

MSNG-2019

6th International conference on materials science and nanotechnology for next generation (MSNG2019)

PROCEEDING BOOK

6thInternational

CONFERENCE ON MATERIALS SCIENCE AND NANOTECHNOLOGY FOR NEXT GENERATION (MSNG2019)

Conference

October 16-18, 2019, Niğde, TURKEY

EDITORIAL BOARD

Prof.Dr.Fahrettin YAKUPHANOGLU	Firat University / Turkey
Assoc.Prof.Dr. Ahmet EKİCİBİL	Çukurova University / Turkey
Dr. Ayşegül DERE	Firat University / TURKEY

COMMITTEES

HONORARY PRESIDENT

Prof.Dr. Kutbeddin DEMİRDAĞ	Rector of Firat University / Turkey
Prof. Dr. Muhsin KAR	Rector of Niğde Ömer Halisdemir University

CONFERENCE PRESIDENT

Prof.Dr.Fahrettin YAKUPHANOGLU	Firat University / Turkey
Assoc. Prof. Dr. Recep ZAN	Niğde Ömer Halisdemir University / Turkey

ORGANIZING COMMITTEE

Ahmet EKİCİBİL	Çukurova University / Turkey
Ali Osman AYAŞ	Adıyaman University / TURKEY
Ayşe SEYHAN	Niğde Ömer Halisdemir University / TURKEY
Ayşegül DERE	Firat University / TURKEY
Bora TİMURKUTLUK	Niğde Ömer Halisdemir University / TURKEY
Canan AKSU CANBAY	Firat University / TURKEY
Faruk KARADAĞ	Çukurova University / TURKEY
Filiz KELEŞ	Niğde Ömer Halisdemir University / TURKEY
İbrahim Karaca	Niğde ömer Halisdemir University / TURKEY
Mehmet Ali OLĞAR	Niğde Ömer Halisdemir University / TURKEY
Mustafa AKYOL	Adana Alparslan Türkeş Science and Technology University / TURKEY
Sevgi DEMİREL	Niğde Ömer Halisdemir University / TURKEY
Yavuz ATASOY	Niğde Ömer Halisdemir University / TURKEY
Yeliz KONUKLU	Niğde Ömer Halisdemir University / TURKEY

SCIENTIFIC COMMITTEE

Abdel Salam Hamdy MAKHLOUF	University of Texas Rio Grande Valley / Unıted States
Abdelkarim MEKKI	King Fahd University of Petroleum Minerals / Saudı Arabıa
Abdullah G. AL-SEHEMI	King Khalid University / Saudı Arabıa
Abdullah YILDIZ	Yıldırım Beyazit University / TURKEY
Abdülmecit TÜRÜT	Medeniyet University / Turkey
Adem TATAROĞLU	Gazi University / Turkey
Adil CANIMOĞLU	Niğde Ömer Halisdemir University / TURKEY
Adnan KAYA	İzmir Katip Çelebi University / TURKEY
Adrian M.T. SILVA	University of Porto / PORTUGAL
Afaf M. BABEER	Jazan University / SAUDI ARABIA
Ahmet EKİCİBİL	Çukurova University / TURKEY
Ahmed A. ALGHAMDI	King Abdulaziz University / SAUDI ARABIA
Ahmad UMAR	Najran University / SAUDI ARABIA
Ahmet ORAL	Middle East Technical University (METU) / TURKEY
Ali COŞKUN,	University of Fribourg / SWITZERLAND
Ali GÜRSEL	International University of Sarajevo / BOSNIA
Ali Osman AYAŞ	Adıyaman University / TURKEY
Ali ÖZER	Cumhuriyet University / TURKEY
Asım SOYLU	Niğde Ömer Halisdemir University / TURKEY
Asmaa HENDI	King Abdulaziz University / SAUDI ARABIA
Atif MUHAMMED	King Saud University / SAUDI ARABIA
Atilla COŞKUN	Muğla Sıtkı Koçman University / TURKEY
Attieh ALGHAMDI	King Abdulaziz University / SAUDI ARABIA
Aziz GENÇ	Bartın University / TURKEY
Bakiye ÇAKIR,	Artvin Çoruh University / TURKEY
Berna BÜLBÜL	Balıkesir University / TURKEY
Birgül YAZICI	Çukurova University / TURKEY
Bora TİMURKUTLUK	Niğde Ömer Halisdemir University / TURKEY
Burhan COŞKUN	Kırklareli University / TURKEY
Byeong-Kwon JU	Korea University / KOREA

Canan Aksu CANBAY,	Fırat University / TURKEY
Canan Aksoy	Karadeniz Technical University / TURKEY
Cahit Tağı ÇELİK	Niğde Ömer Halisdemir University / TURKEY
Cem ÇELEBİ	İzmir Institute of Technology (İYTE) / TURKEY
Christian WENGER	Innov. for High Performance Microelectronics / Germany
Christoph STAMPFER	USA RWTH Aachen University and Forschungszentrum Julich / GERMANY
Chung GWIY-SANG	Ulsan University / KOREA
Darina ARSOVA	Institute of Solid State Physics / BULGARIA
Denis NIKA	Moldova University / MOLDOVA
Dionysios (Dion) DIONYSIOU	University of Cincinnati / USA
D. S. PATIL	North Maharashtra University / INDIA
D. D. ZAITSEV	Moscow State University / RUSSIA
Deniz Sunar ÇERÇİ,	Adıyaman University / TURKEY
Dever NORMAN	Henderson State University / USA
Doğan KAYA	Çukurova University / TURKEY
Ebru ŞENADIM TÜZEMEN	University of Cumhuriyet / TURKEY
Elias STATHATOS	Tecnological-Educational Institute of Patras / GREECE
Emin BACAKSIZ	Karadeniz Technical University / TURKEY
Emin ÇADIRLI	Niğde Ömer Halisdemir University / TURKEY
Emin ÜNAL	Iskenderun Technical University / TURKEY
Emine GÜNERİ	Erciyes University / TURKEY
Emmanuel KOUDOUMAS	Technological Educational Institute of Crete / GREECE
Emmanuel KYMAKIS	Technological Educational Institute of Crete / GREECE
Eren KALAY	Middle East Technical University (METU) / TURKEY
Ertuğrul ŞAHMETLİOĞLU	Kayseri University / TURKEY
Esra ALVEROGLU	Istanbul Technical University / TURKEY
Evangelos VITORATOS	University of Patras / GREECE
Ezgi TAYLAN KOPARAN	Zonguldak Bülent Ecevit University / TURKEY
E. Hassan ALY	Ain Shams University / EGYPT
Farid EL-TANTAWY	Suez Canal University / EGYPT

Faruk KARADAĞ	Çukurova University / TURKEY
Feng Hua ZHANG	Nanyang Technological University / SINGAPORE
Filiz ŞENKAL	Istanbul Technical University / TURKEY
Fumihiko HIROSE	Yamagata University / JAPAN
F. AL-HAZMI	King Abdulaziz University / SAUDI ARABIA
F. M. AMANULLAH	King Saud University / SAUDI ARABIA
Fehiman ÇİNER	Niğde Ömer Halisdemir University / TURKEY
Filiz ŞENKAL	Istanbul Technical University / TURKEY
Gamze BARIM	Adıyaman University / TURKEY
Giorgio SBERVEGLIERI	University of Brescia / ITALY
Gökhan SAVAROĞLU	Osmangazi University / TURKEY
Gökay UĞUR	Gazi University / TURKEY
Grzegorz KARCZEWSKI	Polish Academicy of Sciences / POLAND
Gülfeza KARDAŞ	Cukurova University / TURKEY
Hakan USTA	Abdullah Gül University / TURKEY
Habibe USLU TECİMER	Karabük University (ITU) / TURKEY
Hakan KARAAĞAÇ	İstanbul Technical University (ITU) / TURKEY
Hamad Abdulaziz Hamad ALBRAITHEN	King Saud University / SAUDI ARABIA
Halime ÖMÜR PAKSOY	University of Cukurova / TURKEY
Haluk ŞAFAK	Selçuk University / TURKEY
Hasan ŞAHİN	İzmir Institute of Technology (İYTE) / TURKEY
Hülya Metin GÜBÜR	Mersin University / TURKEY
Hwan Kyu KIM	Korea University / KOREA
H. GHANEM	Fayoum University, Fayoum / EGYPT
Hye-Won SEO	Jeju National University, SOUTH KOREA
İbrahim KARACA	Niğde Ömer Halisdemir University / TURKEY
İbrahim Yasin ERDOĞAN	Bingol University / TURKEY
İlker DOĞAN	The Netherlands Organisation (TNO), NETHERLAND
İsmail POLAT	Karadeniz Technical University / TURKEY
Jingkun XU	Technology Normal University / CHINA
Jongeun RYU	Portugal University of California / USA

José M. KENNY	University of Perugia / ITALY
Juan Carlos Martinez-ANTON	Complutense University of Madrid / SPAIN
Kasım OCAKOĞLU	Tarsus University / TURKEY
Katerina POMONI	University of Patras / GREECE
Khasan S. KARIMOV	GIK Institute / PAKISTAN
Kristina RUSIMOVA	University of Bath / UNITED KINGDOM
Kutsi Savaş ERDURAN	Niğde Ömer Halisdemir University / TURKEY
Lee XINLIANG	Technische Universitat Dresden / GERMANY
Luis BANARES	Universidad Complutense de Madrid / SPAIN
Luisa TORSI	Universita Bari Aldo Moro / ITALY
M. Bülent BAŞOL	Active Layer Parametrics (ALP) Inc., USA
Marco Antonio SCHIAVON	Universidade Federal de São João Del Rei / BRAZIL
Mehmet BAŞOĞLU	Gümüşhane University / TURKEY
Mehmet KABAER	Giresun University / TURKEY
Mehmet PARLAK	Middle East Technical University (METU) / TURKEY
Mehmet Sait BOZGEYİK	Kahramanmaraş Sütçü İmam University / TURKEY
Mehmet ŞENER	Niğde Ömer Halisdemir University / TURKEY
Merih PALANDÖKEN	İzmir Katip Çelebi University / TURKEY
Metin ÖZDEMİR	University of Cukurova / TURKEY
Mikhail I. VASILEVSKIY	University of Minho / PORTUGAL
Mohamed BOUOUDINA	University of Bahrain / KINGDOM OF BAHRAIN
Mohammed Saleh AL-SALIHI	King Saud University / SAUDI ARABIA
Muhammad Hassan SAYYAD	Ghulam Ishaq Khan Institute / PAKISTAN
Muharrem KARAASLAN,	Iskenderun Technical University / TURKEY
Mujdat ÇAĞLAR	Eskişehir Anadolu University / TURKEY
Murat Kaleli	Süleyman Demirel University / TURKEY
Murat SOYLU	Bingöl University / TURKEY
Murat TOMAKİN,	Recep Tayyip Erdoğan University / TURKEY
Mustafa AKYOL	Adana Alparslan Türkeş Science and Technology University / TURKEY
Mustafa ERKOVAN	Sakarya University / TURKEY
Mustafa GENİŞEL	Dicle University / TURKEY

Mustafa GÜNEŞ	Adana Science and Technology University / TURKEY
Nadia ABDEL-AAL	Suez Canal University / EGYPT
Najla M. KHUSAYFAN	King Abdulaziz University / SAUDI ARABIA
Nihal KUŞ	Anadolu University / TURKEY
Niyazi ÖZDEMİR	Fırat University / TURKEY
Nourah AL SENANY	King Abdulaziz University / SAUDI ARABIA
Nouredine SENGOUGA	Université de Biskra / ALGERIA
Nurdan DEMİRCİ SANKIR	TOBB University of Economics and Technology / TURKEY
Nurdoğan CAN	Jazan University / SAUDI ARABIA
Oğuz GÜLSEREN	Bilkent University / TURKEY
Oğuzhan AKGÖL	İskenderun Technical University / TURKEY
Omar A. ALHARTOMY	Tabuk University / SAUDI ARABIA
Orhan YALÇIN	Niğde University / TURKEY
Osman DAYAN	Çanakkale Onsekiz Mart University / TURKEY
Orkun ERSOY,	Hacettepe University
Ömer Faruk YÜKSEL	Selçuk University / TURKEY
Önder METİN	Atatürk University / TURKEY
Panagiotis LIANOS	University of Patras / GREECE
Polycarpos FALARAS	Scientific Research Center / GREECE
Quentin M. RAMASSE	University of Liverpool, UK
Ram K. GUPTA	Pittsburg State University / UNITED STATES
Ramin YOUSEFI	Islamic Azad University / IRAN
Ramazan SOLMAZ	Bingol University / TURKEY
Raşit TURAN	Middle East Technical University / TURKEY
Reem AL-WAFI	King Abdulaziz University / SAUDI ARABIA
Reem M. AL-TUWIRQI	King Abdulaziz University / SAUDI ARABIA
R. H. Al ORAINY	King Abdulaziz University / SAUDI ARABIA
R. O. OCAYA	University of the Free State / SOUTH AFRICA
Roland MAINZ	Helmholtz Zentrum Berlin (HZB), Germany
Saad Hamad BINOMRAN	King Saud Univeristy / SAUDI ARABIA
Safar saaed Saad AL-GHAMDI	King Saud University / SAUDI ARABIA

S. MANSOURI	University of Gabès / TUNUSIA
Saliha ILICAN	Eskişehir Anadolu University / TURKEY
Salem EL-FAIFY	Khalid University / SAUDI ARABIA
Sarani ZAKARIA	Universiti Kebangsaan Malaysia / MALAYSIA
Savaş SÖNMEZOĞLU	Kahramanoğlu Mehmet Bey University / TURKEY
Serap ŞENTÜRK DALGIÇ	Trakya University / TURKEY
Serdar SARIÇİFTÇİ	Johannes Kepler Linz University / TURKEY
Seyfettin ÇAKMAK	Süleyman Demirel University / TURKEY
S. Seyhan TÜKEL	University of Cukurova / TURKEY
Subhash CHAND	National Institute of Technology / INDIA
Şükrü KARATAŞ	Kahramanmaraş Sütçü İmam University / TURKEY
S. MANSOURI	University of Gabès / TUNUSIA
S. WAGEH	Menoufia University / EGYPT
Şakir AYDOĞAN	Atatürk University / TURKEY
Salih YILMAZ	Adana Alparslan Türkeş Science and Technology University / TURKEY
Salim ÇERÇİ	Adıyaman University / TURKEY
Sarani ZAKARIA	Universiti Kebangsaan Malaysia / MALAYSIA
Seda BEYAZ	Balıkesir University / TURKEY
Sefa ERTÜRK	Niğde Ömer Halisdemir University / TURKEY
Selahattin ÇELİK	Niğde Ömer Halisdemir University / TURKEY
Selmin ENER RUŞEN	İstanbul Technical University (ITU) / TURKEY
Serap GÜNEŞ	Yıldız Technical University / TURKEY
Serdar AKSU	APPLE Inc., USA
Serdar ÖNSES	Erciyes University / TURKEY
Serkan TOROS	Niğde Ömer Halisdemir University / TURKEY
Servet TURAN	Eskişehir Technical University / TURKEY
Sezai ALAGÖZ	Cumhuriyet University / TURKEY
Subhash CHAND	National Institute of Technology / INDIA
Şemsettin ALTINDAL	Gazi University / TURKEY
T. M. FARAG,	Al-Azhar University / EGYPT
Tamer ABDALLAH	Ain Shams University / EGYPT

Tayfur KÜÇÜKÖMEROĞLU,	Karadeniz Technical University /TURKEY
Thomas UNOLD,	Helmholtz Zentrum Berlin (HZB) / GERMANY
Tuğrul SENGER	İzmir Institute of Technology (İYTE) / TURKEY
Türker TÜZEMEN,	Cumhuriyet University / TURKEY
Ursel BANGERT	University of Limerick / IRELAND
V. DOROZHKIN,	Kudrinskaja Moscow / RUSSIA
Vasilios Karanikolas,	Patras University / GREECE
Vakkas Bozkurt	Niğde Ömer Halisdemir University
Yashar Azizan - Kalandaragh	Sabalan University of Advanced Technologies, Namin / IRAN
Yasemin ÇAĞLAR	Eskişehir Anadolu University / TURKEY
Yasemin ÇİFTÇİ ÖZTEKİN	Gazi University / TURKEY
Yassine SLIMANI	University of Dammam / SAUDI ARABIA
Young HEE	Sungkyunkwan University / SOUTH KOREA
Yüksel KAPLAN,	Niğde Ömer Halisdemir University / TURKEY
Yusuf Al-TURKI	King Abdulaziz University / SAUDI ARABIA
Yusuf Öner TORAMAN	Niğde Ömer Halisdemir University / TURKEY
Yusuf Selim OCAK,	Dicle University / TURKEY
Zeyad A. ALAHMED	King Saud University / SAUDI ARABIA
Z. LIU	Peking University / CHINA
Zahide BAYER ÖZTÜRK,	HacıBektaşVeli University / TURKEY
Zehra YEĞİNGİL	Çukurova University / TURKEY
V. DOROZHKIN	Kudrinskaja Moscow / RUSSIA
Walid Tawfiq YOUNES	King Saud University / SAUDI ARABIA
Witold Daniel DOBROWOLSKI	Polish Academicy of Sciences / POLAND
Wojtek WLODARSKI	RMIT University / AUSTRALIA
Wolfgang ENSINGER	Technische Universität Darmstadt / GERMANY
W. Aslam FAROOQ	King Saud University / SAUDI ARABIA

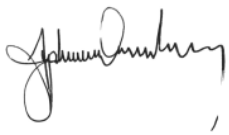
FOREWORD

It is a pleasure for us to offer you Abstracts Book for the 6th international conference on Materials Science and Nanotechnology for Next Generation; MSNG2019. Our goal was to create a a scientific platform that introduces the newest results on internationally recognized experts to local students and colleagues and simultaneously displays relevant Turkish achievements to the world. The positive feedback of the community encouraged us to proceed and transform a single event into a conference series. Now, MSNG2019 is honored by the presence of over 100 colleagues from various countries. We stayed true to the original MSNG2019 concept and accepted contributions from all fields of materials science and technology to promote multidisciplinary discussions. The focal points of the conference emerged spontaneously from the submitted abstracts: energy applications, advanced materials, electronic and optoelectronic devices. Further fields of interest include e.g. new advanced and functional materials, advanced-functional composites, biomaterials, smart materials, dielectric materials, optical materials, magnetic materials, organic semiconductors, inorganic semiconductors, electronic materials, graphene, and more. We can offer free publishing of all peer-reviewed proceedings in international journals Materials Science-Poland, Journal of Nanoelectronics and Optoelectronics, Organo Optoelectronics, Journal of Materials and Electronic Devices and provide the participants with all the commodities of a world – class conference.

Therefore, we hope that getting first-hand access to so many new results, establishing new connections and enjoying the Niğde, Turkey ambience will make you feel that your resources were spent well in MSNG2019.

Our warmest thanks go to all invited speakers, authors, and contributors of MSNG2019 for accepting our invitation, visiting Niğde and using MSNG2019 as a medium for communicating your research results.

We hope that you will enjoy the conference and look forward to meeting you again in one of the forthcoming MSNG2020 event.



Prof. Dr. Fahrettin YAKUPHANOĞLU

Conference Chair

SPONSORS


NİĞDE ÖMER HALİSDEMİR
1992
ÜNİVERSİTESİ


FIRAT ÜNİVERSİTESİ
1975


FOTONiKA
YARI İLETKEN TEKNOLOJİLERİ


ERDEM LAB
LABORATUVAR CİHAZLARI - KİMYASAL ve
SARF MALZEMELERİ


FY
FYTRONiX


Nanomat
nano-engineering


bakkalbaşıoğlu


büronews
ofis mobilyaları


NİĞDE
GAZOZU

INVITED SPEAKERS TALKS

6th International Conference on Materials Science and Nanotechnology For Next Generation (MSNG2019)
October 16-18, 2019, Niğde, TURKEY (ORAL FULL TEXT)

Graphdiyne supported Metal Clusters and Nanoparticles by Multiscale Simulations

S. SENTURK DALGIC
Department of Physics, Faculty of Science, Trakya University, Edirne 22030, Turkey

In this work, the stability and morphological behaviors of atomic clusters and nanoparticles (NPs) on 2D graphdiyne and graphene have performed by multiscale simulations. The interaction energies of the supported metal clusters on Graphdiyne and graphene have calculated and compared with each other and those obtained by other supported surfaces. The difference between the computed energies derived from two methods for the supported metal clusters is getting higher amount by the number of atoms in clusters. The substrate effect on the structure of nanoparticles has defined by binding energies and coordination number analysis as a function of numbers of atoms in the supported particles. This work may present a new route to investigate the GDY-metal nanocomposites in developing renewable energy technologies.

Keywords: Graphdiyne, Clusters, Nanoparticles

Submission date:
Acceptance Date:

Corresponding authors: serapd@trakya.edu.tr dserap@yahoo.com

1. Introduction

Graphdiyne (GDY) is one of the two-dimensional carbon allotropes with a one atom thick layer of carbon sheet having the same symmetry as graphene [1]. In recent years, considerable efforts have been paid attention to the development of the well-defined GDY properties for electrode-materials, catalysts, hydrogen storage material, and cancer drug delivery platforms [2,3]. GDY is a member of the Graphynes family, which is a series of new two dimensional (2D) carbon materials formed by a combination of carbon atoms according to a specific periodic rule [1]. Graphynes is a generic name given to a class of structures, which are graphyne, graphdiyne, graphyne-n. It was noted by experiments that graphynes have completely different properties and structures when compared with other carbon allotropes of graphene and carbon nanotubes (CNTs). Due to the sp-hybridized carbon atoms, graphynes are well-distributed pore structures in contrast to the non-porous structure of graphene. Based on the structural difference, graphynes are a good candidate for the potential applications in catalysis, gas separation, and energy related-fields [4-6]. The first graphynes structure model was proposed by Baughman et al. in 1987 [7]. However, the first graphyne film, defined as γ-graphdiyne (γ-GDY), was not prepared until 2010. [1]. Graphdiyne was synthesized and found to be a semiconductor [8-10]. To date, among all graphyne studies, most of them are related to GDY. The basic properties of GDY, such as stability, electrical, mechanical, and spectroscopic properties, have investigated experimentally and theoretical methods [1-7].

On the other, Alonso and co-workers have investigated the adsorption properties of Pd clusters and their growth on GDY by DFT calculations [8]. By taking consideration of the previous reports, we have investigated the growth of metal clusters and nanoparticles on graphdiyne by multiscale simulations.

To date, the molecular dynamics (MD) investigations on the graphdiyne supported atomic clusters ordering, and stability has rarely reported. In this work, we first obtain the stability of graphdiyne supported small metal clusters by MD simulations using DLPOLY code [9].

Here, the new computational methodology of the supported metal clusters or nanoparticles is presented.

The structural and thermal stability of 2D Graphdiyne supported metal clusters/nanoparticles have investigated by multiscale simulations, which is starting from optimized structures of clusters using first principle simulations and continue with classical MD simulations.

2. Materials and Method

In this work, both the first principle calculations and classical MD simulations of clusters have established by the Gaussian series of program package [10,11] and DLPOLY simulation code [9]. First, the best chemical ordering structures of isolated clusters were optimized by the Gaussian program package using the U3BLYP method and CC-pVTZ basis set [11]. The optimized atomic structures of clusters were initially used for both DFT calculations and classical MD simulations of supported and unsupported small clusters. In order to construct as a hybrid composite of metal clusters, a monolayer of Graphdiyne and alternate substrate of graphene were used. Here, we have focused on the simulation methodology of the optimized small metal clusters supported on graphdiyne. In MD simulations, the many-body potentials of Sutton-Chen (SC) [12-13] was used for the modeling of interatomic interactions in metal clusters or nanoparticles. The Q-SC many-body potential parameters were taken from [13].

In the SC framework, the total energy for a system can be written as an equation (1) given by

$$U = \sum_i U = \sum_i \varepsilon \left[\frac{1}{2} \sum_{j \neq i} V(R_{ij}) - c\sqrt{\rho_i} \right] \quad \textbf{(1)}$$

where V (R_{ij}) is a repulsive pair interaction function between the i and j atomic cores defined by

$$V(R_{ij}) = \left(\frac{a}{R_{ij}} \right)^n . \quad (2)$$

The local electron density function of atom i defined by

$$\rho_i = \sum_{j \neq i} \left(\frac{a}{R_{ij}} \right)^n . \quad (3)$$

In above Eqs (1-3), the R_{ij} is the distance between atoms i and j; ϵ sets the overall energy scale parameter, an a and c are a length and dimensionless parameter scaling the attractive terms, respectively; n and m are integer parameters such that n>m.

QSC parameters for pure elements used in our calculations are given in Table 1.

Table 1: Q-SC Potential parameters of Pd used in MD simulations for pure metals.

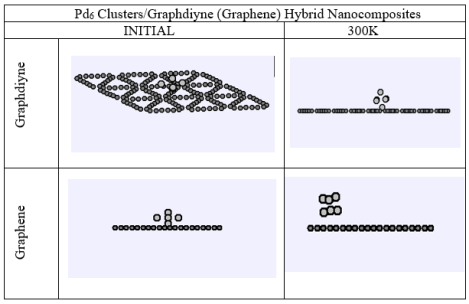
Metal	*n*	*m*	*ϵ* (meV)	c	(A)
Pd	12	6	3.2864	148.205	3.8813

For modeling of the van der Waals type interactions between the metal atoms and ultra-thin 2D static monolayers, the Lennard-Jones (LJ) potentials were considered. The LJ potential parameters were obtained from the values for pure metals given in the study of Neek-Amal [14].

The hybrid nanocomposites of metal/graphdiyne(graphene) were simulated by NVT canonical ensemble and Nose-Hoover thermostat. The time step was that 1fs is used in all simulations. The Verlet-leapfrog algorithm was applied for the integral equation of motions. That nanoparticle was heated from 25K up to high temperatures with a temperature increment of 25K. In order to understand the stability of supported nanoparticles, atomic structure analysis methods were used by the OVITO package [15]. The radial distribution function of (RDF) of supported particles was also obtained from OVITO and used in the coordination number calculations.

3. Results and discussion:

In this work, first we have calculated the optimized geometric structures of Pd_6 clusters using the



Gaussian program package [10,11]. We have also created the graphdiyne and graphene monolayers with 198 and 200 carbon atoms, respectively. The stability of icosahedral Pd_{60}, Pd_{300} clusters supported graphdiyne has presented here. The initial structures for the MD simulations of 3D Pd_6 clusters supported on graphdiyne are shown in Fig1 by the snapshots from GUI editor of DLPOLY. The morphological changes of the supported metal clusters under the heating process are given in the same figure by the snapshots taken from GUI at 300K.

Fig.1: The initial and simulated structures of supported Pd_6 metal clusters

The corresponding g(r) radial distribution functions of metal-metal and metal-substrate at 300K is also shown in Fig. 2.

It has been clear from Fig 1 that 3D Pd_6 cluster supported graphdiyne is maintained its 3D structure, whereas graphene supported Pd_6 cluster has lost its 3D structure and transformed to 2D layer structure. The 3D diffusion coefficients of graphene supported Pd atoms are 10.442 (10^{-9} m^2/sn) while for the graphdiyne supported one is zero. To understand the nature of the interactions, radial distribution function of graphene- Pd atoms give the information about it. The rdf function of C-Pd is given in Fig.2.

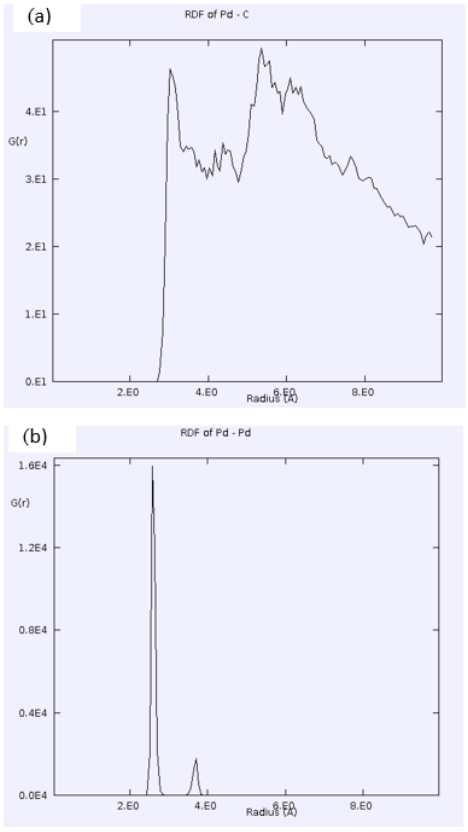
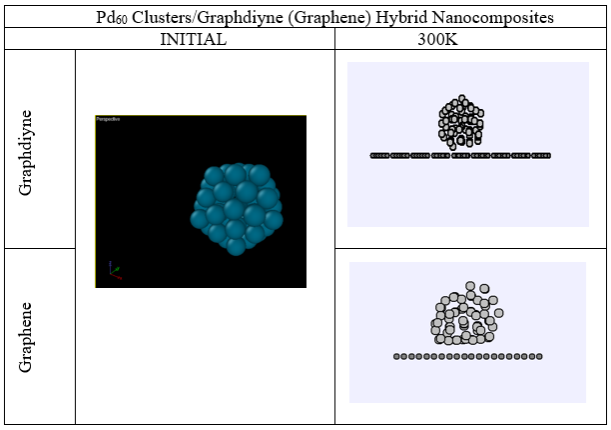


Fig.2: RDFs of Graphene supported Pd_6 clusters.

.

As seen in Fig. 2, for the supported Pd_6 clusters the two peak is observed in RDF of Pd-C interactions. This gives the Pd atoms has two-layer structure on the graphene monolayer. The morphological and structural deformations in graphdiyne supported icosahedral Pd_{60} (ICO Pd_{60}) clusters are given in Fig.3 by comparison with that of graphene supported.

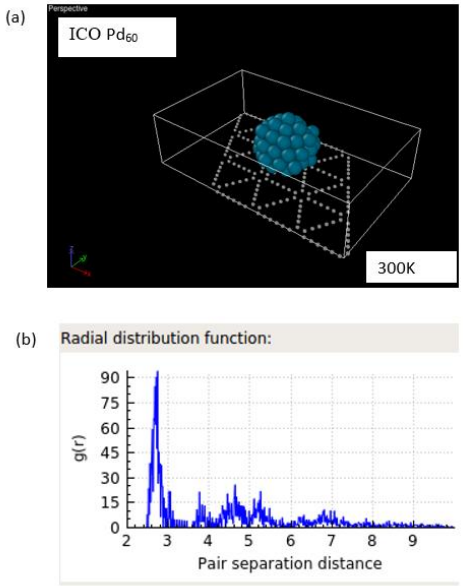
The changes in the local atomic ordering is one of the important property which can be defined by different analysis methods such as radial distribution function g(r), coordination number analysis, bond angle analysis (BAA) or common neighbor analysis (CNA).



The morphology and rdf function of ICO Pd_{60} clusters supported on graphdiyne are shown in Fig. 4

Fig.3: The snapshots from front view of the supported ICO Pd_{60} clusters

It is clear from Fig.3 that graphdiyne supported ICO Pd_{60} clusters are preserved their geometric structure



whatever the graphene supported one has lost and appeared in forming as a new cluster geometry.

Fig.4: The snapshots from OVITO (a) a perspective view and (b) pair distribution function of the supported ICO Pd_{60} clusters

The coordination number of metal clusters/nanoparticles play a crucial role on their catalytic properties. To explore the substrate effect on the structure of metal nanoparticles, the average coordination number were computed from the first peak and the first minimum values of rdfs. In Fig. 5, the changes in the morphology of the graphdiyne supported icosahedral Pd_{300} clusters at 300K. In Fig.5, it is plotted the average coordination number analysis of Pd_{300} clusters.

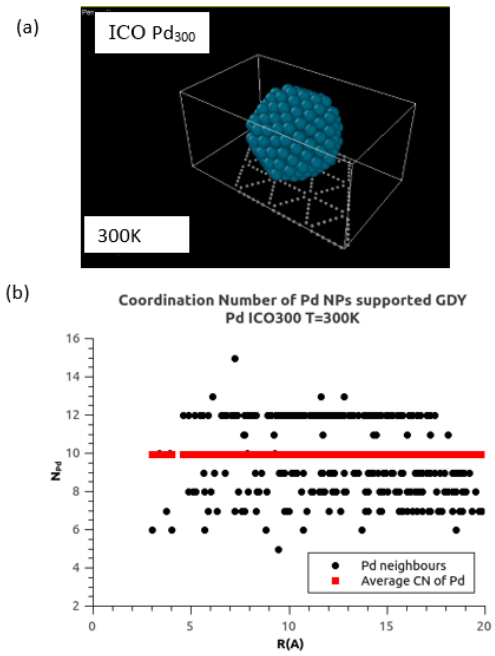


Fig.5: The snapshots from OVITO (a) a perspective view (b) average coordination number analysis of the supported ICO Pd_{300} clusters

It has been shown in Fig.5 that the average coordination number of ICO Pd300 clusters is 9.9 and is smaller than the calculated value of 10.2 for ICO Pd860 clusters and greater than that of 8.1666 for ICO Pd60 at 300K.

Conclusions

It was demonstrated that the metal clusters were optimized by first-principle calculations and then supported on 2D graphdiyne were simulated by classical molecular dynamics (MD) method. The structural stability and morphologies of clusters were presented. The big clusters, namely nanoparticles, supported on graphdiyne, were studied with MD simulations directly. The average coordination number analysis was adopted to supported metal clusters and nanoparticles. It has found that both the calculated cohesive energies and average coordination numbers from clusters to nanoparticles are in good agreement with previously reported values. This computational procedure, namely multiscale simulations, is an efficient method for the supported metal clusters and nanoparticles. It can apply to investigate the stability of different types of supported/unsupported clusters. This work will progress on this line and reported shortly.

References:

[1] X. Gao, H. Liu, D. Wang and J. Zhang, Chem. Soc. Rev. 48 (2019), 908-936.

[2] N. Wang, J. He, K. Wang, Y. Zhao, T. Jiu, C. Huang, and Y. Li, Adv. Mater., 1803202 (2019).

[3] K. Srinivasu, K. S. Ghosh, J. Phys. Chem. C 116, 5951−5956 (2012).

[4] H. Ren, H. Shao, L. Zhang, D. Guo, Q. Jin, R. Yu, L. Wang, Y. Li, Y. Wang, H. Zhao, D. Wang, Adv. Mater., 5 (2015) 1500296.

[5] S. W. Cranford, M. J. Buehler, Nanoscale, 4 (2012) 4587-4593.

[6] H. Zhang, Y. Xia, H. Bu, X. Wang, M. Zhang, Y. Luo, M. Zhao, J. Appl. Phys., 113 (2013) 044309

[7] R. H. Baughman, H. Eckhardt, M. Kertesz, J. Chem. Phys., 87 (1987) 6687-6699.

[8] A. Seif, M. J. Lopez, A. Granja-DelRio, K. Azizi, J. A. Alonso, Phys. Chem. Chem. Phys, 17 (2017) 19094-19102.

[9] DL_POLY: a molecular dynamics simulation package was written by W. Smith, T.R. Forester, and I.T. Todorov obtained from the websitehttp://www.ccp5.ac.uk/DL_POLY

[10] Gaussian 16, M. J. Frisch, G. W. Trucks, H. B. Schlegel, G. E. Scuseria, M. A. Robb, J. R. Cheeseman,

G. Scalmani, V. Barone, G. A. Petersson, H. Nakatsuji, X. Li, M. Caricato, A. V. Marenich, J. Bloino, B. G. Janesko, R. Gomperts, B. Mennucci, H. P. Hratchian, J. V. Ortiz, A. F. Izmaylov, J. L. Sonnenberg, D. Williams-Young, F. Ding, F. Lipparini, F. Egidi, J. Goings, B. Peng, A. Petrone, T. Henderson, D. Ranasinghe, V. G. Zakrzewski, J. Gao, N. Rega, G. Zheng, W. Liang, M. Hada, M. Ehara, K. Toyota, R. Fukuda, J. Hasegawa, M. Ishida, T. Nakajima, Y. Honda, O. Kitao, H. Nakai, T. Vreven, K. Throssell, J. A. Montgomery, Jr., J. E. Peralta, F. Ogliaro, M. J. Bearpark, J. J. Heyd, E. N. Brothers, K. N. Kudin, V. N. Staroverov, T. A. Keith, R. Kobayashi, J. Normand, K. Raghavachari, A. P. Rendell, J. C. Burant, S. S. Iyengar, J. Tomasi, M. Cossi, J. M. Millam, M. Klene, C. Adamo, R. Cammi, J. W. Ochterski, R. L. Martin, K. Morokuma, O. Farkas, J. B. Foresman, and D. J. Fox, Gaussian, Inc., Wallingford CT, 2016.

[11] S. Senturk Dalgic, S. Dalgic, unpublished results

[12] A. P. Sutton, J. Chen, Philos. Mag. Lett., 61 (1990) 139

[13] Y. Kimura, Y. Qi, T. Cagin and W. Goddard III, MRS Symp. Ser., 554 (1999) 43.

[14] M. Neek-Amal, R. Asgari, and M. R. Rahimi Tabar Nanotechnology,20 (2009) 135602-135610.

[15] OVITO: A. Stukowski, Modelling Simul. Mater. Sci. Eng. 18 (2010).015012

ORAL PRESENTATIONS

6th International Conference on Materials Science and Nanotechnology For Next Generation (MSNG2019)
October 16-18, 2019, Niğde, TURKEY (ORAL FULL TEXT)

The Role of Scintillators and Silicon Photomultiplier Tubes in the Development of Detector Technologies

Deniz SUNAR CERCI*, Salim CERCI*

* Department of Physics, Faculty of Arts and Sciences, Adıyaman University, Adıyaman, TURKEY

Single-photon sensitive solid-state detectors (i.e. silicon photomultipliers (SiPMs)) are well developing technology for detection of visible photons. In recent years, a massive improvement has been made to develop the performance of SiPM. Silicon photomultipliers have become popular for various applications. Nowadays, SiPMs are widely used in the high energy and particle physics experiments, nuclear experiments, spectroscopy as well as medical physics applications. One of the main advantages of SiPMs is the possibility to significantly increase the detector granularity with respect to standard photomultiplier tubes.

Scintillator, another widely used detector device, is a kind of material that can provide detectable photons in the visible part of the light spectrum, following the passage of a photon or a charged particle. Scintillators are still under the great of interest for having the characteristics such as the detection efficiency and the precise determination of the position, energy and time of particles.

In this talk, characteristics of scintillators and silicon photomultiplier tubes as well as their roles and applications in various sciences are presented.

Keywords: Scintillators, Silicon Photomultiplier Tubes, Detector Technologies.

Corresponding author: deniz.sunar.cerci@cern.ch

1. Introduction

A Zinc Sulfide (ZnS) screen can be considered as the first scintillation detector which was built by Sir William Crookes in 1903. This detector could be able to flashing light that can be observed by eye through a microscope. This technique had a significant boost after the invention of photomultiplier tube (PMT) which can convert optical light signal into an electrical signal, then amplifies this signal to a measureable amount by emission of secondary particles (i.e. electrons). Due to having features such as low noise, high gain and fast response, PMTs become a traditional tool to be used.

Single-photon sensitive solid-state detectors (i.e. silicon photomultipliers (SiPMs) or multi pixel counter (MPPC)) now offer alternatives to PMTs which are the higher photon detection efficiency, compactness, insensitivity to ionizing radiation, easy usage, lower operating voltage and lower cost [1]. By providing advanced and new properties, SiPMs show a significant potential to be replaced with PMTs in some of the fields such as medical imaging, high energy and particle physics, spectroscopy, biophotonics and light detection and ranging (LIDAR) [2, 3] applications. SiPMs are essentially made of many miniaturized avalanche photodiodes that are connected in parallel [4]. The combination of serially connected avalanche photodiodes and quenching resistors are called as microcell of the SiPM.

Special tools are needed for visualizing and detecting the ionizing radiations that are in the form of gamma-rays, X-rays, alpha or beta particles having an energy from eV to MeV. Those tools are named radiation detectors which have two kinds of solid materials. First one is the ***scintillator*** which converts the energy of the ionizing radiation to a large number of photons with low energy. The second one known as storage phosphors or dosimeter materials.

In this paper the basic properties of scintillators and silicon photomultiplier tubes as well as their roles and applications in various sciences are presented.

2. Basic principles of scintillators

Scintillators, due to its photographic film measurement ability, can be considered as one of the oldest radiation detectors. A sketch of a typical scintillation detector is shown in Figure 1.

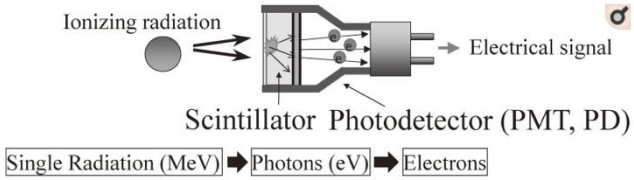


***Figure 1**. A typical scintillator detector [5].*

The light pulse intensity released by a scintillator is proportional to the energy of the absorbed radiation which can be obtained by measuring the height of pulses.
The **size** and **thickness** are the important properties that can affect the *detection efficiency* and *selection sensitivity*. Though, a thin scintillator may be a perfect choice of low energy gamma rays and high energy charged particle, i.e. beta particle. The crystal scintillators are sensitive to low energy X-rays but are insensitive to the radiation of high energy background.
The *timing resolution*, another important parameter for a scintillator, is mainly proportional to the number of photons of the fast component that can be detected and converted to the electrical signal.
In order to have a high detection efficiency the material forming the scintillator should have a high atomic number and high density. For a good scintillator, the refraction index should be in the order of glass index (1.5), wavelength of scintillation needs to be similar to the maximum sensitivity of PMT.
All of these features may influence the energy resolution that is defined as the ability of the scintillator determining the incident radiation energy. High resolution is needed to distinguish various particles at different energies.
In Figure 2, absolute photon yield obtained from various scintillators is shown as a function of the band gap. It can be clearly seen that the high scintillation yield is obtained from the low band gap materials. The material with a band gap of 3 eV gives the maximum light yield ~140 photons/MeV.

*** Inorganic scintillators:** This type of scintillators, including sodium iodide (NaI), lithium iodide (LiI), cesium iodide (CsI), and zinc sulfide (ZnS), are usually utilized in positron emission tomography (PET). Although the scintillation in inorganic scintillators is slower than the organic ones, they show high efficiency in the detection of gamma rays and give high counting rates. A typical pulse decay time is ~10^{-6} sec. The energy band structure in a typical inorganic crystal is shown in Figure 3. A photon can excite an electron from valence band to the conduction band by losing its energy via a photoelectric effect or a Compton effect.

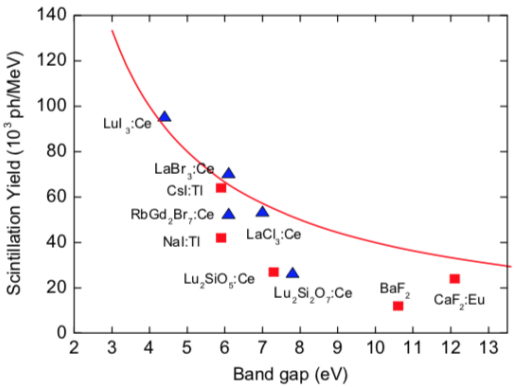


***Figure 2**. Absolute photon yield obtained from various scintillators [6].*

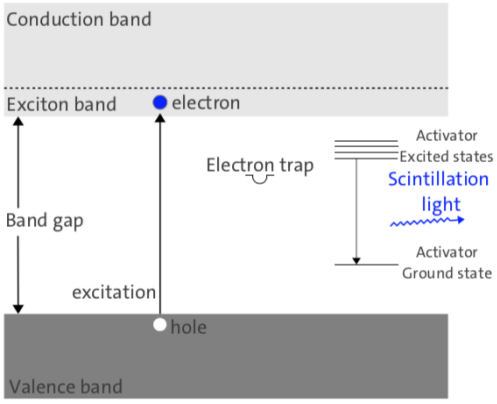


***Figure 3**. The energy band structure in a typical inorganic crystal [7].*

*** Organic scintillators:** This type of scintillator is made of either liquid or solid chemical substances. High response and low light output are the main characteristics

of such scintillators. They are quite different from the inorganic scintillators due to the fluorescence mechanism arising from transitions in the energy levels of a single molecule that is weakly bounded [8].

3. Characteristics of SiPMs

An image of a typical SiPM surface with an array of hundreds or thousands of integrated *single-photon avalanche diodes* (SPADs), named as *microcells* is shown in Figure 4. All microcells are connected in parallel to one common anode and one common cathode output. Interaction of single photon occurs via photoelectric effect resulting with the generation of an electron-hole pair. The final signal of SiPM is the

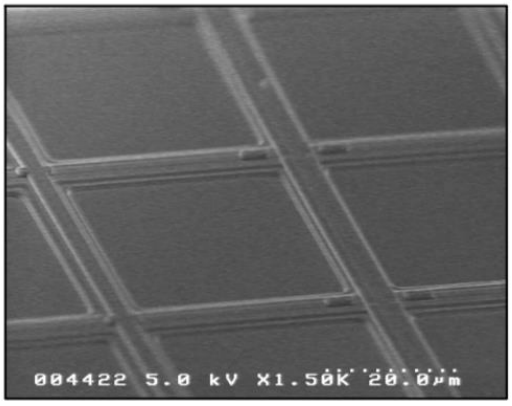


Figure 4*. An image of the SiPM surface with the microcell structure [9].*

superposition of all signals obtained from microcells.
A recent study in Ref. [10] was performed with different SiPMs in order to test the characterization and discrimination abilities of SiPMs from neutrons to gamma ray as well as their timing features. Properties such as easier scalability, the microcell (pixel) size and the overall active area dimension (between less than 1 mm^2 and 100 mm^2) have provided a significant improvement and a noticeable development on SiPM performance [11]. Since PMTs cannot operate properly under the strong magnetic field environment (for instance in PET or in MRI), SiPMs become more attractive to use in such situations. Additionally, SiPMs can achieve to high gain values event with the very low voltages and the noise is almost at the level of single photon. The characteristic features comparison of PMT to SiPMs are given in Table 1.

In order to make development on SiPMs, parameters like breakdown voltage, over voltage, gain, photon detection efficiency, dark count rate (primary noise), optical cross talk, afterpulsing and temperature dependency need to be well understood. Diode structures as either p-on-n or n-on-p type are also crucial to have a better efficiency. The p-on-n structure gives the best sensitivity to shorter wavelengths whereas n-on-p for the longer wavelengths.

Table 1*. Features comparison of PMT to SiPMs.*

	PMT	SiPMs
Quantum Efficiency	25% to 40%	Up to 80%
Single photon resolution	✓	✓
Operation voltage	1 – 3 kV	20 – 40 V
Gain	10^4 - 10^9	10^5 - 10^7
Temperature dependence	Low	Low
Robustness	-	✓
No damage in bright light	-	✓
Insensitivity to magnetic field	-	✓
Miniaturization	-	✓
Production costs	Medium	Low

3. Applications of scintillators and SiPMs

According to the light detection, the applications of SiPMs can be separated in three parts; (a) detection of single photon, (b) detection of multi-photon, (c) high photon time density. Nowadays, scintillation detectors (gamma ray, X-ray, charged and neutral particles detectors) are widely used for the radiation detectors.
Scintillation detectors are also commonly utilized in particle and nuclear physics experiments in order to detect the particles from the processes occurring in atomic nuclei. Large Hadron Collider at the European Centre for Nuclear Research (CERN) in Geneva is a well-known example for the application of scintillators. SiPMs are especially used in the calorimeters to increase the detector granularity. In addition, such calorimeters require magnetic field insensitive tools like SiPMs. Since SiPMs are sensible to voltage changes and temperature, they are also utilized for calibrating and monitoring the gain of devices. Those properties as well as the good energy resolution make SiPMs to get attention to be used in radiation detection and gamma ray spectroscopy.
Among the many fields of applications, SiPMs have strong impact on nuclear medicine which deals with the diagnosis and treatment of patients with ionizing radiation. Positron emission tomography (PET) and computed tomography (CT) machines are utilized in hospitals for diagnosis of cancer lesions. Due to good signal-to-background ratio and high speed properties, SiPMs are particularly important for PET and CT. In addition to those, proton therapy is recently used in various health centers to cure cancer patients more

effectively. Each diagnostic method is based on different scintillator and though different material and detector design need to be taken into account.

Due to its small size, long durability and high sensitivity, SiPMs are also used in military applications to measure radiation as well as to develop radiation protection technology.

An overview about the status and perspectives of solid state as well as the new generation photodetectors is recently published in Ref. [12, 13].

4. Conclusion

This paper is an attempt to give an overview and clearly define the parameters required to describe the performance of scintillators and silicon photomultipliers.

The silicon photomultiplier (SiPM), being a solid-state device, has a broad range of applications from industry to fundamental physics experiments. Given the many new ideas for future applications, SiPMs will certainly continue to expand. The methods of characterization, from which concise specifications can be extracted, will become more and more important. Thanks to the developments and success in the last decades, SiPMs become more interesting for larger markets. However, there are still improvements needed particularly on the electrical behavior and performance parameters. Further studies will undoubtedly continue to meet the challenges of new generation and smart designs.

5. Acknowledgement

The authors would like to acknowledge the Adıyaman University Scientific Activity Foundation for the financial support. The authors also would like to thank the Organisers of the MSNG-2019 Prof. Dr. F. Yakuphanoglu, Assoc. Prof. Dr. A. Ekicibil and Assoc. Prof. Dr. Recep Zan for the nice conference organisation.

References:

[1] RENKER, D., "Geiger-mode avalanche photodiodes, history, properties and problems", Nucl. Instr. and Meth. A vol. 567, pp. 48-5, (2006).

[2] SON, K.T., LEE, C.C., "Multiple-Target Laser Range finding Receiver Using a Silicon Photomultiplier Array". IEEE Trans. Instrum. Meas., 59, 3005–3011, (2010)

[3] RIU, J., SICARD, M.; ROYO, S., COMERON, A. "Silicon photomultiplier detector for atmospheric lidar applications", Opt. Lett. 2012, 37, 1229–1231.

[4] BUZHAN, P. et al., "Silicon photomultiplier and its possible applications", Nucl. Instr. and Meth. A vol. 504, no. 1-3, pp. 48-52, (2003).

[5] YANAGIDA, T., 2018. "Inorganic scintillating materials and scintillation detectors", Proceedings of the Japan Academy. Series B, Physical and biological sciences vol. 94,2 (2018): 75-97. doi:10.2183/pjab.94.007

[6] LECOQ, P., "Development of New Scintillators for Medical Applications", Nuclear Instruments and Methods in Physics Research A 809 p. 130-139, (2016).

[7] XU, C. "Study of the Silicon Photomultipliers and Their Applications in Positron Emission Tomography", Dissertation, Universitat Hamburg and DESY, (2014).

[8] KNOLL, G.F., "Radiation Detection and Measurement No: 28938 3rd edition (Chapters 16 to 18), John Wiley & Sons, (1999).

[9] LLC, "Semiconductor Components Industries", "Introduction to the Silicon Photomultiplier (SiPM)", AND9770/D, (2018).

[10] WONDERS, M.A., CHICHESTER D.L., FLASKA, M., "Characterization of New-Generation Silicon Photomultipliers for Nuclear Security Applications", EPJ Web of Conferences 170, 07015 (2018).

[11] ACERBI, F., PATERNOSTER, G., CAPASSO, M., MARCANTE, M., MAZZI A., REGAZZONI, V., ZORZI N., and GOLA, A., "Silicon Photomultipliers: Technology Optimizations for Ultraviolet, Visible and Near-Infrared Range", Instruments, 3(1), 15 (2019).

[12] VINOGRADOV, S., POPOVA, E., "Status and perspectives of solid state photon detectors", Nuclear Inst. and Methods in Physics Research, A Article in press (2019)

[13] ACERBI, F., GUNDACKER, S., "Understanding and simulating SiPMs", Nuclear Inst. and Methods in Physics Research, A 926 (2019) 16-35. (2019)

6th International Conference on Materials Science and Nanotechnology For Next Generation (MSNG2019)
October 16-18, 2019, Niğde, TURKEY (ORAL FULL TEXT)

Preparation of Boron Mineral Based Phase Change Materials Composites for Thermal Energy Storage

Abdul Malik TURAN[a],, Yeliz KONUKLU[a,b*]

[a]Nigde Ömer Halisdemir University, Department of Chemistry, 51240, Nigde, Turkey

[b]Nigde Ömer Halisdemir University, Nanotechnology Application and Research Center, 51240, Nigde,Turkey

Thermal energy storage in the Phase Changing Materials (PCM) is used to increase the efficiency of heating and cooling applications. In this study, boron mineral(colemanite) based PCM composites were fabricated using direct impregnation method. Lauric acid and decanoic acid was used as supporting material and colemanite was used as composite matrix. Chemical, thermal, and morphological characterization was carried out on the produced composites with Fourier transform infrared (FTIR), Differential scanning calorimetry (DSC) and Scanning electron microscopy (SEM) respectively.It was determined that the produced composites had an energy storage capacity of 34.65 J / g and can be used as energy storage materials in thermal energy storage applications.

Keywords: Phase change material, thermal energy storage, borone, colemanite, composite

Corresponding author: ykonuklu@ohu.edu.

1. Introduction

PCMs are latent heat storage materials which store or release thermal energy during phase change.

Preperation of PCM composites with different supporting materials are one of the important solutions to prevent the leakage of PCMs in thermal energy storage applications. It is reported that different materials can be used as supporting material. For example; Lauric acid composites was prepared using different supporting materials such as; expanded perlite [1], silicon dioxide [2], activated carbon [3], diatomite [4], graphene nanoplates [5]. Furthermore; decanoic acid composites were prepared with different supporting materials such as; halloysite nanotube [6], expanded perlite [7].

Boron is one of the important natural raw material with significant reserves in Turkey. Boron minerals are natural minerals that contain different amounts of boron oxide. Tincal($Na_2B_4O_7.10H_2O$), Colemanite($Ca_2B_6O_{11}.5H_2O$ and Ulexite ($NaCaB_5O_9.8H_2O$) are the most important boron minerals in our country. In this study, boron mineral(colemanite) based PCM composites were prepared with direct impregnation method and characterized.

2. Experimental details

In this work colemanite ($Ca_2B_6O_11.5H_2O$) (Figure 1) was used as the supporting material and lauric acid and decanoic acid as phase change material. In order to obtain 4 composites; 2 recipe and 2 different preparation method was used. The content of the composites is presented in Table 1.

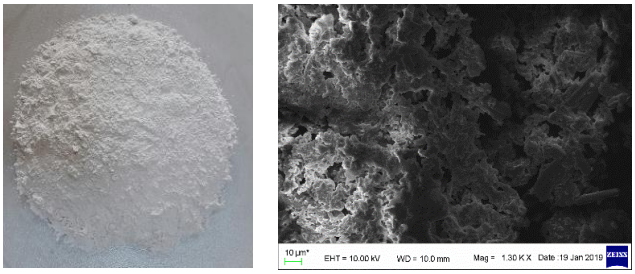


***Figure 1**. Photos of colemanite at a) macro level b)SEM*

Table 1. The contents of the PCM composites

Sample	PCM-(g)	Colemanite(g)	Pretreatment
MK1	LA- 1	9	-
MK4	LA- 2	8	+
MK9	DA- 1	9	-
MK8	DA- 2	8	+

The pretreatment was carried out by heating the colemanite in the high-temperature furnace for one hour.

Colemanite based composites were analyzed for their morphology, chemical composition, thermal and leakage properties using different methods including SEM, FTIR, DSC.

3. Results and discussion

The composites produced in this study as presented in Fig 2-5 have a powder structure similar to the structure of colemanite in room conditions.



Fig. 2. LA, colemanite and MK1



Fig. 3. LA, colemanite (600ºC) and MK4

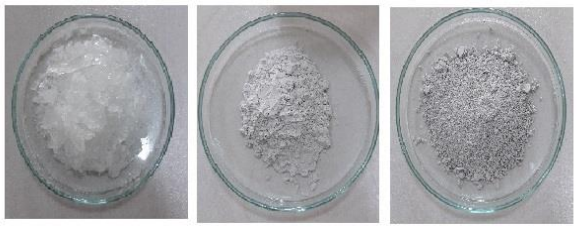


Fig. 4. DA, colemanite (600ºC) and MK8



Fig. 5. DA, colemanite and MK9

The thermal properties of PCMs and colemanite/PCM composites was determined with DSC analysis. All results were summarized in Table 2 and the DSC curves of MK4 presented in Fig.6.

Table 2. DSC analysis of LA, DA and composites

Sample	Tom (◦C)	Hm (J/g)	Toc (◦C)	Hc (J/g)
LA[8]	43.66	196.61	40.98	143.66
MK1	60.27	14.19	57.09	-14.32
MK4	42.07	34.61	39.29	-32.14
DA	30.15	164.64	26.77	−172.14
MK8	29.53	21.80	25.34	-24.38
MK9	27.83	6.37	22.26	8.24

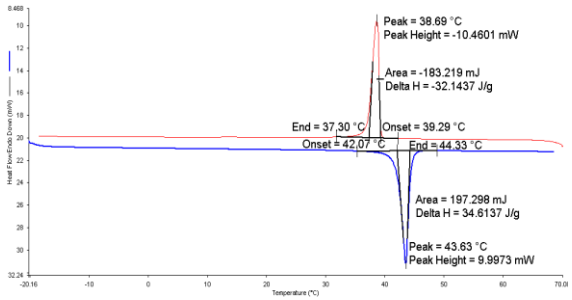
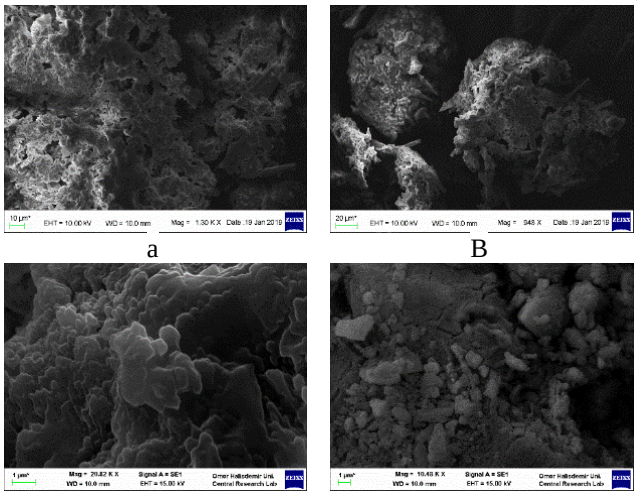


Fig.6. DSC graph of MK4

According to the DSC analysis results the absorption of LA higher than DA to colemanite in prepared composites. Furthermore; PCM absorption of colemanite increased by pretreatment of colemanite at 600ºC. The maximum latent heat storage capacity was obtained with MK4. Melting and freezing point and latent heat storage capacity of MK4 were determined 42.07-39.29 ºC and l 34.6 and -32.14 J / g respectively.

In order to determine the structural properties of MK4, SEM analysis was performed and compared with heated colemanite. The results are presented in Fig.7.



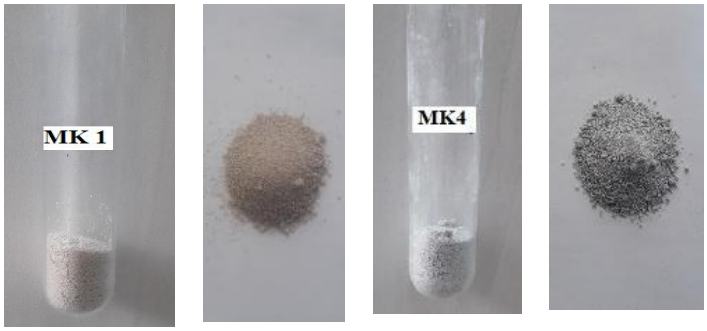
a B

c D

Fig.7. SEM analysis of (a-b) colemanite(600ºC), (c-d) MK4

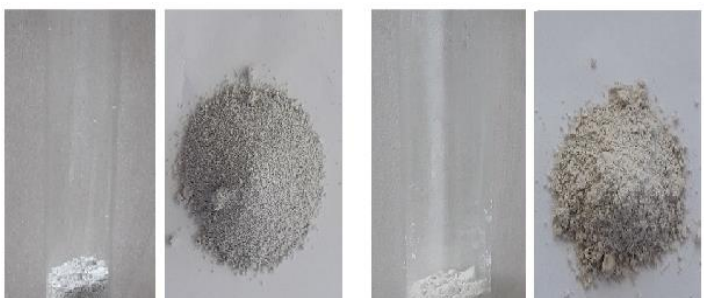
As it is clearly seen from the SEM analysis, structural changes were observed on the surface of colemanite after preparation of composite. It can be concluded that the structure of boron mineral protects LA and DA from environmental effects as a supporting matrix and phase changing occurs in boron mineral structure.

The leakage properties of the composites during phase change were analyzed by high temperature test. For this purpose, the composites were heated to 95 ºC and the results are presented in Fig. 8-9.



MK 1 MK 4

Fig.8. Leakage test of MK1 and MK4



Şekil 4.10. LA içerikli MK1 ve MK4, kompozitinin sızdırmazlık testi

Fig.9. Leakage test of MK8 and MK9

As seen from the high temperature test results; no leakage was observed in the prepared composites.

FTIR analyzes were performed to determine the chemical stability of composites and presented in Figure 10-13.

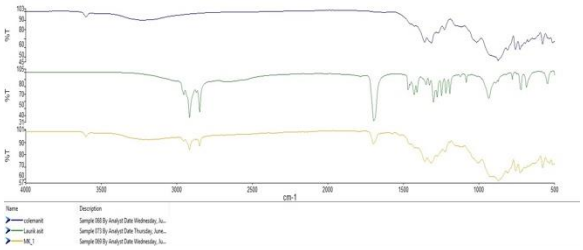


Fig.10. FTIR analyses of colemanite, LA, MK1

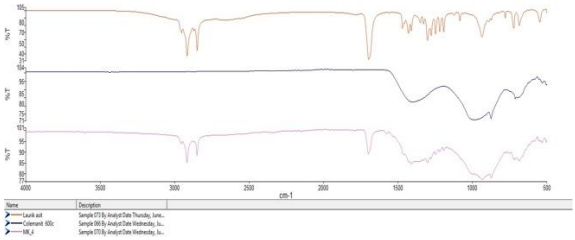


Fig.11. FTIR analyses of LA, colemanite(600 ºC), MK4

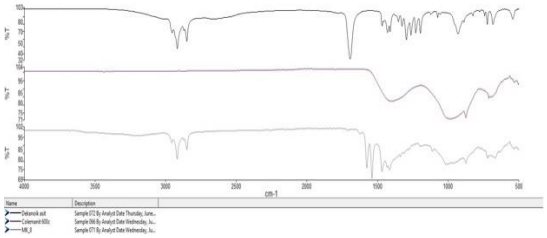


Fig.12. FTIR analyses of DA, colemanite (600 ºC), MK8

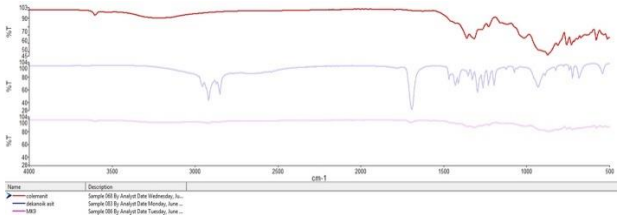


Fig.13. FTIR analyses of DA, colemanite and MK9

According to FT-IR analysis, all composites have the specific spectra of PCM and colemanite which used in their components.

4. Conclusion

In this study, colemanite based LA and DA composites were prepared with direct impregnation method for thermal energy storage. The effect of colemanite pretreatment on latent heat storage was determined.

DSC analyses results show that pretreatment of colemanite at 600ºC have positive effect on latent heat storage capacity of PCM/colemanite composites. The maximum latent heat storage capacity was obtained with MK4 without any leakage. Melting point and latent heat storage capacity of MK4 were determined 42.07ºC and 34.6 J / g respectively.

For further developed investigations, we propose that in order to obtain natural mineral/phase change material composites with a higher latent heat storage capacity, different preparation methods should be determined.

References:

[1] Sarı, A., Karaipekli, A., & Alkan, C. (2009). Preparation, characterization and thermal properties of lauric acid/expanded perlite as novel form-stable composite phase change material. Chemical Engineering Journal, 155(3), 899-904.

[2] Fang, G., Li, H., & Liu, X. (2010). Preparation and properties of lauric acid/silicon dioxide composites as form-stable phase change materials for thermal energy storage. Materials Chemistry and Physics, 122(2-3), 533-536.

[3] Chen, Z., Shan, F., Cao, L., & Fang, G. (2012). Synthesis and thermal properties of shape-stabilized lauric acid/activated carbon composites as phase change materials for thermal energy storage. Solar Energy Materials and Solar Cells, 102, 131-136.

[4] Fu, X., Liu, Z., Xiao, Y., Wang, J., & Lei, J. (2015). Preparation and properties of lauric acid/diatomite composites as novel form-stable phase change materials for thermal energy storage. Energy and Buildings, 104, 244-249.

[5] Harish, S., Orejon, D., Takata, Y., & Kohno, M. (2015). Thermal conductivity enhancement of lauric acid phase change nanocomposite with graphene nanoplatelets. Applied thermal engineering, 80, 205-211.

[6] Mei, D., Zhang, B., Liu, R., Zhang, Y., & Liu, J. (2011). Preparation of capric acid/halloysite nanotube composite as form-stable phase change material for thermal energy storage. Solar Energy Materials and Solar Cells, 95(10), 2772-2777.

[7] Sarı, A., & Karaipekli, A. (2008). Preparation, thermal properties and thermal reliability of capric acid/expanded perlite composite for thermal energy storage. Materials Chemistry and Physics, 109(2-3), 459-464.

[8] Konuklu, Y., & Ersoy, O. (2017). Fabrication and characterization of form-stable phase change material/xonotlite microcomposites. Solar Energy Materials and Solar Cells, 168, 130-135.

6th International Conference on Materials Science and Nanotechnology For Next Generation (MSNG2019)
October 16-18, 2019, Niğde, TURKEY (ORAL FULL TEXT)

Electronic structure and elastic properties of $ScRu_3$ intermetallic compound studied by the GGA method

Mustafa Oğuzhan ALTAY*, Abdullah CANDAN**, Cihan KÜRKÇÜ***, Mustafa ÖZDURAN*

* Department of Physics, Kırşehir Ahi Evran University, Turkey
** Department of Machinery and Metal Technology, Kırşehir Ahi Evran University, Turkey
*** Department of Electronics and Automation, Kırşehir Ahi Evran University, Turkey

The structural, electronic and elastic calculations have been performed on the $L1_2$-type (space number 221) of intermetallic compound $ScRu_3$ using the ab initio density-functional theory within the generalized gradient approximation (GGA). Besides, the basic physical parameters such as lattice constant, bulk modulus, elastic constants, shear modulus, Young's modulus, and Poison's ratio; the band structure, corresponding total and density of states (DOS) are also calculated for this compound.

Keywords: Structural Properties, Electronic Properties, Elastic Properties, Density Functional Theory

Corresponding author: mustafaoguzhanaltay@gmail.com

1. Introduction

$ScRu_3$ crystallizes in cubic CsCl-type structure with space group Pm-3m under ambient conditions. According to the literature researches, there are almost no studies on some physical properties of this material such as structural, electronic, mechanical properties. The basic prototype of this material is Cu_3Au. This structure is also known as $L1_2$. Many experimental and theoretical studies have been done on Cu_3Au for many years [1-5]. However, the lack of sufficient studies on $ScRu_3$ has led us to study this material. We have studied the structural, electronic and elastic properties of this material, in detail. As a result of the calculations, we found that this material has metallic property and is mechanically stable.

2. Theoretical details

$ScRu_3$ compound has a close-packed face-centred-cubic structure with space group Pm-3m. The calculations were performed within the density functional theory, as implemented in the MedeA-Vasp package with the projected augmented wave (PAW). For the exchange-correlation functional, the generalized gradient approximation of Perdew–Burke–Ernzerhof (GGA-PBE) was used [6]. An energy cut-off 500 eV was found to be adequate for the calculation of the structural, electronic, and elastic properties. The k-point sampling was done on an 8x8x8 gamma-point grid for structure. The Fermi distribution function with a smearing parameter of 0.2 eV was used to integrate the bands at Fermi level. The elastic constants C_{ij} are computed using the stress-strain technique.

3. Results and discussion

3.1 Structural Properties:

$ScRu_3$ compound has a cubic CsCl-type structure with Pm-3m symmetry at ambient conditions. The wyckoff positions are located in the following positions. Sc (0,0,0) and Ru (0.5, 0.5, 0.5). The lattice constant, bulk and shear modulus, B/G ratio of $ScRu_3$ were calculated, and the obtained results were given in Table 1.

Moreover, the ratio of B/G has been calculated to investigate the ductility and brittleness properties of the $ScRu_3$ intermetallic compound. This ratio can be considered as an empirical criterion of the extent of the fracture range in the materials. If the ratio of B/G is higher than 1.75, then the material behaves in a ductile manner. If it is less than 1.75, then that material demonstrates brittleness. The B/G value is 2.60 for this material. This indicates the ductile nature of this material.

Table 1. Lattice constant *a* (Å), bulk modulus (B), shear modulus (G), and Young's modulus (E), B/G ratio of $ScRu_3$.

Material	a_0	B	G	B/G	E
$ScRu_3$	3.920	206.58	79.39	2.60	211.13

3.2 Electronic Properties:

The calculated electronic band structure along the high symmetry directions and partial density of states for $ScRu_3$ are given in Figure 2 and Figure 3, respectively. It is clearly from Figure 2 and Figure 3 that the valence and conduction bands are overlapping around the Fermi level. Moreover, there is no band gap at the Fermi level which is obviously indicating that this compound is conductivity. For $ScRu_3$, the electronic bands above the Fermi level are due to the d-states of Ru atoms and Sc atoms. We have also noticed that the group of bands that appears below the Fermi level is mainly due to the d-state of Ru atoms, which can be seen in Figure 3.

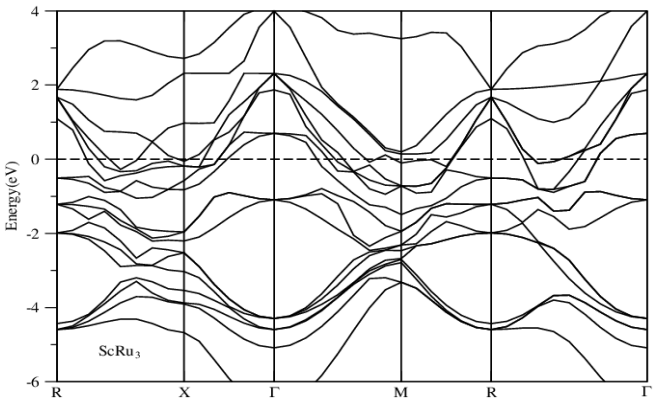


Figure 2. *Calculated the electronic band structure of $ScRu_3$ compound along several lines of high symmetry in the Brillouin zone.*

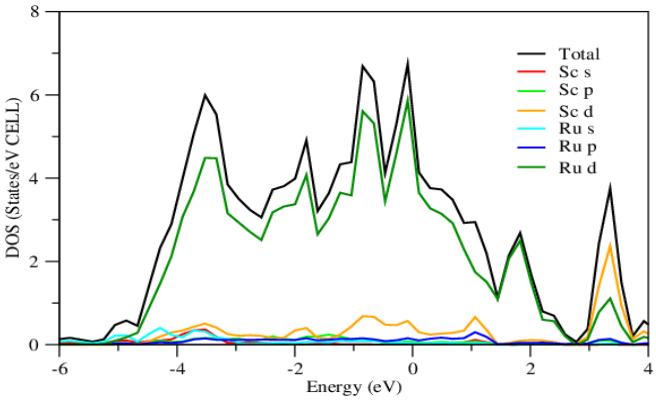


Figure 3. *Calculated partial and total DOS for $ScRu_3$ compound.*

3.3 Elastic Properties

It is very important to know the elastic properties of a solid material. Elastic constants are closely related to various fundamental solid-state phenomena such as phonon spectra, specific heat, thermal expansion, Debye temperature, interatomic bonding, equations of state and sound velocities. In cubic structures, there are only three independent elastic constants (C_{11}, C_{12}, and C_{44}). The calculated values of elastic constants are listed in Table 2. Mechanical stability of these compound has been analysed in terms of their elastic constants. The conditions for mechanical stability for cubic crystals are given by;

$$C_{11} > 0, (C_{11} - C_{12})/2 > 0, B > 0$$

The obtained elastic constants for $ScRu_3$ reveal that this compound is mechanically stable in the studied phase.

Table 2. The calculated elastic constants (C_{11}, C_{12}, C_{44}, in GPa) for $ScRu_3$.

Compound	Ref.	C_{11} (GPa)	C_{12} (GPa)	C_{44} (GPa)
$ScRu_3$	Present	286.76	164.49	95.91

4. Conclusion

The calculated elastic constants verify the Born's mechanical stability criteria for cubic structures. On the other hand, it is observed that the B/G > 1.75, thus classifying this compound as ductile materials in nature. From the electronic band structure figure, the valance and conduction bands are overlapped with each other at the Fermi level which indicates that this material has metallic characteristics.

References:

[1] G.-S. WANG, E.K. DELCZEG-CZIRJAK, Q.-M. HU, K. KOKKO, B. JOHANSSON, L. VITOS, Journal of Physics: Condensed Matter, 25 (2013) 085401.
[2] J. BRINKMAN, C. DIXON, C. MEECHAN, Acta Metallurgica, 2 (1954) 38-48.
[3] T. HASHIMOTO, K. NISHIMURA, Y. TAKEUCHI, Journal of the Physical Society of Japan, 45 (1978) 1127-1135.
[4] M. HIRABAYASHI, S. NAGASAKI, H. KŌNO, Journal of Applied Physics, 28 (1957) 1070-1071.

[5] D. ROY, A. MANNA, S.S. GUPTA, Journal of Physics F: Metal Physics, 2 (1972) 1092.

[6] J. PERDEW, K. BURKE, M. ERNZERHOF, Physical Review Letters, 80 (1998) 891.

6th International Conference on Materials Science and Nanotechnology For Next Generation (MSNG2019)
October 16-18, 2019, Niğde, TURKEY (ORAL FULL TEXT)

Physical Properties of Half-Heusler TbPdBi Alloy

Mustafa Oğuzhan ALTAY*, Ahmet İYİGÖR**, Abdullah CANDAN**, Mustafa ÖZDURAN*

* Department of Physics, Kırşehir Ahi Evran University, Turkey
** Department of Machinery and Metal Technology, Kırşehir Ahi Evran University, Turkey

The structural, electronic and elastic properties of half-Heusler TbPdBi have been studied using first-principles calculation within the generalized gradient approximation based on density functional theory. The optimized lattice constant (a_0), bulk modulus (B), elastic constants (C_{11}, C_{12} and C_{44}) and other mechanical moduli (G, E, B/G and σ) of this alloy has been computed. Mechanical stability for this alloy has been analyzed in terms of their second-order elastic constants. Besides, electronic band structure as well as total and partial density of states have also been plotted for TbPdBi alloy.

Keywords: Half-Heusler alloys, Electronic Structure, Mechanical Properties.

Corresponding author: mustafaoguzhanaltay@gmail.com

1. Introduction

Half-metallic ferromagnets have become one of the most studied classes of materials due to their possible applications in spin electronics and magnetoelectronics [1]. In these materials the two spin bands show a completely different behaviour. While one of them (usually the majority-spin band, henceforth also referred to as spin-up band) shows a typical metallic behaviour with a non-zero density of states (DOS) at the Fermi level EF, the minority (spin-down) band exhibits a semiconducting behaviour with a gap at E_F. The half-metallicity was first predicted by de Groot and collaborators [2] in 1983 when studying the band structure of a half-Heusler alloy NiMnSb. They showed that the spin down state is semiconducting. Since then, many other materials have also been found to be half-metallic. The current advantages in new materials are promising for engineering new spintronic devices soon. Also, the half Heusler materials have been studied experimentally and theoretically by different researchers and different properties have been found [3-5].

2. Method of calculation

The calculations were performed to obtain the structural, electronic and elastic properties of TbPdBi using first-principles calculations based on the Density Functional Theory (DFT) within the Generalized Gradient Approximation (GGA) as implemented in the Vasp-MedeA package [6, 7]. Plane-wave energy cut-offs of 500 eV were used in VASP calculation. The k-points samplings were 7x7x7 for VASP in the Brillouin zone for TbPdBi, according to the Monkhorst–Pack scheme [8]. The structure was relaxed until the convergence in energy of 10^{-5} eV was reached. In the VASP calculations, the Methfessel–Paxton smearing [9] with broadening of 0.225 eV was used for relaxation.

3. Results and discussion

The unit cell of the full Heusler X_2YZ structure (space group: Fm-3m) consists of four inter-penetrating fcc sublattices. If one of the two equivalent sites (0, 0, 0) or (1/2, 1/2, 1/2) (here, occupied by X atoms) is empty, the half Heusler XYZ structure (space group: F43m) appears (See Figure 1).

Table 1. Calculated lattice constants (in Å), bulk modulus (in GPa) for TbPdBi in the $C1_b$ phase.

Material	References	*a* (Å)	B (GPa)
TbPdBi	This Work	6.740	86.094
	Exp. [5]	6.662	

The calculated lattice constant and bulk modulus are listed in Table 1. The computed lattice constant is agreement with the experimental value [5].

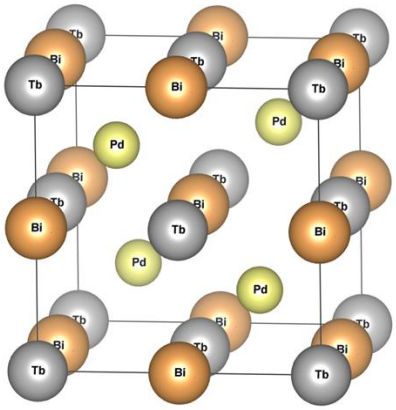


Figure 1. *Crystal structure of TbPdBi half Heusler alloy.*

The elastic constants are among the properties that are not yet studied experimentally and theoretically for this material. In the case of cubic crystals, there are three independent elastic constants (C_{11}, C_{12}, and C_{44}). For cubic crystals, the conditions for mechanical stability are given by [10].

$C_{44}>0$, $C_{11}-C_{12}>0$ and $B=(C_{11}-2C_{12})/3>0$ (1)

These criteria are verified (see Table 2), so it is concluded that this alloy is stable in the $C1_b$ phase. According to the ratio B/G, TbPdBi alloy is ductile manner.

Table 2. Calculated, Shear modulus (in GPa), Young modulus (in GPa), poission's ratio (σ) and elastic constants for TbPdBi in the $C1_b$ phase.

Material	C_{11}	C_{12}	C_{44}	G	B/G	E	σ
TbPdBi	172.65	85.63	20.66	29.80	2.89	80.16	0.35

The calculated electronic band structure along the high symmetry directions in the Brillouin zone and total and partial density of states for TbPdBi are given in Figure 2 and Figure 3. In the figures, the Fermi level was set to 0 eV. It is seen that there is no band gap at the Fermi level. However, it can be said that the conductivity and valence bands of the in the Fermi are gapless semiconductors for this material due to the overlap on the Γ high symmetry. Generally, Pd-d electrons are mainly dominant in valence bands and Tb-d electrons are mainly dominant in conductivity bands.

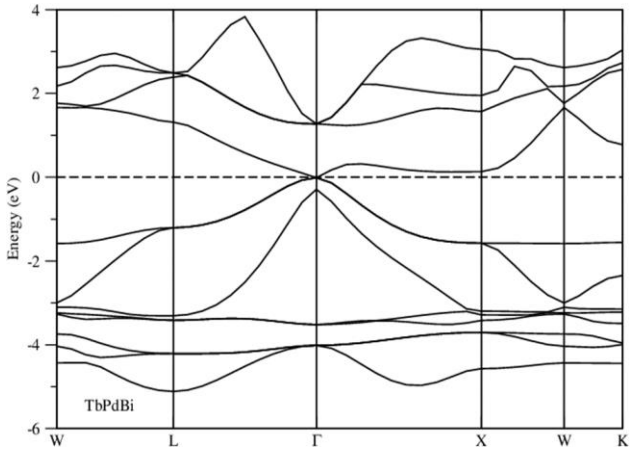


Figure 2. *The electronic band structure of the TbPdBi alloy.*

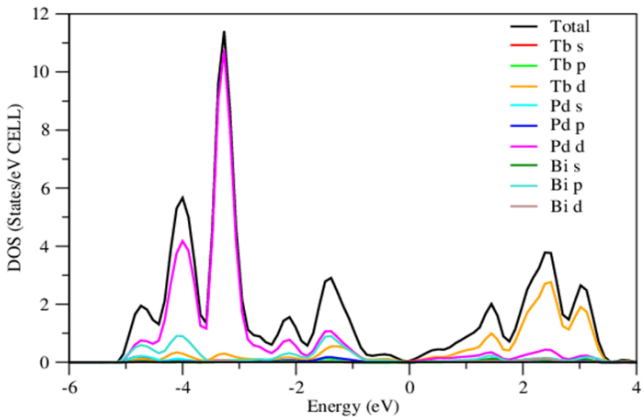


Figure 3. *The total and partial density of states for TbPdBi.*

4. Conclusion

In this study, the structural, mechanical and electronic properties of the half-Heusler TbPdBi alloy have been investigated with the Density Functional Theory. The calculated lattice parameter is good agreement with the available experimental data. The stress-strain method was used to calculate the elastic properties. TbPdBi alloy is mechanically stable in the $C1_b$ phase. According to the ratio B/G, this alloy is ductile manner. From the

electronic band structure calculations, it is seen that this alloy is a gapless semiconductor for $C1_b$ phase.

References:

[1] ZUTIC, I., FABIAN, J., DAS SARMA A., Rev. Mod. Phys 76 (2004) 323.
[2] de Groot R. A., Mueller F. M., van Engen P. G. and Buschow K. H., J. Phys. Rev. Lett. 50 (1983) 2024.
[3] Pavlosiuk, O., Fabreges, X., Gukasov, A., Meven, M., Kaczorowski, D., Wiśniewski, P., "Magnetic structures of R_EPdBi half-Heusler bismuthides (R_E= Gd, Tb, Dy,Ho, Er)", Physica B, 536, 56-59, 2018.
[4] Radmanesh, S. M. A., Martin, C., Zhu, Y., Yin, X. Xiao, H. Mao, Z. Q. and Spinu L., "Evidence for unconventional superconductivity in half-Heusler YPdBi and TbPdBi compounds revealed by London penetration depth measurements", Physical Review B, 98, 241111(R), 2018.
[5] Pavlosiuk, O., Kleinert, M., Wiśniewski P., Kaczorowski D., "Antiferromagnetic Order in the Half-Heusler Phase TbPdBi", Acta Physica Polonica A, 133,3 498-500, 2018.
[6] Kresse G and Hafner J 1993 Phys. Rev. B47 558.
[7] Kresse G and Furthmuller J 1993Phys. Rev. B54 11169.
[8] H.J. Monkhorst and J.D. Pack, Phys. Rev. B 13 (1976) p.5188–5192.
[9] M. Methfessel and A.T. Paxton, Phys. Rev. B 40 (1989) p.3616–3621.
[10] Born M., Huang K., 1954. Dynamical theory of crystal lattices. Clarendon, Oxford

6th International Conference on Materials Science and Nanotechnology For Next Generation (MSNG2019)
October 16-18, 2019, Niğde, TURKEY (ORAL FULL TEXT)

Ab initio study of C15 type Laves phase $LaIr_2$

Mustafa Oğuzhan ALTAY*, Ahmet İYİGÖR**, Cihan KÜRKÇÜ***, Mustafa ÖZDURAN*

* Department of Physics, Kırşehir Ahi Evran University, Turkey
** Department of Machinery and Metal Technology, Kırşehir Ahi Evran University, Turkey
*** Department of Electronics and Automation, Kırşehir Ahi Evran University, Turkey

Structural, elastic, electronic, and vibrational properties of the Laves phase $LaIr_2$ are investigated using the first-principles calculations. The electronic band structure shows that the material behaves metallic nature. The calculated total density of states are 3.60 (electrons/eV) of $LaIr_2$. The different mechanical properties such as elastic constants, bulk modulus B, shear modulus G, Young's modulus E, and Poisson ratio v are derived from Voigt–Reuss–Hill approximation. The ductility nature appears in both the values of Cauchy pressure and Pugh's ratio. Lastly, the phonon dispersion curves of this material along high symmetry directions in the first Brillouin zone are plotted.

Keywords: Laves phases, Electronic Properties, Vibrational Properties, Elastic Properties.

Corresponding author: mustafaoguzhanaltay@gmail.com

1. Introduction

The Laves phases are the structure of AB_2, which is explained by Fritz Laves and divided the Laves phases into three types such as face-centered cubic C15 ($MgCu_2$), hexagonal C14 ($MgZn_2$) and double-hexagonal C36 ($MgNi_2$) [1]. Laves phases have some functional properties, those are excellent corrosion and creep resistance, magnetic and electrical properties [2, 3]. C15-type Laves phase is better than any other two Laves phase because of the cubic structure [4, 5]. Due to the simple structure, the study of different types of physical and superconducting properties are quite interesting and understand very clearly. The agreeable superconductivity is found in the Laves phase cubic $MgCu_2$ (C15) type intermetallic compound with transition temperatures 0.07 K to above 10 K [6]. Shrivastava and co-workers [7] studied structural, electronic and elastic properties of $REIr_2$ (RE = La and Ce) Laves phase intermetallic compounds using full-potential linearized augmented plane wave (FP-LAPW) method within generalized gradient approximation (GGA) as implemented in WIEN2k code. In this study, we have elaborately performed the first-principles calculations to investigate the structural, electronic, elastic and phonon properties of the $LaIr_2$ compound, which crystallizes in C15-$MgCu_2$ type structure.

2. Theoretical details

All the calculations have been performed using the plane-wave pseudo-potential DFT method implemented in the MedeA-VASP package [8, 9]. Projector Augmented Wave (PAW) pseudopotentials were used to present the ionic potentials [10]. The Perdew-Burke-Ernzerhof (PBE) [11] exchange-correlation functional was treated at the generalized gradient approximation (GGA). In fact, the calculated results of GGA (PAW-PBE) are in reasonable agreement with the experimental value in all cases, this shows that the pseudo-potential and our methods are suitable for this study. According to a precise inspection of the convergence of total energy with respect to the energy cut-off of plane wave and size of k-mesh, the energy cut-off was chosen to be 500 eV for $LaIr_2$. The energy convergence criterion for electronic self-consistency is 10^{-6} eV/cell. The Monkhorst-Pack [12] scheme k-points grid sampling was set at $8 \times 8 \times 8$ for the Brillouin zone. The Fermi distribution function with a

smearing parameter [13] of 0.2 eV was used to integrate the bands at the Fermi level. Phonon dispersion curves are calculated using the MedeA-PHONON [14] module with the forces calculated with the Vasp.

3. Results and discussion

The crystal structure of the $LaIr_2$ intermetallic compound is shown in Figure 1. First of all, the equilibrium lattice parameter has been optimized and calculated value is tabulated in Table 1 with the experimental and theoretical data [7, 15]. Besides, the computed lattice constant, bulk modulus B, shear modulus G, and Young's modulus E have also been calculated and listed in Table 1. The calculated lattice constant and bulk modulus agree well with experimental and theoretical data for $LaIr_2$ in C15 phase.

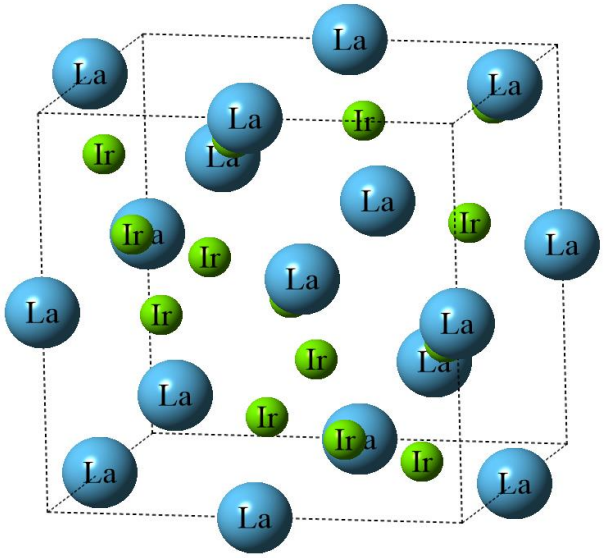


Figure 1. *Crystal structure of C15 type Laves phase $LaIr_2$ compound.*

Table 1. The calculated equilibrium lattice constant (a_0, in Å), bulk modulus (B, in GPa), shear modulus (G, in GPa), ratio B/G and Young modulus (E, in GPa) for $LaIr_2$.

Material	Ref.	a_0 (Å)	B	G	B/G	E
$LaIr_2$	This Work	7.737	175.524	61.281	2.864	164.679
	[7]	7.73	183.09	-	2.78	-
	[15]	7.68	-	-	-	-

Furthermore, Bulk modulus (B), Shear modulus (G), Voigt (G_V) and Reuss (G_R) polycrystalline elastic modulus, and B/G ratio are calculated and given in Table 1. The ratio of B/G has been calculated to investigate the ductility and brittleness properties of the $LaIr_2$ intermetallic compound. This ratio can be considered as an empirical criterion of the extent of the fracture range in the materials [16]. If the ratio of B/G is higher than 1.75, then the material behaves in a ductile manner. If it is less than 1.75, then that material demonstrates brittleness. The B/G value is 2.864 for this alloy. This indicates the ductile nature of this material.

The electronic properties such as electronic band structure, the partial density of state (PDOS), and the total density of state (TDOS) of cubic laves phase $LaIr_2$ have been calculated and given in Figure 2 and Figure 3, respectively. It is clear from Figure 2 that the valence and conduction bands are overlapping around the Fermi level which indicates the metallic nature of $LaIr_2$.

On the other hand, as presented in Figure 3, the calculated total DOS exhibits obvious metallic behavior because the values of total DOS for this phase are continuous at the Fermi level. The density of states at Fermi level $N(E_F)$ are 3.60 (electrons/eV) for $LaIr_2$. The electronic bands above the Fermi level are due to the f-states of La atoms. We have also noticed that the group of bands that appears below the Fermi level is mainly due to the d-state of Ir atoms, which can be seen in Figure 3.

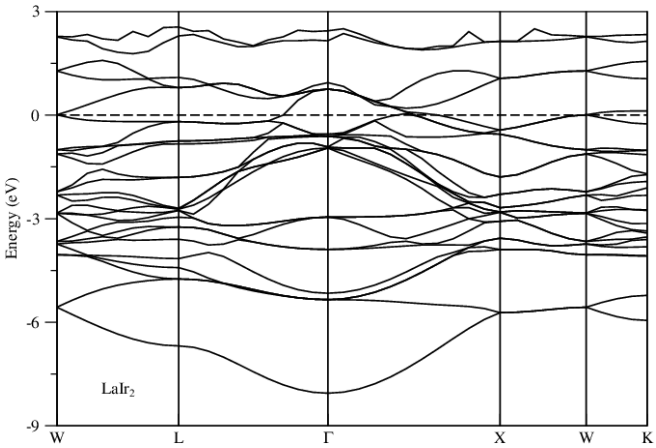


Figure 2. *Calculated the electronic band structure of $LaIr_2$ compound along several lines of high symmetry in the Brillouin zone.*

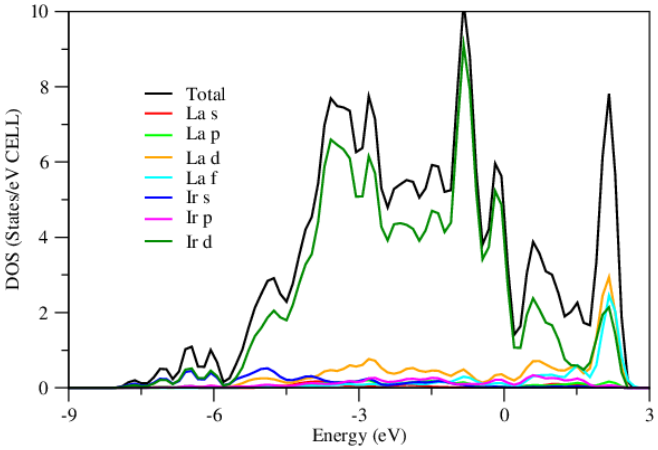


Figure 3. *Calculated partial and total DOS for $LaIr_2$ compound.*

Elastic constants are significant parameters of solid material and also provide valuable information on structural stability. A cubic system has three independent elastic constants (C_{11}, C_{12}, C_{44}). Mechanical stability for this alloy has been analyzed in terms of their elastic constants. For cubic crystals, the conditions for mechanical stability are given by [17]:

$$C_{11} > 0, \quad C_{11} - C_{12} > 0, \quad B > 0, \quad C_{44} > 0 \qquad (1)$$

Table 2. The calculated elastic constants (C_{11}, C_{12}, C_{44}, in GPa) for $LaIr_2$.

	Ref.	C_{11} (GPa)	C_{12} (GPa)	C_{44} (GPa)	C_P (GPa)
$LaIr_2$	Present	241.13	142.72	70.97	71.75
	[7]	253.01	146.87	75.33	71.54

The calculated elastic constants of the $LaIr_2$ intermetallic compound have been tabulated in Table 2. This table clearly shows the compatibility with the previous calculation [7]. The obtained elastic constants satisfy these mechanical stability criterions, thus showing that this compound is mechanically stable.

Figure 4 shows the calculated phonon dispersion curves of the $LaIr_2$ compound. As expected for $MgCu_2$-type cubic crystal structure (space group Fd-3m) with six atoms in the primitive cell, the phonon dispersion curve exhibits 18 branches, three acoustic and fifteen optical branches. All phonon modes exhibit positive frequencies, suggesting that $LaIr_2$ is dynamically stable.

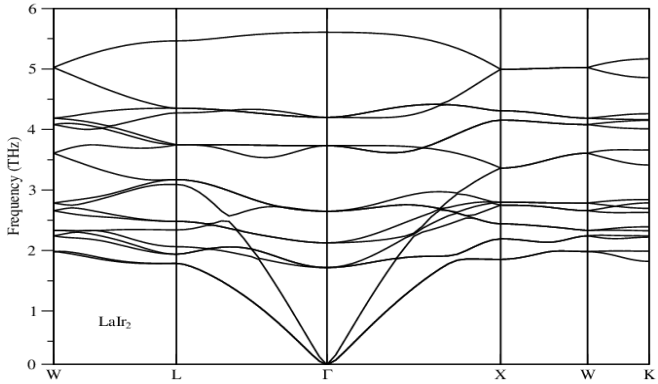


Figure 4. *The phonon dispersion curves of $LaIr_2$ compound.*

4. Conclusion

The calculated equilibrium lattice parameter is in good agreement with available other experimental and theoretical values. Our results for elastic constants suitably verify the Born's mechanical stability criteria for cubic structures. On the other hand, it is observed that the B/G > 1.75, thus classifying this compound as ductile materials in nature. From the band structure diagram, the valance and conduction bands are overlapped with each other at the Fermi level which indicates that this material has metallic characteristics. In addition, the phonon frequencies along high symmetry directions indicate that this compound is dynamically stable without any imaginary phonon frequencies.

References:

[1] LAVES, F., WİTTE, H., "Die Kristallstruktur des MgNi2 und seine Beziehungen zu den Typen MgCu2 und MgZn2", Metallwirtsch, 14(33), 645-649, 1935.
[2] NONG, Z. S., ZHU, J. C., CAO, Y., YANG, X. W., LAİ, Z. H., LİU, Y., "A first-principles study on the structural, elastic and electronic properties of the C14 Laves phase compounds TiX2 (X= Cr, Mn, Fe)", Physica B: Condensed Matter, 419, 11-18, 2013.
[3] RAJAGOPALAN, M., KUMAR, S. P., ANUTHAMA, R., "FP-LAPW study of the elastic properties of Al2X (X= Sc, Y, La, Lu)", Physica B: Condensed Matter, 405(7), 1817-1820, 2010.
[4] MOUSA, A.A., JARADAT, R., AZAR, S.M., ABU-JAFAR, M., JARADAT, E.K., KHALİFEH, J.M., ILAİWİ, K.F., "First principle investigation of the structural, electronic and elastic properties of the Laves

phase compounds SrX2 (X= Pd and Pt)", Chinese Journal of Physics, 59, 210-219, 2019.
[5] SAİDİ, F., SEBAA, N., MAHMOUDİ, A., AOURAG, H., MERAD, G., DERGAL, M., "Structural electronic and mechanical properties of YM2 (M= Mn, Fe, Co) laves phase compounds: First principle calculations analyzed with datamining approach", Solid State Communications, 274, 9-20, 2018.
[6] RAPP, Ö., INVARSSON, J., & CLAESON, T., "Search for superconductivity in Laves phase compounds", Physics Letters A, 50(3), 159-160, 1974.
[7] SHRİVASTAVA, D., FATİMA, B., & SANYAL, S.P., "Structural, electronic and elastic properties of REIr2 (RE= La and Ce) Laves phase compounds", In AIP Conference Proceedings, Vol. 1731, No. 1, p. 090003, 2016.
[8] KRESSE, G., HAFNER, J., "Ab initio molecular dynamics for liquid metals", Physical Review B, 47(1), 558, 1993.
[9] KRESSE, G., FURTHMÜLLER, J., "Efficiency of ab-initio total energy calculations for metals and semiconductors using a plane-wave basis set", Computational materials science, 6(1), 15-50, 1996.
[10] BLÖCHL, P.E., "Projector augmented-wave method", Physical review B, 50(24), 17953, 1994.
[11] PERDEW, J.P., BURKE, K., ERNZERHOF, M., "Generalized gradient approximation made simple", Physical review letters, 77(18), 3865, 1996.
[12] MONKHORST, H.J., PACK, J.D., "Special points for Brillouin-zone integrations", Physical review B, 13(12), 5188, 1976.
[13] METHFESSEL, M.P.A.T., PAXTON, A.T., "High-precision sampling for Brillouin-zone integration in metals", Physical Review B, 40(6), 3616, 1989.
[14] PARLİNSKİ, K., Lİ, Z. Q., KAWAZOE, Y., "First-principles determination of the soft mode in cubic ZrO2", Physical Review Letters, 78(21), 4063, 1997.
[15] IANDELLİ, A., PALENZONA, A., "Crystal chemistry of intermetallic compounds", Handbook on the physics and chemistry of rare earths, 2, 1-54, 1979.
[16] PUGH, S.F., "XCII. Relations between the elastic moduli and the plastic properties of polycrystalline pure metals", The London, Edinburgh, and Dublin Philosophical Magazine and Journal of Science, 45(367), 823-843, 1954.
[17] BORN, M., HUANG, K., Dynamical theory of crystal lattices, Clarendon press, 1954.

6th International Conference on Materials Science and Nanotechnology For Next Generation (MSNG2019)
October 16-18, 2019, Niğde, TURKEY (ORAL FULL TEXT)

Structural, electronic, elastic and phonon properties of $CeIr_2$ Laves phase intermetallic compound

Abdullah CANDAN*, Ahmet İYİGÖR*, Cihan KÜRKÇÜ**

* Department of Machinery and Metal Technology, Kırşehir Ahi Evran University, Turkey
** Department of Electronics and Automation, Kırşehir Ahi Evran University, Turkey

We have performed the first-principles calculations to study the structural, electronic, elastic and phonon properties of $CeIr_2$ Laves phase intermetallic compound using a plane-wave pseudopotential scheme within the density-functional theory (DFT). The electronic exchange–correlation potential is calculated by the generalized gradient approximation and Perdew–Burke–Ernzerhof (PBE). The optimized lattice constant and formation enthalpy are in reasonable agreement with available experimental data. The electronic properties are obtained in relation to band structures, total and partial density of states, which confirm its metallic character. The calculated elastic constants reveal that this compound is mechanically stable in C15 structure and this material also found to be ductile in nature. Finally, the phonon dispersion curves along high-symmetry points at the Brillouin zone and phonon density of states are plotted.

Keywords: Intermetallics, Laves phases, Elastic Properties, Phonon Properties.

Corresponding author: acandan@ahievran.edu.tr

1. Introduction

Intermetallic compounds of Laves phases are intermetallic phases having AB_2 composition and named by Fritz Laves who first described them. They have the face-centered cubic C15 ($MgCu_2$), hexagonal C14 ($MgZn_2$) and double-hexagonal C36 ($MgNi_2$) structures [1, 2]. The three structure types are related to each other but there are some differences in the stacking of a basic unit [3, 4]. These phases form the largest group of intermetallics and having many important applications such as superconducting materials, giant magnetostrictive materials, and hydrogen storage materials. Laves phase compounds show high melting temperature, low density and excellent oxidation resistance which are essential for high-temperature structural applications [5]. Shrivastava et al. [6] reported the structural, electronic and elastic properties of $REIr_2$ (RE = La and Ce) Laves phase intermetallic compounds using full-potential linearized augmented plane wave (FP-LAPW) method within generalized gradient approximation (GGA) as implemented in WIEN2k code.

In the current study, we have extensively performed the first- principles calculations to investigate the structural, electronic, elastic and phonon properties of the $CeIr_2$ compound, which crystallizes in C15-$MgCu_2$ type structure.

2. Theoretical details

All calculations have been carried out by using the quantum-ESPRESSO code [7, 8] based on the density functional theory (DFT). The energy cut-off for the expansion of the eigenfunctions was set to 50 Ry. This cut-off energy was found to be adequate to study the structural and lattice dynamical properties. We have used the generalized gradient approximation (GGA) parameterized by Perdew-Burke-Ernzerhof (PBE) [9] for the exchange and correlation terms in the electron-electron interaction for k-space summation which was 12×12×12 Monkhorst and Pack [10] grid of k-points. The elastic constants can be obtained by calculating the total energy as a function of volume-conserving strains. Having obtained self-consistent solutions of Kohn–Sham equations, the lattice-dynamical properties were calculated within the framework of the self-consistent density functional perturbation theory [11].

3. Results and discussion

The crystal structure of $CeIr_2$ intermetallic compound is given in Figure 1. First of all, the equilibrium lattice

parameter has been optimized and calculated value is shown in Table 1 with the experimental and theoretical data [6, 12]. Besides, the computed cell volume (V_0), density (ρ), and formation enthalpy (E_f) have also been calculated and listed in Table 1.

The calculated lattice parameter agrees well with experimental and theoretical data for $CeIr_2$ in face-centered cubic C15 phase.

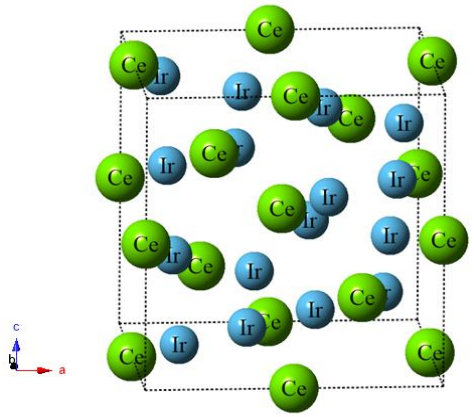


Figure 1. *Total energy versus lattice constant curves of $CeIr_2$ intermetallic compound.*

Table 1. The calculated equilibrium lattice parameter (a_0), cell volume (V_0), density (ρ), and formation enthalpy (E_f) for $CeIr_2$.

	Ref.	a_0 (Å)	V (Å³/f.u.)	ρ (g/cm³)	E_f (eV/atom)
$CeIr_2$	Present	7.622	442.761	15.738	-0.779
	[6]	7.62	-	-	-
	[Exp.-12]	7.573	-	-	-

The electronic band structure analysis of the materials gives us information about the materials' electric types: conductor, semiconductor or insulator. The electronic properties such as electronic band structure, the partial density of state (PDOS), and the total density of state (TDOS) of cubic laves phase $CeIr_2$ have been calculated and given in Figure 2, Figure 3. It is clear from Figure 2 that the valence and conduction bands are overlapping around the Fermi level. Moreover, there is no band gap at the Fermi level which is clearly indicating that this compound is neither insulator nor semiconductor materials but rather conductor one. On the other hand, as presented in Figure 3, the calculated total DOS exhibits obvious metallic behavior because the values of total DOS for this phase are continuous at the Fermi level. The density of states at Fermi level $N(E_F)$ are 6 States/eV for $CeIr_2$. For $CeIr_2$, the electronic bands above the Fermi level are due to the f-states of Ce atoms. We have also noticed that the group of bands that appears below the Fermi level is mainly due to the d-state of Ir atoms, which can be seen in Figure 3.

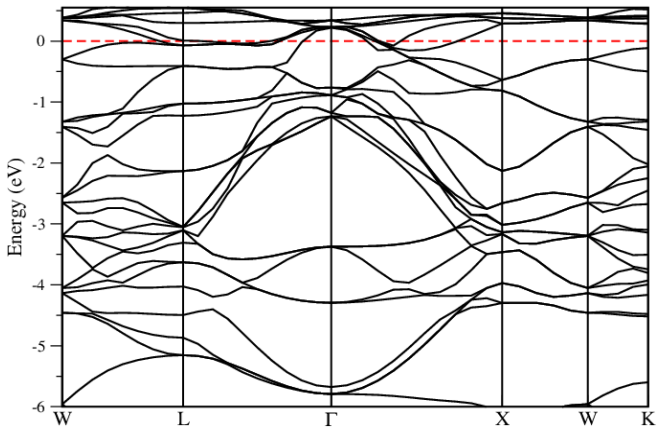


Figure 2. *Calculated the electronic band structure of $CeIr_2$ compound along several lines of high symmetry in the Brillouin zone.*

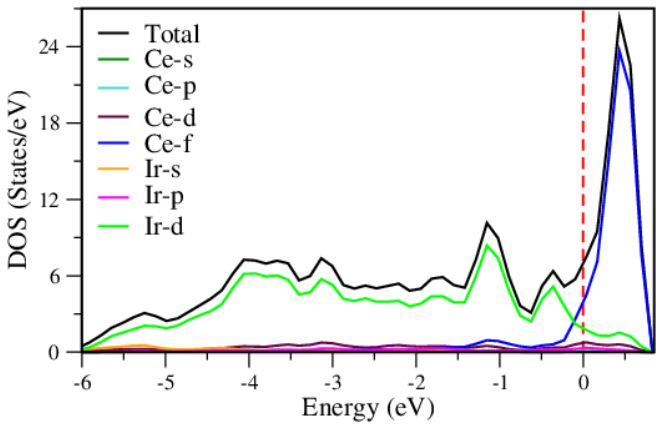


Figure 3. *Calculated partial and total DOS for $CeIr_2$ compound.*

Elastic constants are significant parameters of solid material and also provide valuable information on structural stability. A cubic system has three independent elastic constants (C_{11}, C_{12}, C_{44}). Mechanical stability for this alloy has been analyzed in terms of their elastic constants. For cubic crystals, the conditions for mechanical stability are given by [13]:

$$C_{11} > 0, \quad C_{11} - C_{12} > 0, \quad B > 0, \quad C_{44} > 0 \qquad (1)$$

Table 2. The calculated elastic constants (C_{11}, C_{12}, C_{44}, in GPa) for $CeIr_2$.

Compound	Ref.	C_{11} (GPa)	C_{12} (GPa)	C_{44} (GPa)
$CeIr_2$	Present	280.71	173.23	96.83
	[6]	252.93	182.63	96.95

The calculated elastic constants of $CeIr_2$ intermetallic compound have been tabulated in Table 2. This table clearly shows the compatibility with the previous calculation [6]. The obtained elastic constants satisfy these mechanical stability criterions, thus showing that this compound is mechanically stable.

Moreover, mechanical parameters such as Bulk modulus (B), Shear modulus (G), Voigt (G_V) and Reuss (G_R) polycrystalline elastic modulus, and B/G ratio are given in Table 3. The ratio of B/G has been calculated to investigate the ductility and brittleness properties of the $CeIr_2$ intermetallic compound. This ratio can be considered as an empirical criterion of the extent of the fracture range in the materials [14]. If the ratio of B/G is higher than 1.75, then the material behaves in a ductile manner. If it is less than 1.75, then that material demonstrates brittleness. The B/G value is 2.73 for this alloy. This indicates the ductile nature of this material.

Table 3. The calculated bulk modulus (B, in GPa), shear modulus (G, in GPa), and ratio B/G for Ru_2ZnGa.

Compound	Ref.	B (GPa)	G_V (GPa)	G_R (GPa)	G (GPa)	B/G
$CeIr_2$	Present	209.06	79.59	73.32	76.45	2.73
	[6]	-	-	-	-	3.19

Figure 4 shows the calculated phonon dispersion curves and partial and total density of states of the $CeIr_2$ compound. As expected for $MgCu_2$-type cubic crystal structure (space group Fd-3m) with six atoms in the primitive cell, the phonon dispersion curve exhibits 18 branches, three acoustic and fifteen optical branches. All phonon modes exhibit positive frequencies, suggesting that $CeIr_2$ is dynamically stable. From Figure 4, there is a gap between the optic-optical phonon modes because of the mass difference between the Ce and Ir atoms. This gap is calculated to be 0.71 THz for this compound. Besides, the calculated zone-center phonon frequencies are found to be 0.613-2.697-2.994-3.174-4.758-6.466 THz.

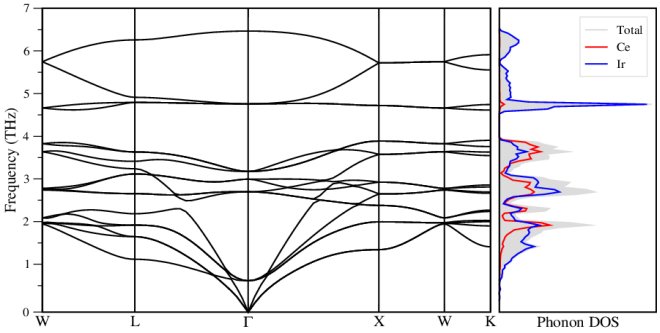


Figure 4. *The phonon dispersion curves and partial and total density of states of $CeIr_2$ compound.*

4. Conclusion

The calculated equilibrium lattice parameter is in good agreement with available other experimental and theoretical values. Our results for elastic constants verify the Born's mechanical stability criteria for cubic structures. On the other hand, it is observed that the B/G > 1.75, thus classifying this compound as ductile materials in nature. From the band structure diagram, the valance and conduction bands are overlapped with each other at the Fermi level which indicates that this material has metallic characteristics. In addition, the phonon frequencies along high symmetry directions indicate that this compound is dynamically stable without any imaginary phonon frequencies.

References:

[1] LAVES, F., WİTTE, H., "Die Kristallstruktur des MgNi2 und seine Beziehungen zu den Typen MgCu2 und MgZn2", Metallwirtsch, 14(33), 645-649, 1935.
[2] NONG, Z. S., ZHU, J. C., CAO, Y., YANG, X. W., LAİ, Z. H., LİU, Y., "A first-principles study on the structural, elastic and electronic properties of the C14 Laves phase compounds TiX2 (X= Cr, Mn, Fe)", Physica B: Condensed Matter, 419, 11-18, 2013.
[3] RAJAGOPALAN, M., KUMAR, S. P., ANUTHAMA, R., "FP-LAPW study of the elastic properties of Al2X (X= Sc, Y, La, Lu)", Physica B: Condensed Matter, 405(7), 1817-1820, 2010.
[4] MOUSA, A.A., JARADAT, R., AZAR, S.M., ABU-JAFAR, M., JARADAT, E.K., KHALİFEH, J.M., ILAİWİ, K.F., "First principle investigation of the structural, electronic and elastic properties of the Laves phase compounds SrX2 (X= Pd and Pt)", Chinese Journal of Physics, 59, 210-219, 2019.

[5] SAİDİ, F., SEBAA, N., MAHMOUDİ, A., AOURAG, H., MERAD, G., DERGAL, M., "Structural electronic and mechanical properties of YM2 (M= Mn, Fe, Co) laves phase compounds: First principle calculations analyzed with datamining approach", Solid State Communications, 274, 9-20, 2018.

[6] SHRİVASTAVA, D., FATİMA, B., & SANYAL, S.P., "Structural, electronic and elastic properties of REIr2 (RE= La and Ce) Laves phase compounds", In AIP Conference Proceedings, Vol. 1731, No. 1, p. 090003, 2016.

[7] VANDERBİLT, D., "Soft self-consistent pseudopotentials in a generalized eigenvalue formalism", Physical review B, 41(11), 7892, 1990.

[8] GIANNOZZI, P., BARONI, S., BONINI, N., CALANDRA, M., CAR, R., CAVAZZONI, C., CERESOLI, D., CHIAROTTI, G.L., COCOCCIONI, M., DABO, I., DAL CORSO, A., FABRIS, S., FRATESI, G., DE GIRONCOLI, S., GEBAUER, R., GERSTMANN, U., GOUGOUSSIS, C., KOKALJ, A., LAZZERI, M., MARTIN-SAMOS, L., MARZARI, N., MAURI, F., MAZZARELLO, R., PAOLINI, S., PASQUARELLO, A., PAULATTO, L., SBRACCIA, C., SCANDOLO, S., SCLAUZERO, G., SEITSONEN, A.P., SMOGUNOV, A., UMARI, P., WENTZCOVITCH, R.M., "QUANTUM ESPRESSO : a modular and open-source software project for quantum simulations of materials", Journal of physics: Condensed matter, 21, 395502, 2009.

[9] PERDEW, J.P., BURKE, K., ERNZERHOF, M., "Generalized gradient approximation made simple", Physical review letters, 77(18), 3865, 1996.

[10] MONKHORST, H.J., PACK, J.D., "Special points for Brillouin-zone integrations", Physical review B, 13(12), 5188, 1976.

[11] BARONİ, S., GİANNOZZİ, P., TESTA, A., "Green's-function approach to linear response in solids", Physical Review Letters, 58(18), 1861, 1987.

[12] IANDELLİ, A., PALENZONA, A., "Crystal chemistry of intermetallic compounds", Handbook on the physics and chemistry of rare earths, 2, 1-54, 1979.

[13] BORN, M., HUANG, K., Dynamical theory of crystal lattices, Clarendon press, 1954.

[14] PUGH, S.F., "XCII. Relations between the elastic moduli and the plastic properties of polycrystalline pure metals", The London, Edinburgh, and Dublin Philosophical Magazine and Journal of Science, 45(367), 823-843, 1954.

6th International Conference on Materials Science and Nanotechnology For Next Generation (MSNG2019)
October 16-18, 2019, Niğde, TURKEY (ORAL FULL TEXT)

Ab initio study of the fundamental properties of Ru_2ZnGa Heusler alloy

Abdullah CANDAN*, Cihan KÜRKÇÜ**, Ahmet İYİGÖR*

* Department of Machinery and Metal Technology, Kırşehir Ahi Evran University, Turkey
** Department of Electronics and Automation, Kırşehir Ahi Evran University, Turkey

The structural, electronic, mechanical, and vibrational properties of Ru_2ZnGa Heusler alloy are investigated in the Fm-3m space group. These properties have been performed in the framework of self-consistent first-principle calculations, using the pseudo-potential plane wave method based on the Generalized Gradient Approximation (GGA). It is seen that calculated lattice constant agree well with the available theoretical result. As well as the electronic band structure along the high symmetry directions, total and partial density of states are presented. The elastic constants and other polycrystalline elastic moduli have been anticipated, and the mechanical stability of Ru_2ZnGa alloy has been verified. Besides, phonon dispersion curves and the corresponding density of states are also obtained using the density functional perturbation theory (DFPT).

Keywords: Full Heusler-type alloys, Electronic Properties, Elastic Properties, Vibrational Properties.

Corresponding author: acandan@ahievran.edu.tr

1. Introduction

During the last century, Heusler alloys [1] have attracted a lot of researchers [2] owing to its various electronic properties. Many researchers have been studying into Heusler alloys to look for spintronic [3] topological insulators and for thermoelectric materials [4]. To date, many of the Heusler alloys have been synthesized and their physical properties have been estimated. Heusler compounds are $L2_1$ type crystal structure and they are of two types full Heusler and half Heusler. The full Heusler type has space group of 225, four interpenetrating fcc lattices with the chemical formula X_2YZ [5]. X and Y atoms are transition metals and Z atoms are mainly from III, IV and V group of elements of the periodic table. The X atoms occupy (0, 0, 0) and (1/2, 1/2, 1/2), Y atoms at (1/4, 1/4, 1/4) and Z atoms at (3/4, 3/4, 3/4). To the best of our knowledge, no studies of electronic band structure, elastic and vibration properties of Ru_2ZnGa alloy have been reported in the literature. Only, Gilleßen in his dissertation has studied the lattice constant and magnetic moment of Ru_2ZnGa Heusler alloy using density functional theory [6]. Therefore, we have aimed to provide some additional information about the physical properties of Ru_2ZnGa to the existing data using the ab initio total-energy calculations.

2. Theoretical details

All calculations have been carried out by using the quantum-ESPRESSO code [7, 8] based on the density functional theory (DFT). The energy cut-off for the expansion of the eigenfunctions was set to 40 Ry. This cut-off energy was found to be adequate to study the structural and lattice dynamical properties. We have used the generalized gradient approximation (GGA) parameterized by Perdew-Burke-Ernzerhof (PBE) [9] for the exchange and correlation terms in the electron-electron interaction for k-space summation which was 12×12×12 Monkhorst and Pack [10] grid of k-points. The elastic constants can be obtained by calculating the total energy as a function of volume-conserving strains that break the cubic symmetry. Having obtained self-consistent solutions of Kohn–Sham equations, the lattice-dynamical properties were calculated within the framework of the self-consistent density functional perturbation theory [11].

3. Results and discussion

The equilibrium lattice constant is determined by minimizing the total energy with respect to different values of the lattice constant. These energy values are

fitted to the Murnaghan's equation of state in order to obtain the lattice constant, and the first-order pressure derivative of the bulk modulus. The total energies corresponding to different lattice constants for the Ru_2ZnGa alloy are shown in Figure 1.

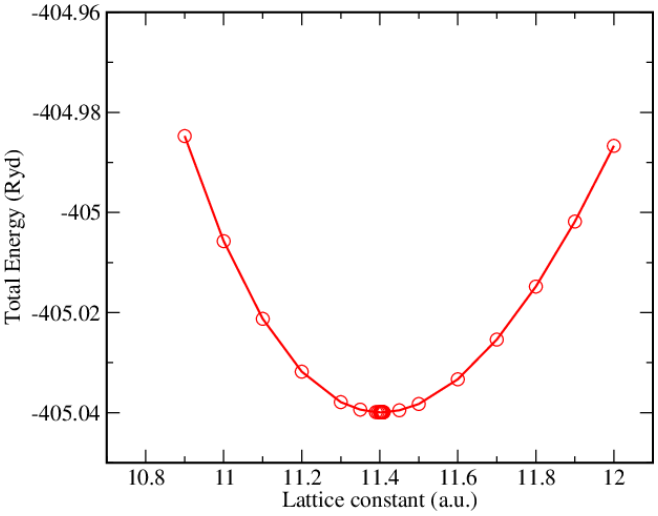


Figure 1. *Total energy versus lattice constant curves of Ru_2ZnGa.*

We also tabulated lattice constant (a_0), Bulk modulus (B) and its pressure derivative (B′) for Ru_2ZnGa alloy in able 1. Our results have been compared with the available result in the literature [6]. There is a good agreement between our lattice constant and that previously reported. The predicted lattice constant is about 0.04 % smaller than the theoretical data [6].

Table 1. The calculated equilibrium lattice constant (a_0), bulk modulus (B), and pressure derivative of bulk modulus (B′) for Ru_2ZnGa.

Material	Reference	a_0 (Å)	B_0 (GPa)	B′ (GPa)
Ru_2ZnGa	Present	6.034	207.2	4.94
	[8]	6.056	-	-

The spin-polarized electronic band structures for Ru_2ZnGa alloy along the high symmetry directions in the Brillouin zone given in Figure 2. It is seen that there is no band gap at the Fermi level, as a result, Ru_2ZnGa alloy exhibit metallic behavior. Furthermore, the total and the partial density of states of Ru_2ZnGa alloy are shown in Figure 3. It is clearly seen that the low-energy part (around -10 and -5 eV) mainly consists of Zn-4d states and also at the Fermi level is dominated by Ru-4d states.

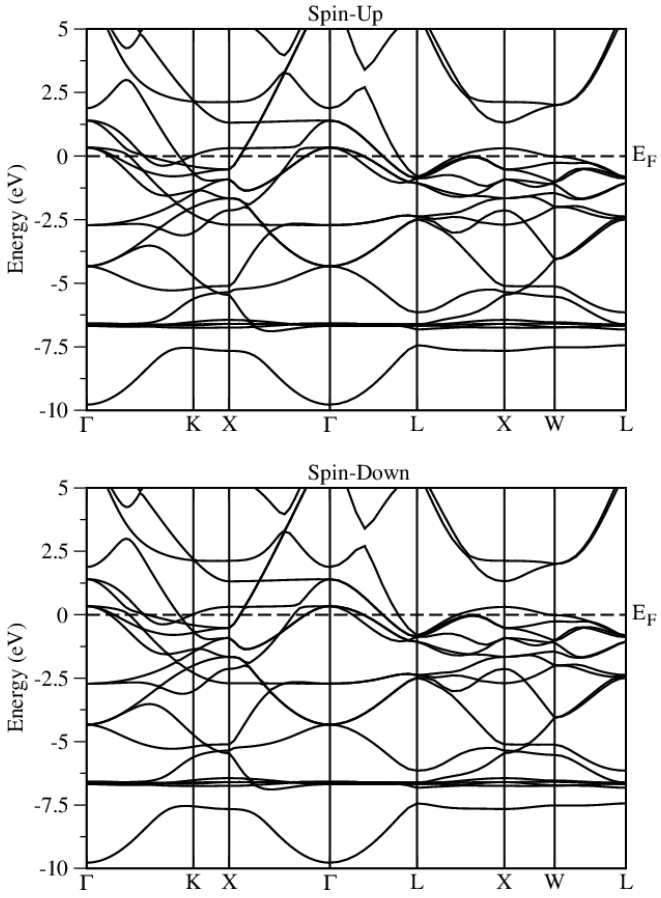


Figure 2. *Electronic band structures in the spin-up and spin-down states of the Ru_2ZnGa alloy. The dotted line indicates the Fermi level at 0 eV.*

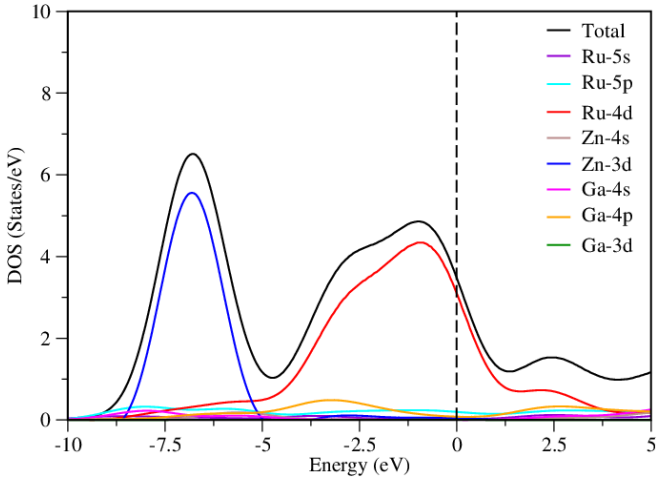


Figure 3. *Total and partial DOS for Ru_2ZnGa alloy, the Fermi level is set at 0 eV.*

Elastic constants are significant parameters of solid material and also provide valuable information on structural stability. A cubic system has three independent elastic constants (C_{11}, C_{12}, C_{44}). Mechanical stability for this alloy has been analyzed in terms of their elastic constants. For cubic crystals, the conditions for mechanical stability are given by [12]:

$$C_{11} > 0, \quad C_{11} - C_{12} > 0, \quad B > 0, \quad C_{44} > 0 \qquad (1)$$

Table 2. The calculated elastic constants (C_{11}, C_{12}, C_{44}, in GPa) for Ru_2ZnGa.

Material	C_{11} (GPa)	C_{12} (GPa)	C_{44} (GPa)
Ru_2ZnGa	280.38	173.97	135.18

The calculated elastic constants of Ru_2ZnGa alloy have been tabulated in Table 2. The obtained elastic constants for this alloy satisfy these mechanical stability criterions, thus showing that the Ru_2ZnGa is mechanically stable.

Moreover, mechanical parameters such as bulk modulus (B), shear modulus (G), Voigt (G_V) and Reuss (G_R) polycrystalline elastic modulus, and B/G ratio are given in Table 3. The ratio of B/G has been calculated to investigate the ductility and brittleness properties of Ru_2ZnGa. This ratio can be considered as an empirical criterion of the extent of the fracture range in the materials [13]. If the ratio of B/G is higher than 1.75, then the material behaves in a ductile manner. If it is less than 1.75, then that material demonstrates brittleness. The B/G value is 2.25 for this alloy. This indicates the ductile nature of this material.

Table 3. The calculated bulk modulus (B, in GPa), shear modulus (G, in GPa), and ratio B/G for Ru_2ZnGa.

Material	B (GPa)	G_V (GPa)	G_R (GPa)	G (GPa)	B/G
Ru_2ZnGa	209.44	102.39	83.64	93.01	2.25

Figure 4 shows the calculated phonon dispersion branches with the inclusion of partial and total density of states of Ru_2ZnGa alloy. As expected for the $L2_1$-type crystal structure with four atoms in the primitive cell, the phonon dispersion curve exhibits 12 branches, three acoustic and nine optical branches. All phonon modes exhibit positive branches, suggesting that this alloy is dynamically stable. The zone-centered optic phonon modes are found as 4.464, 6.425 and 7.147 THz for Ru_2ZnGa. The partial and total density of states show that Ru, Zn, and Ga atoms vibrate in the acoustic and optical regions.

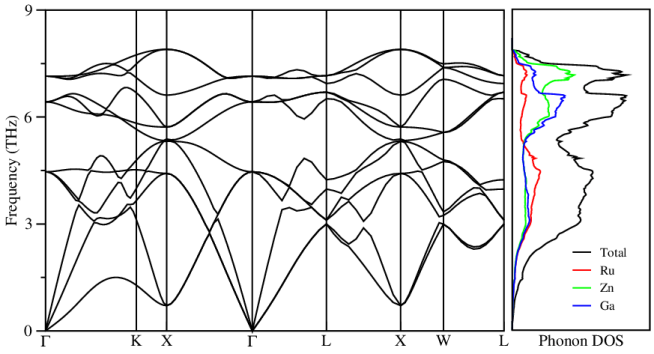


Figure 4. *The calculated phonon dispersions and partial density of states for Ru_2ZnGa.*

4. Conclusion

In this research, electronic band structure, vibrational and some mechanical properties of Ru_2ZnGa which crystallize in fcc structure with space group Fm-3m and 225 space number, have been examined in detail. The calculated spin-polarized electronic band structures for this alloy show that this material has a metallic character. The calculated elastic constants show that this alloy is stable mechanically. We have also calculated the phonon frequencies along the high symmetry directions. The calculated phonon dispersion curves of Ru_2ZnGa alloy confirm that this alloy is dynamically stable in the $L2_1$ structure without any imaginary phonon frequencies.

References:

[1] HEUSLER, F., Verhandlugen der Deutschen Physikalischen Gesellschaft, sec. 5, pp. 219, 1903.
[2] GALANAKİS, I., MAVROPOULOS, P., DEDERİCHS, P.H., "Electronic structure and Slater–Pauling behaviour in half-metallic Heusler alloys calculated from first principles", Journal of Physics D: Applied Physics, 39(5), 765–775, 2006.
[3] BERGMANN, A., GRABİS, J., TOPERVERG, B. P., LEİNER, V., WOLFF, M., ZABEL, H., WESTERHOLT, K., "Antiferromagnetic dipolar ordering in [Co2MnGe⁄V] N multilayers", Physical Review B, 72(21), 214403, 2005.
[4] GRABİS, J., BERGMANN, A., NEFEDOV, A., WESTERHOLT, K., ZABEL, H., "Element-specific x-ray circular magnetic dichroism of Co2MnGe Heusler thin films", Physical Review B, 72(2), 024437, 2005.

[5] FUJİİ, S., SUGİMURA, S., ASANO, S., "Hyperfine fields and electronic structures of the heusler alloys co2mnx (x= al, ga, si, ge, sn)", Journal of Physics: Condensed Matter, 2(43), 8583, 1990.
[6] GİLLEßEN, M., DRONSKOWSKİ, R., Maßgeschneidertes und Analytik-Ersatz: über die quantenchemischen Untersuchungen einiger ternärer intermetallischer Verbindungen (No. RWTH-CONV-113777). Fachgruppe Chemie, 2010.
[7] VANDERBİLT, D., "Soft self-consistent pseudopotentials in a generalized eigenvalue formalism", Physical review B, 41(11), 7892, 1990.
[8] GIANNOZZI, P., BARONI, S., BONINI, N., CALANDRA, M., CAR, R., CAVAZZONI, C., CERESOLI, D., CHIAROTTI, G.L., COCOCCIONI, M., DABO, I., DAL CORSO, A., FABRIS, S., FRATESI, G., DE GIRONCOLI, S., GEBAUER, R., GERSTMANN, U., GOUGOUSSIS, C., KOKALJ, A., LAZZERI, M., MARTIN-SAMOS, L., MARZARI, N., MAURI, F., MAZZARELLO, R., PAOLINI, S., PASQUARELLO, A., PAULATTO, L., SBRACCIA, C., SCANDOLO, S., SCLAUZERO, G., SEITSONEN, A.P., SMOGUNOV, A., UMARI, P., WENTZCOVITCH, R.M., "QUANTUM ESPRESSO : a modular and open-source software project for quantum simulations of materials", Journal of physics: Condensed matter, 21, 395502, 2009.
[9] PERDEW, J.P., BURKE, K., ERNZERHOF, M., "Generalized gradient approximation made simple", Physical review letters, 77(18), 3865, 1996.
[10] MONKHORST, H.J., PACK, J.D., "Special points for Brillouin-zone integrations", Physical review B, 13(12), 5188, 1976.
[11] BARONİ, S., GİANNOZZİ, P., TESTA, A., "Green's-function approach to linear response in solids", Physical Review Letters, 58(18), 1861, 1987.
[12] BORN, M., HUANG, K., Dynamical theory of crystal lattices, Clarendon press, 1954.
[13] PUGH, S.F., "XCII. Relations between the elastic moduli and the plastic properties of polycrystalline pure metals", The London, Edinburgh, and Dublin Philosophical Magazine and Journal of Science, 45(367), 823-843, 1954

6th International Conference on Materials Science and Nanotechnology For Next Generation (MSNG2019)
October 16-18, 2019, Niğde, TURKEY (ORAL FULL TEXT)

First principles study of structural, electronic and elastic properties of perovskite $MgZrO_3$ in cubic phase

Abdullah CANDAN*, Cihan KÜRKÇÜ**, Ahmet İYİGÖR*

* Department of Machinery and Metal Technology, Kırşehir Ahi Evran University, Turkey
** Department of Electronics and Automation, Kırşehir Ahi Evran University, Turkey

First principles study of structural, elastic, electronic properties of the cubic perovskite $MgZrO_3$ have been investigated using the pseudo-potential plane wave method within the generalized gradient approximation (GGA). Structural properties are calculated and the thermodynamics stability of $MgZrO_3$ compound in the cubic perovskite structure has been established with respect to formation enthalpy. Electronic band structure show that this compound is indirect energy band gap (Γ-M) semiconductor. The elastic constants are calculated using the stress-strain technique. Since the calculated elastic constants of this material comply with mechanical stability criterions, $MgZrO_3$ compound is mechanically stable in the cubic perovskite structure. Besides, the shear modulus, B/G ratio, Young's modulus, Poisson's ratio and anisotropic factor are estimated in the framework of the Voigt-Reuss-Hill approximation for ideal polycrystalline $MgZrO_3$ compound.

Keywords: Semiconductor, First-principle calculations, Elastic Properties.

Corresponding author: acandan@ahievran.edu.tr

1. Introduction

The ABO_3 type perovskites are of exceptional importance not
only due to their applications in modern technologies but also for investigating the phase transitions. Recently, perovskites have been investigated with great attention both theoretically as well as experimentally in physics, chemistry, and material science because of their applications in science and technology. The perovskites especially oxides based on general formula ABO_3 have attracted researchers all over the globe as a result of their remarkable properties like multi-ferriocity, superconductivity, thermoelectricity, solid-oxide fuel cells, half-metallicity, ferromagnetism. In this study, we focus on the comparatively less studied $MgZrO_3$ perovskite. This studied perovskite is widely known for thermal barrier coatings owing to their low thermal expansion. Moreover, this perovskite $MgZrO_3$ is used as a base catalyst, due to their high activity and durability in order to produce an efficient biodiesel catalyst. The electronic, optical and thermoelectric properties of the $MgZrO_3$ compound have been investigated theoretically by Noor and co-workers [1] using Wien2k. They calculated the indirect bandgap value for $MgZrO_3$ perovskite as 0.77 eV. The mechanical properties of this material have never been studied. In this investigation, we have made an attempt to discuss and evaluate the structural, electronic, particularly elastic properties of $MgZrO_3$ in the framework of the density functional theory (DFT).

2. Theoretical details

In the present work, the first-principles calculations are performed within quantum-ESPRESSO code based on the density function theory (DFT) [2, 3]. The exchange–correlation energy functional were treated within the generalized gradient approximation (GGA) developed by Perdew–Burke–Ernzerhof (PBE) [4]. The convergence of the performed calculations with respect to the plane-wave cut-off and k-points mesh, were carefully tested. The energy cut-off of the plane-wave basis was of 600 Ry. The sampling of the Brillouin zone was of 12x12x12 k-points with a Monkhorst–Pack grid [5]. Integration up to

the Fermi surface was performed using the smearing technique [6] with smearing parameter 0.02 Ry.

3. Results and discussion

$MgZrO_3$ perovskite has been reported in cubic phase with a lattice constant of 4.08 Å [1]. The Mg atoms are located at corners (0, 0, 0), Zr at center (0.5, 0.5, 0.5) and O atoms are sited at face centers (0.5, 0.5, 0), (0.5, 0, 0.5), (0, 0.5, 0.5) of cubic unit cell (see Figure 1).

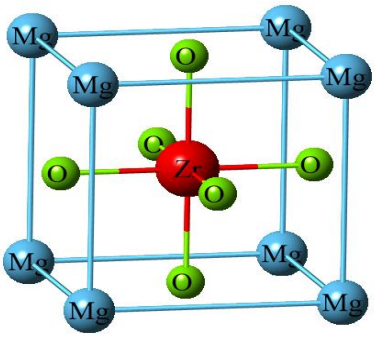


Figure 1. *Crystal structure of perovskite $MgZrO_3$ in cubic phase.*

We also tabulated lattice constant (a_0), equilibrium lattice volumes (V_0) and formation enthalpy (ΔH_f) of the $MgZrO_3$ perovskite in Table 1. Our results have been compared with the available result in the literature [1]. There is a good agreement between calculated lattice constant, formation enthalpy for $MgZrO_3$ and that previously reported.

Table 1. Calculated lattice constant (a_0), equilibrium lattice volumes (V_0) and formation enthalpy (ΔH_f) of $MgZrO_3$.

Compound	Ref.	a_0 (Å)	V_0 (Å^3)	ΔH_f (eV/atom)
$MgZrO_3$	Present	4.106	69.229	-2.522
	[1]	4.08	-	-2.94

In order to investigate electronic nature of our material, the energy band structure within GGA (Generalized Gradient Approximation) for $MgZrO_3$ has been computed and then, plotted along the high-symmetry directions in the Brillouin zone as presented in Figure 2. The valence band maximum (VBM) occur at M point and the conduction band minimum (CBM) occur at Γ point, making $MgZrO_3$ compound to be a indirect band gap material (Γ–M).

Also, the determined total (TDOS) and orbital projected partial density of electronic states (PDOS) of this material have been shown in Figure 3. In the valence band which is below Fermi level (E_F), the bands are mainly d states of Zr atoms and p states of O atoms. The bands above the Fermi level are mainly d states of Zr atoms, p states of O atoms and s states of Mg atoms.

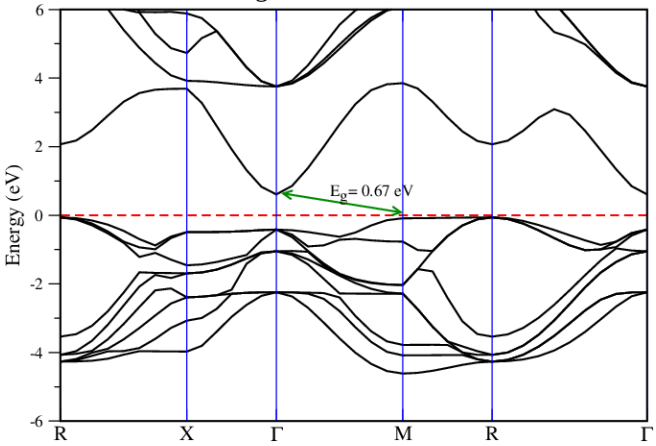


Figure 2. *Electronic band structures of the $MgZrO_3$.*

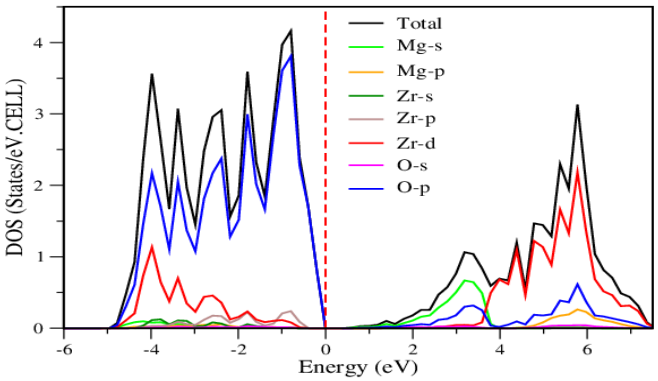


Figure 3. *Total and PDOS of the $MgZrO_3$.*

For any cubic crystal, there are three (C_{11}, C_{12} and C_{44}) independent elastic constants [7] which have been tabulated for $MgZrO_3$ in Table 2.

Table 2. Calculated elastic constants (C_{ij}).

Compound	Ref.	C_{11} (GPa)	C_{12} (GPa)	C_{44} (GPa)
$MgZrO_3$	Present	325.89	75.48	44.26

We have employed Born-Huang criteria [8] to designate mechanical stability of our crystal. These criteria are given by, for a cubic crystal,

$$C_{11} > 0, \quad C_{11} - C_{12} > 0, \quad B > 0, \quad C_{44} > 0 \qquad (1)$$

The obtained elastic constants for the $MgZrO_3$ perovskite respond to these mechanical stability criterions, thus showing that this material is mechanically stable.

Besides, Bulk modulus (B), Shear modulus (G), Voigt (G_V) and Reuss (G_R) polycrystalline elastic modulus, and B/G ratio are given in Table 3. The ratio of B/G has been calculated to investigate the ductility and brittleness properties of this compound. This ratio can be considered as an empirical criterion of the extent of the fracture range in the materials [9]. If the ratio of B/G is higher than 1.75, then the material behaves in a ductile manner. If it is less than 1.75, then that material demonstrates brittleness. The B/G value is 2.33 for this alloy. This indicates the ductile nature of this material.

Table 3. The calculated Bulk modulus (B, in GPa), Shear modulus (G, in GPa), and ratio B/G for $MgZrO_3$.

Compound	B	G_V	G_R	G	B/G
$MgZrO_3$	158.95	76.64	59.70	68.17	2.33

The Poisson's ratio (ν) and Young's modulus (E) are very important properties for industrial applications. E, the ratio between stress and strain, is required to provide information about the measure of stiffness of the solids. The E value at Table 4 indicates that this material can be counted as stiff materials. ν provides more information about the characteristics of bonding forces than any of the other elastic properties. The lower limit and upper limit of ν are given 0.25 and 0.5 for central forces in solids, respectively [10]. Calculated ν value is equal to 0.31. The present result shows that the inter-atomic forces for $MgZrO_3$ is predominantly central forces. The anisotropy shear factor vital mechanical parameter since it is defined to measure elastic anisotropy of a compound. Calculated anisotropy shear factors from the Table 4 indicates that $MgZrO_3$ has anisotropic character.

Table 4. The calculated Young's modulus (E, in GPa), Poisson's (ν) ratio, and anisotropy shear factor (A) for $MgZrO_3$.

Compound	E	ν	A
$MgZrO_3$	178.93	0.31	0.354

4. Conclusion

The optimized lattice constant of $MgZrO_3$ is 4.106 Å. This compound indicates semiconductur character and thus it promising candidate for electronics application. Also, obtained indirect band gap value for $MgZrO_3$ is in accordance with the literature. On the other hand, the obtained elastic constants show that this compound have mechanical stability in cubic Pm-3m crystal structure since they obey the Born-Huang criterions. The calculated B/G ratio indicates that this material is ductile.

References:

[1] NOOR, N.A., RASHİD, M., MAHMOOD, Q., HAQ, B.U., NAEEM, M.A., LAREF, A., "Optoelectronic pressure dependent study of MgZrO3 oxide and ground state thermoelectric response using Ab-initio calculations", Opto-Electronics Review, 27(2), 194-201, 2019.
[2] VANDERBİLT, D., "Soft self-consistent pseudopotentials in a generalized eigenvalue formalism", Physical review B, 41(11), 7892, 1990.
[3] GIANNOZZI, P., BARONI, S., BONINI, N., CALANDRA, M., CAR, R., CAVAZZONI, C., CERESOLI, D., CHIAROTTI, G.L., COCOCCIONI, M., DABO, I., DAL CORSO, A., FABRIS, S., FRATESI, G., DE GIRONCOLI, S., GEBAUER, R., GERSTMANN, U., GOUGOUSSIS, C., KOKALJ, A., LAZZERI, M., MARTIN-SAMOS, L., MARZARI, N., MAURI, F., MAZZARELLO, R., PAOLINI, S., PASQUARELLO, A., PAULATTO, L., SBRACCIA, C., SCANDOLO, S., SCLAUZERO, G., SEITSONEN, A.P., SMOGUNOV, A., UMARI, P., WENTZCOVITCH, R.M., "QUANTUM ESPRESSO : a modular and open-source software project for quantum simulations of materials", Journal of physics: Condensed matter, 21, 395502, 2009.
[4] PERDEW, J.P., BURKE, K., ERNZERHOF, M., "Generalized gradient approximation made simple", Physical review letters, 77(18), 3865, 1996.
[5] MONKHORST, H.J., PACK, J.D., "Special points for Brillouin-zone integrations", Physical review B, 13(12), 5188, 1976.
[6] METHFESSEL, M.P.A.T., PAXTON, A.T., "High-precision sampling for Brillouin-zone integration in metals", Physical Review B, 40(6), 3616, 1989.
[7] MOUHAT, F., COUDERT, F.X., "Necessary and sufficient elastic stability conditions in various crystal systems", Physical review B, 90(22), 224104, 2014.
[8] BORN, M., HUANG, K., Dynamical theory of crystal lattices, Clarendon press, 1954.

[9] PUGH, S.F., "XCII. Relations between the elastic moduli and the plastic properties of polycrystalline pure metals", The London, Edinburgh, and Dublin Philosophical Magazine and Journal of Science, 45(367), 823-843, 1954.

[10] BANNİKOV, V.V., SHEİN, I.R., IVANOVSKİİ, A.L., "Electronic structure, chemical bonding and elastic properties of the first thorium-containing nitride perovskite TaThN3" physica status solidi (RRL)–Rapid Research Letters, 1(3), 89-91, 2007.

6th International Conference on Materials Science and Nanotechnology For Next Generation (MSNG2019)
October 16-18, 2019, Niğde, TURKEY (ORAL FULL TEXT)

First Principles Simulation of Pressure-Induced Phase Transition in Li_2Se

C. Kurkcu[1], A. Iyigor[2], and A. Candan[2]

[1]Department of Electronic and Automation, Kırşehir Ahi Evran University, Kırşehir, Turkey
[2]Department of Machinery and Metal Technology, Kırşehir Ahi Evran University, Kırşehir, Turkey

An ab initio constant pressure technique is carried out to explore the behavior of Li_2Se under high pressure. We have studied the structural properties of Li_2Se using density functional theory (DFT) under pressure up to 250 GPa. For the exchange-correlation energy, we used the Generalized Gradient Approximation (GGA) of Perdew-Burke-Ernzerhof [1]. Li_2Se crystallizes in NaCl-type structure with space group $Fm\bar{3}m$ under ambient conditions. This structure of this material undergoes a structural phase transformation to tetragonal structure with space group I4/mmm at a hydrostatic pressure of 90 GPa. This phase transformation is also studied by total energy and enthalpy calculations.

Keywords: Phase Transition, Enthalpy, ab-initio

Corresponding autor: ckurkcu@ahievran.edu.tr

1. Introduction

Li_2Se is an important material which takes attention thanks to its wide range of applications in solid-state batteries, fuel cells or solid-state gas detectors and photo-emissive ultraviolet light materials and so on [1-3]. This material is expected to have technological properties hence a number of studies on it have been carried out [4-12]. The Li_2Se crystallizes in a cubic-type structure with space group $Fm\bar{3}m$ at ambient conditions. Additionally, some studies have been made on other physical properties of Li2Se. Eithiraj et al. [13] and Seifert-Lorenz and Hafner [14] have studied the electronic band structure of Li_2Se using the Tight-Binding Linear Muffin-Tin Orbital method. In this study, we calculated structural phase transition in Li_2Se and predicted phase transition from cubic structure to tetragonal structure under hydrostatic pressure of 90 GPa.

2. Calculation details

The structural properties of Li_2Se were carried out within Density Functional Theory (DFT) calculations using Siesta software package [15]. The calculations were performed using an GGA-PBE exchange-correlation functional [16]. We have used Troullier-Martins type norm-conserving pseudo-potential for Li and Se atoms [17]. In all calculations were conducted using double-zeta plus polarized (DZP) basis sets of localized atomic orbitals. The energy mesh cut-off, which corresponds to the spacing of the real space grid used to calculate the Hartree, exchange, and correlation contribution to the total energy and Hamiltonian, was set to be 350 Rydberg (Ry). Li_2Se was modelled using **3x2x1** cells with periodic boundary condition for 72 atoms supercells. The Brillouin−zone integration was performed with 8×8×8 and 8×8×6 k−point meshes for cubic and tetragonal structures of Li_2Se, respectively [18]. Structural optimizations were performed via the Parrinello-Rahman technique until the residual force acting on all atoms were smaller than 0.01 eV/Å and pressure is gradually increased by 10 GPa through this method to the system. For analyze each minimization step, we used the KPLOT program and the RGS algorithm that give detailed information about the space groups, atomic positions and lattice parameters of an analyzed structure [19, 20].

3. Results and discussion

The calculations of equilibrium lattice parameters of cubic phase of Li_2Se were performed initially by relaxing 72 atoms supercell at zero pressure. The equilibrium unit cell lattice constant is found to be a = b=c=6.0198 Å. In order to determine the phase transition of Li_2Se, the

pressure−volume relation is obtained by using the constant pressure ab initio simulation. The P−V curve is given in Fig. 1. A sharp change is observed in volume as the pressure increases from 80 GPa to 90 Gpa. This indicates a first order pressure induced phase transition in Li_2Se.

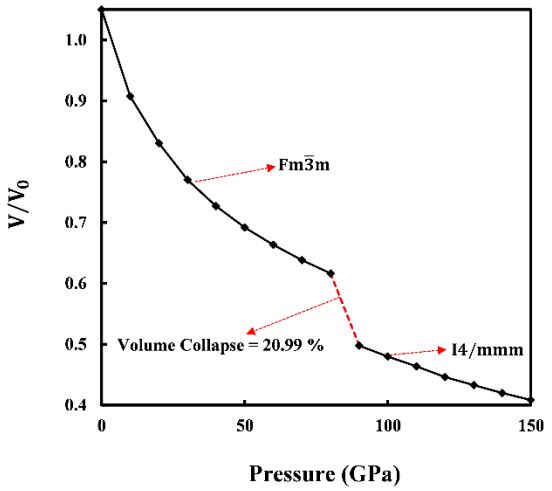


Figure 1. The volume change of the simulation cell as a function of pressure.

The structural analysis make known that the cubic structure transforms to tetragonal structure at 90 GPa pressure as shown in Fig. 2. This result shows that the *ab initio* technique successfully produces the experiment observed high-pressure phase of Li_2Se with an overvalued transition pressure.

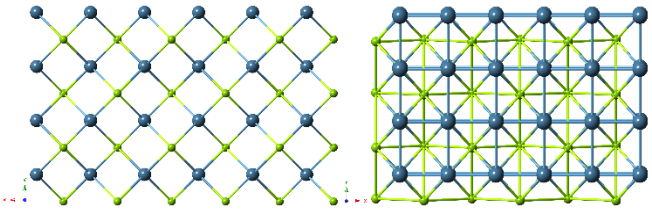


Figure 2. The crystal structures of Li_2Se: cubic structure (left) and tetragonal structure (right).

The results suggest that ab inito technique can successfully generate phase transitions of Li_2Se under high pressure. However, the calculated phase transition pressure is slightly higher than the experimental results. This is due to using a defect free structure with a finite volume where the phase transition occurs over the whole simulation cell instead of nucleation and buildup. Thus, when the particular conditions such as finite size of the simulation cell, the time scale of simulations, etc. are considered, such an overestimated transition pressure is anticipated. In order to avoid this situation, energy−volume calculations are considered to study the stability of cubic and tetragonal structures since the thermodynamic theorem does not take into account the possible existence of such an activation energy barrier separating the two structural phases. The result is presented in Fig. 3.

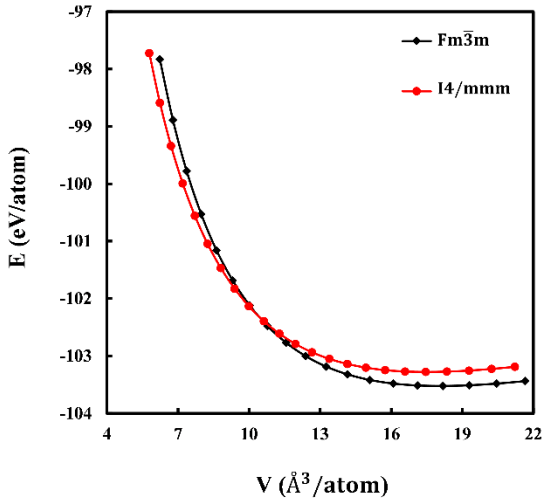


Figure 3. The energy-volume curves of structural phases of Li_2Se.

The energy–volume datas are fitted to the third-order Birch–Murnaghan equation of state. At the phase transition, the two phases have the same enthalpy ($H= E_{tot} + PV$, where $P =-dE_{tot}/dV$ is obtained by direct differentiation of the calculated the energy–volume curves), therefore the transition pressure can be easily determined by equating the enthalpy of the two phases. The computed enthalpy curve of the cubic and tetragonal structures as a function of pressure is shown in Fig. 4. As can be seen in Fig. 4, transition pressure was obtained at about 70 GPa.

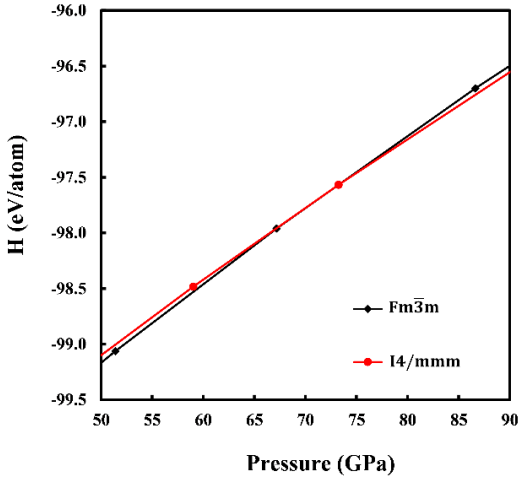


Figure 4. The enthalpy curves of structural phases of Li_2Se as a function of pressure.

4. Conclusion

In this study, ab-initio calculations were performed to examine phase transition behavior of Li_2Se under high pressure with SIESTA. As a result of the calculations, a first-order phase transition was observed from the cubic $Fm\bar{3}m$ phase to the tetragonal $I4/mmm$ phase at 90 GPa. We also obtained lattice parameters that are in good agreement with other studies.

References:

[1] D. Bisero, A. di Bona, P. Paradisi, S. Valeri, K 2 Te photocathode growth: A photoemission study, Journal of Applied Physics 87(1) (2000) 543-548.
[2] A. Piccioli, R. Pegna, I. Fedorko, M. Giunta, N. Malakhov, A. Menzione, F. Raffaelli, A. Braem, E. Chesi, C. Joram, Characterization of a potted 5-in. HPD with Rb2Te photocathode, Nuclear Instruments and Methods in Physics Research Section A: Accelerators, Spectrometers, Detectors and Associated Equipment 518(1-2) (2004) 602-604.
[3] C. Joram, Large area hybrid photodiodes, Nuclear Physics B-Proceedings Supplements 78(1-3) (1999) 407-415.
[4] A. Koh, Systematic variation between cohesive energy and a lattice ratio in alkali chalcogenide crystals, physica status solidi (b) 210(1) (1998) 31-33.
[5] R. Singh, V. Jain, J. Shanker, Relative Stability and Structural Phase Transitions in Alkaline Earth Chalcogenide Crystals, physica status solidi (b) 111(2) (1982) 519-523.
[6] S. Chaturvedi, S. Sharma, P. Paliwal, M. Kumar, Analysis of Crystal Binding and Structural Phase Transition in Alkaline-Earth and Alkali Chalcogenides, physica status solidi (b) 156(1) (1989) 171-179.
[7] F. Kalarasse, B. Bennecer, Elastic properties and lattice dynamics of alkali chalcogenide compounds Na2S, Na2Se and Na2Te, Computational Materials Science 50(5) (2011) 1806-1810.
[8] K. Stöwe, Polymorphic forms of Rb2Te: in-situ high-pressure DAC X-ray diffraction investigations and structure modelling with CASTEP, Zeitschrift für Kristallographie-Crystalline Materials 219(6) (2004) 359-369.
[9] J. Songster, A. Pelton, The li-Te (lithium-tellurium) system, Journal of phase equilibria 13(3) (1992) 300-303.
[10] A. Pelton, A. Petric, The Na-Te (Sodium-Tellurium) System, Journal of Phase Equilibria 11(5) (1990) 447-451.
[11] A. Petric, A. Pelton, The K-Te (Potassium-Tellurium) system, Journal of Phase Equilibria 11(5) (1990) 443-447.
[12] J. Sangster, A. Pelton, The Rb-Te (rubidium-tellurium) system, Journal of phase equilibria 18(4) (1997) 394.
[13] R. Eithiraj, G. Jaiganesh, G. Kalpana, First-principles study of electronic structure and ground-state properties of alkali-metal selenides and tellurides (M2A)[M: Li, Na, K; A: Se, Te], International Journal of Modern Physics B 23(25) (2009) 5027-5037.
[14] K. Seifert-Lorenz, J. Hafner, Crystalline intermetallic compounds in the K-Te system: The Zintl-Klemm principle revisited, Physical Review B 66(9) (2002) 094105.
[15] P. Ordejón, E. Artacho, J.M. Soler, Self-consistent order-N density-functional calculations for very large systems, Physical Review B 53(16) (1996) R10441.
[16] J. Perdew, K. Burke, M. Ernzerhof, Perdew, burke, and ernzerhof reply, Physical Review Letters 80(4) (1998) 891.
[17] N. Troullier, J.L. Martins, Efficient pseudopotentials for plane-wave calculations, Physical review B 43(3) (1991) 1993.
[18] H.J. Monkhorst, J.D. Pack, Special points for Brillouin-zone integrations, Physical review B 13(12) (1976) 5188.
[19] R. Hundt, J.C. SchoÈn, A. Hannemann, M. Jansen, Determination of symmetries and idealized cell parameters for simulated structures, Journal of applied crystallography 32(3) (1999) 413-416.
[20] A. Hannemann, R. Hundt, J. Schön, M. Jansen, A new algorithm for space-group determination, Journal of applied crystallography 31(6) (1998) 922-928.

6th International Conference on Materials Science and Nanotechnology For Next Generation (MSNG2019)
October 16-18, 2019, Niğde, TURKEY (ORAL FULL TEXT)

Investigation of Some Physical Properties of NaS: An Ab-Initio Study

C. Kurkcu[1], A. Iyigor[2], and A. Candan[2]

[1]Department of Electronic and Automation, Kırşehir Ahi Evran University, Kırşehir, Turkey
[2]Department of Machinery and Metal Technology, Kırşehir Ahi Evran University, Kırşehir, Turkey

Some physical properties of NaS were studied using the density functional theory with the generalized gradient approximation (GGA) of Perdew-Burke-Ernzerhof under high hydrostatic pressure. To apply pressure to the system, we used the Parrinello-Rahman method. NaS crystallizes in hexagonal structure with space group $P6_3/mmc$ at ambient conditions. This material undergoes a structural phase transformation from this phase to orthorhombic structure with space group Pmmm at 50 GPa hydrostatic pressure.

Keywords: Phase Transition, Enthalpy, Ab-initio.

Corresponding author: ckurkcu@ahievran.edu.tr

1. Introduction

NAS (Sodium-Sulfur (NaS) batteries) battary is the world's first commercial megawatt-class battery that can store large amounts of energy for hours. The NAS battery system has more capacity, higher energy density and longer lifetime than other battery technologies. Because of these properties, it is more useful for stationary applications compared to lithium-ion batteries, which are suitable for providing high power, which is widely used today. The NAS battery system supports the integration of variable renewable energy sources such as wind and solar into the grid. In addition, NAS battery helps to reduce energy costs and environmental burden. Thanks to its numerous superior features, NaS batteries are very popular today. Within the scope of the literature studies, there are almost no studies on the physical properties of this material. Therefore, in order to cover this deficiency in the literature, we studied some physical properties of NaS under high pressure. NaS crystallizes in hexagonal structure with space group $P6_3/mmc$ at ambient conditions. We observed that this hexagonal type structure transforms into an orthorhombic structure with space group Pmmm under 50 GPa pressure.

2. Calculation details

All the DFT calculations were performed with Perdew-Burke-Ernzerhof (PBE) generalized gradient approximation (GGA) [1] functional using the ab initio program SIESTA [2]. A Parrinello-Rahman technique was used for minimization of geometries under a constant pressure. A cutoff energy of 350 Ryd was used in all calculations.

The self-consistent “norm-conserving” pseudopotentials were generated using the Troullier-Martins scheme [3]. In the calculations, double-zeta plus polarized orbitals were used for a real space grid. We used Γ-point sampling for the Brillouin-zone integration. For the energy-volume calculations, we considered the unit cell of $P6_3/mmc$ and Pmmm phases. The Brillouin-zone integration was performed with $8 \times 8 \times 4$, and $8 \times 8 \times 6$ k-point mesh for $P6_3/mmc$ and Pmmm phases of NaS following the convention of Monkhorst and Pack [4]. We used these k-point meshes for the energy-volume calculations. The simulation cell consist of 144 atoms with periodic boundary conditions. These structures were allowed to relax and to find their equilibrium volumes and lowest energies for each value of the applied pressure by optimizing their lattice vectors and atomic positions. Geometries were relaxed until the forces on all atoms were less than 0.01 eV $Å^{-1}$ and the stress tolerances were getting less until 0.5 GPa.

Parrinello-Rahman technique was used to apply external pressure to the system. Pressure was increased with an increment of 10 GPa. In order to analyze each minimization step, KPLOT program and RGS algorithm was used [5, 6] that gives elaborated knowledge about cell parameters, atomic positions and space group of an analyzed structure.

3. Results and discussion

NaS crystallizes in a hexagonal-type structure at ambient conditions. We studied this structure under the hydrostatic pressure up to 100 GPa. Pressure was gradually increased beginning from the 0 GPa and the structure of NaS at each applied pressure was analyzed via the KPLOT program. NaS undergoes a phase transformation from the hexagonal-type structure with space group $P6_3/mmc$ to the orthorhombic structure with space group Pmmm at 50 GPa. The crystal structures of these two phase at 0 GPa, and 50 GPa are depicted in Fig. 1.

We plotted pressure-volume relation to determine the thermodynamic nature of the phase transitions for NaS in Fig. 2. As seen in Fig. 2, the volume decrease monotonically and indicate the phase transitions at 50 GPa. It is clear that this discontinuity indicates the first order phase transitions.

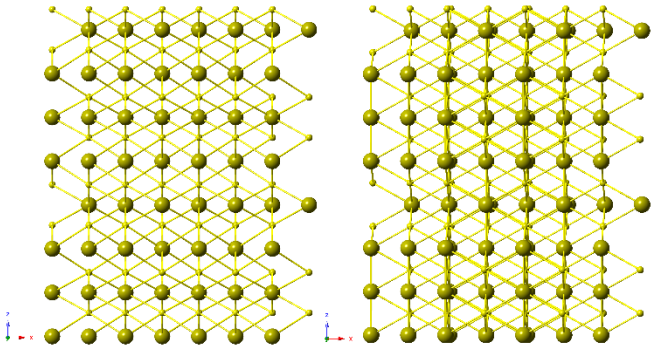


Figure 1. The crystal structures of NaS: $P6_3/mmc$ phase (left) and Pmmm phase (right).

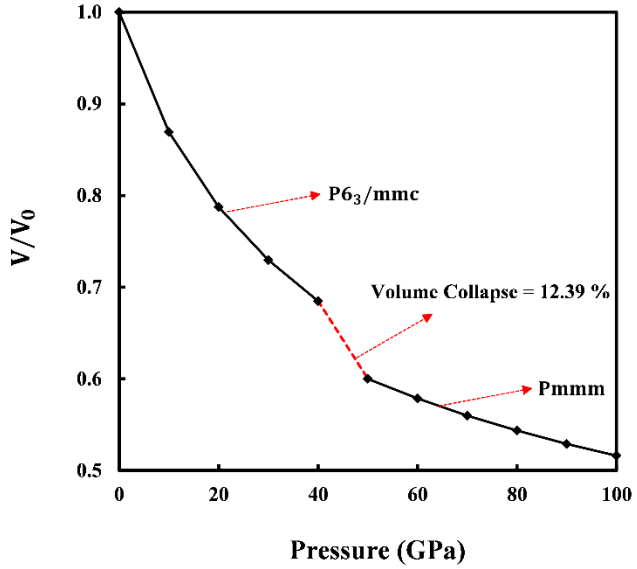


Figure 2. The volume change of the simulation cell as a function of pressure.

Transition pressures obtained in constant-pressure simulations are noticeably larger than the experimental results. This result is anticipated because the simulation conditions such as loading rate, the limited box size, the lack of defects in the simulated structures and the use of periodic boundary conditions are significantly different from the experimental ones. As a result, the systems have to cross a significant energy barrier to transform from one phase to another phase. We then take the energy-volume computations into account so as to study the stability of high pressures phases of NaS. The total energy as a function of volume is depicted in Fig. 3.

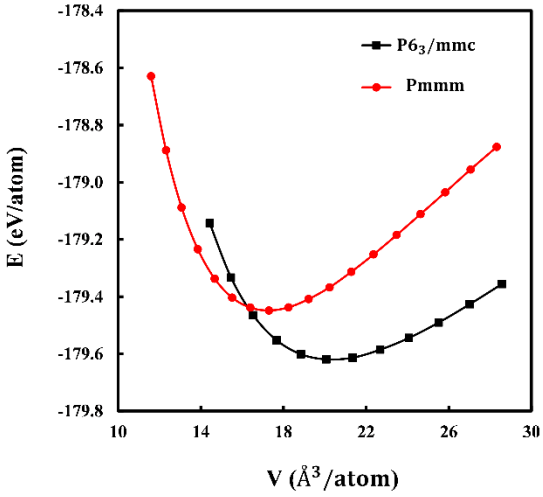


Figure 3. The energy-volume curves of structural phases of NaS.

We used the Gibbs free energy (G) in order to calculate the phase transition pressures from $P6_3/mmc$ to Pmmm phase at 0 K. The Gibbs free energy is given by Eq. 1.

$$G = E_{tot} + PV - TS \quad (1)$$

Where E is the total energy, P is the pressure, V is the volume and S is the entropy. We performed our calculations at 0 K, therefore, the TS term is neglected. Thus, G equals to the enthalpy (H) given by Eq. 2.

$$H = E_{tot} + PV \quad (2)$$

where $P = -dE_{tot}/dV$.

The intersection of two enthalpy curves shows a transition pressure between two phases. The phase transition pressures from $P6_3/mmc$ to Pmmm phase is found to be about 12 GPa, and the related enthalpy versus pressure graphs is depicted in Fig. 4.

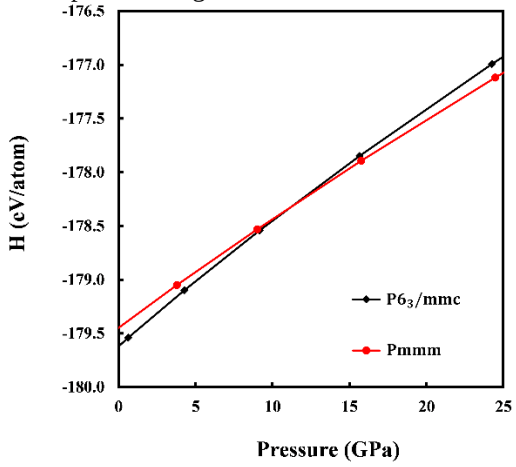


Figure 4. The enthalpy curves of structural phases of NaS as a function of pressure.

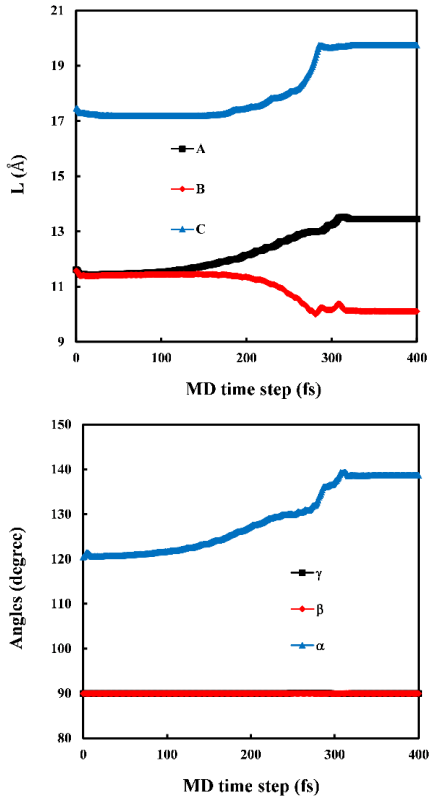


Figure 5. The behavior of the simulation cell lengths (top) and angles (bottom) as function of MD time steps at 50 GPa

As a next step, we studied the atomic movement during the phase transformation by analyzing the modification of the simulation cell. We plot the variation of the simulation cell lengths and angles as a function of minimization step at 50 GPa in Fig. 5. These cell vectors are expressed as A, B, and C are initially along the [100], [010] and [001] directions, respectively. The magnitudes of these vectors are plotted in Fig. 5.

4. Conclusion

In summary, the structural properties of NaS under high hydrostatic pressure ranging from 0 to 100 GPa at zero temperature have been studied using ab initio constant pressure simulations. We obtained phase transition sequence $P6_3/mmc \rightarrow Pmmm$. According to the enthalpy calculations, the transition pressure was estimated as 12 GPa.

References:

[1] J.P. Perdew, K. Burke, M. Ernzerhof, Generalized gradient approximation made simple, Physical review letters 77(18) (1996) 3865.
[2] P. Ordejón, E. Artacho, J.M. Soler, Self-consistent order-N density-functional calculations for very large systems, Physical Review B 53(16) (1996) R10441.
[3] N. Troullier, J.L. Martins, Efficient pseudopotentials for plane-wave calculations, Physical review B 43(3) (1991) 1993.
[4] H.J. Monkhorst, J.D. Pack, Special points for Brillouin-zone integrations, Physical review B 13(12) (1976) 5188.
[5] R. Hundt, J.C. SchoÈn, A. Hannemann, M. Jansen, Determination of symmetries and idealized cell parameters for simulated structures, Journal of applied crystallography 32(3) (1999) 413-416.
[6] A. Hannemann, R. Hundt, J. Schön, M. Jansen, A new algorithm for space-group determination, Journal of applied crystallography 31(6) (1998) 922-928.

6th International Conference on Materials Science and Nanotechnology For Next Generation (MSNG2019)
October 16-18, 2019, Niğde, TURKEY (ORAL FULL TEXT)

Structural phase transition and electronic properties of $LiBH_4$ under high pressure

C. Kurkcu[1], A. Iyigor[2], and A. Candan[2]

[1]Department of Electronic and Automation, Kırşehir Ahi Evran University, Kırşehir, Turkey
[2]Department of Machinery and Metal Technology, Kırşehir Ahi Evran University, Kırşehir, Turkey

We study the pressure-induced phase transition of $LiBH_4$ using a constant pressure ab initio technique with Generalized Gradient Approximation of Perdew-Burke-Ernzerhof. $LiBH_4$ crystallizes under ambient conditions in orthorhombic structure (space group Pnma). We predict the structural phase transformations from this structure to monoclinic structure (space group $P2_1/c$) with the application of hydrostatic pressure. Also, we study the electronic properties of $LiBH_4$ and some physical properties such as the lattice constants, the bulk modulus, the pressure derivative of the bulk modulus, and equilibrium energies. Furthermore, we study these phase transitions using the total energy and enthalpy calculations.

Keywords: Phase Transition, Enthalpy, Ab-initio, Electronic properties.

Corresponding author: ckurkcu@ahievran.edu.tr

1. Introduction

The search for safe, economic, and clean energy has become a major problem with the decrease in unsustainable fuel supplies and increase in world demand for energy. Hydrogen can be an ideal energy carrier, but storage is the main problem the limits its widespread use [1, 2]. Therefore, obtaining practical storage materials with high hydrogen content is the key issue for hydrogen-based propulsion [3]. Recently, interest on complex hydrides (alanates and borohydrides) has increased considerably due to their possible application as hydrogen storage materials. Furthermore, the changes in the structure of these materials under high pressure have been studied in the past decades. Vajeeston et al. predicted a large volume collapse of their structures under high pressure for $LiAlH_4$ and $NaAlH_4$ [4, 5] Talyzin et al. calculated high pressure phase transition in $LiBH_4$ by y Raman spectroscopy
and X-ray diffraction [6] .

2. Calculation details

The calculations in the present work were carried out in the frame of density-functional theory (DFT) calculations with the *ab initio* program SIESTA [7]. Generalized Gradient approximation (GGA) using the Perdew-Burke-Ernzerhof (PBE) functional [8]was used for the exchange-correlation energy. Double-ξ plus polarized basis sets were employed. In order to represent the electron density, the local part of the pseudopotentials, and the Hartree and the exchange correlation potential a uniform mesh with a plane wave cut-off of 350 Ry was used. A simulation cell chosen consists of 48 atoms with periodic boundary conditions. We employed Γ-point sampling for the Brillouin zone integration. To get optimized lattice vectors and atomic positions, the stress tolerance and maximum atomic force were taken less than 0.5 GPa and smaller than 0.01 $eV\,Å^{-1}$, respectively. Firstly the system was equilibrated at zero pressure, and after that the pressure was gradually increased by a rise of 2 GPa applying Parrinello-Rahman technique to the system. In order to find symmetries of the phases observed in the simulations, we used the RGS algorithm and the KPLOT program [9, 10] that permitted detailed data about a given structure such as space group, cell parameters and atomic positions.

3. Results and discussion

Initially, we relax our 48 atoms supercell at zero pressure to obtain the lattice parameters of the orthorhombic Pnma phase. The equilibrium unit cell lattice constants of $LiBH_4$ are obtained as a=7.1068, b=4.5345, and c=6.7427 Å. The pressure-volume relation of $LiBH_4$ is investigated and presented in Fig. 1. The volume gives sharp variations when the applied pressure is increased from 4 GPa to 6 GPa in this material. The structural analysis makes known that the orthorhombic structure transforms to the monoclinic structure with space group $P2_1/c$ at 6 GPa as shown in Fig. 2. The lattice parameters of this monoclinic structure are as follows: a=4.3022, b=6.3410, and c=7.0263 Å.

The obtained phase transition pressure values using gradually increasing pressure technique show that the *ab initio* technique successfully produces the experimental observed high-pressure phase of $LiBH_4$ with an overvalued transition pressure. Since the restricted conditions such as finite size of the simulation cell, the lack of any defect in simulated structure, etc. are considered, such an overestimated transition pressure is expected [ ]. Conversely, the thermodynamic theorem does not take into account the probable presence of an activation barrier separating the two structural phases. Thus, as a next step, we take the energy-volume computations into account to study the stability of high-pressure phases of $LiBH_4$. The computed total energies as a function of volumes are presented in Fig. 3.

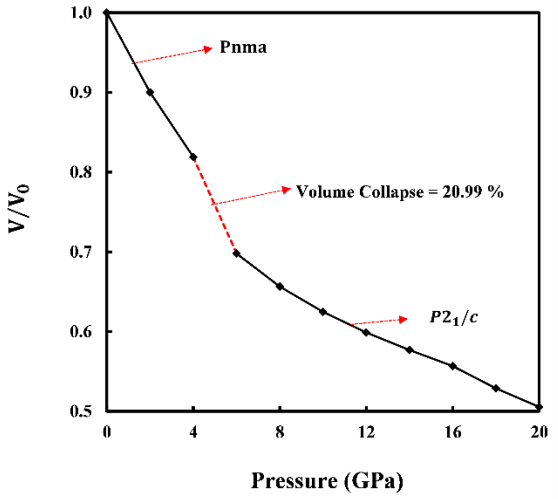


Figure 1. The volume change of the simulation cell as a function of pressure.

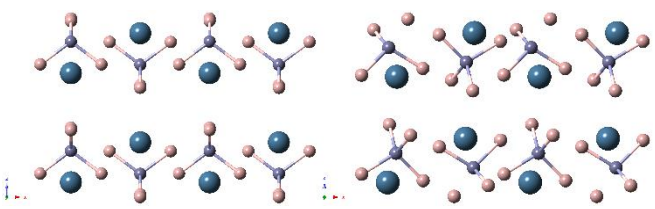


Figure 2. The crystal structures of $LiBH_4$: Pnma phase (left) and $P2_1/c$ phase (right).

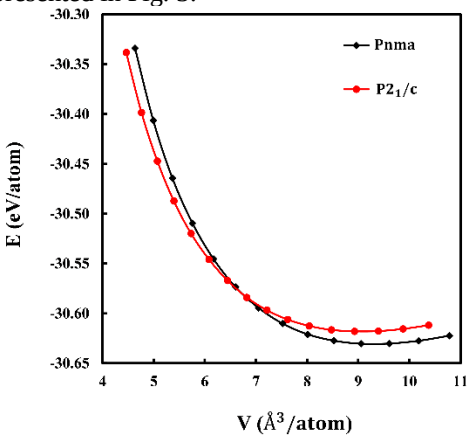


Figure 3. The energy-volume curves of structural phases of $LiBH_4$.

The transition pressure between the different phases of $LiBH_4$ is easily identified by a simple comparison of their static lattice enthalpy since the intersection of two enthalpy curves indicates a pressure-induced phase transition between these two phases. The computed enthalpy curves of the Pnma and $P2_1/c$ stable phases are plotted as a function of pressure in Fig. 4. As can be seen from this figure, the enthalpy curve of the Pnma phase crosses with that of the $P2_1/c$ phase at about 3.8 GPa indicating phase transition between these phases

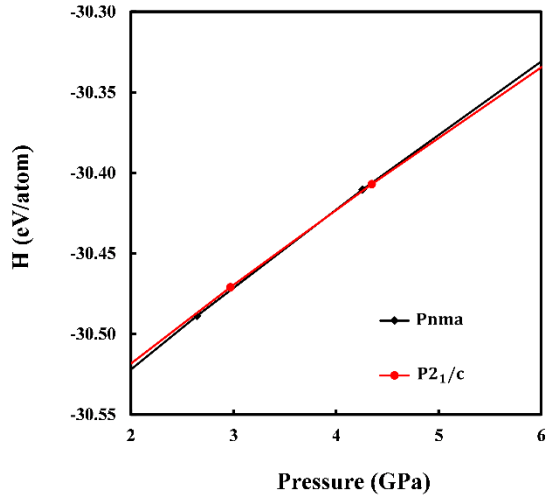


Figure 4. The enthalpy curves of structural phases of $LiBH_4$ as a function of pressure.

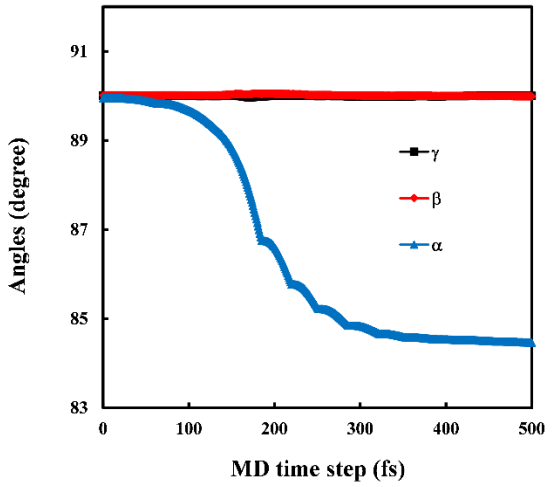
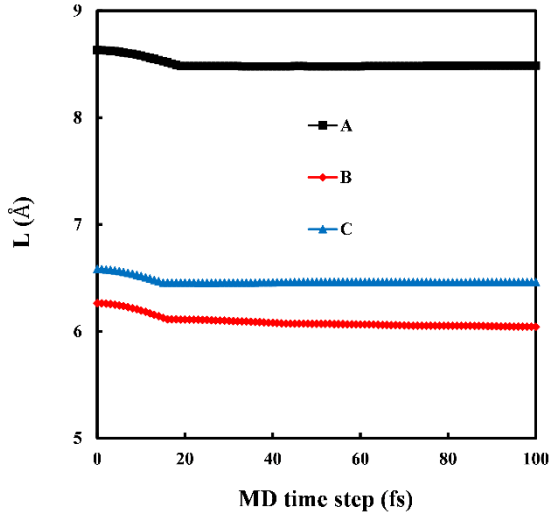


Figure 5. The behavior of the simulation cell lengths (top) and angles (bottom) as function of MD time steps at 6 GPa.

In order to evaluate transformation mechanism at the atomistic level, we investigate the variations of the simulation cell vectors and angles as a function of minimization step. Fig. 5 displays the modification of the simulation cell lengths and angles at 6 GPa. These simulation cell vectors called as **A**, **B**, and **C** which are initially along the [100], [010] and [001] directions, respectively.



We also calculated the band structures along the high-symmetry directions for Pnma and $P2_1/c$ phases of $LiBH_4$. We obtained band gaps as 1.12 eV and 2.1 eV for Pnma and $P2_1/c$ phases, respectively.

4. Conclusion

We have performed an *ab initio* constant pressure technique in order to study the pressure-induced phase transformation in the orthorhombic structured $LiBH_4$. The first-order phase transition is obtained as $\mathrm{Pnma} \rightarrow \mathrm{P2_1}/c$. According to the enthalpy calculations, the transition pressure was estimated as 6 GPa. Additionally, changes in angle and cell vectors were observed at each time step.

References:

[1] L. Schlapbach, A. Züttel, Hydrogen-storage materials for mobile applications, Nature 414(6861) (2001) 353-358.
[2] B. Sakintuna, F. Lamari-Darkrim, M. Hirscher, Metal hydride materials for solid hydrogen storage: a review, International journal of hydrogen energy 32(9) (2007) 1121-1140.
[3] S. Li, X. Ju, C. Wan, Pressure-induced phase transitions in LiBH4: Density functional theory calculations, international journal of hydrogen energy 39(17) (2014) 9330-9338.
[4] P. Vajeeston, P. Ravindran, R. Vidya, H. Fjellvåg, A. Kjekshus, Pressure-induced phase of NaAlH 4: A potential candidate for hydrogen

storage?, Applied physics letters 82(14) (2003) 2257-2259.
[5] P. Vajeeston, P. Ravindran, R. Vidya, H. Fjellvåg, A. Kjekshus, Huge-pressure-induced volume collapse in LiAlH 4 and its implications to hydrogen storage, Physical Review B 68(21) (2003) 212101.
[6] A. Talyzin, O. Andersson, B. Sundqvist, A. Kurnosov, L. Dubrovinsky, High-pressure phase transition in LiBH4, Journal of Solid State Chemistry 180(2) (2007) 510-517.
[7] P. Ordejón, E. Artacho, J.M. Soler, Self-consistent order-N density-functional calculations for very large systems, Physical Review B 53(16) (1996) R10441.
[8] J.P. Perdew, K. Burke, M. Ernzerhof, Generalized gradient approximation made simple, Physical review letters 77(18) (1996) 3865.
[9] A. Hannemann, R. Hundt, J. Schön, M. Jansen, A new algorithm for space-group determination, Journal of applied crystallography 31(6) (1998) 922-928.
[10] R. Hundt, J.C. SchoÈn, A. Hannemann, M. Jansen, Determination of symmetries and idealized cell parameters for simulated structures, Journal of applied crystallography 32(3) (1999) 413-416

6th International Conference on Materials Science and Nanotechnology For Next Generation (MSNG2019)
October 16-18, 2019, Niğde, TURKEY (ORAL FULL TEXT)

Synthesis and Cell Performance Studies of a New Carbazole Based Organic Sensitizer for DSSCs

Merve YANDIMOĞLU[1]*, Kamuran GÖRGÜN[1], Müjdat ÇAĞLAR[2] and Handan CAN SAKARYA[1]

[1] Eskişehir Osmangazi University, Faculty of Art and Science, Department of Chemistry, Eskişehir, TURKEY
[2] Eskişehir Technical University, Faculty of Science, Department of Physics, Eskişehir, TURKEY

The rapid decline in energy resources around the world has increased the demand and interest for effective, safe and harmless energy sources. Among the energy sources, solar energy is the most easily accessible, cheapest and greener resource. Therefore, the studies on DSSCs have increased considerably in recent years. In this study, we synthesized a novel small organic molecule (III) which could be a potential DSSC, derived from carbazole using Ullman and Suzuki-Miyaura coupling reaction (Scheme 1). Photophysical and photovoltaic properties of the synthesized molecule were evaluated by UV-vis/Fluorescence absorption spectroscopy and I-V measurements of the prepared DSSC.

Keywords: Carbazole, Dye-Sensitized Solar Cell (DSSC), Photovoltaic Performance
Corresponding author: mervesag26@gmail.com

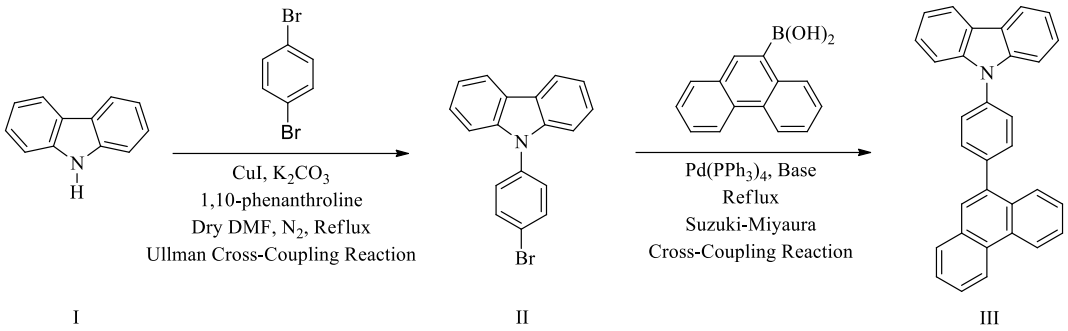
1. Introduction

In recent years organic dyes have been designed to be used as application as electron donors in bulk heterojunction solar cells, emitters in organic light-emitting diodes, and sensitizers in dye-sensitized solar cells (DSSCs) [1,2]. DSSCs discovered by Brian O'Regan and Michael Grätzel in 1991. As a result of the study, it has shown remarkable efficiency with a single layer of ruthenium dye adsorbed into broadband mesoporous semiconductor titanium dioxide (TiO_2) [3]. DSSCs work on the principle of electron formation at the LUMO level of dye by absorbing photons from solar energy to the semiconductor electrode (TiO_2) conductive band and finally to the FTO electrode [4]. Another alternative similar semiconducting material which is inclusively studying to utilize in the preparation of DSSC is Zinc Oxide (ZnO) because of its properties such as band gap (3.28 eV) [5] nearly equal to TiO_2 (3.25 eV) [6], great transparency and ease to fabricate with different nanostructured films [7]. The ZnO based DSSC has low cost, simple construction and higher electron mobility than TiO_2 [8]. Using heterocycles such as carbazole, phenothiazine, indole, and phenoxazine with "push-pull" feature in the sensitizers/co-sensitizers have showed to be an effective strategy [9-11]. Carbazole-derived organic materials which have low oxidation potentials, thermal stability, and hole-conducting capabilities, are interesting because of carbazole's electron rich nature which acts usually as donor in the electronic systems [12,13]. Furthermore, the carbazole unit can be easily functionalized from the different positions (3,6- and 2,7- or *N* positions) with different functional groups for tuning of the electronic properties. In this study, we synthesized a novel small organic molecule (III) which could be a potential DSSC, derived from carbazole using Ullman and Suzuki-Miyaura coupling reaction [14] (Scheme 1). Photophysical and photovoltaic properties of the synthesized molecule were evaluated by UV-vis/Fluorescence absorption spectroscopy and I-V measurements of the fabricated DSSC.

2. Experimental details

2.1 Materials

All chemicals and solvents were obtained from Sigma-Aldrich (Turkey). The organic solvents were purified by a standard procedure before using for reactions. Semiconductors to be used in DSSC production are ZnO and TiO_2. ZnO powder was obtained by hydrothermal synthesis and TiO_2 film was purchased from SOLARONIX as already coated on FTO substrates. Iodide/tri-iodide electrolyte (Iodolyte Z) was purchased from SOLARONIX.



I II III

Scheme 1. *Synthetic route for the compound **III**.*

^{1}H NMR spectra of compound **II** and compound **III** were obtained on a JEOL ECZ500R UltrashieldTM 500 MHz spectrometers at 298 K (Japan). UV–vis absorption of compound III was obtained with SHIMADZU UV2450 UV-vis scanning spectrometer. Photoluminescence spectrum was acquired with a Perkin–Elmer LS-55 spectrophotometer. The current density–voltage (*I–V*) characteristics of the DSSCs were recorded by a solar cell measurement system (FYTRONIX OPTOSENSE).

2.2 Synthesis of the Target compounds

2.2.1 Synthesis of the Compound II

To a solution of carbazole (compound **I**) (2.5 g, 15.0 mmol) in 50 mL dry DMF were added 1,4-dibromobenzene (5.3 g, 22.4 mmol), copper(I)iodide (285 mg, 1.5 mmol), 1,10-phenanthroline (135 mg, 0.75 mmol), and K_2CO_3 (4.1 g, 29.9 mmol) and then the reaction mixture was refluxed for 24 hours under nitrogen atmosphere. Then, this reaction mixture was cooled to room temperature and solvent was removed with using evaporator. The residue was extracted with dichloromethane. The product (compound **II**) was obtained by column chromatography on silica gel using n-hexane as the eluent to give a white solid. (Isolated yield 3.4 g, 71%). ^{1}H NMR: ($CDCl_3$-d_1, 500 MHz, δ): 7.20-7.37 (m, 6H), 7.44 (d, 2H, J=8.3 Hz), 7.69 (d, 2H, J=8.3 Hz), 8.07 (d, 2H, J=7.6 Hz).

2.2.2 Synthesis of the Compound III

9-(4-Bromophenyl)-9H-carbazole (compound **II**) (0,2 g, 1 eq), phenanthracene-9-boronic acid (0.17 g, 1.2 eq), K_2CO_3 (2 M, 0.683 mL), and tetrakis(triphenylphosphine)palladium ($Pd(PPh_3)_4$) 3 mol% were added to 25 mL THF into a double necked flask. The mixture was refluxed at 70 °C for 24 hours. The reaction mixture was cooled to room temperature and solvent was removed with using evaporator. The residue was extracted with dichloromethane and the organic phase dried over Na_2SO_4 and filtered. The product (compound **III**) was obtained by column chromatography on silica gel using a mixture of dichloromethane and n-hexane (1:5, v:v) as the eluent to give a white solid. (Isolated yield 0.17 g, 65%). ^{1}H-NMR ($CDCl_3$-d_1, 500 MHz, δ): 7.50-7.60 (2H, m), 7.64-7.82 (6H, m), 7.93 (2H, dd, J= 7.2 Hz), 8.04 (2H, dd, J= 7.2 Hz), 8.22-8.37 (4H, m), 8.44 (2H, dd, J = 5.0 Hz), 8.47-8.57 (2H, m, Hz), 8.79 (1H, d, J= 2.0 Hz).

2.3 DSSC Fabrication of the Compound III

Fluorine-doped tin oxide (FTO) substates were firstly cleaned in ultrasonic bath of acetone solution for 15 min and then rinsed with distilled water. The ZnO paste was prepared by mixing the ZnO nanopowder, Triton-X 100 and acetyl acetone. The prepared pastes were spread onto the FTO glasses by doctor-blade method and then these FTOs was annealed for 1 hour at 400 °C in air and cooled. On the other hand, TiO_2 electrotes were purchased from Solaronix. The electodes were immersed into a 1.2 mM solution of compound **III** in chloroform; 0.5 mM solution of ruthenizer 535 bis-TBA (N719, Solaronix) and 1% (v/v) N719 – 99% (v/v) compound **III** mixture for 24 h. Later, the dye loaded ZnO/TiO_2 electrodes were assembled by fixing with Pt counter electrode to form a sandwich-type DSSCs. Finally, iodide/tri-iodide redox couple electrolyte (Iodolyte Z, Solaronix) was injected into the DSSC.

The solar cells loaded with N719 co-sensitizer, compound **III** dye and compound **III** dye + N719 co-sensitizer were named **Z1**, **Z2** and **Z3** DSSC, respectively. Furthermore, the TiO_2-based solar cells loaded with N719, compound **III** dye and compound **III** dye + N719 co-sensitizer were named **T1**, **T2** and **T3** DSSC, respectively.

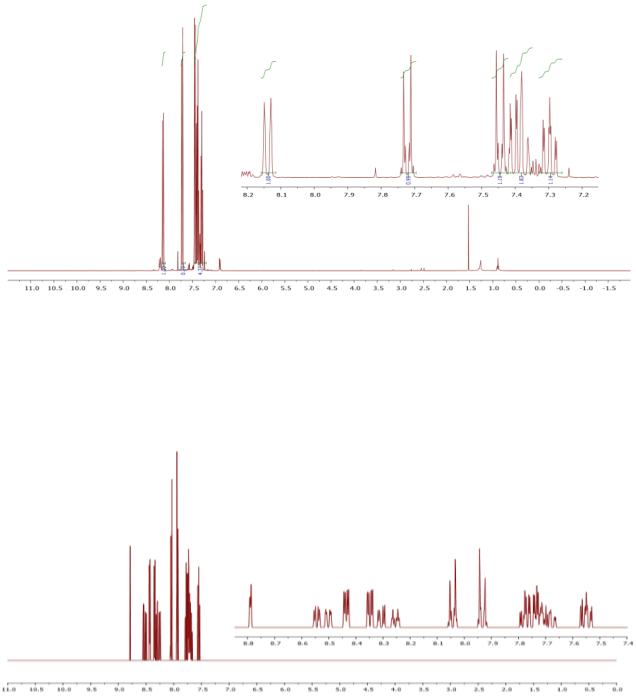


Fig. 2. ^{1}H *NMR Spectrum of Compound* ***III****.*

3. Results and Discussion

Carbazole based compounds **II** and **III** were synthesized by using Ullman and Suzuki coupling reactions. ^{1}H NMR, UV-

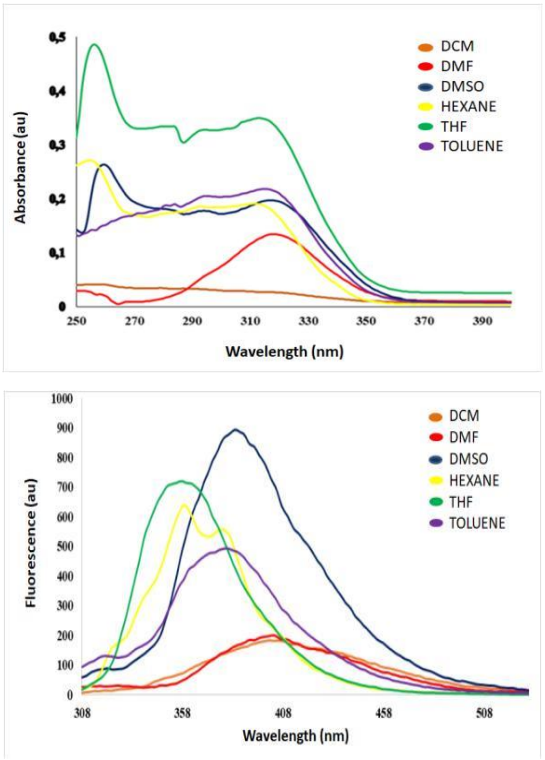
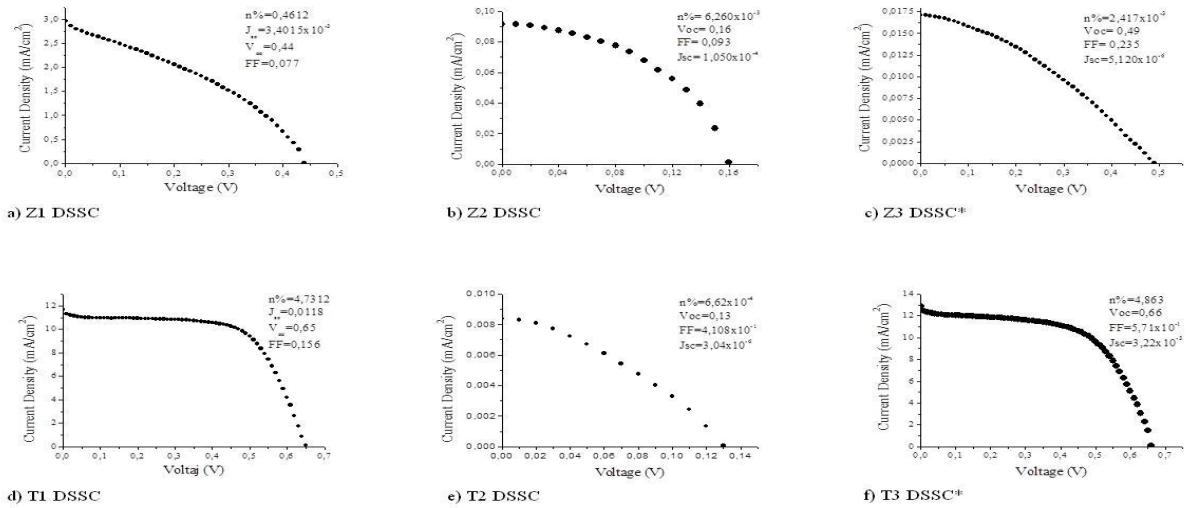


Fig. 3. *Absorption spectrum and emission spectrum of compound* ***III*** *in different solvents.*



*%1 (v/v) N719 - %99 (v/v) Compound III
(N719: 0.5 mM solution of ruthenizer 535 bis-TBA N719, Solaronix)
III: 1.2 mM solution of Compound III in chloroform

Fig. 4. *Current density−voltage (I−V) plots for the fabricated DSSCs based on* ***a)*** *ZnO-N719 (**Z1**),* ***b)*** *ZnO-compound **III** dye (**Z2**),* ***c)*** *ZnO-compound **III** dye + N719 (**Z3**),* ***d)*** *TiO_2- N719 (**T1**),* ***e)*** *TiO_2- compound **III** dye (**T2**),* ***f)*** *TiO_2- compound **III** dye + N719 (**T3**).*

vis and Fluorescence spectra results were confirmed the existence of compound **III**. Synthesis and characterization of compound **II** have been reported previously [15].

Figure 3 shows the absorption spectrum and fluorescence spectrum in different solvents (DCM, DMF, DMSO, n-hexane, THF and toluene) for compound III. As shown in **Figure 3** in dilute (10^{-5} M) different solutions of compound **III**, the absorption maximum wavelengths were carbazole-based peak of n-π* transitions observed at 250-260 nm. The other carbazole-centered π-π* transition of the phenanthrene unit, is observed at 310-320 nm wavelength. The bathocromic effect was observed with increasing polarity of solvents while the hypochromic effect was observed in toluene.

On the other hand, the fluorescence spectrum of compound **III** has emission peaks in the range of 355-410 nm in all solutions. Two-shoulder emission peaks were observed at 358 and 380 nm in the n-hexane. The effect of solvent polarity shows that compound **III** emits at the longest wavelength emission maxima in DMF at 405 nm and the shortest wavelength emission maxima in THF at 355 nm. Fluorescence spectrum showed higher wavelength shift (bathocromic effect) with increasing polarity of solvents.

Fig. 4 shows I-V plots of the fabricated DSSCs based on Z1, Z2, Z3, T1, T2 and T3. As seen in this figure, Z1 has the best performance among Z groups and T1 and T3 have high efficiency values in T group. Also all electrical parameters of DSSCs are tabulated in Table 1.

Table 1. Photovoltaic parameters of *the fabricated DSSCs*.

		J_{sc}(mAcm^{-2})	v_{oc} (V)	FF%	n(%)
a	**Z1 DSSC**	3.4015×10^{-3}	0.44	0.077	4.612×10^{-1}
b	**Z2 DSSC**	1.050×10^{-4}	0.16	0.093	6.26×10^{-3}
c	**Z3DSSC**	5.12×10^{-6}	0.49	0.235	2.417×10^{-3}
d	**T1 DSSC**	1.18×10^{-2}	0.65	0.156	4.7312
e	**T2 DSSC**	3.04×10^{-6}	0.13	0.411	6.62×10^{-4}
f	**T3 DSSC**	3.22×10^{-3}	0.66	0.571	4.863

According to the obtained results, the synthesized molecule used with together N719 has enhanced the performance of DSSC and this result has implied that the improvement in molecular design will play an important role to get higher cell efficiency.

4. Conclusion

DSSC fabrication was performed and the *I-V* measurements shows that **Z2** DSSC more efficient than **Z3** DSSC as shown in **Table 1**. It is thought that co-sensitizer (N719) is not required for ZnO-based DSSC measurements and that a more efficient solar cell is formed by using the substance alone. However, it was concluded that the use of co-sensitizer (N719) in TiO_2-based DSSC measurements significantly increased the efficiency of the solar cell. Among all the DSSCs, the most efficient one is **T3** DSSC. As a result of the measurements, it is seen that compound **III** and N719 can have a synergistic effect (when using TiO_2) or an asynergic effect (when using ZnO) to each other. It is thought that DSSCs with higher cell efficiency can be prepared by improving molecular design.

5. Acknowledgement

This work was supported by Eskişehir Osmangazi University Commission of Scientific Research Projects under Grant No. 2017-1321. I would like to thank Yasemin Çağlar, for the DSSC measurements and all contributions.

References:

[1] LIANG, M., CHEN, J., "Arylamine organic dyes for dye-sensitized solar cells", Chemical Society Reviews, Vol. 42, pp. 3453-3488, 2013.
[2] ZHU, X-H., PENG, J., CAO, Y., RONCALI, J., "Solution-processable single-material molecular emitters for organic light-emitting devices", Chemical Society Reviews, Vol. 40, pp. 5924-5925, 2011.
[3] O'REGAN, B., GRATZEL, M., "A low-cost high-efficiency solar cell based on dye-sensitized colloidal TiO_2 films", Nature, Vol. 353, pp. 737-740, 1991.
[4] GRÄTZEL, M., "Convsersion of sunlight to electric power by nanocrystalline dye-sensitized solar cells", J. Photochem. Photobiol. A: Chemistry, Vol. 164, pp. 3-14, 2004.
[5] SILVA, É. P., CHAVES, M., DURRANT, S. F., LISBOA-FILHO, P. N., BORTOLETO, J. R. R., "Morphological and electrical evolution of ZnO: Al thin filmsdeposited by RF magnetron sputtering onto glass substrates", Materials Research, Vol. 17, No. 6, pp. 1384-1390, 2014.
[6] DÍAZ-URIBE, C. E., VALLEJO LOZADA, W. A., MARTÍNEZ ORTEGA, F., "Synthesis and characterization of TiO_2 thin films doped with copper to

be used in photocatalysis", Iteckne, Vol. 10, pp. 16-20, 2013.

[7] BAXTER, J. B., AYDİL, E. S., "Dye-sensitized solar cells based on semiconductor morphologies with ZnO nanowires", Solar Energy Materials and Solar Cells, Vol. 90, pp. 607-622, 2006.

[8] SUH, D. I., LEE, S. Y., KIM, T. H., CHUN, J. M., SUH, E. K., YANG, O. B., LEE, S. K., "The fabrication and characterization of dye-sensitized solar cells with a branched structures of ZnO nanowires", Chemical Physics Letters, Vol. 442, pp. 348-353, 2007.

[9] MISHRA, A, FISCHER, M. K. R., BAUERLE, P., "Metal-free organic dyes for dye-sensitized solar cells: from structure: property relationships to design rules", Angewandte Chemie International Edition, Vol. 48, pp. 2474–2499, 2009.

[10] OOYAMA, Y, HARIMA, Y., "Molecular designs and syntheses of organic dyes for dyesensitized solar cells", European Journal of Organic Chemistry, Vol. 2009, 2903-2934, 2009.

[11] HAGFELDT, A, BOSCHLOO, G, SUN, L, KLOO, L, PETTERSSON, H., "Dye-sensitized solar cells", Chemical Reviews, Vol. 110, pp. 6595–6663, 2010.

[12] THOMAS, K. R. J., LIN, J. T., TAO, Y.-T., KO, C.-W., "Light-Emitting Carbazole Derivatives: Potential Electroluminescent Materials", Journal of the American Chemical Society, Vol. 123, pp. 9404-9411, 2001.

[13] LI, J., MA, C., TANG, J., LEE, C.-S., LEE, S., "Novel starburst molecule as a hole injecting and transporting material for organic light-emitting devices", Chemistry of Materials, Vol. 17, pp. 615-619, 2005.

[14] MIYAURA, N., SUZUKI, A., "Palladium-Catalyzed Cross-Coupling Reactions of Organoboron Compounds", Chemical Reviews, Vol. 95, pp. 2457-2483, 1995.

[15] GÖRGÜN, K., ÇAĞLAR, Y., "Synthesis of novel carbazole derived substances using some organoboron compounds by palladium catalyzed and investigation of its semiconductor device characteristics", Journal of Molecular Structure, Vol. 1157, pp. 106-111, 2018.

6th International Conference on Materials Science and Nanotechnology For Next Generation (MSNG2019)
October 16-18, 2019, Niğde, TURKEY (ORAL FULL TEXT)

Eco-Friendly Carbazole-Based Molecules Synthesis and Their Photodiode Properties

Kamuran GÖRGÜN[1]*, Müjdat ÇAĞLAR[2], Merve YANDIMOĞLU[1], Handan CAN SAKARYA[1]

[1] Eskişehir Osmangazi University, Faculty of Art&Science, Department of Chemistry, Eskişehir, TURKEY
[2] Eskisehir Technical University, Science Faculty, Department of Physics, Eskisehir, TURKEY

In this study, we designed the targeted molecule in two stages. In the first stage, we synthesized 9-(3,5-dibromophenyl)-9H-carbazole (II) and 9-(4-Bromophenyl)-9H-carbazole (III) using by Ullman coupling reactions. In the second stage, the targeted compounds as 9-(4-(4bH-fluoren-3-yl) phenyl) -9H-carbazole (IV) and 9- (3,5-di(9H-fluoren-2-yl) phenyl)-9H-carbazole (V) were performed successfully by using Suzuki-Miyaura cross coupling reactions. All synthesized compounds (II, III, IV and V) were characterized by using ^{1}H NMR, ^{13}C NMR, spectroscopic analysis. These compounds were dissolved by CH_2Cl_2 and coated onto the borosilicate glass with drop casting method. The heterojunction structure (n-Si/IV) and (n-Si/V) were fabricated by using the obtained compounds. We investigated the electrical properties of photodiodes fabricated with synthesized new molecules.

Keywords: Carbazole, Suzuki-Miyaura coupling, Ullman coupling, photodiode character

Corresponding author: *kgorguntr@gmail.com*

1. Introduction

One of the most significant parts in the rapidly rising organic optoelectronics field is to look for new materials with developed characteristics. For this reason, conjugated compounds are becoming the focus of attention. Because of the effectual hole transport and perfect thermal stability of carbazole derivatives, the electron-rich carbazole moiety is widely used in the design organic solar cell [1], electroluminescence materials [2], optoelectronic applications [3], synthesis carbazole-based liquid crystalline materials [4], carbazole electrochemistry [5], carbazole-containing polymers [6-7], and biological applications [8-9]. Because of that, the great interest in carbazole derivatives results from the reasonably priced of the starting material, easy modification of its structure. It is known that fluorene derivatives also have high emission quantum yields and exhibit ambipolar charge carrier transport characteristics and therefore there are widely used for excellent hole-transporting properties and good solubility of fluorene derivatives. [10-11]. The synthesis of organic compounds containing the heteroaryl structural units has been much paying attention in recent years [12]. So, synthesis in recent years was relied on the use of these types of reactions [13]. The Ullmann reaction [14] which has copper-catalyzed homocoupling is the first efficient process that enabled the synthesis of symmetrical biaryls. In another reaction, Suzuki-Miyaura (SM) cross-linking reaction using aryl halides and aryl boronic acids is one of the important synthetic reactions for the production of asymmetric biaryls. [15], [16], [17], [18], [19], which plays an important role in changing commercial products.
In the present study, we report the synthesis and characterization of carbazole derivatives with 1,4 and 1,3,5 benzene core of well-defined. Firstly, we synthesized novel carbazole derivatives (compound IV-V). Secondly, we determined the carbazole derivatives. The film was coated on n-Si and glass substrates using this material. The optical band gap value was determined from optical transmittance measurements. The photodiode based on these small molecule semiconductor was fabricated and electrical properties of this device were investigated.

2. Experimental details

All reagents and organic solvents were commercial quality. The chemical structure and synthetic route of the targeted material is shown in **Figure 1** and **Figure 2**.

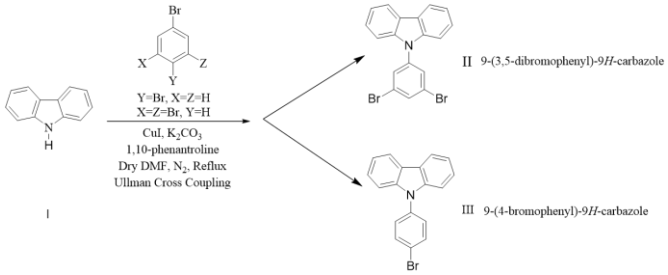


Fig 1. Synthetic rote of 9-(4-bromophenyl)-9H-carbazole (II) and 9-(4-bromophenyl)-9H-carbazole (III)

2.1. Synthesis of 9-(3,5-dibromophenyl)-9H-carbazole (II) (Fig. 1) [20]

Carbazole mixture (I) (5.0 g, 29.9 mmol), 1,3,5-tribromobenzene (14.1 g, 44.9 mmol), copper(I) iodide (570mg, 3.0 mmol), 1,10-phenanthroline (270 mg, 3 mmol), K_2CO_3 (8.3 g, 59.8 mmol), and 60 mL of dried DMF was refluxed under nitrogen atmosphere for 24 h. Cooling to room temperature before the solvent was removed under vacuum and the residue was extracted with CH_2Cl_2. The products were then obtained by column chromatography on silica gel with hexane as the eluent, to get white solid (compound II). Isolated yield (6.0 g, 50%). ^{1}H NMR: ($CDCl_3$-d_1, 500 MHz): 7.35 (t, 2H), 7.42-7.50 (m, 4H), 7.73 (s, 2H, *J*=8,3 Hz), 7.80 (s, 1H), 8.1 (d, 2H, *J*=7.5 Hz).

2.2. Synthesis of 9-(3,5-di(9H-fluoren-2-yl) phenyl)-9H-carbazole (IV) (Fig. 2)

9-(3,5-dibromophenyl)-9H-carbazole (0,5 g, 1 eq), Fluorene-2-boronic acid (0,575 g, 2,2 eq), K_2CO_3 (2M, 4 eq, 2,49 mL), tetrakis(triphenylphosphine) palladium 3 mol% and THF (30 ml) were mixed refluxed under a N_2 atmosphere for 12 h. After being cooled, the mixture was extracted with CH_2Cl_2, dried over Na_2SO_4 and filtered. Solvent was evaporated under a vacuum, after that column chromatography over silica gel with a mixture of CH_2Cl_2 and n-hegzan (1:2, v:v) as eluent, resulted in the product 9-(3,5-di(9H-fluoren-2-yl) phenyl)-9H-carbazole (compound V) as a white solid in 65% yield (0.38 g). ^{1}H-NMR (500 MHz, $CDCl_3$, δ): (0.21 g, %72) 8.20 (2H, d, *J*=7.5 Hz), 8.19 (2H, t, *J*=7.5 Hz), 8.05 (2H, t, *J*=7.5 Hz), 7.93(2H, s), 7.91 (2H, d, *J*=9.0 Hz), 7.86 (3H, s), 7.85 (2H, d, *J*=7.5 Hz), 7.7 (2H, d, *J*=7.5 Hz), 7.47 (2H, t, *J*=7.0 Hz), 7.33 (4H, d, *J*=6.0 Hz), 4.02 (4H, s). ^{13}C-NMR (125 MHz, $CDCl_3$, δ): 144,115, 143,865, 143,529, 141,629, 141,187, 140,909, 138,759, 138,682, 126,981, 126,904, 126,146, 126,050, 125,129, 124,341, 123,938, 123,449, 120,406, 120,339, 120,118, 120,012.

9-(4-bromophenyl)-9H-carbazole (compound III) and 9-(4-(4bH-fluoren-3-yl) phenyl)-9H-carbazole (compound V) was synthesized, presented and discussed in the previous work [21]

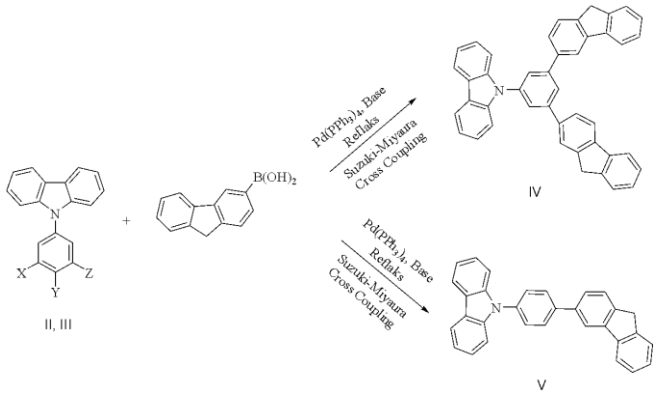
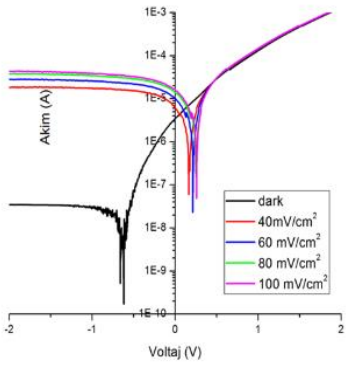


Fig 2. Synthetic rote of 9-(3,5-di(9H-fluoren-2-yl) phenyl)-9H-carbazole (IV) and 9-(4-(4bH-fluoren-3-yl) phenyl)-9H-carbazole (V)

The 9-(3,5-di(9H-fluoren-2-yl) phenyl)-9H-carbazole (IV) and 9-(4-(4bH-fluoren-3-yl) phenyl)-9H-carbazole (V) [21] were ultrasonically dispersed in CH_2Cl_2 for 2 h. The solutions were coated onto the surface of n-Si and borosilicate substrates using drop-casting method and n-Si/p-IV and n-Si/p-V heterojunction diodes were obtained. In this structure, gold top contact and silver bottom contact were used. Gold was evaporated in VAKSIS PVD system and for silver bottom contact, silver paint was used. ^{1}H NMR and ^{13}C NMR of the II, III, IV and V were obtained on a BRUKER DPX FT NMR (500 MHz) and (125 MHz) spectrometers at 298 K (Germany). The current–voltage (I–V) characteristics of the photodiodes were recorded by a semiconductor characterization system (KITHLEY 4200SCS) and a solar cell measurement system (FYTRONIX SOLAR CELL SYSTEM).

3. Results and discussion

9-(4-(4bH-fluoren-3-yl) phenyl)-9H-carbazole (IV) was synthesized in two steps as shown in Figure 2. The structure of compounds is confirmed by ^{1}H NMR and ^{13}C NMR spectra technique. In the ^{1}H NMR of Compound IV, in the phenyl ring bound to the fluorene compound, four kinds of protons with the same chemical environment and their signals were observed. These signals were observed as doublets of two protons at 8.20 and 7.91 ppm and as triplets of two protons at 7.59 and 7.47 ppm, respectively. Three identical protons in the phenyl ring resonated at the same region. These protons were observed as singlet at 7.86 ppm. Two identical protons in fluorene at the 3 and 5 positions of the phenyl ring were observed as singlets at 7.93 ppm. Similarly, identical four-proton in the same compound were assigned at 7.39 ppm as dublets while two identical protons were observed at 8.19 ppm as triplets, the other two identical protons were assigned at 8.05 ppm. In the same way, signals at 7.85 and 7.7 ppm were observed as doublets. The four protons singlet at 4.02 ppm were observed to belong to methylene protons in the fluorene ring. In the ^{13}CNMR spectra, twenty signals were observed as expected due to the symmetry structure of the molecule. As a result of these spectroscopic data, it was determined that the compound **IV** is 9-(4-(4bH-fluoren-3-yl) phenyl)-9H-carbazole.



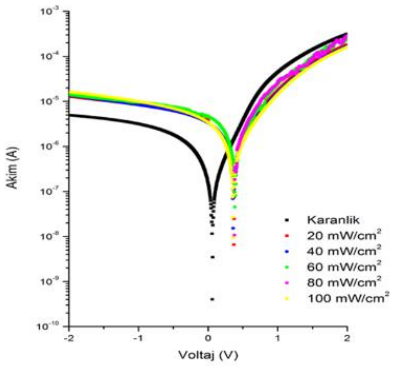


Fig 3. Current-voltage plots of the n-Si/-p-IV (up) and n-Si/-p-V (down) photodiodes

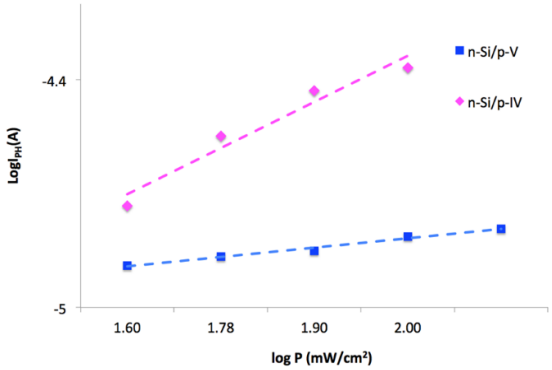
The current-voltage characteristics of the (n-Si/-p-IV and n-Si/-p-V) photodiodes are shown in Figure 3. As seen in these figure, the photocurrent in n-Si/IV increases by 1000 times but in the n-Si/V is less then 10 under 100mW/cm^2 illumination.

The photoconduction mechanism of diodes can be analyzed by the following equation:

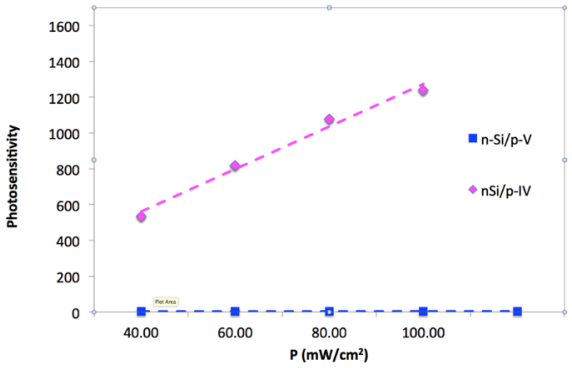
$$I_{ph} = AP^{m} \qquad (1)$$

Where, I_{ph}, A, P and m are photocurrent, constant, light intensity and illumination coefficient, respectively.

Fig. 4 Illustrates the photocurrent and photosensitivity versus illumination intensity plot of n-Si/p-IV and n-Si/p-V photodiode.



(a)



(b)

Fig 4. Photocurrent and photosensitivity versus illumination intensity plot of n-Si/p-IV and n-Si/p-V photodiode

The obtained m values of the photodiodes to determine photoconduction mechanism were 0.1216 (for compound IV) and 0.0246 (for compound V). These values are less then 0.5 which means that the light is absorbed in the metal-semiconductor junction area.

4. Conclusion

9-(4-(4bH-fluoren-3-yl) phenyl)-9H-carbazole (IV) and 9-(3,5-di(9H-fluoren-2-yl) phenyl)-9H-carbazole (V) were synthesized by using Ullman and Suzuki coupling reactions. The structural analysis of this compounds have been elucidated by ^{1}H-NMR and ^{13}C-NMR confirms these structure. These compounds were dissolved by $CHCl_3$ and the borosilicate glass were coated with drop casting method. The synthesized compound IV and compound V were used to fabricate heterojunction structure (n-Si/p-IV and n-Si/p-V). The obtained device exhibited photodiode characteristic and their photoconduction mechanism implied that the light is absorbed in the metal-semiconductor junction area.

5. Acknowledgement

This work was supported by Eskişehir Osmangazi University Commission of Research Project under Grant no. 2017-1321.

References:

[1] SATHIYAN, G., SIVAKUMAR, E.K.T., GANESAMOORTHY, R., THANGAMUTHU, R., SAKTHIVEL, P. "Review of carbazole based conjugated molecules for highly efficient organic solar cell application", Tetrahedron Lett. 57, 243–252, 2016.

[2] JIANG, H., SUN, J., ZHANG, J., "A review on synthesis of carbazole-based chromophores as organic light-emitting materials", Curr. Org. Chem. 16, 2014–2025, 2012

[3] HIGGINBOTHAM, H., KARON, K., LEDWON, P., DATA, P., "Carbazoles in optoelectronic applications", Disp. Imaging 2, 207–216, 2017

[4] MANICKAM, M., IQBAL, P., BELLONI, M., KUMAR, S., PREECE, J.A., "A brief review of carbazole-based photorefractive liquid crystalline materials", Isr. J. Chem. 52, 917–934, 2012.

[5] KARON, K., LAPKOWSKI, M., "Carbazole electrochemistry: a short review", J. Solid State Electrochem. 19, 2601–2610, 2015.

[6] GRAZULEVICIUS, J.V., STROHRIEGL, P., PIELICHOWSKI, J., PIELICHOWSKI, K., "Carbazole-containing polymers: synthesis, properties and applications", Prog. Polym. Sci. 28, 1297–1353, 2003.

[7] PENWELL, R.C., GANGULY, B.N., SMITH, T.W, "Poly(N-vinylcarbazole): a selective review of its polymerization, structure, properties, and electrical characteristics", J. Polym. Sci. Macromol. Rev. 13, 63–160, 1978.

[8] BASHIR, M., BANO, A., IJAZ, A., CHAUDHARY, B., "Recent developments and biological activities of N-substituted carbazole derivatives: a review", Molecules, 20, 13496–1351, 2015

[9] KNÖLKER, H.-J., REDDY, K.R., "Isolation and synthesis of biologically active carbazole alkaloids", Chem. Rev. 102, 4303–4428, 2002.

[10] FUKUDA, M., SAWADA, K., YOSHINO, K., "Synthesis of fusible and soluble conducting polyfluorene derivatives and their characteristics", J Polym Sci Part A: Polym Chem, 31, 2465-2471, 1993.

[11] RANGER, M.; RONDEAU, D.; LECLERC, M. "New Well-Defined Poly(2,7-fluorene) Derivatives: Photoluminescence and Base Doping", Macromolecules 30, 7686-7691, 1997.

[12](a) THOMPSON, M.J., ADAMS, H., B. Chen, "Development of a Diversity-Oriented Approach to Oxazole-5-amide Libraries", J. Org. Chem., 74 (), 3856-3865, 2009.

(b) SHI, B., BLAKE, A., CAMPBELL, I.B., JUDKINS, B.D., MOODY, C.J., Chem. Commun. 2009), pp. 3291-3294

(c) Y.-X. DA, Z. YANG, Z.-J. QUAN, Z. ZHANG, X.-C. WANG J. Heterocycl. Chem., 46, 737-741, 2009.

[13] TIETZE L.-F., BRASCHE G., GERICKE K. "Domino Reactions in Organic Synthesis", Wiley-VCH, Weinheim 2006
[14] ULLMANN, F., P. sponagel ber dtsch Chem Ges, 38, 2211-2212, 1905.
(b) GOLDBERG, I., Ber Dtsch Chem Ges, 39, 1691-1692, 1906.
[15] MIYAURA N., SUZUKI, A. "Palladium-Catalyzed Cross-Coupling Reactions of Organoboron Compounds" Chem. Rev., 95, 2457-2483, 1995.
[16] SUZUKI, A., "Recent advances in the cross-coupling reactions of organoboron derivatives with organic electrophiles", J. Organomet. Chem., 576, 147-168, 1999.
[17] SUZUKI A., "Cross-coupling reactions of organoboranes: an easy way to construct C-C bonds (Nobel Lecture) ". Chem. Int. Ed., 50, 6722-6737, 2011.
[18](a) MIYAURA N. (second ed.), MEIJERE A. DE, DIEDERICH, F., (Eds.), "Metal-Catalyzed Cross-Coupling Reactions", vol. 1, Wiley-VCH, Weinheim, 2004.
(b) TIETZE, L., ILA, H., BELL, H., "Enantioselective palladium-catalyzed transformations", Chem. Rev., 104, 3453, 2004.
[19] YIN, L., LIEBSCHER, J., "Carbon−Carbon Coupling Reactions Catalyzed by Heterogeneous Palladium Catalysts", Chem. Rev., 107, 133-173, 2007.
[20] GÖRGÜN, K., CAGLAR, Y., YAKUPHANOĞLU F., "Synthesis and Photodiode Characterization of Novel Twisted Carbazole Derivatives with 1,3,5-Benzene Core" Silicon, 10, 693–702, 2018.
[21] GÖRGÜN, K., "Carbazole Derivative Molecules, Characterization and Investigation of Dye-Sensitized Solar Cell and Semiconductor Device Characteristics", 5th Internatıonal conference on materials science and nanotechnology for next generation Congress MSNG2018, 04-06 October 2018, Nevşehir, Türkiye, P: 75-78

6th International Conference on Materials Science and Nanotechnology For Next Generation (MSNG2019)
October 16-18, 2019, Niğde, TURKEY (ORAL FULL TEXT)

On the voltage dependent profile of interface traps (Dit) and series resistance (Rs) in the Au/(MgO-PVP)/n-Si (MPS) structures at room temperature

Ayşegül Eroğlu[1]
Seçkin Altındal Yerişkin[2]

[1]Department of Physics, Faculty of Science, Gazi University, Ankara, TURKEY
[2]Department of Chemical Engineering, Faculty of Engineering, Gazi University, Ankara, TURKEY

In this study, both the voltage dependent profiles of the interface traps (D_{it}) and series resistance (R_s) in Au/(MgO-PVP)/n-Si (MPS) structures were extracted from the capacitance-voltage (C-V) and conductance-voltage (G/w-V) characteristics by using low-high frequencies (C_{LF}-C_{HF}) capacitance and Nicollian-Brews methods, respectively. The D_{it}-V plot was obtained from the 10 kHz and 1 MHz and it shows a peak behavior at 3.9 V with $1.6x10^{13}$ $eV^{-1}cm^{-2}$. Such peak behavior of it was attributed to a special density distribution of interface traps at (MgO-PVP)/n-Si interface with energies located in forbidden band-gap of Si. The R_s-V plot was obtained from the measured capacitance and conductance data at 1MHz. The value of R_s decreases with increasing bias voltage and close to a constant value (~298 Ω) which is corresponding to the real value of R_s at strong accumulation region. Experimental results show that these two parameters are more effective on the (C-V) and (G/w-V) measurements, but while D_{it} is effective in inversion and depletion regions at low frequencies, R_s is effective only at accumulation region especially at high frequencies. Therefore, they should be into account in the calculation the main electric and dielectric properties of the MIS/MOS and MPS type structures.

Keywords: Au/(MgO-PVP)/n-Si (MPS) type structure; Capacitance-voltage (C-V) and conductance-voltage (G/w-V) characteristics; Voltage dependent profile of D_{it} and series resistance (R_s)

Submission date:
Acceptance Date:

Corresponding authors: ayseguleroglu06@gmail.com

1. Introduction

In last two decades, especially the metal, metal-oxide, graphene doped organic or polymeric materials which are prepared by simple methods such as spin-coating, electro-spinning, electrostatic spraying, and sol-gel methods become used instead of insulator or oxide materials such as SiO_2 and SnO_2 which are prepared traditional methods such as thermal or wet oxidation and sputtering [1-6]. The using such polymer interfacial layer can be easy polarized under an external electric field and so influence both the electrical and dielectric properties of these structures [7,8]. Usually, such organic materials with and without doped can be used in many electronic devices such as diodes, capacitors, transistors, and solar cells [6-10]. Additionally, PVA and PVP type organic materials are known as a promising candidate for a good gate interfacial layer in the fabrication of polymer thin-film MPS-type devices due to its low-cost production, low- weight in per molecule, low energy consumption, and easy grown processes. MgO has been intensely studied and proved to be a perfect charge-transport material in electronics [10]. Both the quality and performance of the MPS type these structures are depend

on many factors such as the existence of the interface traps (D_{it}) semiconductor/polymer interface, interfacial layer and it's homogeneity, the formation of barrier height (BH) at M/S interface, the magnitude of R_s, and fabrication processes. When these structures have D_{it}, R_s, and an interlayer, the characteristics of them become different from the ideal case of the MS and MIS type structures [11-14]. It is well known that the existence of D_{it} and polarization processes lead to an excess capacitance (C) and conductance (G) the measurement of them. The value of Rs can also affect both the C and G values of these structures especially at accumulation region [11,15]. The main aim of these study is to fabricate the Au/(MgO-PVP)/n-Si (MPS) structures instead of conventional metal-oxide-semiconductor (MOS) structures to increase performance of the MS structures. For this purpose both the capacitance-voltage (C-V) and conductance-voltage (G/w-V) measurements of them were carried out in wide range of frequency and voltage. The voltage dependent profiles of the D_{it} for the Au/(MgO-PVP)/n-Si (MPS) structure show a peak behavior at 3.9 V with $1.6x10^{13}$ $eV^{-1}cm^{-2}$.

2. Experimental details

Au/(MgO-PVP)/n-Si (MPS) type structures were fabricated on the n-Si wafer which have (100) float zone, 1^{-10} W.cm resistivity and 300 mm thickness. Firstly, n-Si wafer was cleaned in the ammonium peroxide for 1 min to remove native oxide layer or organic dirties from the surfaced later they were dipped into sequence of acidic wafer was solutions (H_2SO_4:H_2O_2:H_2O=3:1:1) for 3 minutes. Subsequently, they rinsed in the high-pure deionized water with of 18 MΩ.cm resistivity and then dried with nitrogen (N_2) gas. Secondly, ohmic contacts were formed using thermal evaporation system which evaporated highly pure (99.99%) Au on the whole back side of the wafer at 10^{-6} Torr and annealed in the nitrogen ambient 550 ^oC for 5 min to get a good ohmic contact. After that high-pure Au dots with 1 mm diameter were grown on the front of one of the same n-Si wafer to get MS type SBDs as a reference samples. Thirdly, the prepared MgO-PVP solution was grown on the front of second n-Si wafer by using electro-spining method and then Au was also thermal evaporated on the (MgO-PVP) organic layer and so the fabrication processes of MPS type structure were completed. The C-V and G/w-V measurements were performed by using HP4192A-LF impedance analyzer.

3. Results and discussion:

The C–V and G/ω–V curves of the fabricated Au/(MgO-PVP)/n-Si (MPS) structure were given in Fig. 1(a) and (b), respectively. As shown in these curves, both the C–V and G/w-V characteristics in the frequency range of 10 kHz-5 MHz have inversion, depletion, and accumulation regions like a MOS type capacitor. Both the C and G values increase with decreasing frequency due to the existence of interface traps, dislocations, and dipol or surface polarization [11-15]. In other words, the observed higher values of C and G/ω at low and intermediate frequencies are the result of interface traps and their relaxation time (τ) due to the fact that they can easily follow the ac signal and yield an excess C and G/ω to the measured of them. Additionally, the dipoles can easily orient themselves at low and intermediate frequencies and these lead to an increase in the C and G/ω values.

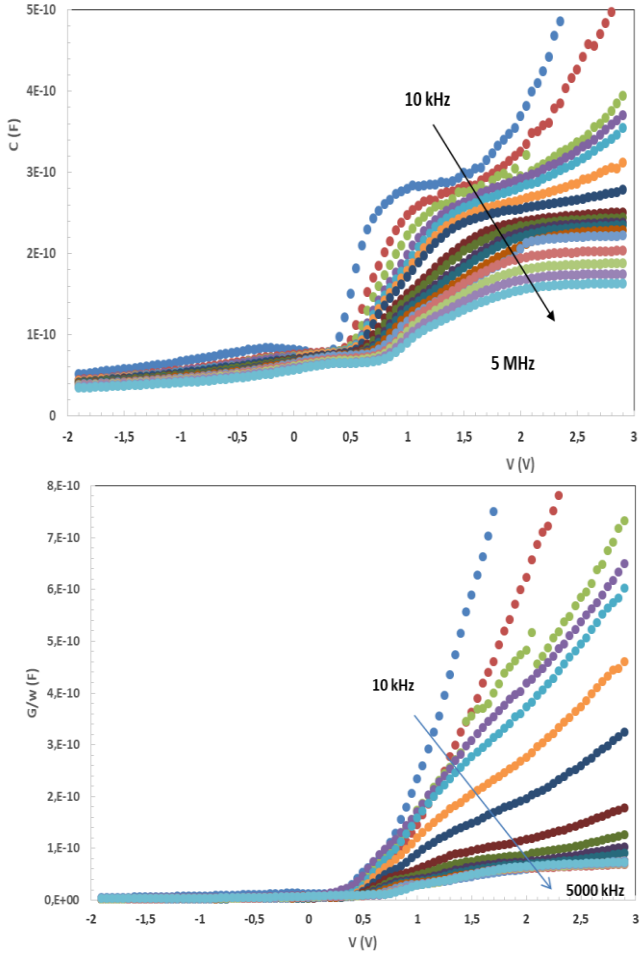


Fig.1: (a) C-V-f and (b) G/w-V-f characteristics of the Au/(MgO-PVP)/ n-Sİ structure.

Therefore, both the voltage-dependent profile of R_s and D_{it} were obtained by using the low-high frequency (C_{LF}–C_{HF}) and Nicollian-Brews methods. [11,15]. In the equivalent circuit of MIS type structure, the interlayer capacitance Ci is connected in series with the parallel combination of the interface traps/states capacitance (C_{ss}) and the space charge capacitance (C_{sc}). Thus, the voltage dependent profile of the D_{it} obtained from the measured high frequency (1 MHz) and low frequency (10 kHz) by using following relation [15].

Thus, the interface state density D_{it} is evaluated as follows:

$$qAD_{it} = C_{it} = \left[\frac{1}{C_{LF}} - \frac{1}{C_i}\right]^{-1} - \left[\frac{1}{C_{HF}} - \frac{1}{C_i}\right]^{-1} \quad (1)$$

In Eq. 1, q is the elementary charge and A is the rectifier contact area of the structure.

As can be seen in Fig 2, the distributions of D_{it} –V show a peak at about 4 V due to a special densisty disturibition of interface traps between organic interlayer and n-Si. The obtained value of D_{it} is suitable for an electronic device when compared MIS or MOS type structures. The obtained low mean value of D_{it} ($\cong 10^{12}$ $ev^{-1}.cm^{-2}$) is the result of passivation effect of the used MgO-doped PVP organic interlayer.

The voltage dependent value of R_s was also extracted from the measured the C and G/w values at 1 MHz by using Nicollian-Brews method [15]. The voltage-dependent profile of R_s was subtracted from the measured C and G values by using the following relation:

$$R_s = \frac{G_m}{G_m^2 + \left(\omega C_m\right)^2} \quad (2)$$

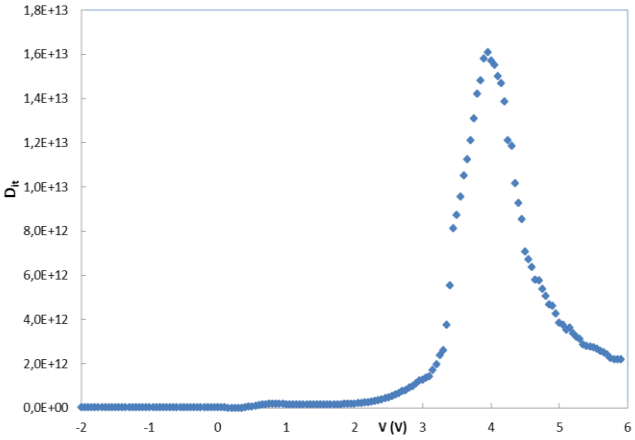


Fig.2: D_{it}-V profile of Au/(MgO-PVP)/n-Si structure.

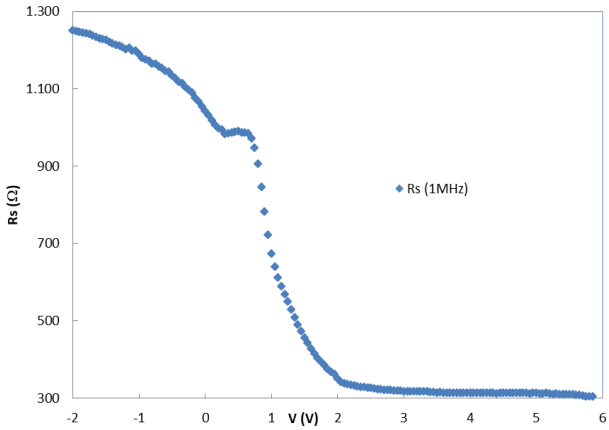


Fig.3: R_s-V profile of Au/(MgO-PVP)/n-Si structure.

As can be seen in Fig. 3, the value of R_s is more effective at accumulation region at high frequency, but the value of D_{it} is more effective both in the depletion and inversion region both at low and intermediate frequencies. These results show that the existence of D_{it}, R_s, and interfacial layer are more effective on the impedance measurements (C-V and G/w-V) characteristics. Therefore, they must be taken into account in the calculations to get more reliable and accuracy results.

Conclusions

In this study, Au/(MgO-PVP)/n-Si (MPS) structures were fabricated on the n-Si wafer instead of conventional MOS structure to increase the performance of the MS structure in respect of get low D_{it}, R_s , and high value of capacitor. For this reason, the capacitance-voltage (C-V) and conductance-voltage (G/w-V) measurements were performed in wide frequency (10 kHz- 5 MHz) and voltage (-2/3 V) at room temperature, respectively. Both of the measured C and G/ω were found as a strong function of frequency and applied bias voltage owing to the frequency-dependent charges and the resistivity effect of the structure. The voltage dependent profile of D_{it} and Rs were extracted from the low (10 kHz) and high (1 MHz) frequencies and Nicollian-Brews methods, respectively. The mean value of D_{it} ($=10^{12}$ $eV^{-1}cm^{-2}$) is considerably low when compared a conventional MOS structure. Such low value of D_{it} is the result of passivation effect of the used (MgO-PVP) organic interlayer. Additional, these results show that while D_{it} is effective in inversion and depletion regions at low-intermediate frequencies, R_s is effective only at accumulation region especially at high frequencies and these two important

parameters must be taken into account both in the electric and dielectric properties of these structures.

References:

[1] İ. Yücedağ, A. Kaya, ¸S. Altındal, and İ. Uslu, "Frequency and voltage dependent electrical and dielectric properties of Al/Co-doped PVA/pSi structures at room temperature," Chin. Phys. B, vol. 23, p. 047304, Feb. 2014.

[2] M. Gökçen, T. Tunç, S. Altındal, and İ. Uslu, "Electrical and photocurrent characteristics of Au/PVA (Co-doped)/n-Si photoconductive diodes, " Mater. Sci. Eng. B., vol. 177, pp. 416–420, Mar. 2012.

[3] S.A. Yerişkin, M. Balbaşı, İ. Orak, The effects of (graphene doped-PVA) interlayer on the determinative electrical parameters of the Au/n-Si (MS) structures at room temperature, Journal of Materials Science: Materials in Electronics. 28 (2017) 14040–14048. doi:10.1007/s10854-017-7255-1.

[4] R.K. Gupta, K. Ghosh, P.K. Kahol, Fabrication and electrical characterization of Au/p-Si/STO/Au contact, Current Applied Physics. 9 (2009) 933–936. doi:10.1016/J.CAP.2008.09.007.

[5] H.E. Lapa, A. Kökce, A.F. Özdemir, İ. Uslu, Ş. Altındal, A comparative study on dielectric behaviours of Au/(Zn-doped PVA)/n-4H-SiC (MPS) structures with different interlayer thicknesses using impedance spectroscopy methods, Bulletin of Materials Science. 41 (2018) 82. doi:10.1007/s12034-018-1602-6.

[6] A. Kaya, S. Alialy, S. Demirezen, M. Balbaşı, S.A. Yerişkin, A. Aytimur, The investigation of dielectric properties and ac conductivity of Au/GO-doped PrBaCoO nanoceramic/n-Si capacitors using impedance spectroscopy method, Ceramics International. 42 (2016) 3322–3329. doi:10.1016/J.CERAMINT.2015.10.126.

[7] T. Tunç, ¸Ş. Altındal, İ. Dökme, and H. Uslu, "Anomalous peak in the forward-bias C–V plot and temperature-dependent behavior of Au/PVA (Ni,Zn-doped)/n-Si(111) structures," J. Electron. Mater., vol. 40, pp. 157–164, Dec. 2010.

[8] P. Chattopadhyay and B. Ray Chaudhuri, "Frequency dependence of forward capacitance-voltage characteristics of Schottky barrier diodes," Solid-State Electron., vol. 36, pp. 605–610, Apr. 1993.

[9] S.-S. Li, Y.-Y. Lin, W.-F. Su, and C.-W. Chen, "Polymer/metal oxide nanocrystals hybrid solar cells," IEEE J. Sel. Topics Quantum Electron., vol. 16, no. 6, pp. 1635–1640, Nov./Dec. 2010.

[10] Y. Azizian-Kalandaragh, "Impedance spectroscopy (IS) and thermally stimulated discharged current (TSDC) studies on CdSe-PVA nanocomposites prepared by ultrasound-assisted method," Optoelectron. Adv. Mater., vol. 4, pp. 174–179, Feb. 2010.

[11] S. M. Sze, Physics of Semiconductor Devices, 2nd ed. New York, NY, USA: Willey, 1981, ch. 7.

[12] P. Chattopadhyay and B. Ray Chaudhuri, "Frequency dependence of forward capacitance-voltage characteristics of Schottky barrier diodes," Solid-State Electron., vol. 36, pp. 605–610, Apr. 1993.

[13] H. C. Card and E. H. Rhoderick, Studies of tunnel MOS diodes I. Interface effects in silicon Schottky diodes, J. Phys. D Appl. Phys. 4 (1971), pp. 1589-1601.

[14] B. L. Sharma, Metal-Semiconductor Schottky Barrier Junctions and Their Applications, Plenum Press, New York and London, 1984.

[15] E. H. Nicollian and J. R. Brews, MOS (Metal Oxide Semiconductor) Physics and Technology. New York, NY, USA: Wiley, 1982, pp. 117–129.

6th International Conference on Materials Science and Nanotechnology For Next Generation (MSNG2019)
October 16-18, 2019, Niğde, TURKEY (ORAL FULL TEXT)

Dye sensitive solar cells based on Mn-doped ZnO photoelectrodes

Halil ESGİN[1], Yasemin CAGLAR[2]

1 Cukurova University, Central Research Laboratory, Adana, TURKEY
2 Eskisehir Technical University, Science Faculty, Department of Physics, Eskisehir, TURKEY

In present study, Manganase (Mn) doped Zinc Oxide (ZnO) nanopowders, which are also used as electrodes in dye sensitive solar cells, have been deposited by hydrothermal synthesis method. Zinc acetate dihydrate, manganese acetate were used as the starting materials and dopant source. Sodium dodecyl sulfate (NaC12H25SO4; SDS) were used as the surfactant and sodium hydroxide (NaOH) as the reactant. The morphological properties of Mn doped ZnO nanopowders were investigated by scanning electron microscopy (SEM) and the structural properties were examined by X-ray diffractometer (XRD). The Mn doped ZnO nanopowders were coated onto the flourine doped tin oxide (FTO) surfaces by the doctor blade method for the first step of the formation of the dye sensitive solar cell. After coating, Mn doped ZnO films were annealed at 450 °C and then immersed in ruthenium-based dye solution for different immersion time. The dye-absorbed Mn doped ZnO films were combined with Pt counter electrodes to form sandwich type DSSC using sealed adhesive. After electrolyte injection into the DSSC, current-voltage (I-V) curves were obtained under a solar simulator with 1 sun intensity and an AM 1.5 filter. The solar cell parameters of the DSSCs were determined. The performances of the fabricated DSSCs have been compared and the ZM01-DSSC showed a better performance as 2.22% efficiency.

Keywords: Mn Doped ZnO, DSSC, Hydrothermal Synthesis, SEM, Solar Performance.

Corresponding author: esginhalil@gmail.com

1. Introduction

Most of the energy used today is supplied by fossil fuels such as coal, petroleum and natural gas. In addition to the depletion of these fuels and the continuous increase in their prices, they cause damages to the environment as a result of their combustion and their effects on human health are also great. In 2009, the rate of renewable energy use was eight percent. The usage amount of renewable energy especially photovoltaics has increased over the years. As of 2017, usage of renewable energy has reached 11,3%. The rate of solar cells in this increase is quite high. Therefore, low-cost and high-performance solar cell production is highly valued. In 1991, A new technology (DSSCs) has developed by Michael Graetzel, which replicates the photosynthesis phenomena in plant leaves, have become a promising technology with their low-cost production and durable structure. The basic structure of DSSCs consists of transparent conductive oxide (TCO) / Photoanode (porous metal oxide) / DYE molecules / Electrolyte / Platinum coated TCO.

In practice, DSSC contains expensive materials such as platinum, ruthenium which are difficult to eliminate. Also, liquid electrolyte presents a serious challenge to making a cell suitable for use in all weather. Although its conversion efficiency is less than the best thin-film cells, in theory its price/performance ratio should be good enough to allow them to compete with fossil fuel electrical generation by achieving grid parity.

In dye-sensitive solar cells, the dye molecules are impregnated on the photoanode which is oxide semiconductor in nano scale such as titanium dioxide, zinc oxide. The most promising results were obtained with ZnO which is used as photoanode material in dye sensitive solar cells [1]. However, the energy conversion

efficiency value in ZnO-based DSSCs is relatively low. The main reason for low efficiency is the limitations in the short-circuit current density, which depend on the surface characteristics of the photoanode and the counter electrode [2]. The resistance, surface morphology, photocatalytic activity and band gap of the ZnO semiconductor can be brought to the desired values with the appropriate doping material.

ZnO nano material doped with 3d transition metals shows wide application areas such as catalysis, field effect transistors, solar cells etc. [3]. In this study, we made an attempt to increase the efficiency of ZnO based DSSCs by doping the element Mn in ZnO photoanode.

There are many techniques such as pulsed laser deposition [4], sol-gel method [5] spraying [6],hydrothermal [7] are used to obtain Mn doped ZnO nanopowder. Although there are many methods in the literature for the production of nanoscale metal oxide materials, hydrothermal synthesis method has been preferred because of the lower working temperatures and lower cost. Hydrothermal synthesis method is a technologically important method for crystal growth and the synthesis of new materials with useful properties. It is also interesting scientifically because using high pressure provides an additional parameter for obtaining fundamental information on the structures, behavior and properties of solids. Furthermore, it is possible to obtain more homogeneous and higher crystallinity material compared to other methods.

In present work, Mn doped ZnO nanopowders were produced by hydrothermal synthesis method at varying concentrations. Doctor blade method was used to produce Mn doped ZnO films. Scanning Electron Microscopy (SEM) was used to determine morphological features of synthesized ZnO nanostructures and X-ray diffraction method (XRD) was used to determine structural features. The solar parameter of the ZnO:Mn-DSSCs were also investigated by using an solar simulator.

2. Experimental details

2.1. Synthesis of Mn doped ZnO

The Mn doped ZnO nanopowders were synthesized by the hydrothermal method. Zinc nitrate hexahydrate ($Zn(NO_3)_2.6H_2O$) and Sodium hydroxide (NaOH) were used as starting materials for the ZnO nanopowders. Manganese Acetate ($(CH_3COO)_2Mn\cdot H_2O$) was used as dopant source. To obtain a homogeneous solution, these were dissolved in water by mixing the appropriate stoichiometric ratios of initial materials in 10 minutes. Then 1g sodium dodecyl sulfate ($NaC_{12}H_2.5SO_4$) was added and stirred for 30 minutes. Then, the solution was placed to 100 mL capacity of Teflon coated stainless steel autoclaves. The Teflon-lined stainless-steel autoclaves was heated at 140°C for 12 h. Subsequently, the autoclave was cooled to room temperature. The resulting white precipitates were collected by filtration and washed with deionized water and ethanol for several minutes. The final products were dried in an oven at 60 °C. The obtained powders were named as ZM0, ZM01, ZM05, ZM1, ZM3 and ZM8, respectively.

2.2. Fabrication of ZnO:Mn-DSSC

For dye-sensitive solar cell production, firstly ZnO paste was prepared by mixing ZnO nanopowder, triton-X 100 and acetyl acetone. ZnO paste was coated by a doctor blade method on the cleaned FTO surface. ZnO film, which is used as electrode in DSSC fabrication is immersed in ruthenium-based dye solution (0.5 mM N719 (Ruthenizer 535 bis-TBA, Solaronix)) at room temperature. ZnO films were kept in a ruthenium-based dye solution for 1-4 h hours to allow dye absorption. In order to form the DSSC structure, the platinum (Pt) coated glass with a small hole in the middle was clipped together with the counter electrode and then the electrolyte was dropped into hole. The active area of the fabricated cells during exposure to light was approximately 0.25cm^2.

The XRD of the nanopowders is carried out using CuKα radiation in a Rigaku SMARTLAB diffractometer. The morphological analyses of the nanopowders are performed using by SEM (TESCAN MAIA3). The photocurrent characteristicsof the prepared cell are measured using a solar cell measurement system (FYTRONIX OPTOSENSE).

3. Results and discussion

The SEM images of the ZnO nanopowders have been shown in Fig.1. Looking at the SEM images of the Mn doped samples, it was observed that each nanoparticle size was reduced with decreasing amount of dopant and that the leaf-like elongated state became shorter and rounded (coin shape). It has been observed that rod-like structures are formed at high additive amount.

XRD pattern of ZnO:Mn nanopowders have been shown in Fig. 2. The synthesized ZnO nanostructures were crystallized in hexagonal zincite structure and polycrystalline form (ICCD card no. 01-079-0206). No characteristic peak of the surfactant or reactant used during production was found. Also, there were no peaks of Mn and Manganese Oxide derivatives. It has been

found that the production method is suitable for obtaining very pure products.

The current density-voltage (*J-V*) graphs for DSSCs are given in Fig. 3-8 at different dipping time (1-4h) under AM 1.5 simulated sunlight at 100 mW/cm^2. From the *J-V* graphs, open circuit voltage (V_{oc}), short circuit current density (J_{sc}), full factor (FF) were estimated and conversion efficiency (n%) was calculated using Equation (1) [8]. All solar parameters were given in inset in Fig. 3-8.

$$n\% = \frac{Fill\ Factor\ x\ I_{sc}\ x\ V_{oc}}{P_{in}} x100\% = \frac{P_m(\frac{mW}{cm^2})}{Light\ Intensity\ (\frac{mW}{cm^2})} x100\% \quad (1)$$

where P_{in} is the intensity of the incident light.

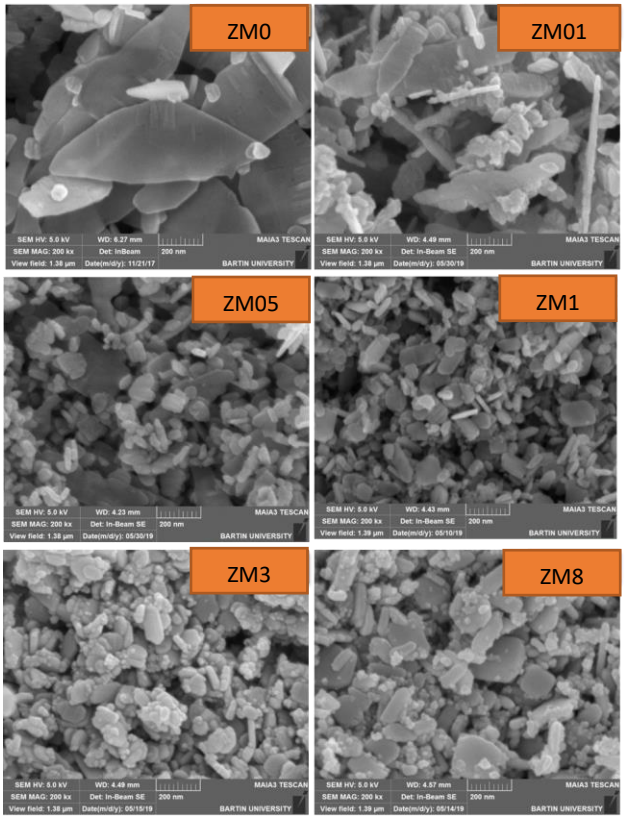


Figure 1. *SEM images of the Mnu doped ZnO powders at different magnifications*

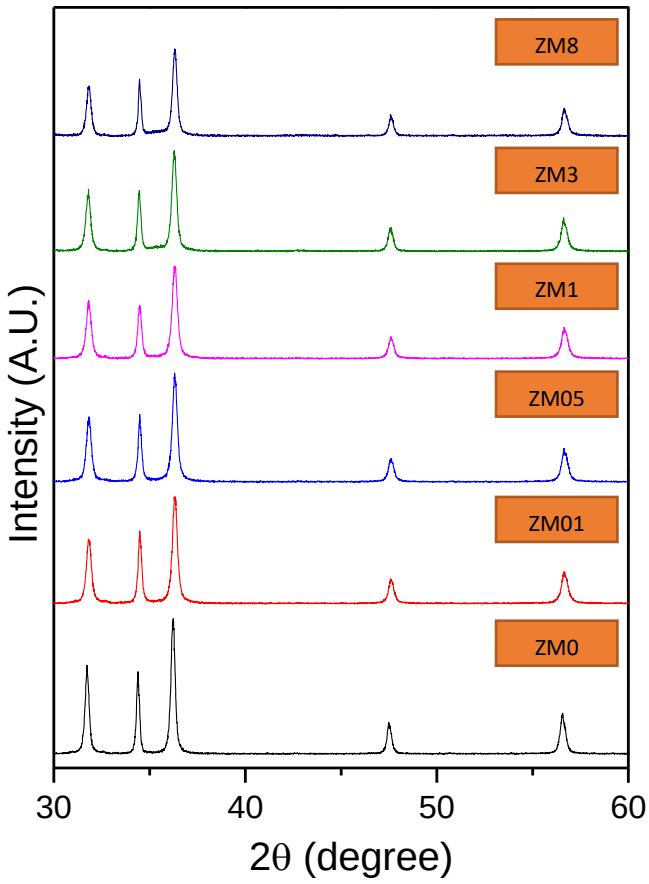


Figure 2. *XRD spectra of the Mn doped ZnO powders*

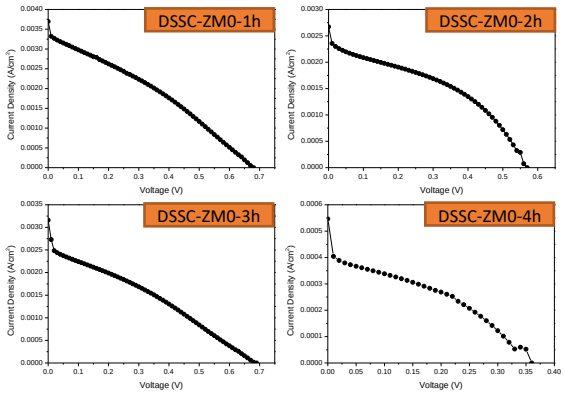


Figure 3. *J-V curves of the ZnO-DSSC*

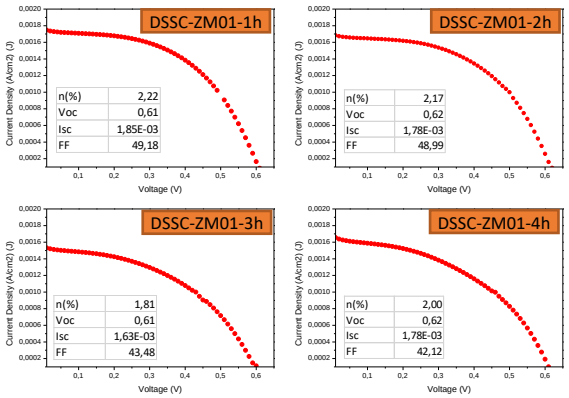


Figure 4. *J-V curves of the ZnO:0.1%Mn-DSSCs*

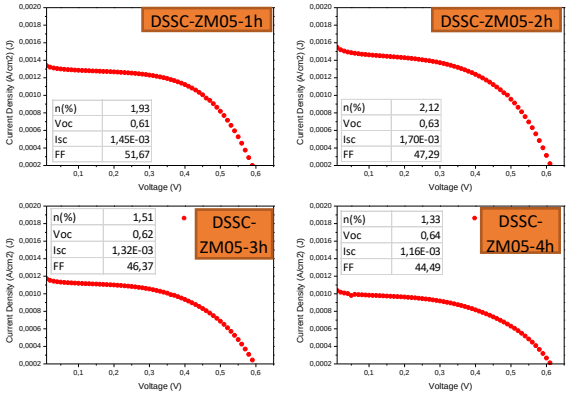


Figure 5. *J-V curves of the ZnO:0.5%Mn-DSSCs*

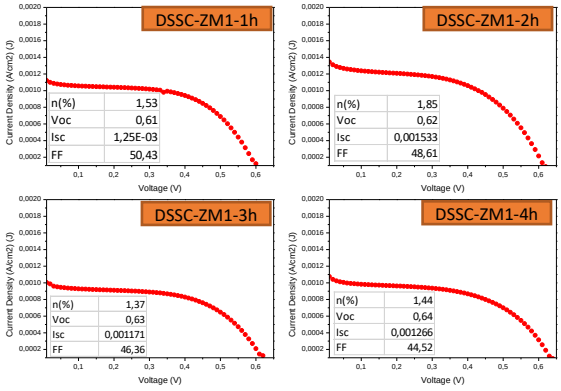


Figure 6. *J-V curves of the ZnO:1%Mn-DSSCs*

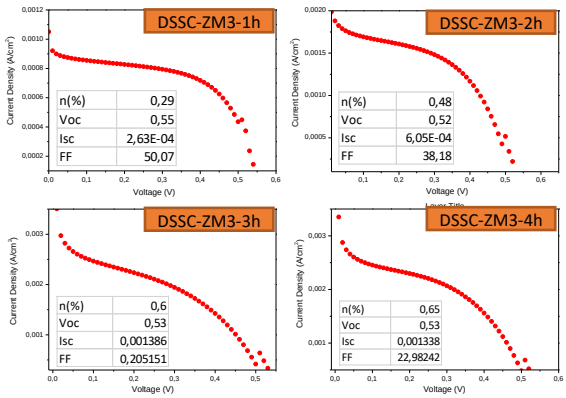


Figure 7. *J-V curves of the ZnO:3%Mn-DSSCs*

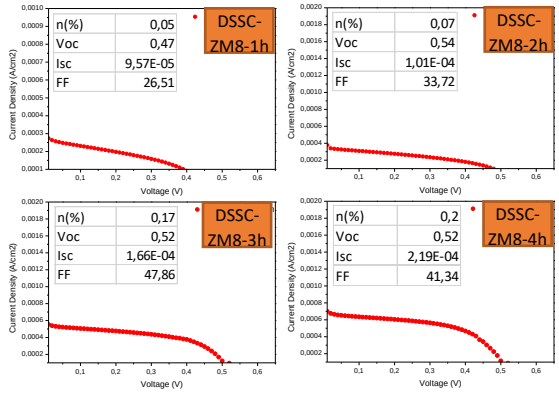


Figure 8. *J-V curves of the ZnO:8%Mn-DSSCs*

These graphs show that the dipping time and the concentration of Mn are highly effective on the solar parameters of the solar cells. The highest efficiency in all cells was achieved in 1-hour dipping time and 0.1% Mn dopant amount. For each dopant concentration, the solar cell parameters such as n%, V_{oc}, I_{sc}, FF value increased to a dipping time of 2 hours and then shifted a downward trend. In addition, the highest values were obtained with 0.1% dopant concentration. As a result, efficiency value increased from 0.71% to 2.22% compared to pure ZnO by doping Mn.

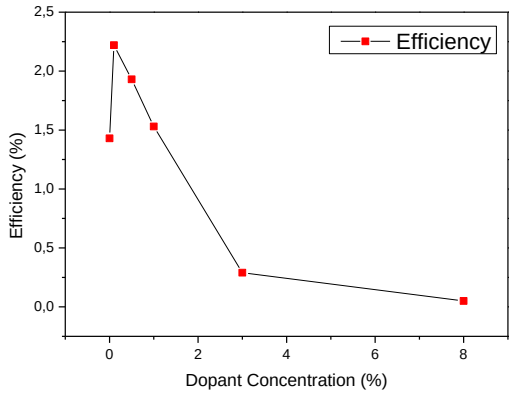


Figure 9. *Efficiency values of the ZnO:Mn-DSSCs at different dopant concentration.*

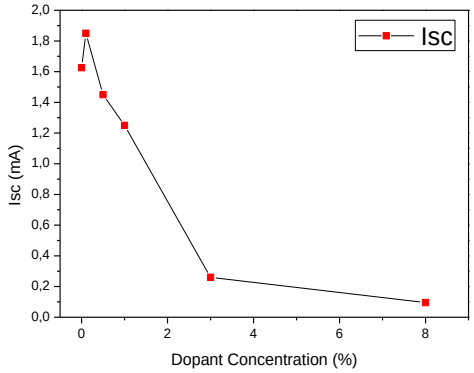


Figure 10. *Short circuit current values of the ZnO:Mn-DSSCs at different dopant concentration.*

The graphs in figure 9-11 show the changes in the solar cell parameters (n%, V_{oc}, I_{sc}) depending on the Mn concentration. It is clear that the solar cell parameters at the dopant concentration of 0.1% are the highest value

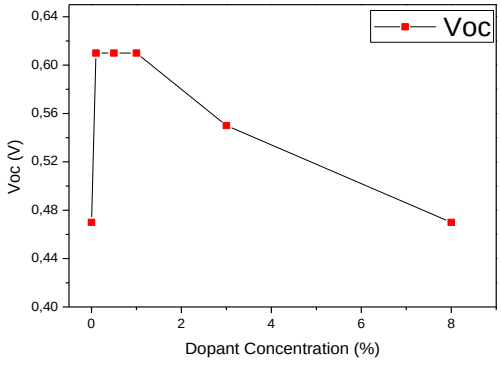


Figure 11. *Open circuit voltage values of the ZnO:Mn-DSSCs at different dopant concentration.*

4. Conclusion

The hydrothermal method was used to synthesize Mn doped ZnO nanopowders. Structural and morphological properties of undoped and Mn doped ZnO nanopowders were investigated by XRD and SEM. ZnO:Mn-DSSCs were fabricated using N719 dye-sensitized at different Mn concentration and different dipping time. The effects of dopant concentration and dye dipping time on DSSC parameters were systematically investigated. The efficiency value increased by approximately 3 times compared with pure ZnO.

5. Acknowledgement

This work was supported by Eskisehir Technical Commission of Scientific Research Project under Grant No. 1706F385 and 19ADP157

References:

[1] L.-Y. Lin, M.-H. Yeh, C.-P. Lee, C.-Y. Chou, R. Vittal, and K.-C. Ho, "Enhanced performance of a flexible dye-sensitized solar cell with a composite semiconductor film of ZnO nanorods and ZnO nanoparticles," *Electrochim. Acta*, vol. 62, pp. 341–347, 2012.

[2] K. Hongsith, N. Hongsith, D. Wongratanaphisan, A. Gardchareon, S. Phadungdhitidhada, and S. Choopun, "Efficiency Enhancement of ZnO Dye-sensitized Solar Cells by Modifying Photoelectrode and Counterelectrode," *Energy Procedia*, vol. 79, pp. 360–365, 2015.

[3] Z. L. Wang, "Zinc oxide nanostructures: growth, properties and applications," *J. Phys. Condens. matter*, vol. 16, no. 25, p. R829, 2004.

[4] T. Fukumura, Z. Jin, A. Ohtomo, H. Koinuma, and M. Kawasaki, "An oxide-diluted magnetic semiconductor: Mn-doped ZnO," *Appl. Phys. Lett.*, vol. 75, no. 21, pp. 3366–3368, 1999.

[5] R. Viswanatha *et al.*, "Synthesis and Characterization of Mn-Doped ZnO Nanocrystals," *J. Phys. Chem. B*, vol. 108, no. 20, pp. 6303–6310, May 2004.

[6] V. R. Shinde, T. P. Gujar, C. D. Lokhande, R. S. Mane, and S.-H. Han, "Mn doped and undoped ZnO films: A comparative structural, optical and electrical properties study," *Mater. Chem. Phys.*, vol. 96, no. 2, pp. 326–330, 2006.

[7] T. Yang *et al.*, "Room-temperature ferromagnetic Mn-doped ZnO nanocrystal synthesized by hydrothermal method under high magnetic field,"

Mater. Sci. Eng. B, vol. 170, no. 1, pp. 129–132, 2010.

[8] Z.-S. Wang, H. Kawauchi, T. Kashima, and H. Arakawa, "Significant influence of TiO2 photoelectrode morphology on the energy conversion efficiency of N719 dye-sensitized solar cell," *Coord. Chem. Rev.*, vol. 248, no. 13, pp. 1381–1389, 2004.

6th International Conference on Materials Science and Nanotechnology For Next Generation (MSNG2019)
October 16-18, 2019, Niğde, TURKEY (ORAL FULL TEXT)

Thermophysical Behaviours of Alumix-431 –Fe Alloy Mixtures prepared by Powder Metallurgy Method

Ayşe Nur Acar*[1,3], Rasiha Nefise MUTLU[2], Abdul Kadir EKSİ[3], Ahmet EKİCİBİL[4]

[1]*Cukurova University, Ceyhan Engineering Faculty, Mechanical Engineering Department, Ceyhan, Adana,Turkey*
[2]*Cukurova University, Sciences and Letters Faculty, Chemistry Department, Sarıçam, Adana,Turkey*
[3]*Cukurova University, Engineering Faculty, Mechanical Engineering Department, Sarıçam, Adana,Turkey*
[4]*Cukurova University, Sciences and Letters Faculty, Physics Department, Sarıçam, Adana,Turkey*

Aluminum and aluminum based alloys possses, physical properties such as good strength. These physical properties can be controlled with additive suitable alloying elements to aluminum base metal. Therefore these aluminum and alumium based alloys use in wide industrial areas such as automotive industry because of improved properties via adding suitable alloying elements.In this study; Alumix-431 alloy powder mixed with %2.5, 5 and %10 Fe. Mixed alooy mixtures pelleted on the 150kPa pressure. These pelleted alloy mixture samples sintered 610°C temperature for an hour under N_2 atmosphere. In order to examine thermophysical properties of these samples; specific heat capacity behaviour has been performed via heat flux type Differential Scanning Calorimeter (DCS). Specific heat capacity measurements supported by SEM images, EDS spectrums and XRD patterns of these alloy samples

Keywords: Aluminium, powder metallurgy, specific heat capacity,y structural characterisation
*Corresponding author: anacar@cu.edu.tr

1. Introduction

For researchers; Powder metallurgy is a widely utilized production method on the preparing of aluminium based alloys. This method provides net or near-net shape, complex shape, good physical properties and high dimensional tolerance. These properties are generally obtained with pressing technique and heat treatment due to nature of this method [1-5]. Heat treatment on the aluminium based alloys acquires binding of Al and other alloying element s (i.e. Fe) each other and obtaining transient liquid phase. This phase leads to densification of the pressed materials and also occurring of intermetallic phases [5]. In this study; the thermophysical properties (specific heat capacity) of alumix -(431)-Fe alloy mixtures with 2.5; 5 and 10 %Fe alloying element prepared by this method have been examined. These properties of these alloy mixtures supported by SEM images, EDS spectrums and XRD patterns.

2. Experimental Details

In this study; the chemical composition of Alumix-(431) alloy powder that is obtained from Ecka Granule in Germany is 89 % of Al, 1.5% of Cu, 2.5 % of Mg 5.5% of Mg with 1.5% of lubricant and the Alumix-(431) powder mixed with different contents of Fe alloying elements (2.5; 5 and 10% Fe).Alumix-(431) –(2.5; 5 and 10% Fe)alloy mixtures placed into cylindrical molds on dimensions of (20×10)mm and alloy mixture powder pelleted on the 150kPa pressure. Pelleted mixture samples sintered at 610°C temperature for an hour under N_2 atmosphere and cooled to room temperature (RT). Heating and cooling temperature rate selected as 20°C/min. In order to examine the specific heat capacity behaviours of these sintered samples; samples cut down to small pieces. These behaviours of these samples were performed at range of 40 to 600°C of Differential Scanning Calorimeter (DSC) with 20 °C/min of heating rate, 50mL/min gas flow and applied under N_2 atmosphere and also this behaviours supported by SEM images with FEI Quanta 650 Field Emission SEM device; EDS spectrums which is subsidiary SEM device and crystal structures of these samples characterized by PANalytical Empyrean XRD (λ=1.54Å) device.

Table 1. *The specific heat capacity values of Alumix-(431)-Fe%2.5 (a) ,%5 (b) and 10%(c) mixtures with fitted values and errors%.*

T(°C)	2.5% Fe	Fitted (2.5%Fe)	Error%	5% Fe	fitted (5%Fe)	Error %	10%Fe	fitted (10%Fe)	Error %
40	1,19	1,206844506	-1,415504668	1,22	1,256	-2,86624203	1,28	1,305857023	-1,98008071
100	1,28	1,225139861	4,285948337	1,46	1,316	10,94224924	1,49	1,333840741	11,70748911
160	1,32	1,250377103	5,274461893	1,53	1,4012	9,19212104	1,58	1,384939685	14,08439061
220	1,31	1,282520552	2,097667821	1,47	1,5116	-2,75205080	1,5	1,459136614	2,80051816
280	1,36	1,321569344	2,825783496	1,72	1,6472	4,419621176	1,6	1,556430873	2,799297289
340	1,63	1,367523369	16,10286078	1,58	1,808	-12,6106194	1,6	1,676822365	-4,581425372
400	1,44	1,4203826	1,362319447	1,94	1,994	-2,70812437	1,93	1,820311068	6,025834462
460	1,45	1,480147028	-2,07910541	1,5	2,2052	-31,9789588	1,53	1,986896974	-22,99550406
520	1,54	1,546816652	-0,44263972	1,46	2,4416	-40,2031454	1,49	2,17658008	-31,54398437
580	1,43	1,620391468	-13,3140886	1,45	2,7032	-46,3598697	1,55	2,389360385	-35,12908268

3. Results and discussion

On this study; Alumix(431) powder that has irregular shaped particle and mean particle size distribution of 108μm utilized.

Specific heat capacity of alloys is needed heat amount which is risen temperature of 1 g of alloys by 1 °C or 1 K [6-8] The Figure 1 gives the Specific heat capacity v.s. temperature curves of sintered Alumix-(431) – (2.5; 5 and 10%) Fe alloy mixtures and on the Table 1; specific heat capacity values of these samples were given with fitted heat capacity values.. Specific heat capcity values fitted according to following equation (1)[8,9]. On the equation (1); c_0,c_1,c_2 and c_3 are coefficients of specific heat capacity.

$$c_p = c_0 + c_1 x + c_2 x^2 + c_3 x^{-3} \quad (1)$$

It was observed that heat capacity values increased with increasing temperatures but not showed perfectly linear increase due to increasing in the amplitude of atomic vibration of the composition of the new material with increasing of temperature[10]. In the first run; at temperature range of 100-200°C, the exothermic peak observed on the all the Alumix (431) – Fe alloy mixtures. In second run; exothermic peak is observed at range of 220- 350 °C temperature for both Alumix (431) -5 and 10% Fe alloy mixtures and at temperature range of 280-400 °C temperatures for Alumix (431) – 2.5%Fe alloy mixture. ın third run, exothermic peak is observed at range of 340- 460°C temperatures for both Alumix (431) -5 and 10% Fe alloy mixtures and at temperature range of 460- 580 °C temperatures for Alumix(431) – 2.5%Fe alloy mixture. The endothermic peaks are observed at range of 450-580°C temperatures for both of Alumix (431) -5 and 10% Fe alloy mixtures and at temperature range of 350-450°C for Alumix (431)-2.5% Fe alloy mixture. According to article of Zahra *et al.*, the first c_p increase is attributed to GP zone reversion and stable η ($MgZn_2$) dissolution and also indirect evidence for the existence of large sized Guinier-Preston (GP) zones[11].

Supersaturated solid solution (SSSα) →GP zones→η phase

From Figure 1 and Table 1; it was apparently observed that specific heat capacity of alloy mixtures increased with increasing of Fe content. Maximum specific heat capacity was obtained on the Alumix-(431)- 10% Fe alloy mixture (1.55 J/°C at 580°C).

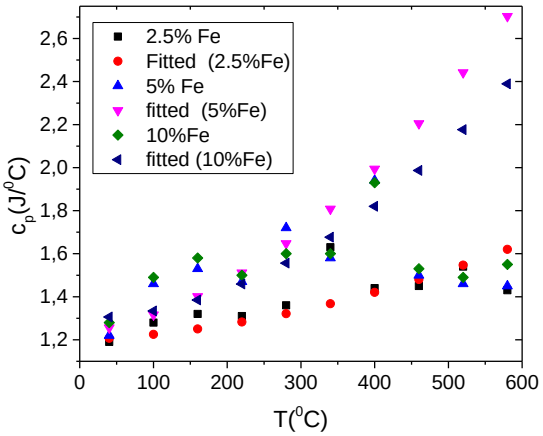


Figure 1. *The Specific heat capacity- temperature curves of Alumix-(431)-(2.5,5 and 10%Fe alloy mixtures*

Table 2. *The fit coefficients and nonlinear –squares regression values of specific heat capacity behaviour of Alumix-(431)-Fe%2.5 (a) ,Fe%5 (b) and Fe 10%(c) mixtures*

	Alumix-(431)-2.5%Fe	**Alumix-(431)-5%Fe**	**Alumix-(431)-10%Fe**
c_0	1,200000618	1,23	1,3
c_1	0,000188166	5,10E-04	1,76E-05
c_2	9,59054E-07	3,50E-06	3,21E-06
c_3	1,199999807	0,000001	1,3
R^2	0,9651	0,9622	0.9444

Table 2 gives The fit coefficients and nonlinear –squares regression values of specific heat capacity behaviour of Alumix-(431)-Fe%2.5 (a) ,Fe%5 (b) and Fe 10%(c) mixtures. According to Table 2, the best fit obtained on the Alumix-(431)- 5% Fe alloy mixture (R^2=0.9622).

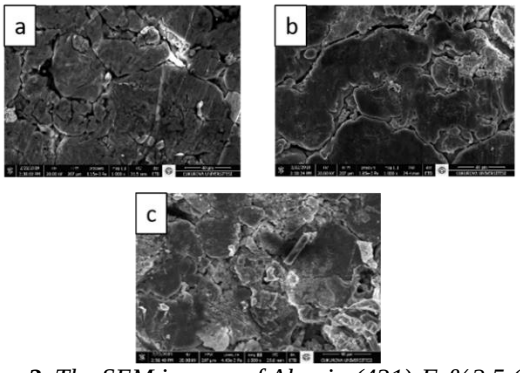


Figure 2. *The SEM images of Alumix-(431)-Fe%2.5 (a) ,5%*
(b) and 10%(c) mixture

The SEM images of Alumix-(431)-Fe alloy mixtures were observed on the Figure 2. As a known; after heat treatment besides shaping technique such as pressing; grain bonding occurs and big particles and grain boundaries forms. It interestingly observed that, as the Fe content on the Alumix-(431) alloy increased; on the surfaces of these alloy mixtures, spongelike formations were apeeared. It was observed that on the Alumix-(431) -2.5%Fe alloy mixture; formation of Fe consisting particles is least to other alloy mixtures and occurring of Fe consisting particles is mostly found on the Alumix-(431)-10%Fe alloy. This case supported by EDS spectrums of these alloy mixtures in Table 3.. from EDS spectrums; decreasing of Fe and Zn alloying elements can be recommended that spinel formation occurs besides Fe-including.

Table 3.*The EDS spectrums of Alumix-(431)-Fe%2.5 (a) ,Fe%5 (b) and Fe 10%(c) mixtures*

Element	**Alumix(431)-2.5%Fe**	**Alumix(431)-5%Fe**	**Alumix(431)-10%Fe**
Al	92.43	79.0	73.13
Mg	3.03	3.22	2.9
Zn	2.48	12.34	16.73
Cu	1.33	2.80	2.42
Fe	0.73	2.63	4.81

According to literature; at high cooling rates, owing to kinetic limitations there is not adequate time for arranging of atoms of alloys themselves into a stable solid structure. Thereby, occurrence of a mostly irregular packed but kinetically preferred metastable structure forms. [12-14]., Whereas only the kinetic approach is not sufficient due to

scarce knowledge of atomic motion throughout solidification; the formation kinetics dominates over the thermodynamics [13,14]. Fe in Al alloys happens the formation Fe- binded phase and Al-Fe phase easily cause to stress concentration.[15,16,5]. Fe is one of the widely used alloy elements in Al alloys and the solid solubility of Fe into Al is relatively low [15,17-19]. Owing to solid solubility of Fe into the Al matrix, Al_3Fe phase can be depurated via rapid solidification that is spreaded via rising of cooling rate [15,20]. XRD patterns of sintered Alumix-(431)-(2. (2.5, 5 and 10wt %) Fe alloy mixtures showed on the Figure 4. On the XRD patterms of sintered Alumix-(431)-(2. (2.5, 5 and 10wt %) Fe alloy mixtures; that $A_{l3}Fe$ formations appeared in the Alumix-431-2.5%Fe mixtures whereas this phase formation is not observed on the other mixtures and this case can be recommended that this phase is also found on the other mixtures and overlapped of diffraction angles of Al and Fe on the XRD patterns of these alloy mixtures [21].

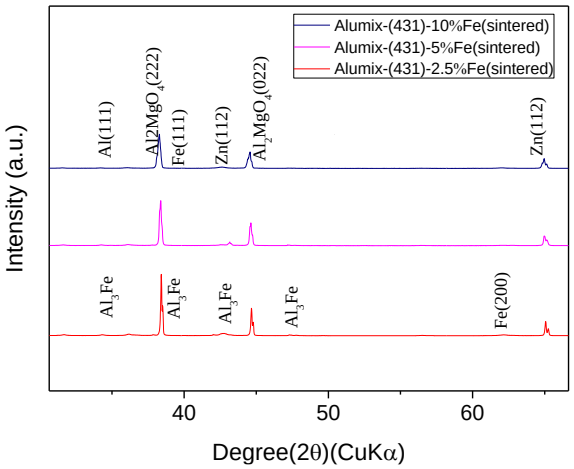


Figure 4. *The XRD Patterns of Alumix-(431)-Fe%2.5, 5% and 10%(c) mixture*

4. Conclusion

In this study; specific heat capacity behaviours of Alumix 431 –Fe alloy mixtures prepared by powder metallurgy method investigated. Following experimental results were given;

-Specific heat capacity values increased with increasing temperatures but not showed perfectly linear increase.

-Maximum specific heat capacity was obtained on the Alumix-(431)- 10% Fe alloy mixture (1.55 J/°C at 580°C).

-On the SEM images; formation of Fe intermetallics and spinel observed

-on the XRD patterms; except that Al_3Fe, other phases is not showed owing to overlap of diffraction angles of Al and Fe alloying elements.

5.Acknowledgement:

The authors are greatly thankful to Cukurova University research funding (FBA-2018-11074)

References:

[1] AZARNIYA A., TAHERI A.K., TAHERI K.K., Recent Advances in Ageing of 7xxx Series Aluminum Alloys: A Physical Metallurgy Perspective Journal Of Alloys And Compounds 781, 945-983,2019.

[2] MISHRA R.S., H. SIDHAR H., Chapter 2 - Physical Metallurgy Of 2XXX Aluminum Alloys, in: Friction Stir Welding Of 2XXX Aluminum Alloys Including Al-Li Alloys, Butterworth-Heinemann, 15-36, 2017.

[3] PANG J., LIU F., LIU J., TAN M., BLACKWOOD D., Friction Stir Pro-cessing of Aluminium Alloy AA7075: Microstructure, Surface Chemistry And Corrosion Resistance, Corrosion Sci. 106,217-228,2016.

[4] ROMETSCH P. A., ZHANG Y., KNIGHT S., Heat Treatment of 7xxx Series Aluminium Alloys—Some Recent Developments, Trans. Nonferrous Met. Soc. China 24, 2003−2017 ,2014.

[5] XINGQING W., SUI YONGJIANG S.,WOOD J. V.,HAIBO L., Formation of Intermetallic Compound in Iron-Aluminum Alloys, Journal. of Shanghaı Unıversıty Vol. 2 No. 4, 305-310 1998.

[6]MORÎNTALE E., HARABOR A., CONSTANTINESCU C., ROTARU P, Use of Heat Flows From DSC Curve For Calculation Specific Heat of the Solid Materials, Physics AUC. Vol. 23, 89-94,2015

[7]FANG H.,WONG M.B., BAI Y.,Use of Kinetic Model for Thermal Properties of Steel at High Temperatures,Australian Journal of Civil Engineering, 13:1, 40-47,2015,

[8]WIELGOSZ E., KARGUL T., FALKUS J., Comparison of Experimental and Numerically Calcuated Thermal Properties of Steels, International Conference on Metallurgy and Materials, May 21 st-23rd 2014,Brno, CzechRepublic, Metal 2014,6 pages.

[9]KELLEY K.K., X. High - Temperature Heat - Content, Heat - Capacity, and Entropy Data for Inorganic Compounds, Bureau of Mines Bull. 476, 192,1949.

[10]KARTHİKEYAN B., RAMANATHAN S., RAMAKRİSHNAN V., A calorimetric study of 7075 Al/SiC_p composites, Materials and Design 31,S92–S95, 2010

[11]ZAHRA A.-M., ZAHRA C.Y., JAROMA – WEILAND G., NEUER G., LACOM W., Heat Capacities of Aluminıium Alloys, Journal of Mtaerials Science 30, 426-436),1995.

[12] ALIRAVCI C.A., PEKGULERYÜZ M Calculatıon Of Phase Dıagrams For The Metastable Aı-Fe Phases Formıng In Dırect-Chıll (Dc)-Cast Alumınum Alloy Ingots,.Calphad. Vol. 22. No. 2, pp. 147-l 55, 1998.

[13]BERTELLI F.,, MEZA E.S., GOULART P.R., CHEUNG N., RIVA R., GARCIA A.,- Laser remelting of Al–1.5 wt%Fe alloy surfaces: Numerical and experimental analyses, Optics and Lasers in Engineering 49 490–497, 2011.

[14]SHINGU P.H., "Light Metals: Science and Technology", eds. Suryana-rayana C.,Prasad P.M., Malhotra S.L.,Anantharaman T.R., Trans Tech, Aedermannsdorf, p. 77 1985.

[15] WANG X., GUAN R.-G., WANG Y, Formation Mechanism of Nanoscale Al_3Fe Phase in Al-Fe Alloy During Semisolid Forming Process, Metallurgıcal And Materıals Transactıons B Volume 49B, 2225-2231,2018.

[16] MOLDOVAN P., POPESCU G., MICULESCU F., Microscopic Study Regarding the Microstructure Evolution of the 8006 Alloy in the Plastic Deformation Process J. Mater. Process. Technol., vol. 153, pp. 408–15, 2004.

[17] SUN S.B., ZHENG L.J., LIU J.H., ZHANG H., Selective Laser Melting Of An Al–Fe–V–Si Alloy: Microstructural Evolution And Thermal Stability, J. Mater. Sci. Technol., Vol. 33, 389–96,2017.

[18]TCHERDYNTSEV V.V., KALOSHKIN S.D., GUNDEROV D.V., AFONINA E.A., BRODOVA I.G., STOLYAROV V.V., BALDOKHIN Y.V., SHELEKHOV E.V., TOMILIN I.A., Phase Composition And Microhardness of Rapidly Quenched Al–Fe Alloys After High Pressure Torsion Deformation, Mater. Sci. Eng. A, vol. 375, 888–93,2004..

[19]CUBERO-SESIN J.M., HORITA Z., Mechanical Properties and Microstructures of Al-Fe Alloys Processed by High-Pressure Torsion, Metall. Mater. Trans. A, vol. 43A, 5182–92,2012.

[20] MI G.F., DONG C.F., ZHAO D.W., Front. Manuf. Des. Sci.,vols. 44–47, 2126–30,2011.

[21] LEE L.S., KAO P.W., HO N.J,,Microstructure and Mechanical Properties of Al–Fe In-Situ Nanocomposite Produced by Friction Stir Processing, Intermetallics 16, 1104–1108,2008.

6th International Conference on Materials Science and Nanotechnology For Next Generation (MSNG2019)
October 16-18, 2019, Niğde, TURKEY (ORAL FULL TEXT)

Adsorption isotherms and thermodynamic studies of methylene blue onto coconut shell based activated carbon prepared by $ZnCl_2$

Hatice Karaer Yağmur*, İsmet Kaya**
**Dicle Üniversitesi, Fen Fakültesi, Kimya Bölümü, Diyarbakır, Turkey*
***Çanakkale Onsekiz Mart Üniversitesi, Kimya Bölümü, Polimer Sentez ve Analiz Lab., Çanakkale, Turkey*

The aim of present work is to study an easy method for methylene blue (MB) removal from water by adsorption on coconut shell based activated carbon as a high capacity adsorbent. Therefore, an activated carbon with high-surface area was prepared from coconut shells by chemical activation with $ZnCl_2$ and was characterized by BET, FT-IR, SEM and TGA measurements. In addition, it is to be a potential for adsorption in removal of methylene blue from the aqueous solution investigated.

Keywords: coconut shell, activated carbon, methylene blue, adsorption

Corresponding author: profhatice23@hotmail.com

1. Introduction

Activated carbons (AC) are good adsorbents to remove various compounds from water owing to its high carbon content, large adsorption capacity, surface area and microporous nature [1]. Commercially available AC, however, is expensive and this leads to a vast research in finding for cheap and efficient materials. Agricultural by-products have been usually used as the raw materials for the production of AC since they are abundant, renewable and cheap [2]. AC may be prepared using a variety of raw materials. Besides, traditional coal and wood, some fruit by products, such as cherry, peach stone, grape seeds and coconut shell, are widely used as preparation precursors due to high carbon content and surface area. Among these raw materials, there has been an increasing interest in using lignocellulosic by-products including agricultural residues and coconut shells as raw materials due to low ash content, high carbon content and high hardness [3-5].
AC can be obtained by two basic processes: chemical activation or physical activation. Chemical activation can be accomplished in a single step by carrying out thermal decomposition of raw material with activating agents such as potassium carbonate (K_2CO_3), phosphoric acid (H_3PO_4), potassium hydroxide (KOH), zinc chloride ($ZnCl_2$) and sodium carbonate (Na_2CO_3) [6]. In physical activation, the sample is heat treated in an inert atmosphere and the activation of the solid residual product (char) is realized at high temperatures (900–1000 °C), in slightly reactive atmosphere, such as steam or carbon dioxide [7]. Although chemical activation is carried out at lower temperatures and reaction time, higher yield, physical activation requires a much longer time [2].
In this study, activated carbon was obtained from coconut shell using zinc chloride ($ZnCl_2$) as activating agent. The effect of different chemical reagents (KOH and $ZnCl_2$) on the pore development and the yield of the prepared activated carbon were investigated. The coconut shell based activated carbons was characterized by use of BET, FT-IR, SEM and TGA measurements. In addition, it is to be a potential for adsorption in removal of methylene blue from the aqueous solution investigated.

2. Experimental Details

2.1. Materials and methods
Coconut shells were bought locally market (Diyarbakır, Turkey). After drying at room temperature coconut shells were crushed using electric grinder.
2.2. Preparation of the activated carbon
Preparation of activated carbon sample from coconut shells materials, using $ZnCl_2$ chemical activation, followed a general procedure similar to literature [2, 6, 8, 9]. Coconut shell was smashed and sieved to a desired particle sizes between 1 and 2 mm prior to its chemical activation. The coconut shells were cleaned with deionized water and dried at 120 °C for 72 h to reduce the

moisture content. The char was impregnated with $ZnCl_2$ solution. The impregnation ratio 1:2 according to the $ZnCl_2$: chars ratio (w/w). The activating agent and the coconut shells were homogeneously mixed at room temperature for 24 h under continuous agitation (1000 rpm). This mixture was dried at 120 ºC for 24 h to prepare the impregnated sample. The impregnated sample was set in a horizontal stainless-steel tubular reactor with 7 cm diameter and 100 cm length. These processes were performed by heating in a horizontal stainless-steel tubular reactor (7.0 cm diameterx100 cm length). At every turn, the impregnated sample was carbonized at 500 °C for 1 h under nitrogen (N_2) flow of 100 mL min-1 at the heated at a rate of 10°C min-1. The carbonized samples were boiled with HCl (0.1 M) solution under reflux to remove impurities and reduce the amount of ash content of the activated carbon. Then, the activated carbon was washed several times with hot distilled water and finally with cold distilled water until chloride ions did not detected. After washing by distilled water, the activated carbon was dried at 120 ºC for 24 h.

2.3. Adsorption studies

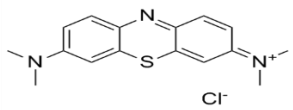
The adsorption studies were carried out on the AC-z using MB (Scheme 1). The adsorption studies can be categorized into two sections: (a) Effect of temperature (b) fitting of data to adsorption isotherms studies. Stock solutions (1000 mgL^{-1}) of MB were prepared by dissolving appropriate amounts of them in distilled water. The solutions ranging from 25 to 300 mgL^{-1} were prepared by diluting the stock solutions. The equilibrium studies were performed 0.15 g of AC-z (as an adsorbent) with 50 mL of dye solution of initial concentrations (25–300 mg L^{-1}) in 100 mL stopper conical flasks at 298, 308 and 318 K at 120 rpm for contact time 7 h. The adsorption capacity at equilibrium (qe, mg g^{-1}), and the percentage removal (removal, %) can be calculated using the following equation 1:

$$qe = \frac{(Co - Ce)V}{m} \quad (1)$$

where Co and Ce (mgL^{-1}) are the initial and equilibrium concentrations of MB in the solution, respectively. V (L) is the volume of the MB solution and m (g) is the mass of the adsorbents. All batch adsorption experiments were conducted in 100 mL stopper erlenmeyer flasks and shaken on a temperature controlled shaker at 120 rpm and natural pH.

2.4. Characterization

The raw coconut shell and activated carbons were characterized by use of Fourier transform infrared spectroscopy (FT-IR), scanning electron microscopy (SEM), thermogravimetric analysis-differential thermal analysis (TGA) and Brunauer–Emmett–Teller (BET). Analyzes were performed via universal ATR sampling accessory between 4000–450 cm^{-1}. The surface properties of activated carbons were identified via a scanning electron microscopy SEM-EDX (Zeiss Evo 40, Ametek EDX). The measurements of specific surface areas of activated carbons produced from coconut shell have been made by the BET surface area (SBET) was determined based on the standard Brunauer–Emmett–Teller multipoint method in the region of relative pressures (0.05–0.35) near completed monolayers. The pore size distribution of the samples was obtained according to the Barrett-Joyner-Halenda (BJH) method. The total pore volume (VT) was calculated from the amount of nitrogen adsorbed at P/P0 = 0.99. The mesoporous volume (Vmeso) was calculated by subtracting Vmicro from Vtotal (Vmeso = Vtotal - Vmicro).



Scheme 1. *The chemical formula of methylene blue.*

3. Results and Discussion

The FT-IR spectrums for raw coconut shell (CS, natural coconut shell), AC-n (activated carbon without $ZnCl_2$) and AC-z (obtained activated carbon by $ZnCl_2$) were given in Figure 1 and Figure 2. According to Figure 1, the bands at 3334 cm^{-1}, 2924 cm^{-1} and 1739 cm^{-1} are related to the hydroxyl groups (-OH), the C-H stretching and the carbonyl groups (C=O). The bands are related to 1373 cm^{-1} and 1604 cm^{-1} showed the presence of aromatic rings because of C=C stretch. The band at 1233 cm^{-1} and a relatively intense band at 1030 cm^{-1} can be related to the C-O stretching in phenols, alcohols or ethers. The existence of hydroxyl groups, ethers, carbonyl groups, phenols and aromatic compounds confirms the lignocellulosic structure of coconut shell [2]. The FT-IR spectrum of activated samples indicated in Figure 2 shows a decrease of bands when compares with the raw material spectrum. This shows a decrease of functional groups in the raw material. It can be seen that bands at around 3300 cm^{-1}, 1739 cm^{-1} and 1233 cm^{-1}, which refers to the presence of –OH, C=O, and aromatic C=C stretch have disappeared in the activated carbons spectrum. These

changes indicated that there was a break of chemical bonds during the carbonization and activation process [2].

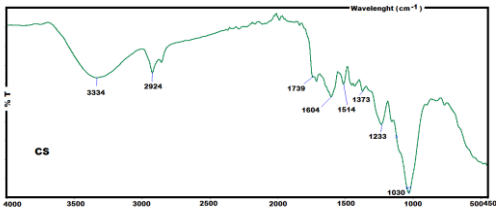


Figure 1. *FT-IR spectrum of CS.*

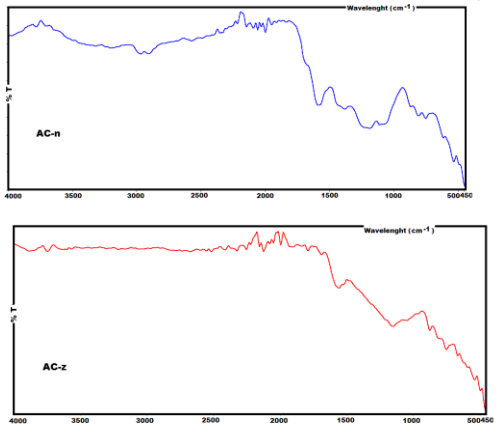


Figure 2. *FT-IR spectra of AC-n and AC-z.*

The TGA curves of CS, AC-n and AC-z were given in Figure 3. The specific temperatures of the CS and ACs were given in Table 1. The coconut shells, usually consists of hemicellulose, cellulose and lignin. The pyrolysis of coconut shells could be related to the pyrolysis of these polymers. Based on literature [10], reported that the decomposition of hemicellulose, cellulose and lignin occurred at ranges of 180–240, 230–310, and 300–400 ◦C, respectively. Beyond 400◦C, the most important reaction leads to the aromatization process, at low mass loss rate. Researchers have already confirmed that lignin starts decomposing at low temperatures (160–170 ◦C) and continues to decompose at low rate until approximately 900 ◦C. Hemicellulose is the second component to start decomposing, followed by cellulose, in a narrow temperature interval from about 200 to 400 ◦C. The main decomposition takes place and accounts for the greatest decomposition in the biomass pyrolysis process consisting of degradation reactions in this interval. Beyond 400 ◦C, the most important reaction leads to the aromatization process, at low mass loss rate [10]. According to TGA, it was observed that the first mass loss started with an initial temperature of 130 °C. The weight loss percentage recorded 5.3 (CS), 3.4 (AC-n) and 2.1(AC-z) wt.% which was expected to be due to moisture loss and lower molecular weight volatile matter [11]. According to Table 1, it can be observed that the AC-z had higher thermal stability other than AC-n.

Table 2 shows surface area, pore volume, and pore diameter of activated carbons. The data show that the SBET of the AC-n increased from 3.4 m^2 g^{-1} to 935.5 m^2 g^{-1} when the $ZnCl_2$: char ratio 1:2. An increase in pore volume was observed for the ACs. Moreover, the most of the pores had sizes smaller than 2.5 nm (25A˚), indicating a development of micro porosity of the material. VT is directly related to the development of porosity of the material. The activation process rearranges the carbon structure producing a more ordered structural skeleton. The pore development occurs from four stages: (a) opening of previously inaccessibly pores, (b) creation of new pores, (c) widening of the existing pores and (d) merger of the existing pores due to pore wall breakage. The micro pores were the responsible for the increase of VT. In additionally, the increase of development of mesoporous promoted and a decrease in the microspore percentages (Vmicro/Vt (%)) [13]. The values of Vmicro/Vt (%)) were 75.4 and 62.2 for the AC-n and AC-z, respectively. Based on the table, it was observed that AC-z has the high surface area and pore volume.

Figure 4 shows the SEM images for the AC-n and AC-z. According to Figure 4, SEM image of AC-z shows a slightly damaged and uneven surface, which may be due to the release of volatile materials during carbonization process. After activation process, the image of AC-z shows uneven surface, caused by the dehydrating action of activating agent, which leads to the porosity development [14].

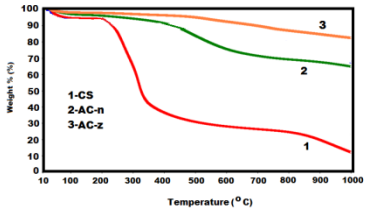


Figure 3. *TGA curves of CS, AC-n and AC-z.*

Table 1. *The results of thermal analysis.*

	T_{on} (°C)	T_{20} (°C)	T_{50} (°C)	% Char at 1000 °C
CS	233	278	339	17.8
AC-n	387	590	-	68.2
AC-z	442	-	-	84.5

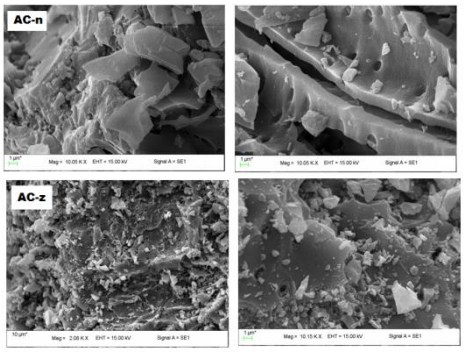


Figure 4. *SEM images of the AC-n and AC-z.*

Table 2. *Textural characteristics of the prepared activated carbons.*

Active carbons	SBET (m^2g^{-1})	Micro volume (V_{micro})	Meso volume (V_{meso})	Total volume (Vt)	percentage of micro pores	Average pore diameter
AC-n	3.4	0.001216	0.00039	0.001613	75.4	1.90
AC-z	935.5	0.25593	0.155302	0.411232	62.2	1.76

3.1. Adsorption isotherms

The adsorption isotherms study was performed at three different temperatures (298, 308 and 318 K) with the initial MB concentrations of 25–300 mg L^{-1}, as shown in Figure 5. The data was further analyzed with two isotherm models including Langmuir and Freundlich (as illustrated in Table 3). The Langmuir model is valid for monolayer adsorption for specific homogenous areas as the Freundlich isotherm is used to recognize heterogeneous adsorption processes [15].
Figure 6 shows the non-linear isotherm plots obtained for the adsorption MB onto AC-z adsorbent at 298, 308 and 318 temperatures. The Qm, b, k and n were calculated based on Table 3 and the obtained data are given in Table 4. As can be seen from Table 4, the experimental data were in good consistency with the Langmuir model owing to high coefficient of determination (R^2).

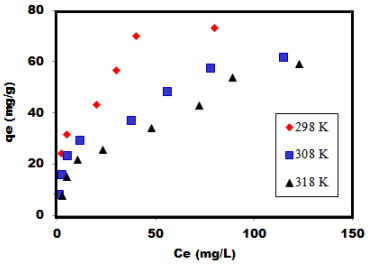


Figure 5. *Adsorption isotherms for MB onto AC-z at 298, 308 and 318 K*

Table 4. *Langmuir and Freundlich isotherm parameters.*

Dye	T (K)	Langmuir isotherm			Freundlich isotherm		
		Qm (mg g^{-1})	b (L mg^{-1})	R^2	k (mg g^{-1})	1/n	R^2
MB	298	76.92	0.1538	0.9723	18.39	2.67	0.9383
	308	65.36	0.0729	0.9677	36.18	2.46	0.9556
	318	66.67	0.0369	0.9338	33.10	2.12	0.9619

Table 3. *Adsorption isotherm models*

Ce /qe = 1 /b Qm + Ce/Qmax (2)	Langmuir isotherm
logqe = log k + (1/n) logCe (3)	Freundlich isotherm
Qm = maximum adsorption capacity; b = Langmuir constant; k and 1/n = Freundlich constants.	

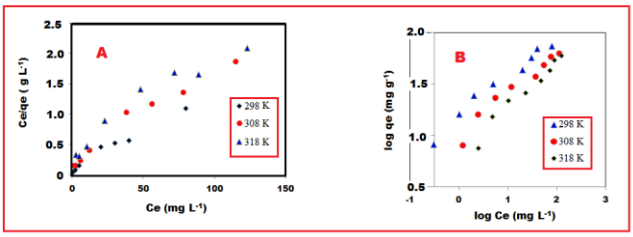


Figure 6. *Langmuir (A) and Freundlich (B) isotherm for MB removal by AC-z.*

3.2. Adsorption thermodynamics

The thermodynamic parameters, namely, standard Gibb's free energy (ΔG^o), enthalpy change (ΔH^o), and entropy change (ΔS^o) were estimated in order to understand the feasibility and nature of the adsorption process (figure not shown).

$$\Delta G^o = -RT \ln Kc \quad (2)$$

$$\ln Kc = \Delta S^o / R - \Delta H^o / R\,T \quad (3)$$

$$\Delta G^o = \Delta H^o - T\Delta S^o \quad (4)$$

where T (K), R are the absolute temperature and the gas constant (8.314 J $mol^{-1}K^{-1}$), espectively [1]. Kc (L g^{-1}) is calculated by using the Langmuir constants Qm and b (Kc = Qm x b) and known as a the equilibrium constant. The thermodynamic parameters ΔH^o and ΔS^o were computed by using the slope and intercept of the plot of ln Kc versus 1/T. The negative values of (ΔG^o), -6.12 kJ mol^{-1}, -3.99 kJ mol^{-1} and -2.38 kJ mol^{-1} at 298 K, 308 K and 318 K. The negative ΔG^o values at 298, 308 and 318 K proposed a feasible and spontaneous process of adsorption[16]. The ΔS^o and the ΔH^o were computed as 187.8 J mol^{-1} K^{-1}, -62.01 kJ mol^{-1}, respectively. The positive value of ΔS^o (187.8 J mol^{-1}) suggests that the degree of randomness at the solid-liquid interface increased during MB dye adsorption on the AC-z [15]. The negative enthalpy change (ΔH^o) values confirmed that the adsorption process for AC-z were exothermic in nature.

4. Conclusion

The results of this study showed that the AC-z obtained from coconut shell high BET surface area other than AC-n. The textural characterization showed that the ACs are essentially microporous and that BET surface area of 935 m^2 g^{-1} was obtained for AC-z. Because of their textural and chemical properties, the coconut shell activated carbon obtained in this study is potential material in the wastewater treatment for the removal of some organic pollutants.

Acknowledgements

This research was funded by the Dicle University Scientific Research Projects Unit (DUBAP) under the project number of FEN.18.008.

References:

[1] Guo,F., Li, X., Jiang, X., Zhao, X., Guo, C., Rao, Z., 2018. Characteristics and toxic dye adsorption of magnetic activated carbon prepared from biomass waste by modified one-step synthesis. Colloids and Surfaces A 555, 43–54.

[2] Joseph, C., Anısuzzaman, S., Abang, S., Musta, B., Quek, K., Wong, X., 2017. Adsorption Performance and Evaluation of Activated Carbon from Coconut Shell for the Removal of Chlorinated Phenols in Aqueous Medium. Materıals Scıence (Medžıagotyra) 23, No: 4.

[3] Zhao, X., Zeng, X., Qin, Y., Li, X., Zhu, T., Tang, X., 2018. An experimental and theoretical study of the adsorption removal of toluene and chlorobenzene on coconut shell derived carbon. Chemosphere 206, 285-292.

[4] Promdee, K., Chanvidhwatanakit, J., Boonmee,S. C., Kawichai, T., Jarernprasert, S., Vitidsant, T.,2017. Characterization of carbon materials and differences from activated carbon particle (ACP) and coal briquettes product (CBP) derived from coconut shell via rotary kiln. Renewable and Sustainable Energy Reviews 75, 1175–1186.

[5] Islam, A., Ahmed, M., Khanday, W., Asif, Hameed, M. B.,2017. Mesoporous activated coconut shell-derived hydrochar prepared via hydrothermal carbonization-NaOH activation for methylene blue adsorption. Journal of Environmental Management 203,237-244.

[6]Karagöz, S., Tay, T., Uçar, S., Erdem,M.,2008. Activated carbons from waste biomass by sulfuric acid activation and their use on methylene blue adsorption. Bioresource Technology 99, 6214–6222.

[7] Pereira, R., Veloso, C., Silva,N., Sousa, L., Bonomo, R., Souza, A., Souza, M., Fontan, R., 2014. Preparation of activated carbons from cocoa shells and siriguela seeds using H_3PO_4 and $ZnCl_2$ as activating agents for BSA and α-lactalbumin adsorption. Fuel Processing Technology 126, 476–486.

[9] Uçar, S., Erdem, M., Tay, T., Karagöz, S., 2009. Preparation and characterization of activated carbon produced from pomegranate seeds by $ZnCl_2$ activation. Applied Surface Science 255, 8890–8896.

[10]Song, C., Wu, S.,Cheng, M., Tao, P., Shao, M., Gao, G.,2014. Adsorption Studies of Coconut Shell Carbons Prepared by KOH Activation for Removal of Lead(II) From Aqueous Solutions. Sustainability 6, 86-98.

[11] Danish, M., Ahmad, T., Hashim, R., Said, N., Akhtar, M., Saleh, J.,Sulaiman, O.,2018.Comparison of surface properties of wood biomass activated carbons and their application against rhodamine B and methylene blue dye. Surfaces and Interfaces 1,11–13.

[12] Khalili, N., Campbell, M., Sandi, G., Golas, J.,2000. Production of micro and mesoporous activated carbon from paper mill sludge I. Effect of zinc chloride activation. Carbon 38,1905–1915.

[13] Cazettaa, A., Vargasa, A., Nogamia, E., Kunitaa, M., Guilherme, M., Martins, A., Silva, T., Moraes, J., Almeida, V., 2011. NaOH-activated carbon of high surface area produced from coconut shell: Kinetics and equilibrium studies from the methylene blue adsorption. Chemical Engineering Journal 174,117– 125.

[14] Pezoti, O., Cazetta, A., Souza, I., Bedin, K., Martins, A., Silva, T., Almeida, V.,2014.Adsorption studies of methylene blue onto $ZnCl_2$-activated carbon produced from buriti shells (Mauritia flexuosa L.). Journal of Industrial and Engineering Chemistry 20, 4401–4407.

[15] Vasu1, A., Reddy, C., Danaboyina,S., Manchala, G., Chavali, M., 2017.The Improvement in Mechanical Properties of Coconut Shell Powder as Filter in HDPE Composites, Journal of Polymer Science & Applications 1:2.

[16] Li, W., Yang, K., Peng, J., Zhang, L., Guo, S., Xia, H., 2008.Effects of carbonization temperatures on characteristics of porosity in coconut shell chars and activated carbons derived from carbonized coconut shell chars. Industrial Crops and Products 28,190–198.

6th International Conference on Materials Science and Nanotechnology For Next Generation (MSNG2019)
October 16-18, 2019, Niğde, TURKEY (ORAL FULL TEXT)

Comprehensive Investigation on Dielectric Properties of Al/CdS-PVA/p-Si Structures at 5 kHz-5 MHZ

A. Yashar Azizian-Kalandaragh
Department of Physics, Faculty of Basic Sciences, University of Mohaghegh Ardabili, Ardabil 179, Iran
B. İbrahim Yücedağ
Department of Computer Engineering, Technology Faculty, Düzce University, Düzce 81000, Turkey
C. Gülçin Ersöz Demir
Department of Management Information Systems, Faculty of Management, Selçuk University, Konya 42700, Turkey
D. Şemsettin Altındal
Department of Physics, Faculty of Sciences, Gazi University, Ankara 06500, Turkey

In this study, we investigated the effect on the dielectric properties of an CdS-PVA interfacial layer grown by sol-gel method onto p-Si. Structural defects were passivated effectively with an CdS-PVA interfacial layer. The voltage dependence of electrical and dielectric characteristics such as the real and imaginary parts of complex dielectric parameters (ε', ε''), tangent loss ($tan\delta$) and real and imaginary part of electrical modulus (M' and M'') of Al/CdS-PVA/p-Si structures were analyzed at in the wide range of frequency (5 kHz-5 MHz). The ε', ε'' $tan\delta$, M' and M'' were found a powerful function of frequency and voltage. The change in dielectric parameters can be ascribed to the interfacial layer, interfacial/dipole polarization and their relaxation time at metal/semiconductor interface.

Keywords: Al/CdS-PVA/p-Si structures, dielectric parameters, electrical modulus
Submission date:
Acceptance Date:

Corresponding authors:glcnersoz@gmail.com

1. Introduction

The presence of the polymer nanocomposites between the metal and the semiconductor affects the performance, reliability and stability of the electronic and optoelectronic and photo-electrochemical applications. Polymer nanocomposite materials have application area such as light emitting diodes [1, 2], photodetectors [3], hybrid solar cells [4, 5], field effect transistors [6] and sensing devices [7, 8]. Among polymer nanocomposite materials, cadmium sulphide-polyvinyl alcohol (CdS-PVA) shone through as an attractive compound for semiconductor device applications. The doping of CdS nanostructures into polyvinyl alcohol (PVA) makes the polymer suitable for use in many applications in terms of its high viscosity, excellent water solubility and biocompatibility. In this work, Al/CdS-PVA/p-Si structures observed as a function of the frequency and applied bias voltage. The real and imaginary parts of complex dielectric parameters (ε', ε''), loss tangent ($tan\delta$) and real and imaginary part of electrical modulus (M' and M'') of Al/CdS-PVA/p-Si structures were investigated in the frequency range of 5 kHz-5 MHz.

2. Experimental details

To begin fabrication of Al/CdS-PVA/p-Si structures, firstly, p-type silicone substrates (p-Si) were cut to the appropriate size and cleaned by standard chemical procedure. On the back surface of p-type silicon, ohmic contact was formed by coating Al metal by thermal evaporation method. To improve the quality of the ohmic contact, it was annealed in a nitrogen gas environment for 30 minutes at 450 degrees. Then CdS nanoparticles were added to the PVA polymer by ball-milling method to form CdS-PVA nanocomposites. CdS-PVA nanocomposites were formed by sol-gel technique on the p-Si wafer at 300 K. Schottky contacts have been constituted as Al dots by thermal evaporating process which has been performed at 4.10^{-6} Torr.

3. Results and discussion

The investigation of dielectric spectroscopies such as ε', ε'', $tan\delta$, M' and M'' were obtained capacitance and conductance measurements were carried out at 0.3 V by using a HP 4192 A LF impedance analyzer. All these parameters were calculated by the following formulas [9-11]:

$$\varepsilon' = \frac{C}{C_0} \quad (1)$$

$$\varepsilon'' = \frac{G/\omega}{C_0} \quad (2)$$

$$tan\delta = \frac{\varepsilon''}{\varepsilon'} \quad (3)$$

$$M^* = \frac{1}{\varepsilon^*} = M' + jM'' = \frac{\varepsilon'}{\varepsilon'^2 + \varepsilon''^2} + j\frac{\varepsilon''}{\varepsilon'^2 + \varepsilon''^2} \quad (4)$$

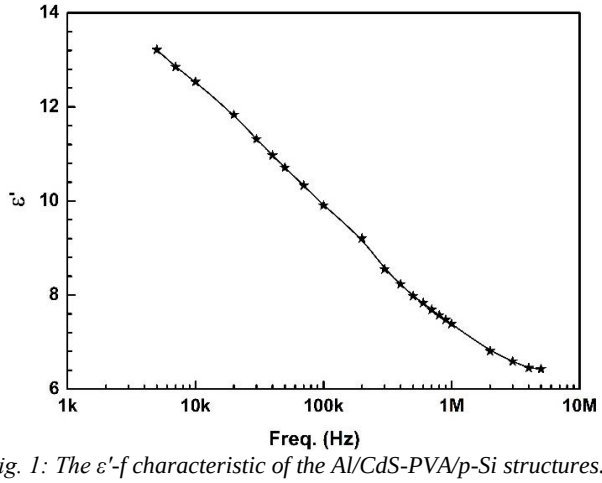


Fig. 1: The ε'-f characteristic of the Al/CdS-PVA/p-Si structures.

Fig. 1, Fig. 2, Fig. 3, Fig. 4 and Fig. 5, the frequency dependent plot of the ε'-f, ε''-f, $tan\delta$-f, M'-f and M''-f characteristics at 0.3 V bias of the Al/CdS-PVA/p-Si structures, respectively. Experimental results indicate that all these parameters are strong functions of voltage and frequency. The value of ε' decrease with increasing frequency. The values of ε'' and $tan\delta$ of Al/CdS-PVA/p-Si structures show a broad peak. This peak is usually a result of the particular density distribution of surface states (N_{ss}) at the M/S interface, dipole polarizations and R_s of the device [12]. The ε''-f curve has a peak at about 200 kHz, while $tan\delta$-f curve has a peak at about 300 kHz. Both ε''-f and $tan\delta$-f characteristics decrease with increasing frequency after peak behaviors. The ε'' and the $tan\delta$ are bigger at low frequency because of the possible interface polarization mechanism since N_{ss} cannot follow the ac signal at high frequency. The existing of polarization in the material is because of ionic, electronic, dipolar and space charge polarization [13].

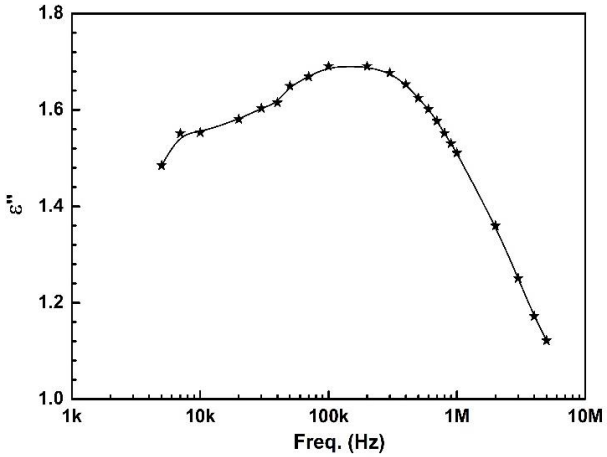


Fig. 2: The ε''-f voltage characteristic of the Al/CdS-PVA/p-Si structures.

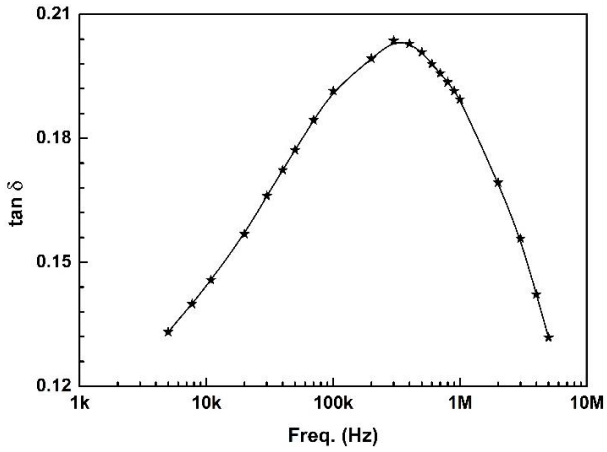


Fig. 3: The tanδ-f characteristics of the Al/CdS-PVA/p-Si structures.

The behavior of M' vs. f curve increase with increasing frequency, whereas the behavior of M'' vs. f curve shows a peak behavior at about 1 MHz. These changes of M' and M'' with frequency can be ascribed to the distribution of the interface states located between the interfacial layer, relaxation/life time and Debye theory [14]. According to this theory, for lower frequencies, the value of relaxation time (τ) is lower than the period (T = 1/ f). In this case, dipoles can follow the external ac signal. As shown in figure 4 and 5, M' and M'' reached a maximum value at high frequency due to the relaxation process ($M\infty = 1/\varepsilon\infty$) [15].

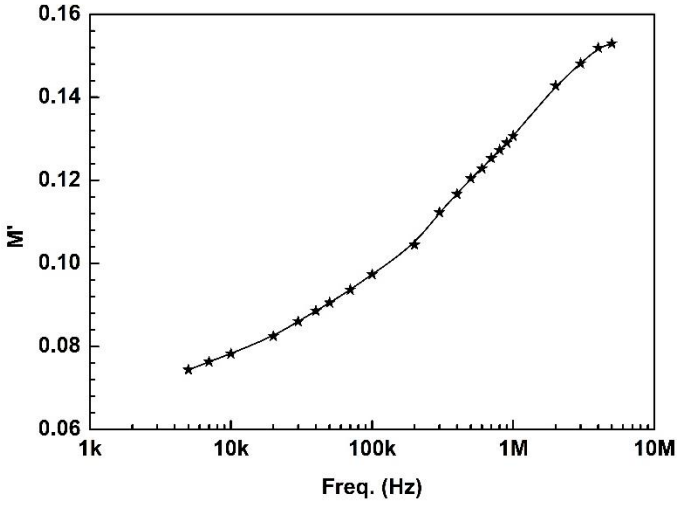


Fig. 4: The M'-f characteristics of Al/CdS-PVA/p-Si structures.

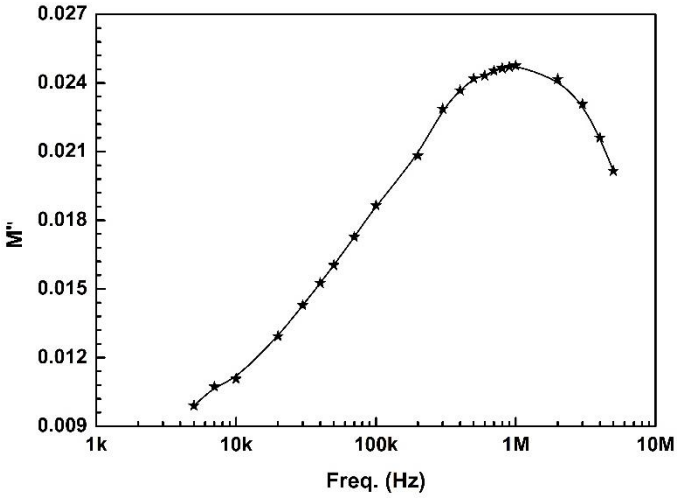


Fig. 5: The M''-f characteristics of Al/CdS-PVA/p-Si structures.

Conclusions

The main aim of this study is determining of basic dielectric properties of Al/CdS-PVA/p-Si structures. As a result of the interfacial layer, surface states, series resistance and polarization processes have effect on the dielectric properties. The obtained high values of ε' and ε'' especially at low frequencies can be attributed to the conductivity directly related to the increase in the mobility of charge carriers at traps or states and the Maxwell-Wagner polarization mechanism. The observed behaviors of M' and M'' for all frequency can be ascribed the polarization mechanisms and Debye relaxation model. The effect of N_{ss} and polarization decrease with increasing frequency because of the charges at traps and dipole cannot follow the ac signal due to low values of the relaxation time. This results show that CdS-PVA nanocomposites can be used quite conveniently as an interfacial layer in the production of electronic devices technology.

References:

M.C. Schlamp, X. Peng, A.P. Alivisatos, J. Appl. Phys., 82 (1997) 5837-5842. **[1]**

J. Zhao, J.A. Bardecker, A.M. Munro, M.S. Liu, Y. Niu, I. Ding, J. Luo, B. Chen, A.K. Y. Jen, D.S. Ginger, Nano Lett., 6 (2006) 463-467. **[2]**

S.A. McDonald, G. Konstantatos, S. Zhang, P.W. Cyr, E.J.D. Klem, L. Levina, E. H. Sargent, Nat. Mater., 4 (2005) 138-142. **[3]**

W.U. Huynh, J.J. Dittmer, A.P. Alivisatos, Science, 295 (2002) 2425-2427. **[4]**

L. Wang, Y. Liu, X. Jiang, D. Qin, Y. Cao, J. Phys. Chem. C, 111 (2007) 9538-9542. **[5]**

O. Gunaydin, A. Demir, G. Ersöz Demir, İ. Yücedağ, B. Çoşut, Macromol. Res., 26 (2018) 164-172. **[6]**

S.P. Mondal, S. Bera, G. Narender, S.K. Ray, Appl. Phys. Lett., 101 (2012) 173108. **[7]**

S. Pandey, G.K. Goswami, K.K. Nanda, Sci. Rep., 3 (2013) 2082. **[8]**

A. Gümüş, G. Ersöz, İ. Yücedağ, S. Bayrakdar, Ş. Altındal, J. Korean Phys. Soc., 67 (2015) 889-895. **[9]**

[10] G. Ersöz Demir, İ. Yücedağ, Y. Azizian-Kalandaragh, Ş. Altındal, J. Electron. Mater., 47 (2018) 6600-6606.

[11] N. Baraz, İ. Yücedağ, Y. Azizian-Kalandaragh, G. Ersöz, İ. Orak, Ş. Altındal, B. Akbari, H.Akbari, J. Electron. Mater., 56 (2017) 4276- 4286.

[12] P. Dutta, S. Biswas, S.K. De, Mater. Res. Bull., 37 (2002)193-200.

[13] I. Yücedağ, A Kaya, Ş Altındal, I Uslu, Chinese Phys. B, 23 (2014) 47304.

[14] T. Badapanda, S. Sarangi, S. Parida, B. Behera, B. Ojha, S. Anwar, J. Mater. Sci. Mater. Electron., 26 (2015) 3069-3082.

[15] S. Sze, Physics of semiconductor devices (1981) New York: Wiley.

6th International Conference on Materials Science and Nanotechnology For Next Generation (MSNG2019)
October 16-18, 2019, Niğde, TURKEY (ORAL FULL TEXT)

Comparative Investigation on Main Electrical Parameter of Structures with (MIS) and without (MS) Al_2O_3 Interfacial Layer

A. Gülçin Ersöz Demir
Department of Management Information Systems, Faculty of Management, Selçuk University, Konya 42700, Turkey
B. İbrahim Yücedağ
Department of Computer Engineering, Technology Faculty, Düzce University, Düzce 81000, Turkey

The current study was carried out by forming the thin film of the by using atomic layer deposition (ALD) technique of Al_2O_3 insulator material onto n-type Silicon carbide (n-SiC) in order to better understand the effects of interfacial materials on conventional MS structures. Then current-voltage (*I-V*) characteristics were obtained by applying a voltage between (-2.5V) and (+2.5V) to compare both the Metal/Semiconductor (MS) structure and the Metal/Insulator/Semiconductor (MIS) structure in terms of electrical properties. Thanks to the obtained *I-V* characteristics, rectification ratios (RR), ideality factors (n), reverse saturation currents (I_0), shunt resistances (R_{sh}) and series resistances (R_s) were obtained for both structures. When the results obtained are evaluated in depth in terms of these parameters, it is seen that the interface layer increases the device performance.

Keywords: Au/4H-n/SiC (MS), Au/Al_2O_3/4H-n/SiC (MIS), Current transmission mechanism

Submission date:
Acceptance Date:

Corresponding authors:glcnersoz@gmail.com

1. Introduction

Many researchers have been working on the development of interface materials and interface properties for decades to prevent interfacial traps and defects in traditional MS structures and to improve device performance [1, 2]. MIS structures can be obtained with these interface materials used to improve the interfacial properties of MS structures. So many interface materials have been tried for this purpose up to date and remarkable results have been obtained [3, 4]. One of these materials is the Al_2O_3 material known as sapphire. The Al_2O_3 material is an inorganic insulator with excellent insulating properties due to the band gap of about 9 eV [5]. It usually occurs quickly with the immediate oxidation of aluminum and is abundant in nature. Thanks to this feature, Al_2O_3 has been used in many applications and devices production in the electronics industry. In order to obtain Al_2O_3 thin film in desired thickness, chemically and physically stable, homogeneous and uniform structure, Atomic Layer Deposition (ALD) technique is preferred because of these properties [6]. In current study, Al_2O_3 was chosen as the interface material and its application in Schottky diodes was realized. For this purpose, both MS and MIS structures were obtained. The structures were measured electrically between (-2.5V) and (+2.5V) in order to determine the basic electrical parameters.

2. Experimental details

In order to form both MS and MIS structures, firstly, n-SiC substrate was cut in appropriate dimensions and technique and subjected to standard chemical cleaning process. Al metals were coated along all surfaces by Physical Vapor Deposition (PVD) method to form ohmic contacts to the back surfaces of two n-SiC substrates. Coated Al contacts were kept at 450 degrees for 30 minutes in nitrogen environment to improve contact quality. Then, Al_2O_3 insulating material onto one of the n-SiC substrates were grown at 70 Å thickness as an interface layer by ALD method. In the final stage of the fabrication process, the gold contacts in the form of

circular dots were coated on both substrates by the PVD method. Thus both MS and MIS structures were fabricated under the same experimental conditions in order to make an accurate comparison. Schematic illustrations of both structures made ready for measurement are given in Figure 1. Both MS and MIS structures, which were fabricated, were connected to Keithley 2400 SMU from ohmic and rectifier contacts and measured by applying voltage between (-2.5V) and (+2.5V) for electrical measurements.

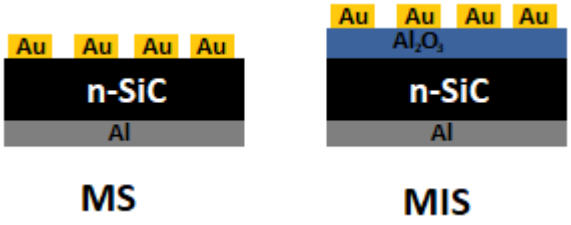


Fig.1: Schematic illustrations of MS and MIS structures

3. Results and discussion

I-V graphs of both structures whose fabrication is completed and measured are as shown in Figure 2.

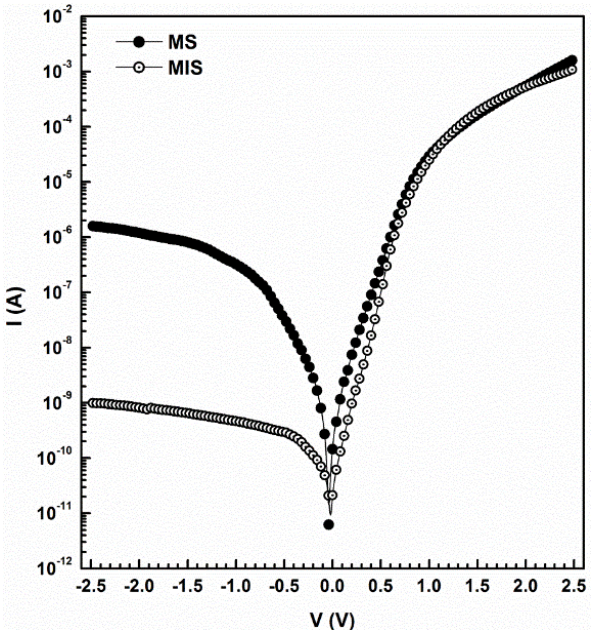


Fig. 2: Current-Voltage characteristics of Au/4H-n/SiC (MS) and Au/Al_2O_3/4H-n/SiC (MIS) structures.

When the *I-V* graph is examined carefully, it is seen that the Al_2O_3 insulation layer used as the interface layer increases the rectification rate of the MIS structure by approximately 1000 times compared to the MS structure. This result can be attributed to improving the interface states of the MIS structure [7]. The following formulas are used respectively to obtain basic electrical parameters such as reverse saturation current, barrier height and ideality factor of both structures [8, 9]:

$$I_0 = AA^*T^2 exp\left(-\frac{q\Phi_{B0}}{kT}\right) \quad (1)$$

$$\Phi_{B0} = \frac{kT}{q} ln\left[\frac{AA^{**}T^2}{I_0}\right] \quad (2)$$

$$n = \frac{q}{kT}\frac{d(V-IR_s)}{d(ln(I))} \quad (3)$$

where A is the area of the circular contacts, T is the absolute temperature, ϕ_{B0} is the barrier height, q is the elemental charge, k is the Boltzmann constant, I_0 is the inverse saturation current, n is the ideal factor and R_s is the series resistance.

Resistance values of both structures (MS and MIS) were calculated from *I-V* data. From the obtained data, R_i-*V* graphs of both structures are plotted and shown in Figure 3. When the R_i-*V* graph is examined in depth, it gives the rectification ratio for according to Ohm's Law both structures just as the *I-V* graph. On the other hand, the values of the shunt and series resistans for both structures can be found from this graph.

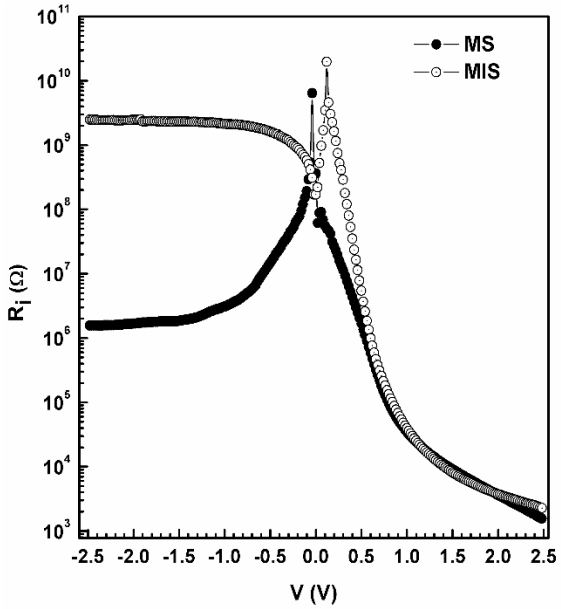


Fig. 3: Ri-V characteristics of Au/4H-n/SiC (MS) and Au/Al_2O_3/4H-n/SiC (MIS) structures.

In order to calculate these basic electrical parameters for both structures, the Ln (*I*)-*V* characteristic, which is a semi-logarithmic *I-V* graph, is plotted as in Figure 4. According to Figure 4, linearity is observed in the mid-voltage region of both structures, but this linearity is disturbed by the effect of R_s at high voltage. This can be attributed not only to the

effects of R_s but also to the effects of the interface states [10]. On the other hand, the slopes of the graphs are used to calculate the basic electrical parameters of both structures. According to the calculations and the data obtained from these slopes, it can be seen that the Al_2O_3 interface material improves the device performance.

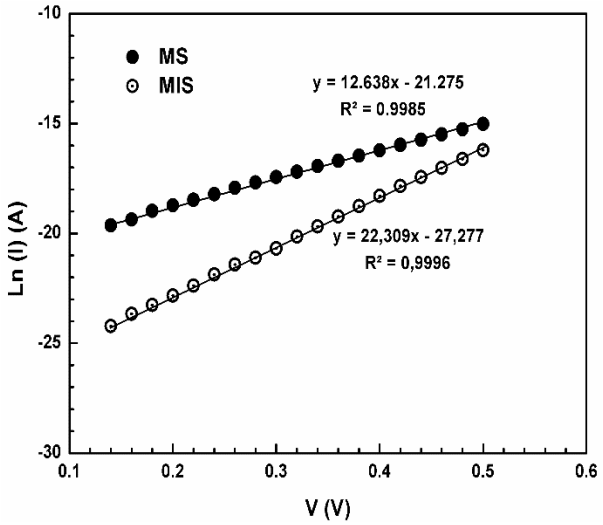


Fig. 4. A semi-logarithmic I-V graph of Au/4H-n/SiC (MS) and Au/Al_2O_3/4H-n/SiC (MIS) structures.

4. Conclusions

In the present study, MS and MIS devices were fabricated by forming Al_2O_3 on n-SiC using ALD technique. For this research, the *I-V* measurements of both devices were realized by applying a (-2.5V) - (+2.5V) bias voltage. Al_2O_3 (70 Å thick) was used as a high dielectric interfacial insulating layer between the metal and the semiconductor to enhance the performance of the MIS device compared to the MS device. R_s values in the depletion zone are decreasing irrespective of the frequency change. The rectification ratio of the MIS device is about 1085 times greater than the MS device is clearly understood from the measurement results. For all devices the sheet resistance is almost worth close to each other, whereas difference of series resistance is quite high. The value of the current increases exponentially with the increase in applied voltage from the mid region of the positive voltage, but due to the R_s effect, there is a considerable deviation from the linearity in the high positive voltage region for both devices. In conclusion, Al_2O_3 interfacial insulator layer leads to a considerably of the capacitance or dielectric constant compare to native SiO_2 so that can more storage of charges or energy.

References:

İ. Yücedağ, A. Kaya, Ş. Altındal, Int. J. Mod. Phys. B., 28 (2014) 1450153. **[1]**

B. Kınacı, S. Çörekçi, K. Kızılkaya, S. Özçelik, Optoelectron. Adv. Mat., 6 (2012) 327-330. **[2]**

S. Abermann, G. Pozzovivo, J. Kuzmik, G. Strasser, D. Pogany, J.F. Carlin, N. Grandjean, E. Bertagnolli, Semicond. Sci. Technol., 22 (2007) 1-4. **[3]**

P. Kordoš, G. Heidelberger, J. Bernát, A. Fox, M. Marso, H. Lüth, Appl. Phys. Lett., 87 (2005) 143501. **[4]**

G. Puzzilli, B. Govoreanu, F. Irrera, M. Rosmeulen, and J. V. Houdt, Microelectron. Reliab., 47 (2007) 508-512. **[5]**

G. Agostinelli, A. Delabie, P. Vitanov, Z. Alexieva, H.F.W. Dekkers, S. De Wolf, G. Beaucarne, Sol. Energ. Mat. Sol. C, 90 (2006) 3438-3443. **[6]**

A. Chawanda, C. Nyamhere, F. D. Auret, W. Mtang, M. Diale, J. M. Nel, J. Alloy. Compd., 492 (2010) 649-655. **[7]**

G. Ersöz, İ. Yücedağ, S. Bayrakdar, Ş. Altındal, A. Gümüş, J. Mater. Sci: Mater. Electron., 28 (2017) 6413-6420. **[8]**

S. Sze, Physics of semiconductor devices (1981) New York: Wiley. **[9]**

N. Baraz, İ. Yücedağ, A. Demir, G. Ersöz, Ş. Altındal, M. Kandaz, Polym. Advan. Technol., 28 (2017) 952-957. **[10]**

6th International Conference on Materials Science and Nanotechnology For Next Generation (MSNG2019)
October 16-18, 2019, Niğde, TURKEY (ORAL FULL TEXT)

Synthesis and Electrical Admittance (Y) Properties of Co Doped $LaCrO_3$ Compounds

Fatih M. Coşkun[1*], Özgür Polat[2, 3], Mustafa Coşkun[1], Abdülmecit Türüt[1]
[1]Faculty of Engineering and Natural Sciences, Department of Engineering Physics, Istanbul Medeniyet University, 34700 Uskudar, Istanbul, Turkey.
[2] CEITEC BUT, Brno University of Technology, Purkyňova 123, 612 00 Brno, Czech Republic
[3]Institute of Physical Engineering, Brno University of Technology, Technická 2, 616 69 Brno, Czech Republic

The cobalt (Co) doped $LaCrO_3$ (LCO) powder was synthesized by solid-state reaction method using La_2O_3 (ACROS, 99.9%), Cr_2O_3 (ACROS, 99%) and Co_2O_3 (Alfa Aesar, 99%) powders were used as starting materials. For the preparation of Co doped $LaCrO_3$ powders, Co_2O_3 (Alfa Aesar, 99%) powder with various mol % (1, 10, 15) were mixed with La_2O_3 (ACROS, 99.9%) and Cr_2O_3 (ACROS, 99%) powders. The obtained powders were calcined at 1200 °C for 12 h in air ambient in order to obtain desired homogeneity and crystalline structure. After the calcination, the powders were pressed under 10 tons pressure to prepare pellets. Those pellets were annealed at 1150 °C to obtain enough hardness. Novocontrol Broadband Dielectric/Impedance Spectrometer equipped with liquid nitrogen dewar was employed for frequency dependent electrical admittance (Y) measurements of prepared pellet samples. Measurement temperature of the samples was gradually varied from -100 °C to 100 °C with 20 °C step. Real part of admittance (Y') showed both frequency independent (lower frequency region) and frequency dependent (higher frequency region) regions for all samples. Imaginary part of admittance (Y'') first decreased with increasing frequency and reached a minimum value and increased with increasing frequency for all samples. The total admittance showed similar behavior to real part one. Finally, the increasing Co doping ratio caused admittance parameter to decrease.

Keywords: $LaCrO_3$, Cobalt (Co), Solid-State Reaction, Electrical Admittance (Y)
Submission date:30 October 2019
Acceptance Date:

Corresponding authors: fatihmehmetcoskun@gmail.com

1. Introduction

Perovskite-oxide materials stated by ABO_3 chemical formula, have considerable attention among the researchers due to their physical and chemical properties such as high crystallinity, high electrical conductivity, high stability in air, high temperature processability etc. Such unique properties of perovskite-oxides offer very large application areas including gas sensing [1], fuel cell [2], membrane [3], heating element [4], catalysis [5] so on.

$LaCrO_3$ (LCO) is one of the important members of perovskite-oxide family with high optical band gap (3.4-3.5 eV), orthorhombic crystalline structure with a = 5.513 Å, b = 5.476 Å, c = 7.759 Å lattice parameters (space group Pbnm), high p-type conductivity, and high temperature durability in reducing atmosphere, high physical and chemical stability in air ambient etc [7].

In the literature, many researchers studied LCO compounds and reported its structural, chemical, dielectric and magnetic properties at room temperature [8-10]

There is a few number of studies on LCO in terms of wide temperature and frequency range electrical admittance properties.

It is known that the ionic radius and oxidation states of the doped/foreign cations play key roles on the electrical and magnetic properties of the parent materials [11,12]. The substitution of Co to Cr site will distort the unit cell of LCO due to lattice mismatch between Co and Cr. Hence, such distortion will have influence on the electrical and dielectric properties of LCO compound.

In this investigation, the impact of the substitution of Co into Cr site on the electrical admittance (Y) and activation energy (Ea) were investigated at a wide range of frequency and temperature region. The powders of all compounds were prepared via solid state reaction. Scanning electron microscopy (SEM) and X-ray photoelectron spectroscopy (XPS) were employed to study crystalline morphology and the surface characteristics of synthesized powders, respectively. It has noticed that the activation energy tends to decreases with increase in the doping ratio.

2. Experimental details

The Co dop $LaCrO_3$ (LCCO) powder was prepared by the solid-state reaction method. For the preparation of Co doped $LaCrO_3$ powders, Co_2O_3 (Alfa Aesar, 99%) powder with various mol % (1, 10, 15) were mixed with La_2O_3 (ACROS, 99.9%) and Cr_2O_3 (ACROS, 99%) powders. First, the high purity La_2O_3 and Cr_2O_3 powders were mixed in an agate mortar for 1 h with ethanol and calcined at 900 °C for 10 h in the air to obtain LCO compound. After the first step calcination the powders were reground for homogeneity purpose. After reground the powder for several hours the second calcination was carried out at 1200 °C for another 12 h in the air. The LCO powder was pressed into 13 mm pellets at 10 tons pressure for several minutes in order to study electrical properties. After that, the pellet was heated at 1150 °C for 4 h in air to sinter the pellets.

The chemical and structural analysis of LCCO powder were carried out using a FEI scanning electron microscope (SEM), X-Ray photoelectron spectroscopy (XPS) X-ray diffractometer (XRD, Bruker D8 Discover) analyses. Novocontrol Broadband Dielectric/Impedance Spectrometer was employed to study frequency-depended electrical admittance property measurements varied temperature from – 100 °C to 100 °C with 20 °C step. In order to investigate of electrical properties of LCO, the LCO pellet was sandwiched between two platinum (Pt) electrodes and placed into Dielectric Spectrometer for measurements.

3. Results and discussion:

SEM images of Co doped LCO at various percentages are shown in fig. 1. As seen from the figure, the grain sizes incerease as the the dopping ratio is increased.

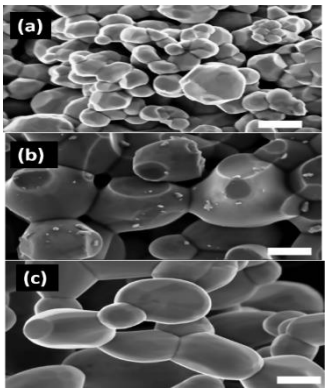


Fig.1: SEM images of (a) 1% Co doped LCO, (b) 10% Co doped LCO (c) 15% Co doped LCO [13]. (The scale is 1 μm)

The real part of the admittance (Re Y) behavior of LCCO samples are demonsrated in fig. 2. Real part of admittance (*Y'*) or conductance (G) shows both frequency independent (lower frequency region) and frequency dependent (higher frequency region) regions for all samples. The frequency independent region is called the dc region. The *dc* region extends to the higher frequency with increasing temperature. The strongly frequency dependent region is called the *ac* region.

On the other hand fig. 3. demonstrates the imaginary part of the admittance (Im Y), namely susceptance (B) of LCCO, at various temperature. Imaginary part of admittance (Y") first decreases with increasing frequency and reaches a minimum value and increases with increasing frequency for all samples.

In fig. 4(a), Re (Y) comparison graph for all compounds at 100 °C can be seen. From this figure, we can infer that the increasing Co doping ratio causes admittance parameter to decrease. The real part of the admittance, which is Conductance (G), decreases with increasing Co dop ratio. This leads to activation energy to increase, as shown in fig. 4(c). The activation energies at fig. 4(c) are calculated from the arhenius relation which is:

$$f_{min}=f_0 e^{-(Ea/kT)} \qquad (1)$$

From the figure 4(b) we can compare the minimum values of imaginary admittance graphs for T=100 °C.

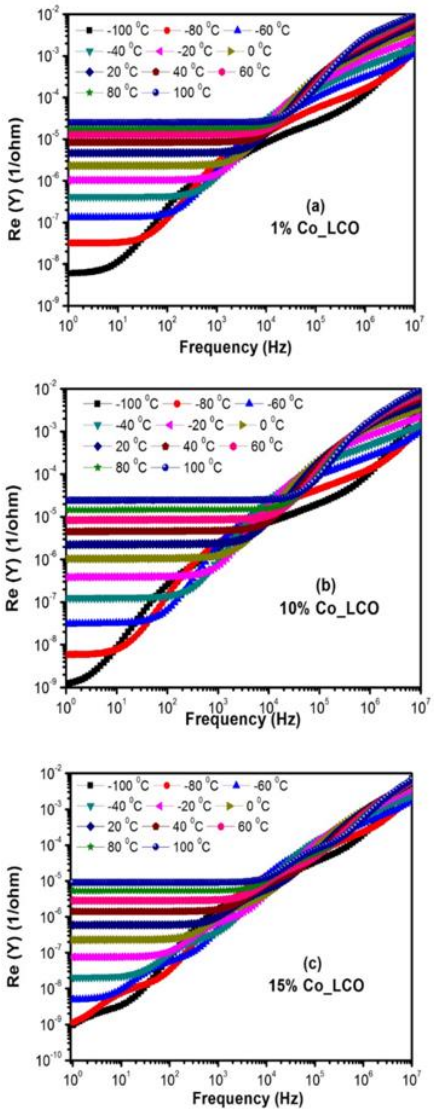


Fig. 2: Real part of admittance (Y') for (a) 1% Co doped LCO, (b) 10% Co doped LCO, (c) 15% Co doped LCO samples under a temperature range from -100 C to 100 C

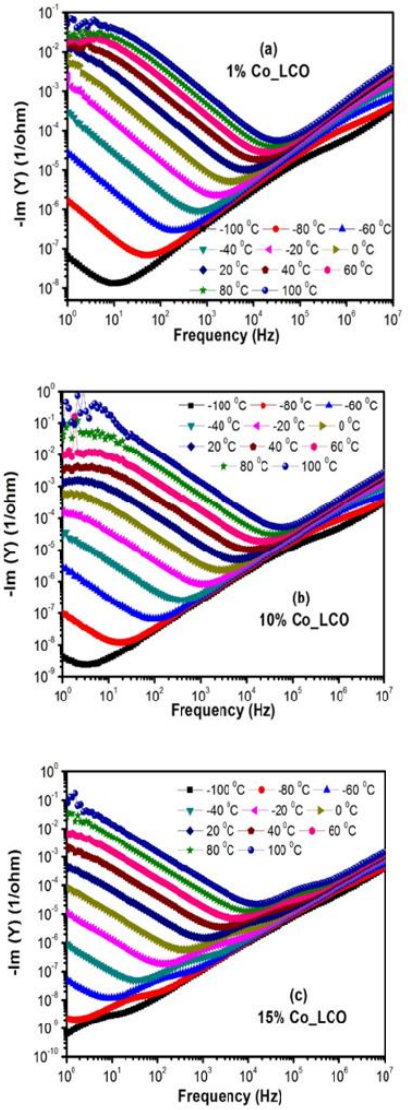


Fig. 3: Imaginary part of admittance (Y') for (a) 1% Co doped LCO, (b) 10% Co doped LCO, (c) 15% Co doped LCO samples under a temperature range from -100 C to 100 C

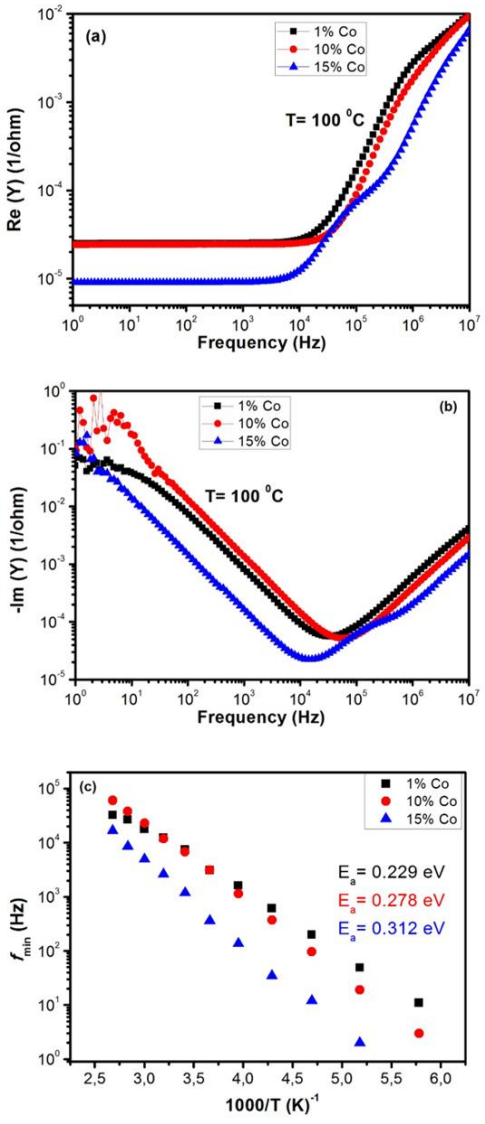


Fig. 4: (a) Re (Y) comparison graph for all compounds at 100 °C (b) Im (Y) comparison graph for all compounds at 100 °C (c) Temperature dependent activation energies for all compounds.

Conclusions

In this study we prepared pellets of 1%, 10% and 15% Co doped LCO compounds After the dielectric measurements, we have seen that the Real part of admittance (Y') shows both frequency independent (lower frequency region) and frequency dependent (higher frequency region) regions for all samples. The Im (Y'') of the LCCO samples at various temperatures first decreases with increasing frequency and reaches a minimum value and increases with increasing frequency for all samples. The Im(Y'') graphs have negative value which leads us to conclude that the compounds show capacitive reactance rather than inductive.

References:

[1] Z. Panpan, Q. Hongwei, Z. Heng, L.Wei, H. Jifan, Journal of Rare Earths 35(6), (2017) 602.
[2] K. Hilpert, R.W. Steinbrech, F. Boroomand, E. Wessel, F. Meschke, A. Zuev, O. Teller, H. Nickel, L. Singheiser, J. Eur. Ceram. Soc. 23, (2003) 3009-3020.
[3] S. Wang, Y. Dong, B. Lin, J. Gao, X. Liu, G. Meng, Mater. Res. Bull., 44, (2009) 2127-2133.
[4] A. M. Azad, R. Sudha, O. M. Sreedharan, TJ. Less Common Metals. 166, (1990) 57–62.
[5] K. Rida, A. Benabbas, F. Bouremmad, M. A. Pen, E. Sastre, A. Martinez-Arias, Appl. Catal. B Environ., 84, (2008) 457-467.
[6] D. Fu and M. Itoh, (2011) ISBN: 978-953-307-332-3, InTech, Available from: http://www.intechopen.com/books/ferroelectrics-material-aspects/ferroelectricity-in-silver-perovskite-oxides.
[7] O. Polat, Z. Durmus, F. M. Coskun, M. Coskun, A. Turut, J. Mater. Sci., 53, (2018) 3544– 3556.
[8] Y. Kenji, I. Naoshi, S. Yutaka, I. Yoshinobu, Materials Chemistry and Physics, 190, (2017) 96-101.
[9] S. M. Khetre, A. U. Chopade, C. J. Khilare, C. J. Jadhav, P. N. Jagadale, S. R. Bamane, J. Mater. Sci: Mater. Electron., 24, (2013) 4361–4366.
[10] V.D. Nithya, J. R. Immanuel, S.T. Senthilkumar, C. Sanjeeviraja, I. Perelshtein, D. Zitoun, K. R. Selvan, Materials Research Bulletin, 47 (2012) 1861–1868
[11] S. Halder, Md.S. Sheikh, B. Ghosh, T.P. Sinha, Ceram. Int. 43 (2017) 11097–11108.
[12] H. Qi, Y. Luan, S. Che, L. Zuo, X. Zhao, C. Hou, Inorg. Chem. Commun. 66 (2016) 33–35.
[13] M. Coskun, O. Polat, F.M. Coskun, Z. Durmus, M. Caglar, A. Turut, Materials Science&Engineering B 248 (2019) 114410.
[14] J. Li, L. Guanzhong, W. Guisheng, D. Mao, Y. Guo, Y. Wang, Y. Guo, Catal. Sci. Technol. 4 (2014) 1268.

6th International Conference on Materials Science and Nanotechnology For Next Generation (MSNG2019)
October 16-18, 2019, Niğde, TURKEY (ORAL FULL TEXT)

Application of the TG and DTA to the Turkish Soma Peat.

Canan AKSU CANBAY[1], Jale GÜLEN[2,*], Fikret SÜNER[3]
[1] Firat University, Faculty of Science, Department of Physics, Elazig 23169, Turkey
[2]Yıldız Tech. Uni. Chem. Metal. Faculty Chem Eng Dept., 34210 Esenler İstanbul
[3]İstanbul Tech. Uni. Mining Faculty Geological Eng. Dept., 34469 Ayazağa İstanbul

In this study,a Soma peat sample was heated with different heating rates. DTA and TG results were investigated. Maximum weight loss percetages (%) was observed on TG curves and corresponding DTA peak start/finish temperatures were determined. The thermal parameters obtained from both TG and DTA data were evaluated for determining the kinetic and Arrhenius parameters.

*Keywords:*Turkish Soma (Değirmisaz) peat (lignite), TG-DTA thermogravimetry, Proximate analysis, Pyrolysis kinetics.
Submission date:12October 2019
Acceptance Date:20January2020

*Corresponding author:gulenj@yildiz.edu.tr

1. Introduction

Coal as an energy source marked the economic and political development in the world. The severe oppurtunity is seen in the Europe especially during the 19th and 20th centuries. At the beginning of the 21 century, coal energy accounts for 36% of the total energy produced in Europe. So, it is the most important energy source [1]. Turkey has low coke but huge lignite reserves. But those lignite reserves are high ash and volatile matter and low calorific value. The coal evaluation in the air or in free medium can be done via thermo analytical methods such as thermogravimetry (TG), differential thermogravimetry (DTG), differential thermal analysis (DTA), differential scanning calorimetry (DSC), thermogravimetry-Fourier transform infrared spectroscopy (TG-FTIR) and thermogravimetry-mass spectrometry (TG-MS) techniques were employed at a growing rate in the evaluation and characterization of fossil fuels from the point of determining the combustion characteristics or kinetic parameters [2]. Thermogravimetry (TG) and differential thermal analyses (DTA) have been defined to be an effective tool to study coal behavior in different medium [3, 4]. Previous TG studies showed that the sample composition [5], the rank of coal [6], the maceral groups of coal [7, 8] have some effects on the characteristics of the plots.

The objective of this research was to investigate the pyrolysis kinetics of Değirmisaz peat.

2. Experimental details

Soma has 0.265 billion tone of lignite reserves and the calorific value of them is 4000-6000 kcal/kg. Experimental peat sample was supplied from those area. It is located in the Agean district of Turkey.The samples were ground to grain size down to 1 mm. Proximate analysis (which includes the moisture, the ash, the volatile matter and the fixed carbon contents determination) was performed on the peat sample. Moisture content was measured according to DIN 51718 [9], the ash content according to DIN 51719 [10] and volatile matter according to DIN 51720 [11]. Fixed carbon was calculated from volatile matter by difference. Gross calorific value was measured according to DIN standards, using an IKA C-400 adiabatic calorimeter.One-hundred millilitre of each sample were placed in an aluminium crucible in a Shimadzu DTG 60AH Thermal Analyser. Al_2O_3 was used as reference material. Samples were heated from ambient temperature up to 950 ºC with

different heating rates of 5, 10, 15 and 20 ºC/min in a 150 cm^3/min flow of argon gas.

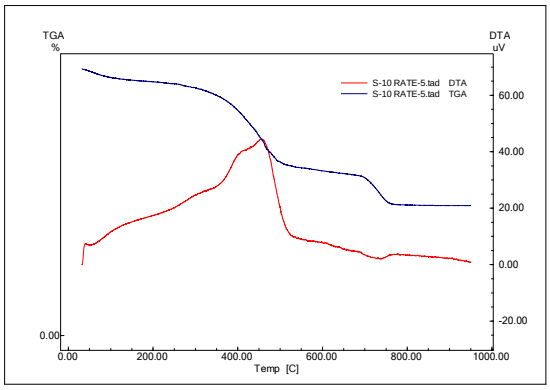
3. Results and discussion:

The results of proximate analysis and obtained calorific value of the Soma peat are shown in Table 1.

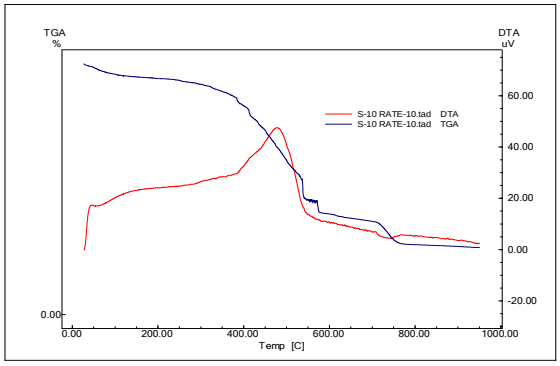
Table 1. Analysis of the Soma peat (peat amount 10 %).

Proximate analysis (%)	Soma peat (dry basis)
Volatile matter	32.5
Ash	44.7
Fixed carbon	22.8
Calorific value	4707 kcal/kg

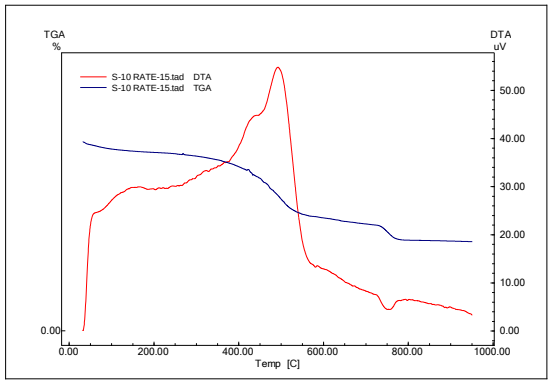
The thermal characterisation of mineral substances can be made by thermogravimetry (TG) and Differential Thermal Analysis (DTA). These methods are widely used



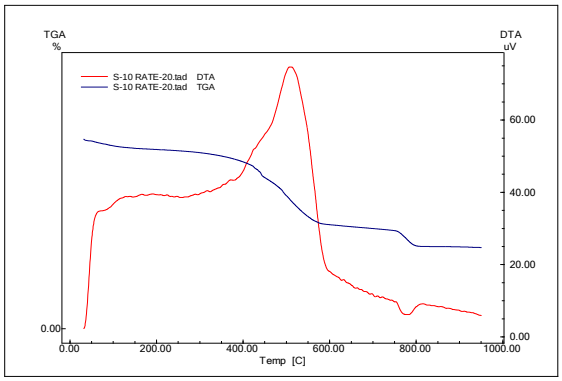
-a-



-b-



-c-



-d-

Figure 1. *The TG and DTA curves of the sample at;* ***a)*** *5 ˚C/min,* ***b)*** *10 ˚C/min,* ***c)****15 ˚C/min. and* ***d)*** *20 ˚C/min. heating rates.*

for the characterisation of organic and inorganic substances. The results of TG and DTA curves are shown in Fig. 1.a, b, c and d.The samples were heated from room temperature to 950 ˚C with different heating rates as 5, 10, 15 and 20 ˚C/min. in a 150 mL/min. flow of argon. On these graphics, the blue and red lines depict the TG and DTA behavior of the blends, respectively. As seen from the TG trends of figures; with increasing the heating rate, the weight loss of the blends decreased. The related weight losses of the samples were given at the following Table 2. As seen from the Fig. 1.a-Fig.1.d, the weight loss occured in two steps.

Table 2. Mass loss (wt.%) of the sample at different heating rates.

Heating Rates (˚C/min.)	1.Step (%)	2. Step (%)
5	33.340	11.847
10	52.799	9.798

15	32.278	8.471
20	38.516	8.846

The DTA curves (Fig.1.a-d) of the blends are observed in the stages one is exothermic and the other is endothermic. The first peak is caused by the volatilization of volatile matter released from the coal and the second peak is caused by decomposing of the residual char. For heterogeneous ignition with O_2 usage, on the other hand, only one strong exothermic peak appears on the DTA curve, as a result of burning of the whole coal particle. However, in the case of hetero-homogeneous ignition, after release of part of the volatile matter, one strong exothermic peak appears on the DTA curve with a remarkable weight loss on the TG curve [12].Similar to the TG curves,the first peak of DTA has been sharpening with increasing the heating rate. The onset and end point of the exothermic and endothermic reaction peaks during heating were given in Table 3 and Table 4.

Table 3. DTA curve values of the exothermic reaction during heating.

Heating Rate (˚C/min)	Peak Start Temperature (˚C)	Peak Finish Temperature (˚C)	Enthalpy (kJ/g)
5	369.90	511.22	2.13
10	406.44	536.83	2.18
15	435.09	548.81	2.42
20	422.12	589.26	2.75

Table 4. DTA curve values of the endothermic reaction during heating.

Heating Rate (˚C/min)	Peak Start Temperature (˚C)	Peak Finish Temperature (˚C)	Enthalpy (J/g)
5	729.32	740.36	-48.78
10	710.78	761.53	-67.89
15	730.08	777.29	-58.33
20	756.37	802.92	-51.99

The weight loss (W) of the samples is assumed to react via the first order reaction. It is written at the following equations (1);

$$dW / dt = k.W^n \qquad (n=1) \qquad (1)$$

where; k is the reaction constant. The thermal effect that is seen at the peak areas is taken place according to the Arrhenius law. The k constant can be written as below;

$$k = A.Exp(-E/RT) \qquad (2)$$

After substituting Eq (2) in the Eq (1) the following equation can be obtained;

$$dW\ dt = A.Exp(-E/\ RT).W \qquad (3)$$

taking the logarithm of both sides;

$$log\left(\frac{1}{W}\cdot\frac{dW}{dt}\right) = logA - E\ /2.303RT \qquad (4)$$

where dW/dt is the rate of weight change of the reacting material in % min^{-1}, A is the Arrhenius constant or pre-exponential factor in 1 min^{-1}, E is the activation energy in $kJ.mol^{-1}$, T is the temperature in K, n is the reaction order and R is the gas constant in 8.314 $J.mol^{-1}.K^{-1}$.In the model, the plot of log[(dW/dt).(1/W)] against 1/T (given in Fig.-2) is a straight line with a slope of – E/2.303R. The magnitude of the slope can be used to calculate the activation energy (E).

For 5 ºC/min heating rates, weight losses approximately 33 % and 12 % were seen for 425 and 728 ºC mid point temparatures, respectively. From the first order reaction mechanism, the related activation energy is found from yhe slope given below.

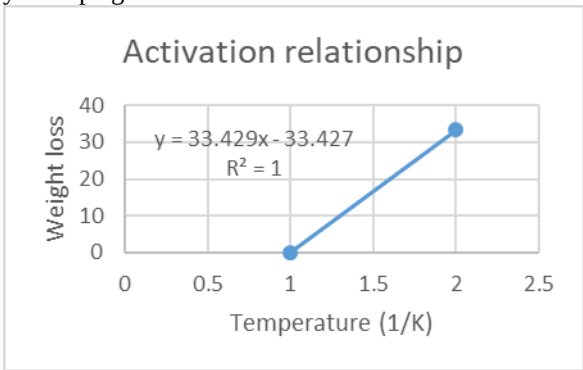


Figure 2. Activation energy relationship for 5 ºC/min heating rates of Manisa peat

Thus, the activation energy of the sample was found as 640.07 J/mol.

Conclusions

A peat sample taken from Manisa city of Agean area of Turkey was investigated with DTA and TG analyses. Two characteristic peaks (exothermic and endothermic) were seen in DTA plots and maximum weight loss in Soma peat sample was observed at 5 ºC/min of heating rate and this occurredmost probablybecause at small heating rates the sample staysunder heating (at a temperature region)for longer timespans. The reaction activation energy was also evaluated.

References:

[1] Coal industry across Europe, Association for coal and lignite (Euracoal) Brussels, 2003.
[2] K. Jayaramana, M. V. Kok, I. Gokalp, Thermogravimetric and mass spectrometric (TG-MS) analysis andkinetics of coal-biomass blends, Renewable Energy, 101(2017)293-300
[3] Y Chen, LB Suida, VN Misra,Biodepyritizarion of coal J Chem Technol Biotechnol 79 (2004) 1-12
[4] S. Küçükbayrak, Influence of the mineral matter on the combustion characteristics of Turkish lignires. Thermochim Acta 216 (1993) 119-129
[5] O. P. Mahajan, P. L. Walker, Effect of inorganic matter removal from cıals and chars on their surface areas. Fuel 58 (1979) 333-337
[6] SE Smith, R.C. Neavel, E.J. Hippo, R.N Miller, DTGA combustion of coal in the Exxon coal library. Fuel 60 (1981) 458-462
[7] A White, M.R. Davies, S.D. Jones, Reactivity and characterization of coal maceral contents. Fuel 68 (1989) 511
[8] J.C. Crekllıng, E.J. Hippo, B.A. Woerner, D.P. West, Combustion characteristics of selected whole coals and macerals Fuel 71 (1992) 151
[9] Deutsche Norm, Testing of solid fuels determination of the water content and the moisture of analysis sample, DIN 51718, 1995.
[10] Deutsche Norm, Testing of solid fuels determination of ash content, DIN 51719, 1978.
[11] Deutsche Norm, Testing of solid fuels determination of volatile matter, DIN 51720, 1978.
[12] Y. Chen, S. Mori, W-P Pan, Studying the mechanism of ignition of coal particles by TG-DTA. Thermochimica Acta 275 (1996) 149-158
[13] R.Junga, W.Knauer, P. Niemiec, M. Tanczuk, Experimental tests of co-combustion of laying hens manure with coal by using thermogravimetric analysis. Renewable Energy 111(2017) 245-255.

6th International Conference on Materials Science and Nanotechnology For Next Generation (MSNG-2019)
October 16-18, 2019, Niğde, TURKEY (ORAL FULL TEXT)

Thermal and Electrical Properties of Poly(isobornyl methacrylate) and Poly(cyclohexen-3-yl-methyl methacrylate) Doped Multi Wall Carbon Nanotubes.

Gamze BARIM[1,*], Canan AKSU CANBAY[2], Gülay YENICE[1]
[1]University of Adiyaman, Faculty of Science and Arts, Department of Chemistry, 02040, Adiyaman, Turkey
[2]University of Firat, Faculty of Science, Department of Physics, 23169 Elazığ, Turkey

We have examined the thermal and electrical aspects of poly(cyclohexen-3-yl-methyl methacrylate) poly(CHMA) doped multi-walled carbon nanotubes (MWCNTs) composites. We acquired cyclohexen-3-yl-methyl methacrylate (CHMA) monomer from the reaction of 3-cyclohexene-1-methanol compound with methacryloyl chloride with this connection. Free radicals at 70 ° C in the presence of AIBN initiator in 1,4-dioxane solvent was employed to perform the homopolymerization of the synthesized monomer. We preferred solution processing method with the various weight ratios (%1, %3, %5) of MWCNTs in order to prepare the poly(CHMA):MWCNTs nanocomposites. We also examined thermal and electrical aspects of the nanocomposites which were composed of poly(cyclohexen-3-yl-methyl methacrylate) and multi-walled carbon nanotubes. Furthermore, the thermal and electrical properties of poly (isobornyl methacrylate) poly(IBMA) doped multi-walled carbon nanotubes composites were investigated. Thermal stability and electrical conductivity of composites increased with increasing multi-walled carbon nanotubes dopant.

Keywords: Multi Wall Carbon Nanotubes, Poly(isobornyl methacrylate), Poly(cyclohexen-3-yl-methyl methacrylate)

Submission date:12 October 2019
Acceptance Date:20 January 2020

**Corresponding author*:gbarim@adiyaman.edu.tr

1. Introduction

Functional polymers, which can be utilized as reagents, catalysts, protecting groups, etc, are macromolecules and chemically bound functional groups are attached to them.. Functional polymers do not cost must, are easily-processed and they have a range of attractive mechanical characteristics for functional organic molecules. It is possible to modify the aspects of the polymer either by means of chemical reactions on pendant groups or by altering the physical nature of the polymers. Dopants are employed in order to improve the properties of polymers as well. The kind of carbon nanotube is one of the most commonly used dopants. In the last two decades, polymer/carbon nanotube (CNT) nanocomposite materials have been developed a lot. Thanks to its outstanding physical and chemical aspects, carbon nanotube has generated enormous interest in most areas of science and engineering. At low CNT loading, polymer materials get good mechanical properties and high electrical and thermal conductivities from the CNT. Micro- and nano-scale particles have been regarded as filler material for polymers in order to generate high potential composites with improved characteristics. When the CNT content exceeds a critical value, known as a percolation threshold, the polymer/CNT nanocomposites become conductive due the formation of a 3D conductive network of the CNT within the polymer matrix [1–5]

2. Experimental details

In order to synthesize the Poly(CHMA)/MWCNTs and Poly(IBMA)/ MWCNTs composites; 3-cyclohexene-1-methanol (Aldrich), methacryloyl chloride (Merck), isobornyl methacrylate (IBMA) (Sigma), Azobisisobutyronitrile (AIBN) (Fluka), tetrahydrofurane (THF), multi wall carbon nanotubes and other chemicals and solvents were used without further purification. Firstly, we acquired cyclohexen-3-yl-methyl methacrylate (CHMA) monomer from the reaction of 3-cyclohexene-1-methanol

compound with methacryloyl chloride. Free radicals at 70 °C in the presence of AIBN initiator in 1,4-dioxane solvent were employed to perform the homopolymerization of the synthesized monomer [6]. In order to prepare the poly(CHMA):MWCNTs nanocomposites, solution processing method with the various weight ratios (%1, %3, %5) of MWCNTs was preferred following the synthesis of the poly(cyclohexen-3-yl-methyl methacrylate). 1 g of poly(CHMA) was dissolved 10 mL of THF to prepare the composites. The various weight ratios (%1, %3 and %5) of MWCNTs were dispersed in separate beakers in 2 mL of THF for 5h by means of using an ultrasonic bath. We added 2 mL of polymeric solution to this mixture and stirred it with the help of a magnetic stirrer. The solvent was evaporated under vacuum so that the polymer/ MWCNTs composites can be obtained. Poly(IBMA)/ MWCNTs composites were prepared identically. Thermal stabilities of the Poly(CHMA)/ MWCNTs composites were investigated on a Perkin- Elmer TGA/DTA 7300 thermal analysis systems under N_2 flow with a heating rate of 20 0C/min. To determine the electrical conductivity values of Poly(CHMA)/MWCNTs and Poly(IBMA)/MWCNTs composites in pellet forms the current-voltage (I-V) measurements made by using Fytronix FY 7000 Solar Simulator and two probe method were taken by steps of 0.2 Volt from 0 Volt to 6 Volt under dark and in room conditions. The thickness values of the composite samples in pellet forms were measured by using a digital micrometer.

3. Results and discussion

3.1. Thermal properties of composites

Thermal stabilities of the Poly(CHMA)/ MWCNTs composites were investigated on a Perkin- Elmer TGA/DTA 7300 thermal analysis systems under N2 flow with a heating rate of 20 0C/min. The thermogravimetric curves of composites are shown in Figure 1. If the temperatures

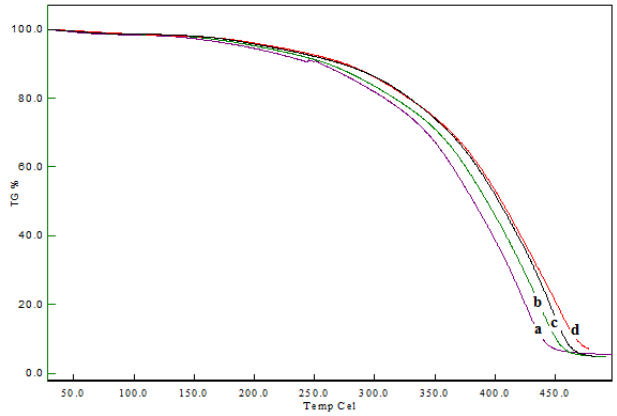


Fig.1: *Thermal degradation curves of composites; a:Poly(CHMA) b: Poly(CHMA)/ MWCNTs:%1 c: Poly(CHMA)/ MWCNTs:%3 d: Poly(CHMA)/ MWCNTs:%5*

corresponding to 50 wt% loss of the polymers were taken as a measure for their thermal stability, these temperatures would be 382, 390, 401, 403 0C for poly(CHMA) and P(CHMA):MWCNTs (%1, %3, %5) respectively. Data in Table 1 clearly show that thermal stability of composites increased with increasing multi-walled carbon nanotubes dopant [7–9].

Table 1: Thermal decomposition temperatures of composites

		%Weight loss at different temperature (^{0}C)		
Samples	**T_{max}**	**%10**	**%50**	**%90**
Poly(CHMA)	448	255	382	440
Poly(CHMA)/MWCNTs:%1	412	259	390	450
Poly(CHMA)/MWCNTs:%3	416	270	401	455
Poly(CHMA)/MWCNTs:%5	422	272	403	458

T_{max}: Temperature for maximum rate of decomposition.

In order to determine the electrical conductivity values of the synthesized Poly(CHMA)/ MWCNTs and Poly(IBMA)/MWCNTs composites, severally five resistance (R) and their standard error values for each sample were obtained from analyses of repeating I-V measurements and their average values were also calculated. The I-V graphs of Poly(CHMA)/ MWCNTs composites were given in Figure 2, 3 and 4 and those of Poly(IBMA)/MWCNTs composites were placed in Figure 5, 6 and 7. The conductivity (σ) and resistivity (ρ) values for each composite sample were determined by taking linear fitting to the obtained graphs and were listed in Table 2. The electrical resistivity and conductivity values of the samples were computed by using these simple formulas as below;

$$R = \frac{1}{slope} \quad (1)$$

$$\rho = \frac{R.A}{t} \quad (2)$$

$$\sigma = \frac{1}{\rho} \quad (3)$$

here, slope refers to the slope value obtained by taking linear fitting of an I-V plot, *A* is probe needle contact area (=0.5 mm^2) and *t* is the thickness of sample (=1 mm).

Table 2: The electrical resistivity and conductivity parameters of the samples.

Sample ID	Resistance R (Ω)	Resistivity ρ (Ω.m)	Conductivity σ (S/m)	Standard error (%)
Poly(CHMA)/ MWCNTs :%1	$1.442x10^{11}$	$7.210x10^{7}$	$1.387x10^{-8}$	±3.85
Poly(CHMA)/ MWCNTs :%3	$9.606x10^{8}$	$4.803x10^{5}$	$2.082x10^{-6}$	±5.82
Poly(CHMA)/ MWCNTs :%5	$2.972x10^{6}$	$1.486x10^{3}$	$6.727x10^{-4}$	±4.58
Poly(IBMA)/ MWCNTs :%1	$1.537x10^{8}$	$9.852x10^{5}$	$1.015x10^{-6}$	±4.71
Poly(IBMA)/ MWCNTs :%3	$1.145x10^{7}$	$5.727x10^{3}$	$1.746x10^{-4}$	±6.46
Poly(IBMA)/ MWCNTs :%5	$1.435x10^{7}$	$7.176x10^{3}$	$1.393x10^{-4}$	±8.43

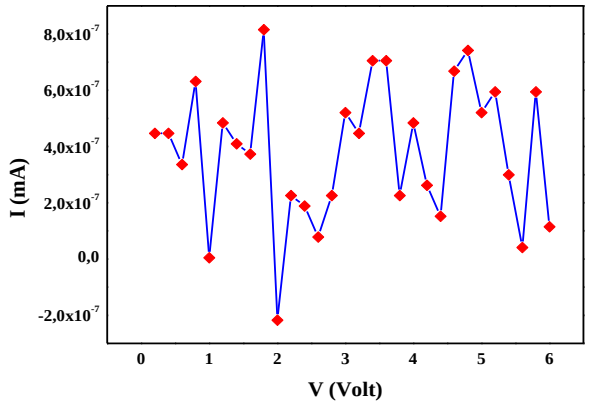


Fig.2: *I-V graph of Poly(CHMA)/ MWCNTs:%1 composite sample.*

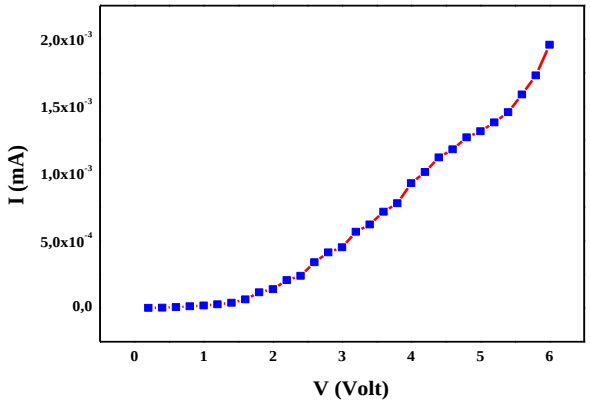


Fig.4: *I-V graph of Poly(CHMA)/MWCNTs:%5 composite sample.*

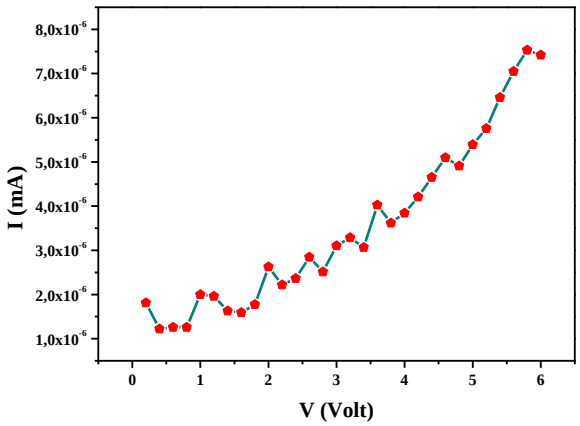


Fig.3:*I-V graph of Poly(CHMA)/ MWCNTs:%3 composite sample.*

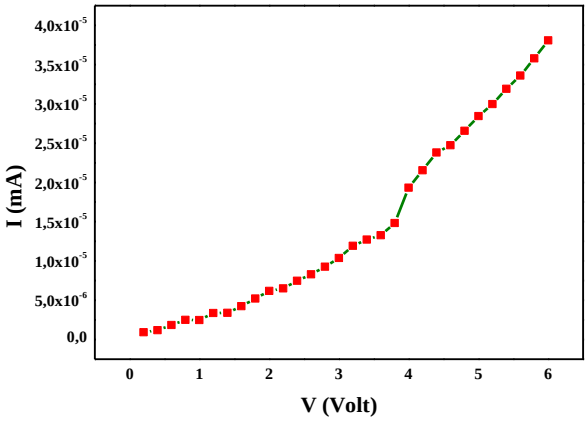


Fig.5: *I-V graph of Poly(IBMA)/ MWCNTs:%1 composite sample.*

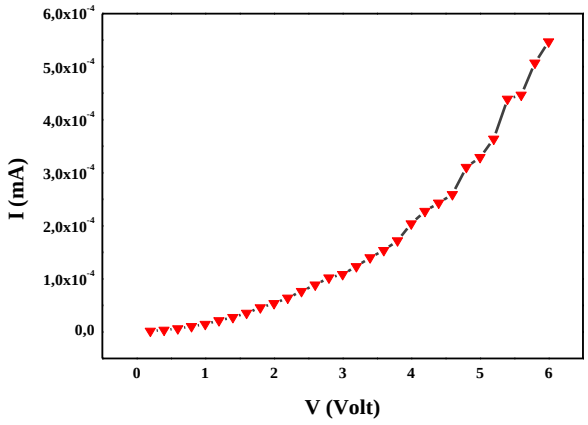


Fig.6: *I-V graph of Poly(IBMA)/ MWCNTs:%3 composite sample.*

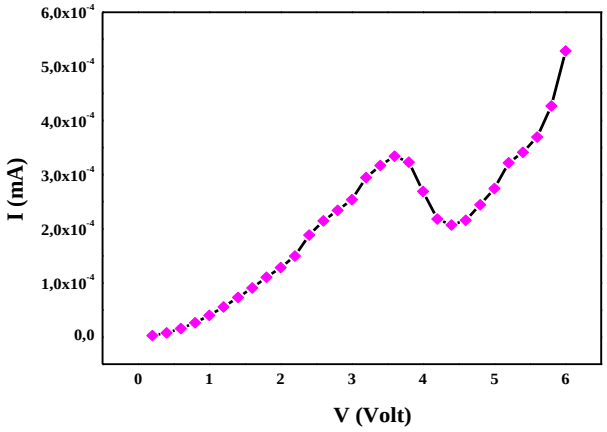


Fig.7:*I-V graph of Poly(IBMA)/ MWCNTs:%5 composite sample.*

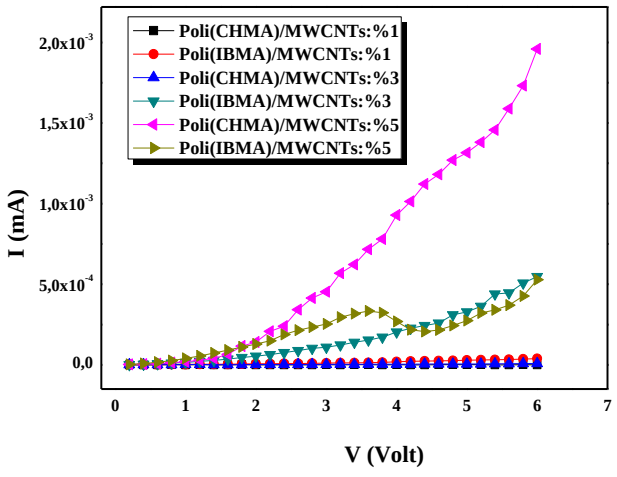


Fig.8: *MultipleI-V graphs of Poly(CHMA)/MWCNTs and Poly(IBMA)/ MWCNTs composite samples.*

As it is understood from both multiple I-V graphs of Poly(CHMA)/ MWCNTs and Poly(IBMA)/ MWCNTs composite samples in Figure 8 that the electrical conductivities of the samples were increased due to increment in MWCNTs proportion, so inversely their resistivities were decreased. Therefore, it can be deduced that while the doping ratio increased, the electrical properties of the samples upgraded from insulating to semiconducting properties.

Conclusions

Poly(CHMA) and Poly(IBMA) were prepared by free radical polymerization. The Poly(CHMA):MWCNTs and Poly(IBMA): MWCNTs nanocomposites were prepared by solution processing method with the various weight ratios (%1, %3, %5) of MWCNTs. Thermal and electrical properties of the nanocomposites comprised of polymers and multiwalled carbon nanotubes were investigated. Thermal stability and electrical conductivity of composites increased with increasing multi-walled carbon nanotubes dopant.

References:

[1] D. Braun, H. Cherdron, M. Rehahn, H. Ritter, B. Voit, Polmer Synthesis: Theory and Practice, 375-395, 2012.
[2] F. Yakuphanoglu, I. S. Yahia, G. Barım, B. F. Şenkal, “Double-walled carbon nanotube/polymer composites: Electrical properties under dc and ac fields”, Synthetic Metals,160, 1718-1726, 2010
[3] M. T. Byrne, Y. K. Gun’ko, “recent advances in research on carbon nanotube-polymer composites”,advanced Materials, 22, 1672-1688, 2010.
[4] K. Hayashida, H. Tanaka, “Ultrahigh electrical resistance of poly(cyclohexyl methacrylate)/carbon nanotube composites prepared using surface initiated polymerization”, Advanced Functional Materials, 22, 2338-2344, 2012.
[5] M. Moniruzzaman, K. I. Winey, “Polymer nanocomposites containing carbon nanotubes”, Macromolecules, 39, 5194-5205, 2006.
[6] G. Barim, M.G. Yayla, M. Degirmenci, “Copolymerization of cyclohexene-3-yl methyl methacrylate with styrene: synthesis, characterization, monomer reactivity ratios and, thermal properties”, Designed Monomers and Polymers, 17, 610-614, 2014.
[7] E. Logakis, C. Pandis, P. Pissis, J. Pionteck, P. Poetschke, “Highly conducting poly(methyl methacrylate)/carbon nanotubes composites: Investigation on their thermal, dynamic-mechanical, electrical and dielectric properties”, Composites Science and Technology, 71, 854-862, 2011.
[8] S. Kumar, T. Rath, B. B. Khatua, A. K. Dihibar, C. K. Das, “Preparation and characterization of poly(methyl

methacrylate)/multi-walled carbon nanotube composites", Journal of Nanoscience and Nanotechnology, 9, 4644-4655, 2009.
[9] R. Haggenmueller, H. H. Gommans, A. G. Rinzler, J. E Fischer, K. I. Winey, "Aligned single-wall carbon nanotubes in composites by melt processing methods", Chemical Physics Letters, 330, 219-225, 2000.

6th International Conference on Materials Science and Nanotechnology For Next Generation (MSNG-2019)
October 16-18, 2019, Niğde, TURKEY (ORAL FULL TEXT)

Synthesis and Characterization of PVA/ZnO Nanocomposite Films Prepared in Different Ratios

E.BARIM[1*], C. AKSU CANBAY[2], G. BARIM[3]

[1]Munzur University Vocational School of Tunceli, 62000, Tunceli, TURKEY, [2]Firat University, Faculty of Science, Department of Physics, Elazig/TURKEY, [3]Adiyaman University, Faculty of Science and Education, Department of Chemistry, Adiyaman/TURKEY

Abstract. Nanoparticles have recently attracted attention in the fields of biology, medicine and electronics due to their biological, chemical and physical properties. In particular, nano-ZnO (Zinc oxide) is very popular in recent years due to its antibacterial properties.In addition to this property of nano-ZnO which is a metal oxide group, it has electrical conductivity, photo oxidizing capacity against chemical and biological species, photocatalyticability and self-sterilization. ZnO is a multifunctional material and has found application areas such as semiconductors, UV-shielding materials, photochemical, polymer coating. PVA (Polyvinyl alcohol) is a non-toxic, water-soluble polymer. Because it is a polymer with many technological, pharmaceutical and biomedical applications, it is widely used in various fields of industry. PVA is also a good host material for metal and semiconductor nanomaterials because of their thermo-stability and good film-forming capabilities.

Keywords: Zinc oxide, Poly (Vinyl Alcohol), Nanocomposite Films

Submission date:12 July 2016
Acceptance Date:20 October 2016

Corresponding authors:esrabarim@gmail.com

1. Introduction

Polymer-based metal oxide nanocomposites have applications in some fields such as medical and engineering technology due to their electrical, mechanical and optical properties [1,2]. Shapememory polymer (SMP) nanocomposites can be obtained by incorporating metal or metal oxide fillers such as ironoxide (III), ferro magnetic particles, NdFeB particles, Ni-Mn-Gasingle crystal and nickelpowder, which exhibit thermomagnetic or electromagnetically induced shapememory effect (SME) [3-8].Among these nanocomposites, having thermally shapememory effect are generally used which are magnetic or electromagnetically induced materials. SMP nanocomposites, by mixing different nanodoles with elastomeric matricesor SMPs, recover their permanent shape when exposed to externalstimuli such as temperature, humidity/water, light (UV, IR andvisible) electric and magnetic field and can memorize their temporary shape. Unique (original) functions have been developed to expand the range of SMP applications such as smart implants, controlled medical devices, adaptive optical devices, dry/wetadhesives, fasteners. However, the performance of the nanocomposites depends on the ratio, dispersion and nano-fill type [9]. Polyvinylalcohol (PVA) is used in many technical applications since it is a polymer with many interesting physical properties. PVA is a semi-crystalline, water soluble material with lowel ectrical conductivity. Furthermore, It is used in many technological, pharmaceutical and biomedical applications due to its excellent film forming and bonding properties [3,4].

Because of their optical and electrical properties, metal oxide semiconductor films have attracted much attention in recent years. Zincoxide exists in nature as a “mineral zinkite and is grouped as a semiconductor of the II-IV group. Due to its boundary ionism, it is located be tween covalent and ionic semiconductors. Zincoxide (ZnO) based polymeric nanocomposite materials are very interesting because of their good transparency, high electron mobility [5, 6], direct wide band gap (3.37 eV at room temperature)

[7]. This enables applications in optoelectronics in the blue / UV region, including light-emitting diodes, laser diodes and photo detectors [8- 10], short-wave length light emitting diodes, transparent conductors, dye-sensitized solar cells, piezo electric materials, gas sensors, photovoltaic cells, varistors (alsocalled as variable resistors), as a high resistance semiconducting device and fully transparent thin film transistors [11].

In this study, a new nanocomposite based on Polyvinylalcohol/Zinc oxide (PVA/ZnO) was synthesized. First, ZnO nanoparticles were synthesized with hydrothermal method. Then, 4 films were prepared by using different rates of acquired ZnO and provided PVA. Prepared PVA-ZnO nanocomposite films were characterized with X-Ray Diffraction (XRD), Scanning Electron Microscope (SEM), FT-IR devices.

2. Experimental details

2.1. Materials

Zinc nitrate hexahydrate $Zn(NO_3)6.H_2O$ (≥ 99 %) and polyvinyl alcohol (PVA, Mw=125000, 88 % hydrolyzed, AR Grade) were provided from Merck company.

2.2. Characterization Techniques and Measurements

All the analyzes were taken in the laboratories of the Munzur University. Prepared PVA-ZnO nanocomposite films were characterized with Rigaku MiniFlex 600 X-Ray Diffraction (XRD) device. The morphological surface structure of Nanocomposite films was viewed with Hitachi SU3500 Scanning Electron Microscope (SEM) device. Their Infrared spectrums were gathered with JASCON FT-IR device.

2.3. Preparation of PVA/ZnO Nanocomposite Films

ZnO nanoparticles were synthesized with hydrothermal method. First, 1.19 g of Zinc nitrate hexahydrate $Zn(NO_3).6H_2O$, was mixed with 40 mL distilled water in ultra-sonication device until completely dissolved. While the mixing was still in process, 5 mL ammonia (NH_3) solution was added to a solution which includes Zinc nitrate hexahydrate drop by drop and the pH value was ensured around 8-9. The prepared basic solution was put in the hydrothermal device that was set to 180 ºC and it was taken out of the device after 12 hours, filtered and dried.4 films were prepared by using different rates of acquired ZnO and provided PVA. In the first sample, 0.05 g PVA was dissolved in 20 mL of water, other three samples were prepared in accordance with (PVA)1-X and (ZnO)X formula. To achieve this; beakers containing 1%, 5%, %10 ZnO and matching PVA in weight were dissolved in distilled water after heating in ultra-sonication device for 3 hours at 80 ºC. Prepared PVA-ZnO mixtures were poured onto 4 different petri plates, and were contained in a dust-free environment at room temperature for 3 days to acquire nanocomposite films. Only the first sample that contained PVA was named as (P) and other 3 samples were named accordingly with their ZnO rates as (PZ1), (PZ5), and (PZ10).

3. Results and discussion

3.1. FT-IR Analysis

FT-IR spectrums of PVA-ZnO nanocomposite films were gathered with JASCON FT-IR device. Their Infrared spectrums were observed between 4000 and 400 cm^{-1} wavelengths (Figure 1). When the spectrums were examined; while large and flat peak at 3252 cm^{-1} of pure PVA belongs to hydroxyl group (OH), peaks of the asymmetric stretching vibrations at 2930 cm^{-1} and 2852 cm^{-1} respectively indicate CH and CH_2. Further, peaks are observed at 1711 cm^{-1} and 1656 cm^{-1} resulting from C=O stretching vibration. When the FT-IR spectrums of PVA-ZnO nanocomposite films were examined; the new peak that belonged to ZnO at 458 cm^{-1} showed us that the synthesis of the nanocomposites were successful.

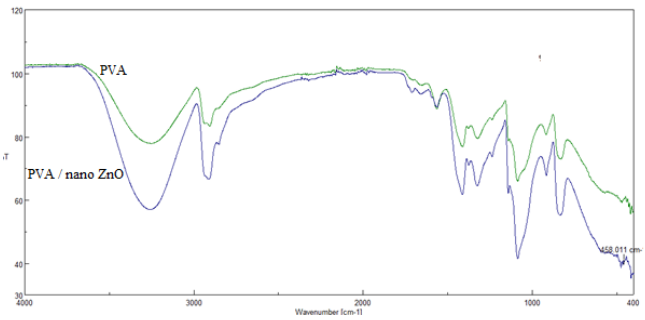
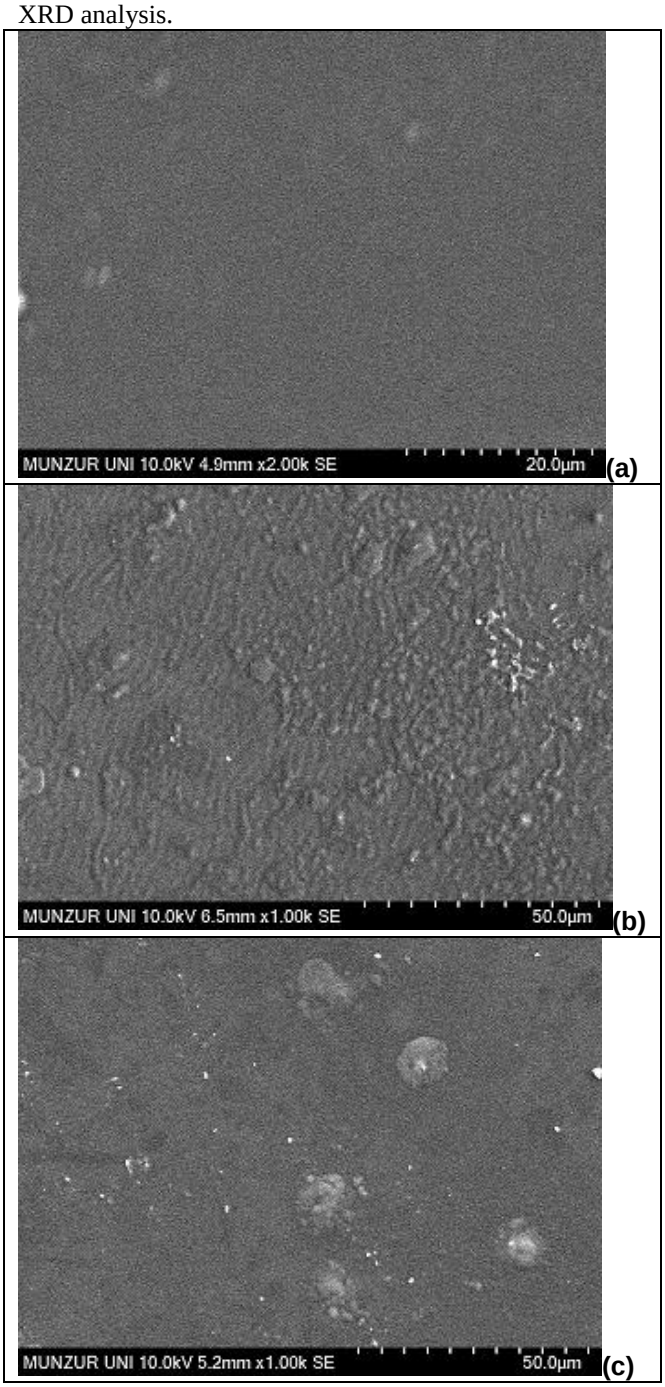


Figure 1. FT-IR spectra ZnO/PVA nanocomposites.

3.2. SEM Observations

Scanning electron microscopy (SEM) imagines taken at different magnification rates for all samples and SEM images taken in these imagines at 1.00k and 2.00k magnification ratios are given in Fig.2. When the SEM image (Fig.2a) of the PVA sample is examined, it is seen that particles and fibers (microtubes) are formed that do not exceed a few micrometers. The images were shown that, uncoated ZnO PVA were aggregated and compressed, while coated PVAs had a better distribution and homogeneity. SEM images were also shown that, sample with medium

concentraction (Fig.2c) had a better distribution. This is due to the less agglomeration of nanocomposites in medium concentraction of samples. This fact confirms the results of XRD analysis.



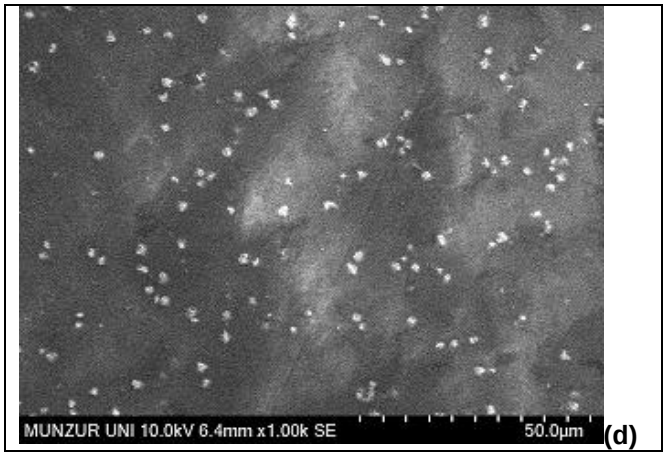


Figure 2. Sem İmages of theSamples; a) PVA, b) PVA/ZnO(%1), c) PVA/ZnO(%5), d) PVA/ZnO(%10).

3.3. X-Ray Analysis

PVA composites with different proportions of ZnO were analyzed by X-ray diffraction to examine the nature of the crystallinity of the samples. X-ray diffraction graphs of ZnO / PVA samples are given in Fig.3. PVA/ZnO nanocomposites at a scatteringangle of 2θ=~19° can be matched to there flection plane of crystalline PVA [101] [12-20]. The crystalline nature of PVA can be attributed to the strong interaction between the PVA chains through intermolecular hydrogen bonding. The X-ray diffraction pattern of the ZnO nanoparticles describes the hexagonal wurtzite structure. As the lower ZnO concentration was used in the PVA matrix, the intensity of peaks in the shapewasal so reduced.

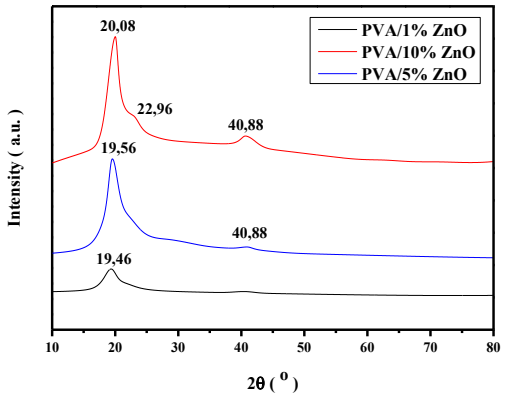


Figure 3. XRD spectraZnO/PVA nanocomposites.

Conclusions

In this study, nano-composite films were produced by adding ZnO produced by hydrothermal method to PVA

polymer in three different ratios (1,5,10%). In order to investigate the structural properties of these materials, FT-IR, X-Ray and SEM analyzes were performed. In FT-IR spectra, the characteristic peak values of the PVA sample are 1000-1300 cm^{-1} and the wide range of 3000-3500 cm^{-1} is characteristic of PVA, and these peak values correspond to the C-O and O-H tensile bands, respectively. When ZnO is added to PVA, these peak values decrease. These results are consistent with the literature. This result suggests that produced nanocomposite films have become more thermally stable. According to SEM images were shown that, sample with medium concentraction had a better distribution. This is due to the less agglomeration of nanocomposites in medium concentraction of samples. In addition the XRD analysis peaks for ZnO/PVA were in good agreement with those of hexagonal wurtzite structure. According to these results, produced ZnO/ PVA nanocomposite films can be used in wide range applications.

References:

[1]. N. Bouropoulos, G.C. Psarras, N. Moustakas, A. Chrissanthopoulos, S. Baskoutas, Phys Status Solidi A 205 (2008) 2033–2037.
[2]. J. Lee, D. Bhattacharyya, A. J. Easteal, J. B. Metson, Curr. Appl. Phys. 8 (2008) 42–47.
[3].Yu X. J., Zhou S. B., Zheng X. T., Guo T., Xiao Y., Song B. T., 2009. A biodegradable shape-memory nanocomposite with excellent magnetism sensitivity, Nanotechnology, 20:235070/1–235070.
[4]. Kumar U. N., Kratz K., Behl M., Lendlein A., 2012. Shape-memoryproperties of magnetically active triple-shape nanocomposites based on a grafted polymer network with two crystallizables witchingsegments, Express PolymerLetters, 6:26–40.
[5].Cuevas J. M., Alonso J., German L., Iturrondobeitia M., Laza J. M., Vilas J. L., Leon L. M., 2009. Magneto-active shapememory composites by incorporating ferro magnetic microparticles in a thermo-responsive polyalkenamer, Smart Materials and Structures, 18:075003/1–75003.
[6].Golbang A., Kokabi M., 2010. Magnetic field actuation of shapememory nanocomposites, Advanced Materials Research, 123–125:999–1002.
[7].Zeng M., Or S. W., Chan H. L. W., 2010. dc- andac-magnetic field-induced strain effects in ferro magnetic shape memory composites of Ni-Mn-Gasingle crystal and polyurethane polymer, Journal of AppliedPhysics, 107:09A942/1–3.
[8].Zhang D. W., Liu Y. J., Leng J. S., 2010. Magnetic field activation of thermo responsive shape-memory polymer with embedded micronsized Ni powder, Advanced Materials Research, 123–125:995–8.
[9].Jinlian Hu., Yong Zhu., 2012. HuahuaHuang., Jing Lu., Recentadvances in shape–memorypolymers: Structure, mechanism, functionality, modelingandapplications, The Hong Kong PolytechnicUniversity, 37 (2012) 1720– 1763.
[10]. C. M. Hassan, N.A. Peppas, Adv. Polym. Sci. 153 (2000) 37- 65.
[11]. M. Kokabi, M. Sirousazar, Z. Hassan, Eur. Polym. J. 43 (2007) 773- 781.
[12]. Y.W. Heo, D.P. Norton, L.C. Tien, Y. Kwon, B.S. Kang, F. Ren, Mater SciEng R 47 (2004)1–2.
[13]. E.M.C. Fortunato, P.M.C. Barquinha, A.C.M.B.G. Pimentel, A.M.F. Goncalves, A.J.S. Marques, L.M.N. Pereira. Adv Mater 17(2005) 590–4.
[14]. A. Mang, K. ReimannandRubenackeSt, Solid StateCommun, 94(1995) 251- 254.
[15]. Ü. Özgür, Ya. I. Alivov, C. Liu, A. Teke, M. A. Reshchikov, S. Dogan, V. Avrutin, S-J. Choand H. Morkoç, J. Appl. Phys., 98 (2005) 041301.
[16]. N. H. Nickeland E. Terukov, ZincOxide - A Materialfor Micro- andOptoelectronic Applications, (ed) 2005, (Netherlands:Springer).
[17]. C. Jagadishand S. J. Pearton, ZincOxideBulk, ThinFilms, andNanostructures, (ed) 2006, (New York: Elsevier).
[18].Husam S. Al-Salman, M.J. Abdullah, SuperlatticesandMicrostructures 60 (2013) 349–357.
[19].Gupta, S.;Webster, T.J.; Sinha, A.; J. Mater. Sci. Mater. Med., 2011, 22, 1763. DOI: 10.1007/s10856-011-4343-2
[20]. Kumar, A; Negi, Y.S.;Bhardwaj, N.K.; Choudhary, V.; Adv. Mater. Lett., 2013, 4, 626.
DOI: 10.5185/amlett.2012.12482

6th International Conference on Materials Science and Nanotechnology For Next Generation (MSNG2019)
October 16-18, 2019, Niğde, TURKEY (ORAL FULL TEXT)

Improvement of Growth Time in Graphene Synthesis on Nickel Substrate

Meryem BOZKAYA[1], Ali ALTUNTEPE[2], Hakan ATEŞ[3], Recep ZAN[2*]

1 Gazi University, Graduation of Nature and Applied Sciences, Department of Advanced Technologies, Ankara TURKEY
2 Niğde Ömer Halisdemir University, Nanotechnology Applied and Research Center, Niğde,
3 Gazi University, Faculty of Technology, Department of Metallurgy and Materials Engineering, Ankara, TURKEY

Graphene is the two-dimensional materials which formed the sp^2-hybritization of carbon atoms arranged like honeycomb structure. It has been good candidate optoelectronic technologies especially as transparent conductive electrodes due to excellent electrical and optical properties. Currently, Chemical vapor deposition is considered rising methode for graphene synthesis on transition metal oxide substrate but, Nickel and cooper substrate is mostly used to grow large scale and high-quality graphene. Graphene synthesis on nickel substrate has a lot of challenged such as controlled number of layer graphene because of high solution carbon atoms. However, Graphene synthesis can be controlled by optimizing parameters of CVD methode like growth time, cooling process, flow rate of carbon source. In this study, growth time was improving to synthesize quality graphene by using methane gas on nickel surface via CVD methode. Bilayer graphene was obtained for 10 min. growth time.

Keywords: Graphene, Nickel substrate, Chemical vapor deposition (CVD)

Corresponding author: recepzan@gmail.com

1. Introduction

Graphene is an one atom thick nano materials and it has sp^2 hybritization [1]. Graphene is one of the attractive materials for both researcher and industrial company due to exciting optical, mechanical and electrical properties [2]. Specially, it has been gleaming of hope for optoelectronic devices such as solar cells, liquid crystal display, super capacitors and transistors, bendable and wearable technology [3]. Several chemical and mechanical methodes can be used for graphene synthesis such as mechanical exfoliation, epitaxial growth. However, chemical vapor deposition is an ideal methode to synthesize homogenous and large-scale graphene by using various carbon source and carrier gas on the transition metal oxide substrate [4,5].
Firstly, carbon atoms are exposed to segregation because of high temperature in substrate at mechanism of carbon segregation especially nickel substrate then, segregated carbon on to substrate is deposited with the aid cooling process [6]. On the other hand, graphene synthesis in copper substrate is directly occurred by depositing carbon atoms at surface without carbon segregation [7]. Nickel substrate can be used to as catalyst for graphene synthesis large scale and homogenously due to that has high carbon solubility [8]. But Nickel has some drawbacks because of both carbon segregation and carbon decomposition, thus, it has been caused precipitation of extra carbon occurs at the nickel surfaces substrate [9]. So, control of graphene layer is can be difficult. Different methods are used overcome these drawbacks most of parameters can be optimized to control number of layer graphene by CVD such as flow rate of gas, growth time, temperature, cooling process etc. [10]. Aim of this study, improvement of growth time has been purposed to synthesize homogeneous graphene on to nickel substrate.

2. Experimental details

Firstly, 20 µm Nickel foil was pre-cleaned for high-quality graphene synthesis with acetone (5 min.), deionized water (5min.) and isopropyl alcohol (5 min.),

respectively. After cleaning, nickel substrate was treated with plasma cleaner for 5 min. Plasma cleaner eliminates organic contaminants from the surface of nickel which is important to synthesized graphene. Then, the substrate was loaded into the CVD furnace shown fig.1.



Figure 1.*CVD system*

Firstly, CVD system was heated to 1000 °C in 20 sccm Ar and 80 sccm H_2 ambient for 60 min., the substrate was annealing during 30 min. with the same gases. The substrate was annealing during 30 min. with the same gases to occur grain boundaires and to make sure eliminated contamination. After the annealing process was started growth time with 20 sccm methane (CH_4) gase during 40 min. All the process was repeated in order to investigate affecting of growth time for graphene synthesis on nickel substrate by reducing from 40 min. to 10 min.
Graphene was characterizated by Raman spectroscopy with 633 nm. wavelength laser to determine structure and of film layer of graphene.

3. Results and discussion

Analysis of graphene synthesis on nickel substrate was characterizated by using Raman spectroscopy and results are shown Fig.2 in which is four different samples for different growth time. Graphene has some peak positions in Raman spectra in which is called D, G and 2D peaks. While G peak is showing to exist carbon structure especially graphite, D peak shows contamination such that the sp^2 hybritization carbon structure as called graphite and 2D peak is indicator for the thickness of the graphene layer. The reason for the appearance of the D peak could be associated with surface contamination, defect or insufficient annealing process.

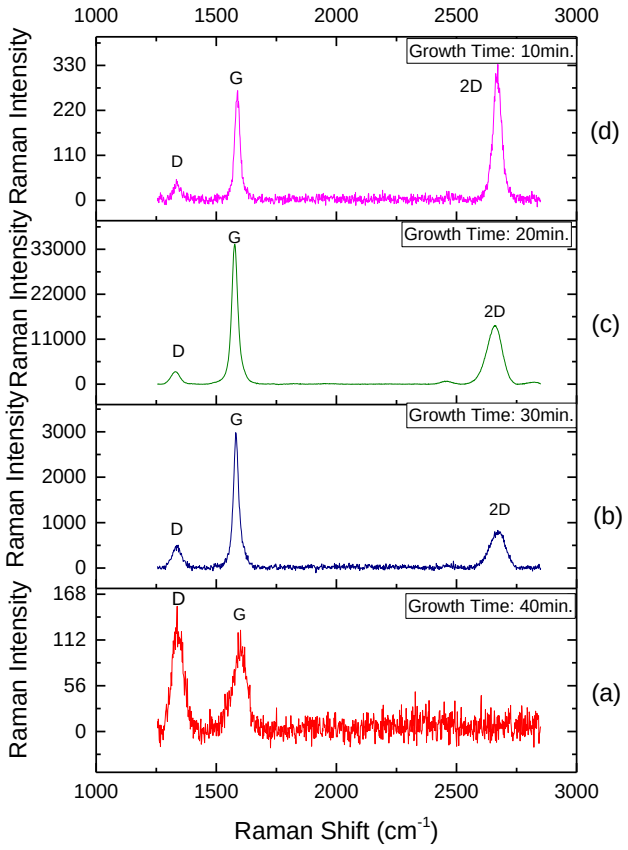


Figure 2. *Raman Spectra of Graphene Synthesis*
- *(a) Raman spectroscopy of 40min. growth time of graphene synthesis*
- *(b) Raman spectroscopy of 30min. growth time of graphene synthesis*
- *(c) Raman spectroscopy of 20 min. growth time of graphene synthesis*
- *(d) Raman spectroscopy of 10min. growth time of graphene synthesis*

Fig.2(a) is shown that the Raman spectra of obtained sample with the 40 min. growth time, in which shows D and G peaks and it is not observed 2D peaks. This ob Fig.2(b) is shown raman peak positions of the obtained sample with the 30 min. growth time. These peak positions represent D, G and 2D peaks. Ratio of $I_{2D}/_G$ which is determined plenty of graphene structure layer was calculated 0,27 and value of full width half maximum (FWHM) of the 2D peak was measured as 76.60. FWHM was also used to control graphene quality along with peak positions. Based on this result multi-layer graphene was

obtained with 30 min. growth time during flowed methane gase. Moreover, When the growth time was more reduced than previous step, both number of graphene layer and D peak was reduced, in which is shown Fig.2. (c) of synthesized graphene sample with 20 min. growth time. Also, ratio of $I_{2D}/_G$ was measured as 0.41 and value of FWHM was calculated as 73,85. Growth time was reduced as 10 min. shown fig. 2 (d), it was observed that sharp of 2D peak was increased. Besides, Ratio of $I_{2D}/_G$ was measured 1,16 and value of FWHM was calculated as 29.67. Meaning of the results is shown that obtained sample is bilayer graphene and when the growth time is reduced, it was observed that D peak is reduced. As a result, it is said that growth time is affected removing the defect or surface contamination of graphene synthesis on nickel substrate. In addition, growth time is getting reduced, it was observed that number of graphene layer is reduced. However, graphene was synthesized under 20 sccm methane gase with 5 min. growth time, it was not obtained any sp^2 hybridization of carbon structure. Flow rate of methane gas can be reduced, or cooling rate can be optimized to grow mono layer graphene. Also, thickness of nickel substrate can be reduced for high-quality monolayer graphene.

4. Conclusion

It was demonstrated that control of number of graphene layer by optimizing growth time on nickel substrate. The obtained samples were characterizated by using Raman spectroscopy. Plenty of graphene layer were determined with 2D and G peaks.

5. Acknowledgement

The authors greatfully acknowledge the funding from The Scientific and Technological Research Council of Turkey (TÜBİTAK-117M401).

References:

[1] GEIM, A. K., NOVOSELOV, K. S., “The rise of graphene.”, Nature Publising Group. Vol. 6, pp. 183-191 2007.
[2] JO, W. J., LEE, J. U., JO, W. H., “Graphene-based electrodes for flexible electronics.”, Society of Chemistry Industry. Vol. 64 pp. 1676-1684 2015.
[3] CHOI, W., LAHIRI, I., SEELABOYINA, R., KANG, Y. S., “Synthesis of graphene and its applications: A Review.” Critical Reviews in Solid State and Materials Sciences, 35:52-71, Pp. 52-71. 2010.
[4] ZHANG, Y., ZHANG, L., ZHOU, C., “Review of chemical vapor deposition of graphene and related applications.”, Accounts of Chemical Research, Vol.46 No. 10, pp.2329-2339, 2010.
[5] SEE, J., LEE, J., JANG, A., R., CHOI, Y., KIM, U., SHIN, H., S., “Study of cooling rate on the growth of graphene via chemical vapor deposition.”, Chemistry of Materials, Vol.29 pp.4202-4208, 2017.
[6] CHEN, X., ZHANG, L., CHEN, S., “Large area CVD growth of graphene.”, Synthetic Materials, Vol.210 pp. 95-108, 2010.
[7] UMAIR, A., RAZA, A., “Controlled synthesis of bilayer graphene.”, Nano Express, 7:437, pp.1-5, 2012.
[8] AL-SHURMAN, K., M., NASEEM, H., “CVD graphene growth mechanism on nickel thin films.”, Excerpt from the Proceedings of the 2014 COMSOL Conference in Boston.
[9] BARATON, L., HE, Z., B., LEE, C., S., COJOCARU, C., S., LEE, Y., H., PRIBAT, D., “On the mechanisms of precipitation of graphene on nickel thin films.” A Letters Journal of Exploring, 96 (2011) 46003.
[10] YU, Q., LIAN, J., SIRIPONGLERT, S., LI, H., CHEN, Y., P., PEI, S., S., “Graphene segregated on Ni surface and transferred to insulators.” Applied Physics Letters. 93, 113103, 2008.

6th International Conference on Materials Science and Nanotechnology For Next Generation (MSNG2019)
October 16-18, 2019, Niğde, TURKEY (ORAL FULL TEXT)

Study on The Doping Effect of Spin Coated ZnO:N

S. GÜLLÜLÜ CATAKCI[1*] and M. CAGLAR[2]

[1] Graduate School of Sciences, Eskişehir Technical University, Eskisehir, Turkey
[2] Department of Physics, Eskişehir Technical University, Eskişehir, Turkey

In this study, we have produced nitrogen (N) (0; 0,4; 0,8; 1.2; 1.6 and 2 at.%) doped ZnO films on n-Si and glass substrates by sol gel spin coating method. The effect of nitrogen concentration on the structural, morphological, optical and electrical properties of the films was investigated. X-ray diffraction (XRD) measurements of the films revealed the formation of the hexagonal ZnO wurtzite structure. Atomic force microscopy (AFM) and scanning electron microscopy (SEM) analyses have been performed to make the general morphological characterizations. The optical properties have been investigated with UV_VIS spectrometry. The conductivity type, resistivity and carrier concentration were determined from Hall Effect measurements.

Keywords: N doped zinc oxide, Sol gel spin coating, p-type ZnO.

Corresponding author: suheyla_gullulu@eskisehir.edu.tr

1. Introduction

Nowadays, Zinc oxide (ZnO), which is of great importance for device technology, attracts attention with its excellent properties. ZnO has great properties such as wide band gap (3.37 eV), large exciton binding energy (60 meV), ease in doping, non-toxicity, easy to find in nature, electrochemical stability and good optical transparency in the visible region and so it has been used in many studies because of having these advantages [1]. ZnO has been used in many devices, which are the basis of today's technology, such as solar cell, transistor, field effect transistors, sensors and diodes etc. [2]. There are many methods like pulsed laser deposition [3], molecular beam epitaxy [4], magnetron sputtering [5], atomic layer deposition [6], microwave plasma-assisted chemical vapor deposition [7] for producing ZnO-based devices. Among these methods, the sol-gel method (simplicity, safety, vacuum-free deposition system) has many advantages [8].
Recently; in order to obtain better optical and electrical properties, p-type ZnO is tried to be made by adding V-group elements (such as N, P, As, Sb and Bi) of metal oxide material whose natural state is n type ZnO. And among these elements, N is preferred because of its low toxicity, easy addition and abundance in nature [9-13].

2. Experimental details

In this study, we produced undoped and N doped ZnO films were prepared using sol gel spin coating technique on n-Si and glass. To obtain a p-type ZnO solution, a 0.4 M sol of zinc acetate dihydrate $Zn(CH_3COO)_2$, in isopropyl alcohol (C_3H_8O) was solved and diethanolamine ($C_4H_{11}NO_2$) was used as a stabilizer. And then Ammonium acetate ($C_2H_3O_2NH_4$) as nitrogen source was added to the sol in the volumetric ratio of Zn/N of 1:1. The prepared solutions were stirred at room temperature and then n-Si and glass surfaces were rotated at 3000 rpm for 30 s and coated using a Laurell WS-400B-6NPP/Lite spin coater. Samples were named as Z0, ZN0.4, ZN0.8, ZN1.2, ZN1.6 and ZN2 depending on N doping ratio. After the first coating process, the substrates were dried at 300 °C for 10 min in air by using a Protherm PTF 12/38/150 tube furnace. This process was repeated ten times and then finally for crystallization and phase formation all films were annealed at 500 °C for 1 hr in air using the furnace.
The surface morphology of the films was investigated by atomic force microscope (NT-MDT; AFM) and scanning electron microscope (ZEISS ULTRA PLUSS, SEM). The structural analysis has been carried out x-ray diffraction spectroscopy (BRUKER D2 PHASER). A sealed x-ray tube was used at 30 kV and 30 mA with CuK_α (λ=1.5406

Å) radiation and the measurements were carried out in the reflection geometry (30° ≤2θ ≤60°).

For optical transmittance measurements, a double beam Shimadzu UV 2450 spectrophotometer with an integrated sphere in the wavelength range of 200-900 nm was used. The thickness of the films was calculated using Envelope Method**.** And finally to investigate electrical properties, we used Hall effect measurement system (ECOPIA HMS-5000).

3. Results and discussion

Atomic force microscope was used to obtain information about surface morphology from 3D images of undoped and N doped ZnO films. Figure 1 shows the AFM images of all films. The root-mean-square (RMS) roughness values of active layers for Z0, ZN0.4, ZN0.8, ZN1.2, ZN1.6 and ZN2 are 6.54 nm, 9.76 nm, 8.44 nm, 12.70 nm, 11,96 nm and 14.46 nm, respectively. It was seen from AFM images that the lowest RMS value is Z0 film with the 6.54nm.

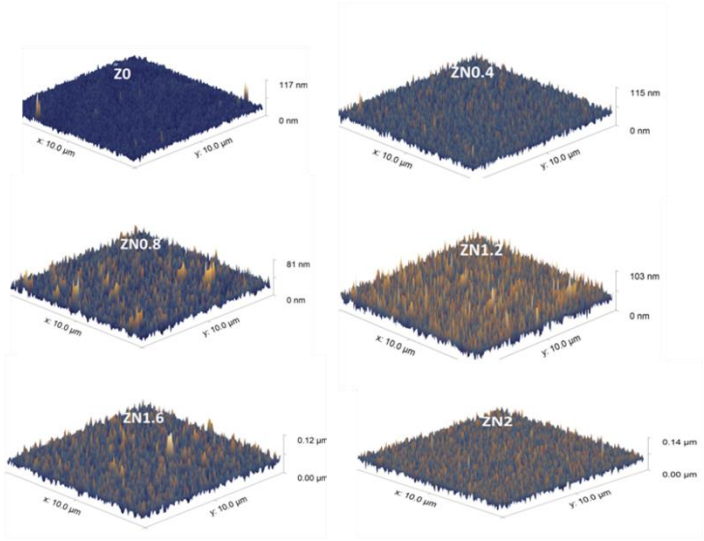


Figure 1. *AFM images of the different N concentrations ZnO films.*

Undoped and N doped ZnO films surface morphologies were investigated by SEM. Figure 2 shows the view of FESEM images the films.
In these SEM images, a smooth, uniform microstructures are clearly seen. It can be seen from Fig. 2 that they consist of densely packed particles in the order of nm. Also, it is shown that the voids between grains (particles) slightly decrease with increase in N ratio.
X-ray diffraction (XRD) analysis of the films was carried out with an X-ray powder diffractometer (BRUKER D2 PHASER) in air. The XRD spectrum of the films is shown in the Fig. 3. These spectra indicate that the films have polycrystalline nature. Grain size values were calculated by using Scherrer equation (Eq.1) [15] according to the peak having high intensity.

$$D = \frac{k\lambda}{\beta cos\theta} \qquad (1)$$

Where D is crystallite size, λ is the X-ray wavelength used, β is the angular line width of half maximum intensity and θ is Bragg's diffraction angle. As seen from Fig. 3, grain size slightly increases with N doping concentration.

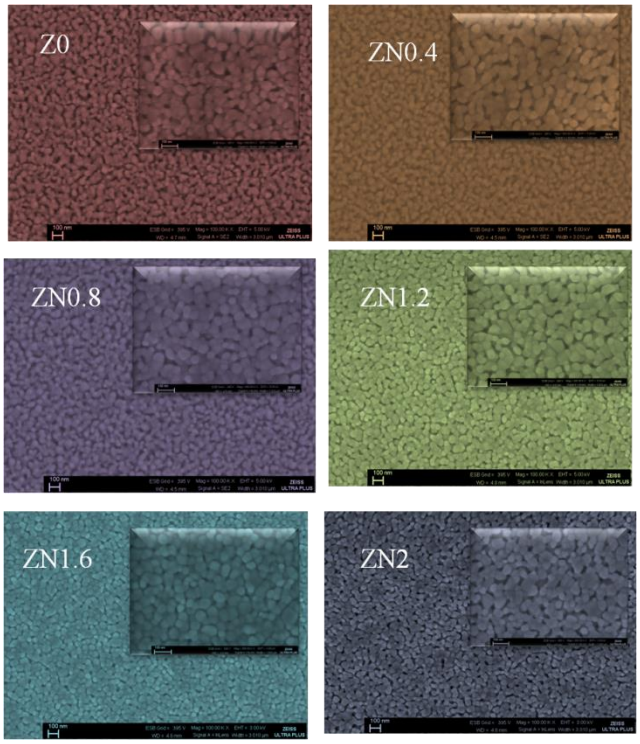


Figure 2. *SEM images of the films for different N doping concentrations.*

To investigate the optical properties of the obtained films, transmittance and absorption spectra were taken and these data were used in the analyses.
By using absorption data of the films optical band gaps were calculated from $(\alpha h\upsilon)^2$ versus energy graphs. The

optical band gap value are about between 3.23 eV and 3.25 eV. A decrease is shown on the band gap values with increasing N content. Minimum band gap value belongs to 1.2%N.

All the films are transparent with average transmission (>80%) in the visible range.

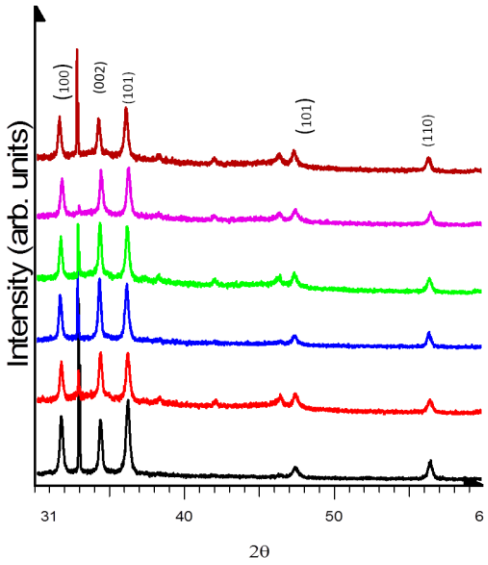


Figure 3. *XRD spectra of the undoped and N doped ZnO films.*

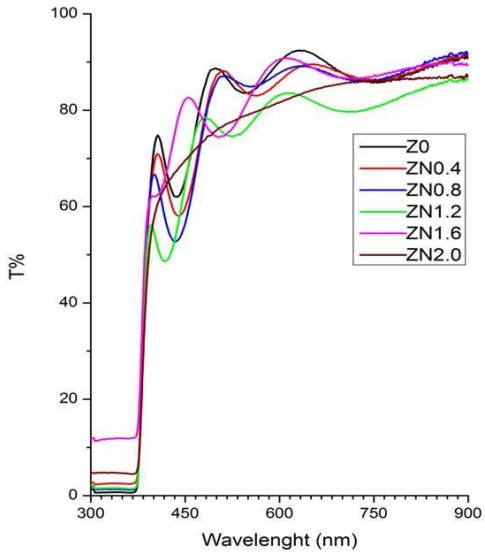


Figure 4. *Optical transmittance spectra of the ZnO films.*

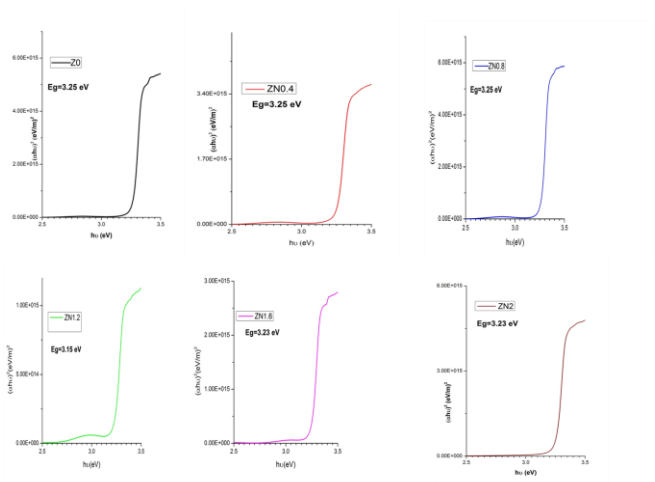


Figure 5. $(\alpha h\nu)^2$ *-h*ν *graphs and band gaps of thin films*

Table 1. About structural and optical properties

Doping concentration	Grain size (nm)	Band gap (eV)	Transmission (%)
0	30.21	3.25	84
0.4	29.59	3.25	82
0.8	29.99	3.25	81
1.2	33.83	3.15	82
1.6	33.45	3.23	82
2	29.99	3.23	81

The thickness of the films was determined using Swanepoel's Envelope Method [16]. The ZnO thin films' thicknesses were calculated from interference fringes of transmission data. For the calculation the index of refraction n at different wavelengths, we used the envelope curve. T_{max} and T_{min} show the max. and min. values in the transmission spectrum, respectively. The expression for refractive index is given by equation (2).

$$n = [N + (N^2 - {n_s}^2)^{1/2}]^{1/2} \quad (2)$$

Where

$$N = 2n_s \frac{T_M - T_m}{T_M T_m} + \frac{{n_s}^2 + 1}{2} \quad (3)$$

n_s is the refractive index of the substrate (in our case n_s =1.52 (glass)).

$$t = \frac{\lambda_1 \lambda_2}{(\lambda_1 n_2 - \lambda_2 n_1)} \quad (4)$$

The thickness of the films was calculated using equation (4).

Where n_1 and n_2 are the refractive indices corresponding to wavelengths $\lambda_1$and λ_2 respectively. And the calculated film thickness value is about 200 nm.

Finally, to determine the some electrical properties of deposited N doped ZNO films at room temperature, Hall effect measurement system was used. In Table 2, carrier concentration, resistivity and mobility values of the films depending on the N doping are tabulated. Undoped and 0.4 % N doped ZnO films illustrate n-type property. But an increase in N amount converts the conductivity type from n to p and the highest hole concentration, minimum resistivity and high mobility values belong to 1.2% N doped ZnO film. Finally N incorporation causes to have p-type property of ZnO.

Table 2. Hall effect measurements results

DOPANT CONCENTRATİON(%)	BULK CONCENTRATION (cm^{-3})	RESISTIVITY($ohmcm$)	MOBILITY (cm^2/Vs)
0	-1.45×10^{21}	1.07×10^{-1}	1.96×10^{-1}
0.4	-6.83×10^{20}	2.27×10^{-1}	7.24×10^{-2}
0.8	9.25×10^{18}	7.5	9.17×10^{-2}
1.2	2.34×10^{19}	1×10^{-2}	4.41
1.6	-1.87×10^{17}	5.89	2.22
2	-3.93×10^{19}	7.96	1.27×10^{-1}

4. Conclusion

We deposited undoped and N doped ZnO thin films with using a sol gel spin coating technique. SEM images of films illustrated smooth and uniform surface. And also, voids between grains (particles) slightly decrease with increase in N ratio. XRD results showed that the films have polycrystalline nature and grain size values calculated by Scherrer formula slightly increased with N doped. As a result of optical measurements, the band gap tended to decrease and minimum band gap value showed 1.2 %N ZnO film. To calculate film thickness value, Envelope Method, was used and it was found as about 200 nm. Hall effect measurement carried out at room temperature in the scope of electrical characterization showed that an increase in N amount converted the conductivity type from n to p and the highest hole concentration, minimum resistivity and high mobility values belong to 1.2% N doped ZnO film. Finally N incorporation was successfully performed to acquire p-type property to n-type ZnO.

5. Acknowledgement

The authors would like to thank Seda AKTAŞ, Fatma ÜNÜGÜR, Kıvanç SEVER, Ebru ÇELİK and Utku ERGÜL for their assistance in all measurements.

References:

[1] AKSOY, S., CAGLAR, Y., "Synthesis of Mn doped ZnO nanopowders by MW-HTS and its structural, morphological and optical characteristics", Journal of Alloys and Compounds, 2019

[2] CAGLAR, Y., CAGLAR, M., ILICAN, S., "XRD, SEM, XPS studies of Sb doped ZnO films and electrical properties of its based Schottky diodes", Optik, 2018

[3] MAJUMDAR, S., BANERJI, P., "Temperature dependent electrical transport in p-ZnO/n-Si heterojunction formed by pulsed laser deposition", Journal of Applied Physics 105, 2009

[4] OPEL, M., GEBRAGS, S., ALTHAMMER, T. B., GROSS, R., "Laser molecular beam epitaxy of ZnO thin films and heterostructures", Journal of Physics D: applied Physics 47 034002, 2014

[5] GAO, W., LI, Z., "ZnO thin films produced by magnetron sputtering", Ceramics International 30 (1155-1159), 2004

[6] LIN Y.Y., HSU, C. C., TSENG, M. H., SHYUE J. J., TSAI F. Y., "Stable and high-performance flexible ZnO thin-film transistors by atomic layer deposition" ACS Appl. Mater. Interfaces, 7, 40, 22610–22617, 2015

[7] MELENDREZA M.F., SOLIS-POMAR F., GUTIERREZ-LAZOS C.D., FLORES P., JARAMILLO A.F., FUNDORA A., PEREZ-TIJERINA E., "A new synthesis route of ZnO nanonails via microwave plasma-assisted chemical vapor deposition", Ceramics International, 42, 1160–1168, 2016.

[8] CAGLAR, Y., ILICAN, S., CAGLAR, M., "FESEM, XRD and DRS studies of electrochemically deposited boron doped ZnO films", Materials Science-Poland, 35(4), 2017, pp. 824-829

[9] HON GEN, N., SUNG H., H., KEE-KAHB, K., EUN, W., S., EUI, J., K., "Sol-gel derived N-doped ZnO thin films", Material Letters 63 (2246-2248), 2009

[10] SONMEZOGLU, S., "Current Transport Mechanism of n-TiO2/p-ZnO Heterojunction Diode", Applied Physics Express, October 2011

[11] GUAN-RU, H., YOW-JON, L., "Current transport mechanism of heterojunction diodes based on the sol-gel p-type ZnO and n-type Si with H_2O_2 treatment", Materials Chemistry and Physics, 136 (179-183), 2012

[12] YONGGE, C., LEI, M., SAKAE, T., MASAKI, T., YOHEI, K., YASUHIKO, H., "Low resistivity p-ZnO films fabricated by sol-gel spin coating", Applied Physiscs Letters, 88, 251116, 2006

[13] DUTTA, M., BASAK, D., "p-ZnO/n-Si heterojunction: Sol-gel fabrication, photoresponse properties, and transport mechanism", Applied Physics Letters 92, 2008

[15] CAGLAR, M., ILICAN, S., CAGLAR, Y., "Influence of substrate tempererature on structural and electrical properties of ZnO films" Trakya Univ J Sci, 7(2): 153-159, 2006

[16] CAGLAR, M., YAZICI CAGLAR, Y., ILICAN, S., "The determination of the thickness and optical constants of the ZnO crystalline thin film by using envelope method", Journal of Optoelectronics and Advanced Materials, 8(4):1410-1413 · September 2006

6th International Conference on Materials Science and Nanotechnology For Next Generation (MSNG2019)
October 16-18, 2019, Niğde, TURKEY (ORAL FULL TEXT)

The Yb Doping Effects on Levitation Force in Sm123 Superconductors.

İ. Karaca
Department of Physics, Faculty of Science, Niğde Ömer Halisdemir University, Niğde, 51240, Turkey

S. Özen, and M.T. Güler
Graduate School of Sciences, Niğde Ömer Halisdemir University, Niğde, 51240 Turkey

We produced Yb doped Sm123 superconductors by the melt growth method. The samples have investigated in terms of levitation force. The magnetic levitation calculated by using our newly designed vertical magnetic levitation force measurement system. It has the Nb-Fe-B permanent magnet (~0.5T) at 77 K with Zero Field Cooled process. The levitation force results analyzed by dynamic curve fit method. The best fit curve and their equation were determined as $F=F_0+ae^{(-bz)}$. The higher hysteresis was determined on the sample SmYb6 during the ascending process. All sample regression nearly equals to 1. On the other hand, the curve fittings are suitable and correct. These results showed that the produced samples can be applied to bearing systems, magnetic sensors and others in technological respect.

Keywords: Yb dopant, Sm123 superconductor, Levitation Force

Corresponding authors: i.karaca@ohu.edu.tr

1. Introduction

Since the discovery of the high-temperature superconductor ceramic materials, which has a critical temperature above 90 K (−183 °C) in 1986 [1], many researchers have focused various production methods and different additives investigation to improve materials superconducting properties. Recently, the most widely studied production methods are the solid-state reaction method [2] and melt-growth method (MGM) [3, 4]. There are several reports on the additive material, gold (Au), silver (Ag) [5-6], zinc (Zn) [7], etc. elements. It was investigated by Yan, et al. [8] with 17 different oxide dopants on the YBa2Cu3O7 and by Kanai, et al. [9] with 34 different dopants on the BiSrCaCu2Oy.

In the 21st century, the magnetic levitation technology based on the superconductivity is favorable to attractive in the forthcoming transportation systems with its high-velocity operation, better riding comfort, friendliness to environment, and saving of maintenance labor [10]. The magnetic levitation force (MLF) change were relevant to distance becomes different from increasing or decreasing, indicates that the steady levitation with using the permanent magnet (PM) [11]. Also, the results of MLF showed that its data used to identify experimentally further about levitation systems and as the fast procedure to test superconductor samples nature, led to further development of this measuring technique.

The high levitation force and field trapping ability of melt–textured (RE) BCO (RE is a light rare earth element or yttrium) is associated with function of the size of the shielding current loop (grain size) and the Jc [12, 13]. During peritectic reaction of (RE)-BaCuO, RE-211 particles form in the Ba-Cu-O molten liquid. As a result, for coarsening of RE-211 particles numerous attempts have been made which yields more effective flux pinning centers and hence increased Jc

In this work, the superconductor samples were produced by the melt-growth method (MGM). Also, Yb make assistance on the purification [12] and in grain growth [9]. Because of this it was doped to the Sm123 superconductor and its effects were investigated on the levitation force by experimentally and theoretically.

Basics of Magnetic Levitation

The force between high temperatures superconductors (HTS) originated from the permanent magnet (PM) system can be written as

$$F = \mu \frac{dH}{dx} \quad (1)$$

Where dH/dx is the field gradient produced by the magnet, μ is the magnetic moment related with the bulk magnetization M which is defined as

$$M = \sum_{i=1}^{n} (\mu_i) \quad (2)$$

The trapped field in HTS originated from the PM, an attractive force occurs when the sample is moved away from the PM. This result can be attributed to the number of pinning centers in the HTS sample, which results in an increase of trapped magnetic field inside the samples. In addition, the levitation force is related to the grain size and crystallographic orientation [14]. This is also seen in Fig.2 and Fig.8 from the exponentially decline in the vicinity of about 30 mm, the transition is clearly verified. This transition point in the decay is well-known in the literature depending on the critical current. It can be seen from the Table 1 and 2, regression parameters of the curve are very high.

Chang et al. [15] reported that the relationship between levitation force and distance for a magnet levitated over a flat ceramic superconductor has an apparent paradox. If the force were modeled as an interaction between two dipole magnets, then one should expect an inverse power law relation. However, experiments with small test magnets levitated over large ceramic superconducting show an exponential decay relation:

$$F = F_0 e^{(-bz)} \quad (3)$$

where z is the distance from the center of the test magnet to the superconductor surface. It was used, in this study, that small ceramic superconducting levitated over large test magnets, this is the same as their assumption.

2. Experimental details

2.1 Sample Prepare

Sm1.46Ba1.54Cu3.20Oy (Sm123) precursor powders were prepared by melt growth method (MGM) with starting materials Sm2O3, Yb2O3, BaCO3, and CuO (>99.99%) powders. Yb2O3 powders which are 0.3, 0.4, 0.5 and 0.6 g were added before the calcination process as the dopant. The precursor powders were manually grounded twice for 5 h and calcined at 900°C for 10 h in presence of air atmosphere. Then, selected four different amounts of powders were pressed into pellets under the 300 MPa pressure. The pressed MgO were calcined 600°C for 5 h and into a pellet under the 250 MPa pressure, which was used to a substrate bottom of the samples. All cylindrically shaped pellets, which has a 4-6 mm high and 8 mm radius, were sintered at 1050°C for 12 h. The annealing procedure was applied within the oxygen atmosphere at 650 °C for 5 h. The five samples which are 0.0, 0.3, 0.4, 0.5 and 0.6 g doped Yb2O3 are named brevity of the whole manuscript as SmYbP, SmYb3, SmYb4, SmYb5, SmYb6, respectively.

2.2 Levitation Experimental System

The stable levitation of a magnet over a flat superconducting disk was offered, a model which flux penetration makes possible based on the energy cost of vortices, by Hellman [16]. Moon et al. [17] have suggested a useful experimental setup which the measurement of the forces on a permanent magnet levitated above bulk superconductors properties. Maglev systems have become very important in the future life is generally based on the superconductor technology ranging from in a superconducting wind turbine generator [18], [19] and a superconducting magnetic energy storage (SMES) [20] to an Infra-Red (IR) sensor leads to Earth Orbit Systems (EOS) [21]. The magnetic field associated with each normal core is spread over a region and each normal core is surrounded by a vortex of circulating supercurrents. A considerable magnetic field can be trapped by a superconductor when it exhibits large flux pinning forces [22]. The force-distance (permanent magnets and superconductor) hysteresis loops during the descending and ascending process expanded with critical current density increases. The hysteresis curves strongly depend on the size of grains and their connectivity in these materials.

Magnetic properties were measured at 77 K with liquid nitrogen. Measurements were performed in the ZFC regimes by the Nb-Fb-B magnet (PM~0.5T). The analysis data were taken during the descending and ascending procedure. The distance was changed with a velocity of about 0.2 mm/s. Magnetic repulsive and attractive forces between the superconductor and a PM were measured using a handmade levitation measurement experimental system, as figure out in Fig 1.

The samples (in 14 mm diameter) was were immobilized at the bottom of a liquid nitrogen-filled receptacle container which is movable free to move in the vertical direction. This receptacle container was then placed just above the plate of the balance without touching it. Thus, the observed weight change of the magnet directly reflected the magnetic force induced in the system [23].

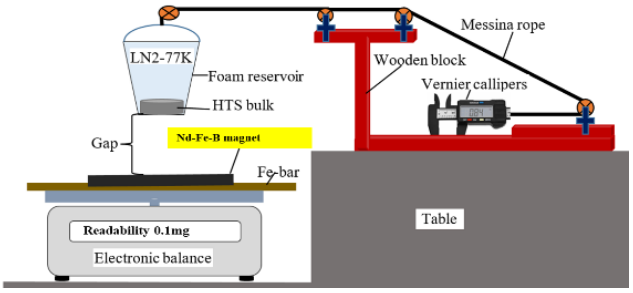


Fig.1: Levitation force determination experimental setup.

3. Results and discussion

The solidification of the materials leads to the growth of superconducting grains [24]. This grain yields to improve the physical properties as the critical current (***J***c) and the magnetic levitation force. The levitation occurs with a magnet levitated over a flat ceramic superconductor, reported by several researchers, it has a mysterious nature [25-29]. This property has been investigated since it was applied to Maglev and other industrial applications. If the force modeled as a relation between two dipole magnets, then one should expect an inverse power law relation. But the levitation test results of a small permanent magnet with a ceramic superconductor which shows an exponential decay relation as given in Eq. 3.

In this work, a small superconducting ceramic was used to levitate overlarge test magnets as given in Figure 1 and suitable for Eq. 3. The experimental results of all samples were analyzed according to the Eq. 3.

From regression analysis, during the descending and ascending process with a velocity of about equal to 0.2 mm / s, the F0 and the best fit values were obtained and the results were given in Table 1-2.

The magnetic levitation force occurs while the pinning of flux happens, i.e., by their interaction with imperfections. The increases of the pinning centers within the superconductor has become the greater levitation force. The measured and calculated results are consistent with each other.

The trapped field in superconductors is originated from the permanent magnet. An attractive force occurs when the superconductor has moved away from the permanent magnet. This result is assigned to the number of pinning centers in the superconductor sample. In addition, the magnetic levitation force is related to the grain size and the crystallographic orientation [30]. So, it correlated to the grain boundary connectivity, orientation and size, cracks, and the pinning center density within the bulk superconductor. From the analysis, the regressions are suitable for the Bean's model, which describe the critical current density by the magnetic field differences versus the distance [30-31].

3.1. Descending Process results:

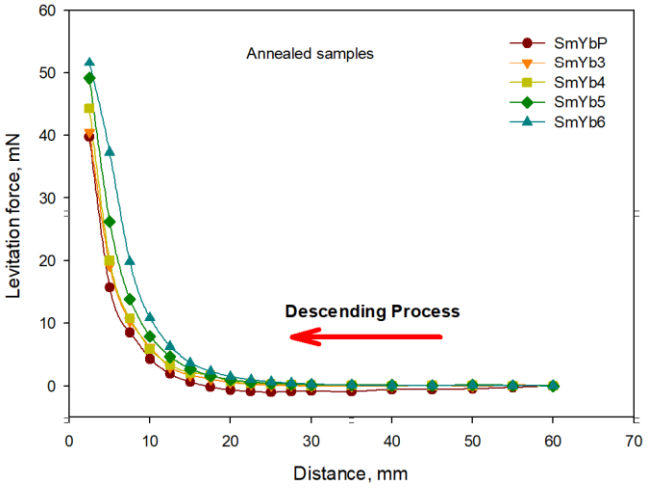


Fig.2: Annealed samples descending process.

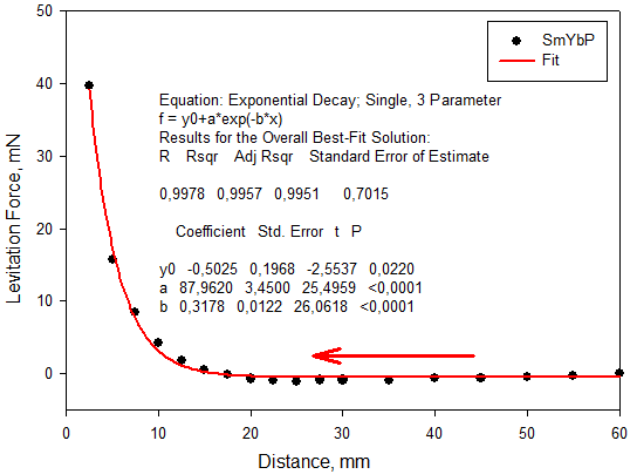


Fig.3: Annealed SmYbP sample fit curve descending process.

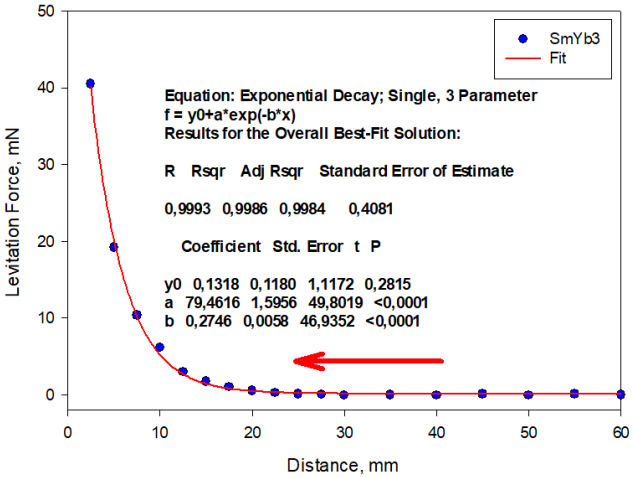


Fig.4: Annealed SmYb3 sample fit curve descending process.

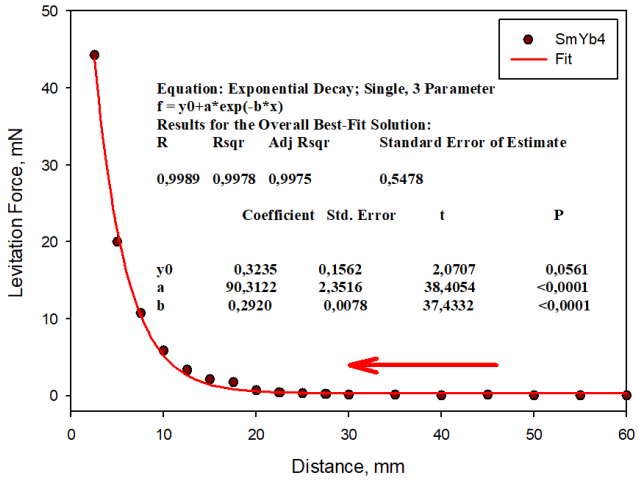


Fig.5: Annealed SmYb4 sample fit curve descending process.

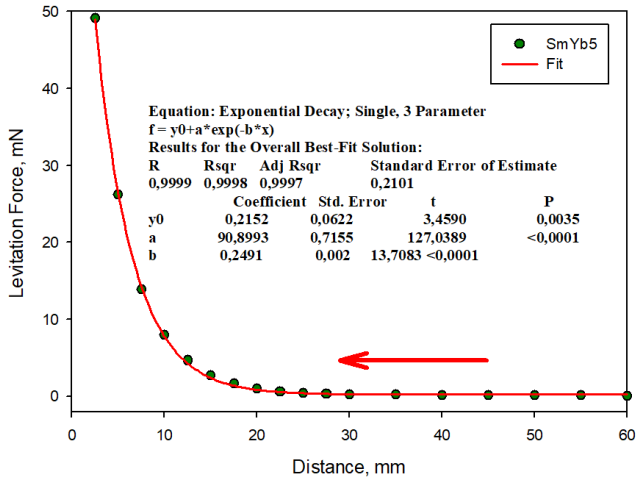


Fig.6: Annealed SmYb5 sample fit curve descending process.

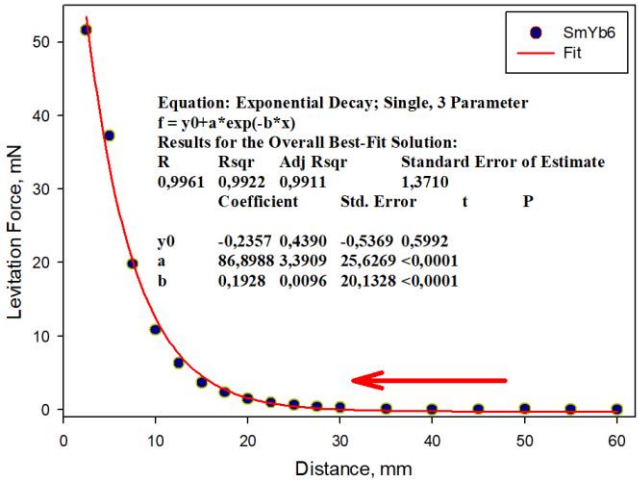


Fig.7: Annealed SmYb6 sample fit curve descending process.

Table 1: Best-fit results descending process

Sample	$F = F_0 + ae^{-bz}$			r^2
	F_0	a	b	
SmYbP	-0.5025	87.9620	0.3178	0.9957
SmYb3	0.1318	79.4616	0.2746	0.9986
SmYb4	0.3235	90.3122	0.2920	0.9978
SmYb5	0.2152	90.8993	0.2491	0.9998
SmYb6	-0.2357	86.8988	0.1928	0.9922

3.1. Ascending Process results:

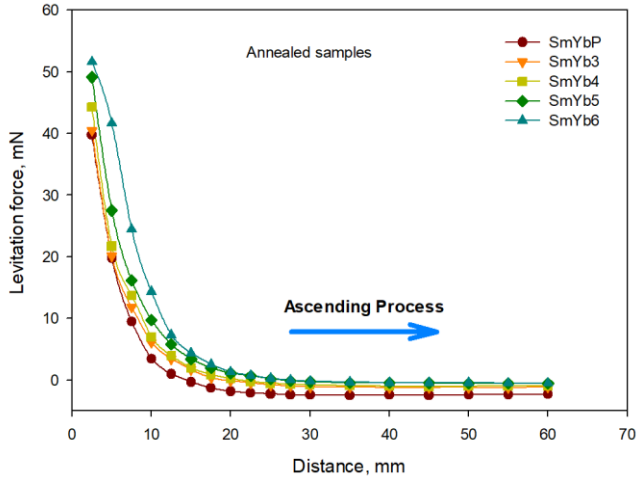


Fig.8: Annealed samples asscending process.

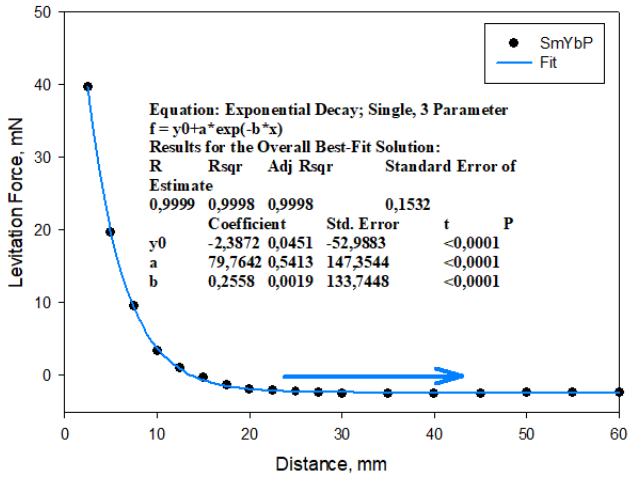


Fig.9: Annealed SmYbP sample fit curve ascending process.

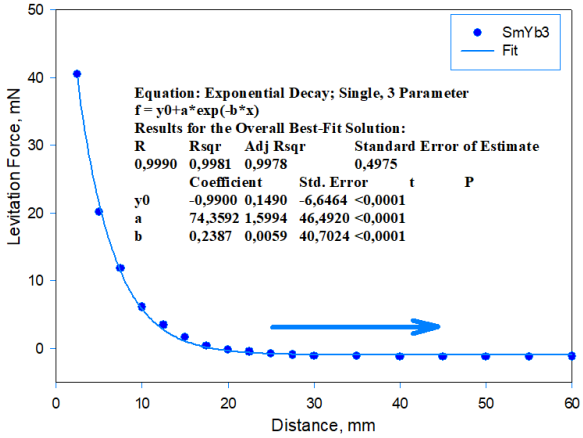


Fig.10: Annealed SmYb3 sample fit curve ascending process.

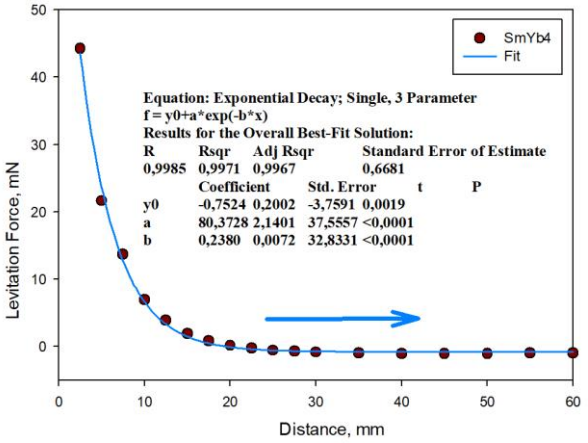


Fig.11: Annealed SmYb4 sample fit curve asscending process.

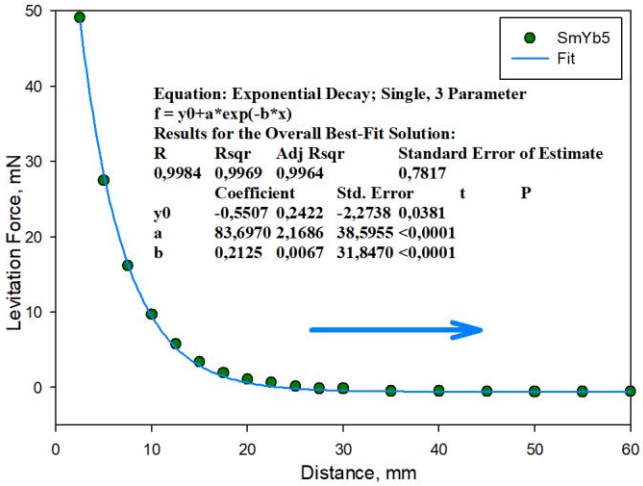


Fig.12: Annealed SmYb5 sample fit curve ascending process.

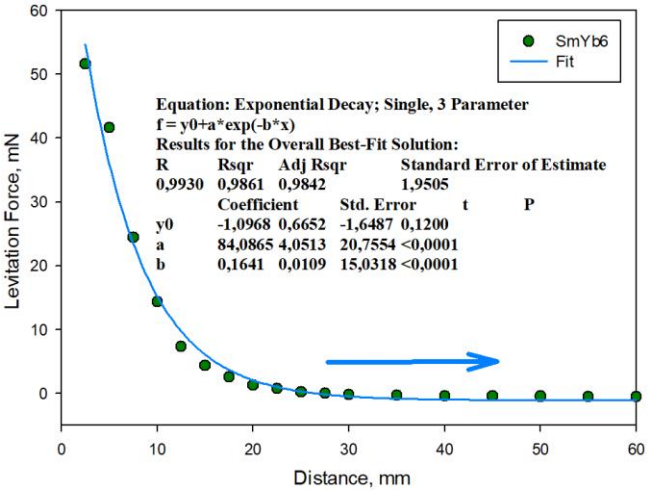


Fig.13: Annealed SmYb6 sample fit curve ascending process.

Table 2: Best-fit results ascending process

Sample	$F = F_0 + ae^{-bz}$			r^2
	F_0	a	b	
SmYbP	-2.3872	79.7642	0.2558	0.9998
SmYb3	-0.9900	74.3592	0.2387	0.9981
SmYb4	-0.7524	80.3728	0.2380	0.9971
SmYb5	-0.5507	83.6970	0.2125	0.9969
SmYb6	-1.0968	84.0865	0.1641	0.9861

In Table 1 and 2, the samples regression analysis results have been show in descending and ascending processes, respectively. Through the descending results, we have obtained in sample SmYb4 the most significant F0 (F0=0.3225mN) and the largest coefficient b value

determined (b=0.3178 mm^{-1}). However, the lowest value of F0 and b coefficient are -0.5025 mN in SmYbP and 0.1928 mm^{-1} in SmYb6. In the ascending results attractive force seen only, the most significant F0 is -2.3872 mN and the highest b coefficient is 0.2558 mm^{-1} in SmYbP. But, the lowest value of F0 and b coefficient are -0.5507 mN in SmYb5 and 0.1641 mm^{-1} in SmYb6. These implies that the Yb doping increments don't affected the coefficients linearly. Nevertheless, Yb doping generally changed the levitation force.

Chang et al. [15] measured as a function of vertical separation for a composition disk. Their samples obey an exponential relationship as in Eq. 3. They have found that the highest value in sample YBCO no1 F0 is 168 mN and in sample, TBCCO b coefficient is 786 m^{-1}.

Our results as a function of the distance are in a good agreement with the literature [4, 9, 12, 15, 17, 20, 23, 30], especially with that of Chang et al. [15].

Conclusions

High temperature superconducting (HTS) material has attractive potential applications due to its magnetic levitation property, e.g., a levitated small magnet over an HTS disc cooled by liquid nitrogen.

1. We designed the handmade setup vertical levitation force measurement system and used it for sample measurement. Although many workers have reported about superconducting bearing systems [1-32], there is no standardized method for measuring or reporting magnetic levitation force [30]. Magnetic levitation force between the RE-123 samples and PM was measured in the different vertical distances in the ZFC procedure.

2. The magnetic levitation force is originated from the pinning of flux lines, i.e., by their interaction with imperfections. The increase of the pinning centers density within the superconductors is brought out to the greater magnetic levitation force and hysteresis. It is considered that the changes in the levitation force are related to the grain orientation, the homogeneity, and the number of the pinning centers in the samples [32].

3. Yb doping increments don't affect the coefficients linearly. Nevertheless, Yb doping generally changed the levitation force. Our results as a function of the distance are in a good agreement with the literature [4, 9, 12, 15, 17, 20, 23, 30], especially with that of Chang et al. [15]. All the parameters are in well agreement with previous works.

Consequently, this study has shown that the results agree with the application of the bearing system in the literature [1-32]. The magnetic properties of our samples will be undertaken in a leadership role in the fabrication of new generation materials for technological applications.

References:

[1] J. G. Bednorz, K. A. Müller, Z. Phys. B., 64 (1986) (1): 189–193.
[2] Y. Yamada, Y. Shiohara - Physica C: Superconductivity, 217, 1–2, (1993) 182-188.
[3] K. Devendra, Namburi, Y. Shi, R. A. Dennis, H. John, D, David, A. Cardwell, Supercond. Sci. Technol., 31 (2018) 044003.
[4] H.T.Ren, L. Xiao, Y.L. Jiao, M.H. Zheng, Physica C: Superconductivity, 412–414, 1, (2004) 597-601.
[5] A. Jabbar, M. Mumtaz, K. Nadeem, Eur. Phys. J. Appl. Phys., 69 (2015) 30601,
[6] V. Bartůněk, O. Smrčková, J. Supercond Nov Magn., 24 (2011) 1241.
[7] M. Tian, N. Kumar, S. Xu, J. Wang, S. James, Kurtz, and M. H. W. Chan, Physical Review Letters, 95 (2005) 076802.
[8] M. F. Yan, W. W. Rhodes, P. K. Gallagher, Journal of Applied Physics, 63 (1988) 821.
[9] T. Kanai, T. Kamo, Shin-pei Matsuda, The Japan Society of Applied Physics, Japanese Journal of Applied Physics, 28, 2, 4 (1989) L2188-L2191.
[10] H. Fujimoto, H. Kamijo, Physica C, 335 (2000) 83–86.
[11]İbrahim Karaca, Chinese Journal of Physics, 47 (2009) 690-696.
[12] J.S. Choi, S.D. Park, B.H. Jun, Y.H. Han, N.H. Jeong, B.G. Kim, J.M. Sohn, C.J. Kim, Physica C, 468 (2008)1473-1476.
[13] S. Nariki, N Sakai, M. Murakami, I. Hirabayashi, Physica C, 439 (2006) 62-66.
[14] K. Iida, N.H. Babu, T.D. Withnell, Y. Shi, S.Haindl, H. W. Weber, D.A. Cardwell, Physica C, 445-448 (2006) 277-281.
[15] Francis C. Moon, p-110, New York, John Wiley & Sons, (1994).
[16] F. Hellman, E. M. Gyorgy, D. W. Johnson, Jr., H. M. O'Bryan, and R. C. Sherwood, J. Appl.Phys. 63, (1988) 477.
[17] F. C. Moon, M. M. Yanoviak, and R. Raj, Appl. Phys. Lett. 52, (1988) 1534.
[18] F. Díaz-González, A. Sumper, O. Gomis- Bellmunt, R. Villafáfila-Robles, Renewable and Sustainable Energy Reviews 16 (2012) 2154–2171.
[19] P.N. Barnes, M.D. Sumption, G.L. Rhoads, Cryogenics 45 (2005) 670–686.
[20] S.A. Pullano, A.S. Fiorillo, A. Morandi, P.L. Ribani, 2015 AEIT International Annual Conference (AEIT), 14-16 Oct. 2015, p. 1-3.
[21] S. Raouf, Potential aerospace applications of high-temperature superconductors, Hampton Univ., 1994 NASA-HU American Society for Engineering Education (ASEE) Summer Faculty Fellowship Program; pp.104.

[22] H. Fujimoto, H. Kamijo, Physica C 335 (2000) 83–86.
[23] A. Benlhachemi, S. Golec, J. R. Gavarri, Physica C, 209 (1993) 353.
[24] J. Unsworth, J. Du, B. J. Crosby, J. C. Macfarlane, IEEE Transactions on Mag., 29 (1993) 1
[25] W. Zhao, Y. Shi, M. Radušovská, A. R. Dennis, J. H. Durrell, P. Diko and D. A. Cardwell, Supercond. Sci. Technol., 29 (2016) 125002.
[26] K. Iida et al, Supercond. Sci. Technol., 18, (2005) 1421-1427.
[27] C. J. Kim, S. D. Park, H. W. Park and B. H. Jun, Supercond. Sci. Technol., 29, (2016) 034003.
[28] J. Unsworth, J. Du, B. J. Crosby, J. C. Macfarlane, IEEE Transactions on Mag., 29, (1993) 1
[29] A. Sanchez, C. Navau, Physica C, 268, (1996) 46.
[30] F.C. Moon, Superconducting Levitation: Applications to Bearing and Magnetic Transportation. (USA, John Wiley & Sons, 2008).
[31] D. Tripathi, T.K. Dey, Physica C, 507, (2014) 1.
[32] E. Yanmaz, S. Balci and T. Küçükömeroğlu, Materials Letters 54, (2002) 191.

6th International Conference on Materials Science and Nanotechnology For Next Generation (MSNG2019)
October 16-18, 2019, Niğde, TURKEY (ORAL FULL TEXT)

Investigation of the suitability of various turbulence models for numerical analysis of flow characteristics in minichannels

Fuat Kaya, Umut Unal

Nigde Omer Halisdemir University, Faculty of Engineering, Department of Mechanical Engineering, 51240 Nigde/TURKEY

The aim of this study is to investigate the suitability of various turbulence models for numerical analysis in minichannels. The governing equations for the fluid flow were solved by using Fluent CFD code. The prediction performance of two popular turbulence models and various options available for these models were evaluated by comparing the computed pressure drop with the data given in the literature. Since rotating and other terms are added separately to the RNG k-ε turbulence model from the standard k-ε, it has been found to be more appropriate in predicting results. In addition, RSM turbulence model is more suitable than RNG k-ε turbulence model in estimating the turbulent flow characteristics in minichannels. However, the time taken to meet convergence criteria in the RSM turbulence model is much higher than the RNG k-ε turbulence model, whereas the results obtained are close to each other. Therefore, RNG k-ε turbulence model is suitable for solving turbulent flow problems in minichannels.

Keywords: Minichannel, CFD, Pressure Drop, Heat Transfer, Turbulence Models

Corresponding authors: fkaya@ohu.edu.tr

1. Introduction

Nowadays, miniaturization of devices is becoming more important as a result of rapid progress in production tools and equipment. In this context, the use of micro-mini channels for the removal of the heat generated emerges. In these channels, it is aimed to improve the two main parameters which the researchers emphasize. These are pressure drop and heat transfer.

Hrenya et al. [1] performed applications using a k-ε turbulence model for fully developed pipe flow for different Reynolds number values. As a result of the analysis, he compared turbulent kinetic energy, dissipation of turbulent, reynold sheer stress, skin friction coefficient values compared with experimental and numerical results. Vijipurapu and Cui [2] compared

different turbulence models including RNG k-ε, k-ω and RSM and LES (Large Eddy Simulation) model using RANS (Reynolds averaged Navier-Stokes) equations in rough pipes. As a result of these comparisons, they have obtained results having k-ε, k-ω which have low computational cost and close to the actual results within the scope of certain tolerance values in numerical calculations in an average time. However, it is insufficient in case of any results regarding the instantaneous flow area. With this comparison, this gives consistent results with the LES instant flow area, which has a high calculation cost.

Escue and Cui [3] examined swirling flow velocity profiles in a straight pipe using RSM and RNG k-ε turbulence models. The analyses were performed using the Fluent CFD program. They concluded that it was insufficient for developing swirl flow compared to experimental data.

Ahsan [4] investigated the relationship between pressure drop and flow rate values of friction factor value using FVM (Finite Solved Method) and k-ε turbulence model and enhancement Wall treatment in a fully developed turbulent flow. As a result of the analysis, it was found to be in harmony with the experimental and analytical data in the literature.

In their numerical studies, Lim et al. [5] studied turbulence intensity and friction factors for different Reynolds number values in a fully developed turbulent flow. In this study, RNG k-ε turbulence model, SST k-ω turbulence model and RSM (Reynold Stress Model) models were analyzed for different wall functions. As a result of the analysis, they found that the turbulence models they used gave close results with the analytical results. When the RNG k-ε turbulence model was analyzed with enhancement Wall, it gave better results than other models. On the other hand, the

SST k-ω turbulence model yielded stable and close results for turbulence intensity compared to other models.
Sharma [6] experimentally studied the heat transfer coefficient and pressure drop in the turbulent flow regime in circular cross-section minichannels. The experiments were carried out under constant heat flux. As a result of the analysis, it is observed that they are in harmony with the numerical results.
Ghobadi and Muzychka [7] investigated pressure drop and heat transfer in two different channels with flat and spiral geometry for the purpose of cooling. They used pure water as a fluid. They found that spiral geometry minichannel had higher pressure drop and heat transfer rate than straight minichannel.
Xie et al. [8] examined numerically the pressure drop in the laminar flow regime for a 20 x 20 mm square cross-section. Constant heat flow was applied along the wall. When the pressure drop value in the system is compared with experimental data, it is seen that it reaches convergence with a maximum 12% error.
Zunaid et al. [9] In this study, examined straight rectangular and semi-cylindrical projections channels pressure drop characteristics under constant heat flux. They concluded that the pressure drop increased with an increasing number of reynolds. At the same time, semi-cylindrical projections have a higher pressure drop compared to straight channels due to hindrances on the channel surface.

In this study, the suitability of the turbulence models used for numerical solutions of turbulent flows in the Ansys Fluent program was investigated.

2. Numerical Method

Governing equations for an incompressible fluid in three-dimensional steady flow are given below [6]. These equations are solved by using Ansys-Fluent CFD software.

$$\nabla.(\rho\vec{U}) = 0 \quad (1)$$

$$\vec{U}.\nabla.(\rho\vec{U}) = -\nabla P + \nabla.(\mu\nabla\vec{U}) \quad (2)$$

$$\vec{U}.\nabla.(\rho c_p T) = \nabla.(k\nabla T) \quad (3)$$

Solution geometry is a square channel with an edge length of 10 mm and a length of 1000 mm. A constant heat flux of 500000 W / m^2 was applied to the channel along the wall. Water was used as a fluid and analyzes were performed at varying velocities of inlet velocity 2, 4 and 6 m/s. Channel geometry was given schematically in Figure 1. Thermophysical properties of water are given in Table 1.

Table 1. Thermophysical Properties of Water

density (ρ) kg/m^3	Specific heat (C_p)	Thermal Conductivity (w/m.K)	Viscosity (kg/m.s)
	j/kg.K		
998.2	*4182*	*0.6*	*0.001003*

In this study, the mesh structure given in Figure 2 as a result of grid refinement tests was obtained. Mesh structure consists of 90 * 90 * 70 and 587951 cells. Numerical tests were carried out with the residuals less than 10^{-6}.

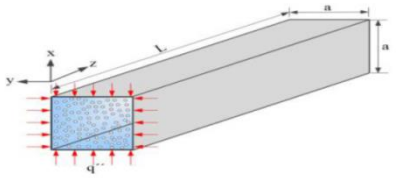


Figure 1. *Schematic demonstration of Minichannel given in Ref. [10]*

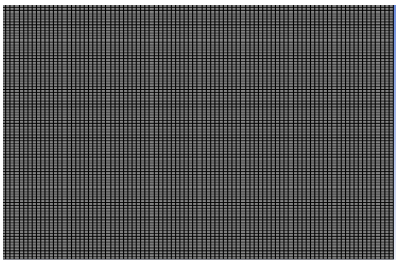


Figure 2. *Geometry Mesh Structure*

Different turbulence models commonly used in the literature to determine minichannel flow characteristics in turbulent flow have been tested and their results analyzed.
Detailed information on turbulence models can be found in the relevant literature.

3. Results and discussion

In the analysis of flow characteristics in minichannels, the suitability of turbulence models commonly used in the literature was investigated.
In order to confirm the numerical technique, the results of the pressure drop in the literature were compared with the results obtained from numerical tests and it is also given in Fig. 3.

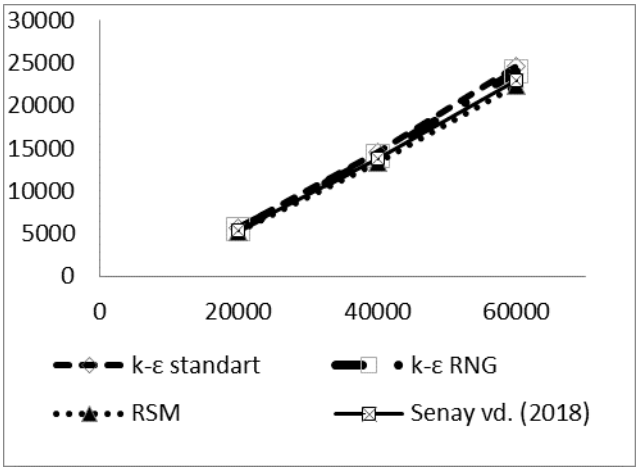
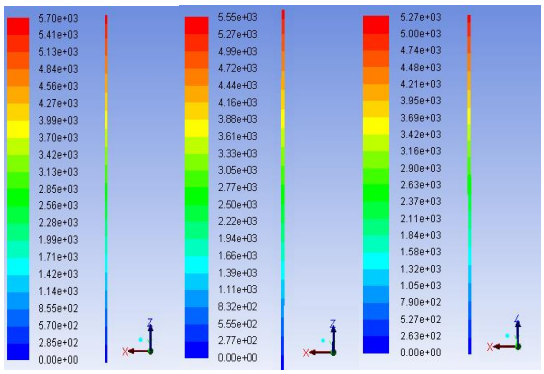


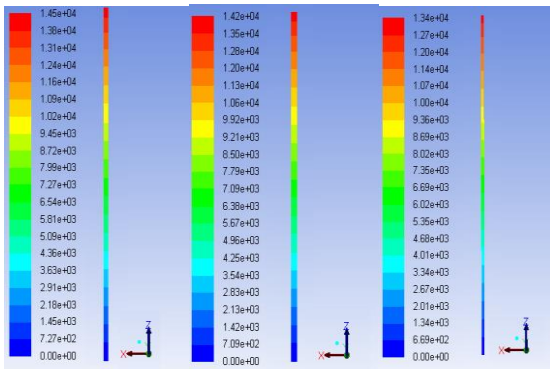
Figure 3. *Pressure Drop at Different Reynolds Numbers*

As can be seen from Figure 3, there is an increase in the pressure drop due to the increase of Reynolds number. In addition, when compared with the results of the study in the literature, RSM converged with a maximum error rate of 3.35%, k-ε RNG maximum 4.16%, and k-ε Standard maximum 6.6% error rate.



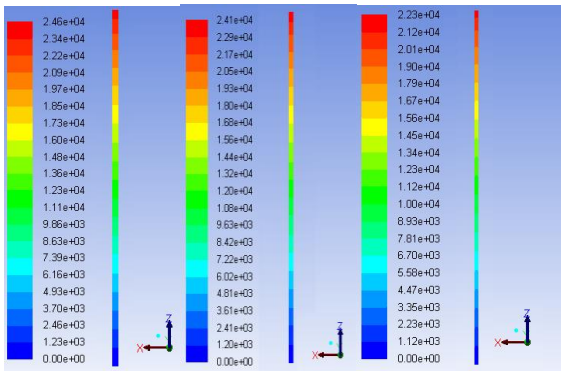
a. $k-\varepsilon$ Standart b. $k-\varepsilon$ RNG c. RSM

Figure 4. *Pressure Contours for Re 20000*



a. $k-\varepsilon$ Standart b. $k-\varepsilon$ RNG c. RSM

Figure 5. *Pressure Contours for Re 40000*



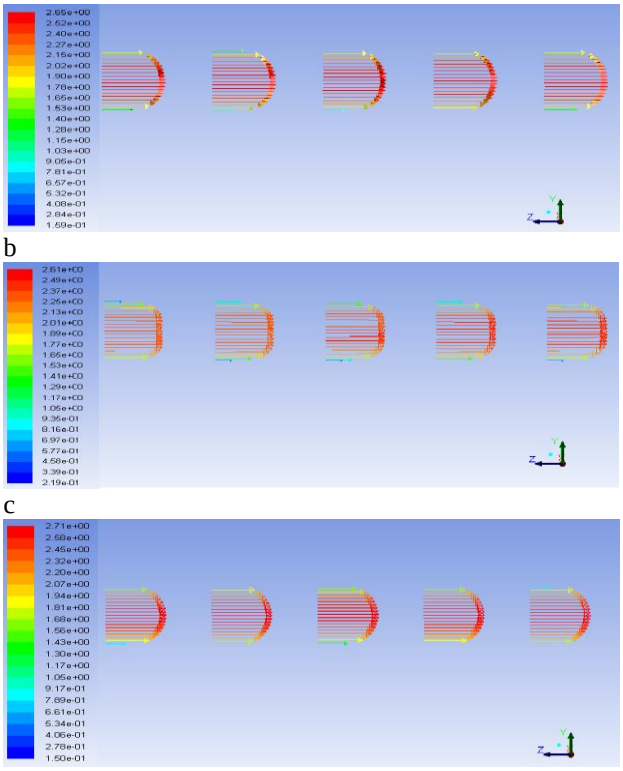
a. $k-\varepsilon$ Standart b. $k-\varepsilon$ RNG c.RSM

Figure 6. *Pressure Contours for Re 60000*

Fig. 4, 5 and 6 give the pressure contours obtained for different Reynolds Numbers.

Figures 7 demonstrates the velocity vectors for turbulent flow at different Reynolds numbers. As can be seen from the figures, the velocity profiles reflect the turbulence characteristics and the increasing number of Reynolds shows that the velocity vectors are flattened.

a



b

c

Figure 7. *Velocity Vectors for Re 20000*

a. $k-\varepsilon$ Standart b. $k-\varepsilon$ RNG c. RSM

4. Conclusions

In this study, different turbulence models were analyzed as k-ε Standard, k-ε RNG, RSM in a minichannel. In order to validate the results in the literature and to investigate the effects of turbulence models, it was carried out under

constant wall heat flux along a straight square cross-section channel and thus the numerical solution of the energy equation was also made.

The results obtained from the Numeric tests show that the pressure drop increases with increasing inlet Reynolds number.

Comparing the results obtained from the numerical tests with the results in the literature, the RSM model has a better approach with a maximum error rate of 3.35% for pressure drop, but requires longer processing time in order to meet the convergence criterion and the RNG k-ε model has been found to achieve convergence in a shorter time and with a maximum error of 4.16%. it was found to provide convergence with 4.16 error. The standard $k-\varepsilon$ turbulence model is considered to be an unsuitable model since the convergence value is a maximum error rate of 6.6 %. When all the criteria are evaluated, it is recommended that the most suitable turbulence model for determining turbulent flow characteristics in minichannels is RNG k-ε model.

References

[1] Hrenya, C. M., Bolio, E. J., Chakrabarti, D., and Sınclair J. L., "Comparison of Low Reynolds Number $k-\varepsilon$ Turbulence Models in Predicting Fully Developed Pipe Flow", Chemical Engineering Science 50 (12), 1923-1941, 1995.

[2] Vijapurapu, S., Cui, J., "Performance of turbulence models for flows through rough pipes" Applied Mathematical Modelling 34, 1458-1466, 2010.

[3] Escue, A., Cui, J., "Comparison of turbulence models in simulating swirling pipe flow", Applied Mathematical Modelling 34, 2840-2849, 2010.

[4] Ahsan, M., "Numerical analysis of friction factor of a fully developed turbulent flow using $k-\varepsilon$ turbulence model with enhanced wall treatment", Beni-Suef University Journal of Basic and Applied Sciences 3,269-277, 2014.

[5] Lim, D., C., Al-Kayiem H., H., Jundika C. Kurnia, "Comparison of Different Turbulence Models in Pipe Flow of Various Reynolds Number", 6th İnterneational Conference on Production, Energy, and Reliability, 2018.

[6] Sharma, P., "Forced Convective Heat Transfer Characteristics of Water Through a Minichannel at Higher Reynolds Number", International Journal for Scientific Research & Development Vol. 1, Issue 11, 2321-0613,2014.

[7]Ghobadi, M, & Muzychka, Y., S., "Heat Transfer and Pressure Drop in Mini Channel Heat Sinks", Heat Transfer Engineering, 36:10, 902-911,2015.

[8] Xie, X., L., Liu, Z., J., He, Y., L., Tao, W., Q., " Numerical study of laminar heat transfer and pressure drop characteristics in a water-cooled minichannel heat sink", Applied Thermal Engineering 29, 64–74, 2009

[9] Zunaid, M., Jindal, A., Gakhar, D., Sinha, A., "Numerical Study of Pressure Drop and Heat Transfer in Straight Rectangular and Semi Cylindrical Projections Microchannel Heat Sink", Journal of Thermal Engineering, Vol. 3, No. 5, pp. 1453-1465, 2017.

[10] Kaya F., "Numerical Investigation of Effects of Ramification Length and Angle on Pressure Drop and Heat Transfer in a Ramified Microchannel", Journal of Applied Fluid Mechanics, Vol. 9, No. 2, pp. 767-772, 2016.

[11] Şenay, G., Kaya, M., Gedik, E. and Kayfeci, M., "Numerical investigation on turbulent convective heat transfer of nanofluid flow in a square cross-sectioned duct", International Journal of Numerical Methods for Heat & Fluid Flow, Vol. 29 No. 4, pp. 1432-1447, 2019.

, S. Alayoğlu, B. Eichhorn, J. Electroanal. Chem., 655 (2011) 140−146.

[10] J. Xie, Q. Zhang, L. Gu, S. Xu, P. Wang, J. Liu, Y. Ding, Y. F. Yao, C. Nan, M. Zhao, Y. You, Z. Zou, Nano Energy, 21 (2016) 247-257.

[11] J. Zou, M. Wu, S. Ning, L. Huang, X. Kang, S. Chen, ACS Sustainable Chem. Eng., 7 (2019) 9007−9016.

[12] DL_POLY: a molecular dynamics simulation package was written by W. Smith, T.R. Forester, and I.T. Todorov obtained from the websitehttp://www.ccp5.ac.uk/DL_POLY

[13] A. P. Sutton, J. Chen, Philos. Mag. Lett., 61 (1990) 139

[14] Y. Kimura, Y. Qi, T. Cagin and W. Goddard III, MRS Symp. Ser., 554 (1999) 43.

[15] B. Prasai, Y. Ren, S. Shan, Y. Zhao, H. Cronk, J. Luo, C-J. Zhong, V. Petkov, Nanoscale, 7 (2015) 8122-8134.

[16] F. Cleri, V. Rosato Phys. Rev. B **48**, (1993) 22

[17] S. Senturk Dalgic, unpublished results

[18] OVITO: A. Stukowski, Modelling Simul. Mater. Sci. Eng. 18, (2010) 015012.

6th International Conference on Materials Science and Nanotechnology For Next Generation (MSNG2019)
October 16-18, 2019, Niğde, TURKEY (ORAL FULL TEXT)

Aniline Monomers on the Gold (111) Nanosurfaces

Serap Senturk DALGIC *, Sebile Sibel YAVUZ*, Seyfettin DALGIC*, Fatma KANDEMİRLİ**

*Trakya University, Faculty of Science, Department of Physics, Edirne 22030, TURKEY
** Kastamonu University, Faculty of Engineering, Department of Biomedical Engineering, 37200 Kastamonu, TURKEY

In this study, we have investigated the interaction energies and conductivities of Gold (Au) (111)/ Aniline (ANi) nanocomposites and compared with each other. For this purpose, composite structures constructed by optimized aniline organic molecule and gold (111) hollow and nanolayer surfaces which are formed from gold nanoparticles in diameter of 2nm [1,2]. The optimization has been done by using Gaussian program package in the ground state with density functional method (DFT/B3LYP) on the Lanl2dz basis set. Some Occupied Frontier Orbital energies and Virtual Frontier Orbital energies have been obtained and the electronic properties (ionization energy, electron affinity, electronegativity, chemical hardness and softness) have calculated. We have also computed interaction energies between conducting organic molecules of ANi and Au (111) surfaces as hollow and nanolayer.

Our results are in a good agreement with experiments [3] show that interaction energy between ANi molecules and hollow Au (111) nanosurface is higher than that of layer Au (111) nanosurfaces. Also, according to the band gap energies and ionization energies of the nanocomposites, hollow Au (111)/ANi nanocomposite is more conductive than layer Au (111)/ANi nanocomposite.

Keywords: Aniline/Gold nanocomposites
Corresponding authors: sebilesibel@hotmail.com, dserap@yahoo.com

1. Introduction

Nanocomposites are materials resulting from combinations of two or more compounds in nanoscale that results in new physicochemical properties and high potential materials for electrocatalysis, chemical sensors and microelectronic devices. The production of new nanocomposites based on metal nanoparticles and conductive polymers will provide a variety of interesting properties and novel properties in nano-technological applications. Conductive metallic or semiconductor nanocomposites formed with conductive polymers such as polyaniline (PANI) are of interest due to the strong electronic interaction between the nanoparticles and the polymer matrix. Among the nanomaterials, gold nanoparticles will be the building block of nanomaterials science in the 21st century due to its excellent biocompatibility, conductivity, catalytic properties, high surface / volume ratio, high density and various interesting properties [1-3].

2. Experimental details

In this work, the adsorption of aniline molecule on Au (111) hollow and layer nanosurfaces was performed and the importance of the design of 2D Aniline (ANi)/Au (111)

nanocomposite structures was emphasized for the new generation electronic applications. Therefore, we investigated and compared the physicochemical properties of 2D ANi/Au (111) nanocomposites as hollow and layer.

Considering the interface interactions, the adsorbed energy between polymer molecules and monolayer nanosheet can also be calculated as

$$E_{int} = (E_{comp} - (E_{sheet} + E_{poly})) / n \quad (1)$$

where E_{int} is the interaction energy between monolayer-sheet and polymer monomer, E_{comp} is the total energy of the polymer/monolayer-sheet composite, E_{sheet} is the total energy of the nanosheet, E_{poly} is the total energy of the polymer and n: the number of the polymer monomers [4].

HOMO (The highest occupied molecular orbital) and LUMO (the lowest unoccupied molecular orbital) of molecules represent electron donor and electron acceptor capabilities. In charge transfer, the groundstate complex is stabilized by including an amount of charge transfer configuration in which an electron is transferred from donor HOMO to the receiving LUMO. The gap between HOMO and LUMO energy values is defined as the chemical stability of the molecule given by $\Delta E = E_{LUMO} - E_{HOMO}$. The closer the molecular orbitals interact with each other, that is, the smaller the energy difference, the easier the interaction and reaction of the reagents is. The ionization potential energy ($I = -E_{HOMO}$) is the minimum energy required to extract an electron in the gas phase to the molecule. Electron affinity ($A = -E_{LUMO}$) is defined as the amount of energy that increases when an electron is added to the gas phase molecule. Electronegativity ($\chi=(I+A)/2$) means the ability of an atom within the molecule to attract electrons. Chemical hardness ($\eta=(I-A)/2$) is a measure of charge inhibition. The chemical softness can be defined as $S=1/2\eta$ [5].

Some Occupied Frontier Orbital energies and Virtual Frontier Orbital energies have been obtained by using Gaussian-16W series of program package. The electronic properties (ionization energy, electron affinity, electronegativity, chemical hardness and softness) and the interface interactions between aniline molecule and hollow / layer gold (111) nanosurfaces have been calculated with the results of optimized geometries in the ground state. All the results have been computed by using the density functional method (DFT/B3LYP) with the Lanl2dz basis set.

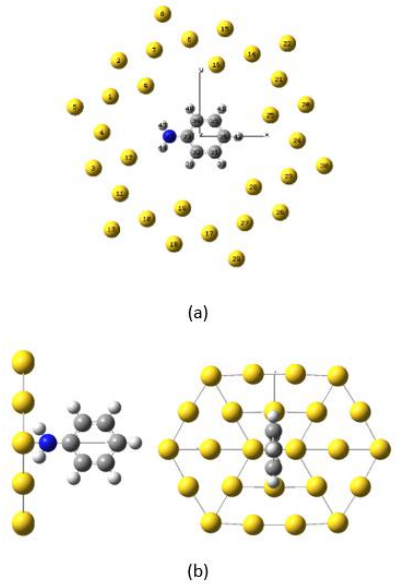


Fig.1: View of Ani/Au (111) nanocomposites before optimization from different sides a) C6H7Au30N (Hollow) b) C6H7Au24N (Layer)

3. Results and discussion:

First, we prepared Au (111) nanosurfaces as hollow and layer using a special Fortran program. After individual optimization of the aniline molecule and gold nanosurfaces by Gaussian 16W with DFT/B3LYP and Lanl2dz basis set, Ani/Au nanocomposites have been formed. One of the Ani molecule has placed parallel to the hollow Au (111) nanosurface The other Ani molecule was perpendicular to the layer Au (111) nanosurface in x dimension and at the center of it as seen in Fig1. The new structures were re-optimized to get stable ANi / Au nanocomposites in Fig.2.

After optimization, we calculated the absorbed energies of the hollow Ani/Au (111) and layer Ani/Au (111) nanocomposites are -0,02831 a.u. and -0,009355 a.u. respectively as seen in Table 1. So, the hollow nanocomposite has more interfacial interaction than the layer nanocomposite.

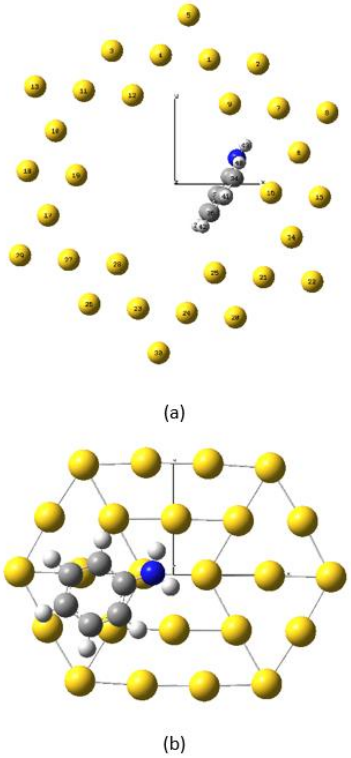


Fig.2: The optimized structures of Ani/Au (111) nanocomposites a) C6H7Au30N (Hollow) b) C6H7Au24N (Layer)

	Ani/Au (111) C6H7Au30N Hollow	Ani/Au (111) C6H7Au24N Layer
E_poly (a.u.)	-287,564867	-287,564867
E_sheet (a.u.)	-4064,705729	-3252,082765
E_comp (a.u.)	-4352,298906	-3539,656987
E_int (a.u.)	-0,02831	-0,009355

***Table 1**: Adsorbed Energy at Interface of Ani/Au (111) Nanocomposites.*

The HOMO-LUMO energies and virtual frontier orbital energies were obtained using the quantum calculations of nanocomposites. The bandgap energy, the ionization energy, electron affinity, electronegativity, chemical hardness, and softness have been calculated by HOMO-LUMO energies of ANi/Au nanocomposites and given in Table 2.

	Ani/Au (111) C6H7Au30N Hollow	Ani/Au (111) C6H7Au24N Layer
LUMO (a.u.)	-0,17548	-0,17181
HOMO (a.u.)	-0,18647	-0,21477
Band Gap Energy (a.u.)	**0,01099**	0,04296
Ionization Energy (I) (a.u.)	**0,18647**	0,21477
Electron Affinity (A) (a.u.)	0,17548	0,17181
Electronegativity (χ) (a.u.)	0,180975	0,19329
Hardness (η) (a.u.)	0,005495	0,02148
Softness (S) $(a.u)^{-1}$	90,991811	23,277467

Table 2: Physicochemical properties of the Ani/Au (111) Nanocomposites.

Considering the physicochemical properties, especially bandgap (ΔE) and ionization energy (I) of the studied hybrid structures, hollow Ani/Au (111) nanocomposite is more stable than layer ANi/Au (111). The other physicochemical properties also support the means of the bandgap energy.

Conclusions

In this study, we studied with 2D hollow and layer Au (111) nano surfaces and Aniline to form nanocomposites. The absorbed energy of the nanocomposites was investigated with the Gaussian 16W program with DFT / B3LYP function on LANL2DZ basis. We found that the hollow nanocomposite is more stable than layer ANi/Au (111) nanocomposite. Consequently, using hollow nanosurfaces to form a nanocomposite is important for conductivity. All the results are in good agreement with previously reported values.

References:

[1] S. Senturk Dalgic, S. S. Yavuz, S. Dalgic, F. Kandemirli, The Structural and Electronic Properties of n-pyrrole/Hollow Gold Monolayer Hybrid Nanostructures by ab-inito Simulations, J. Optoelectronic and Biomedical Materials, 11, 9-18 (2019).

[2] S. Senturk Dalgic, unpublished results

[3] V Sridevi, S Malathi, CS Devi. Synthesis and Characterization of Polyaniline/Gold Nanocomposites, Chemical Sciences Journal, Volume 2011: CSJ-26.

[4] A, Hamed Mashhadzadeh, A, Fereidoon, M, Ghorbanzadeh Ahangari, Superlattices and Microstructures, 111 (2017) 23-31.

[5] T. Abbaz, A. Bendjeddou, D. Villemin, Molecular structure, HOMO, LUMO, MEP, natural bond orbital analysis of benzo and anthraquinodimethane derivatives, Pharmaceutical and Biological Evaluations, April 2018; Vol. 5 (Issue 2): 27-39.

6th International Conference on Materials Science and Nanotechnology For Next Generation (MSNG2019)
October 16-18, 2019, Niğde, TURKEY (ORAL FULL TEXT)

Thiophene/ Copper Nanocomposite Structures

Serap Senturk DALGIC *, Sebile Sibel YAVUZ*, Seyfettin DALGIC*, Fatma KANDEMİRLİ**

*Trakya University, Faculty of Science, Department of Physics, Edirne 22030, TURKEY
** Kastamonu University, Faculty of Engineering, Department of Biomedical Engineering, 37200 Kastamonu, TURKEY

In recent years, nanocomposites formed using nano-sized metals and organic materials are remarkable in terms of materials used and differences in design [1-3]. Thiophene (Th) based nanocomposites, preferred in biological sensors, capacitors, solar cells and other electronic applications due to their efficient charge carrying properties, excellent environmental and thermal stability, are also cost-effective [3]. In this study, properties of nanocomposites constructed by Th organic molecule and 2D copper nanosheet in different structural directions have been examined. For this purpose, the interfacial interaction energies and some physicochemical properties of Th/Cu monolayer nanocomposites have been researched. The initial geometries have been constructed by optimized Th monomer and optimized Cu (100), (110) and (111) monolayer nanosurfaces. The quantum chemical calculations and some physicochemical properties of the optimized geometries of Th/Cu monolayer nanocomposites have been calculated by using the Gaussian program package in the ground state with a density functional method (DFT/B3LYP) on the Lanl2dz basis set.

The results show that the ionization energy and bandgap energy of Th/Cu (100) nanocomposites is lower than those obtained by Cu (110) and Cu (111) nanocomposite. So, it is the most conductive nanocomposite produced in this study. Therefore, we concluded that nanocomposites formed in different structural directions using the same material are an essential factor for the proper use of electronic applications. Our results are in good agreement with experiments.

Keywords: Thiophene, Copper nanocomposites

Corresponding authors: sebilesibel@hotmail.com, dserap@yahoo.com

1. Introduction

The ability of understanding and predicting molecular surface systems used nanoelectronic devices is the main subject of molecular electronics. Since the adsorbate-substrate interactions control the electron flow in molecular-based devices, it takes special attention. From this perspective, the organic conductive thiophene (Th) molecule on the copper (Cu) nanosurface may be an attractive choice among molecular surface systems. Because Th is a basic functional unit of oligothiophene used to build a molecular field-effect transistor or molecular wires [4]; copper nanoparticles (CuNPs) have impressive properties such as good thermal and electrical conductivity, nonlinear optical properties and are much less costly than other metals and their potential applications in cooling fluids are well known for electronic systems, conductive inks, switches or photochromic glasses in optical systems and nonlinear optical materials [5].

2. Experimental details

In this work, we performed the adsorption of thiophene molecule on Cu nanosurfaces and emphasized the importance of the design of 2D monolayer thiophene (Th) /copper (Cu) nanocomposite structures consisting of organic (Th) monomer and monolayer copper (Cu) nanoparticles for the new generation electronic applications. Therefore, some physicochemical properties of Th/Cu monolayer nanocomposites optimized with Cu (100), (110) and (111) monolayer nanosurfaces were investigated.

Considering the interface interactions, the adsorbed energy between polymer molecules and monolayer nanosheet can also be calculated as

$$E_{int} = (E_{comp} - (E_{sheet} + E_{poly}))/n \quad (1)$$

where E_{int} is the interaction energy between monolayer-sheet and polymer monomer, E_{comp} is the total energy of the polymer/monolayer-sheet composite, E_{sheet} is the total energy of the nanosheet, E_{poly} is the total energy of the polymer and n: the number of the polymer monomers [6].

HOMO (The highest occupied molecular orbital) and LUMO (the lowest unoccupied molecular orbital) of molecules represent electron donor and electron acceptor capabilities. In charge transfer, the groundstate complex is stabilized by including an amount of charge transfer configuration in which an electron is transferred from donor HOMO to the receiving LUMO. The gap between HOMO and LUMO energy values is defined as the chemical stability of the molecule given by $\Delta E = E_{LUMO} - E_{HOMO}$. The closer the molecular orbitals interact with each other, that is, the smaller the energy difference, the easier the interaction and reaction of the reagents is. The ionization potential energy ($I = -E_{HOMO}$) is the minimum energy required to extract an electron in the gas phase to the molecule. Electron affinity ($A = -E_{LUMO}$) is defined as the amount of energy that increases when an electron is added to the gas phase molecule. Electronegativity ($\chi=(I+A)/2$) means the ability of an atom within the molecule to attract electrons. Chemical hardness ($\eta=(I-A)/2$) is a measure of charge inhibition. The chemical softness can be defined as $S=1/2\eta$. The dipole moment is other important electronic property of materials. The bigger the dipole moment represents the stronger intermolecular interactions. Molecular electrostatic potential (MEP) shows that the re-location of the electron density.

The interface interactions between organic molecule thiophene and copper (100), (110) and (111) nanosurfaces have been performed from the optimized geometries by using Gaussian-16W series of program package. The frontier orbital energies HOMO and LUMO energies of the Th/Cu nanocomposites in the ground state have been obtained by using density functional method (DFT/B3LYP) with the Lanl2dz basis set.

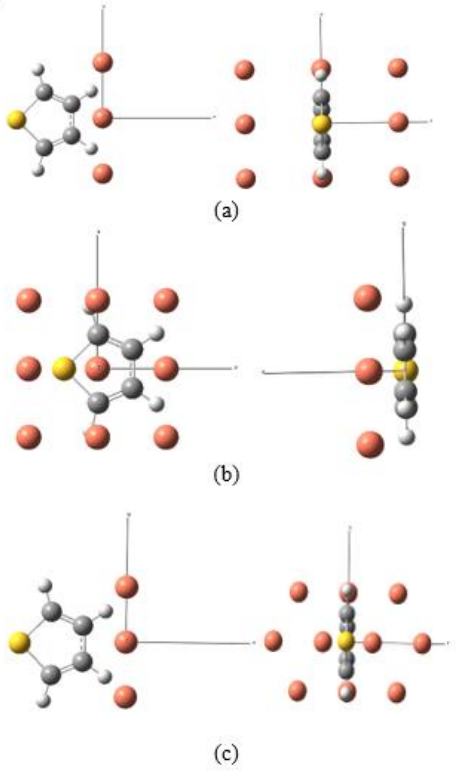


Fig.1: View of nanocomposites before optimization from different sides a) Th/Cu (110) b) Th/Cu (100) c) Th/Cu (111).

3. Results and discussion:

First, the thiophene monomer and Cu (110), (100) and (111) nanosurfaces were obtained by a special Fortran program. After individual optimization of the thiophene molecule and copper nano surfaces by Gaussian 16W with DFT/B3LYP and Lanl2dz basis set, Th/Cu nanocomposites have been formed such that the Th molecule has perpendicular to the z-axis in dimension x as seen in Fig1. The new structures were re-optimized to get stable Th / Cu nanocomposites in Fig.2.

After optimization, we calculated the absorbed energy of the Th/Cu nanocomposites. As seen in Table 1, differences of nanosurfaces of Cu

have profoundly influenced the interface interaction. It is important to understand the interfacial interaction between Th monomer and different Cu nanosurfaces guiding the fabrication of nanocomposites. The interface interaction of Th / Cu (100) is stronger than Cu (110) and Cu (111).

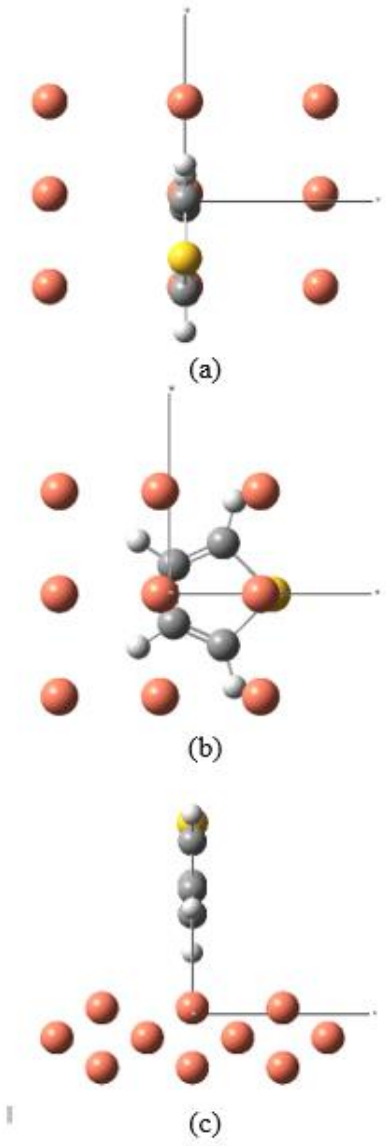


Fig.2: The optimized structures of nanocomposites a) Th/Cu (110) b) Th/Cu (100) c) Th/Cu (111).

	Th/Cu(110)	Th/Cu(100)	Th/Cu(111)
E_{poly} (a.u.)	-164,8788272	-164,8788272	-164,8788272
E_{sheet} (a.u.)	-1765,397975	-1765,527813	-1961,793447
E_{comp} (a.u.)	-1930,278333	-1930,409852	-2126,675330
E_{int} (a.u.)	-0,00153043	**-0,00321185**	-0,00305585

***Table 1**: Adsorbed Energy at Interface of Th/Cu Nanocomposites.*

The HOMO-LUMO energies and virtual frontier orbital energies were obtained using the quantum calculations of nanocomposites. The bandgap energy, the ionization energy, electron affinity, electronegativity, chemical hardness, and softness have been calculated by HOMO-LUMO energies of Th/Cu nanocomposites and given in Table 2.

	Th/Cu (110)	Th/Cu (100)	Th/Cu (111)
LUMO (a.u.)	-0,13038	-0,12084	-0,10734
HOMO (a.u.)	-0,17842	-0,14917	-0,18349
Band Gap Energy (a.u.)	0,04804	**0,02833**	0,07615
Ionization Energy (I) (a.u.)	0,17842	**0,14917**	0,18349
Electron Affinity (A) (a.u.)	0,13038	0,12084	0,10734
Electronegativity (χ) (a.u.)	0,1544	0,135005	0,145415
Hardness (η) (a.u.)	0,02402	0,014165	0,038075
Softness (S) (a.u)-1	20,8160	35,2983	13,1320

Table 2: Physicochemical properties of the Th/Cu Nanocomposites.

The bandgap energies (ΔE) values and the ionization energies (I) of the studied hybrid structures in Table 2 shows that Th/Cu (100) nanocomposite is most stable among the that of Th/Cu nanocomposites. The hardnesses of

nanocomposites are 0,02402 a.u., 0,014165 a.u. and 0,038075a.u. which are compatible with the means of the bandgap energy. The dipole moments of studied hybrid structures in Table 3 show that there is the weakest intermolecular interactions are in the Th/Cu(100) nanocomposites, so that means the most stable nanocomposite again.

	Th/Cu(110)	Th/Cu(100)	Th/Cu(111)
Dipole Moments (Debye)	0,97681	0,213620	1,064794

Table 3: Dipole Moments of the Th/Cu Nanocomposites.

Conclusions

In this study, 2D Copper (110), (100), (111) nano surfaces and Thiophene were used to form nanocomposites. The absorbed energy of the nanocomposites was investigated with the Gaussian 16W program with DFT / B3LYP function on LANL2DZ basis. It has been found that the use of different copper nanosurfaces for design is profoundly effective for the physicochemical properties of the nanocomposites. Th / Cu (100) is the most stable nanocomposite of Th / Cu nanocomposites corresponding to bandgap energies. Thus, the interaction energy and the dipole moment of the nanocomposite are the lowest among others. Consequently, the design of materials to form a nanocomposite is important for conductivity. All the results are in well agreement with previously reported values.

References:

[1] C. Zhan, G. Yu, Y. Lu, L. Wang, E. Wojcik, S. Wei, Conductive polymer nanocomposites: a critical review of modern advanced devices, J. Mater. Chem. C, 5, 1569-1585 (2017).
[2] S. Senturk Dalgic, S. S. Yavuz, S. Dalgic, F. Kandemirli, The Structural and Electronic Properties of n-pyrrole/Hollow Gold Monolayer Hybrid Nanostructures by ab-inito Simulations, J. Optoelectronic and Biomedical Materials, 11, 9-18 (2019).
[3] F-H Lu, F-C Chang, M-G Mohamed, T-F Liu, C-G Chao, S-W Kuo, Conducting Ag/oligothiophene complex pastes through a simple quenching/chelation method, J. Mater. Chem. C, 2 ,6111-6118 (2014).
[4] M. Callsen, N. Atodiresei, V. Caciuc, S. Blügel, Semiempirical van derWaals interactions versus ab initio nonlocal correlation effects in the thiophene-Cu(111) system, Physical Review B 86, 085439 (2012).
[5] M. Rhazi, S. Majid, M. Elbasri, F. Ezzahra Salih, L. Oularbi. K. Lafdi, Recent progress in nanocomposites based on conducting polymer: application as electrochemical sensors, International Nano Letters (2018) 8:79–99.
[6] A, Hamed Mashhadzadeh, A, Fereidoon, M, Ghorbanzadeh Ahangari, Superlattices and Microstructures, 111 (2017) 23-31.

6th International Conference on Materials Science and Nanotechnology For Next Generation (MSNG2019)
October 16-18, 2019, Niğde, TURKEY (ORAL FULL TEXT)

The Hugoniot Equation of State of Boron Carbide Determined by Molecular Dynamics Simulations

H.C. Çekil, M. Özdemir
Cukurova University, Faculty of Arts and Sciences, Department of Physics, Adana 01330, TURKEY

Boron Carbide[1,2] has been investigated via non-equilibrium molecular dynamics simulations[3] to determine the Hugoniot equation of state. Simulations are carried out at 0 K and 10 K initial temperatures in different crystallographic directions. Momentum mirror technique is used to mimic shock wave compression. Dimensions of samples used in simulations are 30x30x1200 A^3 and 30x46x2242 A^3. Hugoniot curves are determined for <001> and <100> directions at initial temperatures mentioned above. Hugoniot elastic limits (HEL) and the corresponding impact velocities are obtained. The results are compared with available experimental results. HEL point occurs at about 20 GPa in <001> direction. It is observed that resistance of material to structural deformations is higher for <100> direction compared to <001> direction.

Keywords: Boron Carbide, Molecular Dynamics, ReaxFF, Shock Compression, Hugoniot State
Corresponding author: hccekil@student.cu.edu.tr

1. Introduction

Boron carbide is a ceramic material widely studied because of its peculiar properties. These are low density, high hardness, high melting point and neutron absorption. The properties allow to use boron carbide in refractory, abrasive powder, coating and nuclear applications.

Ballistic applications require lightweight and high-strength materials. When one considers these properties, boron carbide is one of the candidate materials. In order to reveal the mechanical behavior of it on loading a great deal of research is carried out by different groups. Shock compression experiment is an important tool to test material strength on dynamic compression. Shock compression experiments are available in literature [4-10].

In addition to the studies conducted to examine the behavior under dynamic load, there are many studies investigating the elastic properties and its strength on static loading[11-20].

To induce a shock wave in material allows one to investigate the physical and chemical processes take place at extreme pressures and temperatures. Analysis of propagation of shock wave gives information about rapidly dynamical changes.

Although shock compression experiments are successful for understanding processes on dynamic loading it is not possible to observe events on an atomic scale and in very narrow time intervals. Shock simulations can overcome this challenge.

In this study, non-equilibrium molecular dynamics simulation is employed to reveal the equation of state of boron carbide. The interatomic potential used is reactive force field (ReaxFF). Momentum mirror technique is used to create shock wave. Simulations has been done at 0K-10K initial temperatures. Boron carbide impact resistance is investigated for two crystal planes.

2. Simulation Details

The sample used in simulations consist of 16200 and 432000 atoms for <001> and <100> crystal directions, respectively. The general form of boron carbide unit cell is depicted in Fig 1. Boron carbide has different stoichiometric forma and $B_{12}C_3$ stoichiometry is examined in this study. The samples are formed with replication of hexagonal unit cells of 6x6x100 and 6x6x400 in three directions. These correspond to a length of 1200 A^o and 2260 A^o for shock wave propagation, respectively. We explore two main crystallographic directions as the shock loading direction. Periodic boundary conditions are maintained for perpendicular directions to shock propagation to

eliminate edge effects. ReaxFF potentials are employed to describe the interaction between atoms[22]. LAMMPS software is used to perform simulations[3]. Before simulation the system was equilibrated with NPT ensemble at desired temperature and zero pressure. NVE ensemble is used for conserving the energy during shock simulation. The time step to integrate the equations of motions was chosen 0.25 fs.

Shock wave is initiated with the throw of atoms to a massive stationary piston that is used as momentum mirror which reflects back the z component of velocity of atoms that reach the piston. The desired impact velocity toward piston was given as initial velocity of atoms. Impact velocities are chosen between 0.5 km/s and 4.0 km/s. The simulation sample is virtually divided into parts of equal width along the impact direction. All variables are obtained by taking averages over these parts.

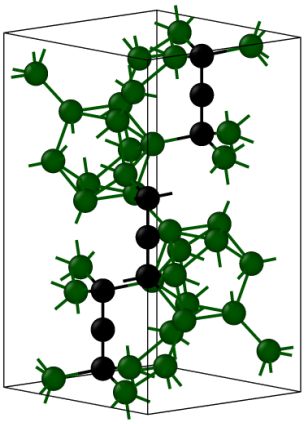


Figure 1. *Hexagonal unit cell of boron carbide.*

3. Results and discussion

The shock velocity versus particle velocity behaviour of the material obtained from simulations are given in Fig 2. for 0 and 10 K initial temperatures and <001> and <100> crystallographic directions. The relationship between shock velocity and particle velocity is expressed as

$$U_s = C_0 + sU_p \quad (1)$$

where C_0 represents the sound velocity and s is constant. Shock propagation velocity has two different regimes as in Fig 2. When the impact velocity exceeds a certain value, shock wave splits into an elastic and a plastic front. The velocity at which the splitting begins to appear is 0.7 km/s for <001> direction and 1.5 km/s for <100> direction. The curves that correspond to elastic regime (upper curves) in Fig. 2 are fitted to equation (1) to determine the sound velocity. Sound velocity is found to be 16 km/s for the two different directions studied. The constant s that appears in equation (1) is found to be 0.89 and 0.99 for <001> and <100> directions, respectively. The Hugoniot curve of the material is shown in Fig. 3 where available experimental results are also depicted.

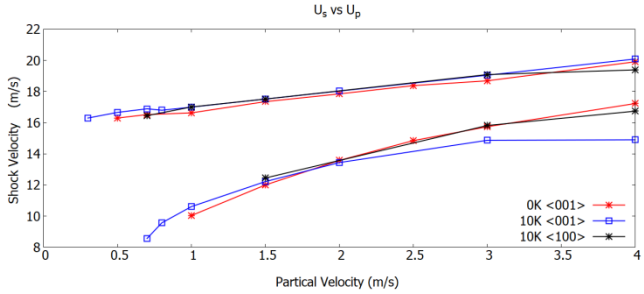


Figure 2. *Shock propagation velocity versus impact velocity for B_4C.*

Our results compare with experimental results favorably as seen in Fig. 3. HEL point occurs at about 20 GPa at 0 K and 10 K initial temperatures in <001> direction. It is our conclusion that it takes place at about 40 GPa in <100> direction. Therefore one can conclude that the resistance of the material to structural deformations is higher for <100> direction compared to <001> direction.

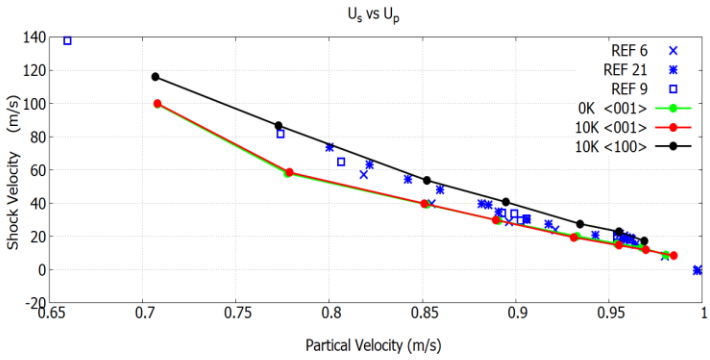


Figure 3.*Hugoniot curve for B_4C. the simulation result was represented with point and line. Experimental result represented with blue circle*

4. Conclusions

B_4C was examined by non-equilibrium molecular dynamics simulations to understand the mechanical

behavior of the material under dynamic loading. Shock propagation velocity and P-V diagram are extracted from the simulation data. Hugoniot elastic limit was determined to be 20 GPa and 40 GPa for <001> and <100> directions, respectively. These values are determined from shock wave propagation inside the material and by observing the piston velocity at which a plastic wave front begins to appear besides the elastic wave.

5. Acknowledgement

This research was funded in part by the Cukurova University Research Projects Development and Coordination Unit under the project number FDK-2016-7282. The numerical calculations reported in this paper were partially performed at TUBITAK ULAKBIM, High Performance and Grid Computing Center (TRUBA resources).

References:

[1] F. Thevenot, Journal of the European Ceramic society, 6(4), 205-225 (1990).

[2] V.Domnich, S. Reynaud, R. A. Haber, M. Chhowalla, Journal of the American Ceramic Society, 94(11), 3605-3628(2011).

[3] Plimpton, S. (1995). Fast Parallel Algorithms for Short-Range Molecular Dynamics, *J Comp Phys*, 117, 1-19. (http://lammps.sandia.gov).

[4] M.L. Wilkins. Use of boron compounds in lightweight armor. In *Boron and refractory borides* (pp. 633-648). Springer, Berlin, Heidelberg..

[5] W. H. Gust, Royce, E. B. Royce. (1971). Dynamic yield strengths of B4C, BeO, and Al2O3 ceramics. *Journal of Applied Physics*, *42*(1), 276-295.

[6] Grady, D. E. (2015). Hugoniot equation of state and dynamic strength of boron carbide. *Journal of Applied Physics*, *117*(16), 165904.

[7] Dandekar, D. P. (2001). *Shock response of boron carbide* (No. ARL-TR-2456). ARMY RESEARCH LAB ABERDEEN PROVING GROUND MD.

[8] Bourne, N. K. (2002). Shock–induced brittle failure of boron carbide. *Proceedings of the Royal Society of London. Series A: Mathematical, Physical and Engineering Sciences*, *458*(2024), 1999-2006.

[9] Zhang, Y., Mashimo, T., Uemura, Y., Uchino, M., Kodama, M., Shibata, K., ... & Sekine, T. (2006). Shock compression behaviors of boron carbide (B 4 C). *Journal of applied physics*, *100*(11), 113536.

[10] Holmquist, T. J., & Johnson, G. R. (2006). Characterization and evaluation of boron carbide for plate-impact conditions. *Journal of applied physics*, *100*(9), 093525.

[11] Nelmes, R. J., Loveday, J. S., Wilson, R. M., Marshall, W. G., Besson, J. M., Klotz, S., ... & Hull, S. (1995). Observation of inverted-molecular compression in boron carbide. *Physical review letters*, *74*(12), 2268.

[12] Niihara, K., Nakahira, A., & Hirai, T. (1984). The effect of stoichiometry on mechanical properties of boron carbide. *Journal of the American Ceramic Society*, *67*(1), C-13.

[13] Hollenberg, G. W., & Walther, G. (1980). The elastic modulus and fracture of boron carbide. *Journal of the American Ceramic Society*, *63*(11-12), 610-613.

[14] Champagne, B., & Angers, R. (1979). Mechanical properties of hot-pressed B-B4C materials. *Journal of the American Ceramic Society*, *62*(3-4), 149-153.

[15] Domnich, V., Gogotsi, Y., Trenary, M., & Tanaka, T. (2002). Nanoindentation and Raman spectroscopy studies of boron carbide single crystals. Applied Physics Letters, 81(20), 3783-3785.

[16] Chen, M., & McCauley, J. W. (2006). Mechanical scratching induced phase transitions and reactions of boron carbide. *Journal of applied physics*, *100*(12), 123517.

[17] Gieske, J. H., Aselage, T. L., & Emin, D. (1991, July). Elastic properties of boron carbides. In *AIP Conference Proceedings* (Vol. 231, No. 1, pp. 376-379). AIP.

[18] Werheit, H., Leithe-Jasper, A., Tanaka, T., Rotter, H. W., & Schwetz, K. A. (2004). Some properties of single-crystal boron carbide. *Journal of Solid State Chemistry*, *177*(2), 575-579.

[19] Lee, S., Bylander, D. M., & Kleinman, L. (1992). Elastic moduli of B 12 and its compounds. *Physical Review B*, *45*(7), 3245.

[20] McClellan, K. J., Chu, F., Roper, J. M., & Shindo, I. (2001). Room temperature single crystal elastic constants of boron carbide. *Journal of materials science*, *36*(14), 3403-3407.

[21] Vogler, T. J., Reinhart, W. D., & Chhabildas, L. C. (2004). Dynamic behavior of boron carbide. *Journal of applied physics*, *95*(8), 4173-4183.

[22] An, Q., Goddard III, W. A. (2015). Atomistic origin of brittle failure of boron carbide from large-scale reactive dynamics simulations: suggestions toward improved ductility. *Physical Review Letters*, *115*(10), 105501.

6th International Conference on Materials Science and Nanotechnology For Next Generation (MSNG2019)
October 16-18, 2019, Niğde, TURKEY (ORAL FULL TEXT)

Usage of Enzyme Catalysts Supported With Magnetic Nanomaterials In Polymer Synthesis

S. Sakar[1], S.Sanduvac[2*], E. Sahmetlioglu[1,3] , E. Yılmaz[1] and E. Turaç[4]
[1]Ernam-Erciyes University Nanotechnology Application and Research Center, Kayseri 38090, Turkey
[2]Bünyan Vocational School, Kayseri University,Kayseri 38600, Turkey
[3]Safiye Cikrikcioglu Vocational School, Kayseri University, Kayseri 38039, Turkey
[4]Department of Chemistry, Nigde Omer Halisdemir University, Nigde 51240,Turkey

In this study, synthesis, characterization and use of magnetic Fe_3O_4 supported nanocatalysts in polymer synthesis have been investigated. In the first stage, magnetic Fe_3O_4 was obtained by using $FeCl_3$ with hydrothermal method. The resulting magnetic iron oxide was modified with aminopropyltriethoxysilane, glutaraldehyde, respectively, and coated with horseradish peroxidase (HRP). The synthesized catalyst was used in the polymerization reaction of acrylamide. To prepare magnetic enzyme catalyst and use in polymerization reaction is first study in the literature. With this method, the catalyst easily recovered by magnetic separation. The catalyst with include HRP enzyme has been reused 16 times in the polymerization reaction of acrylamide was performed. The optimum conditions have been determined. The structure of the polymer and nanocatalyst have been evaluated by XRD, FT-IR, SEM, EDX, ^{1}H-NMR, and RAMAN techniques. The white polyacrylamide has been successfully synthesized by using the water as the solvent. The resulting white polymer has a molecular weight of 14500 g/mol.

Keywords: Nanocatalysts, aminopropyltriethoxysilane, glutaraldehyde, horseradish peroxidase (HRP)
Submission date:

Corresponding author: senemtapan@gmail.com

1. Introduction

In few decades, polymerizations catalyzed by enzymes (enzymatic polymerizations) have received more attention as a new methodology for polymer synthesis [1]. Enzymes are regarded as environmentally friendly and green catalysts than conventional initiators since they can be obtained from renewable raw materials.

Horseradish peroxidase (HRP), one of the most widely used catalysts in enzymatic reactions, is found in horseradish roots [2]. There are many organic and inorganic electron donor compounds (such as phenols, amines, indoles, phenolic acids and sulfonates) that can be oxidized with peroxidase catalyst and H_2O_2. However, HRP is not stable under various conditions. The stabilization of HRP may be achieved by medium engineering, chemical crosslinking, protein engineering or enzyme immobilization.

Enzyme immobilization can be defined as the chemical and physical retention of the enzyme molecules in a catalytic process in order to maintain the catalytic activity and ensure its reusability. Immobilized enzymes are more useful and advantageous molecules than free enzymes and can be easily removed from the medium at the end of the reaction. They can be used many times in the reaction and are more resistant to environmental factors [3].

In recent years, many studies have been carried out on the development of immobilized enzymes due to their important advantages such as low production costs, control of the process and reusability of the immobilized enzymes [4].

In this study, synthesis, characterization and use of magnetic Fe_3O_4 supported nanocatalysts in polymer

synthesis were investigated. The resulting magnetic iron oxide was modified with aminopropyltriethoxysilane and glutaraldehyde, respectively, and HRP was immobilized on the surface of the particles. The synthesized catalyst was used in the polymerization reaction of acrylamide. Optimum conditions were determined. Polyacrylamide was synthesized successfully.

2. Experimental details

Magnetic Fe_3O_4 was obtained by using $FeCl_3.6H_2O$ with hydrothermal method. The resulting magnetic iron oxide was modified with aminopropyltriethoxysilane, glutaraldehyde, respectively, and coated with horseradish peroxidase (HRP).
0.40 grams of magnetic nanocatalyst and 2 grams of acrylamide were dissolved in 10 ml of purified water. 50µ L of 99.8% purity H_2O_2 was added dropwise to the reaction 5 times in 10 minutes. Polyacrylamide has been successfully synthesized.The structure of the polymer and nanocatalyst have been evaluated by XRD, FT-IR, SEM, EDX, ^{1}H-NMR, and RAMAN techniques.

3. Results and discussion

The catalyst and polymer have been synthesized successfully. It is shown in the table 1 that the catalyst can be used repeatedly.
Table 1: Experimental table of enzymatic oxidative polymerization.

Monomer g	catalyst g	Solvent	H_2O_2 µL	t (hour)	Color	Yield, %
2	0,40	H_2O	50	24	White	59
2	0,40	H_2O	50	24	White	69
2	0,40	H_2O	50	24	White	56
2	---	H_2O	50	24	---	0
2	0,40	H_2O	50	24	White	65
2	0,40	H_2O	50	24	White	97
2	0,40	H_2O	50	24	White	57
2	---	H_2O	50	24	---	0
2	0,40	H_2O	50	24	White	66
2	0,40	H_2O	50	24	White	72
2	0,40	H_2O	50	24	White	78
2	---	H_2O	50	24	---	0
2	0,40	H_2O	50	24	White	64
2	---	H_2O	50	24	---	0
2	0,40	H_2O	50	24	White	78
2	0,40	H_2O	50	24	White	80

The monomer was completely soluble in following organic solvents: DMF, DMSO, THF, acetone, methanol,water, chloroform and ethanol. It was insoluble in chloroform and water. The product, polymer, was also readily soluble in water. However, it was insoluble in DMF, DMSO, THF, acetone, methanol, chloroform and ethanol.
The crystalline structure of Fe_30_4 particles was investigated by XRD. As shown in Figure 1, 30.1, 31.8, 35.5, 43.1, 53.4, 57.0, 62.6 and 74.0 ° coincided with the standard data of Fe_30_4 (JCPDS no. 01-088-0315), respectively.

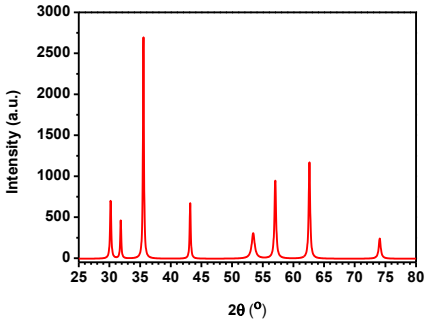


Figure 1. *XRD Spectrum of Fe_30_4.*

In Figure 2-a-d and Figure 3, SEM images of MNP, MNP-APTES, MNP-APTES-GA, catalyst and polymer structures are given respectively. In addition, EDX results are given in Figure 4.a-e.

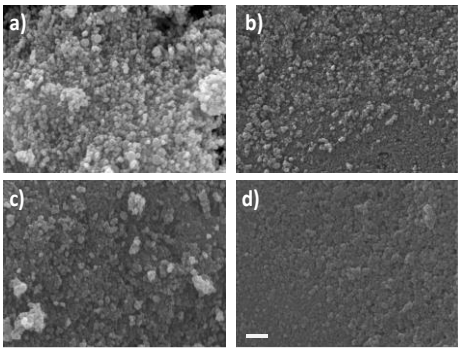


Figure 2. *SEM images a) MNP b) MNP-APTES c) MNP-APTES-GA d) Catalyzer*

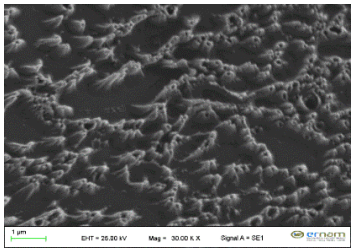


Figure 3. *SEM image of Polymer*

In the EDX analysis of MNP molecule, it is seen that only iron and oxygen elements are present in the structure. As a result of the modification, silicon element from APTES and carbon elements from gluteraldehyde are seen. In Figure 4.d, it is seen that Fe ratio increases with Fe element coming from the structure of HRP. In Figure 4.e, it is seen that there is nitrogen element coming from acrylamide in polymer structure[5].

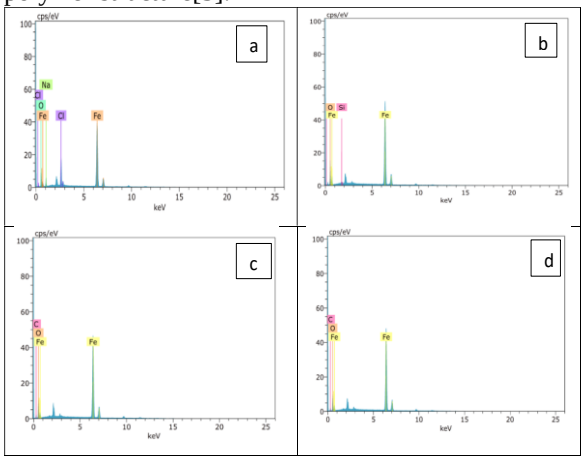


Figure 4. *EDX a) MNP b) MNP-APTES c) MNP-APTES-GA d) Catalyzer*

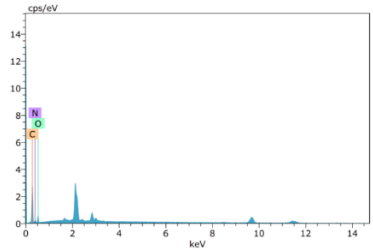


Figure 4.e*: EDX graphic of polymer*

In Figure 5, the distribution of magnetic iron in the catalyst is shown in red.

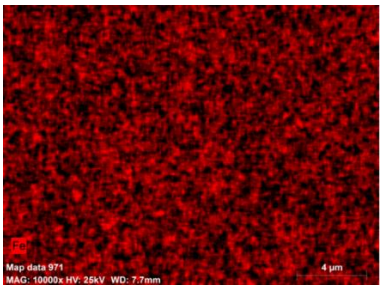


Figure 5*. EDX mapping image of catalyst*

Figure 6 shows the FTIR spectra of the catalyst. In this spectrum; (a) The peak at 3744 cm^{-1} results from the O – H stretching band. The characteristic band at the wavelength of 539,11 cm^{-1} is due to the stretching vibration of the Fe – O bond. (b) The peak at 2329.8 cm^{-1} is provided by the presence of stretching vibration on the aminopropyl group. At 1257,5 cm^{-1}, it corresponds to the presence of Si-O-H and Si-O-Si groups. The peak at 527,12 cm^{-1} shows Fe – O – Si bonds.
(c) Symmetrical stretching vibrations of peak - $CH_2CH_2CH_2$ - groups at 2901.1 cm^{-1}. (d) represents the stretching bands of peak $–CH_2$ groups at 2982.8 cm^{-1}. The peak at 1387.7 cm^{-1} comes from the –CONH– bonds [6].

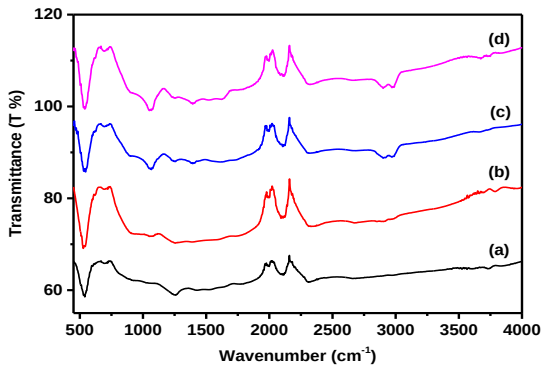


Figure 6. *FT-IR Spectrum of Catalyst*

a) Fe_3O_4 b) Fe_3O_4 – APTES c) Fe_3O_4 – APTES – GA d) Fe_3O_4 – APTES – GA – HRP

Figure 7 shows the FTIR spectra of the polymer. In the FT-IR spectrum of the polymer, symmetrical and asymmetric stretching of NH_2 groups was observed at polyacrylamide 3325 cm^{-1}. The band at 3160 cm^{-1} is thought to belong to symmetrical stretching vibrations of O – H or N – H groups [7]. The peak at 2976 cm^{-1} belongs to the stretching vibration C – H. The band at 1608-1647 cm^{-1} is the stretching vibration frequencies in the carboxyl and amide groups ($CONH_2$) [8].

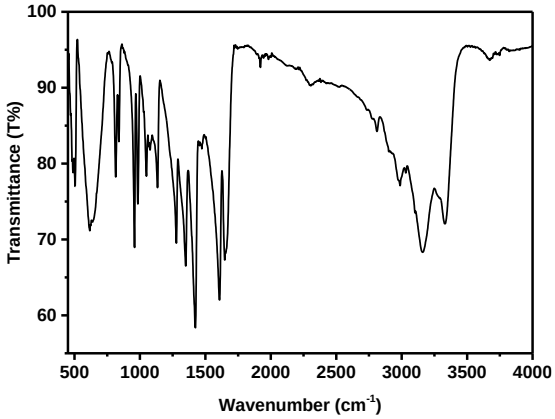


Figure 7. *FT-IR Spectrum of Polymer*

-NH_2 protons in polyacrylamide were released at 7.08-7.52 ppm. Signals in the range of 5.56-6.21 ppm come from CH_2 and CH protons[9].

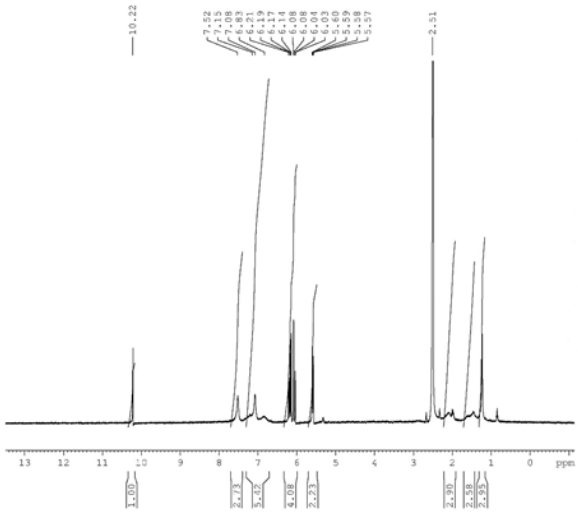


Figure 8. *^{1}H-NMR Spectrum of polymer*

The peaks of the catalyst at 224.95 cm^{-1}, 292.86 cm^{-1}, 409.43 cm^{-1}, 494.65 cm^{-1} are caused by magnetic iron oxide. The peaks at 609,90 cm^{-1} and 1316,39 cm^{-1} are caused by the stress of Fe – O. These peaks can be assigned to the visible raman peak of the HRP [10]. In the raman spectrum of PAA, C – H band at 1240,13 cm^{-1} and the peak C – N stretch at 1417,71 cm^{-1}. The peak at 1572,38 cm^{-1} is thought to come from the NH_2 bending (amide II) band [11].

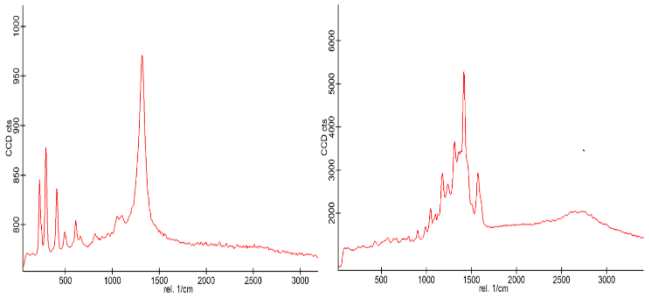


Figure 9. *(a) Raman Spectrum of Magnetic Nanocatalyst, (b) Raman Spectrum of Polymer*

4. Conclusion

In this study, synthesis, characterization and use of magnetic Fe_3O_4 supported nanocatalysts in polymer synthesis have been investigated. Magnetic nanoparticles immobilized with HRP were used for polymerization reaction of acrylamide in the presence of H_2O_2. After the used catalysts were recovered and washed with water to remove the substrate and products. The reusability of the immobilized enzyme was investigated. With this method, the catalyst easily recovered by magnetic separation. The catalyst with include HRP enzyme has been reused 16 times. The white polyacrylamide has been successfully synthesized by using the water as the solvent. The resulting white polymer has a molecular weight of 14500 g/mol.

References:

[1] KUMBUL, A., GOKTURK, E., TURAC, E. AND SAHMETLİOGLU, E., Enzymatic oxidative polymerization of para-imine functionalized phenol catalyzed by horseradish peroxidase. Polymers for Advanced Technologies, 26(9), 1123–1129, (2015).
[2] KUMBUL, A., GOKTURK, E. AND SAHMETLİOGLU, E.,Synthesis, characterization, thermal stability and electrochemical properties of

ortho-imine-functionalized oligophenol via enzymatic oxidative polycondensation. Journal of Polymer Research, 23(3), 16-22 (2016).

[3] CHANG, Q., TANG H., Immobilization of Horseradish Peroxidase on NH2-Modified Magnetic Fe3O4/SiO2 Particles and Its Application in Removal of 2,4-Dichlorophenol, Molecules 2014, 19, 15768-15782.

[4]VANDAMME, EJ., 1983. Peptide antibiotic production through immobilized biocatalyst technology. Enzyme and Microbial Technology, 5(6), 403–415.

[5]CHOGHAMARANİ, A. G., GHASEMİ, B., SAFARİ, Z., AZADİ, G., 2014. Schiff base complex coated Fe_3O_4 nanoparticles: a highly reusable nanocatalyst for the selective oxidation of sulfides and oxidative coupling of thiols. Catalysis Communications.

[6] H.J., KİM, Y., SUMA, S.H., LEE, J., KİM, H.S., KİM, 2012. Journal of Molecular Catalysis B: Enzymatic, 83, 8-15.

[7]HUİJUN, W., MAO, P., JUN, Z., PENG, L., 2008. Encapsulation of silica nanoparticles by redox-initiated graft polymerization from the surface of silica nanoparticles. Journal of Colloid and Interface Science, 326(1), 151-157.

[8]VAN DER MAAS, J.H., 1969. Basic infrared spectoscopy, 2. Heyden & Son Limited, London.
Demchenko, O., Zheltonozhskaya, T., Turov, A., Tsapka, M., Syromyatnikov, V., 2005.

[9]Poly(vinylalcohol)-graft-polyacrylamide with different grafts numbe and lengt has studied by ^{1}HNMR spectroscopy. Molecular Crystals and Liquid Crystals, 427, 225–233.

[10]HASHİMOTO, S., TATSUNO, Y., KİTAGAWA, T., 1984. 88. Resonance Raman Evidence for the Presence o f the FeIV = 0 Bond in Horseradish Peroxidase Compound II. Proceedings of the Japan Academy, 60, 345-348.

[11]GUPTA, M.K., BANSİL, R., 1981. Laser raman spectroscopy of polyacrylamide. Journal of Polymer Science: Polymer Physics Edition, 19(2), 353-360.

6th International Conference on Materials Science and Nanotechnology For Next Generation (MSNG2019)
October 16-18, 2019, Niğde, TURKEY (ORAL FULL TEXT)

A New Electrospun Material for Photocatalytic, SERS and Antibacterial Applications

Sultan KARAGOZ [a*], N. Burak KİREMİTLER [a,b], Menekse SAKİR [a], Samaa SALEM [a,c], M. Serdar ONSES [a,b], Ertugrul SAHMETLİOGLU [a,d], Ahmet CEYLAN [c], Erkan YİLMAZ [a,c,e]

[a]ERNAM - Erciyes University Nanotechnology Application and Research Center, Kayseri 38039, Turkey
[b]Department of Materials Science and Engineering, Faculty of Engineering, Erciyes University, Kayseri 38039, Turkey
[c]Faculty of Pharmacy, Erciyes University, Kayseri 38039, Turkey
[d]Safiye Cikrikcioglu Vocational School, Kayseri University, Kayseri 38039, Turkey
[e]Technology Research & Application Center (TAUM), Erciyes University, Kayseri 38090, Turkey

In this study, multifunctional Ag and TiO_2 modified polycaprolactone (PCL) electrospun nanofiber (NF) mats were fabricated by one-step electrospinning. It was exploited for three different purposes (i) reusable SERS substrate for quantitative analysis to trace organic pollutants, (ii) photocatalyst for degradation of organic pollutants and (iii) antibacterial agent for killing of bacteria. Three different nanofiber patterns, PCL, PCL-TiO_2, PCL/TiO_2-Ag NFs were fabricated and further investigated. The detailed morphological and structural characterizations of the PCL/TiO_2-Ag NFs samples were performed by scanning electron microscope (SEM), X-ray diffraction spectroscopy (XRD), fourier transform infrared spectroscopy (FT-IR) techniques, UV-Vis spectroscopy and Surface enhanced Raman scattering (SERS).

Keywords: Electrospinning, nanofibers, SERS, photocatalytic degradation, antibacterial agent.
Corresponding author: sultan.krgz88@gmail.com

1. Introduction

In recent years, with increasing industrialization and the world's population, water pollution has become one of the most important issues for the environment. With the use of new technologies, economic and renewable energy resources that necessitate less energy and time are required. For this reason, it is of vital importance to develop more effective and economical approaches to the synthesis of materials and to provide effective solution methods. Due to modern industrialization and frequent water pollution problems, there is increasing demand for cost-effective techniques for the detection and production of multifunctional nanomaterials, as well as degradation of organic pollutants in wastewater.

Effective and economic approaches have been developed for the removal of environmental pollutants that harm living organisms such as organic pollutants and heavy metal ions [1]. Recently, a green chemical pathway photocatalysis is applied for the degradation of hazardous organic chemicals to water, carbon dioxide, and simple mineral acids [2-4]. The photocatalytic system, which offers us sustainable, advanced treatment technology with lower energy consumption, is known as the most effective method in this field.

For this purpose, semiconductor nanostructures emerge as promising building blocks for the development of photocatalyst platforms for environmental improvement due to usability, non-toxic natural and biological/chemical stability [5]. Titanium dioxide (TiO_2) with broad bandgap of ~3.2 eV and ~3.27 eV has been reported to be the most promising photocatalyst due to its fascinating properties low cost, high catalytic stability and relatively high yield [6].

The appropriate noble metal nanoparticles for this intent is silver nanoparticles (AgNPs); it demonstrates enormous surface plasmons (320–450 nm) approached to the adsorption bandgap of TiO_2 [7]. As a result, TiO_2 functionalized AgNPs has the highest ability to enhance the substrate photocatalytic efficiency. In addition, Ag NPs was also chosen due to its extraordinary properties includes the non-toxicity, chemically stable and low-cost as well as its well-known ability as an antibacterial agent, which will add further virtues to the fabricated functionalized scaffold.

Surface-enhanced Raman spectroscopy (SERS) is an ultra-sensitive technique that provides molecular-level information about surface adsorbed molecules. Due to its ability to detect even a single molecule, it has given great hope in recent years to detect organic contaminants such as dye molecules [8,9]. Effectively, the electromagnetic enhancement of Raman signals will be achieved through utilizing the high-density growth of these metallic nanostructures to generate hot spots, where electromagnetic fields are concentrated.

In this study, the capability of the fabricated NFs mats toward the SERS quantitative measurements and bactericidal attributes were investigated. Intriguingly, the findings inferred that the modified electrospun fiber-based SERS substrate sufficiently; due to their photocatalytic ability, degraded various organic contaminants.

2. Experimental details

The PCL/TiO_2-Ag solution was prepared in 3 steps and nanofiber mats (NFs) were produced using electrospinning method. NFs of PCL/TiO_2-Ag were fabricated by using a commercial electrospinner (Holmarc HO-NFES-040). During the electrospinning process, the following parameters were used: the applied electrical voltage was 18 kV, the distance between collector and needle was 15 cm, and the flow rate kept at 1 $mL \cdot h^{-1}$.

3. Results and discussion:

Uniform NFs without any beads were observed in all the samples (PCL, PCL/TiO_2-Ag NF mats) as confirmed by SEM analyses (Fig. 1). Their average diameters determined by randomly measuring 100 fibers within each sample are pure PCL (307±98 nm) and PCL/TiO_2-Ag (663±266 nm) NFs. As compared to pure PCL (Fig. 1c); PCL/TiO_2-Ag (Fig. 1f) exhibited NFs with larger diameters.

The structural properties of the PCL/TiO_2-Ag nanofibers were explored by XRD analysis (Fig. 2a). Two characteristic main peaks attributed to the semicrystalline hydrophobic biodegradable polymer PCL and ascribed to the diffraction pattern ranged between between 20°–25° (2θ=21.42º and 23.9°) can easiy be observed. For the anatase phase of TiO_2, the characteristic peaks and the corresponding lattice planes were assigned at 25.4° (101), 38.0° (004), 48.2° (200), 54.3° (105), 55.2° (211), 62.9° (204), 69.0° (116), 70.0° (220) and 75.1° (215); and rutile at 27.5° (110) and 36.2° (103) can be identified. Identification peaks at 37.8° (111) and 54.3° (006) related to Ag NPs also can be distinguished.

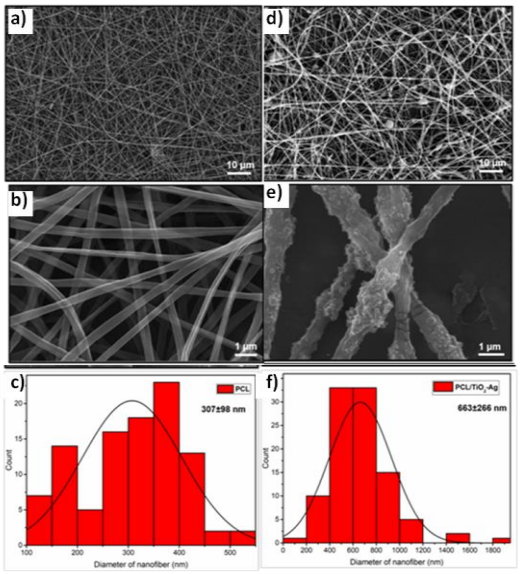


Figure 1: *SEM images and diameter distribution of NFs.*

Figure 2b present the FT-IR spectra of PCL, PCL/TiO_2, PCL-Ag and PCL/TiO_2-Ag NFs. The peaks which appear ~2900 cm^{-1} are attributed to stretching of C-H bonds. The strong band at about 1750 cm^{-1} is related to C=O carbonyl stretching while the band at 1200 cm^{-1} corresponds to C-O stretching in the crystalline phase of the PCL. Ti-O-Ti bond in TiO_2 is identified with peaks ~646 cm^{-1}.

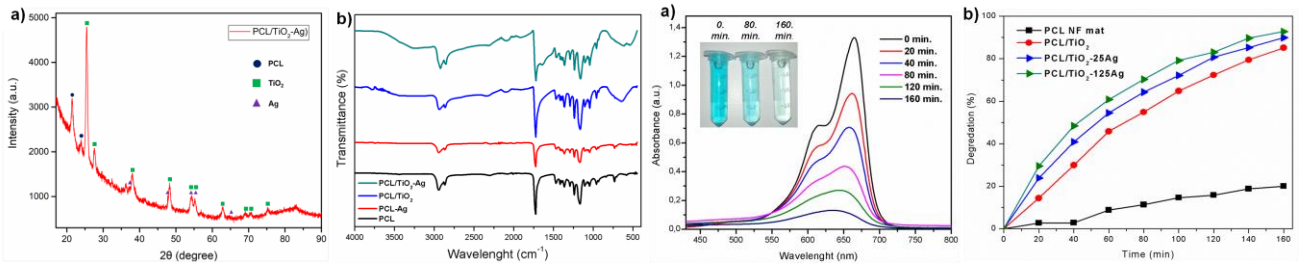


Figure 2: *(a) XRD patterns of PCL/TiO_2-Ag NFs. (b) FT-IR studies of PCL, PCL/TiO_2, PCL-Ag and PCL/TiO_2-Ag NFs.*

The use of PCL/TiO_2-Ag NFs enables detection of the characteristic peaks of MB based on the SERS effect (Fig. 3a). In order to examine the impact of Ag nanoparticle (NP) concentration on the SERS intensity; Raman spectrum of 100 µM MB was obtained by using NFs prepared at different Ag NP loadings (Fig 3b.). The intensity of the SERS spectrum obtained from the NFs containing 25 mg·$mL^{-1}$of Ag^+ ions was higher than the intensity obtained from the NFs containing 12.5 mg·mL^{-1} of Ag^+ ions.

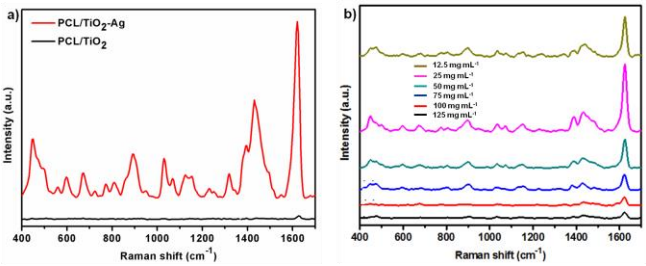


Figure 3: *(a) Comparison of SERS spectra of 1mM of MB obtained from PCL/TiO_2-Ag NF mat (red line) and PCL/TiO_2 NFs mat (black line). (b) SERS spectra of 100 µM of MB obtained from PCL/TiO_2-Ag NF mats prepared with different Ag^+ concentrations.*

Photocatalytic degradation of MB in aqueous solution on PCL/TiO_2 and PCL/TiO_2-Ag NF mats is shown in Fig. 4. Fig 4a shows the UV-vis absorbance of aqueous MB solution (10 mg·L^{-1}) on PCL/TiO_2-125Ag NF mats at different time intervals (0 to 160 min), whereby, the intensity of the characteristic peak of MB, assigned at 644 nm, was decreasing throughout time. As shown in Fig. 4b, the best results were obtained for PCL/TiO_2-Ag NFs mats (125 mg·mL^{-1} of Ag^+) with ~93% photocatalytic degradation in 160 min.

Figure 4: *(a) UV-vis absorbance of aqueous MB solution (b) Graphic of photocatalytic degradation % of MB on pure PCL, PCL/TiO_2 and with different concentration of Ag of PCL/TiO_2-Ag NF mats (t=160 min).*

The in-vitro antibacterial activity of PCL/TiO_2-Ag NFs mats was qualitatively assessed through the presence or absence of inhibition zones. PCL/TiO_2-Ag NF mats showed a promising antibacterial impact against both Escherichia coli and Staphylococcus aureus their respective diameter zones of inhibition of 6.9-7.6 and 8.9-9.2 mm (Fig. 5). In this study, the antibacterial activity of the PCL/TiO_2-Ag NF mats was higher against S. aureus (Gram-positive) than against E. coli (Gram-negative).

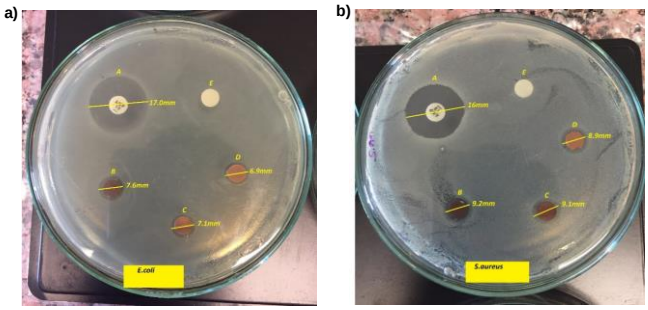


Figure 5: *Zone of inhibition plates treated with PCL/TiO_2-Ag NFs mats containing different Ag-NPs contents. (a) Escherichia coli and (b) Staphylococcus aureus.*

4. Conclusions

The results showed PCL/TiO_2-Ag nanofiber mats can be used as an effective SERS substrate to detect organic pollution at the level of 10nM. The addition of silver nanoparticles increased the photocatalytic properties of TiO_2, thereby achieving high yields. Since Ag NPs increased the photocatalytic performance of TiO_2 NPs, photocatalytic complete degradation of MB occurred within 160 minutes. Nanofiber mats

exhibit antibacterial activity against both *E. coli* and *S. aureu.*

References:

[1] JİANG, L., HUANG, Y., LİU, T., "Enhanced visible-light photocatalytic performance of electrospun carbon-doped TiO2/halloysite nanotube hybrid nanofibers", Journal of colloid and interface science, Vol. 439, pp. 62-68, 2015.

[2] RAVELLİ, D., DONDİ, D., FAGNONİ, M., ALBİNİ, A., "Photocatalysis. A multi-faceted concept for green chemistry", Chemical Society Reviews, Vol. 38(7), pp. 1999-2011, 2009.

[3] MOHAPATRA, D. P., BRAR, S. K., PİCARD, P., TİYAGİ, R. D., "Preparation of a new class of whey-stabilized ZnO nanoparticles for degradation of bisphenol A in water", Science of Advanced Materials, Vol. 5(1), pp. 57-63, 2013.

[4] Lİ S., SHEN, X., LİU, J., ZHANG, L., "Synthesis of Ta3N5/Bi2 MoO6 core–shell fiber-shaped heterojunctions as efficient and easily recyclable photocatalysts", Environmental Science: Nano, Vol. 4(5), pp. 1155-1167, 2017.

[5] LEE, H., KİM, M., SOHN, D., KİM, S. H., OH, S. G., LM, S. S., KİM, I. S., "Electrospun tungsten trioxide nanofibers decorated with palladium oxide nanoparticles exhibiting enhanced photocatalytic activity", RSC Advances, Vol. 7(10), pp. 6108-6113, 2017.

[6] KUMAR, S. G., DEVİ, L. G. "Review on modified TiO2 photocatalysis under UV/visible light: selected results and related mechanisms on interfacial charge carrier transfer dynamics", The Journal of physical chemistry A, Vol. 115(46), pp. 13211-13241, 2011.

[7] BAİ, C., LİU, J. Q., LİU, W. L., REN, M. M., LİU, Q. Z., WANG, X. Q., WU, Y. Z., "Fabrication of hierarchical hollow silica/silver/silica/titania composite particles", Journal of Sol-Gel Science and Technology, Vol. 77(3), pp. 565-573, 2016.

[8] BEJABER, S., PEVELER, W. J., QUESADA-CABRERA, R., CORTES, E., SOTELO-VARQUEZ, C., ABDUL-KARİM, N., PARKİN, I. P., "Photo-induced enhanced Raman spectroscopy for universal ultra-trace detection of explosives, pollutants and biomolecules", Nature communications, Vol. 7, pp. 12189, 2016.

[9] PRAKASH, J., HARRİS, R. A., SWART, H. C., "Embedded plasmonic nanostructures: Synthesis, fundamental aspects and their surface enhanced Raman scattering applications", International Reviews in Physical Chemistry, Vol. 35(3), pp. 353-398, 2016.

6th International Conference on Materials Science and Nanotechnology For Next Generation (MSNG2019)
October 16-18, 2019, Niğde, TURKEY (ORAL FULL TEXT)

Comparison of Structural Properties of Hydroxyapatite and Strontium Apatite Produced by Hydrothermal Method

Turan GURGENC*

* Firat University, Faculty of Technology, Department of Automotive Engineering, Elazig, TURKEY

In this study, pure strontium apatite (SrAp) and hydroxyapatite (HAp) were synthesized at same conditions by hydrothermal method. Hydrothermal treatment was carried out at 180 ^{0}C for 12 hours. The synthesized apatite particles are characterized by X-Ray diffraction (XRD), Fourier transform infrared spectra (FTIR), Field emission scanning electron microscope (FE-SEM) and Energy-dispersive X-ray spectroscopy (EDS). Nanosized hydroxyapatite and pure strontium apatite particles were successfully produced by hydrothermal method. The lattice parameters a, c, volume of unit cell and crystallinity of strontium apatite particles are higher than the hydroxyapatite particles. The hydrothermally synthesized strontium apatite's Sr/P atomic ratio was 1.74 and the hydrothermally synthesized hydroxyapatite's Ca/P atomic ratio was 1.75.

Keywords: Hydroxyapatite, Strontium apatite, Hydrothermal method, Biomaterial.

Corresponding author: tgurgenc@firat.edu.tr

1. Introduction

Calcium phosphate compounds are very interesting in many areas such as medicine, chemistry and biology. The first studies to determine the composition of calcium phosphate compounds were carried out by Berzelius in the first half of the 18th century. A hundred years after this attempt, Hausen introduced the idea of different calcium phosphate phases, and until then, their mixture was called apatite [1]. Among calcium phosphate compounds, hydroxyapatite $Ca_{10}(PO_4)_6(OH)_2$, is the most widely used biocompatible ceramic material. This is because the chemical composition is similar to the mineral phase of the bone and tthermodynamically most stable crystalline phase of calcium phosphate in body fluid, and is therefore highly biocompatible [2]. Naturally occurring calcium phosphates have calcium deficiency and have Ca/P ratios below 1.67 and are generally carbonated. Therefore, synthetically produced hydroxyapatites (HAp) are of great interest due to their high biocompatibility and osteogenic potential [3].

Strontium (Sr) has similar chemical and physical properties as calcium (Ca) and about 98% of the Sr in the total body is found in bone tissues. Sr has special features such as improving the mechanical properties of bone, increasing the proliferation of pre-osteoblastic cells, increasing the formation of bone cells, and therefore, there has been increasing interest in biomedical studies with this element in recent years [4].

Although apatite powders can be produced by many different methods, the main production methods are divided into wet methods and solid state reactions. Wet methods in HAp production can be divided into three as precipitation, hydrolysis of other calcium phosphates and hydrothermal method. Solid state reactions generally give stoichiometric and well crystallized powders, but the process is long, requires high temperatures and heat treatment times. Again, the sintering ability of some powders is generally low. The hydrothermal method has advantages over these methods such as good reproducibility, wide reaction temperature range, good crystallization and process simplicity. Apatites with different morphology, chemical composition and degree of crystallinity can be obtained depending on the production technique [5, 6].

Kuśnieruk et. al. [7], were synthesized nano-hydroxyapatite at different parameters by hydrothermal method. In another study, hydroxyapatite were synthesized with hydrothermal method by using cetyltrimethylammonium bromide and hexamethylenetetramine as additives [8]. Neira et. al. [9], were synthesized hydroxyapatite at different molar concentrations by hydrothermal method. Liu et. al. [10], were synthesized hydroxyapatite at different pH concentrations by hydrothermal method. Pure strontium apatite particles were synthesized by nanoemulsion method [11]. Edwin and Wilson were synthesized strontium apatite at different sonification times by precipitation method [12]. Ma et. al. [13], were synthesized pure strontium apatite particles by precipitation method.

In recent years interest in strontium apatites has been increasing. Again, there are not many studies on the production of pure strontium apatites by hydrothermal method. For this reasons, in present study, it is aimed to compare the structural properties of strontium apatite which has attracted the attention of researchers in recent years with hydroxyapatite which is frequently used as implant material.

In this study, strontium and hydroxyapatite particles were synthesized by hydrothermal method at same conditions. The synthesized particles were characterized by XRD, FT-IR, FE-SEM and EDS. The structural results of the synthesized apatite particles were compared and explained in detail.

2. Experimental details

0.1 M Merck brand $Ca(NO_3)_2.4H_2O$ and Fluka analytical brand 0.06 M $H_9N_2O_4P$ were individually dissolved in 30 ml of water. The two solutions were stirred with magnetic stirrer for 30 minutes. Mixture containing $H_9N_2O_4P$ was added dropwise into the mixture containing $Ca(NO_3)_2.4H_2O$ slowly while stirring continue and was stirred with magnetic stirrer at room temperature for 30 min. The resulting mixture' s pH was adjusted to 10 by adding dropwise ammonia solution while stirring continue. After that the mixture was stirred with magnetic stirrer for 10 min and then ultrasonicated for 30 min. All these were performed at room temperature. Final mixture was dropwise to hydrothermal autoclave, put in to hydrothermal reactor and hydrothermally treated at 180 °C for 12 h. After the slow cooling to room temperature, the solution was filtered and precipitates washed with distilled water a few times and dried at 60 °C for 5 h. After drying, the synthesized particles were ground in a mortar and the synthesized hydroxyapatite was named as HAp. The strontium apatite particles were synthesized in the same procedure, using only Acros organics brand strontium nitrate ($Sr(NO_3)_2$) instead of $Ca(NO_3)_2.4H_2O$. Phase analysis of the synthesized apatite particles were determined by X-ray diffraction using Rigaku D/Max 2200 with a Cu Kα (target) radiation (λ = 1.5406Å) and the scan range from 2θ = 2 to 80° (scan rate: 6°/min.) under 25 mA and 35 kV current. The functional groups of the synthesized apatite particles were analyzed by Fourier transform infrared spectroscopy with a scan range from 4000 cm^{-1} to 400 cm^{-1}.

The lattice parameters of synthesized apatite particles were calculated from (0 0 2) and (3 0 0) peaks using Equation (1) for hexagonal structure (a=b and c) [14, 15]:

$$\frac{1}{d^2} = \frac{4}{3}\left(\frac{h^2 + hk + k^2}{a^2}\right) + \frac{l^2}{c^2} \quad (1)$$

where d is the distance for two adjacent planes and h, k and l are the Miller indices. The volumes of unit cells (V) were calculated from following relation [14, 15]:

$$V = 0.866\, a^2 c \quad (2)$$

where a and c is lattice parameters. The crystallinity degree of synthesized strontium apatite particles (X_C) were calculated from Equation 3 [16]:

$$X_C = 1 - \frac{V_{112/300}}{I_{300}} \quad (3)$$

where $V_{112/300}$ is the intensity of the hollow between (112) and (300) planes and I_{300} is the intensity of the (300) plane.

3. Results and discussion

In Figure 1, FT-IR spectra of synthesized apatite particles are shown. Synthesized particles absorption bands correspond to absorbed water of apatite, carbonate group, vibrations of phosphate group, hydrogen phosphate group and OH group. The peak at 457 cm^{-1} in SrAp and the peak at 473 cm^{-1} in HAp correspond to υ_4 bending vibration of phosphate (PO_4^{3-}) [17]. Also the peak from about 555 to about 592 cm^{-1} in SrAp and the peak from about 563 to about 600 cm^{-1} in HAp correspond to same PO_4^{3-} vibration [18, 19]. The band observed at 623 cm^{-1} in SrAp and the band observed at 631 cm^{-1}

in HAP are ascribed to OH^- ions [18, 19]. The peak at 870 cm^{-1} in SrAp and 875 cm^{-1} in HAp correspond to HPO_4^{2} [4]. The peak at 949 cm^{-1} in SrAp and 962 cm^{-1} in HAp correspond to υ_1 bending vibration of PO_4^{3-} [19]. The peaks observed from about 1010 to about 1078 cm^{-1} in SrAp correspond to υ_3 stretching vibration of PO_4^{3-}. Same PO_4^{3-} vibration also observed at from about 1024 to about 1090 cm^{-1} in SrAp [18, 19]. The peak at 1438 cm^{-1} in SrAp and 1441 cm^{-1} in HAp correspond to CO_3^{2-} [4, 18]. The broad band stretching from about 2500-3700 cm^{-1} in SrAp and stretching from about 2700-3600 cm^{-1} in HAp correspond to H_2O molecules in the apatite particles. The peak at 1600 cm^{-1} in SrAp and 1651 cm^{-1} in HAp correspond to H_2O molecules in the apatite particles [4, 17].

The XRD results of synthesized particles are seen in Figure 2. The diffraction peaks of hydrothermally synthesized SrAp are identical with standard ASTM data-card 33-1348 and the diffraction peaks of hydrothermally synthesized HAp samples are identical with standard ASTM data-card 09-032. Also the XRD results are in good agreement with previous literature studies [13, 17]. The diffraction peaks of HAp shifted to higher 2θ values than SrAp. The reason for this is that Sr' s ionic radius (1.13 Å) is higher than Ca (0.99 Å) [18]. The lattice parameters, volume of unit cells and crystallinity of the samples are given in Table 1. As it seen, the lattice parameters a, c, volume of unit cell and crystallinity of SrAp are higher than the HAp. This is thought to be due to the high atomic radius of Sr, as mentioned above [17, 18]. FE-SEM images of the apatite particles are shown in Fig. 3. The synthesized particles size is in nanoscale range. Hydrothermally synthesized SrAp particles are in rod like form and HAp particles are almost spherical. According to the EDS analysis, Sr/P and Ca/P atomic ratios of SrAp and HAp samples were 1.74 and 1.75, respectively.

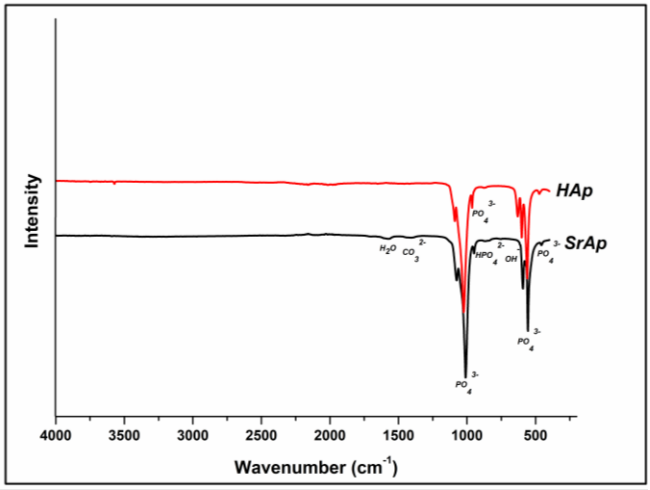


Figure 1. *FT-IR spectra of synthesized apatites.*

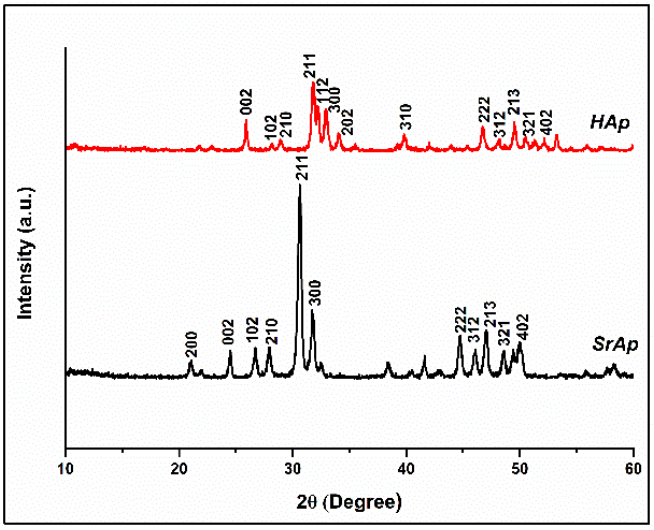
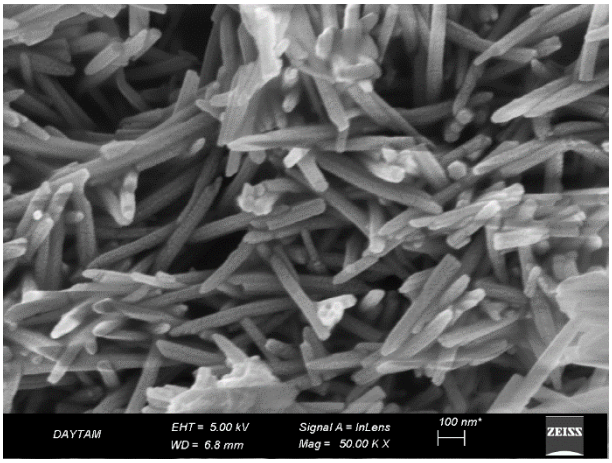


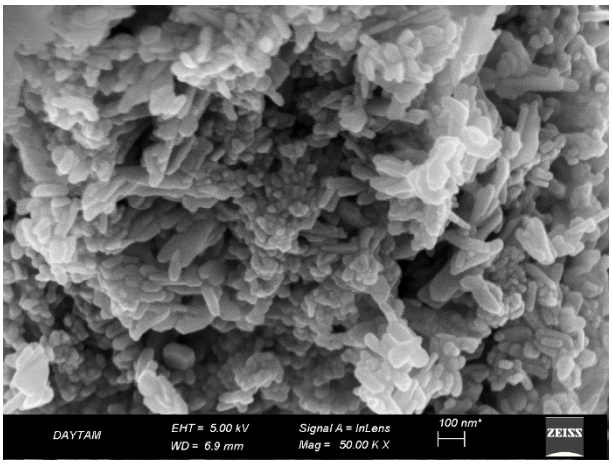
Figure 2. *XRD results of synthesized apatites.*

Table 1. *The lattice parameters, volume of unit cells and crystallinity of the samples*

Sample	a (nm)	c (nm)	V (nm^3)	X_C
SrAp	0.9758	0.7255	0.5982	0.864
HAp	0.9412	0.6870	0.5269	0.773



a)



b)

Figure 3. *FE-SEM images of synthesized particles a) SrAp and b) HAp.*

4. Conclusion

Nano sized pure strontium apatite and hydroxyapatite were successfully synthesized with hydrothermal method. The characteristic XRD peaks of hydroxyapatite appeared to higher 2θ values than SrAp. Atomic radius size is effective on crystal parameters. The nano sized strontium apatite particles are in rod like form and the nano sized hydroxyapatite particles are almost spherical. The Sr/P and Ca/P atomic ratios of apatite particles are close to stoichiometric ratio of apatite. The synthesized nanoparticles may find use as implant material.

References:

[1] KOUTSOPOULOS S., "Synthesis and characterization of hydroxyapatite crystals: a review study on the analytical methods", Journal of Biomedical Materials Research: An Official Journal of The Society for Biomaterials, The Japanese Society for Biomaterials, and The Australian Society for Biomaterials and the Korean Society for Biomaterials. 2002; 62, No. 4: 600-612.

[2] FARZADI A., BAKHSHI F., SOLATI-HASHJIN M., ASADI-EYDIVAND M., ABU OSMAN N. A., "Magnesium incorporated hydroxyapatite: Synthesis and structural properties characterization", Ceramics International. 2014; 40, No. 4: 6021-6029.

[3] SADAT-SHOJAI M., KHORASANI M.-T., DINPANAH-KHOSHDARGI E., JAMSHIDI A., "Synthesis methods for nanosized hydroxyapatite with diverse structures", Acta biomaterialia. 2013; 9, No. 8: 7591-7621.

[4] RAVI N. D., BALU R., SAMPATH KUMAR T., "Strontium-substituted calcium deficient hydroxyapatite nanoparticles: Synthesis, characterization, and antibacterial properties", Journal of the American Ceramic Society. 2012; 95, No. 9: 2700-2708.

[5] MOBASHERPOUR, I., HESHAJIN, M. S., KAZEMZADEH, A., ZAKERI M., "Synthesis of nanocrystalline hydroxyapatite by using precipitation method", Journal of Alloys and Compounds. 2007; 430, No. 1-2: 330-333.

[6] JIN, X., ZHUANG, J., ZHANG, Z., GUO, H., TAN, J., "Hydrothermal synthesis of hydroxyapatite nanorods in the presence of sodium citrate and its aqueous colloidal stability evaluation in neutral pH", Journal of colloid and interface science. 2015; 443, No. 125-130.

[7] KUŚNIERUK, S., WOJNAROWICZ, J., CHODARA, A., CHUDOBA, T., GIERLOTKA, S., LOJKOWSKI, W., "Influence of hydrothermal synthesis parameters on the properties of hydroxyapatite nanoparticles", Beilstein journal of nanotechnology. 2016; 7, No. 1: 1586-1601.

[8] ORTIZ, G. M. H., PARRA, R., FANOVICH, M. A., "Comparative hydrothermal synthesis of hydroxyapatite by using cetyltrimethylammonium bromide and hexamethylenetetramine as additives", Ceramics International. 2018; 44, No. 4: 3658-3663.

[9] NEIRA, I. S., KOLEN'KO, Y. V., LEBEDEV, O. I., VAN TENDELOO, G., GUPTA, H. S., GUITIÁN, F., YOSHIMURA, M., "An effective morphology control of hydroxyapatite crystals via hydrothermal synthesis", crystal growth and design. 2008; 9, No. 1: 466-474.

[10] LIU, J., YE, X., WANG, H., ZHU, M., WANG, B., YAN, H., "The influence of pH and temperature on the morphology of hydroxyapatite synthesized by hydrothermal method", Ceramics international. 2003; 29, No. 6: 629-633.
[11] PREKAJSKI, M., MIRKOVIĆ, M., TODOROVIĆ, B., MATKOVIĆ, A., MARINOVIĆ-CINCOVIĆ, M., LUKOVIĆ, J., MATOVIĆ, B., "Ouzo effect—New simple nanoemulsion method for synthesis of strontium hydroxyapatite nanospheres", Journal of the European Ceramic Society. 2016; 36, No. 5: 1293-1298.
[12] NIMMY, E., WILSON, P., "Investigations on sonofragmentation of hydroxyapatite crystals as a function of strontium incorporation", Ultrasonics sonochemistry. 2019; 50, No. 188-199.
[13] MA, X., LIU, Y., ZHU, B., "Synthesis and characterization of pure strontium apatite particles and nanoporous scaffold prepared by dextrose-templated method", Materials Research Express. 2018; 5, No. 2: 025002.
[14] CULLITY, B., "Elements of X-ray Diffraction, Addison-Wesely", Reading, MA, USA. 1978.
[15] BADRAN, H., YAHIA, I., HAMDY, M. S., AWWAD, N., "Lithium-doped hydroxyapatite nano-composites: synthesis, characterization, gamma attenuation coefficient and dielectric properties", Radiation Physics and Chemistry. 2017; 130, No. 85-91.
[16] LANDI, E., TAMPIERI, A., CELOTTI, G., SPRIO, S., "Densification behaviour and mechanisms of synthetic hydroxyapatites", Journal of the European Ceramic Society. 2000; 20, No. 14-15: 2377-2387.
[17] STANIĆ, V., JANAĆKOVIĆ, D., DIMITRIJEVIĆ, S., TANASKOVIĆ, S. B., MITRIĆ, M., PAVLOVIĆ, M. S., KRSTIĆ, A., JOVANOVIĆ, D., RAIČEVIĆ, S., "Synthesis of antimicrobial monophase silver-doped hydroxyapatite nanopowders for bone tissue engineering", Applied Surface Science. 2011; 257, No. 9: 4510-4518.
[18] GENG, Z., CUI, Z., LI, Z., ZHU, S., LIANG, Y., LIU, Y., LI, X., HE, X., YU, X., WANG, R., "Strontium incorporation to optimize the antibacterial and biological characteristics of silver-substituted hydroxyapatite coating", Materials Science and Engineering: C. 2016; 58, No. 467-477.
[19] NASKER, P., MUKHERJEE, M., KANT, S., TRIPATHY, S., SINHA, A., DAS, M., "Fluorine substituted nano hydroxyapatite: Synthesis, bio-activity and antibacterial response study", Ceramics International. 2018; 44, No. 17: 22008-22013.

6th International Conference on Materials Science and Nanotechnology For Next Generation (MSNG2019)
October 16-18, 2019, Niğde, TURKEY (ORAL FULL TEXT)

Optical Measurement (UV) Results of Zinc Oxide (ZnO) and Cadmium Oxide (CdO) Nano Powders Produced by Chemical Precipitation Method.

Fehmi ASLAN[1], Hikmet ESEN[1] and Fahrettin YAKUPHANOGLU[2]

[1]Department of Energy Systems Engineering, Firat University, Turkey
[1]Department of Energy Systems Engineering, Firat University, Turkey,
[2]Department of Physics, Firat University, Turkey,

Abstract

The changes of transmittance and absorbance of ZnO and CdO nano powders produced by chemical precipitation method according to different wavelengths were investigated. The mean transmittance values of the semiconductor metal oxides in the visible region were calculated as approximately 88% and 80% for ZnO and CdO, respectively. From the transmittance spectra of the produced nano powders, it was seen that there were sudden increases up to 90% in wavelengths between 400-500 nm. Absorbance plots of nano powders, significant scattering was not observed at 400 nm as the lower wavelength. After 350 nm wavelength, the absorption was found to be reduced. The optical band ranges of ZnO and CdO powder samples produced in this study were found to be 3.07 and 2.31 eV, respectively.

Keywords: Zinc oxide (ZnO), Cadmium oxide (CdO), Nano powder, Optical properties

Corresponding authors: faslan558@gmail.com

1. Introduction

Metal oxide semiconductor nano powders have a wide range of applications such as electronics, optics and optoelectronics. Among the nanostructured materials, zinc oxide (ZnO), cadmium oxide (CdO) and titanium dioxide (TiO2) are among the most important metal oxides. The superior electrical and optical properties of these semiconductors can be improved to the desired level thanks to organic semiconductors to be added to the structure from the outside [1].

Zinc oxide (ZnO) is a very popular material due to its excellent electro-optical properties such as wide band range (~ 3.3 eV), large excitatory binding energy (60 meV), apparent range transparency and no toxic effect. ZnO's excellent electro-optical properties and easily adjustable morphological structure make this semiconductor metal oxide important for solar cell and sensor applications [2]. Zinc oxide (ZnO) ln, Mg and Er by adding various elements such as electrical properties can be changed. Zinc oxide (ZnO) is also considered as a metal oxide material attached between metal and semiconductor [3, 4]. Scientists use ZnO thin films produced by various techniques or doping as the interface material between semiconductor and metal [5, 6]. There are many techniques for obtaining ZnO thin film layer such as atomic layer doposition [7], spray pyrolysis [8], spin coating, drop casting [9] and SILAR technique [10]. Among these techniques, spin coating technique is the cheapest and simplest technique to make a good thin film [11].

Thin films produced with cadmium oxide have an important place in the production of

optoelectronic devices due to their excellent optical transmittance and wide band gap [12]. CdO metal oxide semiconductor is used extensively in phototransistor, photodiode, solar cell and gas sensor applications [13, 14]. A device having excellent electrical properties and transmittance can be produced using a semiconductor metal oxide with a wide optical band range. Cadmium oxide is known to have a low band gap (approximately 2.2 eV). This low bandwidth can be increased by doping externally [15]. Thin films formed using CdO nano powders are produced using drop casting, spray pyrolysis, chemical vapor deposition and chemical bath deposition methods [16].

Experimental details

In this study, chemical precipitation method was used in the production of metal oxide nano powders. The synthesis was performed with the Fytronix nano particle production system shown in Fig. 1. Nano powders were obtained by passing the acetate salts through some processes. In order to obtain the ZnO paticules, zinc acetate was taken in a specific amount and dissolved in 125 ml of methanol to a gel position to form a 0.1 molar solution. NaOH was dissolved in 65 ml of methanol to form a gel to form a 0.4 molar base solution. The two solutions obtained were placed in a beaker and stirred for 10 minutes with the aid of a magnetic stirrer. This mixture was centrifuged at 5000 rmp for 5 minutes. The resulting precipitate was washed three times with methanol. This precipitate was dried on a heating plate at 50 ° C for 1 hour and then fired in a laboratory oven at 400 ° C for 1 hour.

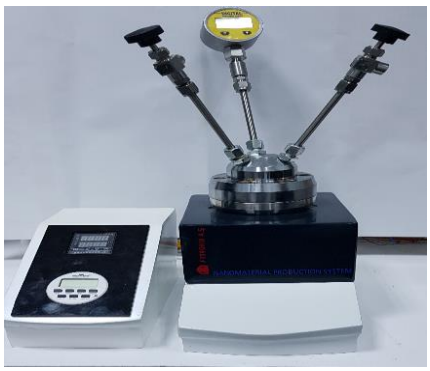


Figure 1. *Nono powder production device designed by FYTRONIX.*

Zinc esatate was taken in a certain amount to obtain the CdO paticules and dissolved in 125 ml of methanol until the gel position to form a 0.1 molar solution. NaOH was dissolved in 65 ml of methanol to form a gel to form a 0.4 molar base solution. the resulting two solutions were placed in a beaker and stirred for 10 minutes with the aid of a magnetic stirrer. This mixture was centrifuged at 5000 rmp for 5 minutes. The resulting precipitate was washed three times with methanol. This precipitate was dried on a heating plate at 50 ° C for 1 hour and then fired in a laboratory oven at 400 ° C for 1 hour.

Optical characterization of the produced powders was performed with UV 1200 Spectrophotometer.

3. Results and discussion:

The variation of the tranmittance and absorbance of the produced nano powders according to different wavelengths is shown in Fig. 2(a-b) and Fig. 3(a-b). The mean tranmittance values of the semiconductor metal oxides in the visible region were calculated as approximately 88 % and 80 % for ZnO and CdO, respectively. From the transmittance values of the produced nano powders shown in Fig. 2(b) and Fig. 4(b). It is seen that there are sudden increases up to 90 % in wavelengths between 400-500 nm. The transmittance values of synthesized nano powders affect parameters such as crystallinity, porosity, thickness and surface roughness of the structure [17]. The transmittance values of nano-powders produced are consistent with the current literature [16, 18, 19]. No significant scattering was observed at the lower wavelengths, such as 400 nm, from the absorbance graphs of the nano powders given in Fig. 2(a) and Fig. 4(a). After 350 nm wavelength, the absorption was found to be reduced. Diffuse reflection spectroscopy was used to determine the forbidden energy (Eg) ranges of the synthesized nanoparticles. This method provides information about the absorption properties of thin films. The reflectance values of the produced powders were determined by the following equation with the help of Kubelka-Munk function [20, 21].

$$F(R) = \frac{(1-R)^2}{2R} \quad (1)$$

Wherein R is diffuse reflection, F (R) represents the absorbance corresponding Kubelka-Munk function. F(R) values in the equation are converted to linear absorption coefficient [22, 23].

Optical transitions of semiconductor materials are characterized as direct and indirect passages. The absorption coefficient (α) of the semiconductor materials produced is used to determine the band structure and the forbidden energy range. The relationship between the absorption coefficient (α) and photon energy (hυ) was calculated using the following equation [24]:

$$(\alpha h\upsilon) = \left(\frac{F(R)h\upsilon}{t}\right) = B\left(h\upsilon - E_g\right)^n \quad (2)$$

Here α represents the absorption coefficient, Eg band gap energy, hυ photon energy. Direct optical band ranges were

determined from (hυ) versus $(\alpha h\upsilon)^2$ curves of the samples given in Fig. 3 and Fig. 5. The optical band ranges of ZnO and CdO powder samples produced in this study were found to be 3.07 and 2.31 eV, respectively. The forbidden energy ranges found correspond to previous literature studies [16, 18, 22].

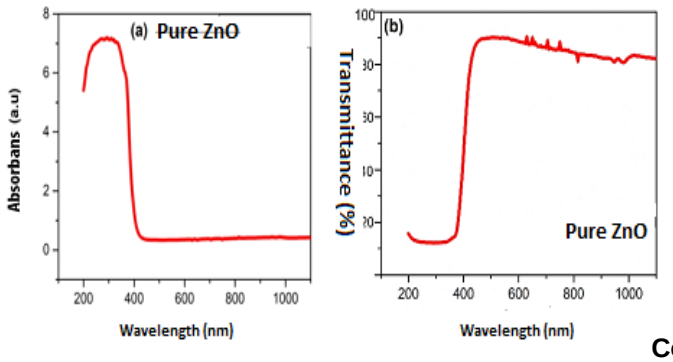


Figure 2. *ZnO nano powder a) absorption b) transmittance spectrum.*

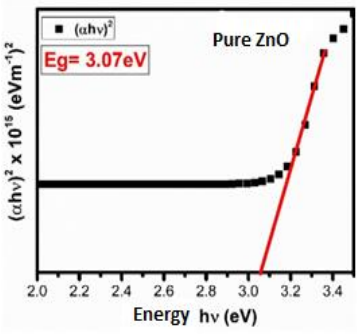


Figure 3. *Energy-band gap graph of ZnO nano powder.*

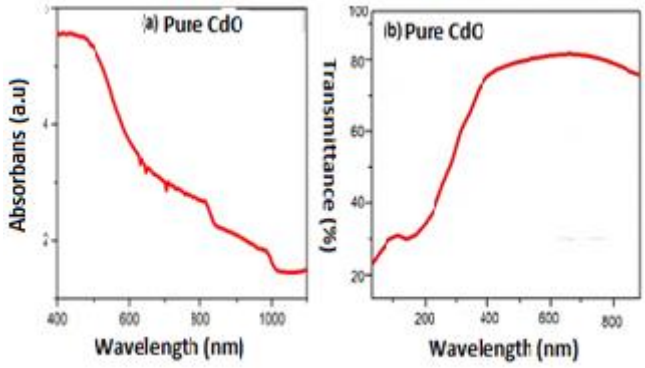


Figure 4. *CdO nano powder a) absorption b) transmittance spectrum.*

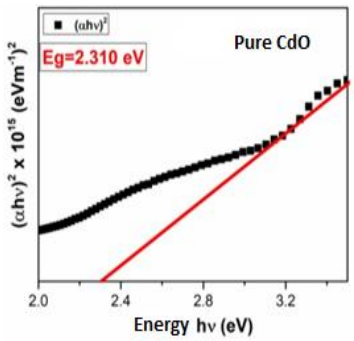


Figure 5. *Energy-band gap graph of CdO nano powder.*

Conclusions

In this study, optical measurement (UV) results showed that the produced nono powders are of high quality. The calculated transmittance, absorbance and forbidden energy range values of ZnO and CdO nano powders obtained by precipitation method confirmed that these samples are suitable for optical device and thin film applications.

References:

[1] ASLAN F, Esen H, Yakuphanoglu F (2019) Electrical and fotoconducting characterization of Al/coumarin:ZnO/Al novel organic-inorganic hybrid photodiodes. J Alloys Compd 789:595–

606. https://doi.org/10.1016/j.jallcom.2019.03.090

[2] KAHRAMAN S, Çakmak HM, Çetinkaya S, et al (2013) The effects of coumarin additive on the properties of ZnO nanostructures. J Phys Chem Solids. https://doi.org/10.1016/j.jpcs.2012.12.005

[3] GOZEH BA, Karabulut A, Yildiz A, Yakuphanoglu F (2018) Solar light responsive ZnO nanoparticles adjusted using Cd and La Co-dopant photodetector. J Alloys Compd. https://doi.org/10.1016/j.jallcom.2017.10.167

[4] NAM Y, Hwang I, Oh S, et al (2013) Switchable Schottky diode characteristics induced by electroforming process in Mn-doped ZnO thin films. Appl Phys Lett. https://doi.org/10.1063/1.4803088

[5] SINGH SK, Hazra P, Tripathi S, Chakrabarti P (2016) Performance analysis of RF-sputtered ZnO/Si heterojunction UV photodetectors with high photo-responsivity. Superlattices Microstruct. https://doi.org/10.1016/j.spmi.2015.12.036

[6] EL-ATAB N, Alqatari S, Oruc FB, et al (2013) Diode behavior in ultra-thin low temperature ALD grown zinc-oxide on silicon. AIP Adv. https://doi.org/10.1063/1.4826583

[7] ORAK I, Kocyigit A, Alindal S (2017) Electrical and dielectric characterization of Au/ZnO/n-Si device depending frequency and voltage. Chinese Phys B. https://doi.org/10.1088/1674-1056/26/2/028102

[8] AYDOĞAN Ş, Grilli ML, Yilmaz M, et al (2017) A facile growth of spray based ZnO films and device performance investigation for Schottky diodes: Determination of interface state density distribution. J Alloys Compd 708:55–66. https://doi.org/10.1016/j.jallcom.2017.02.198

[9] BAIK DG, Cho SM Application of sol-gel derived ®lms for ZnO/n-Si junction solar cells

[10] RAIDOU A, Lharch M, Nouneh K, et al (2014) Effect of substrate on ZnO thin films grown by SILAR method. In: Proceedings of 2014 International Renewable and Sustainable Energy Conference, IRSEC 2014

[11] YILMAZ M, Caldiran Z, Deniz AR, et al (2015) Preparation and characterization of sol–gel-derived n-ZnO thin film for Schottky diode application. Appl Phys A Mater Sci Process. https://doi.org/10.1007/s00339-015-8987-5

[12] ORTEGA M, Santana G, Morales-Acevedo A (2000) Optoelectronic properties of CdO/Si photodetectors. Solid State Electron 44:1765–1769. https://doi.org/10.1016/S0038-1101(00)00123-4

[13] ISMAIl RA, Al-Samarai AME, Mohmed SJ, Ahmed HH (2013) Characteristics of nanostructured CdO/Si heterojunction photodetector synthesized by CBD. Solid State Electron 82:115–121. https://doi.org/10.1016/j.sse.2013.02.035

[14] NASER GY, Raja WN, Faris AS, et al (2013) Some optical properties of CdO thin films. Energy Procedia 36:42–49. https://doi.org/10.1016/j.egypro.2013.07.006

[15] YAKUPHANOGLU F, Caglar M, Caglar Y, Ilican S (2010) Electrical characterization of nanocluster n-CdO/p-Si heterojunction diode. J Alloys Compd 506:188–193. https://doi.org/10.1016/j.jallcom.2010.06.174

[16] YAKUPHANOGLU F (2011), Synthesis and electro-optic properties of nanosized-boron doped cadmium oxide thin films for solar cell applications. Sol Energy 85:2704–2709. https://doi.org/10.1016/j.solener.2011.08.008

[17] BALAKRISHNAN G, Bandi VR, Rajeswari SM, et al (2013) Effect of oxygen partial pressure on microstructural and optical properties of titanium oxide thin films prepared by pulsed laser deposition. Mater Res Bull 48:1901–1906. https://doi.org/10.1016/j.materresbull.2013.07.009

[18] TEMEL S, Nebİ M, Peker D (2017) Sol-Gel Döndürerek Kaplama Tekniği i le Saydam İletken Zn O İnce Filmlerin Üretilmesi ve Karakterizasyonu. 5:51–59

[19] SARIGUL H, Sorar İ (2016) Sol-Jel Yöntemiyle Hazırlanan TiO2 Filmlerin

Optik ve Elektrokromik Özellikleri. Marmara Fen Bilim Derg 28:81–88. https://doi.org/10.7240/mufbed.14319

[20] ESCOBEDO A. Morales, Mora ES, Pal U (2007) Use of diffuse reflectance spectroscopy for optical characterization of un-supported nanostructures. 53:18–22

[21] YAKUPHANOGLU F, Mehrotra R, Gupta A, Munoz M (2009) Nanofiber organic semiconductors: The effects of nanosize on the electrical charge transport and optical properties of bulk polyanilines. Journal of Applied Polymer Science. journol Appl Polym Sci 114(2).:794–799. https://doi.org/doi:10.1002/app.28535

[22] YAKUPHANOGLU F (2012), Semiconducting and quartz microbalance (QCM) humidity sensor properties of TiO 2 by sol gel calcination method. Solid State Sci 14:673–676. https://doi.org/10.1016/j.solidstatesciences.2012.03.016

[23] YAKUPHANOGLU F (2010), Electrical characterization and device characterization of ZnO microring shaped films by sol-gel method. J Alloys Compd 507:184–189. https://doi.org/10.1016/j.jallcom.2010.07.151

[24] KARTHIK K, Pandian SK, Jaya NV (2010) Effect of nickel doping on structural, optical and electrical properties of TiO2 nanoparticles by sol-gel method. Appl Surf Sci 256:6829–6833. https://doi.org/10.1016/j.apsusc.2010.04.096

Fırat University, Faculty of Engineering, Department of Metallurgical and Materials Engineering, Elazığ, TURKE

6th International Conference on Materials Science and Nanotechnology For Next Generation (MSNG2019)
October 16-18, 2019, Niğde, TURKEY (ORAL FULL TEXT)

On The Frequency-Voltage Dependence Profile of Complex Dielectric, Complex Electric Modulus and Electrical Conductivity in Al/(0.05Gr-PVA)/p-Si Structures at Room Temperature.

Seda KARADAŞ[1]*, Muzaffer BALBAŞI*

* Gazi University, Faculty of Engineering, Department of Chemical Engineering, Ankara, TURKEY

Metal/semiconductor (MS) with and without an interlayer have been intensely studied due to their some very important physical, optical and chemical properties. Al/(0.05Gr-PVA)/p-Si (MS) type structures have been fabricated. The second aim is to get more reliable and accurate results on the real and imaginary parts of complex dielectric parameters, complex electrical modulus, and ac conductivity of the Al/(0.05Gr-PVA)/p-Si (MPS) structure have been investigated in wide range of frequency (5 kHz-5 MHz) and ± 4 V at room temperature by using impedance spectroscopy method including in wide range of C-V and G/ω-V measurements. The real and imaginary parts of complex dielectric parameters (ε′, ε″), complex electrical modulus (M′, M″), and ac electrical conductivity (σ_{ac}) of samples were studied as a function of frequency and voltage at room temperature. It is also found that ε′ and ε″ decrease together with rising frequency whereas M′, M″ and σ_{ac} increase under the same circumstances.

Keywords: Dielectric parameters (ε′,ε″); Electric Modulus; MPS structures; AC conductivity

Submission date:10 September 2019

Acceptance Date: 16 September 2019

Corresponding authors: sedakaradass93@gmail.com

1. Introduction

Metal-semiconductor (MS) contacts/structures with and without an interfacial layer have been much studied due to some important characteristics [1-3]. The investigation their conduction mechanisms (CMs) in wide range of frequency and voltage can be supplied more information both on the electric and dielectric properties conduction of them. Conduction mechanism and their performance are dependent on a lot of factors such as the existence of surface states or dislocation (Nss), native or deposited interlayer, barrier in-homogeneities at M/S interface, series resistance (Rs)[4,5]. In this study, the used poly-vinyl-alcohol (PVA) has high- water solubility, process ability, and high formation capacity [6]. Graphene is also a very new material which is discovered by Geim in 2004 and gain Nobel-prize in 2010 which has excellent electric conductivity and superior mechanical stability [7]. Al/(0.05Gr-PVA)/p-Si (MPS) structures were fabricated and their complex dielectric parameters (ε*=ε′-jε″), complex electrical modulus (M*=M′+jM″), and conductivity were investigated in wide range of frequency and voltage by using C-V-f and G/ω-V-f characteristics.

2. Experimental details

Before the fabrication of the Al/(0.05Gr-PVA)/p-Si/Al (MPS) structures, p-Si wafer was cleaned in the ultrasonic bath using standard cleaning processes. After that high-pure Al (150 nm) layer was grown on the back side of wafer at 10-6 Torr and then was annealed at 450°C to perform ohmic contact. Subsequently, the prepared (0.05Gr-PVA) solution was grown on the wafer by electrospinning technique. Finally, high-pure Al (150 nm) was grown on the interlayer. In order to perform C/G-w measurements, samples were pasted on the copper holder by the help of silver paste. The schematic diagram of the fabricated sample was represented in Fig.1.

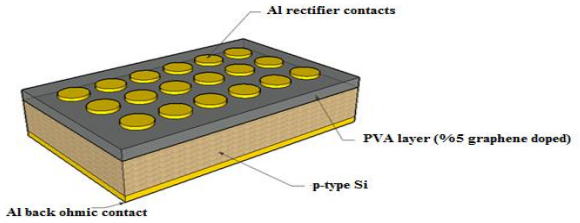


Fig.1: The schematic diagram of the fabricated Al/(0.05Gr-PVA)/p-Si structure

3. Results and discussion:

The frequency and voltage dependent profile of ε' and ε" were obtained by using C-V-f and G/ω-V-f characteristics and represented Fig.2 (a and b) by using following relations:

$$\varepsilon^* = \varepsilon' - j\varepsilon'' = \frac{Cd_i}{A\varepsilon_0} - j\left(\frac{Gd_i}{\omega A\varepsilon_0}\right) = \left(\frac{C}{C_o} - j\frac{G}{\omega C_o}\right) \quad (1)$$

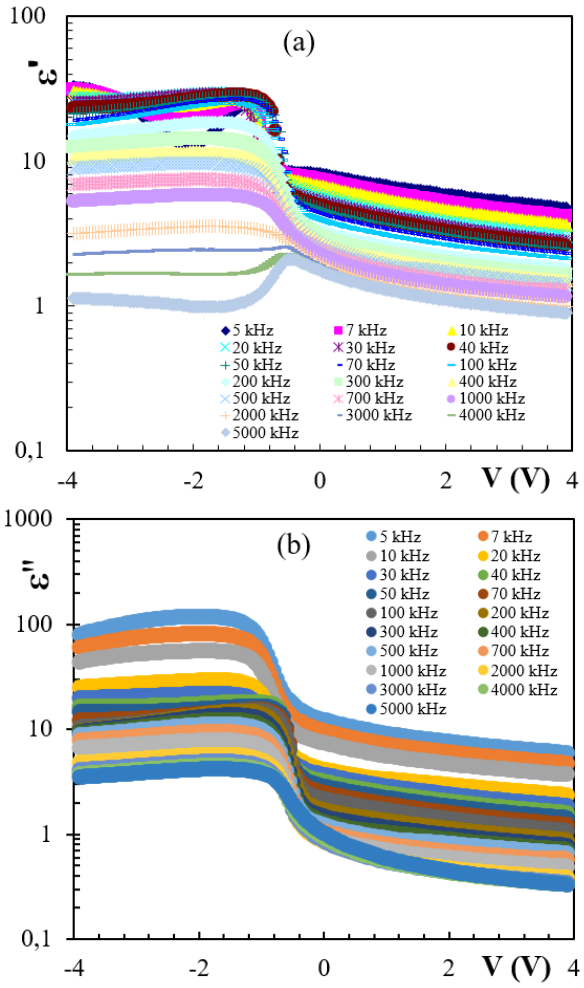


Fig.2: (a) ε'- V (b) ε''-V plots of the Al/(0.05Gr-PVA)/p-Si structure.

Complex electric modulus (M*) were calculated from the values of ε′ and ε″ data as follow:

$$M^* = \frac{\varepsilon'}{\varepsilon'^2 + \varepsilon''^2} + J\frac{\varepsilon''}{\varepsilon'^2 + \varepsilon''^2} \quad (2)$$

M'-V and M"-V plots were calculated Eq. 2 and represented in Fig. 3 (a,b), respectively. . It is clear that both the M' and M" are strong function of frequency and voltage. The observed peak behavior in the M″-V plots are the result of a particular density distribution of N_{ss} and their relaxation times in this region. Because at enough high frequency, charges at traps cannot follow ac signal and similarly dipoles have not enough time to orient in themselves [9,10].

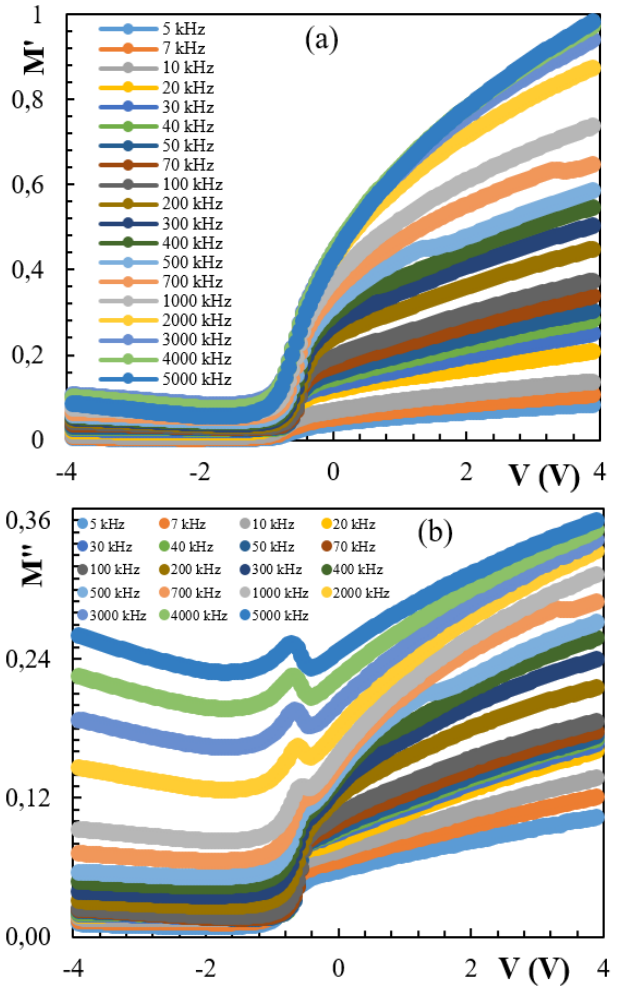


Fig.3: (a)M'-V (b) M"-V plots of the Al/(0.05Gr-PVA)/p-Si

Conclusions

In this study, (MPS) type structures were fabricated on the p-Si wafer and their reel and imaginary components of complex dielectric ($\varepsilon^*=\varepsilon'-j\varepsilon''$), complex electric modulus ($M^*=M'+jM''$), and electrical conductivity have been intensely investigated in wide range of frequency (5 kHz-5MHz) and voltage (± 4 V). In this study, (0.05Gr-PVA) polymer was used an interlayer to increase the values of capacitance and so storage more energy. Both the complex dielectric parameters (ε′, ε″), complex electrical modulus (M′, M″) were found a strong function of frequency and voltage. The obtained value of ε' (=1291) even at 5kHz is 340 times higher than the maximum value of conventional SiO2 and so it can be successfully used instead of insulators which are prepared by traditional methods such as SiO_2, SnO_2, and Si_3N_4.

References:

[1] H.U. Tecimer, M.A. Alper, H. Tecimer, S. Altındal, Integration of Zn-doped organic polymer nanocomposites between metal semiconductor structure to reveal the electrical qualifications of the diodes, Polym. Bull. 75 (2018) 4257-4271.

[2] M.S. Pratap Reddy, L. Jung-Hee, J. Ja-Soon, Frequency dependent series resistance and interface states in Au/bio-organic/n-GaN Schottky structures based on DNA biopolymer, Synth. Met. 185-186 (2013) 167-171.

[3] S. Altındal Yerişkin, M. Balbaşı, İ. Orak, The effects of (graphene doped-PVA) interlayer on the determinative electrical parameters of the Au/n-Si (MS) structures at room temperature, J. Mater. Sci.: Mater. Electron. 28: (2017) 14040–14048.

[4] C.V.S. Reddy, X. Han, Q.Y. Zhu, M.L.Q. Mai, W. Chen, Dielectric spectroscopy studies on (PVP+ PVA) polyblend film, Microelectron. Eng. 83 (2006) 281-285.

[5] A. Buyukbas-Ulusan, S. Altındal-Yerişkin, A. Tataroğlu, Forward and reverse bias current-voltage (I-V) characteristics in the metal-ferroelectric-semiconductor (Au/(SrTiO3)/n-Si) structures at room temperature, J. Mater. Sci.: Mater. Electron. 29 (2018) 16740–16746.

[6] Li Hongling, Jiao Wei, Yanan Ojan, Jianling Zhang, Jian Yu, Guosheng Wang, Colloids and Surfaces A: Physochemical and Engineering Aspects, 449 (2014) 148-156.

[7] KS Novoselov, AK. Geim, SV Morozov, D. Jiang, Y. Zhang, SV Dubonos, Science 306 (2004) 666-669.

[8] Z. Wang, W. Zhou, L. Dong, X. Sui, H. Cai, J. Zuo, Q. Chen, Journal of Alloys and Compounds, 682 (2016) 738-745.

[9] H.Y. Şafak Asar, T. Asar, Ş. Altındal, S. Özçelik, J. Alloys and Compounds, 628 (2015) 442.

[10] M. Popescu, I. Bunget, Physics of Solid Dielectrics, Elsevier, Amsterdam, 1984.

6th International Conference on Materials Science and Nanotechnology For Next Generation (MSNG2019)
October 16-18, 2019, Niğde, TURKEY (ORAL FULL TEXT)

Photoluminescence Properties of Tetra- and Octa-Substituted Double Decker Lu(III) Phthalocyanines

E. Yabaş[1*], P. Başer[2], M. Kul[3]

[1]Advanced Technology Research and Application Center, University of Sivas Cumhuriyet, Sivas, 58140, Turkey

[2]Department of Physics, Science Faculty, University of Sivas Cumhuriyet, Sivas, 58140 Turkey

[3] Sivas Science and Technology University, Sivas, 58140, Turkey

Fluoreccence and photoluminescence properties of tetra and octa-substituted double decker Lu(III) phthalocyanines to which imidazole groups are attached have been investigated under the same conditions. The changes in these properties were examined with increasing number of substituents. Thus, the effect of imidazole groups on the optical properties of double decker Lu(III) phthalocyanines were determined. The photoluminescence spectra of the compounds show indicating the strong π-π interaction along with electron and energy transition between the tetrapyrolic macrocycles.

Keywords: Double-decker phthalocyanine, Photoluminescence, Fluorescence, Optoelectronics

Submission date:
Acceptance Date:

Corresponding authors: yabasebru@gmail.com

1. Introduction

Phthalocyanine with stable π-conjugated system is a synthetic analogue of porphyrin macrocycle. Phthalocyanines are organic semiconductor compounds. The intense blue-green color of phthalocyanines, combined with their thermal and chemical stability, has gained importance in many areas of application. Phthalocyanines with stable π-conjugated systems are of interest in many applications because of their photo-sensitivity, high fluorescence quantum yield, and strong absorption at high wavelengths such as 600-750 nm [1-6]. Phthalocyanines draw interest as materials for optical recording media, nonlinear optical application, light absorption, electric conduction, photoconduction, energy conversion, electrodes, chemical sensors and catalyst [3,7-9]. Phthalocyanines are known for their very poor solubility in many solvents. This property seriously limits potential applications of these compounds. Their solubility can be increase by substituents and metals. The substituted groups may be attached to the phthalocyanine ring at peripheral, non-peripheral or axial positions [1].

Double-decker ftalosiyanin metal complexes, in which two rings of phthalocyanine are coupled by a metal ion, shows high chemical and thermal stability, redox activity and intriguing optical, electrical and magnetic properties [3,10-12]. These properties allow double-decker phthalocyanines to become promising organic molecule candidates for optical materials and devices such as optical logic displays, electrochromic display, photovoltaic cells, and organic light emitting diodes [7,13,14]. Double-decker phthalocyanine complexes, known as stable radicals, with an uncommon electron in the delocalized π- orbital on two phthalocyanine rings, can be formulated as $Ln^{3+}(Pc^{2-})(Pc^{-})$ or $Ln^{3+}(Pc_2)^{3-}$. Strong π-π interactions are observed in such structures [3]. Lanthanide ions are also well known for their particular photoluminescent characters [10,11]. Photoluminescence spectra can be used to obtain information about the optical properties of these compounds [15,16].

It is desirable that organic semiconductor compounds to be used in optoelectronic applications do not exhibit aggregation behavior, have high fluorescence quantum yield, have absorbtion at high wavelengths and have appropriate orbital levels to permit electron transfer [5,17,18].

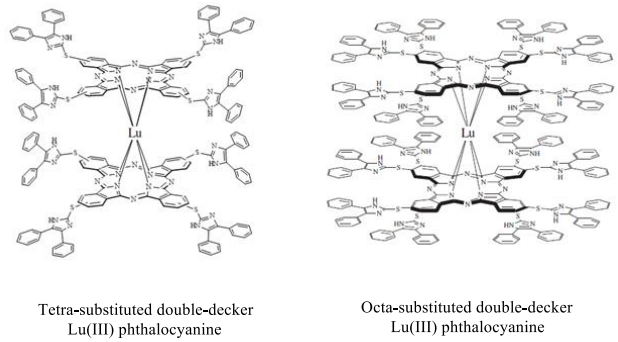
In this work, we examined the photoluminescence (PL) and fluorescence properties of tetra- and octa-substituted double decker Lu(III) phthalocyanine compounds. We have determined that these compounds have the potential to be used in optoelectronic applications.

2. Experimental details

The tetra- [19] and octa-substituted [20] double decker phthalocyanine compounds were prepared according to the literatures (Figure 1). Spectroscopic purity solvents were used in the whole study. Andor-Solis UNIRAM Raman and Fotoluminescence spectrometer was used for PL measurements of thin films. UV-vis spectra were recorded on a Shimadzu UV-1800 UV-vis spectrophotometer. A Shimadzu RF 5301 fluorescence spectrophotometer was used for spectrofluorometric measurements of solutions. Scanning Electron Microscope (SEM) images were taken at Tescan MIRA3 XMU. Thin films of the compounds were prepared by drop casting method. In this method, the compounds were dissolved separately in THF, the solutions were dropped onto the glass surface and allowed to dry.

3. Results and discussion:

The phthalocyanine compounds used in this study are tetra- and octa-substituted double decker phthalocyanine compounds whose molecular structures are shown in Figure 1. Photoluminescence and fluorescence properties of these compounds were investigated and their potential to be used in optoelectronic applications was determined. In addition, the aggregation properties of thin films of the compounds were examined by UV-vis spectrophotometer and the surface properties of the solids of the compounds were examined by SEM.



Tetra-substituted double-decker Lu(III) phthalocyanine

Octa-substituted double-decker Lu(III) phthalocyanine

Figure 1. Molecular structures of tetra- and octa-substituted double decker phthalocyanine compounds

PL properties of the compounds were examined by thin films prepared by drop casting method. The PL spectra of the compounds are shown in figures 2 and 3. The energy gaps for tetra- and octa-substituted lutetium(III) phthalocyanines were 1.73 eV and 1.72 eV, respectively. No significant difference was observed between the energy gaps of the compounds.

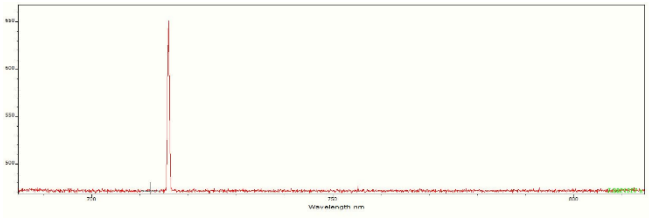


Figure 2. PL spectra of thin film tetra-substituted lutetium(III) phthalocyanine.

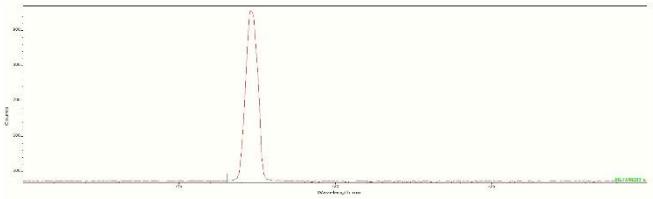


Figure 3. PL spectra of thin film octa-substituted lutetium(III) phthalocyanine.

The fluorescence properties of compounds in solution phase were examined (Figures 4 and 5).

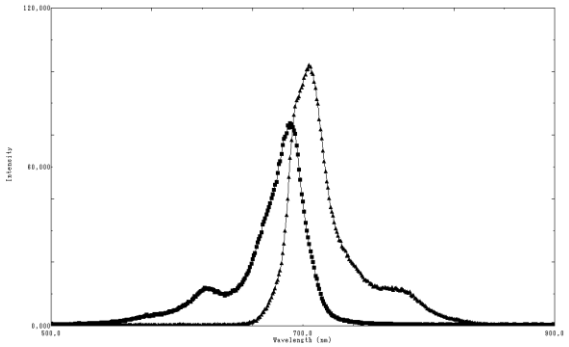


Figure 4. Emission and excitation spectra of tetra-substituted lutetium(III) phthalocyanine.

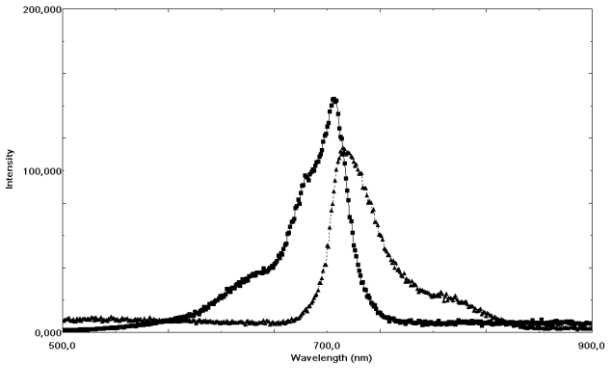


Figure 5. Emission and excitation spectra of octa-substituted lutetium(III) phthalocyanine.

Fluorescent quantum yields were calculated from measured emission spectra of compounds. The fluorescence quantum yields of compounds were determined by a comparative method in equation 1.

$$\Phi_F = \Phi_F(\mathrm{Std})\frac{FA_{\mathrm{Std}}\eta^2}{F_{\mathrm{Std}}A\eta^2_{\mathrm{Std}}} \qquad (1)$$

Where F and F_{Std} are the areas under the fluorescence emission curves of the compound and the standard, respectively. A and A_{Std} are the absorbance of the samples and standard at the excitation wavelength, respectively, η and η_{Std} are the refractive indexes of solvents used for compound and standard, respectively. Unsubstituted ZnPc was used as standard (Φ_F = 0.18 in DMSO) [21].

Fluorescence quantum yields for tetra- and octa-substituted double decker Lu(III) phthalocyanines were found to be 0.30 and 0.39, respectively. Binding of imidazole groups to phthalocyanine macrocycle significantly changed the fluorescence quantum yield and this difference increased as the imidazole groups increased. Imidazole groups appear to contribute to phthalocyanine in energy transfer.

Aggregation behaviors of these compounds in solution phase were investigated with UV-vis spectrophotometer. In addition, the aggregation behavior of these compounds in solid phase thin films were also examined (Figure 6). No significant shift or new peak formation was observed in the UV-vis spectra. Therefore, we can say that the compounds did not show aggregation behavior.

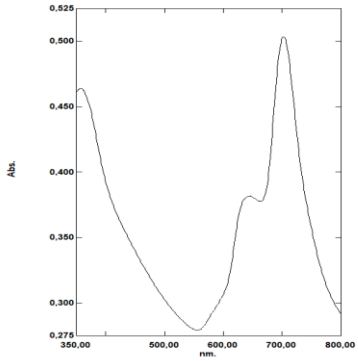
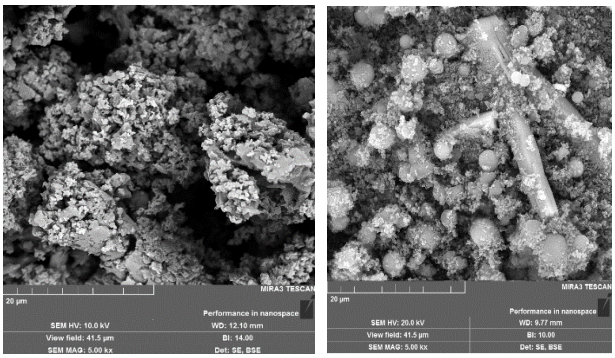


Figure 6. UV-Vis spectrum of thin film tetra-substituted lutetium(III) phthalocyanine.

The SEM images were also taken in solid form of tetra- and octa-substituted double decker Lu(III) phthalocyanine compounds. As observed from the SEM images, a more regular solid surface was obtained as a result of the increase of substituted imidazole groups (Figure 7).



A **B**

Figure 7. SEM images of (A) tetra-substituted and (B) octa-substituted double decker Lu(III) phthalocyanines solids.

Conclusions

In this study, we examined the photoluminescence and fluorescence properties of tetra- and octa-substituted double decker Lu(III) phthalocyanine compounds. The changes in these properties were examined with increasing number of substituents. The photoluminescence spectra of the compounds show indicating the strong π-π interaction along with electron and energy transition between the tetrapyrolic macrocycles. It was observed that the fluorescence quantum yield of the compounds was much higher than that of the standard unsubstituted phthalocyanine compound and increased as the number of substituted imidazole groups increased. Compounds also showed no significant aggregation. As the substituted imidazole groups increases, the molecule becomes more organized and has been superior properties. According to the results, these compounds have the potential to be used in optoelectronic applications.

Acknowledgments

In this study, the laboratory facilities of the Advanced Technology Application and Research Center (CÜTAM) of Sivas Cumhuriyet University were used.

References:

[1] C.C. Lenzoff, A.B.P. Lever, Phthalocyanines Properties and Applications, Cilt 1, VCH publishers, (1989).
[2] C.C. Lenzoff, A.B.P. Lever, Phthalocyanines Properties and Applications, Cilt 2, VCH publishers, (1993).
[3] C.C. Lenzoff, A.B.P. Lever, Phthalocyanines Properties and Applications, Cilt 3, VCH publishers, (1993).
[4] C.C. Lenzoff, A.B.P. Lever, Phthalocyanines Properties and Applications, Cilt 4, VCH publishers, (1996).
[5] Y. Zhang, X. Cai, Y. Bian, J. Jiang, Struct. Bond., 135 (2010) 275.
[6] T. Nyokong, Coord. Chem. Rev., 251 (2007) 1707.
[7] D. Atilla, N. Kılınç, F. Yüksel, A. G. Gürek, Z. Z. Öztürk, V. Ahsen, Synth. Met., 159 (2009)13.
[8] J.Jıang (Editor), Structure and Bonding, Springer-Verlag Berlin Heidelberg, ISBN 978-3-642-04751-0, 135 (2010)1.
[9] N. Kobayashi, Coord. Chem. Rev., 227 (2002) 129.
[10] X. Sun, C. Ma and J. Jiang, Synth. Met., 139 (2003) 497.
[11] A. Altındal, Ş. Abdurrahmanoğlu, M. Bulut, Ö. Bekaroğlu, Synth. Met. 150, 181 (2005).
[12] J. A. Saja, M.L. Rodriguez-Mendez, Adv. Colloid Interface Sci., 116 (2005) 1.
[13] D. K. P. Ng, J. Jiang, Chem. Soc. Rev., 26 (1997) 433.
[14] Ş. Abdurrahmanoğlu, A. R. Özkaya, M. Bulut, Ö. Bekaroğlu, Dalton Trans., (2004) 4022.
[15] Y. Sakakibara, R. N. Bera, T. Mizutani, K. Ishida, M. Tokumoto, T. Tani, J. Phys. Chem. B, 105 (2001) 1547.
[16] A. R. Gómez, C. M. Sánchez-Hernández, I. Fleitman-Levin, J. Arenas-Alatorre, J. C. Alonso-Huitrón, M. E. S. Vergara,Materials,7(2014)6585.
[17] F. Babudri, G. M. Farinola, F. Naso, R. Ragni, Chem. Commun., 10 (2007).
[18] G. Torre, G. Bottari, U. Hahn, T. Torres, Struct. Bond, 135(2010)1.
[19] E. Yabaş, M. Sülü, F. Dumludağ, A. R. Özkaya, B. Salih, Ö. Bekaroğlu, Polyhedron, 42 (2012) 196.
[20] E. Yabaş, M. Sülü, F. Dumludağ, B. Salih, Ö. Bekaroğlu, Polyhedron, 153 (2018) 51.
[21] M. Durmuş, T. Nyokong, Spectrochim. Acta A, 69 (2008) 1170.

6th International Conference on Materials Science and Nanotechnology For Next Generation (MSNG2019)
October 16-18, 2019, Niğde, TURKEY (ORAL FULL TEXT)

Development of anode/cathode electrodes for solid oxide fuel cells working at medium temperatures

Seda EVCİMEN [1, 2]

[1] Nigde Omer Halisdemir University, Mechanical Engineering Department, 51245, Nigde, Turkey
[2] Nigde Omer Halisdemir University Prof. Dr. T. Nejat Veziroglu Clean Energy Research Center, 51245, Nigde,Turkey

Solid oxide fuel cells (SOFC), are high efficient energy conversion systems utilizing hydrogen, natural gas, propane, diesel etc. as a fuel with the help of an oxidizer that convert chemical energy directly into electricity and heat energy. Although energy efficiency is high, SOFCs are facing with major problems in the way of commercialization such as long-term stability, production cost and high operating temperatures. Researchers make great efforts to reduce the operating temperature of SOFC; however, the key challenge is to develop high-ion-conductivity electrolyte materials at lower operating temperatures. SOFC is composed of a porous anode, a dense electrolyte and a porous cathode. While the anode is responsible for the fuel oxidation, the oxygen ions generated at the cathode as a result of the cathode electrochemical reaction are transferred through the electrolyte to the anode layer. In this study, it is aimed to increase the cell performance and to decrease the working temperature (600-800°C). ScSZ as electrolyte material and GDC with low temperature microstructural stability in electrodes are used. In literature, NiO / GDC is generally used as an anode material for solid oxide fuel cells operating at low temperatures. In these materials, metallic Ni acts as a catalyst for the fuel oxidation and provides an electronic path for the conduction. On the other hand, GDC acts as a matrix to support the catalyst (Ni), preventing its agglomeration under operation, and providing mixed ionic and electronic conductivity. The performance analyzes of 1 cm2 anode supported SOFC prepared by following the methods in the literature are examined and a power density of 800 mW / cm2 was obtained at 800 °C.

Corresponding author: sedaevcimen@hotmail.com

Keywords: Solid oxide fuel cells, SOFC, medium temperature, anode / cathode electrode, impedance analysis, performance analysis

1. Introduction

With the rapidly developing technology and increasing population, the difference between the amount of energy produced and the amount of energy consumed is increasing day by day. The trend towards renewable energy sources such as wind and solar energy, hydrogen technologies and fuel cells, which are more reliable, clean and sustainable in order to get rid of the negative effects of fossil energy sources in the world, is rapidly increasing.

Solid oxide fuel cells (SOFC), are high efficiency systems as fuel hydrogen, natural gas, propane, diesel etc. and with the help of an oxidizer that convert chemical energy directly into electricity and heat energy.

Despite their high energy conversion efficiency, SOFC's face major challenges to commercialization, such as long-term stability, production costs and high operating

temperatures. Particularly, the most important problems are the deterioration caused by the high operating temperature and the failure to ensure full sealing. In addition, the use of expensive corrosion-resistant flow plates (Crofer 22 APU, etc.) increases the costs of the system considerably. Operating temperatures for SOFC can be divided into 3 zones; 800 ° C and above: high temperature, 600 ° C to 800 ° C: medium temperature and below 600 ° C: low temperature SOFC. If the operating temperature is lowered from the high temperature to the medium temperature range, stainless steel may be used as the flow plate, thus making it possible to achieve a significant reduction in costs. However, lowering the operating temperature of the system increases the electrolyte resistance and thus adversely affects the performance of the fuel cell. To minimize the loss of performance, reducing the electrolyte thickness, using electrolyte materials with high ionic conductivity, and enabling the production of fuel cell components using thin film techniques are preferred.

In this study, it was aimed to increase cell performance and decrease working temperature by adding microstructural stability GDC to low and medium temperatures as an electrolyte material for medium working SOFCs and to anode and cathode electrolytes at low and medium temperatures [1-2].

2. Experimental details

Anode supported SOFC with active area of 1 cm^2 was manufactured to be used in experimental studies. Anode supported cells are produced by strip casting, co-sintering and silk printing methods.

The anode consists of two parts, the anode functional layer (AFL), the first layer being NiO / GDC (70: 30% by mass) and the anode active layer (AAL), the second layer being NiO / GDC (50: 50% by mass) [3] . Sludge was prepared by adding tovar, alcohol, starch and PEG and fish oil to AFL and AAL powders prepared in different containers. The prepared slurry was mixed with zirconium balls for 24 hours to ensure homogeneous mixing. The alcohol in the homogeneously prepared slurry was removed with a magnetic stirrer for 30 minutes. AAL 190 µm and AFL 140 µm thickness were cast on the myler in strip casting machine [4].

For an MEG with an active area of 1 cm^2, the anode leaves cut into appropriate sizes were bonded to each other using a hydraulic press with a pressure of 200 MPa by the addition of electrolyte. Finally, the membrane consisting of anode and electrolyte was sintered at 1375 ° C.

The cathode paste was prepared by adding certain amounts of butvar, alcohol, and starch to the cathode material LSM / GDC and LSM / both. The cathode paste was stirred for 24 hours to increase homogeneity as in anode and electrolyte production. The functional layer LSM / GDC (50: 50% by mass) and the active layer were treated on the electrolyte surface. Cathode production was completed by sintering at 1075 ° C.

3. Results and discussion

In the first stage of the experimental studies, AFL ratio AAL ratios were changed for anode supported SOFCs in which the use of the electrolyte material as an ScSZ material and LSM / GDC as the cathode material. The samples produced with these parameters are shown in Fıgure 1.

	AAL	AFL	ScSZ
N1	14	3	1
N2	16	3	1
N3	18	3	1
N4	20	3	1
N5	16	4	1
N6	16	2	1
N7	16	1	1

Figure 1. *AAL and AFL ratio*

In the second part of the experimental study, in the first stage, anode supported SOFCs were produced by using LSM /ScSZ instead of LSM / GDC which is used as cathode material. The AAL and AFL ratios of the samples prepared using LSM /ScSZ are shown in Figure 2.

	AAT	AİT	ScSZ
N8	14	3	1
N9	16	3	1
N10	18	3	1
N11	20	3	1
N12	16	4	1
N13	16	2	1
N14	16	1	1

Figure2. *AAL and AFL ratios of the samples prepared using LSM /ScSZ*

Current / voltage performance and impedance measurements were investigated for characterization. The cell and interconnectors used in the experimental apparatus are shown in Figure 3.

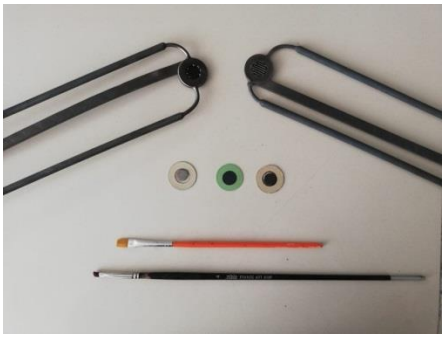


Figure3. *Anod supported SOFC and interconnectors*

4. Conclusion

GDC doped cathode layers were examined parametric at different temperatures (700, 750, 800 ° C) with different ScSZ doped cathodes in order to reduce ion conduction and electrical resistance. According to the performance results, a power density of 800 mW / cm^2 was obtained from the MEG with 16-1 layer LSM / GDC cathode at 800 ° C. These results have been achieved by using LSM / GDC and LSM / ScSZ for SOFCs using high temperature YSZ electrolyte without compromising performance at medium temperatures (700-800 ° C) and even higher power density. In addition, this study showed that GDC, which has ion conduction at lower temperatures, provides high performance such as, and that coating temperatures can be further reduced by improving coating techniques.

References:

[1] DİNG, C., LİN, H., SATO, K., KAWADA, T., MİZUSAKİ, J. AND HASHİDA, T., "Improvement of electrochemical performance of anode-supported SOFCs by NiO–Ce0. 9Gd0. 1O1. 95 nanocomposite powders", *Solid State Ionics*, 181(25-26), 1238-1243, 2010.

[2] ARAÚJO, A. J., GRILO, J. P., LOUREIRO, F. J., CAMPOS, L. F., PASKOCIMAS, C. A., NASCIMENTO, R. M. AND MACEDO, D. A., "Designing experiments for the preparation of Ni-GDC cermets with controlled porosity as SOFC anode materials: effects on the electrical properties", *Ceramics International*, 44(18), 23088-23093, 2018.

[3] JADHAV, S., PURI, V. AND JADHAV, L., "NiO-GDC-BCY composites as an anode for SOFC", *Journal of Alloys and Compounds*, 685(626-632, 2016.

[4] TORKNIK, F. S., KEYANPOUR-RAD, M., MAGHSOUDIPOUR, A. AND CHOI, G. M., "Effect of microstructure refinement on performance of Ni/Ce0. 8Gd0. 2O1. 9 anodes for low temperature solid oxide fuel cell", *Ceramics International*, 40(1), 1341-1350, 2014.

6th International Conference on Materials Science and Nanotechnology For Next Generation (MSNG2019)
October 16-18, 2019, Niğde, TURKEY (ORAL FULL TEXT)

Thermoluminescence Studies of SIM Card Chips Used In Mobile Phone For Different Operators In Turkey

A.Kandemir[*], and H.Toktamış[**]

[*]*Department of Physics, of Natural and Applied Sciences, Çukurova University, 01330 Adana, Turkey*
[**]*Department of Engineering Physics, Faculty of Engineering, Gaziantep University, 27310, Gaziantep, TURKEY*

The materials found close to human body such as IC (Integrated Circuit), USB and mobile phone can be used as a dosimetry. SIM card chip used in mobile phone is a silicon rich material and a potential candidate of dosimetry. In this study, thermoluminescence (TL) properties of the SIM card chips of three different operators in Turkey were investigated and analyzed as suitable or not for a dosimeter after β – irradiation ^{90}Sr-^{90}Y at room temperature. Chip composition can be detected by X-Ray Fluorescence (XRF) method. Kinetic parameters of the glow curves were determined by computerized glow curve deconvolution (CGCD) methods. These parameters are number of peaks, carrier concentration (n_0), trap activation (eV), and frequency factor (s^{-1}) of operator 1. The main results from these experiments are all SIM card chips show the TL properties but the chip which was extracted from operator 1 has better TL properties as a dosimeter. The chip which gives the best TL intensity exhibits a distinct peak around 230 ˚C and a shoulder peak around 130 ˚C.

Keywords: SIM Card Chip, Thermoluminescence, Kinetic Parameters.

Corresponding author: ardakandemir88@gmail.com

1. Introduction

Thermoluminescence can be defined as the emission of light from a semiconductor or an insulator when it is heated, due to the previous absorption of energy from irradiation. Because of the heating process sample must be inorganic material. Generally, application areas are; radiation dosimetry, age determination, and geological researches.
On the other hand, for the fabrication process for SIM Card, main sample is semiconductor wafer. It needs to dice into individual chips. More commonly, the dies are separated from the wafer by the use of a diamond saw. Gold and aluminum wires bonded between chip and substrate. A mylar sheet is stuck to the back of the wafer so that following separation the dies remain attached to the mylar film.

2. Experimental Details

According to X-Ray Fluorescence Method, SIM chip composition is made by SiO_2 [1].

SIM card chip was exposed by ^{90}Sr - ^{90}Y beta radiation source at room temperature. It was irradiated from 2.4 Gy to 2.4 kGy. Before and after irradiation process, sample was heated up from 30°C to 400°C in 1°C per second increments by Harshaw 3500 TLD Reader. Process before the irradiation is determination of natural dose (background radiation) and its purpose is evacuation of the traps which are located in the forbidden band gap of the material. Glow curves and the other results were obtained by using WINREMS software program. During experiments were not performed, the sample placed inside a box in a completely dark environment to avoid light contamination.

3. Results and Discussion

Figure 1 shows kinetic parameter of variations of carrier concentration (n_0) as a function of dose. For the low dose region, there is no important change in the carrier concentration, but after 20 Gy, the carrier concentration increases with increasing dose. At higher dose, the

structure of traps and the number of traps is being changed are the reasons of this increment.

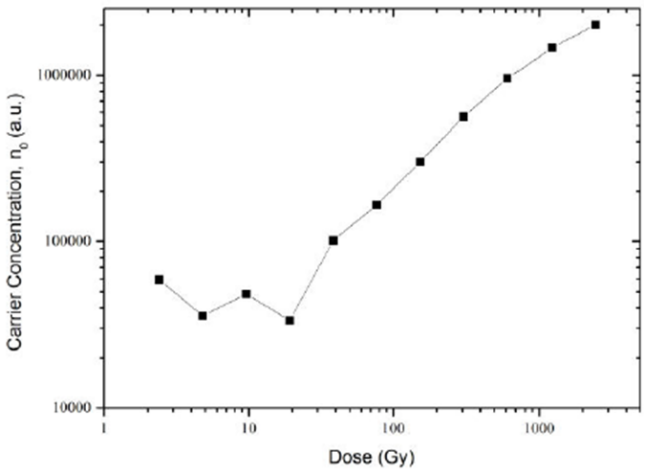


Figure 1. *Carrier concentration* (n_0) *of the Operator 1.*

4. Conclusion

In this study, investigations were performed on Operator1. After all experiments, results show that the Operator 1 has good results and may be use as a core material of the dosimeters. SIM card chip that we used shows thermoluminescence property and its material can be a candidate to use as an accidental dosimeter. However, more testing will be required in order to make proper determination

5. Acknowledgement

This study was conducted within the scope of "THERMOLUMINESCENCE STUDIES OF SIM CARD CHIPS USED IN MOBILE PHONE FOR DIFFERENT OPERATORS IN TURKEY" (Project No MF.13.09) supported by Scientific Research Projects Commission of Gaziantep University. We are grateful for their support.

References:

[1] Correcher, V., Garcia-Guinea, J., Rivera, T., 2009. Thermoluminescence sensitivity of daily-use materials. Radiat. Eff. Defects Solids 164, 232–239.

6th International Conference on Materials Science and Nanotechnology For Next Generation (MSNG2019)
October 16-18, 2019, Niğde, TURKEY (ORAL FULL TEXT)

Multiband and Polarization Insensitive Perfect Metamaterial Absorber

B. P. Bozoğlan[1], G. Öğücü Yetkin[1], M. Karaaslan[2], O. Altıntaş[2]
[1] Department of Electrical and Electronics Engineering, Gaziantep University, Gaziantep, Turkey
[2] Department of Electrical and Electronics Engineering, İskenderun Technical University, İskenderun, Hatay, Turkey

In this study, design and simulation of a novel multiband perfect metamaterial absorber which is operating at X band region are investigated. The designed structure consists of double square split ring resonators, and the resonator layer made of copper with a thickness of 0.035 mm. Moreover, the used dielectric layer is FR-4 dielectric material with a thickness and dielectric constant of 1.6mm and 4.3, respectively. In addition, microwave simulation program which is based on finite integration technique (FIT) is employed to perform design and simulation. According to simulation results, proposed structure capable to absorb energy of incident microwave at 9.03 GHz, 9.84 GHz and 11.71 GHz for transverse electromagnetic (TEM) mode. Absorption ratios of these resonant frequencies are calculated and equal to 99.8%, 99.6% and 99.8%, respectively. Moreover, the realized metamaterial has same absorption level regardless of polarization angle (phi) that means able to absorb energy with same level (0^0-90^0). Finally, metamaterial absorbers have wide range of application area such as medical, radar, military, visibility, etc.

Keywords: Absorber, Multiband, Perfect Metamaterial.

Corresponding authors: bpinar92@gmail.com

1. Introduction

Metamaterial is artificially produced engineering substance that is not found in nature. In recent years, along with developing technology, interest in metamaterials with unusual electromagnetic (EM) properties such as negative refractive index has increased. Due to their exotic EM features, metamaterials are applying in many different areas such as cloaking [1], absorber [2, 3], solar cell [4, 5], radar [6], and so on. After Landy et al. firstly proposed perfect metamaterial absorber (PMA) in 2008 [7], many scientists have focused on studies in this topic. In the last decade scientific studies, researchers had proposed a dual band [8, 9], three bands [10], multi band [11, 12] and broadband [13, 14] of the metamaterial absorber by using various methods to broaden the absorption band. In recent years, perfect absorber studies that have multiple band structure and polarization independent and wide angle properties have become a great importance owing to high absorption and wide application area.

In this study, a multiband metamaterial absorber (MA) structure has been proposed which shows three different absorption peaks with perfect absorption. Design and simulation parts of the MA absorber have been realized by Finite Integration Technique (FIT) that supports under transverse electromagnetic (TEM) mode. This proposed structure is also simulated for transverse electric- transverse magnetic (TE-TM) mode, and the results obtained for TEM mode and TE-TM mode are compared. Furthermore, the proposed structure has been observed for polarization independency with distinct polarization angle of phi in both mode cases.

2. Design and Simulation

The proposed structure consists of combined double square split rings with single-layer. The front side of the periodic structure of proposed absorber was demonstrated in Fig.1. This absorber includes a metallic sheet and ground plane separated by dielectric substrate. FR4 with a thickness of 1.6 mm has been chosen as

dielectric with relative permittivity of ε_r = 4.3. Copper sheet (conductivity σ = 5.8 x 10^7 S/m) has been utilized on both of the upper and lower layers with a thickness of 0.035 mm.

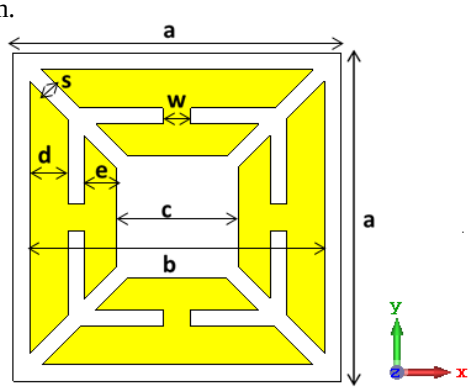


Fig.1: The unit cell of the proposed structure with geometric dimensions: a=30 mm, b=28 mm, c=12 mm, d=3.2 mm, e=3.8 mm, s=1.4 mm, w=2 mm.

Design of the proposed structure has been simulated by using FIT. For TEM mode, boundary conditions are set to perfect electric conductor (at x-plane), perfect magnetic conductor (at y-plane) and open (at z-plane) in simulation. For TE-TM mode, boundary conditions are set as unit cell (at x and y directions) and open (at z direction).

The absorptivity A(w) of the metamaterial absorber can be defined according to equation A(w) = 1 – R(w) – T(w), where R(w) and T(w) indicates reflection and transmission coefficient, respectively. Since the down layer is totally copper, the transmission value T(ω) is zero. Hence, the absorptivity can be represented by A(w) = 1 – R(w).

In Fig.2, absorption and reflection of the structure is given for TEM mode. According to the simulation results, structure consists of three absorption peaks at 9.03 GHz, 9.84 GHz and 11.71 GHz with absorptivity of 99.8%, 99.6% and 99.8%, respectively.

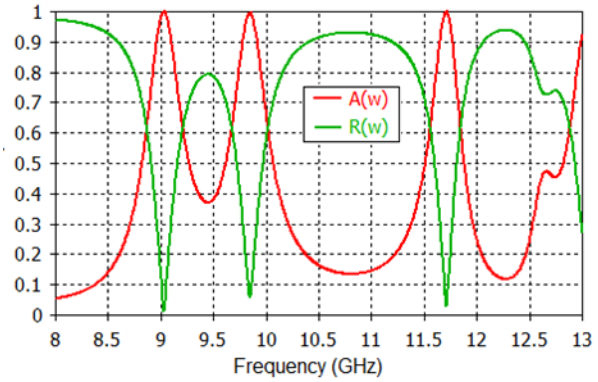


Fig.2: Simulation results of absorption and reflection for TEM mode

In Fig.3, absorption and reflection of the structure is given for TE-TM mode. According to the simulation results, structure consists of three absorption peaks at 9.06 GHz, 9.85 GHz and 11.71 GHz with absorptivity of 99.9%, 99.5% and 99.9%, respectively.

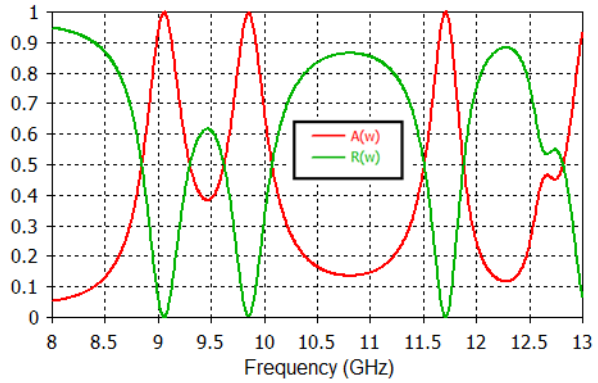


Fig.3: Simulation results of absorption and reflection for TE-TM mode

According to the simulation results, absorption and reflection results and also absorption peak values are almost identical for both two modes as shown in the Fig.2 and Fig.3.

Moreover, as shown in Fig.4 and Fig.5, due to the symmetry of the structure, the proposed MA is polarization independent for transverse electromagnetic (TEM) and transverse electric- transverse magnetic (TE-TM) modes at 0°-90°.

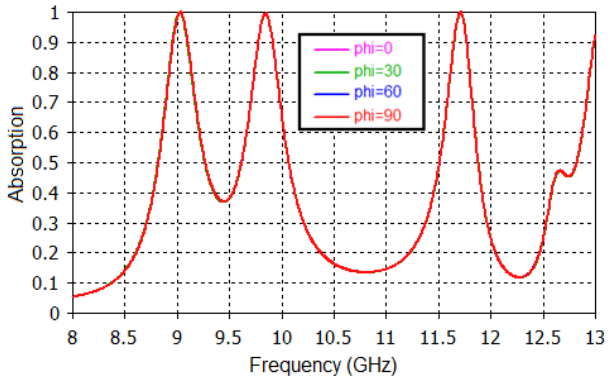


Fig.4: Simulated absorption with different polarization angle phi for TEM mode

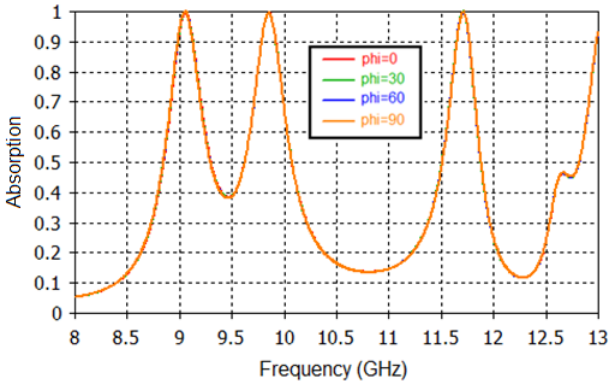


Fig.5: Simulated absorption with different polarization angle phi for TE-TM mode

Conclusions

In this study, a novel perfect metamaterial absorber based on double square split ring resonator structure has been presented. Perfect absorption has been obtained at three different frequencies by changing structure dimensions and frequency range in simulation program. According to the simulation results, the proposed metamaterial absorber has been observed to be polarization independent with distinct polarization angles and also has nearly same absorption peak values at determined operating frequency under TEM and TE-TM modes. The proposed multiband MA is low cost and shows efficient results for the operating frequency range in microwave regime. Proposed structure which has high absorption and polarization independence is suitable to utilize in many application areas such as energy harvesting, radar cross section reduction.

References:

[1] D. Schurig, J.J. Mock, B.J. Justice, S.A. Cummer, J.B. Pendry, A.F. Starr, and D.R. Smith, "Metamaterial electromagnetic cloak at microwave frequencies," Science, vol. 314, pp. 977–980, 2006.
[2] O. Ayop, M.K.A. Rahim, N. A. Murad, and N. A. Samsuri, "Dual-directional polarization insensitive multiband metatametrial absorber," 2015 IEEE International FR and Microwave Conference (RFM2015), Kuching Malaysia, 14-16 Dec 2015
[3] Jin Woo Park, Pham Van Tuong, Joo Yull Rhee, Ki Won Kim, Won Ho Jang, Eun Ha Choi, Liang Yao Chen, and YoungPak Lee, "Multi-band metamaterial absorber based on the arrangement of donut-type resonators," Opt. Express 21, 9691-9702 (2013)
[4] F. Dincer, O. Akgol, M. Karaaslan, E. Unal and C. Sabah, "Polarization angle independent perfect metamaterial absorbers for solar cell applications in the microwave, infrared, and visible regime," Progress In Electromagnetics
Research, vol. 144, pp. 93-101, 2014.
[5] P. Rufanguraa, C. Sabah, "Design and characterization of a dual-band perfect metamaterial absorber for solar cell applications", Journal of Alloys and Compounds, vol. 671, p. 43-50, June 2016.
[6] D. Chaurasiya, S. Ghosh and K. V. Srivastava, "Dual band polarization-insensitive wide angle metamaterial absorber for radar application," 2014 44th European Microwave Conference, Rome, 2014, pp. 885-888.
[7] N. I. Landy, S. Sajuyigbe, J. J. Mock, D. R. Smith and W. J. Padilla, "Perfect metamaterial absorber," Physical Review Letters, vol. 100, 207402, 2008.
[8] H. Xiong, L. L. Zhong, C. M. Luo, J. S. Hong, "Dual-band polarization-/angle-insensitive metamaterial absorber", AIP Advances 5, 067162 (2015).
[9] H. Cheng, S. Cheng, H. Yang, et al., "A polarization insensitive and wide-angle dual-band nearlyperfect absorber in the infrared regime", Journal of Optics, vol. 8, p. 085102, August 2012.
[10] X. Shen, T. J. Cui, J. Zhao, et al., "Polarization-independent wide-angle triple-band metamaterial absorber", Optic Express, vol. 10, pp. 9401-9407, May 2011.
[11] H. Li, L. H. Yuan, B. Zhou, et al., "Ultrathin multiband gigahertz metamaterial absorber", Journal of Applied Physics, vol. 4, p. 044902, February 2012.
[12] L. Huang, H. Chen, "Multi-band and polarization insensitive metamaterial absorber", Progress In Electromagnetics Research, Vol. 113, p. 103-110, 2011.

[13] Sijia Li, Jun Gao, Xiangyu Cao, Zhao Zhang, Yuejun Zheng, and Chen Zhang, "Multiband and broadband polarization -insensitive perfect absorber devices based on a
tunable and thin double split-ring metamaterial," Opt. Express 23, 3523-3533 (2015).
[14] Young Ju Kim, Young Joon Yoo, Ki Won Kim, Joo Yull Rhee, Yong Hwan Kim, and YoungPak Lee, "Dual broadband metamaterial absorber," Opt. Express 23, 3861-3868 (2015).

6th International Conference on Materials Science and Nanotechnology For Next Generation (MSNG2019)
October 16-18, 2019, Niğde, TURKEY (ORAL FULL TEXT)

Wideband and Polarization Insensitive Perfect Metamaterial Absorber

B. P. Bozoğlan[1], G. Öğücü Yetkin[1], M. Karaaslan[2], F. Ö. Alkurt[2], O. Altıntaş[2]
[1] Department of Electrical and Electronics Engineering, Gaziantep University, Gaziantep, Turkey
[2] Department of Electrical and Electronics Engineering, İskenderun Technical University, İskenderun, Hatay, Turkey

In this study, design and simulation of a novel wideband perfect metamaterial absorber which is effect at X band region are investigated. The proposed structure includes four split ring resonators with same dimensions, and the resonator layer made of copper with the thickness of 0.035 mm. The back side of the structure is completely copper to reduce reflection coefficient level. Moreover, the used dielectric layer is FR4 dielectric material with the thickness and dielectric constant of 1.6mm and 4.3, respectively. The proposal has absorption of 99% at between 9.76 GHz and 11.25 GHz frequency range and bandwidth is 1.49 in Transverse Electromagnetic (TEM) mode. Also in this frequency range, the proposed structure is polarization independent at different polarization angles. Since the proposed structure works in the X band, it is suitable for use in radar applications.

Keywords: Absorber, Wideband, Perfect metamaterial (PM).

Corresponding authors: bpinar92@gmail.com

1. Introduction

Metamaterials (MMs) are materials that do not exist in the nature but can be produced artificially and their light refraction properties are negative. In 1967, Victor Veselago et al. put forward the term of the negative refractive index [1]. In 1996, Pendry et al. [2] presented the theoretical studies to obtain a medium with negative constitutive parameters and, Smith et al. carried it out experimentally in 2000 [3]. In the last decade, scientists have increased their researches on metamaterials. Due to their unique electromagnetic properties, these metamaterials have been widely used in various fields such as cloaking [4, 5], antennas [6, 7], absorbers [8, 9], perfect lens [10] and radar applications [11]. One of the important studies on perfect metamaterial absorbers was proposed by Landy et al. in 2008 [12]. In the literature, after this study, the fact, which metamaterials show perfect absorption in a wide band from microwave band to the optical band of the electromagnetic spectrum, has led to a significant increase in research on these structures [13, 14]. After a single resonance study by Landy, polarization and angle independent structures that showed absorption at two or more resonant frequencies have been studied intensively [15, 16]. However, in these structures, absorption shows itself in a narrow band. By multiplexing the unit cell vertically and horizontally, absorption was carried out in wide band [17, 18].

In this study, a wideband metamaterial perfect absorber comprised of split ring resonators operating in X band has been proposed. The study is numerically achieved by CST based on Finite Integration Technique (FIT) that supports under Transverse Electromagnetic (TEM) mode. The absorption results are obtained with and without resistive load between the split parts of resonator. Moreover, the proposed structure has been examined by different polarization angles.

2. Design and Simulation

Design of the proposed structure has been simulated in the full wave CST Microwave Studio and for TEM mode simulation. Boundary conditions have been set to perfect electric conductor (at x- plane), perfect magnetic conductor (at y-plane) and open (at z-plane) in simulation.

As shown in the Fig.1, unit cell of the proposed structure comprises of four split ring resonators which are the same sizes and dimensions. Bottom layer of the absorber design is coated with copper to eliminate the transmitted power. Resonators are formed of copper that has a conductivity of 5,8 x 10^7 S/m and it has a thickness of 0,035 mm. The proposed structure is constructed on a FR4 type dielectric substrate with a thickness and dielectric constant

of 1,6 mm and 4,3 respectively. The size of the unit cell is 20 mm x 20 mm at the x-y plane.

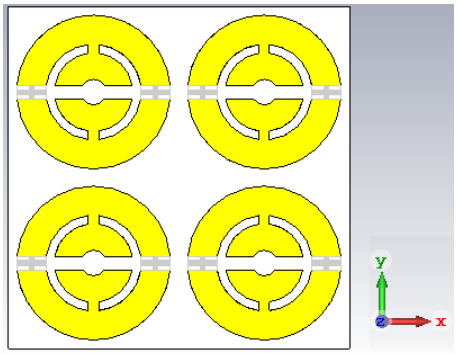


Fig.1: Top view of the proposed structure

The unit cell dimensions of the split ring resonator based structure have shown in Fig.2 and the parameter list has given in Table 1.

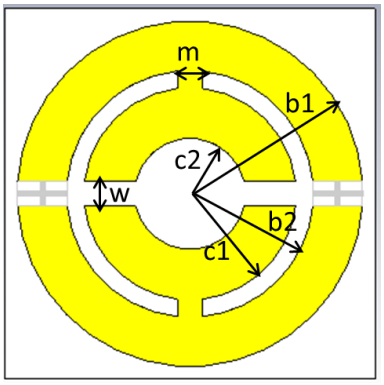


Fig.2: Dimensions of the unit cell

Table 1: Parameter list of unit cell

Parameter	b1	b2	c1	c2	m	w
Value (mm)	4,5	2,8	2,3	0,75	0,6	0,8

The absorptivity A(w) of the metamaterial absorber can be defined according to equation A(w) = 1 – R(w) – T(w), where R(w) and T(w) indicates reflection and transmission coefficient, respectively. When the ground plane is used metal, T(w) = $|S_{21}|^2$ = 0. So we get the following equation:

$$A(w) = 1 - R(w) = 1 - |S_{11}|^2 .$$

Operating frequency range has been determined between 7 and 13 GHz for use in radar applications. In the proposed structure, effect of the resistance load on the absorptivity has researched. Fig.3 shows the result of the structure without using resistive load, and Fig.4 shows the results of the structure using 300 Ω resistors placed in the gaps seen in Fig.1.

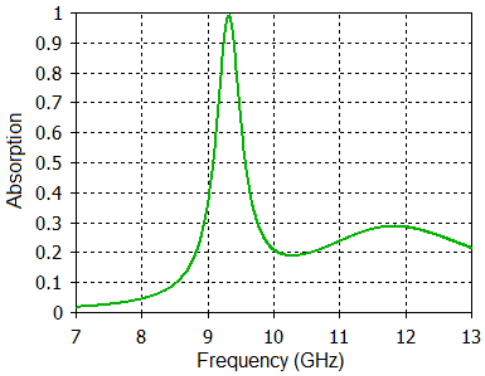


Fig.3: Absorption of the metamaterial absorber without resistive loads

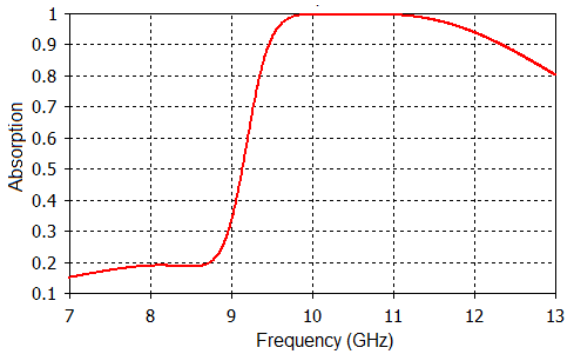


Fig.4: Absorption of the metamaterial absorber with resistive loads

The perfect absorption peak is observed 9.32 GHz without using resistive load demonstrated in Fig.3. A perfect absorption bandwidth is obtained by adding the resistive load at the split gaps of the resonator. According to obtained results using TEM mode, absorption value is 90 % at between 9.47 GHz and 12.32 GHz, and bandwidth is 2.85 GHz. Also the perfect absorption value is 99 % at between 9.76 GHz and 11.25 GHz, and bandwidth is 1.49 GHz illustrated in Fig.4. Furthermore, independency of polarization angle is another important factor for metamaterial absorber in different polarization angle phi applications. As shown in Fig.5, the proposed structure is demonstrated to be polarization independent at the polarization angle phi (0°- 60°).

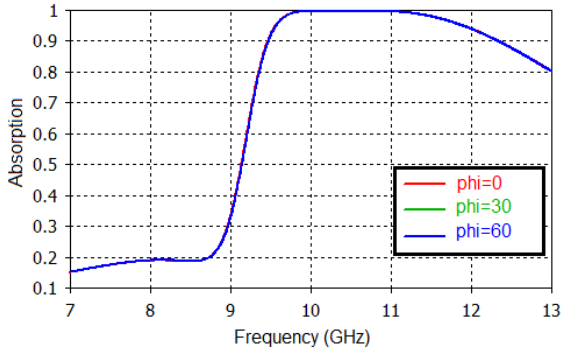


Fig.5: Absorption under different polarization angle phi for TEM mode

Conclusions

In this paper, design and numerical study of the wideband and polarization independent perfect metamaterial absorber in the microwave has been achieved. Proposed absorber structure is composed of multiple split ring resonators and resistors. Simulation results show that the absorber has perfect absorption characteristic with absorptivity more than 99% from 9.76 GHz to 11.25 GHz. Moreover, since the structure is symmetrical, it was also supported by the simulation results in which it is polarization independent at different polarization angles. The proposed structure could be efficiently integrated in radar applications considering the operating frequency band.

References:

[1] Veselago, V.G. The Electrodynamics of Substances with Simultaneously Negative Values of and μ Soviet Physics Uspekhi 10 (4) 1968: pp. 509.
[2] Pendry, J. B., Holden, A. J., Stewart, W. J. and Youngs, I., 1996, Extremely Low Frequency Plasmons in Metallic Mesostructures, Phys. Rev. Lett. 76: 4773-4776.
[3] Smith, D. R., Padilla, W. J., Vier, D. C., Nemat-Nasser, S. C., and Schultz, S., 2000, Composite Medium with Simultaneously Negative Permeability and Permittivity, Phys. Rev. Lett., 84: 4184.
[4] Schurig, D., Mock, J.J., Justice, B.J., Cummer, S.A., Pendry, J.B., Starr, A.F., Smith, D.R. Metamaterial Electromagnetic Cloak at Microwave Frequencies Science 314 (5801) 2006: pp. 977 – 980.
[5] Pendry, J. B., Schurig, D., Smith, D. R. Controlling Electromagnetic Fields Science 312 (5781) 2006: p. 1780 – 1782.
[6] He-Lin, G.L.Y.Y., Chao-Song, L.M.H.G., Yuan, T. A, Microstrip Antenna with Single Square Ring Structured Left-Handed Metamaterial Acta Physica Sinica 1 2012: pp. 021.
[7] Ziolkowski, R.W., Erentok, A. Metamaterial-Based Efficient Electrically Small Antennas IEEE Transactions on Antennas and Propagation 54 (7) 2006: pp. 2113 – 2130.
[8] Bağmancı M, Akgöl O, Özaktürk M, Karaaslan M, Ünal E, Bakır M., Polarization Independent Broadband Metamaterial Absorber for Microwave Applications. Int J RF Microwave Comput Aided Eng. 2019;29: e21630.
[9] F. Ö. Alkurt et al. Octagonal Shaped Metamaterial Absorber Based Energy Harvester, Vol. 24, No: 3 (2018).
[10] Pendry J.B., Negative Refraction Makes a Perfect Lens, Physical Review Letters, 85 (18), 3966, 2000.
[11] K. Özden, A. Özer, O. M. Yücedağ, H. Koçer, Journal of the Faculty of Engineering and Architecture of Gazi University 31:4 (2016) 1105-1112
[12] Landy N.I.,Sajuyigbe S., Mock J.J., Smith D.R., Padilla WJ., Perfect Metamaterial Absorber, Physical Review Letters, 100 (20), 207402, 2008.
[13] Tao H., Landy N.I., Bingham C.M., Zhang X., Averitt R.D., Padilla W.J., A Metamaterial Absorber for the Terahertz Regime: Design, Fabrication and Characterization, Optics Express, 16 (10), 7181-7188, 2008.
[14] Avitzour Y., Urzhumov Y.A., Shvets G., Wide-angle Infrared Absorber Based on a Negative-index Plasmonic Metamaterial, Physical Review B, 79 (4), 045131, 2009.
[15] M. H. Li, H. L. Yang, X. W. Hou, Y. Tian, D. Y. Hou, Perfect Metamaterial Absorber with Dual Bands, Progress In Electromagnetics Research, Vol. 108, 37-49, 2010
[16] Lee J., Lim S., Bandwidth-enhanced and Polarization-insensitive Metamaterial Absorber Using Double Resonance, Electronics Letters, 47 (1), 8-9, 2011.
[17] M. Karaaslan, M. Bağmancı, E. Ünal, O. Akgöl, O. Altıntaş, C. Sabah, Opt Quant Electron (2018) 50:225
[18] J. Fengi, L. Si, L. Sun, Y. Tian, D. Li, Proc. of the 2017 International Symposium on Electromagnetic Compatibility - EMC EUROPE 2017, Angers, France, September 4-8, 2017

.

6th International Conference on Materials Science and Nanotechnology For Next Generation (MSNG2019)
October 16-18, 2019, Niğde, TURKEY (ORAL FULL TEXT)

Influence of extrusion slurry composition on the properties of NiO-YSZ anode supported micro-tubes

C. Timurkutluk[1, 2, 3*], G. Atalmıs[2,3], U. Aydın[1], B. Timurkutluk[2,3] and Y. Kaplan[2,3]

[1] Vestel Defense Industry, Üniversiteler Mah. İhsan Doğramacı Bul. Titanyum Blok 17/B Teknokent ODTÜ, 06800, Ankara, Türkiye
[2] Nigde Omer Halisdemir University, Mechanical Engineering Department, 51245, Nigde, Turkey
[3] Nigde Omer Halisdemir University Prof. Dr. T. Nejat Veziroglu Clean Energy Research Center, 51245, Nigde, Turkey

Solid oxide fuel cells (SOFCs) are high temperature energy conversion devices, converting chemical energy of a fuel directly into electrical and heat energy through electrochemical reactions of fuel and air. They have received great attention since they provide clean and efficient operation together with fuel flexibility. SOFCs can be broadly classified according to their geometry as planar, tubular and micro-tubular. Micro-tubular SOFCs are advantageous over planar and tubular SOFCs in terms of ease of sealing, small in size, high power density, short start-up and shutdown periods, quick response to dynamic loads and high resistance to thermal shock. The extrusion technique is widely used to manufacture support micro-tubes. In this respect, the properties of the extrusion solutions have a great impact on the final product. In this study, therefore, the effects of components in the extrusion slurry of NiO- YSZ anode support micro-tubes are systematically studied for a successful anode support micro-tube fabrication via extrusion. For this purpose, the amounts of solvent, pore former and plasticizer are considered. It is determined that the appropriate amount of organic solvent, pore former and plasticizer in the extrusion slurry for the fabrication of NiO-YSZ anode support micro-tube with desired properties should be 50 wt. %, 10 wt. % and 5 wt. %, respectively. The optimized anode-support micro-tube is then dip coated with YSZ electrolyte and LSM-YSZ cathode. The anode supported micro-tubular cell is tested under hydrogen and open cathode conditions. The cell exhibits a peak power of 1.43 W at an operating temperature of 800 °C

Keywords: Solid oxide fuel cells, SOFC, micro-tubular, extrusion, slurry composition.

Corresponding authors: cigdem.timurkutluk@vestel.com.tr

1. Introduction

Today, the need for energy, most of which is obtained from fossil-based fuels, has an increasing trend due to developments in technology and increasing world population. The fact that fossil resources are finite and the irreversible damages they cause to our world in the long term, especially global warming, have led the commercial and scientific circles to research for new and renewable environmentally friendly energy sources. In this respect, fuel cells, which convert the chemical energy of a fuel directly into electrical

and useful heat energy by an electrochemical way, have received great interest due to their high efficiency and environmentally friendly operation. Over the other available fuel cell types, solid oxide fuel cells offer some advantages including relatively higher efficiency due to high operation temperature (600-1000°C), fuel flexibility, no need for precious catalysts like Pt and tolerance

impurities in the fuel. SOFCs can be broadly divided into two according to geometry: tubular and planar. Beside these, tubular SOFCs with few millimeters in diameter are called micro-tubular SOFCs.

The concept was first introduced by Kendall [1], who fabricated YSZ electrolyte supported micro-tubular cells having 1 mm diameter. This SOFC design, providing easy sealing, high power density, good thermal cycling and high thermal shock resistance due to having cylindrical geometry and small size, together with rapid start up and shut down times, can be used for stationary applications as well as mobile applications [2-4]. In the literature, micro-tubular SOFCs have commonly anode-supported structure to improve the cell performance by reducing the thickness of the electrolyte. In the fabrication of micro-tubular SOFCs, classical extrusion method has been often employed to fabricate this support micro-tube, whereas other layers have been generally coated via dip coating. In addition, the anode support and the electrolyte layer have been generally co-sintered. Beside the processing parameters such as pre-sintering temperature of the anode support micro-tube [5, 6] and co-sintering temperature [7, 8], the properties of the extrusion slurry used in anode support micro-tube fabrication such as the powder size and ratio, the type and ratio of the additives as well as the composition have also great impact on the final product, since they mainly decide the final anode support microstructure thus the cell performance. There exist some studies in the literature investigating the effects of the extrusion slurry. Suzuki et al. [9], for example, focused on the powder size of NiO in the fabrication of NiO-GDC anode support micro-tube via extrusion on the cell performance and microstructure. They tested NiO powders having 0.5 µm and 5 µm particle sizes. The micro-tubular cell including fine NiO powders exhibited relatively higher power densities at all operating temperatures studied. This was explained by the more optimized anode microstructure for better cell performance as a result of fine NiO powders used. Monzon et al. [7] reported that the optimum solid powder content in the extrusion slurry of NiO-YSZ anode support micro-tube should be 65 vol % in terms of acceptable homogeneity, torque values and thermoplastic behavior.

In this study, on the other hand, the amount of solvent, pore former and plasticizer used in the extrusion slurry of NiO-YSZ anode support micro-tube are optimized for a successful extrusion process including sintering step without any structural and geometrical defects.

2. Experimental detail

Commercially available NiO (NiO-F, Novamet, New Jersey, USA) and YSZ (Tosoh, Tokyo, Japan) powders are mixed at a weight ratio of 3:2. An appropriate amount of fish oil (Sigma-Aldrich, Munich, Germany) as a dispersant and solvent (a mixture of ethanol and ethyl methyl ketone, Sigma-Aldrich) are then added to the mixture. In order to study the effects of the amount of solvent, solvent content of the extrusion slurry was varied between 40 and 55 wt. % with respect to solid anode support powders. Next, plasticizer (polyethylene glycol, Sigma-Aldrich) and pore former (activated charcoal, Sigma-Aldrich). Similarly, the amount of plasticizer and pore former was changed from 1 to 10 wt. % and from 0 to 20 wt. % with respect to solid powders, respectively, to investigate their effects on the anode support micro-tube extrusion process. Following the ball milling around 24 h, the solutions were subjected to stirring by a transmission type mechanical stirrer with addition of paraffin wax and stearic acid at suitable ratios. After the desired viscosity is achieved, the slurry is extruded by a home-made extrusion machine with a die having inner and outer diameter of 4 mm and 5.25 mm, respectively. The green tubes were then dried under atmospheric conditions for 24. The sintering of the anode support micro-tubes was performed at 1300 °C for 4h.

3. Results and discussion:

3.1. Effect of solvent content

Anode support micro-tubes are obtained after the extrusion of slurries with various solvent contents. Extrusion slurry with 40 wt. % solvent fails in the homogenization step during the stirring due to agglomeration. Therefore, the extrusion process could not be proceeded for this solution. This can be explained by inadequate solvent content of the extrusion slurry, resulting in agglomeration of the anode support powders. It is possible to extrude the anode support micro-tube slurry having 45 wt. % solvent. However, after the drying steps, some micro-cracks are observed on the tube surface, which cause mechanical failure during sintering as shown in Figure 1.

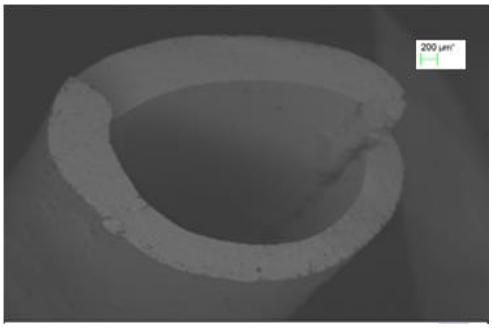
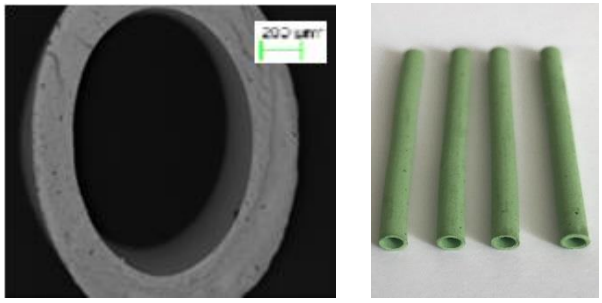


Fig.1: SEM images of anode support micro-tube prepared with 40 wt. % solvent

50 wt. % solvent concentration provides a successful extrusion and sintering step as shown in Figure 2. A further increase in the solvent content (55 wt. %) leads to piling up of the slurry during the extrusion step as illustrated in Figure 3. This may be due to relatively low viscosity of the corresponding extrusion slurry as a result of relatively higher amount of solvent addition.



(a) (b)

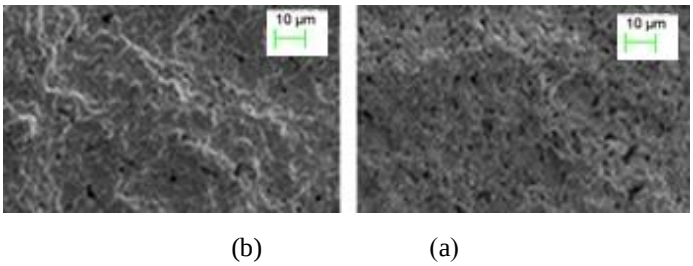
Fig. 2: SEM images (a) and photo after sintering (b) of anode support micro-tubes with 50 wt. % solvent



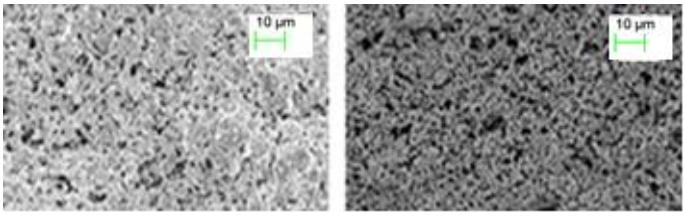
Fig.3: Photo of the extrusion step of the slurry having 55 wt. % solvent

3.2. Effect of pore former content

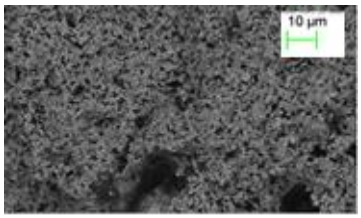
After deciding the amount of solvent in the extrusion slurry, pore former content is studied since SEM images shown in Figure 1 and Figure 2 indicate an inadequate porosity. In order to investigate the effect of pore former content in the extrusion slurry of NiO-YSZ anode support micro-tubes, various solutions including 5-20 wt. % pore former with respect to solid powders are prepared. The resultant microstructures are shown in Figure 4. As expected, the porosity tends to increase with increasing the pore former content. On the other hand, the mechanical strength of the tubes is inversely affected. Although an improvement in the gas diffusion can be achieved at higher pore former contents, the number and the length of the anode triple phase boundaries, where anode electrochemical reactions take place, certainly decrease. Therefore, it is reasonable to expect relatively low cell performances at high anode porosities. Considering the decrease in both mechanical strength and the number of electrochemical reaction zones with the porosity together with long experience in planar SOFCs, the pore former content in the NiO-YSZ anode support micro-tube extrusion slurry is selected as 10 wt. %.



(b) (a)



(c) (d)

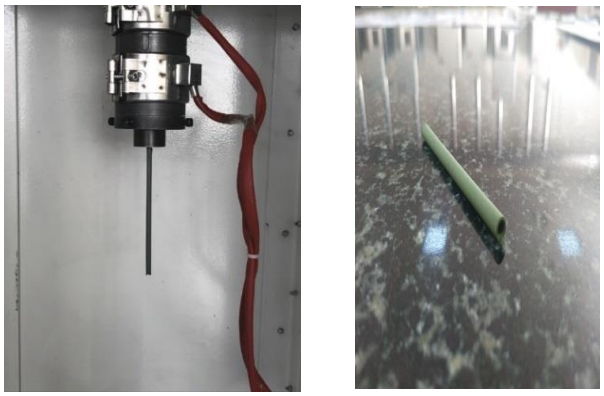


(e)

Fig.4: Micrograph of NiO-YSZ anode support micro-tube without pore former (a) and with 5-20 wt. % pore former (c-e)

3.3. Effect of plasticizer content

With the addition of pore former into the extrusion slurry, it is observed that the workability of the extrudates decreases, leading to broken structure during cutting the micro-tubes after the extrusion at a desired length. To solve this problem, 1, 5, 7 and 10 wt. % plasticizer with respect to solid powders is added into the mixture. According to the observations during the extrusion process, it is seen that at 7 and 10 % loadings the hardness of the extrudates is inadequate, resulting in micro-tubes with non-uniform thickness and irregular geometry. At 1 wt. % plasticizer content, on the other hand, there is no significant change observed in the workability of the extrudates. Therefore, the optimum plasticizer content is decided to be 5 wt. % with respect to solid anode powders. Photos of the extrusion process and of the micro-tube after sintering at this plasticizer content are given in Figure 5.



(a) (b)

Fig.5: Extrusion process of the slurry having 5 wt. % plasticizer (a) and the resultant micro-tube after sintering (b)

After determining the suitable amounts of solvent, pore former and plasticizer, anode support micro-tubes are coated with YSZ electrolyte and LSM-YSZ cathode in an order via dip coating to fabricate anode-supported micro-tubular cell. The active cathode length is adjusted to 50 mm whereas the total length is 70 mm. The inner and outer diameter of the anode support is measured to be 3 mm and 4.5 mm, respectively while both the electrolyte and the cathode layers have a thickness of 20 µm. The cell is then tested under hydrogen and open cathode conditions at 700-800 °C operation temperatures in a temperature-controlled furnace. The performance results are depicted in Figure 6. As expected, the cell performance tends to increase with the operating temperature due to enhanced reaction rate at elevated temperatures. Open circuit potentials are close to theoretical value indicating dense and crack free electrolyte layer together with achieved gas tightness in the tests. The cell exhibits 1.43 W/cm2 peak power density at an operation temperature of 800 °C, which is compatible with the current literature.

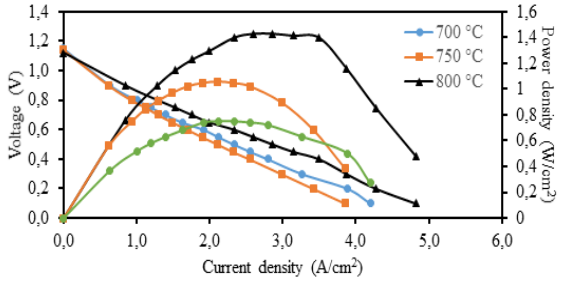


Fig.6: Performance curves of NiO-YSZ supported anode supported micro-tubular SOFC

Conclusions

In this study, the amounts of solvent, pore former and plasticizer used in the extrusion slurry of NiO-YSZ anode support are experimentally optimized, considering a successful extrusion process without any defects together with microstructural observations. The results indicate that at low solvent contents, it is not possible to extrude the slurry due to agglomeration while at high solvent contents, the slurry cannot proceed further and conglomerate on the die due to relatively low viscosity. In addition, in spite of the additives in the extrusion slurry, the final porosity of the anode support micro-tube is found to be inadequate for the desired gas diffusion. Therefore, some amount of pore former addition into the extrusion slurry is required. On the other hand, the mechanical strength and the number of the reaction zones decrease with the pore former content. In addition, the workability of the extrudate is observed to be not enough

with the addition of pore former. To eliminate this problem, addition of certain amount of plasticizer into the extrusion slurry is suggested. However, it is observed that at higher plasticizer contents, the slurry shows a fluidization behavior, thus low hardness. As a conclusion, the amount of solvent, pore former and plasticizer should be carefully decided to obtain anode support micro-tubes with desired properties. Within the ranges considered in this study, the appropriate amount of organic solvent, pore former and plasticizer in the extrusion slurry for the fabrication of NiO-YSZ anode support micro-tube with desired properties are found to be 50 wt. %, 10 wt. % and 5 wt. %, respectively.

References:

[1] K. Kendall, "Progress in Microtubular Solid Oxide Fuel Cells", International Journal of Applied Ceramic Technology, 7(1) (2010), 1-9.

[2] J. Van herle, R. Ihringer, N. M Sammes, G. Tompsett, K. Kendall, K. Yamada, C. Wen, T. Kawada, M. Ihara, and J. Mizusaki, "Concept and technology of SOFC for electric vehicles", Solid State Ionics, 132(3) (2000), 333-342.

[3] T. Suzuki, Y. Funahashi, T. Yamaguchi, Y. Fujishiro, and M. Awano, "Performance of the Micro-SOFC Module Using Submillimeter Tubular Cells", Journal of The Electrochemical Society, 156(3) (2009b), B318-B321.

[4] D. Panthi, B. Choi, and A. Tsutsumi, "Fabrication and Evaluation of a Micro-Tubular Solid Oxide Fuel Cell with an Inert Support Using Scandia-Stabilized Zirconia Electrolyte", Journal of the Electrochemical Society, 162(14) (2015), F1555-F1560.

[5] Y. H. Du, and N. M. Sammes, "Fabrication and properties of anode-supported tubular solid oxide fuel cells", Journal of Power Sources, 136(1) (2004), 66-71

[6] T. Yamaguchi, T. Suzuki, S. Shimizu, Y. Fujishiro, and M. Awano, "Examination of wet coating and co-sintering technologies for micro-SOFCs fabrication", Journal of Membrane Science, 300(1-2) (2007), 45-50.

[7] H. Monzon, M.A. Laguna-Bercero, A. Larrea, B. I. Arias, A. Varez, and B. Levenfeld, "Design of industrially scalable microtubular solid oxide fuel cells based on an extruded support", International Journal of Hydrogen Energy, 39(10) (2014), 5470-5476.

[8] H. Sumi, T. Yamaguchi, K. Hamamoto, T. Suzuki, Y. Fujishiro, T. Matsui, and K. Eguchi, "AC impedance characteristics for anode-supported microtubular solid oxide fuel cells", Electrochimica Acta, 67 (2012), (159-165).

[9] T. Suzuki, Y. Funahashi, T. Yamaguchi, Y. Fujishiro, and M. Awano, "Effect of anode microstructure on the performance of micro tubular SOFCs", Solid State Ionics, 180(6-8) (2009), 546-549.

6th International Conference on Materials Science and Nanotechnology For Next Generation (MSNG2019)
October 16-18, 2019, Niğde, TURKEY (ORAL FULL TEXT)

Synthesis and Thermal Properties of Iron-Based Different Alloy Nano Structures and Characterization with Molecular Dynamic Simulation

Ö. Savaş Pekdur[1], and S. Öztürk Yıldırım[1]*
[1] Department of Physics, Faculty of Sciences, Erciyes University, Kayseri 38039, TURKEY

This study presents for obtaining both theoretical and experimental nanoparticles, DFT (Density Functional Theory) and hydrothermal methods were used. In our calculations, Gaussian 09W and Gauss View programs including molecular mechanics, quasi-experimental and ab-initio methods, which have a large number of theories and basic set options used and also for characterizing structures fourier transform infrared spectroscopy are used and also obtaining size and structure of nanoparticles were studied by analyzing X-ray diffraction and morphology of surface and structure of synthesized nanoparticles were studied

Keywords: DFT, Hydrothemal process
Corresponding authors: ozturk@erciyes.edu.tr

1. Introduction

Especially 21st century nanoparticles have become a very important part of our lives. The types of nanoparticles investigated have extended our lives and brought great convenience to our lives due to their useful properties [1]. Iron oxides are compounds used in nanoparticles. The size of the iron oxides obtained at the nanoscale is very low. Because they are nanoscale, they stack together and reduce surface energies. Surfactant (surface coating) is added to the structures to influence magnetic interaction. The oxidation caused by the external environment is minimized by the coating, the distribution of the particles in different environments is ensured and thus the application areas are increased. In general, there are various synthesis processes used in the development of magnetic nanoparticles. Before the experimental process, there are many chemical calculations made using computer in chemical research. The data obtained by theoretical calculations are very consistent with the data obtained by experimental methods such as ^{13}C and ^{1}H-NMR spectral data, IR frequency values, bond angles, bond lengths, dihedral angles, Mulliken atomic charges, HOMO-LUMO energies, dipole. Most of the features are available in less time and more reliably. Here, depending on the physical, chemical, thermal and mechanical properties, nanoparticle size, surface growth and composition density can be changed by experimental processes [2-4]. As is known, nanostructures range from 1 nm to 100 nm [5]. Nanoparticles of these dimensions have different physical properties compared to other structures [6]. Accordingly, the change in particle sizes changes the magnetic properties of the particles. When we look at these structures, it is very important to extend the application areas which are known to determine the superparamagnetic or ferromagnetic properties of the structure depending on the magnetization values of the structure.

The size of the iron oxides obtained at the nanoscale is very low. Because they are nanoscale, they stack together and reduce surface energies. The magnetic interaction added to the surfactant (surface coated) structures is important. Oxidation caused by the external environment is minimized [7]. With the coating, dispersions of the particles in different media are obtained, thereby increasing the application area. The particles may be coated with an organic layer (polymer or surfactant) or an inorganic layer (gold, silver, silica, carbon) [8].

Magnetic nanostructures are seen in 3 structures as magnetite (Fe_3O_4), maghemite (γ-Fe_2O_3) and hematite (α-Fe_2O_3). These structures have a wide range of applications. Due to its low toxicity and low magnetic crystal anisotropy, it is preferred in technological and biomedical applications, drug therapy, magnetic cell separation and biosensor applications.

Today, iron oxide (Fe_3O_4) nanoparticles can be synthesized in many different ways. These methods include hydrothermal method, co-precipitation, microemulsion, thermal precipitation, sol-gel method. [9-11]. In the synthesis of nanostructures, the hydrothermal method is the most preferred method due to the high crystallinity and temperature-dependent variation of the particle size.

The first stage of the study consists of theoretical calculations. Nowadays, there are many chemical calculations made using computer in chemical research. In our calculations, Gaussian 09W [12] and GaussView [13] programs including molecular mechanics, quasi-experimental and ab-initio methods, and a large number of theories and basic set options are used. Hartree-Fock method (HF) and Becke's three-parameter energy function hybrid approach [14] and Lee-Yang and Parr [15]'s correlation function within the program, B3LYP theory 6 -31G (d, p) Basic set was used. In addition, the basic sets DFT / 6-31G (d, p) and HF / 6-31G (d, p) are used. In our study, the basic bond angles, bond lengths, bond angles, HOMO-LUMO and Mulliken atomic charges of the molecules we synthesized theoretically were calculated. The structures formed are iron based structures. The detailed analysis of these structures, the highest occupied molecular orbital and the lowest empty orbital eigenvalues and other parameters were examined meticulously and the probability and yield of the compound were investigated depending on these parameters. We have once again observed that many features are obtained in a shorter time and more reliably

It has been a challenge to accurately describe the magnetic and electronic properties, especially from conventional density functional theory DFT that explain iron oxide which have electronic band gap. The electronic and equilibrium structure density function theory of Fe_3O_4 used in our experiments was calculated by calculating the hybrid density of DFT and B3LYP, and the structure equilibrium of the cubic cell was calculated. Particularly, α-FeOOH, α-Fe_2O_3, Fe_3O_4 and FeO are the most common compositions in many heterogeneous catalysis.

DFT and B3LYP density functions were used to calculate phonons at the point of the Brillouin region. The frequencies predicted for these crystal structures are compared to frequencies of infrared conductivity.

There have been several studies about structure of magnetite Fe3O4 which computed using DFT and B3LYP hybrid density functional[16-18] Studied electronic structure and crystal structure of Fe_3O_4 in the cubic and monoclinic unit cells using generalized gradient approximation _GGA_–density functional theory _DFT_ or B3LYP hybrid DFT[19]. Classified oxide based on the stres condition. They work interface of properties from DFT calculations and they are using to find failure modes in metal-metal-oxide interfaces are searched the charge redistribution between systems by CCD charge density differences [20].

In the second stage of our study, experimental method was followed. In this study, the controlled changes in the crystallinity and size of the superparamagnetic nanoparticles synthesized by hydrothermal methods and the changes in their magnetic properties were investigated. Changes in particle size depend on surfactant, temperature,

2. Experimental details

2.1. Iron Oxide (Fe_3O_4)

Magnetite is a natural iron oxide magnet, so the name offers a very pleasant distinguishing feature. Magnetite is the most magnetic of all minerals in the world.

Magnetite is shown as as the formula A (B) 2O4. A and B are shown atom's ions which covered possible regions of the crystal structure. Because of the magnet, Fe_3O_4, A metal Fe^{+2} and B metal Fe^{+3}; Two different metal ions in two special area. This arrangement causes electron transfer between different irons in a structured path or vector. This electric vector produces a magnetic field.

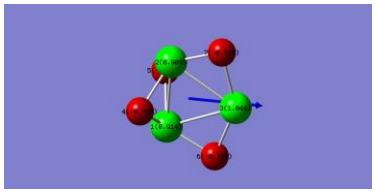


Fig.1: Conformation of Fe_3O_4

The most suitable form of structure iron oxide is drawn as a result of several stages. A conformation is optimized with Gaussian 03 B3LYP / 6-31 (d, p) calculated method package. The optimized conformation

of the steady state is shown in Fig. 1. To determine the most suitable conformation, many conformations are drawn and the relative energies of the conformations are calculated. Energies of molecule, bond lenghts, bond angles, distance between atoms, standard orientation and HOMO-LUMO values were examined. Accordingly, B3LYP / 6-31 (d, p) was optimized using the method and Table 1, Table 2 and Table 3 collected.

Table 1: Energies of conformation (eV).

Energy	Gibbs Free Energy	ZFC
4091.83321	4091.874778	4091.840865

It was concluded that the structure formed was determined by looking at the energies of the conformation. According to the results, the difference between the energy of the structure, Gibbs energy and zero point energies is very small. This is an indication that the structure is stable.

According to HF / 6-31G (d, p) calculations change of bond length and bond angles in Fe_3O_4 are given in Table 2 and Table 3.

Table 2: Fe_3O_4's bond lengths [Å].

Parameter	Bond Lenghts
Fe1-Fe2	2.1956
Fe1-Fe3	2.3371
Fe1-O1	1.765
Fe1-O2	1.765
Fe1-O3	1.6646
Fe2-Fe3	2.3351
Fe2-O1	1.7648
Fe2-O2	1.7649
Fe2-O4	1.6643
Fe3-O3	1.8468
Fe3-O4	1.8468

B3LYP / 6-311 ++ with G (d, p) base set In another study, the average length of this bond 1.795Å, 1.822Å and 2,2371Å is given as [21-26]. Our calculations are consistent with these studies

Table 3: Fe_3O_4's bond angles [°].

Parameter	Bond Angles
FE2-Fe1-O3	113.6232
Fe3-Fe1-O1	87.719
Fe3-Fe1-O2	87.6906
O1-Fe1-O2	93.5545
O1-Fe1-O3	120.792
O2-Fe1-O3	120.7633
Fe1-Fe2-O4	113.7687
Fe3-Fe2-O1	87.7895
Fe3-Fe2-O2	87.7604
O1-Fe2-O2	93.5683
O1-Fe2-O4	120.8618
O2-Fe2-O4	120.8455
Fe1-Fe3-O4	101.1089
Fe2-Fe3-O3	101.0797
O3-Fe3-O3	146.1297
O3-Fe1-Fe2-O4	-0.0079
O1-Fe1-Fe3-O4	-46.8059
O2-Fe1-Fe3-O4	46.8466
O1-Fe2-Fe3-O3	46.8169
O2-Fe2-Fe3-O3	- 46.8434

The longest Fe-Fe bond is Fe2-Fe3, 2,33510197Å and the longest Fe3-O4 bands is 1,8433 Å as calculated. And also Fe1-Fe2 band and the other Fe-O bands are expected value and also while we look at the angles, the values have good agreement with the literature. Mean bond lengths from the B3LYP functional calculation, where bond lengths were allowed to calculation.

Table 4: Standard Orientation Coordinates.

Center number	Atomic Number	x	y	z
1	**26**	-1.11936	-0.59927	-0.00201
2	**26**	1.07263	-0.67363	0.00270
3	**26**	0.05137	1.42840	-0.0015
4	**26**	-0.03077	-1.1472	-1.28590
5	**26**	-0.04906	-1.1348	1.29094
6	**26**	-1.73062	0.95014	-0.00314
7	26	1.7954	0.8261	0.00100

Standard orientation is shown that in the gas is the form of iron oxide in cartesian coordinates and is given that Table 4.

Mulliken load distribution, the main idea of the method is to distribute the wave functions to atoms while the overlap is possible. But this distribution does not show the complete electronegativity of the elements. Mulliken loads experimental data used to make qualitative estimates other than quantitative prediction.

Table 5: Mulliken atomic charges.

Fe1	1.073331
Fe2	1.071951
Fe3	1.038357

O4	-0.768009
O5	-0.772577
O6	-0.822345
O7	-0.820708

Sum of Mulliken charges summed into heavy atoms as shown tahat the moleculer of Fe_3O_4 is determined.



Fig.2: HOMO AND LUMO of Fe_3O_4

Molecular orbital theory due to interactions between HOMO-LUMO p-p * transitions are observed in transition states according to other works [27]. HOMO energy ionization LUMO energy is related to electron activation HOMO and LUMO. The energy difference between is called energy band gap. Structures is an important parameter for stability.

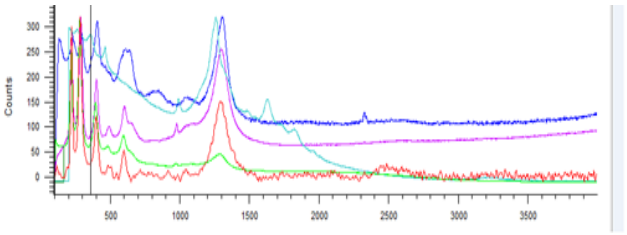


Fig.3: Raman spektra of Fe_3O_4

The method used in the experimental study is the hydrothermal method. In experimental results as shown by Raman spektra Figure 3. And the results are discussed in Ref 29. The structural and magnetic properties of the synthesized nanoparticles were investigated. Changes in the structural and magnetic properties of the nanoparticles were investigated depending on the reaction time, temperature and pH parameters. On the other hand, the surfaces of the particles were coated with the surfactant TA, which we call surfactant.

2.2. Metarials

The chemical reagents used in this work were this Iron (III) sulfate($(Fe_2(SO_4)_3)$ Sigma Aldrich >99%) and ferrous sulphate heptahydrate. ($FeSO_4$.7H2O sodium hydroxide (NaOH, Sigma Aldich >99%) and PEG (Sigma Aldich >99%) All the chemical reagents were of analytical degree.

2.3. Synthesis

The samples of magnetite nanoparticles were prepared according to our last study to Ref 28. All the steps are told there.

2.4. Characterization

The devices are the same which we have used our last experimental and analyses are given Ref 29. The properties of these devices appropriate the search our expectations that we suspect.

3. Results and discussion

We have preapered nanoparticles with the hydrothermal synthesis method which increases heat and time. We performed this based on the mixing of ferric sulfate and iron sulphate during a wet process involving the Fe 2 + and Fe 3 + reaction.

The results which we have found our last study that are given that Ref 28. By XRD purity of samples prepared at different temperatures and amount of TA. The XRD peaks are e five diffraction peaks (220), (311), (400), (422), (440). And the their highest intensity peak was (311). A spinel structure of the Fe3O4 crystal, and the resulting nanoparticles are a magnetic structure [30]. To search the effect of the reaction temperature on the nanoparticle size without surfactan, the temparature was increased from 100 °C to 150 °C, the d_{XRD} increased from 14 to 16 nm.

As a result that using surfactan, particle size is become smaller and when temperature increased 150°C to 180°C, the particle's size increased from 16 nm to 67,5 nm. At 150°C iron oxide was found, d_{XRD} is 13 nm. We have identified TA as both surfactant and modulators.

The d_{FESEM} of the nanoparticles are also listed in Table 5 and some selected FESEM images of the nanoparticles were displayed Ref 28. In the absence TA hydrothermal process are well crystallized, exhibiting a broad size distribution and a relatively small mean size ~24 nm (Table 6). During the hydrothermal process in the absence of TA. The S1-150-0 particles grow intensely and reach 80 nm at 150°C. Because of the founding such a big particles we purposed that absence of the TA caused the growth. Presence of tartaric acid, d_{FESEM} of nanoparticles decreased in order of 80nm and 18 nm. As a result that the growth is strongly inhibited, even at elevated temperatures, when the value of amount of TA is high. We purposed that while increasing temperature the

growing of particle size is bigger than 30 nm But TA is inhibit the growing so at optimal temperature we get superparamagnetic and ferromagnetic particles nanopartizles. Reflections are a magnetite feature with a hollow structure [31-32]

However, when the temperature of the solution was 180 °C, the absorption intensity decreased. And the d_{XRD} of the nanoparticles are not observed to be consistent with the d_{FESEM}. We deducted that when the solution reaches supersaturation, crystal nuclei are formed and the release of iron ions is stopped. Weak change in such a different temperatures interval will depend on the inhibition of TA to grow iron oxide crystals. However, crystal growth is quite slow due to the inhibitory effect of TA and the increase in absorption curve. This trend can then be explained by the fact that FeOOH must correspond to the dehydration phase and the Fe_3O_4 crystals to the growth phase.

Table 6: The crystal parameters, d_{XRD}, lattice parameters, d_{FESEM} of nanoparticles calculated from the broadened peak data using the Scherer equation and represented.

Sample	T (°C)	a (nm)	d_{XRD}(nm)	d_{SEM}(nm)	Reaction Time	H (Oe)
S1-100-0	100	8.366	14	24.0±2	6	99
S1-150-0	150	8.366	16	80±2.3	6	99
S1-150-1	150	8.366	13	18±5.8	6	99
S1-150-2	150	8.366	20	10±3.0	6	99
S1-180-1	180	8.366	67,3	18±3.4	1	99
S1-180-2	180	8.366	67,3	20±5.0	1	99

Conclusions

As a result of the bond lengths and bond angles of the structure of iron oxide structure and better understand the structure can be added to the structure we can work on what we can understand the possible work This simulation study was a preliminary data study for us. We examined the basic properties of the structures that may occur by centering iron oxide. We have worked on new ligands and new surface coatings that can be added to this structure .As we found that bond lengths and angles are avarege.

In experimental section we examined nanoparticles at different temperatures which coated with surfactant. The XRD results are given as we told that Ref 23. We can say that some of the particles we find as a result of the particle are superparamagnetical.

We can say that when we use TA as a surfactant in the synthesis of magnetic Fe3O4 nanoparticles, the particles become smaller.

We can also come to the conclusion that using DFT we can say that by analyzing iron oxide we can find bond charecteristics as a atomic orbital. Altough the bond's energies are too low, O atoms are has got a ability to electron exchange.

Acknowledgement

This research is part of second author's Ph.D. thesis and was financially supported by the Erciyes University Scientific Research Project Coordination Unit, Turkey (Project no: 2017- FDK-7785).

References:

[1] L. Xiao, J. Li, D.F. Brougham, E.K. Fox, N. Feliu, A. Bushmelev, A. Schmidt, N. Mertens, F. Kiessling, M. Valldor, B. Fadeel and, S. Mathur, Water-soluble superparamagnetic magnetite nanoparticles with biocompatible coating for enhanced magnetic resonance imaging, ACS Nano, (2011). 5(8), 6315.

[2] M. Veverka, P. Veverka, O. Kaman, A. Lancok, K. Zaveta, E. Pollert, K. Knizek, J. Bohacek, M. Benes, P. Kaspar, E. Duguet and S. Vasseur, Magnetic heating by cobalt ferrite nanoparticles, Nanotechnology, 18, (2007), 345704.

[3] S. Gyergyek, D. Makovec, M. Jagodic, M. Drofenik, K. Schenk, O. Jordan, J. Kovac, G. Drazic and H. Hofmann, Hydrothermal growth of iron oxide NPs with a uniform size distribution for magnetically induced hyperthermia: Structural, colloidal and magnetic properties. Journal of Alloys and Compounds, (2017), 691, 261.

[4] B. Rožič, M. Jagodič, S. Gyergyek, M. Drofenik, S. Kralj, G. Cordoyiannis and Z. Kutnjak, Multiferroic Behaviour in Mixtures of the Ferroelectric Liquid Crystal and Magnetic Nanoparticles, Mol. Cryst. Liq. Cryst. (2011),545, 1323.

[5] S. Lefebure, E. Dubois, V. Cabuil, S. Neveu and R. Massart, Monodisperse magnetic nanoparticles: Preparation and dispersion in water and oils, J. Matter. Res. 13, (1998), 2975.

[6] H., Goesmann, and C., Feldmann, "Nanoparticle Function Materials", Angew. Chem. Int. Ed., 49, (2010), 1362-1395.

[7] U., Jeong, X.,Teng, Y., Wang, H., Yang, and , Y., Xia Superparamagnetic Colloids: Controlled Synthesis and Niche Applications, Adv. Matter, 19, (2007), 33-60.

[8] A., Lu, E.L., Salabas, and F., Schüth, "Magnetic Nanoparticles: Synthesis, Protection, Functionalization and Application", Angew. Chem. Int. Ed., 46, (2007), 1222-1244
[9] R. M., Cornell, U., Schwertmann, The Iron Oxides, Wiley-VCH 2nd Edition (2003).
[10] R., Fan, X., Chen, H., Gui, Z., L., Liu,. and Z. Y., Chen, A new simple hydrothermal preparation of nanocrystalline magnetite Fe3O4, Materials Research Bulletin, 36, (2001), 497-502.
[11] Z.L., Liu, Y. J., Liu, K. L., Yao, Z. H., Ding, J., Tao, and X., Wang, Synthesis and magnetic properties of Fe3O4 nanoparticles, Journal of Materials Synthesis and Processing, 10, (2002), 83-87.
[12] M.J. Frisch, G.W Trucks, H.B. Schlegel, A Complete DFT, TD-DFT and Non-Linear Optical Property Study on 6-Amino-2-Methylpyridine-3-Carbonitrile (2009) Gaussian 09 Revision C 01 Gaussian 09 Revis B01. Gaussian Inc., Wallingford.
[13] J.B. Foresman, and A. Frisch, NBO Population Analysis and Electronic Calculation of Four Azopyridine Ruthenium Complexes by DFT Method, Exploring Chemistry with Electronic Structure Methods. (1996) 2nd Edition, Gaussian Inc., Pittsburgh.
[14] A. D. Becke, Density-functional exchange-energy approximation with correct asymptotic behavior,Phys. Rev. A 38, 3098 – Published 1 September 1988.
[15]C. Lee, W. Yang, and R. G. Parr,Development of the Colle-Salvetti correlation-energy formula into a functional of the electron density,Phys. Rev. B 37, (1988),785.
[16] Andrew D. Rowan and Charles H. Patterson School of Physics, Trinity College Dublin, Dublin 2, Ireland Hybrid density functional theory applied to magnetite:Crystal structure, charge order, and phonons, PHYSICAL REVIEW B 79, (2009), 205103.
[17] Y. Meng, X.-W. Liu, C.-F. Huo, W.-P. Guo, D.-B. Cao, Q. Peng, A. Dearden, X. Gonze, Y. Yang, J. Wang, H. Jiao, Y. Li, and X.-D. Wen, When Density Functional Approximations Meet Iron Oxides (2016), J. Chem. Theory Comput.
[18] J. H. Noh, I. Osman, A. Saadullah, P. Winget, J.-L. Bredas, Magnetite Fe3O4 (111) Surfaces: Impact of Defects on Structure, Stability, and Electronic Properties (2019)American Chemical Society (ACS).
[19] K. Schütze, J.C. Wilson, S. Weinbruch, N. Benker, M. Ebert, G. Günther,R. Weigel, and S. Borrmann,Sub-micrometer refractory carbonaceous particles in the polar stratosphere, Atmos. Chem. Phys., 17, 2017.12475–12493, 17-12475-2017.
[20] W. Tang , E. Sanville and G. Henkelman, A. grid-based Bader analysis algorithm without lattice bias,Journal of Physics: Condensed Matter, Volume 21, Number 8, Published 30 January 2009 • IOP Publishing Ltd
[21] P., Keith, F. H., McKenna, G., Daniel, V. K. Lazarov, C. Chen, Z. Wang& Y. Ikuhara-Atomic-scale structure and properties of highly stable antiphase boundary defects in Fe3O4.
[22] A.Pratt, , M. Kurahashi, , X., Sun, D. Gilks, & Y. Yamauchi, Direct observation of a positive spin polarization at the (111) surface of magnetite. Phys. Rev. B 85, Hibma, T. et al. Anti-phase domains and magnetism in epitaxial magnetite layers. J. Appl. Phys. 85, (1999), 5291–5293.
[23] S. Celotto, W. Eerenstein, & T. Hibma, Characterization of anti-phase boundaries in epitaxial magnetite films. Eur. Phys. J. B Condens. Matter 36, (2003), 271–279.
[24] E. Verwey, Electronic conduction of magnetite (Fe3O4) and its transition point at low temperatures. Nature 144, (1939),327–328.
[25] A. Rowan, C. Patterson, & L. Gasparov, Hybrid density functional theory applied to magnetite: crystal structure, charge order, and phonons. Phys. Rev. B 79, (2009), 205103.
[261] W. Wang, et al. Fe t2g band dispersion and spin polarization in thin films of Fe3O4(001)/MgO(001): half-metallicity of magnetite revisited. Phys. Rev. B 87, (2013), 085118.
[27] K. Fukui, Theory of Orientation and Stereo Selection. Springer-Verlag, Berlin,(1975) 58.
[28] S. Ö. Yıldırım, Ö. S. Pekdur, A. Ekicibil and M. Akkurt, Determination of the Dimensions of Iron Oxide Nanowires by Hydrothermal Method, International Conference of Strategic Research on Scientific Science and Education 2018 (ICoSReSSE 2018).
[29] Ö. S. Pekdur, S. Ö. Yıldırım, Synthesıs And Characterızatıon Of Fe3O4 Nanopartıcles, Imstec 2018.
[30] Gasparov, L.V.,Patterson, C.H.; Rowan, A.D. (2002) p.66.
[31] T. Taniguchi, K. Nakagawa, T. Watanabe, N. Matsushita, M. Yoshimura, Hydrothermal Growth of Fatty Acid Stabilized Iron Oxide Nanocrystals,(2008) American Chemical Society.
[32] N. G., Shrıramjı, S., Sharma, R. S., Ningthoujam, A., Nigam (2008) p.181-185.

6th International Conference on Materials Science and Nanotechnology For Next Generation (MSNG2019)
October 16-18, 2019, Niğde, TURKEY (ORAL FULL TEXT)

Histopathological Analysis of the Liver Tissue Across Different Cytotypes of the Blind Mole Rat: *Nannospalax xanthodon*

Burcu BİTERGE SÜT[1], Ayşe İKİNCİ KELEŞ[2], Teoman KANKILIÇ[3]

[1]*Niğde Ömer Halisdemir University, Faculty of Medicine, Department of Medical Biology*
[2]*Niğde Ömer Halisdemir University, Faculty of Medicine, Department of Histology and Embryology*
[3]*Niğde Ömer Halisdemir University, Faculty of Science and Literature, Department of Biotechnology*

Blind mole rats (genus *Nannospalax*) are wild rodents with significant adaptation to subterranean life. These organisms are best known for their high tolerance to hypoxia and resistance to cancer. Blind mole rats exist in several different cytotypes with chromosome numbers ranging from 2n=36 to 2n=62 and are represented as four major species living in Turkey; *N. xanthodon, N. leucodon, N. ehrenbergi,* and *N. tuncelicus*. This study aimed to comparatively analyze the liver tissue to determine possible cellular and structural changes between different cytotypes.

Liver tissues from different *Nannospalax* cytotypes (2n=52, 54, 58 and 60) harvested, formalin-fixed and paraffin embedded through histological procedures. 5 micron sections were cut using a microtome. Liver sections were stained with hematoxylin-eosin (H&E) and their histopathology was evaluated under the light microscope. Additionally, in order to have a better view of the nuclear organization, sections were stained with DAPI (4′,6-diamidino-2-phenylindole) and analyzed using a fluorescent microscope. Our results did not identify significant structural differences in the liver parenchyma, portal areas, hepatocytes as well as their nuclear organization.

This study provides the first comparative analysis on the liver tissue of *Nannospalax* cytotypes with varying chromosome numbers. Our finding that liver tissue from different cytotypes of *Nannospalax* did not have unique histological structures suggest that these tissues are unlikely to possess distinct functions. Liver is a vital organ for an organism; therefore, it is highly similar in structure across different organisms, which is in line with our findings.

Keywords: Histopathology, blind mole rat, liver tissue, nuclear organization

Corresponding author: bbitergesut@ohu.edu.tr

1. Introduction

Subterranean mammals often converge at molecular and organismal levels while developing adaptations to life underground [1]. Blind mole rats (genus *Nannospalax*) are wild rodents with significant adaptation to subterranean life. Due to external factors that drive evolution such as the climate change, through affecting vegetation that acts as a population filter, "*Spalax*" lineage has split into various clades [2]. Turkey is one of the main habitats of the blind mole rats, which are represented as four major species; *N. xanthodon, N. leucodon, N. ehrenbergi,* and *N. tuncelicus*. Several studies have indicated that it is very complicated to clearly define the taxonomic status of these rodents as their chromosomal variations are not reflected in the extent of morphological differentiation [3-5]. Karyological studies have reported that different *Nannospalax* cytotypes display distinct chromosomal polymorphisms [6]. In Turkey, 21 different karyotypic forms have been described, which exist in several different cytotypes with chromosome numbers ranging

from 2n=36 to 2n=62 [7]. Although the morphologies, chromosomal properties and the mitochondrial DNA composition of the different cytotypes of the blind mole rats are widely studied; there are no studies that extensively analyze the histopathology of the liver tissue across *Nannospalax* cytotypes. Therefore, this study aimed to comparatively analyze the liver tissue from blind mole rats with different chromosome numbers (2n=52, 54, 58 and 60) to determine possible cellular and structural changes.

2. Experimental details

All animal procedures were approved by the Institutional Ethics Committee at Niğde Ömer Halisdemir University (Date: 10.09.2019, Protocol number: 2019/25) and were carried out in accordance with the principles of the Guide for the Care and Use of Laboratory Animals (NIH Publication No. 85-23, revised 1996).
Without any treatment, animals were sacrificed via ether inhalation. Liver tissues were harvested, fixed in 10% formaldehyde and embedded into paraffin through routine procedures. 5 micron sections were cut using Leica Biosystems RM 2245 Microtome (Germany) and stained with Hematoxylin & Eosin (H&E) as described in[8].

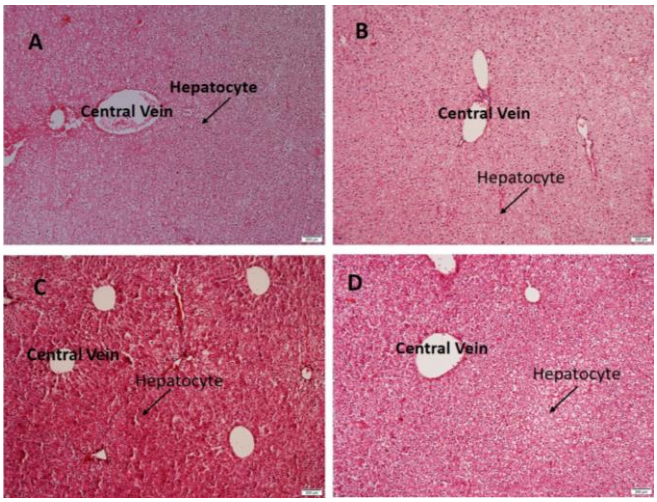


Figure 1. *Histopathological analysis of the liver tissue across Nannospalax cytotypes with chromosome numbers A) 2n= 52, B) 2n= 54, C) 2n= 58, D) 2n= 60 (H&E, x10).*

For immunofluorescent staining with DAPI (4′,6-diamidino-2-phenylindole), the sections were deparaffinized by passing them sequentially through 100%-95%-70%-50% of EtOH. For heat induced antigen retrieval, samples were boiled in 10 mM Sodium Citrate buffer (pH 6.0) for 10 minutes. Sections were permeabilized in 0.4% Triton X-100 in PBS for 20 minutes and blocked with 4% BSA-PBS-Triton X for 1 hour at room temperature. After washing the sections 3x10min in PBS, the sections were mounted in Fluoroshield mounting medium containing the DNA intercalating dye DAPI (Abcam). The sections were sealed with nail varnish and stored at 4°C in the dark.
Microscopic analyses were performed using a microscope (Olympus, BX53, Japan) equipped with a digital camera (DP 80, Olympus, Japan) and Cellsens standard program (version1.17) at different magnifications.

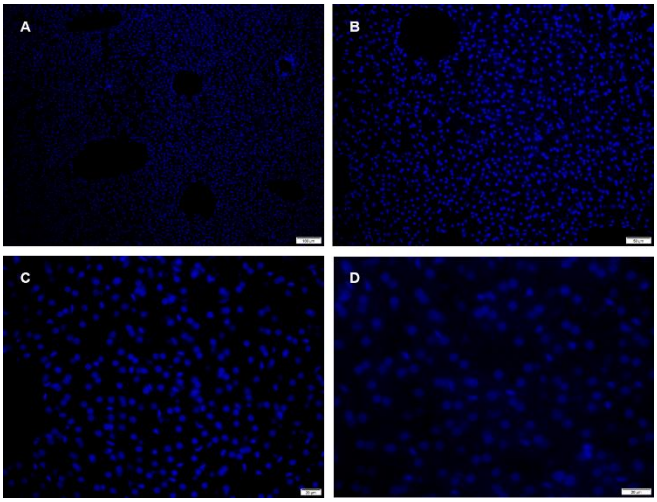


Figure 2. *Nuclear organization of the liver tissue in Nannospalax at a) x10, b) x20, c) x40, d) x60 (DAPI).*

3. Results and discussion

Mammalian livers differ significantly in size in accordance with their body weight [9]. However, structurally and functionally rodent livers share many similarities both within themselves and even with humans [10]. Likewise, the microscopic architecture of the liver is generally similar in all mammals. Our results did not identify significant structural differences in the liver parenchyma, portal areas, hepatocytes as well as their nuclear organization.
The histopathological analysis of the liver parenchyma, portal areas, and hepatocytes from different cytotypes of Nannospalax no difference was observed (Figure 1).
Blind mole rats have evolved into different cytotypes with varying chromosome numbers. However, the functional

reflection of these genomic variations has not been clearly defined yet. In mammals, one copy of the two X chromosomes in females is randomly silenced by tightly packaging the DNA into heterochromatin to provide dosage compensation [11]. In order to investigate whether *Nannospalax* cytotypes with more chromosome numbers undergo a similar heterochromatinization and silencing, we performed immunofluorescent staining using DAPI, which is a DNA-binding dye (Figure 2 and Figure 3). This technique allowed us to evaluate the nuclear organization within the liver tissue across different *Nannospalax* cytotypes, which was quite similar between different specimens despite having significant genomic differences.

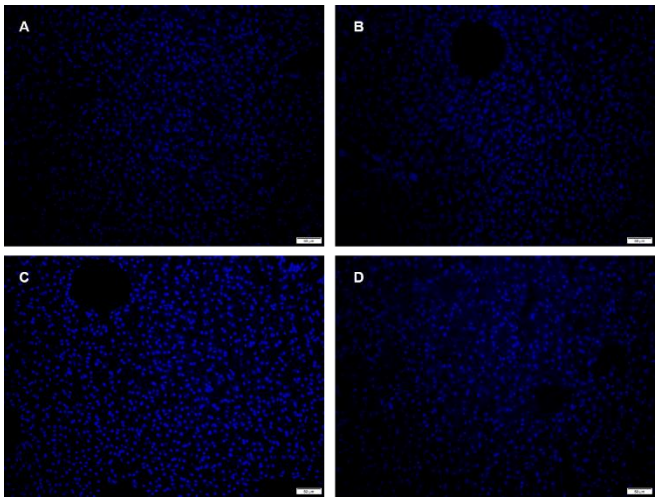


Figure 3. *Nuclear organization of the liver tissue in Nannospalax cytotypes with varying chromosome numbers A) 2n= 52, B) 2n= 54, C) 2n= 58, D) 2n= 60 (DAPI, x20).*

4. Conclusion

This study provides the first comparative analysis on the liver tissue of Nannospalax cytotypes with varying chromosome numbers. Our finding that liver tissue from different cytotypes of Nannospalax did not have unique histological structures or nuclear organization suggests that these tissues are unlikely to differ functionally. Liver is a vital organ for an organism; therefore, it is highly similar in structure across different organisms, which is in line with our findings.

5. Acknowledgements

This research has been supported by a grant to Dr. BİTERGE SÜT by the Scientific Research Projects Coordination Unit of Niğde Ömer Halisdemir University [Project number: SSB2018/05-BAGEP].

6. Author Contributions

BBS and AIK performed the histological procedures. Immunfluorescent stainings and H&E stainings were carried out by BBS and AIK, respectively. TK provided wildtype *Nannospalax* specimens.

References:

[1] Nevo, E. 2000. Mosaic Evolution of Subterranean Mammals Regression Progression and Global Convergence. Oxford University Press. 512.

[2] Hadid, Y., Németh, A., Snir, S., Pavlíček, T., Csorba, G., Kázmér, M., Major, A., Mezhzherin, S., Rusin, M., Coşkun, Y., Nevo, E. 2012. Is evolution of blind mole rats determined by climate oscillations? PLoS One. 7(1):e30043.

[3] Kankılıç, T., Çolak, E., Kankılıç, Tol., 2009. Macro-Anatomical and karyological features of two blind mole rat subspecies (Rodentia: Spalacidae) from Turkey. Anatomia Histologia Embryologia, 38, 145–153.

[4] Sözen, M., M. Sevindik, and F. Matur, 2006a. Karyological and morphological characteristics of Spalax leucodon Nordmann, 1840 (Mammalia: Rodentia) superspecies around Kastamonu Province, Turkey. Turk. J. Zool.30,205–219.

[5] Arslan, A., Arısoy, A., Zima, J. 2014. Comparison of the chromosome banding pattern in the 2n = 56 cytotypes of Nannospalax leucodon and N. xanthodon from Turkey. Scientific World Journal. 2014:121690.

[6] Matur, F., Colak, F., Sevindik, M., Sözen, M. 2011. Chromosome differentiation of four 2n = 50 chromosomal forms of Turkish mole rat, Nannospalax nehringi. Zoolog Sci. 28(1):61-7.

[7] Kankılıç, T., T. Kankılıç, R. Çolak, E. Çolak, and A. Karataş. 2007. Karyological comparison of populations of the Spalax leucodon Nordmann, 1840 supersupecies (Rodentia: Spalacidae) in Turkey. Zool. Middle. East.42,15–24.

[8] Topal, Z., Hanci, H., Mercantepe, T., Erol, H.S., Keleş, O.N., Kaya, H., Mungan, S., Odaci, E. 2015. The effects of prenatal long-duration exposure to 900-MHz electromagnetic field on the 21-day-old newborn male rat liver. Turkish Journal of Medical Sciences. 45: 291-7.

[9] Prothero, J.W. 1982. Organ scaling in mammals: the liver, Comp Biochem Physiol A Comp Physiol, 71:567-577.

[10] Kruepunga, N., Hakvoort, T.B.M., Hikspoors, J.P.J.M., Köhler, S.E., Lamers, W.H. 2019. Anatomy of rodent and human livers: What are the differences? Biochim Biophys Acta Mol Basis Dis. 1865(5):869-878.

[11] Brockdorff, N., Turner, B.M. 2015. Dosage compensation in mammals. Cold Spring Harb Perspect Biol. 7(3):a019406.

6th International Conference on Materials Science and Nanotechnology For Next Generation (MSNG2019)
October 16-18, 2019, Niğde, TURKEY (ORAL FULL TEXT)

Usage of 3d Printing Materials in Creative Industry Applications

B. Ucan, C. Bilsel
Department of Communication Design, Faculty of Art and Design, Yildiz Technical University, 34220 Esenler Istanbul, Turkey

3d printing techniques are widely used in manufacturing applications, mass customization, cloud-based additive manufacturing, rapid manufacturing, rapid prototyping, food, medical applications, bio-printing, pills, automotive industry, computers and robots, 3d selfies, communication, cultural heritage, etc. In this research, usage areas of 3d printer materials in creative industry applications are investigated and examined on samples. It has been determined how the material technology is used in creative industry applications; the future of 3d printer technologies and innovative materials in this field. The examples are based on the usage of 3d technologies in design, the applications of the materials in this field have been evaluated and the scope of the study has been limited in this way. The aim of this research is to examine the historical process of design-based 3d printers and materials, the different application techniques in today's fields and the effects of new approaches in the future.

Keywords: 3d printing, casting, design.

Corresponding authors: bucan@yildiz.edu.tr

1. Introduction

The three-dimensional printer and material technology are the subjects of this article and they have been researched within the following headings. It is aimed to create awareness about 3D technology and 3D printing materials.



Figure 1 Charless Hull, 3D Systems

The first three-dimensional printer and SLA technology was developed in 1984 by Charless Hull [12]. First 3D printer technology company was founded by 3D Systems in 1986, and the first color printing was produced in the USA in 1993. At the same time, NASA (National Aeronautics and Space Administration) created the deficiencies and hardware needs of astronauts and scientists in space through 3D printer technology reduced the cost of sending spare parts. [3], [4]. In the 2000s, open source codes influenced the expansion of the mass of users in the future of smart printers, while at the Massachusetts Institute of Technology (MIT) scientists printed programmable 3D formats using pure glass material. By RepRap project [5], [6], 3D printers have become available to users, thus reducing the cost of 3D printers.

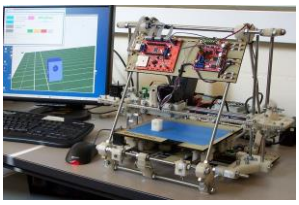


Figure 2 RepRap project

Working principles of 3D printers start with sketch design; drawings with programs such as AutoCAD, Solid works and 3DsMax are transformed into 3D models. The formation of the model is completed by overlapping the filament melting with heat. There are more than 100 trademarks and machines in the 3D printer industry. Zortrax, Stratasys, Leapfrog 3D printers and Form labs Form 1+ are the most well known 3D printers.

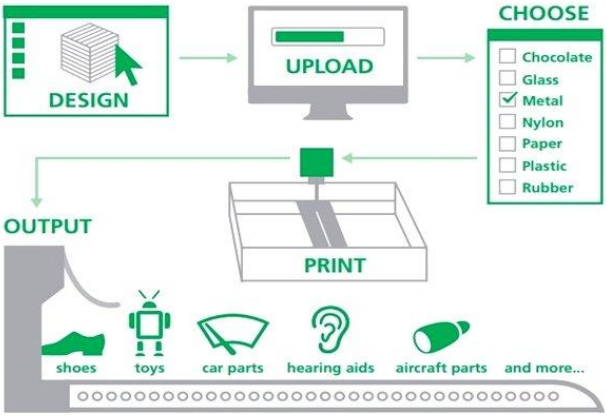


Figure 3 Working principles of 3D printers

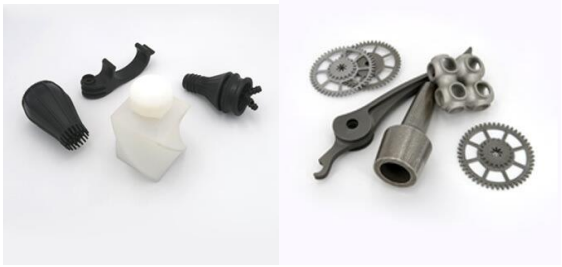


Figure 4 Plastic, SLS, Carbon AND Poly jet resins with DLS, Metal, SLM, DMLS, Binder Spraying and wax casting metal 3DP.

Filaments used in three-dimensional printer technology are listed below:
• PLA (Polyactiric Acid)
• ABS (Acrylonitrile Büdadiene Styrene)
• PETG (Polyethylene Terephthalate Glycol-Modified)
• Flexible (Flex)
• TPU (Thermoplastic Polyurethane)
• Special Filaments (copper, carbon fiber, water soluble, metal, phosphorous, PVA, polycarbonate filaments).

3D printers use the production method with filaments; chemical properties with thermo-plastic materials (Additive Manufacturing) as a result of the production. 3D printers have features, heat sensitivity and different types of filaments. The properties of Filament used in printing models in 3D printers affect the printing quality and accuracy.
ABS, PLA, PETG, Flex and TPU, Bamboo and Antibacterial filaments are used as filaments suitable for personal use. The methods used in 3D printers are Polymerization, Laser Stereo lithography (SLA), Polymer Jet Method, Digital Light Method, Micro Stereo lithography, Laser Sintering, Laser Melting, Melting with Electron Beam, Laminated Object Production, Powder Binding Production and Extrusion Layer Modelling methods are used. [7].

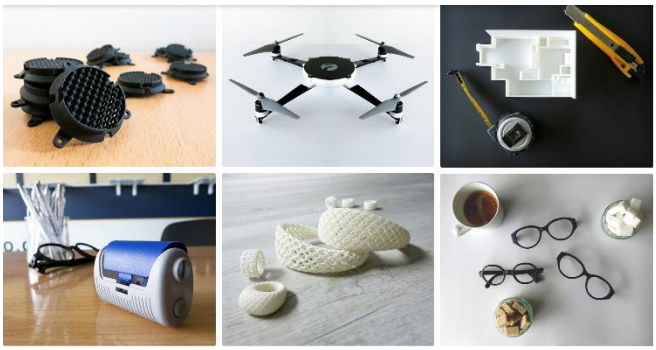


Figure 5 Application areas of 3D printers

3D printers support production in wearable technology, orthopaedic solutions, accessories and similar areas. The developments in the medical field are about to be able to break new ground. [8] The positive effects of organs such as prostheses, joints, skulls, heart, and bone structures have become noticeable. 3D printer technology creates prefabricated houses from the architectural field by pouring concrete or fibreglass from robot 3D printers and extruder used in this field. Gantri, which produces design objects in the field of illumination, produces modern home lighting products. Italian designer Libero Rutilo uses innovative plastic bottles and 3D printers to create innovative designs. Dinara Kasko, who has moved from interior design to the food industry, is a Ukrainian chef cake designer who has set an outstanding example of creativity in cake and cake baking with 3D printer technology.



Figure 6 Ukrainian cake designer Dinara Kasko

2. 3d printing technology

2.1. Rapid Tooling and Casting

3D printing techniques based on layer-by-layer manufacturing are extending their fields of application, from the building of aesthetic and functional prototypes to the production of tools and moulds for technological prototypes or pre-series. In particular, additive construction applied to the production of dies and electrodes, directly from digital data, is defined as rapid tooling (RT). Patterns, cores and cavities for metal castings can be obtained through rapid casting (RC) techniques [8], [9]. In both cases, since the tooling phase is highly laborious, great competitive advantages can be achieved thanks to solutions ensuring shorter time to market.

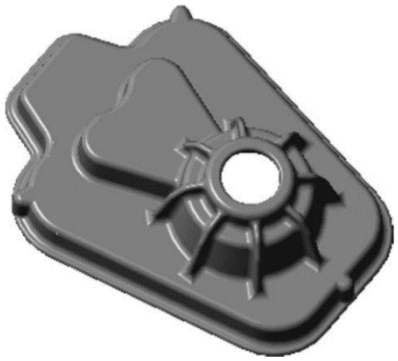


Figure 7 Computer based model of a benchmark

Moreover, RT and RC processes allow the simultaneous development and validation of the product and of the manufacturing process. Technological prototypes can constitute a strategic means, not only for functional and assembly tests or to obtain the customer's acceptance, but mainly to outline eventual critical points in the production process [9].

In this field, innovative solutions are now available based on 3D printing process, which can extend RC possibilities thanks to the lower costs with respect to previous technologies such as selective laser sintering of sand [10]. One such technological solution consists in investment casting starting from starch patterns produced on 3D-printing conceptual modellers. A second solution is another process, in which 3D-printing technology with the use of a ceramic material allows the production of complex cavities and cores, suitable for casting light alloys which is named as ZCast^{TM} technique [9].

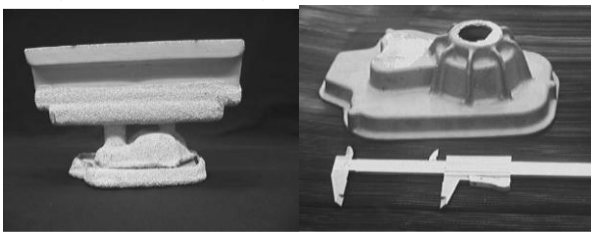


Figure 8 Shell after casting removal (left), prototype obtained by rapid casting (right).

Due to technological advances, new techniques are developed in industry. As a result, customer based solutions can be gathered with higher efficiency. ZCast^{TM} technique is an example of that approach and it can be used for steel casting and Aluminium alloys. ZCast^{TM} technique is proved to be effective for the production of cast technological prototypes in very short times, avoiding any tooling phase and with dimensional tolerances that are completely consistent with metal casting processes [9]. Technological advances in 3d printing techniques are extended the usage of 3d printing materials as ceramic materials, alloys, steel and composites. Through advances in rapid tooling and casting, possible defects in 3d material is minimized with less time and lower cost.

2.2. Bio-Printing

Bio-printing is another variant of rapid prototyping technology as rapid casting (fig. 7 & fig. 8). It is based on organic fluidity. Bio-printing is applied on one layer at a time until a particular 3D material is formed by computer based positioning of natural materials. The disadvantage of this printing type is occurred as the inability to exactly place organic material (cell or matrix) or cell aggregation on recent applications. In upcoming future, through clarifications on bio-printing technology, bio-printing will become more beneficial.

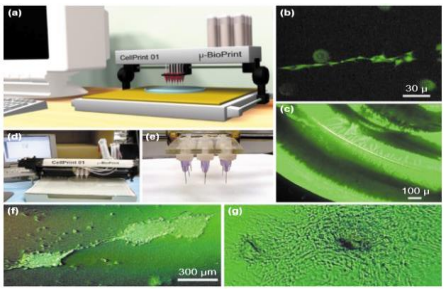


Figure 9 Bio-printer, related devices and cell printer.

Bio-printing can be defined as a rapid prototyping computer aided 3D printing technology with using layer to layer positioning of organic material and/or organic material aggregates into 3D gel the printed structure into vascularised living tissue or organ (fig.9). This definition of organ printing includes the many different printer designs and components of the deposition process such as, for example, jet-based cell printers, bio plotters and the different types of 3D hydro gels and varying cell types [11].

Bio-printing can be classified into three main steps: pre-processing, processing and post processing. Pre-processing refers to the development of a computer-aided design or blueprint of a specific organ. The design can be varied through the complexity of desired organ. Computerized tomography or detailed 3D reconstruction of organs can be used as imaging data. As the second step processing can be summarized as actual computer-aided printing or layer by-layer placement of cells or cell aggregates into a 3D environment using CAD or blueprints. Third step which is post-processing concerned with the perfusion of printed organs and their biomechanical conditioning to both direct and accelerate organ maturation [11].

2.3. Automotive Industry

In the automotive sector where three-dimensional printers are used, the production consists of models produced by SLA technology. In the pre-production and production stage, jig and fixture, thermoforming and injection [9] coating materials are used, but 3D printer technology is used effectively in the intermediate stages of production. Customization and Customization in the automotive field provides high temperatures, durability, humidity, diversity and sustainability in the production of parts, while the advantages in the automotive industry are performance, lightweight polymers and metal parts that combine three-dimensional printer technology with light and durable parts to provide a positive impact on time and cost.

'Strati' is the world's first 3D printed car with all components (basically PLA), processed in as little as two days and can extend its speed up to 37.2822715 miles or 60 kilometres per hour.

Moreover, companies like Koenigsegg One, Local Motors, Audi, Honda, WilliamsF1, BMW and Ford use 3D printers because of the advantages of innovative technologies in product development, performance, diversification, customization, cost reduction and R & D.



Figure 10 "Strati (2014)".

Ford uses silver PLA as the printed material of the engine block, which lasts more than 77 hours, with three-dimensional printer technology, the advantages of innovative technologies in R & D.

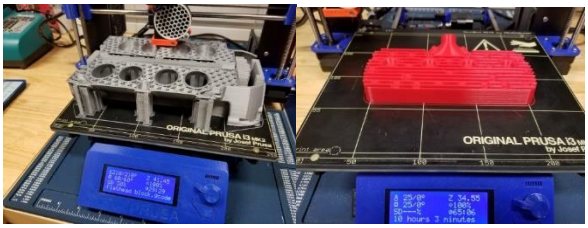




Figure 11 Ford automobile motor blog

2.4. Medical Applications

Artificial organs, bones, face and leg prostheses, reconstructive dental applications, audiology, orthopedic implants, surgical instrument manufacturing, soft tissue and cell printing, bio-medical skeletal systems, which are considered to be the definitive solutions for many diseases in the health sector in the future The researches have led to the development of a new sector in the field of human life and health.

Artificial organs and joints created by 3D printer technology used in patients in the UK and the Netherlands have enabled patients to be healthy thanks to these innovative methods.

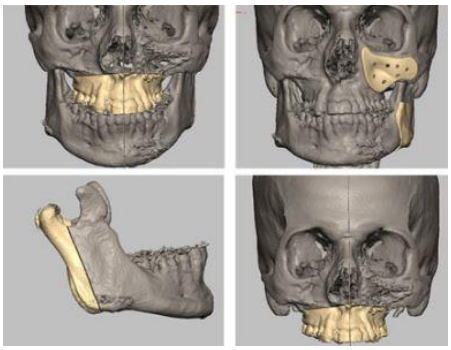


Figure 12 Some medical applications based on 3d printing.

In the 21st century, thanks to researchers and scientists, 3D printer technology has been replaced by a new field of 4-dimensional biomass (which is compatible with human body gel production technology) and biomaterials using bio ink technology to develop dynamic tissue production methods. As a result of a warning, the Lewis laboratory in the USA used gel technology that moves and swells, folds and opens mimics tissues.

3. Results and discussion:

3.1. Rapid Tooling and Casting Technology

Rapid tooling and rapid casting are developing techniques having recent problems on obtaining the exact material due to defects and production process. Even though new, creative and effective solutions are produced such as ZCast™ technique. With technological improvements, problems on having complex cavities and cores will be overcome and usage of RC and RT will get more popular as their advantages on time, cost and material diversity as ceramic materials and light alloys.

3.2. Bio-Printing Technology and related areas

Bio-printing, which can be classified under rapid casting, is a medical based technology including printing cells, organs or any living units of human or animal body. Thus, bio-printing has importance on health and any kind of medical companies. Bio-printing technology is an interdisciplinary area related with computer engineering, materials science engineering and medical sciences. Advances on bio-printing technology will extend human health and quality of human life.

Conclusions

The promise of 3D printing is based on custom products that are made to order, such as dental and medical devices, and low-turnover replacements parts. These goods are typically ordered in unique configurations and in very small quantities. A significant advantage of 3D printing is a firm's ability to quickly and cost-effectively supply low-demand parts without the risk of carrying an unsold finished goods inventory. Since items are made only when ordered and paid for, designers are able to undertake risks they would not otherwise pursue. With 3-D printing, the risk of a poor design is based on wasted design time rather than inventory investment.

A major advantage of 3D printing is the separation of product design from manufacturing capabilities. Since design and manufacturing can be easily outsourced in 3D printing, designers can contract with firms such as shape ways to produce, ship, and collect proceeds for goods based on their designs. Alternatively, a consumer can download a CAD software design for a replacement part online, as easily as he/she would download digital music and then download and print the part on his/her 3-D printer [12,13].

In up-coming future, 3D printing will be used for general purposes-more individually and widely. Since today's 3d printers' investment cost seems to be high, as for other communication devices, 3d printer will be available for any budget as well. 3D printing materials will reach to higher amounts and diversity in materials will be obtained as ceramics, alloys, metals and differing composites. Today, the main disadvantage on using 3d printer is the cost and time-printing time can extend to some hundred hours depending on the complexity of desired material-and such problems will be solved in some years. New technological methodologies are being developed-such as ZCast™ technique and these developments are signing the bright future in 3d printing materials and technology.

References:

[1] Chimento J, Jason HM, Crane N. Three-dimensional printed tooling for thermoforming of medical devices. Rapid Pro Journal, 17 (5), 387-392, 2011.

[2] Malik H, Darwood R, Shaunak S, Kulatilake P, Abdulrahman A, Mulki O, Baskaradas A. Three-dimensional printing in surgery: A review of current surgical applications. J Surgic Res, 199(2), 512-522, 2015.

[3] Chimento J, Jason HM, Crane N. Three-dimensional printed tooling for thermoforming of medical devices. Rapid Pro Journal, 17 (5), 387-392, 2011.

[4] Palousek D, Rosicky J, Koutny D, Stoklásek P, Navrat T. Pilot study of the wrist orthosis design process. Rapid Pro Journal, 20 (1), 27-32, 2014.
[5] Lee J, Cudihy J, Kotov A. Three-dimensional cell culture matrices: State of the art. Tissue Eng Part B Rev, 14 (1), 61-86, 2008.
[6] Cantinoti M, Valverde I, Kuty S. Three-dimensional printed models in congenital heart disease. Int J Cardiovasc Imaging, 33 (1), 137-144, 2017.
[7] Fantini M, De Crescenzio F, Persiani F, Benazzi S, Gruppioni G. 3D restitution, restoration and prototyping of a medieval damaged skull. Rapid Pro Journal, 14 (5), 318-324, 2008
[8] Rankin M, Giovinco A, Cucher J, Watts G, Hurwitz B, Armstrong G. 3D printing surgical instruments: Are we there yet?. J Surg Res, 189 (2), 193-7, 2014.
[9] A. Bernard, J.C. Delplace, N. Perry, S. Gabriel, "Integration of CAD and rapid manufacturing for sand casting optimisation", Rapid Prototyping Journal, 5 (2003) 327-333.
[10] E. Bassoli, A. Gatto, L. Iuliano, M.G. Violante, "3D printing technique applied to rapid casting", Rapid Prototyping Journal, 13/3 (2007) 148-155.
[11] A. Gatto, L. Iuliano, "Effect of the post curing process parameters choice on part produced by direct croning process", Leonardo, P.M. (Ed.), Proceedings of PRIME 2001 –1st International Seminar on Progress in Innovative Manufacturing Engineering (2001), Sestri Levante (Genoa).
[12] V. Mironov, T. Boland, T. Trusk, G. Forgacs, R. R. Markwald, "Organ printing: computer-aided jet-based 3D tissue engineering", TRENDS in Biotechnology, 4 (2003) 157-161.
[13] B. Berman, "3-D printing: the new industrial revolution", Business Horizons, 55 (2012), 155-162.
[14] https://3dprint.com/72171/first-3d-printer-chuck-hull/
[15] Olla P. "Opening Pandora's three-dimensional printed box". Technology and Society Magazine, 34 (3), 74-80, 2015.
[16] https://reprap.org/wiki/File:Mendel.jpg
[17]https://www.neoldu.com/3d-yazici-nedir-nasil-calisir-204h.htm
[18] https://www.sculpteo.com/en/
[19]http://2biy4djn37s2xoe622u8h9g1-wpengine.netdna-ssl.com/wp-content/uploads/2016/04/strati-e1439284623815.jpg
[20]https://www.bocabearings.com/blogs/2018/3d-printed-ford-flathead-v8-engine-working-model[
[21]http://www.voksel.com.tr/blog/saglik-sektorunde-cigir-acan-devrim-3d-yazici-teknolojisi.

Figures 1-12:

[1] https://3dprint.com/72171/first-3d-printer-chuck-hull/.
[2]https://www.kickstarter.com/projects/relativedesign/reprap-self-replicating-3d-printer-fuel-the-moveme.
[3]https://www.neoldu.com/3d-yazici-nedir-nasil-calisir-204h.html.
[4] https://www.sculpteo.com/en/.
[5] https://www.sculpteo.com/en/.
[6] http://sintesistv.com.mx/la-pasteleria-combina-diseno-la-tecnologia-sabor-inolvidable/.
[7] E. Bassoli, A. Gatto, L. Iuliano, M.G. Violante, "3D printing technique applied to rapid casting", Rapid Prototyping Journal, 13/3 (2007) 148-155.
[8] E. Bassoli, A. Gatto, L. Iuliano, M.G. Violante, "3D printing technique applied to rapid casting", Rapid Prototyping Journal, 13/3 (2007) 148-155.
[9] V. Mironov, T. Boland, T. Trusk, G. Forgacs, R. R. Markwald, "Organ printing: computer-aided jet-based 3D tissue engineering", TRENDS in Biotechnology, 4 (2003) 157-161.
[10] https://www.drive2.com/e/BkeHAEAABBI.
[11] https://www.bocabearings.com/blogs/2018/3d-printed-ford-flathead-v8-engine-working-model.
[12] http://www.voksel.com.tr/blog/saglik-sektorunde-cigir-acan-devrim-3d-yazici-teknolojisi.

6th International Conference on Materials Science and Nanotechnology For Next Generation (MSNG2019)
October 16-18, 2019, Niğde, TURKEY (ORAL FULL TEXT)

Structural, Electronic and Elastic Properties of $BeTiH_3$: A Density Functional Theory Study

Ahmet İYİGÖR*, Cihan KÜRKÇÜ**, Abdullah CANDAN*

* Department of Machinery and Metal Technology, Kırşehir Ahi Evran University, Turkey
** Department of Electronics and Automation, Kırşehir Ahi Evran University, Turkey

The structural, electronic and elastic properties of $BeTiH_3$ in Pm-3m space group are studied by performing density functional theory (DFT) within the generalized gradient approximation of Perdew-Burke-Ernzerhof (GGA-PBE). The optimized lattice constant of $BeTiH_3$ is 3.438Å. In addition, electronic band structure calculations are carried out for this material. From the electronic calculations made for $BeTiH_3$, it was found that this alloy was metallic in nature. The obtained second-order elastic constants (C_{ij}) for $BeTiH_3$ do not satisfy mechanical stability criterions, indicating that $BeTiH_3$ is mechanically unstable in the studied phase.

Keywords: Density Functional Theory, Electronic Structure, Elastic Properties.

Corresponding author: ahmetiyigor@ahievran.edu.tr

1. Introduction

The world's growing energy demand, depletion of fossil fuels and environmental concerns have increased the critical need for clean and sustainable energy resources. Various alternatives such as renewable energy sources, nuclear and hydrogen energy are being investigated to produce clean and sustainable energy. Among these sources, hydrogen energy is the most promising technology because it does not present problems such as nuclear waste, regional sensitivity and noise [1,2]. Metal or complex hydrides, many alloys, and metalorganic frameworks have been under investigations as hydrogen storage materials. MgTiX (X = Ni and Si) is also considered; however, dehydrogenation of these materials were found to be low for practical applications [3].
This study adopts first principles calculations in order to investigate and evaluate the structural, electronic and elastic properties of $BeTiH_3$ alloy for hydrogen storage.

2. Computational details

All herein done total energy calculations were carried out using a pseudopotential plane-wave (PP-PW) scheme within density functional theory (DFT) as implemented in the Quantum-ESPRESSO package [4]. The electronic Exchange-correlation potential was calculated within the generalized gradient approximation (GGA) in the scheme of Perdew-Burke-Ernzerhof (PBE) [5]. In all done total energy calculations, Vanderbilt-type ultra-soft pseudo-potential was used to treat the potential seen by the valence electrons because of the nucleus and the frozen core electrons. The wave functions were expanded in a plane-wave basis set with a kinetic energy cut-off of 50 Ry. The electronic charge density was evaluated up to the kinetic energy cut-off of 500 Ry. Brillouin-zone integrations were performed using 12×12×12 k-points. Integration up to the Fermi surface was performed using the smearing technique [6] with smearing parameter σ = 0.02 Ry.

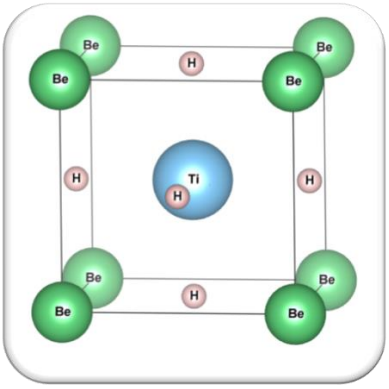


Figure 1. *Crystal Structure of $BeTiH_3$*

3. Results and discussion

$BeTiH_3$ alloy is a lattice with Pm-3m symmetry where the Wyckoff positions 1a (0, 0,0), 3c (0, 1/2, 1/2) and 1b (1/4,1/4,1/4) are occupied by Be, H and Ti respectively (see Figure 1). For $BeTiH_3$ alloy, the lattice parameter, bulk and shear modulus, B/G ratio was calculated, and the results were given in Table 1. Since B / G ratio is 6.05 > 1.75, Pm-3m symmetrical $BeTiH_3$ alloy was found to be ductile.

Table 1. Lattice parameter *a* (Å), Bulk B, Shear G, and Young's E modulus (GPa), B/G ratio, Poisson's ratio σ of $BeTiH_3$.

Alloy	*a*	B	G	B/G	E	σ
$BeTiH_3$	3.440	90.80	14.99	6.05	42.62	0.42

In cubic materials, there are only three independent elastic constants. The calculated values of elastic constants are listed in Table 2.

Table 2. Elactic constants (C_{11}, C_{12} and C_{44} (GPa)) for $BeTiH_3$ alloy.

Alloy	C_{11}	C_{12}	C_{44}
$BeTiH_3$	197.36	37.53	-0.87

Mechanical stability of this alloy has been analysed in terms of its elastic constants. The conditions of mechanical stability for a cubic crystal are given by [7]

$$C_{11} > 0, C_{11} - C_{12} > 0, B > 0, C_{44} > 0 \quad (1)$$

The obtained elastic constants for $BeTiH_3$ do not satisfy these mechanical stability criterions, indicating that the $BeTiH_3$ is mechanical unstable in the studied phase.

The calculated electronic band structure and partial densities of states for $BeTiH_3$ along the high symmetry directions in the Brillouin zone given in Figure 2. In the figures, the Fermi energy level is taken as 0 eV. It is seen that there is no band gap at the Fermi level, as a result, $BeTiH_3$ alloy exhibit a metallic behavior. As seen from the partial densities of states, the bands near the Fermi level are formed mainly by the Ti 3d-states for $BeTiH_3$. Besides, the energy region between −7 and -3 eV consists mainly of the electrons of H 1s and Ti 3d atoms.

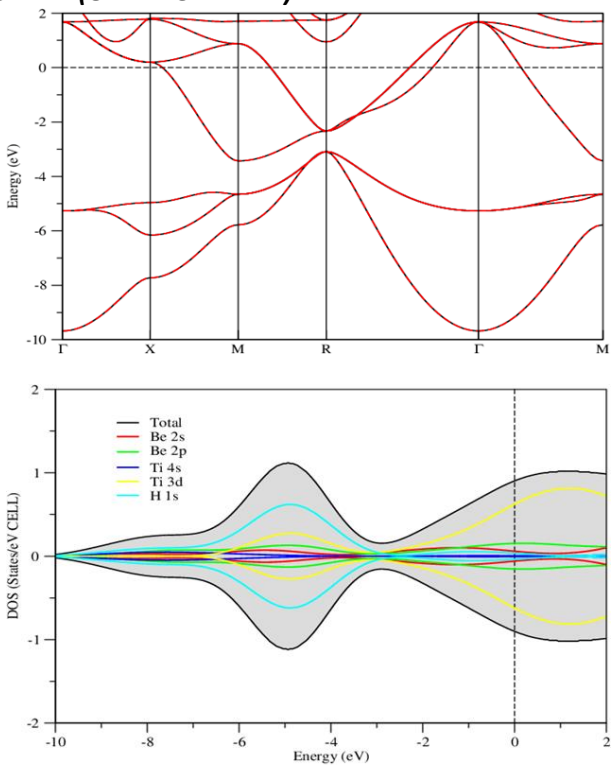


Figure 2. *Calculated electronic band structure, total and partial DOS for $BeTiH_3$ alloy*

4. Conclusion

$BeTiH_3$ alloy's structural, elastic and electronic properties are examined using first principle calculations. The evaluation of elastic constants in terms of mechanical stability shows that $BeTiH_3$ is mechanically unstable because it does not meet known mechanical stability criteria. In addition, the electronic band structure of $BeTiH_3$ shows that this alloy is metallic in nature.

References:

[1] PUKAZHSELVAN, D., KUMAR, V., SINGH, S.K., "High capacity hydrogen storage: basic aspects, new developments and milestones", Nano Energy, 1,4, 566-589, 2012.
[2] AL, S., "Theoretical investigations of elastic and thermodynamic properties of $LiXH_4$ compounds for hydrogen storage", International Journal of Hydrogen Energy
44, 3, 1727-1734, 2019.

[3] AL, S., "Investigations of Physical Properties of $XTiH_3$ and Implications for Solid State Hydrogen Storage", Zeitschrift für Naturforschung A, 2019.
[4] GIANNOZZI, P., BARONI, S., BONINI, N., CALANDRA, M., CAR, R., CAVAZZONI, C., CERESOLI, D., CHIAROTTI, G.L., COCOCCIONI, M., DABO, I., DAL CORSO, A., FABRIS, S., FRATESI, G., DE GIRONCOLI, S., GEBAUER, R., GERSTMANN, U., GOUGOUSSIS, C., KOKALJ, A., LAZZERI, M., MARTIN-SAMOS, L., MARZARI, N., MAURI, F., MAZZARELLO, R., PAOLINI, S., PASQUARELLO, A., PAULATTO, L., SBRACCIA, C., SCANDOLO, S., SCLAUZERO, G., SEITSONEN, A.P., SMOGUNOV, A., UMARI, P., WENTZCOVITCH, R.M., "QUANTUM ESPRESSO : a modular and open-source software project for quantum simulations of materials", J Phys. Condens. Matter, 21, 395502, 2009.
[5] PERDEW, J.P., BURKE, K., ERNZERHOF, M., "Generalized gradient approximation made simple", Phys. Rev. Lett., 77, 3865–3868, 1996.
[6] METHFESSEL, M., PAXTON, A.T., "High-precision sampling for Brillouin-zone integration in metals", Phys. Rev. B, 40, 3616–3621, 1989.
[7] BORN, M., HUANG, K., Dyn. Theor. Cryst. Lattices, Clarendon, Oxford, 1954.

6th International Conference on Materials Science and Nanotechnology For Next Generation (MSNG2019)
October 16-18, 2019, Niğde, TURKEY (ORAL FULL TEXT)

Ab-initio study of the Structural, Electronic and Mechanical Properties of the Intermetallic Co_3Nb in the $L1_2$ Phase

Ahmet İYİGÖR*, Abdullah CANDAN*, Cihan KÜRKÇÜ**

* Department of Machinery and Metal Technology, Kırşehir Ahi Evran University, Turkey
** Department of Electronics and Automation, Kırşehir Ahi Evran University, Turkey

This study employs first principles method to run a investigation on structural, electronic and mechanical properties of Co_3Nb in $L1_2$ phase. The optimized lattice constant (a_0), bulk modulus (B) and the elastic constants (C_{ij}) are evaluated. Young and Shear modulus, Poisson's ratio of Co_3Nb have been analysed. Evaluation of mechanical stability via obtained elastic constants is exhibited a stable nature for this alloy. The present band structure calculations predict that the Co_3Nb alloy is metallic.

Keywords: Intermetallic, Electronic Structure, Mechanical Properties.

Corresponding author: ahmetiyigor@ahievran.edu.tr

1. Introduction

Intermetallic compounds with formula AB_3 are currently under intensive research due to their structural and physical properties. These compounds have interesting mechanical properties, those having the $L1_2$ atomic order are much softer than the compounds which crystallize in D_{22} phase, are used for ultra-high temperature applications and generally have high melting points and good corrosion resistance [1]. However, Cobalt-based superalloys are promising candidates for widespread use as high-temperature materials in aircraft engines, gas turbines and electric generator systems, as they have more qualified high temperature properties than Nickel-based superalloys [2-5]. In the present work, the structural, electronic and mechanical properties of Co_3Nb alloy have been studied.

2. Computational details

The Co_3Nb alloy is in the $L1_2$ phase and is found in the Pm-3m space group as shown in Figure 1 and crystallize in the cubic structure. The crystal structure of Co_3Nb is occupied by three Co atoms and one by Nb atom, while it appears as a simple cubic sub-lattice with four atoms behind each other. The atoms are placed according to Wyckoff locations: Co 3c (0; 1/2; 1/2) and Nb 1a (0; 0; 0). First-principles studies of the Co_3Nb alloy was performed by employing the self-consistent ultrasoft pseudopotential method [6] based on the density functional theory, within the generalized gradient approximation (GGA), incorporated into the quantum-Espresso code [7]. The electronic exchange-correlation potential was calculated within the generalized gradient approximation (GGA) in the scheme of Perdew-Burke-Ernzerhof (PBE) [8]. In all done total energy calculations, ultra-soft pseudo-potential was used to treat the potential seen by the valence electrons because of the nucleus and the frozen core electrons. The wave functions were expanded in a plane-wave basis set with a kinetic energy cut-off of 40 Ry for $L1_2$ structure. The electronic charge density was evaluated up to the kinetic energy cut-off 400 Ry. Brillouin zone integrations were performed using a 10×0×10 k-points mesh. Integration up to the Fermi surface was performed using the smearing technique [9] with smearing parameter σ= 0.02 Ry

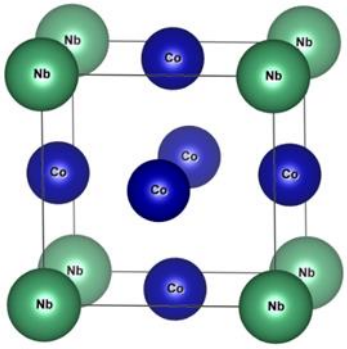


Figure 1. *The crystal structure of Co_3Nb alloy in the $L1_2$ phase.*

3. Results and discussion

Firstly, the equilibrium lattice constants is determined by minimizing the total energy, according to the different values of the lattice constants. Secondly, we have fit the calculated total energy into the Murnaghan equations of state to obtain the lattice constant (a_0), Bulk modulus (B) and its pressure derivative (B′). The a_0, B and B′ values obtained for Co_3Nb compound are presented in Table 1.

Table 1. Calculated lattice constant a_0 (in Å), Bulk modulus B (in GPa), its pressure derivative (B′) and total magnetic moment M (in μ_B).

Alloy	References	a_0	B	B′	M
Co_3Nb	Present	3.653	215.48	4.27	1.77
	VASP [10]	3.654	-	-	

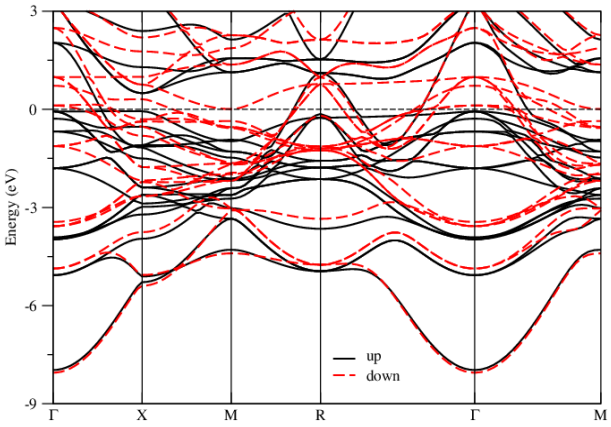


Figure 2. *Band structure along the high symmetry directions for Co_3Nb*

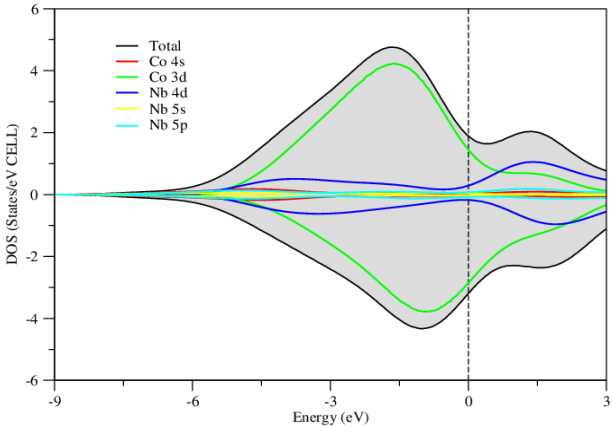


Figure 3. *Calculated total and partial density of states for Co_3Nb*

To get an insight into this alloy, its examined the band structure. The band structure of Co_3Nb along selected high-symmetry lines within the first Brillouin zone is shown in Figure 2. It is clearly seen that there is no gap at the Fermi level (E_F). The valence and conduction bands overlap greatly and there are many bands across E_F, which is like those in many $AuCu_3$-type structure phases. As a result, Co_3Nb is expected to exhibit metallic conductivities, such as good thermal and electrical conductivities. The calculated partial and total density of states (DOS) are shown in Figure 3. It is clear that this alloy is metallic due to the fact that the DOS values differ from zero at the Fermi level. The most dominant contribution to DOS comes from Co-3d and Nb-4d states.

Table 2. Bulk modulus B (in GPa), elastic constants (C_{11}, C_{12} and C_{44}, (in GPa)), Shear moduli G (in GPa), and B/G ratio.

Alloy	C_{11}	C_{12}	C_{44}	B	G	B/G
Co_3Nb	289.70	178.37	147.03	215.48	99.62	2.16

In the case of cubic system, there are only three independent elastic constants, namely, C_{11}, C_{12} and C_{44}. The calculated values of elastic constants are listed in Table 1. The key criteria for mechanical stability of a crystal is that the strain energy must be positive [11], which means in a cubic crystal that the elastic constants should satisfy the following inequalities:

$$C_{44} > 0,\ C_{11} > |C_{12}|,\ C_{11} + 2C_{12} > 0 \quad (1)$$

The obtained elastic constants for Co_3Nb satisfy these mechanical stability criterions, indicating that the Co_3Nb is mechanical stable in the studied phase. According to Pugh [12], if B/G ratio is smaller than 1.75, the material behaves in a brittle manner; otherwise, the material behaves in a ductile manner. It is clearly seen from Table 2 that Co_3Nb is ductile material.

4. Conclusion

The structural, electronic and mechanical properties of Co_3Nb alloy has been studied. According to the calculations, the Co_3Nb alloy is of a metallic nature with magnetic property. Furthermore, according to Pugh, Co_3Nb alloy behaves in a ductile manner.

References:

[1] ARIKAN, N., İYİGÖR, A., CANDAN. A., UĞUR, Ş., CHARIFI, Z., BAAZIZ, H., UĞUR, G., "Structural, elastic, electronic and phonon properties of scandium-based compounds ScX3 (X= Ir, Pd, Pt and Rh): an ab initio study" Computational Materials Science, 79, 703-709, 2013.

[2] SHISHIDO, T., YE, J., KUDOU, K., ET AL., "Solid solution range of boron, microhardness and oxidation resistance of the perovskite type RERh3Bx (RE=Gd, Y, Sc) compounds", J. Alloys Compd., 291, 52-56, 1999.

[3] GEBALLE, T.H., MATTHIS, B.T., COMPTON, V.B., CORENZWIT, E., HULL, G.W., LONGINOTTI, L.D., "Superconductivity in binary alloy systems of the rare earths and of thorium with Pt-group metals", Phys. Rev., 137 (1965), p. A119-A127

[4] DWIGHT, A.E. DOWNY, J.W. CONNER, R.A. "Some AB_3 compounds of the transitiom metals", Acta Cryst., 14, 75, 1961.

[5] SCHAAK, R.E., AVDEEV, M., ET AL., "Formation of transition metal boride and carbide perovskites related to superconducting MgCNi3", J. Solid State Chem., 177, 1244-1251, 2004.

[6] VANDERBILT, D., "Soft self-consistent pseudopotentials in a generalized eigenvalue formalism", Phys. Rev. B, 41, 7892-7895, 1990.

[7] GIANNOZZI, P., BARONI, S., BONINI, N., CALANDRA, M., CAR, R., CAVAZZONI, C., CERESOLI, D., CHIAROTTI, G.L., COCOCCIONI, M., DABO, I., DAL CORSO, A., FABRIS, S., FRATESI, G., DE GIRONCOLI, S., GEBAUER, R., GERSTMANN, U., GOUGOUSSIS, C., KOKALJ, A., LAZZERI, M., MARTIN-SAMOS, L., MARZARI, N., MAURI, F., MAZZARELLO, R., PAOLINI, S., PASQUARELLO, A., PAULATTO, L., SBRACCIA, C., SCANDOLO, S., SCLAUZERO, G., SEITSONEN, A.P., SMOGUNOV, A., UMARI, P., WENTZCOVITCH, R.M., "QUANTUM ESPRESSO : a modular and open-source software project for quantum simulations of materials", J Phys. Condens. Matter, 21, 395502, 2009.

[8] PERDEW, J.P., BURKE, K., ERNZERHOF, M., "Generalized gradient approximation made simple", Phys. Rev. Lett., 77, 3865–3868, 1996.

[9] METHFESSEL, M., PAXTON, A.T., "High-precision sampling for Brillouin-zone integration in metals", Phys. Rev. B, 40, 3616–3621, 1989.

[10] Internet: https://materialsproject.org/materials/mp-1018021/

[11] BORN, M., HUANG, K., Dyn. Theor. Cryst. Lattices, Clarendon, Oxford, 1954.

[12] PUGH, S. F., "XCII. Relations between the elastic moduli and the plastic properties of polycrystalline pure metals", Phil. Mag. J. Sci. 45, 367, 823-843, 195

6th International Conference on Materials Science and Nanotechnology For Next Generation (MSNG2019)
October 16-18, 2019, Niğde, TURKEY (ORAL FULL TEXT)

Investigation of the effect of grape seed, silver nitrate and silver nanoparticle on kidney damage induced by lipopolysaccharide (LPS)

Züleyha Doganyiğit[1*], Emin Kaymak[1], Aslı Okan Oflamaz[1], Tuğrul Akin[2], Fatma Öztürk Küp[2]

[1] Bozok University, Histology-Embriyology Department, Medical Faculty, YOZGAT
[2] Erciyes Universıty, Department of Biology, Faculty of Science, KAYSERI

In this study, biosynthesis of silver nanoparticles with grape seed extracts was determined by using in vivo animal experiments in order to determine whether there is any effect on kidney damage caused by LPS.
80 Wistar albino male adult rats were used for the study. 8 equal groups were made. Groups consists of Group 1 (Control Group), Grup 2 (LPS Grubu), Group 3 (LPS + Silver Nanoparticle), Group 4 (LPS + Grape Seed Extract), Group 5 (LPS + Ag), Group 6 (Grape Seed Extract), Group 7 (Silver Nanoparticle), Group 8 (Ag ion). The histopathological damage and the number of Tunel positive cells in LPS were higher than the other groups ($P < 0.05$). We observed that this damage was reduced in the drug treated groups.

Keywords: lipopolysaccharide, kidney, silver nanoparticle
***Corresponding E-mail:** zuleyha.doganyigit@gmail.com

1. Introduction

Nanoparticles have entered many fields including energy storage, textile, paint industry and health.In addition, it is noteworthy that the share of nanotechnology in these areas is increasing day by day [1]. For the synthesis of silver nanoparticles, environmentally safe materials such as plant extract [2], bacteria [3], fungus [4] and enzymes [5] are used.

Septic acute kidney injury (AKI) is one of the most common disorders and is known to be associated with high mortality [6].

The most important application of silver (Ag) and silver nanoparticles (AgNP) is the use in the medical industry such as topical ointments to prevent infection against burns and open wounds. [7].

2. Method

In this study, biosynthesis of silver nanoparticles with grape seed extracts was determined by using in vivo animal experiments in order to determine whether there is any effect on kidney damage caused by LPS.

Group 1 (Control Group): Only saline (SF) (0.9% NaCl solution) 0.1 ml.

Group 2 (LPS Group): LPS (30 mg / kg) (SF + LPS) 30 minutes after SF administration (n = 10). It was administered intraperitoneally.

Group 3 (LPS + Silver Nanoparticle): AgNP was given orally 60 minutes after LPS administration. (200mg / kg)

Group 4 (LPS + Grape Seed Extract): LPS (30 mg / kg) was given orally after 60 min. (200mg / kg) (n = 10).

Group 5 (LPS + Ag): AgNO3 was given orally after 60 minutes to animals given LPS (30 mg / kg). (200mg / kg) (n = 10).

Group 6 (Grape Seed Extract): Grape seed extract was given orally 30 minutes after SF administration. (200 mg / kg) (n = 10).

Group 7 (Silver Nanoparticle): AgNP was given orally 30 minutes after SF administration. (200 mg / kg) (n = 10).

Group 8 (Ag ion): SF (30 mg / kg) was given orally to AgNO3 after 30 minutes (200 mg / kg n = 10).

Histopathological evaluation

Hematoxylin and Tunel staining was performed on the sections from kidney tissues obtained from sacrified rats. Kidney tissue was examined and

evaluated in random order under blinded conditions with standard light microscopy by a histologist.

Glomerular degeneration, tubular lumen enlargement, hemorrhage, epithelial atrophy, vacuolization, shedding of cells in the tubule and tubular residues were evaluated in renal sections. Histopathological results in each category were scored as follows: 0 = none, 1 = mild, 2 = moderate, and 3 = severe.

The TUNEL method was utilized to show apoptosis of kidney tissue. TUNEL-positive cells in kidney in 20 randomly chosen fields were counted.

Statistical analysis

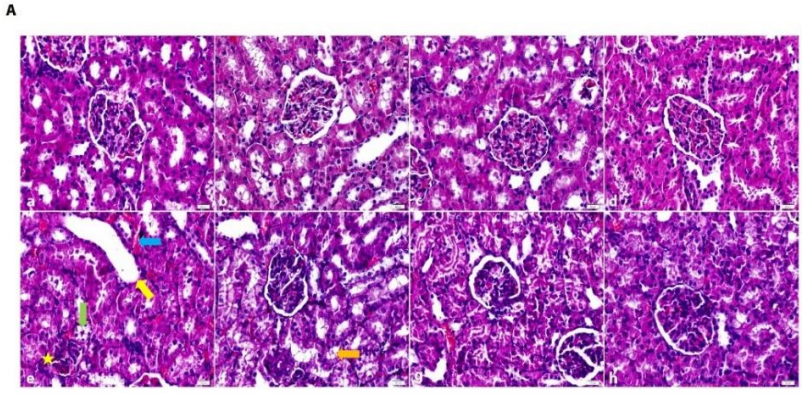
All statistical analyses were carried out using SPSS statistical software (SPSS for Windows, SPSS Inc., Chicago, IL, USA, version 15.0). The Kolmogorov–Smirnov test was used to identify normal distribution of the data. In case of normal distribution, quantitative variables were compared using one-way analysis of variance (ANOVA) and post hoc Tukey test. These differences were considered significant when probability was less than 0.05.

3. Results

Histopathological findings

AgNP, Ag and Grape seed treated groups were observed to show a similar structure histologically similar to those in the control (Figure 1A). Bleeding (blue arrow), enlargement of tubular lumen (yellow arrow), tubular residues (green arrow) and glomerular degeneration (asterisk) are observed in LPS-treated kidney tissue. Vacuolization (orange arrow) was more intense especially in the LPS+AgNP group.

The histopathological damage observed in LPS was higher than all other groups (P <0.05). It is seen that there is a decrease in damage in LPS + drug groups compared to LPS group.



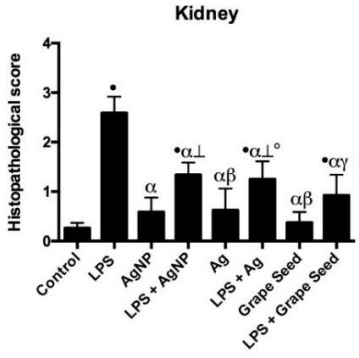


Figure1: *A Control group, B grape group, C Silver nanoparticle group, D Silver nitrate group, E LPS group, F LPS + grape group, G LPS + Silver nitrate group, H LPS + Silver Nitrate group.X400.*

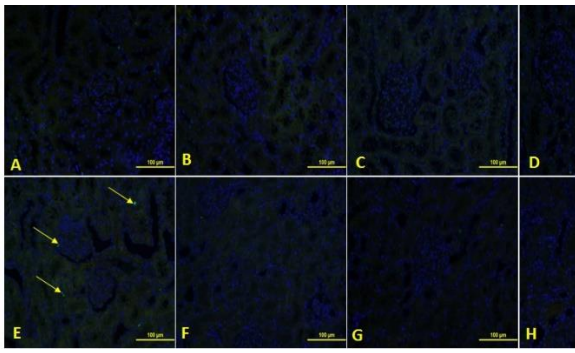
Apoptotic findings

The number of TUNEL positive cells increased significantly in LPS group compared to control, grape seed, nanoparticle and silver nitrate groups. In LPS+grape seed and LPS+nanoparticle groups, there was a statistically significant decrease in the number of Tunel positive cells compared to LPS group (Table 1).

Table 1. TUNEL values in kidney tissue

Groups	Control	Grape	NP	GN	LPS	LPS+Grape	LPS+NP	LPS+GN	*p*
TUNEL	0.52±0.9 1[a]	0.24±0.5 2[a]	0.25±0.5 4[a]	0.16±0.4 7[a]	1.20±1.3 5[b]	0.44±0.8 2[a]	0.48±0.8 2[a]	0.80±0.8 1[ab]	0.001

Data were shown as mean± standard deviation. P<0.05 accepted as significant. There is not statistically significant difference among the groups containing the same letter.



Şekil 2. *A Control group, B grape group, C Silver nanoparticle group, D Silver nitrate group, E LPS group, F LPS + grape group, G LPS + Silver nitrate group, H LPS + Silver Nitrate group. Yellow arrows indicate Tunel Positive cells. X400.*

4. Discussion

LPS administration caused histologically kidney tissue damage. In a study, the histopathology shown that acute tubular damage in the cortex and acute necrosis from the cortex to medulla [8].
In our study, we observed that kidney damage increased significantly with Lps and the number of apoptotoic cells increased in renal tissue. We observed that this damage was reduced in the drug treated groups. We believe that it will be important to reduce endotoxic damage with new studies and similar results. The present results might point to AGNP, grape sees and AG being an important new therapeutic target for the treatment of LPS-induced acute kidney injury.

5. Acknowledgement

The study protocol was approved by the Committee on the Ethics of Animal Experiments of the University of Erciyes (Permit Number: 16/058).

References:

1. Liu, F.K., Huang, P.W., Chang, Y.C., Ko, F.H., Chu, T.C, '' Microwave-assisted synthesis of silver nanorods'', Journal of materials research, 19,469-473,2004.

2. Jain, D., Daima, H.K., Kachhwala, S., Kothari S.L, ''Synthesis of plant- mediated silver nanoparticles using papaya fruit extract and evaluation of their antimicrobial actives'', Digest Journal of Nanomaterials and Biostructures, 4(3), 557-563, 2009.

3. Saifuddin, N., Wong, C.W., Yasumira, A.A.N, ''Rapid Biosynthesis of Silver Nanoparticles Using Culture Supernatant of Bacteria with Microwave Irradiation'', E-Journal of Chemistry, 6, 61-70, 2009.

4. Bhainsa, K.C., Sauza S.F.D, ''Extracellular biosynthesis of silver nanoparticles using the fungus Aspergillus fumigates'', Coll. Surf. B: Biointerfaces 47, 160–164, 2006.

5. Willner, I., Basnar, B., Willner, B., '' Nanoparticle-enzyme hybrid systems for nanobiotechnology'', FEBS J, 274, 302–309, 2007.

6. Silvester, W, Bellomo, R., Cole, L., '' Epidemiology, management, and outcome of severe acute renal failure of critical illness in. Australia'', Critical Care Med, 29(10),1910-1915, 2001.

7. Ip, M, Lui, S.L., Poon, V.K., Lung, I., Burd, A,'' Antimicrobial activites of silver dressings: an in vitro comparison'', J. Medical Microbiol, 55, 59–63, 2006

8. Kadkhodaee, M., Osami, A.,'' Inhibition of inducible nitric oxide synthase reduceslipopolysaccharide-induced renal injury in the rat'', Clin Exp Pharmacol Physiol, 31(12),842-846, 2004.

6th International Conference on Materials Science and Nanotechnology For Next Generation (MSNG2019)
October 16-18, 2019, Niğde, TURKEY (ORAL FULL TEXT)

Developing new MgO luminophors with different dopants for dosimetry applications and determination of ESR properties

V. Guckan[1*], V. Altunal[1], A. Ozdemir[1], E. Erunal[2] and Z. Yegingil[1]

[1]Cukurova University, Faculty of Art and Sciences, Department of Physics, Adana01330, TURKEY
[2]Cukurova University, Ceyhan Engineering Faculty, Chemical Engineering Department, Adana, TURKEY

This work presents the preliminary TL and OSL studies of MgO phosphors produced by the Solution Combustion Synthesis (SCS) method. The aim of this study is to obtain the high sensitivity magnesium oxide (MgO) luminophors doped with different ions to be used as Thermoluminescence (TL) and Continuous-wave Optically stimulated luminescence (CW-OSL) dosimeters. Differences in TL glow curves and OSL decay curves obtained from doped MgO phosphors, were investigated and compared. During the production, the Al, Ca, Li and Na ions were added as the dopants with different molar concentrations by the SCS method. Structure characterization analyzes of the synthesized materials were performed by X-ray Diffraction (XRD) and Scanning Electron Microscope (SEM) methods. The TL and OSL curves of doped and undoped MgO phosphors were compared. It was observed that TL and OSL signals of Na doped and Li doped MgO phosphors increased about 25 times compared to undoped MgO sample. X-Band room temperature Electron Spin Resonance (ESR) measurements of undoped and doped materials were conducted. A sharp intense central peak together with 5 smaller peaks in the undoped material was found. The g-factor of the sharp and intense signal was recorded around 1.977 which is different than free radical g-factor. This refers to the structure of MgO material itself. On the other hand, the spectra of MgO:Li and MgO:Na samples were very similar but they also possess sharp intense central peak and 5 less intense peaks. The MgO:Li,Na spectrum consists of the overlap of a broad single signal and the central sharp single signal.

Keywords: Magnesium oxide (MgO), Solution Combustion synthesis, Radiation Dosimetry, Luminescence, Thermoluminescence (TL), Electron spin resonance (ESR).

Corresponding author: veysiguckan@gmail.com

1. Introduction

Magnesium oxide (MgO) is a wide band-gap (Eg=7.8 eV) insulator with a rock-salt crystal structure under ambient pressure. The Mg ions occupy the octahedral sites within the anion close-packed structure [1].
MgO, or magnesia, is a white hygroscopic solid mineral that occurs naturally as periclase and is a source of magnesium. MgO powders have long been great interest owing to its applications in many industrials' area. Therefore, many extensive studies have been performed to synthesize nanoscale MgO powders using various novel wet chemical methods, e.g. sol-gel synthesis, followed by supercritical drying [2] and spray pyrolysis [3]. But these techniques usually consume much longer time and include many complicated processes. The solution combustion synthesis can be an alternative technique a solution to some of the above-mentioned problems [4].
MgO has long been accepted as a luminescence dosimetry material, mainly for use with the thermoluminescence (TL) technique. In order to increase the number of materials suitable for optically stimulated luminescence (OSL) dosimetry, many researchers have investigated the luminescence characteristics of this material [5-7].
The luminescence occurring in MgO as a results of radiation exposure has been associated with charge transfer processes involving impurities such as lanthanides, V-type centers, transitions metal ions or other crystal defects. There are many reports about MgO doped

with lanthanides, including Ce, Eu, Tb, and Dy to increase the TL or OSL signals and to improve its dosimetric characteristics[5, 8, 9].In addition to the lanthanides, TL emission spectra of MgO doped with transition metals (Mn, Cr, Ni, Fe, Co, Cu) are also reported by some authors.

This study presents the preliminary TL and OSL studies of MgO phosphors produced by the SCS method. Several ions were doped into the MgO phosphors during synthesis process such as Al, Ca, Li and Na as dopants to obtain high sensitivity MgO luminophors that can be for TL and CW-OSL dosimeters, . Structure and morphology of the synthesized materials were checked by XRD and SEM methods. The TL and OSL curves of doped and undoped MgO phosphors were compared with each other. X-Band room temperature ESR measurements of undoped and doped materials were conducted and the effects of dopants on luminescence mechanism were interpreted.

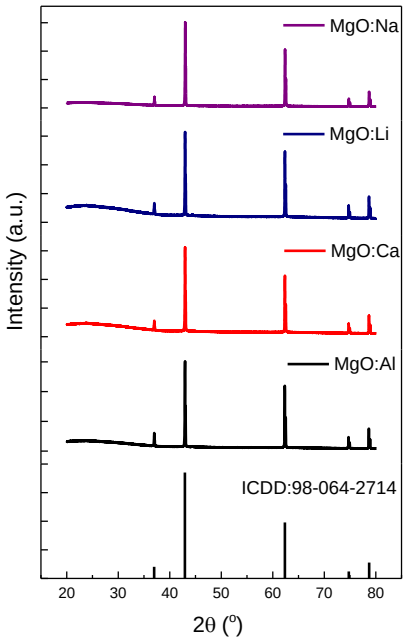


***Figure 1**. XRD analysis of MgO pellets doped with Al, Ca, Li*

2. Experimental details

MgO phosphors were prepared using SCS method as a powder form. Firstly, magnesium nitrate hexahydrate, Mg(NO3)2.6H2O, were stirred in the pure water with chemicals from which dopant ions were taken such as; aluminum oxide, Al(NO3)3.9H2O, calcium nitrate, Ca(NO3)3.4H2O, lithium nitrate, LiNO3, and sodium nitrate, Na(NO3). Then, urea was added into the solution. After the solution became homogenous, it was gradually heated up to 350 oC on the magnetic heater and the water was removed, and the material was burned. Finally, charred material was calcinated at 800 oC – 4h and white powder of MgO phosphors were obtained. Each sample were prepared as pellet form using ~25 mg powder sample and sintered at 1200 oC – 4h before all of the luminescence measurements.

TL and CW-OSL measurements were carried out using a Risø TL/OSL reader model DA-20. Blue light stimulation (470 nm) was performed with the blue light emitting diodes equipped in the reader. Luminescence emission were measured in the VIS region using a Schott BG-39 filter (300–700 nm) and UV region using a (Hoya, U-340, transmittance range from 250 to 390 nm) glass bandpass filter with thickness of 7.5 mm in front of the photo multiplier tube (PMT) tube. In order to the detection of light, a bialkali PMT was used (model 9235QB, Electron Tubes Ltd.). Samples were irradiated at room temperature using an in situ 90Sr/90Y beta source which emits beta particles with a maximum energy of 2.27 MeV. All TL measurements were performed by heating each sample from room temperature up to 450 °C with a heating rate of 5 oC/s. ESR measurements were conducted at room temperature with a Bruker EMX X-band ESR spectrometer operating at 9.5 GHz equipped with a highly sensitive cylindrical cavity.

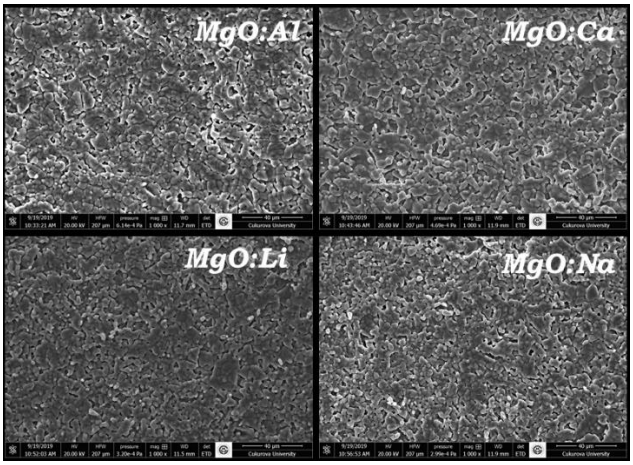


***Figure 2.** SEM images ofMgO pellets doped with Al,Ca,Li and Na ions.*

3. Results and discussion

The XRD pattern of doped MgO pellets are given in Fig. 1. It shows that the pattern matched well with International Center for Diffraction Data (ICDD 98-064-2714) in terms of peak positions. It has cubic structure with lattice parameters of a =b=c=4.2080 Â.

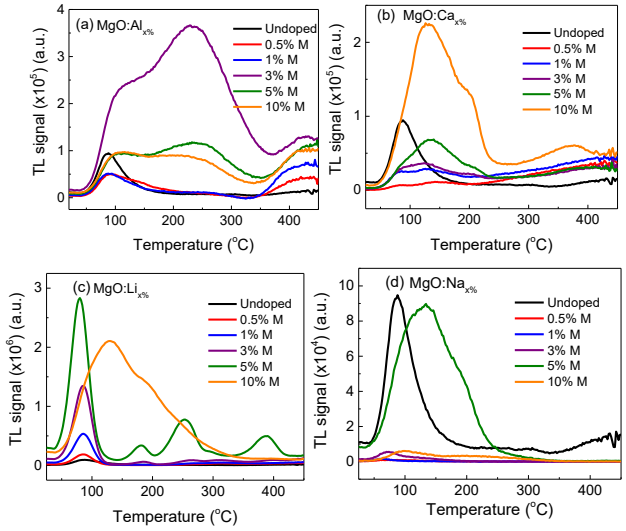


Figure 3. *TL glow curves from (a) MgO:Al$_{x\%}$, (b)MgO: Ca$_{x\%}$, (c) MgO:Li$_{x\%}$ and (d) MgO:Na$_{x\%}$ pellets with different dopant concentrations.*

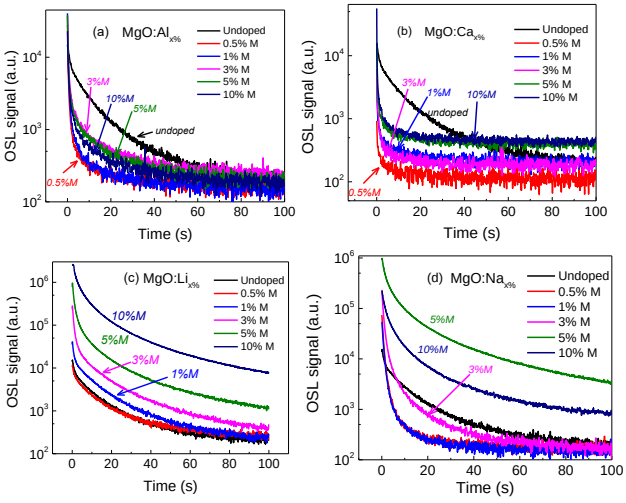


Figure 4. *OSL decay curves from (a) MgO:Al$_{x\%}$, (b)MgO: Ca$_{x\%}$, (c) MgO:Li$_{x\%}$ and (d) MgO:Na$_{x\%}$ pellets with different dopant concentrations.*

The morphology of the MgO pellets has been investigated using SEM. The images show the homogeneous and non-porous structure. This nonporous structure is known to increase thermal interaction in the material. Therefore, it it is expected to contribute to TL signal in good direction[10].

Fig. 3 shows the TL glow curves of MgO pellets doped with different ions with different concentrations (abbreviated as MgO:Abx%) after 2 Gy beta irradiation in comparison with that of the undoped sample. TL readouts were performed by heating each sample from room temperature up to 450 °C with a heating rate of 5 °C/s.

Fig.4 demonstrate the OSL glow curves of MgO pellets doped with different ions with different concentrations (abbreviated as MgO:Abx%) after 2 Gy beta irradiation in comparison with that of the undoped sample. OSL measurements were performed with stimulation time as 100 s with 470 nm blue lights at a power density of ∼70mWcm−2. Compared to the undoped sample, no increase in OSL signal were observed in Al doped and Ca doped MgO samples, but up to 25 times increase were obtained in Li and Na doped samples.

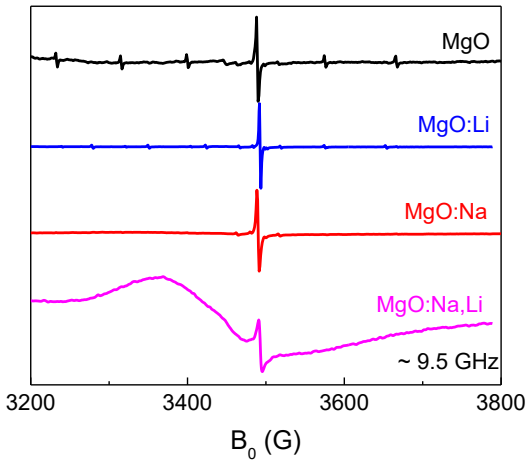


Figure 5. *Room temperature ESR spectra of doped and undoped MgO samples*

Room temperature X-band (9.5 GHz) ESR measurements of undoped MgO and Li, Na doped MgO without irradiation are given in Figure 5. Undoped samples poses 5 small peaks together with a sharp central peak. When the samples are doped with either Na or Li, the smaller peaks vanish but still can be detectable. The g-factor of the intense signal was recorded around 1.977 which is

different than free radical g-factor. Hence, it refers to a paramagnetic center emanating from MgO structure itself. On the other hand, a broad peak appears when two ions are doped at the same time. This shows a synergy between these ions. In all samples, the vicinity of sharp central peak due to MgO presents the strong crystal field created by MgO. However, for a better understanding, ESR measurements should be done on the radiated samples as well.

4. Conclusion

Al, Ca, Li and Na doped MgO samples produced by solution combustion synthesis method were verifiedby XRD measurements and it was observed that our MgO samples which did not contain different phases were highly compatible with the reference number "ICDD 98-064-2714". SEM images showed that all samples had cubic structure of MgO particles with no hollow structure between the grains. Moreover, a structure that contribute to TL signal was formed. According to TL measurements Li doped MgO samples showed up to 25-fold increase in signal. However, it is evident that the trap structures formed in the material could not be formed at high energy levels by the dopants. Therefore, TL peaks were obtained at temperatures lower than desired. It was observed that the increase in OSL signals increases with TL signals proportionally. ESR measurements show a paramagnetic center due to MgO structure itself. By doping the intensity of this center was decreased but still could be detectable. In order to have a full understanding about the structure and free electron formation, radiated samples should also be investigated in detail.

5. Acknowledgement

This research was partly funded by the Cukurova University Research Projects Development and Coordination Unit under the project number FDK-2018-10599. We thank Cukurova University for supporting the project.

References:

[1] C. Klein, C. Hurlbut Jr, Manual of Mineralogy. John Wiley & Sons, Inc., New York (1999).
[2] A.F. Bedilo, M.J. Sigel, O.B. Koper, M.S. Melgunov, K.J. Klabunde, Synthesis of carbon-coated MgO nanoparticles, Journal of Materials Chemistry 12(12) (2002) 3599-3604.
[3] D.J. Seo, S.B. Park, Y.C. Kang, K.L. Choy, Formation of ZnO, MgO and NiO nanoparticles from aqueous droplets in flame reactor, Journal of Nanoparticle Research 5(3-4) (2003) 199-210.
[4] S.T. Aruna, A.S. Mukasyan, Combustion synthesis and nanomaterials, Current opinion in solid state and materials science 12(3-4) (2008) 44-50.
[5] L. Oliveira, B. Doull, E. Yukihara, Investigations of MgO: Li, Gd thermally and optically stimulated luminescence, J Lumin 137 (2013) 282-289.
[6] L. Oliveira, E. Milliken, E. Yukihara, Development and characterization of MgO: Nd, Li synthesized by solution combustion synthesis for 2D optically stimulated luminescence dosimetry, J Lumin 133 (2013) 211-216.
[7] A. Bos, M. Prokić, J. Brouwer, Optically and thermally stimulated luminescence characteristics of MgO: Tb3+, Radiat Prot Dosim 119(1-4) (2006) 130-133.
[8] E. Yukihara, E. Milliken, L. Oliveira, V. Orante-Barrón, L. Jacobsohn, M. Blair, Systematic development of new thermoluminescence and optically stimulated luminescence materials, J Lumin 133 (2013) 203-210.
[9] L. Oliveira, E. Yukihara, O. Baffa, Lanthanide-doped MgO: A case study on how to design new phosphors for dosimetry with tailored luminescent properties, J Lumin (2019).S.J. Pearton, D.P. Norton, K. Ip, Y.W. Heo, T. Steiner, J. Vac. Sci. Technol. B, 22 (2004) 932–948.
[10] V. Altunal, V. Guckan, A. Ozdemir, A. Sotelo, Z. Yegingil, Effect of sintering temperature on dosimetric properties of BeO ceramic pellets synthesized using precipitation method, Nuclear Instruments and Methods inPhysics Research Section B: Beam Interactions with Materials.

6th *International Conference on Materials Science and Nanotechnology For Next Generation (MSNG2019)*
October 16-18, 2019, Niğde, TURKEY (ORAL FULL TEXT)

The Effect of Mn Dopant to the Electrical Performance of ZnO-TFT

S. AKSOY PEHLIVANOGLU[1*], Y. CAGLAR[2], and M. CAGLAR[2]

[1] Department of Physics, University of Sinop, Sinop, Turkey
[2] Department of Physics, University of Eskişehir Technical, Eskişehir, Turkey

In this study, undoped (ZnO) and Mn doped ZnO (ZM) films were deposited by sol gel spin coating technique on 100 nm SiO2 coated Si wafer. Then, The ZnO:Mn-TFTs were fabricated. The effect of different concentrations (0–10 at.%) of Mn on the morphological properties of films was investigated. From AFM images, the lowest RMS value was found to be in undoped ZnO film. From SEM images, it is seen that all films have a smooth, uniform nanostructure. Then electrical performance of ZnO:Mn-TFTs was investigated. The I_{ds}-V_{ds} graphs for all transistor exhibit a transition from linear to saturation behavior. The μ, V_{th}, I_{ON}/I_{OFF} and *SS* values of the ZnO:Mn-TFTs were determined.

Keywords: Mn doped Zinc oxide, Sol Gel Spin Coating, thin film transistor.

Corresponding author: saksoy@sinop.edu.tr

1. Introduction

Metal oxide semiconductors (MOS) are a very versatile material for optoelectronic applications. Among the MOSs, the well-known ZnO has excellent properties such as wide band gap (3.37 eV), large free excitation binding energy (~ 60 meV), high transmittance. Also, ZnO films have great potential applications such as photovoltaic solar cells [1], photo detectors [2], chemical or biosensors [3] and liquid crystal displays [4], transistor [5]. Thin-film transistors (TFTs) are electronic devices based on the FET principle, which are finely obtained on an insulating substrate of the semiconductor such as ZnO. The electrical parameters (field effect mobility, on/off ratio, threshold voltage, sub-threshold swing) of the TFTs are very important for the evaluation of their performance.
ZnO films can be obtained by different methods; magnetron sputtering [6], pulsed laser deposition [7], atomic layer deposition [8], metal–organic chemical vapor deposition [9], sol gel processing [10]. The sol gel process has some advantage such as; excellent compositional control, homogeneity, low cost, simplicity and low annealing temperature. In addition, the doping process can be easily carried out with this method. The structural, morphological and electrical properties of the main material can be easily changed with the doping material. At the same time, the effect of the contribution to ZnO films is also important in affecting the performance of TFTs.
In this study, undoped and Manganese (Mn) doped ZnO films were produced by using sol gel spin coating technique. The effect of Mn doping on the surface properties of the films was investigated. In addition, TFTs were produced and investigated to determine how the electrical performance of these TFTs was influenced by the Mn doping.

2. Experimental details

In this study, undoped and Mn doped ZnO films were prepared using sol gel spin coating technique. The starting material, dopant, stabilizer and solvent were used zinc acetate dihidrate [$Zn(CH_3COO)_2.2H_2O$], Manganase acetate [$Mn\ (CH_3COO)_2.4H_2O$], monoethanolamine (C_2H_7NO) and 2-methoxyethanol ($C_3H_8O_2$), respectively. All solutions were prepared as 0.05 M. Mn doping in ZnAc solution was made at different volume ratio (1, 3 and 10%). 100 nm SiO_2 coated Si wafer was used as substrate. Deposition temperature and annealing temperature were determined as 300°C (10min) and 750°C (2h), respectively. After coating the films, aluminum sources and drain electrodes were formed by metal evaporation system (Vaksis PVD Handy-MT/101T). In addition, silver paste was used for gate contact. The transistors are labeled ZM0, ZM1, ZM3 and

ZM10 after production (taking into account the Mn dopant amount) respectively. The schematic diagram of the TFTs is shown in Figure 1.

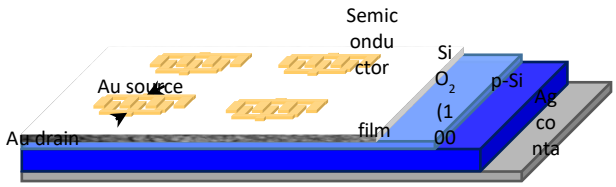


Figure 1. *Schematic diagram of the transistors.*

The surface morphology of the ZnO:Mn films were investigated by atom force microscope (NT-MDT; AFM) and scanning electron microscope (ZEISS ULTRA PLUSS, SEM). Electrical measurements of the TFTs were performed with Keithley 4200 SCS with connected Signatone Probe Station.

3. Results and discussion

Atomic force microscope (AFM) was used to obtain 3-D images of undoped and Mn doped ZnO films and to examine the effects of Mn dopant on the morphology of films. Figure 2 shows the AFM images of all films. The root-mean-square (RMS) roughness values of active layers for ZM0, ZM1, ZM3 and ZM10 are 4.068 nm, 8.379 nm, 5.687 nm and 11.760 nm, respectively. It is seen from AFM images that the film with the lowest RMS value is ZM0 film. This may cause the film to perform better in device applications.

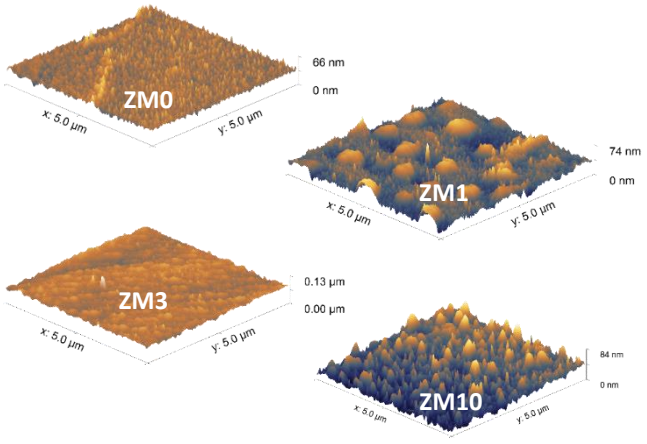


Figure 2. *AFM images of the films.*

The surface morphology of the films was examined and FESEM images are given in Figure 3. In these SEM images, a smooth, uniform microstructure is clearly visible. It can be seen from Figure 3 that all films exhibit a small-grained microstructure. All films were densely coated. This shows that the coating is very suitable for use as a device.

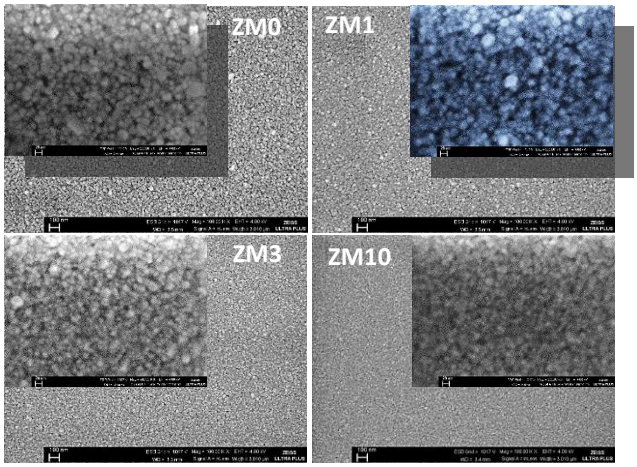


Figure 3. *SEM images of the films.*

To investigate the effect of Mn dopant amount on the device performance, TFT devices containing semiconductor films deposited at different dopant amounts were fabricated. Figure 4-7 indicate the transfer characteristics of ZM0, ZM1, ZM3 and ZM10 transistors respectively (V_{ds} = 30 V). All measurements were performed at room temperature and under a dark. Electrical parameters of all TFTs are given in Table 1. As shown in Figure 4-7, the current of the devices is increased by positive Vg. When the positive gate voltage is applied to the transistor, it exhibits n-type behavior, which has a characteristic that shows a linear behavior at small source-drain voltages (V_{ds}) and a good saturation at V_{ds} values near the gate voltages (V_{gs}). The mobility (µ) and threshold voltage (V_{th}) values are determined using Equation (1) from the slope and intercept values obtained in the saturation region of the $I_{ds}^{1/2}$ - V_g graph (satisfying the V_{ds}> Vgs-Vth condition) [11].

$$I_{ds} = \frac{\mu_{sat} C_i W}{2L} \left(V_{gs} - V_{th}\right)^2 \qquad (1)$$

C_i, W and L are the gate capacitance per unit area, the width of the channel and the length of the channel, respectively (in our study, W = 50µm and L = 1000µm). The threshold voltages of ZM0-TFT and ZM10-TFT were

obtained -5.87V and -7.73V, respectively. This result indicates that these TFTs are operating in depletion mode mode. Because the detectable drain current flows at zero gate voltage. However, the threshold voltages for ZM1 and ZM3 were calculated 17 V and 40.85 V, respectively. A positive threshold voltage indicates that the transistor is operating in enhancement mode, at Vgs = 0 V, the device is in the off position and a positive gate bias is required to form a conductive channel. [12, 13]. The subthreshold swing (SS) is expressed by Equation (2) and is determined from the slope of the linear part of the log (I_{ds}) -V_{gs} graph [14].

$$SS = \left[\frac{dlog_{10}I_{ds}}{dV_{gs}}\right]^{-1} \quad (2)$$

The SS value of the TFTs indicates the presence of interface trap states between the active layer and the gate dielectric layer, thus expressing the interface quality. The SS values for the transistors values for ZM0, ZM1, ZM3 and ZM10 are 30.87, 59.77, 87.41 and 31.21 V/decade, respectively.

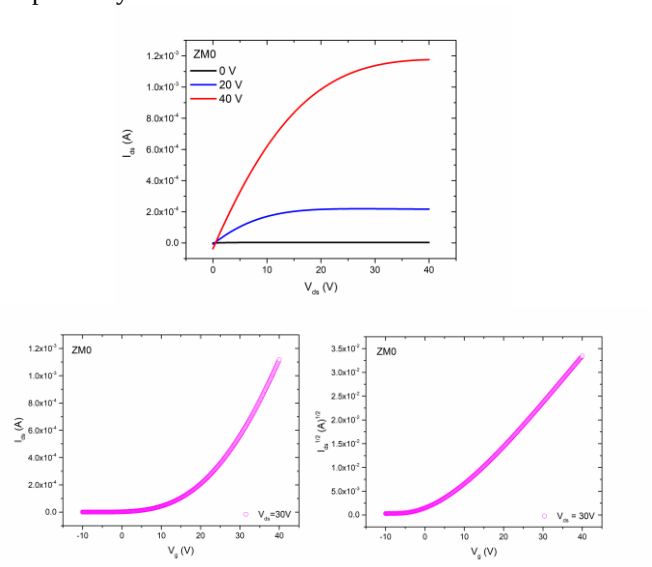


Figure 4. *Output characteristics, transfer characteristics and plot of I_{ds} versus V_g for the ZM0 TF*

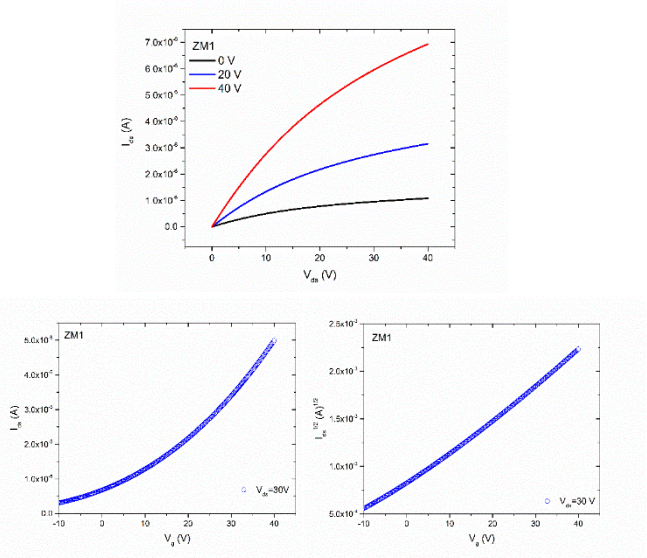


Figure 5. *Output characteristics, transfer characteristics and plot of I_{ds} versus V_g for the ZM1 TFTs.*

Table 1. Electrical properties of the TFTs.

Transistor code	μ (cm^2/Vs)	V_{th} (V)	I_{on}/I_{off}	SS (V/decade)
ZM0	2.78	-5.87	$1.15x10^4$	30.87
ZM1	$4.04x10^{-3}$	17	16.10	59.77
ZM3	$2.12x10^{-3}$	40.85	2.60	87.41
ZM10	$5.81x10^{-4}$	-7.73	511	31.21

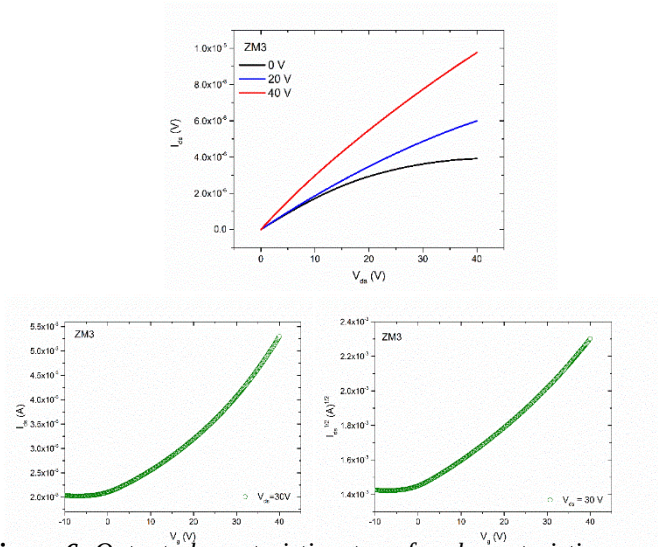


Figure 6. *Output characteristics, transfer characteristics and plot of I_{ds} versus V_g for the ZM3 TFTs.*

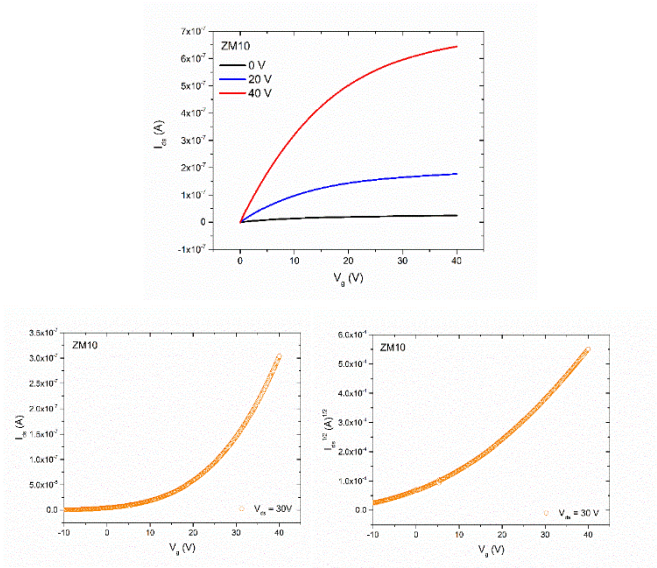


Figure 7. *Output characteristics, transfer characteristics and plot of I_{ds} versus V_g for the ZM10 TFTs.*

4. Conclusion

Using the sol-gel process, undoped and Mn doped ZnO films were produced. The morphological properties of the films were examined and then the necessary contact procedures were performed to examine the device performances. The effect of Mn doping on the performance of the devices was investigated. The ZM0 TFT exhibited an good mobility of 2.78 cm^2/Vs. For ZM0 and ZM10 TFT's, a negative threshold voltage was calculated and it was an indication that TFT operated in depletion mode. The threshold voltages for ZM1 and ZM3 were calculated as 17 V and 40.85 V. Furthermore, the device with the highest I_{on}/I_{off} ratio is the ZM0-TFT.

5. Acknowledgement

This work was supported by Eskisehir Technical University Commission of Scientific Research Project under Grant No. 1706F385

References:

[1] KUMAR, V., SINGH, N., KUMAR, V., PUROHIT, L.P., KAPOOR, A., NTWAEABORWA, O.M., SWART, H.C., "Doped zinc oxide window layers for dye sensitized solar cells", J. Appl. Phys. 114, 134506, 2013.

[2] LIU, K., SAKURAI, M., AONO, M., "ZnO-Based Ultraviolet Photodetectors", Sensors, 10, 2010.

[3] LI, C.F., HSU, C.Y., LI, Y.Y., "NH3 sensing properties of ZnO thin films prepared via sol–gel method", J. Alloys Comp. 606, 27, 2014.

[4] PARK, H. G., KIM, E. M., HEO, G. S., JEONG, H. C., LEE, J. H., HAN, J. M., KIM, T. W., SEO, D. S., "Electro-optical properties of liquid crystal displays based on the transparent zinc oxide films treated by using a rubbing method", 75, 252-257, 2018.

[5] RUZGAR, S., OZKAN, A. E., CAGLAR, M., AKSOY, S., ILICAN, S., CAGLAR, Y., YAKUPHANOGLU, F., "Effect of the deposition temperature on the device performance of the nanostructured ZnO thin film transistor by sol gel method", 9, 689-693, 2014.

[6] HAN, D., ZHANG, Y., CONG, Y., YU, W., ZHANG, X, WANAG, Y., "Fully transparent flexible tin-doped zinc oxide thin film transistors fabricated on plastic substrate" Sci. Rep., 6, 38984, 2016.

[7] D. H., LEE, PARK, K. H., KIM, S., LEE, S. Y., "Effect of Ag doping on the performance of ZnO thin film transistor" Thin Solid Films, 520, 3, 1160–1164, 2011.

[8] LIN Y.Y., HSU, C. C., TSENG, M. H., SHYUE J. J., TSAI F. Y., "Stable and high-performance flexible ZnO thin-film transistors by atomic layer deposition" ACS Appl. Mater. Interfaces, 7, 40, 22610–22617, 2015.

[9] MELENDREZA M.F., SOLIS-POMAR F., GUTIERREZ-LAZOS C.D., FLORES P., JARAMILLO A.F., FUNDORA A., PEREZ-TIJERINA E., "A new synthesis route of ZnO nanonails via microwave plasma-assisted chemical vapor deposition", Ceramics International, 42, 1160–1168, 2016.

[10] CAGLAR Y., CAGLAR M., ILICAN S., AKSOY S., YAKUPHANOGLU F,. "Effect of channel thickness on the field effect mobility of ZnO-TFT fabricated by sol gel process", Journal of Alloys and Compounds, 621, 189–193, 2015.

[11] ORTEL M., TROSTYANSKAYA Y.S., WAGNER V., "Spray pyrolysis of ZnO–TFTs utilizing a perfume atomizer", Solid-State Electron. 86, 22–26, 2013.

[12] RUZGAR, S., CAGLAR, M., "The effect of Sn on electrical performance of zinc oxide based thin film transistor" Journal of Materials Science: Materials in Electronics, 2018.

[13] RUZGAR, S., AKSOY, S., "Electrical performance of ZnO thin film transistors having different active layer thickness", Journal of Materials and Electronic Devices 1 (1) 38-41, 2017.

[14] SHIMODA T., 2019, Nanoliquid Processes for Electronic Devices: Developments of Inorganic Functional Liquid Materials and their Prossesing, pp. 516, Springer Nature Singapore.

6th International Conference on Materials Science and Nanotechnology For Next Generation (MSNG2019)
October 16-18, 2019, Niğde, TURKEY (ORAL FULL TEXT)

Cu: ZnO-DSSC Fabrication and Characterization

Halil ESGİN[1], Yasemin CAGLAR[2]

1 Cukurova University, Central Research Laboratory, Adana, TURKEY
2 Eskisehir Technical University, Science Faculty, Department of Physics, Eskisehir, TURKEY

In this study, Cu doped ZnO nanopowders were deposited by hydrothermal method. To investigate the crystalline structure and the orientation of the Cu:ZnO films, XRD patterns were used. The structural, optical and morphological properties of ZnO nanopowders and films were investigated. The effect of Cu dopant concentrations on the morphology of ZnO and the performance of DSSCs were systematically investigated. According to kubelka munk theory, the band gap values of the films were found and the band gap values decreased with increasing Cu concentration. Then, Cu:ZnO-DSSC was fabricated. The current–voltage characterization of fabricated DSSCs was performed by AM 1.5 simulated sunlight at different light intensity. The cell parameters (the short circuit current, the open circuit voltage, the conversion efficiency and the fill factor) of Cu:ZnO-DSSCs were determined.

Keywords: Cu doped ZnO, hydrothermal synthesis, dye sensitized solar cell.

Corresponding author: yasemincaglar@eskisehir.edu.tr

1. Introduction

Solar energy is one of the most promising alternative energy sources in the future. Producing devices with low production costs and high efficiency is essential for capturing sunlight and saving energy. Dye sensitized Solar Cells (DSSCs) have many advantages compare to other photovoltaic devices, such as a superior performance in conditions of low intensity, low angle of incidence and high temperature. DSSC uses dye molecules adsorbed on the nanocrystalline oxide semiconductors such as titanium oxide (TiO2) or zinc oxide (ZnO) to collect sunlight. A DSSC comprises a series of different component layers stacked in series. These are counter electrodes coated with glass substrate, transparent conductive layer, photoanode (TiO2 or ZnO), dye, electrolyte and sealing gasket. Since Zinc oxide (ZnO) has better electrical properties, its use in DSSCs is considered to be the best alternative to TiO2.[1]. However, ZnO-based DSSCs suffer from lower cell efficiencies than TiO2 nanoparticle-based DSSCs, mainly due to the recombination of injected electrons [2]. Improvement in electrical and optical properties of ZnOs is realized with contribution. In particular, the electrical resistance of ZnO is improved by the addition of trivalent elements such as aluminum, indium, gallium and boron.
It is known that the Copper (Cu) element doped in ZnO changes the morphology, narrows the band gap and increases the absorption wavelenght. In the literature, techniques such as pulsed laser deposition [3], sol-gel method [4], spraying [5], hydrothermal [6] are used to obtain Cu doped ZnO nanopowder. Among them hydrothermal technique is a promising alternative synthetic method because of the simple equipment, catalyst-free growth, low cost, large area uniform production, environmental friendliness and less hazardous.
In present work, Cu doped ZnO nanopowders were produced by hydrothermal synthesis method at varying concentrations. The Cu doped ZnO films have been fabricated by doctor blade method. The structural and morphological properties of the ZnO nanopowders and films were characterized by XRD and SEM, respectively. The electrical performance of the ZnO:Cu-DSSCs were investigated.

2. Experimental details

2.1. Synthesis of Cu doped ZnO

The Cu doped ZnO nanopowders were deposited by the hydrothermal method. Zinc nitrate hexahydrate ($Zn(NO_3)_2.6H_2O$) and Sodium hydroxide (NaOH) were used as initail materials for the ZnO nanopowders. Copper Acetate ($((CH_3COO)_2Cu\cdot H_2O$) were used as dopant source. To obtain a homogeneous solution, these were dissolved in water by mixing the appropriate stoichiometric ratios of initial materials in 10 minutes. Then 1g sodium dodecyl sulfate ($NaC_{12}H_2.5SO_4$) was added and stirred for 30 minutes. Then, the solution was placed to 100 mL capacity of Teflon coated stainless steel autoclaves. The Teflon-lined stainless steel autoclaves was heated at 140°C for 12 h. Subsequently, the autoclave was cooled to room temperature. The resulting white precipitates were collected by filtration and washed with deionized water and ethanol for several minutes. The final products were dried in an oven at 60 °C. The obtained powders were named as ZC-0, ZC-05, ZC-1, ZC-3 and ZC-8.

2.2. Fabrication of ZnO:Cu-DSSC

Firstly, Fluorine-doped tin oxide (FTO) substates were firstly cleaned and the FTOs were dried at nitrogen ambiant. And then, the ZnO:Cu paste was prepared by mixing the nanopowders, Triton-X 100 and acetyl acetone. The resulting pastes were spread onto the FTO glass by doctor-blade method and annealed for 2 h at 450◦C in air and then cooled. Then the ZnO:Cu-DSSCs were prepared by squeezing the paste onto the FTO substrates using plastic tapes. And then, The ZnO:Cu films were immersed into a 0.5 mM N719 (Ruthenizer 535 bis-TBA, Solaronix)) for 1-4 hours. Finally, the dye loaded films were assembled with the prepared Pt counter electrodes to form a sandwich-type DSSCs using a sealing plastic. The active area of the ZnO:Cu films were adjusted to around 0.25 cm^2.

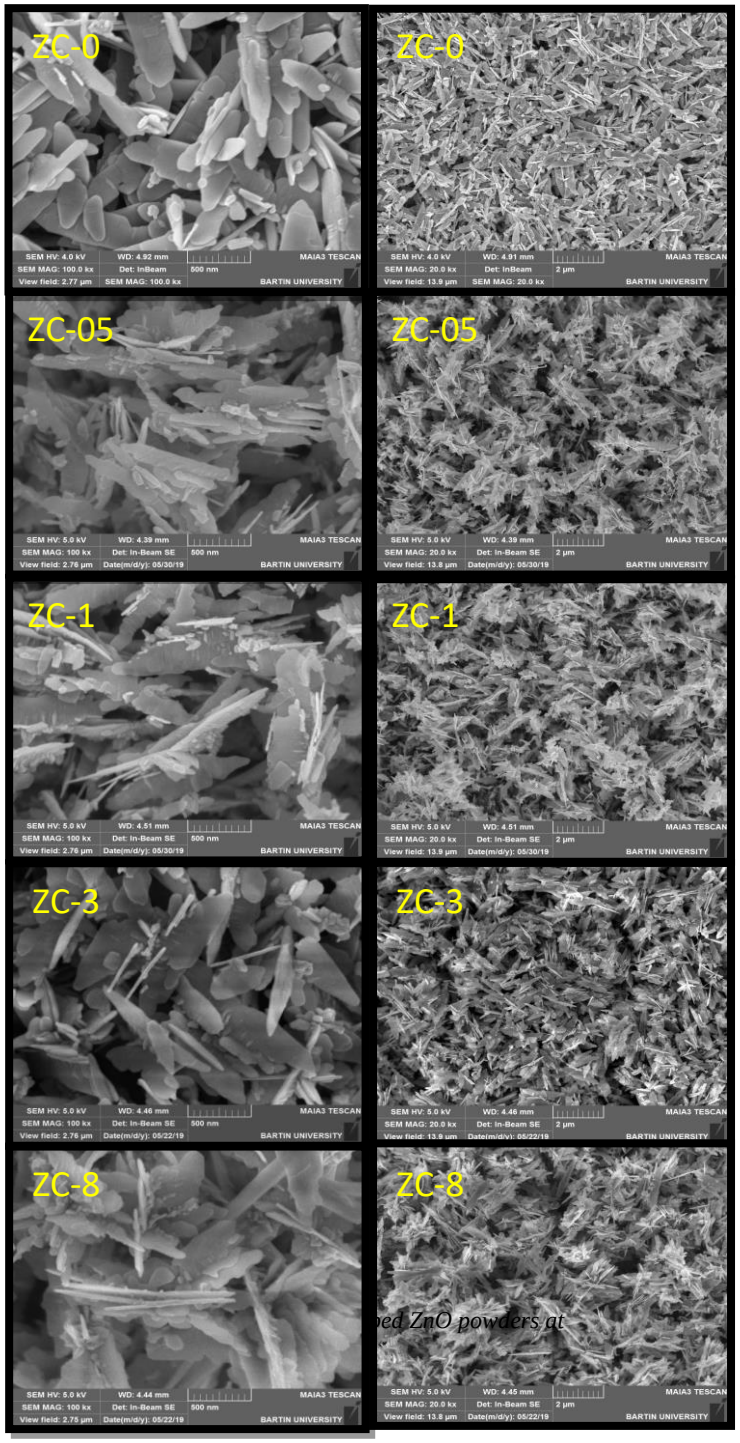
2.3. Characterizations and measurements

Phase identifications of the nanopowders were characterized by X-ray diffraction (XRD, Rigaku SMARTLAB). The morphologies of the nanopowders were investigated by scanning electron microscope (SEM, TESCAN MAIA3). The current–voltage (I–V) characteristics of the DSSCs were recorded by a solar cell measurement system (FYTRONIX OPTOSENSE). SCHIMADZU UV-2450 spectrophotometer was used for reflectance measurements.

3. Results and discussion

Undoped and Cu doped nanopowders have been studied using field emission electron microscopy (FESEM). The SEM images of the films have been shown in Fig.1. It is seen that the leafy structure is disturbed by the copper contribution and it starts to become irregular.

XRD pattern of ZnO:Cu nanopowders are shown in Fig. 2. Fig. 2 confirms that all nanopowders are a polycrystalline nature. The diffraction planes (100), (002), (101) (102), (110) (103) and (112) are in good consent with ZnO-JCPDS card no. 36-1451 and belong to hexagonal wurtzite structure.



ed ZnO powders at

different magnifications

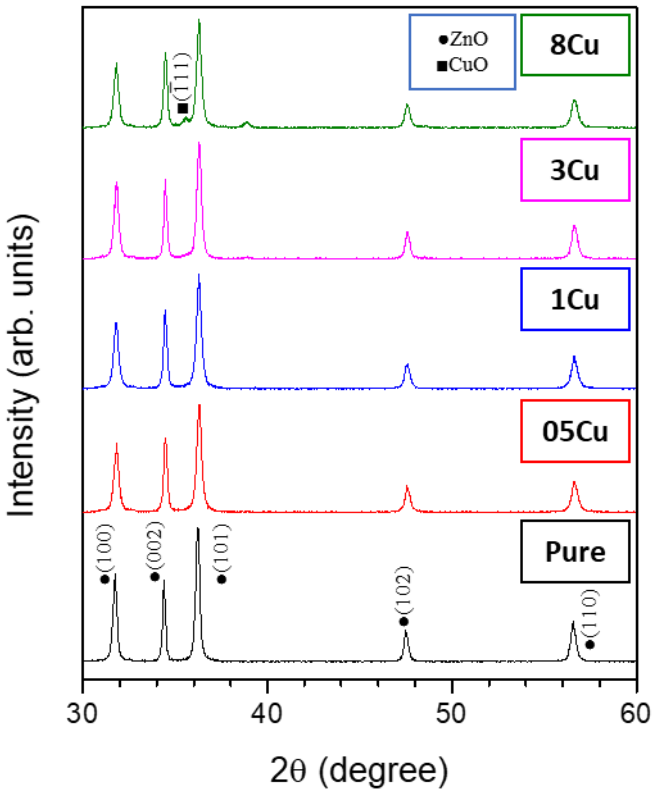


Figure 2. *XRD spectra of the Cu doped ZnO powders*

As seen from XRD patterns, only ZnO peaks were observed up to 3% Cu doped ZnO nanopowders, while CuO peaks were observed in 3 and 8% Cu doped ZnO nanopowders.

The diffuse reflectance measurements were used to find the band gaps of the obtained nanopowders. The diffuse reflectance spectra of all ZnO nanopowders are given in Fig. 3. It is shown that the R% values in this figure decrease with increasing Cu content.

Using reflectance measurements, $(F(R)h\nu/t)^2$ vs $h\nu$ graphs were drawn according to Kubelka-Munk theory [7]. The band gap values of all nanopowders were determined from the point that cuts the energy axis of the linear part of the graph given in Fig. 4. and the band gap values were found to be 3.27 eV, 3.26 eV, 3.25 eV, 3.24 eV, respectively ZC-05, ZC-1, ZC-3 and ZC-8. As expected, the band gap values decrease with Cu incorporation.

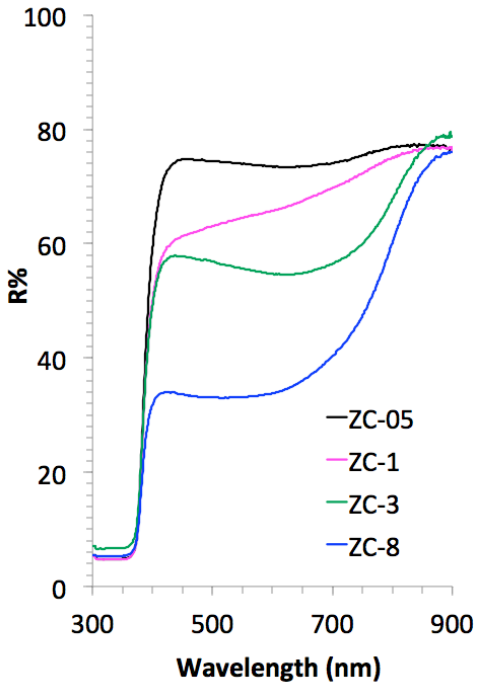


Figure 3. *Reflectance spectra of the Cu doped ZnO powders*

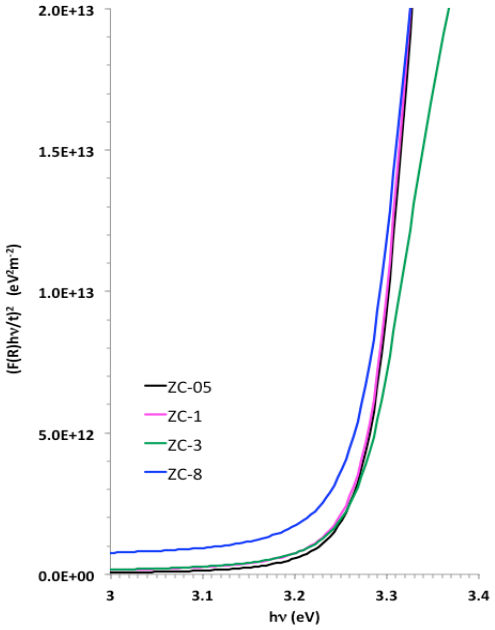


Figure 4. *$(F(R)h\nu/t)^2$ vs. $h\nu$ graph of the Cu doped ZnO powders*

Fig. 5-9 are given in the current density-voltage (*J-V*) graphs for ZnO-DSSC and ZnO:Cu-DSSCs at different loading time (1-4h) under 100mW/cm^2 simulated sunlight illumination. From the *J-V* graphs, DSSC parameters such as open circuit voltage (V_{oc}), short circuit current density (J_{sc}), and conversion efficiency (n%) are estimated using Equation (1) [8] and given in inset in Fig. 5-9.

$$n\% = \frac{FFxV_{oc}xI_{sc}}{P_{in}} x100 \quad (1)$$

where *FF* is the Fill factor and P_{in} is the intensity of the incident light.

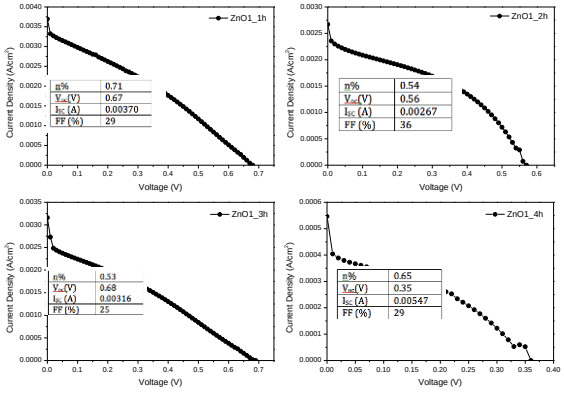


Figure 5. *J-V curves of the ZnO-DSSC*

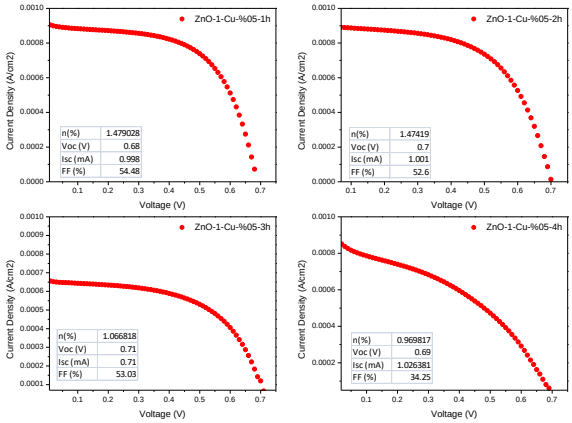


Figure 6. *J-V curves of the ZnO:0.5%Cu-DSSCs*

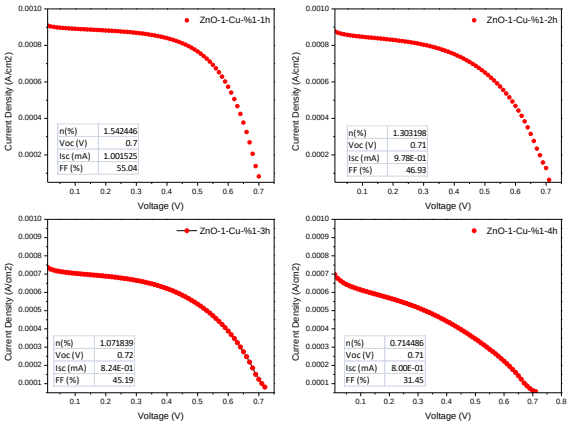


Figure 7. *J-V curves of the ZnO:1%Cu-DSSCs*

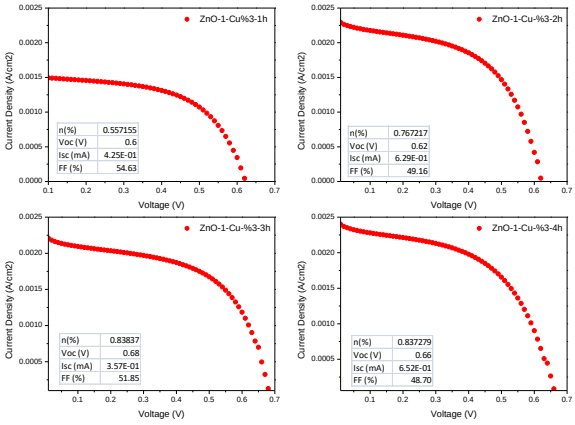


Figure 8. *J-V curves of the ZnO:3%Cu-DSSCs*

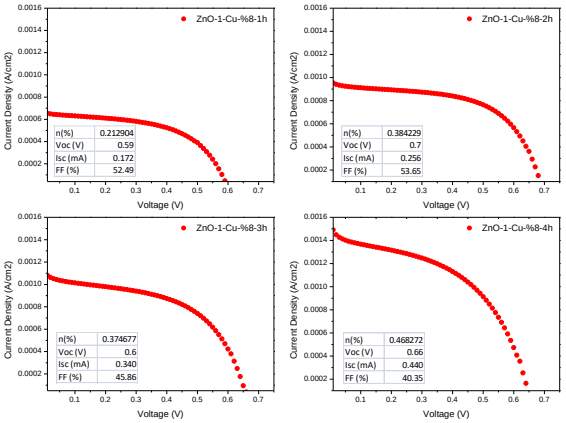


Figure 9. *J-V curves of the ZnO:8%Cu-DSSCs*

It can be seen in these Figures that the dye loading time and Cu content generates a significant effect on the photovoltaic performance of the DSSCs. The highest efficiency (n%) among all DSSCs is the cells immersed in 1 h. The ideal dye loading time was optimized to be 1 hours. It was obvious that the all cell parameters (n%, V_{oc}, I_{sc}, FF) enhanced with first addition of Cu and then declined with the Cu content increasing. The n increased by approximately 2 times compared with that of DSSCs with pure ZnO.

4. Conclusion

In this study, ZnO:Cu nanopowders were deposited by the hydrothermal method. The effects of different Cu concentration on the structural and morphological properties of ZnO powders were investigated. ZnO:Cu-DSSCs were fabricated using N719 dye-sensitized. The effects of dye loading time and Cu concentration on DSSC parameters were systematically investigated.

5. Acknowledgement

This work were supported by Eskisehir Technical Commission of Scientific Research Project under Grant No. 1706F385 and 19ADP157.

References:

[1] VITTAL, R. and HO, KUO-CHUAN, “Zinc oxide based dye-sensitized solar cells: A review”, Renewable and Sustainable Energy Reviews, (2017), 70, 920-935

[2] YANG W., WAN F., CHEN S., JIANG C., “Hydrothermal Growth and Application of ZnO Nanowire Films with ZnO and TiO_2 Buffer Layers in Dye-Sensitized Solar Cells”, Nanoscale Research Letters, (2009), 4, 1486-1492

[3] AMIT K. D., P. MISRA, R.S. AJIMSHA, V.K. SAHU, B. SINGH, “Electron interference effects and strong localization in Cu doped ZnO thin films”, Materials Science in Semiconductor Processing, (2017), 68, 275-278

[4] ASIKUZUN, E., OZTURK, O., ARDA L., TERZİOGLU C., "Preparation, growth and characterization of nonvacuum Cu-doped ZnO thin films", Journal of Molecular Structure, (2018), 1165, 1-7.

[5] NARAYANAN N., and N. K. DEEPAK, "Enhancement of visible luminescence and photocatalytic activity of ZnO thin films via Cu doping", Optik, (2018), 158, 1313-1326

[6] ABINAYA, C., MAIKANNAN M., MANIKANDAN M, MAYANDI J., SURESH P., SHANMUGAIAH V., EKSTRUM C., PEARCE J.M., . "Structural and optical characterization and efficacy of hydrothermal synthesized Cu and Ag doped zinc oxide nanoplate bactericides", Materials Chemistry and Physics, (2016), 184, 172-182.

[7] AVCI B., CAGLAR Y., and CAGLAR M., "Controlling of surface morphology of ZnO nanopowders via precursor material and Al doping", Materials Science in Semiconductor Processing, (2019), 99, 149-158

[8] OCAKOGLU K., YAKUPHANOGLU F., DURRANT J. R., ICLI S., “The effect of temperature on the charge transport and transient absorption properties of K27 sensitized DSSC”, Solar Energy Materials and Solar Cells, (2008) 92, 1047-1053

6th International Conference on Materials Science and Nanotechnology For Next Generation (MSNG2019)
October 16-18, 2019, Niğde, TURKEY (ORAL FULL TEXT)

Pressure Effect on Phase Transition for CaTe Compound

Y. Öztekin Çiftci[1] and İ. Kars Durukan[1]

Department of Physics, Faculty of Science, Gazi University, Ankara 06500, Turkey

Especially, over the last two decades, the alkaline earth chalcogenides gain importance in terms of the structural phase transition under high pressure. Calcium chalcogenides are substantial for constructing ternary compunds, which have a wide application field in technology. CaTe compound is decided to examine as a member of this family and its significant physical properties are calculated via VASP (Vienna Ab initio Simulation Package). A first-principles study is carried out within DFT (density functional theory) and GGA-PBE (generalized gradient approximation with Perdew, Burke and Ernzerhof correction) is used during the computation process. CaTe crystallizes in NaCl (rocksalt) type at ambient conditions and has mechanical stability due to obtained elastic constants. Lattice constants and the other elastic parameters are also reported in present work. The plotted energy-volume curve indicates that NaCl phase of this compound is the most stable one and a phase transition to CsCl phase is predicted under pressure. Furthermore, the pressure effects on structural, electronic and elastic behavior of CaTe are discussed even the focus of this paper is phase transition. The DOS (density of states) is given with the band structure and the phonon curves calculated by PHONOPY are analyzed. Briefly, a systematic method is used to comprehend pressure effect on the characteristics of CaTe and it is concluded that this calcium chalcogenide is dynamically stable in the ground state. A good agreement is reached in comparison of our results with other available theoretical and experimental data in the literature.

Keywords: CaTe, Elastic properties, Phase Transition

Submission date:
Acceptance Date:

Corresponding authors: ilknurdurukan@gazi.edu.tr

1. Introduction

The structural and electronic properties of the heavy alkaline earth chalcogenides (AECs) at high pressures are a subject of considerable theoretical and experimental interest [1]. High pressure, along with ambient-pressure studies on materials, can help with analyzing the nature of interaction among the atoms. These compounds crystallized in the NaCl-type (B1) structure at ambient conditions. The AECs form a very important group of semiconductors with large band gap and valence-band width. Pressure is an attractive thermodynamical variable to reveal the mechanical properties of most of the solids and alloys. Since cohesion of solids is crucial, the interatomic distance changes as a consequence of the application of pressure. A noticeable feature in the electronic band structure of the CaX compounds is that there is no d electron in the valence band. The application of pressure on the NaCl structure of the alkaline earth chalcogenides undergoes a structural phase transition to CsCl- type (B2) structure with eight fold-coordination.

Luo et al. [2] have performed an extensive experimental study of the behavior of CaS, CaSe and CaTe under pressure using energy-dispersive X-ray diffraction. They found that the first two compounds have a phase transition from the B1 (NaCl) to the B2 (CsCl) phase at a pressure of 40 and 38 GPa, respectively. However, CaTe first transforms to an intermediate
state, which is a mixture of the NaCl and MnP phases at 25 GPa and then, at a pressure slightly greater than 33 GPa, to

the B2 phase. Zimmer et al. [3] obtained pressure–volume relationships and structural transitions in CaTe using X-ray diffraction. Khenata et al. [4] calculated electronic band structures and the total energies of CaSe and CaTe in NaCl and CsCl-type structures using full-potential linearized augmented plane wave method (FP-LAPW) within the generalized gradient approximation (GGA).

In this study structural phase transition, elastic, electronic, and vibrational properties of CaTe compound have been associated with these physical properties in CsCl (B2) and NaCl(B1) type crystal structures. In our study, we also have evaluated the vibrational properties of CaTe.

2. Method of Calculation

The calculations have been performed using the Vienna Ab-initio Simulation Package (VASP) [5-9] based on the density functional theory (DFT). The interaction between ions and electrons is described by the projector-augmented wave (PAW) method [10, 11]. The number of k-points in irreducible part of the Brillouin zone has a great influence on the accuracy of the calculations. The k-points of 15×15×15 have been generated by the Monkhorst-Pack grid [12] for the sampling of the Brillouin zone. The algorithm implemented in VASP is based on the conjugate gradient scheme for this study. This algorithm calculates atomic forces and electronic ground state situations for a given geometry in a few iterations. These steps are repeated until energy and force convergence criteria are satisfied. The gradient-corrected functional in the form of the generalized-gradient approximation (GGA) by Perdew and Wang [13, 14] and the projector-augmented wave (PAW) method developed by Blöchl [15] have been used for calculations. All results presented below have been obtained by using a plane wave basis set with 700 eV cut off energy.

3. Results and discussion:

At 0GPa, the CaTe crystallize in the NaCl-type structure, with Fm3m as a space group and it undergoes a first-order transition, from the sixfold coordinated rocksalt (B1) structure to the eightfold coordinated Cesium chloride (B2) structure under compression. To determine the equilibrium geometry, we relaxed (ISIF=3 in VASP) the volume of unit cell and the all atomic positions. With the relaxed equilibrium lattice constant, the Murnaghan equation of state was fitted to the E (V) curves in order to determine the Bulk modulus (B)and its pressure derivative for B1 and B2 structure of CaTe. The obtained results of investigated compound are given in Table . The unit cells of CaTe compound in B1 and B2 crystal structures are shown in Figure 1.

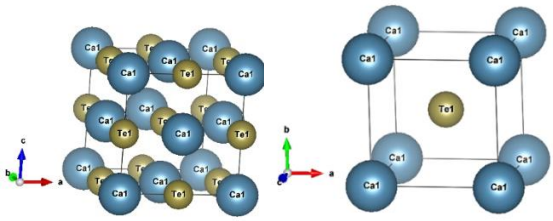


Fig.1: The unitcell of CaTe in B1 and B2 structure.

It is seen from Table I, calculated lattice constant a_0, Bulk module B and derivative of bulk module B', and formation energy of $Co_xA_{1-x}Al$ compound is in good agreement with the other theoretical and experimental study.

Table 1: Calculated equilibrium lattice constant (a_0), bulk modulus (B_0), and its pressure derivative (B_0') and total energies (E_{tot}) of CaTe compound.

Structure	Reference	a_0 (Å)	B_0(GPa)	B_0'	E_{tot}(eV)
NaCl (B1)	Present	6.397	38.55	4.318	-8.47
	Theory[a]	6.396	48.75	3.40	
	Exp.[b]	6.348	41.8	4.3	
CsCl (B2)	Present	3.926	40.022	4.04	-7.84
	Theory[a]	3.653	51.41	3.8	
	Exp[b]	3.93	50	4.2	

a:[16], b:[2]

It is seen from Table 1, calculated lattice constants of B1 and B2 structure is very compatible with the experimental value (a= 6.348, 3.93 Å) [2] and quite compatible with the theoretical value in Ref. [16]. The variations are due to the difference in the method of calculation. The total energies were calculated as a function of volume CaTe are given in Figure 2. According to the Fig. 2, it is clear that the B1 crystal structure is more stable than the B2 crystal structure of CaTe compound.

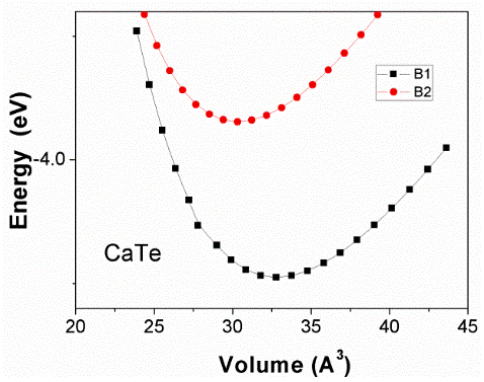


Fig.2: Energy versus volume curves for B1 and B2 crystal structures of CaTe compound

The phase transition behavior of CaTe is also investigated to see the high pressure structural properties. The total energy curves of CaTe for two different crystal structures (B1 and B2) are shown in Fig. 2. It is clear from Fig. 2 that CaTe compound undergoes a phase transition from B1 to B2 structure. This transition pressure (Pt) is determined by calculating the Gibbs free energies at 0 K. The related enthalpy changes (ΔH)-pressure (P) graph is presented in both phases for CaTe compound as shown in Figure 3. The transition pressure is a pressure at which H-P curves for both phases crosses. The transition pressures are calculated to be 28.5 GPa for CaTe and this value is good agreement with other theoretical study (30.41GPa)[16] and lower than the experimental value (33GPa) [2]. It is depicted that B1 crystal structure is more stable than the B2 crystal structure.

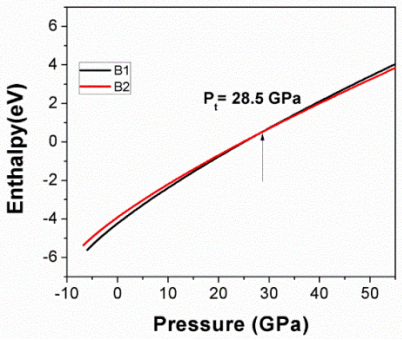


Fig.3: Estimation of phase transition pressure from B1 to B2 structure for CaTe

In order to understand the electronic and phase stability of CaTe the energy band structure along with total electronic density of states in B1 and B2 structure of CaTe are presented in Figure 4 and Figure 5. Fermi level is set 0 eV. Our calculation shows that CaTe in B1 structure is semiconductor which has indirect band gap of 1.45 eV in Γ and X (lower than 2.57 eV of other study) while in B2 structure this compound is of metallic conductivity as there is no band gap near the Fermi level and there are many bands crossing the Fermi level.

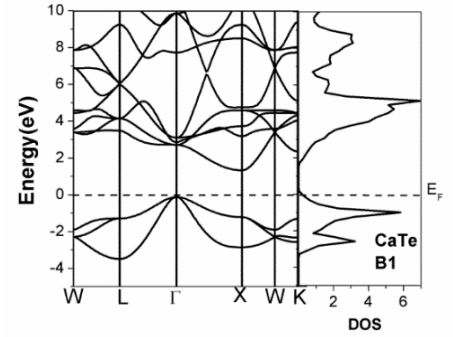


Fig.4: Electronic band structure in B1 structure for CaTe.

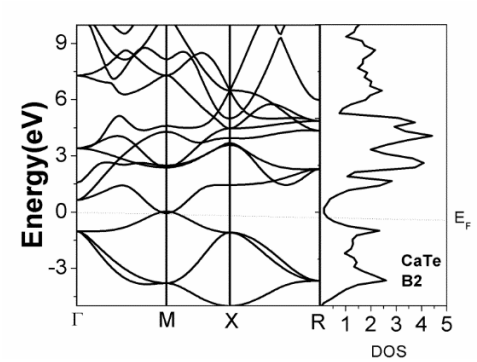


Fig.4: Electronic band structure in B2 structure for CaTe.

Elastic properties are very important properties for materials, which can be determined elasticity, mechanical stability, and stiffness of crystals that is essential to understand the chemical bonding and the cohesion of material [17]. In this study, the second-order elastic constants (Cij) are calculated using the "stress-strain" relations [18]. Calculated elastic constants at zero pressure for B32 and B2 crystal structures of CaTel are listed in Table II and given with Zener anisotropy factor, Poisson's ratio and G/B ratio.

Table 2 Calculated single-crystal elastic constants, Cij [GPa]; Zener anisotropy factor (A) and Poisson's ratio (v) , G/B ratio and Young modulus

Structure	C_{11}	C_{12}	C_{44}	A	v	B/G	E
NaCl(B1)	89.1	14.96	18.55	0.5	0.243	1.615	61.1
Theory[17]	95.17	25.56	27.11				
CsCl (B2)	114.52	4.92	-1.67				
30GPa	216.65	67.15	31.78	0.42	0.329	2.59	119.9
Theory[17]	93.48	14.92	20.98				

The traditional conditions for the mechanical stability of cubic crystals are: C_{11}-C_{12}>0, C_{11}>0, C_{44}>0, C_{11}+2C_{12}>0, C_{12}<B<C_{11}. Our calculated elastic constants satisfy these stability conditions for both phases of CaTe. Therefore, B1 and B2 structures of CaTe are mechanically stable to support the stability conditions.

Conclusions

In our study, as a summary, we have used the first principles calculations have been performed to investigate the structural, electronic and elastic properties of CaTe compound in B1 and B2 crystal structures. The obtained lattice parameters of B1 and B2 structures are in good agreement with experimental data. Our results for the elastic constants satisfy the traditional mechanical stability conditions for both phases of CaTe compound. The transition pressures are calculated to be 28.5 GPa for CaTe and this value is good agreement with other theoretical study. CaTe in B1 structure exhibits a semiconductor but in B2 structure exhibits metalic behavior.

References

[1]A.L. Ruoff, T.A. Grzybowski, Solid State Physics Under Pressure, Terra Scientific, 1985, pp 46.
[2] H. Luo, R.G. Greene, K.G. Handehari, T. Li, A.L. Ruoff, Phys. Rev., B 50 (1994) 16232.
[3] H.G. Zimmer, H. Winzen, K. Sayassen, Phys. Rev., B 32 (1985) 4066.
[4] R. Khenata, M. Sahnoun, H. Baltache, M. Rerat, D. Rached, M. Driz, B. Bouhafs, Physica B, 371 (2006) 12.
[5] G. Kresse, J. Hafner, Phys. Rev., B 47 (1993) 558.
[6] G. Kresse, J. Hafner, J. Phys.: Condens. Matter, 6 (1994) 8245.
[7] G. Kresse, J. Hafner, Phys. Rev., B 49 (1994) 14251.
[8] G. Kresse, J. Furthmüller, Comput. Mater. Sci., 6 (1996) 15.
[9] G. Kresse, J. Furthmüller, Phys. Rev., B 54 (1996) 169.
[10] D. Vanderbilt, Phys. Rev., B 41 (1990) 7892
[11] P.E. Blöchl, Phys. Rev., B 50 (1994) 17
[12] H.J. Monkhorst, J. D. Pack, Phys. Rev., B 13 (1976) 518
[13] J.P. Perdew, Y. Wang, Phys. Rev., B 45 (1992) 1324
[14] J.P. Perdew, J.A. Chevary, S.H. Vosko, K.A. Jackson, M.R. Pedersen, D.J. Singh, C. Fiolhais, Phys. Rev., B 46 (1992) 6671.
[15] P.E. Blöchl, Phys. Rev., B 50 (1994) 17953
[16] Z Charifi, H Baaziz, F El Haj Hassan and N Bouarissa, J. Phys.: Condens. Matter, 17 (2005) 4083–4092.
[17] S. Boucenna , Y. Medkour , L. Louail, M. Boucenna , A. Hachemi , A. Roumili, Computational Materials Science, 68 (2013) 325–334
[18]G.V. Sin'ko, N.A. Smirnov, J. Phys. Condens. Matter, 14 (2002) 6989.

6th International Conference on Materials Science and Nanotechnology For Next Generation (MSNG2019)
October 16-18, 2019, Niğde, TURKEY (ORAL FULL TEXT)

The effect of Rh, Ir doping on the structural and elastic properties of CoAl: An ab-initio study.

İ. Kars Durukan[1*], and Y. Öztekin Çiftci[1]

Department of Physics, Faculty of Science, Gazi University, Ankara 06500, Turkey

The main research purpose of this study is to report on the effect of A(Rh,Ir) doping on CoxA1-x Al in different concentrations (x=0, 0.25, 0.5, 0.75, 1). We have performed first-principles calculations based on density functional theory via the CASTEP packed program. The ground state properties such as lattice constant, bulk modulus and pressure derivative of bulk modulus and formation energy have been calculated which are in good agreement with available experimental and other theoretical data. Mechanical properties have been calculated and compared other experimental and other theoretical data.

Keywords: CoAl, Ab initio, doping effect

Submission date:
Acceptance Date:

Corresponding authors: ilknurdurukan@gazi.edu.tr

1. Introduction

Intermetallic compounds include a class of metallic materials that are studied extensively by material scientists and engineers today. These compounds are already indispensable in many applications and offer additional breakthroughs in their performance[1,2]. These compounds, such as nickel, titanium, cobalt and niobium aluminates, are known as promising compounds in the tecnology because they are highly suitable materials for high temperature structural applications [3-6].

A relatively small proportion of the many intermetallic compounds studied so far have been regarded as suitable candidates for high temperature applications. CoAl intermetallic compound crystallizing in B2 structure is an excellent material for many high temperature applications due to its melting temperature density, moderate oxidation resistance and thermal conductivity[7].

In this work, we have reported theoretical studies to explore the structural and mechanical properties of CoxA1-xAl, CoxA1-xAl compounds at some specified dopant concentrations x= 0.0, 0.25, 0.5, 0.75 and 1.0 using DFT.

2. Method of Calculation

The density functional theory (DFT) [8, 9] has successfully been carried out using the first principles calculations for ground state properties. We have applied to the GGA (Generalized Gradient Approximation) [10] for the exchange-correlation functional. All properties of calculations are investigated by using the CASTEP packed program [11-14]. The plane-wave basis sets with energy cut-off 650 eV and the 16x16x16 Monkhorst and Pack [15] k-points are used in the Brillouin zone for $Co_xA_{1-x}Al$ (A=Rh,Ir). Elastic properties are estimated using the stress-strain method [16,17].

3. Results and discussion:

The crystal structure of $Co_xA_{1-x}Al$ (A=Rh,Ir) compounds is cubic, with the space group Pm-3m, the Pearson symbol is cP2, the prototype is CsCl. The structure is shown in Fig. 1, the A atom in the center represents Rh and Ir atoms.

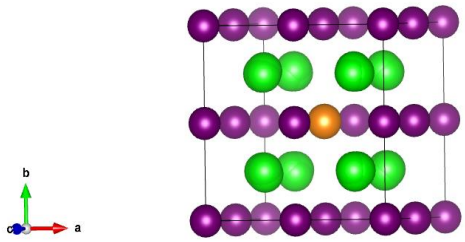


Fig.1: Crystal structure of Co_xA_{1-x} Al (A=Rh,Ir) compounds showing the three occupied sub-lattices. Purple circles: Co atoms, Green circles Al atoms, orange circles Rh or Ir atoms.

It is seen from Table I, calculated lattice constant a_0, Bulk module B and derivative of bulk module B', and formation energy of $Co_xA_{1-x}Al$ compound are in good agreement with the other theoretical and experimental study.

Table 1: Lattice constant, Bulk module, first derivative bulk module and formation energy of Co_xA_{1-x} Al compound.

$Co_xA_{1-x}Al$	Approximation	a_0(Å)	B(GPa)	B'	ΔH_f(ev/f.u.)
RhAl	GGA	3.004	194.9	4.57	-94.640
$Co_{0.25}Rh_{0.75}Al$	GGA	2.980	190.1	4.54	-92.352
$Co_{0.50}Rh_{0.5}Al$	GGA	2.939	186.3	4.48	-90.279
$Co_{0.75}Rh_{0.25}Al$	GGA	2.902	182.1	4.40	-88.173
IrAl	GGA GGA[18] VASP[19] Exp. [20] Exp. [21] Exp. [22] Exp. [23]	3.018 3.012 3.020 2.980 2.9867 2.983 2.986	229.2 229.3[18]	4.67	-103.345
$Co_{0.25}Ir_{0.75}Al$	GGA	2.989	216.6	4.57	-99.098
$Co_{0.50}Ir_{0.5}Al$	GGA	2.948	205.1	4.49	-94.852
$Co_{0.75}Ir_{0.25}Al$	GGA	2.917	191.0	4.38	-90.495
CoAl	GGA LDA[24] LSDA[24] GGA[24] Exp.[25] [26,27]	2.853 2.78 2.79 2.85 2.86 2.80	178.3 199[24] 198.8[24] 181.7[24] 207[26,27]	4.30 4.13[24] 3.31[24] 4.48[24]	-86.363

Figs. 2, and 3 illustrate the Lattice parameters and bulk modulus as a function of composition x. From Fig. 2 and, Fig.3 we can say that the lattice constants and bulk modulus decrease almost linearly with composition.

Elastic constants provide information about the dynamic and mechanical properties of solids as well as the properties of forces in solids [28,29]. It also provides information about the hardness and stability of the material. Therefore, to study the stability of these compounds in Pm-3m structure, we have calculated the elastic constants at equilibrium lattice parameter.

The elastic properties of a cubic crystal are defined exactly by three independent elastic constants, C_{11}, C_{12} and C_{44}. The mechanical stability of the cubic crystals must be in accordance with the Born stability criteria, which are very good for their elastic constants[30]. The calculated elastic constants are compatible with other theoretical and experimental constants.

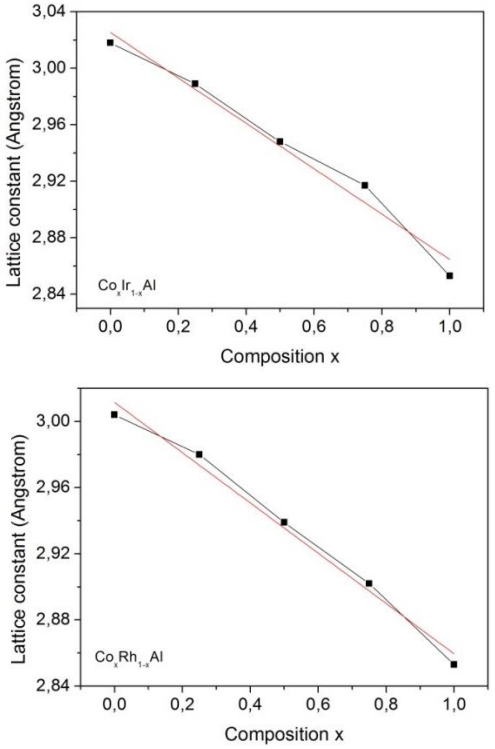
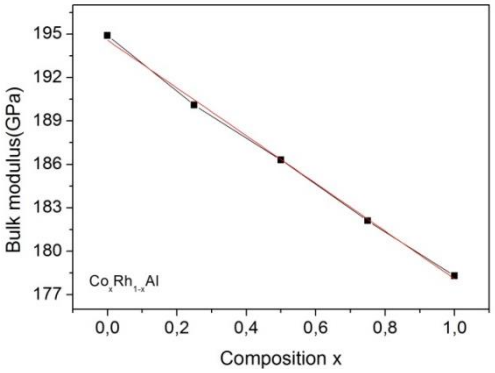


Fig.2: Lattice Constants of Co_x A_{1-x} Al compound



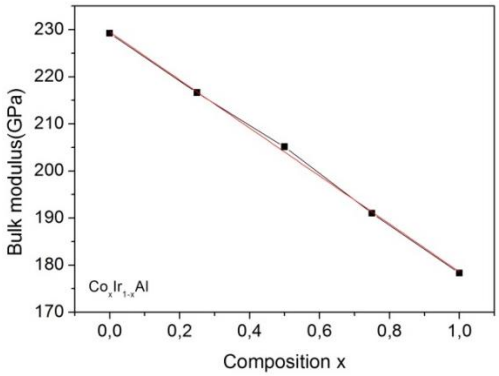


Fig.3: Bulk modulus of $Co_xA_{1-x}Al$ compound

Table 2 Elastic constants Cij (GPa) of $Co_xA_{1-x}Al$ compound.

$Co_xA_{1-x}Al$	C_{11}	C_{12}	C_{44}
RhAl	307.7	142.5	107.7
$Co_{0.25}Rh_{0.75}Al$	300.0	139.6	112.9
$Co_{0.50}Rh_{0.5}Al$	298.5	139.9	119.3
$Co_{0.75}Rh_{0.25}Al$	293.0	130.4	129.2
IrAl	340.3 394.63[18]	179.3 196.28[18]	125.7 229.86[18]
$Co_{0.25}Ir_{0.75}Al$	344.5	155.1	127.8
$Co_{0.50}Ir_{0.5}Al$	337.3	147.1	128.9
$Co_{0.75}Ir_{0.25}Al$	307.1	138.4	133.8
CoAl	291.4 297.8[24] 251±4[25]	125.3 113.45[24] 101±3[25]	139.4 151.69[24] 134±1[25]

Conclusions

In this study, the first principles calculations have been performed to investigate the structural, and elastic properties of $Co_xA_{1-x}Al$ (A=Rh,Ir) compound. The obtained lattice parameter and Bulk module and pressure derivative of bulk modulus of $Co_xA_{1-x}Al$ (A=Rh,Ir) compound is in good agreement with experimental and other data. According to elastic measurements, $Co_xA_{1-x}Al$ (A=Rh,Ir) alloy is mechanically stable.

References:

[1] J.H. Westbrook, (1967), Intermetallic compounds. Huntington, NY: R.E. Krieger Pub. Co, 1967,pp. 19.
[2] R.L Fleischer, A.I. Taub, Science 243 (1989) 616-621.
[3] K. Morsi, Review: reaction synthesis processing of Ni – Alintermetallic materials,Mater. Sci. Eng. A299 (2001)1–15.
[4] M.N. Mungole, R. Balasubramaniam, A. Ghosh, Intermetallics, 8 (2000) 717–720.
[5] B.M. Warnes, N.S. DuShane, J.E. Cockerill, Surf. Coat. Technol. 148 (2001) 163–170.
[6] V. Gauthier, F. Bernard, E. Gaffet, D. Vrel, M. Gailhanou, J.P. Larpin, Intermetallics. 10 (2002) 377–389.
[7] Y. Takano: J. Am. Ceram. Soc., 2001, 84, 2445.
[8] P. Hohenberg, W. Khon, Phys. Rev., 136 (1964) B864.
[9] W. Khon, L. J. Sham, Phys. Rev., 140 (1965) A1133.
[10] J P Perdew, J A Chevary, S Vosko, K A Jackson, M R Pederson, D J Singh, and C Fiolhais, Phys. Rev. B, 46 (1992) 6671.
[11] G Kresse and J Hafner, Phys. Rev. B, 47 (1993) 558.
[12] G Kresse and J Hafner, Phys. Rev. B, 49 (1994) 14251.
[13] G Kresse and J Furthmüller, Comput. Mat. Sci., 6 (1996) 15.
[14] G Kresse and J Furthmüller, Phys.Rev. B, 54 (1996) 11169.
[15] H J Monkhorst and J D Pack, Phys.Rev. B, 13 (1976) 5188.
[16] L Page and P Saxe ,Phys. Rev. B, 65 (2002) 104104.
[17] M J Mehl, J E Osburn, D A Papaconstantopoulos, and B M Klein, Phys. Rev. B, 41 (1990) 10311.
[18] N. Arıkan , Z. Charifi , H. Baaziz , Ş. Uğur , H. Ünver , G. Uğur , Journal of Physics and Chemistry of Solids, 77 (2015) 126–132.
[19] C. Jiang, B. Gleeson, Acta Mater., 54 (2006) 4101.
[20] P. Esslinger, K. Schubert, Z. Metallk., 48 (1957) 126.
[21] K.M. Axler, R.B. Roof, Adv. X-Ray Anal., 29 (1986) 333
[22] H. Schulz, K. Ritapal, W. Bronger, W. Klemm, Z. Anorg. Allgem. Chem., 357 (1968) 299.
[23] A. Chiba, T. Ono, X.G. Li, S. Takahashi, Intermetallics, 6 (1998) 35.
[24] B. Fatima, S. Singh Chouhan, N. Acharya , Sankar P. Sanyal, Advances in Physics Theories and Applications,19 (2013) 24-32.
[25] G.L. Zhao, B.N. Harmon Phys. Rev.B 45 (1992) 2818-2824.
[26] S.C. Lui, E.W. Davenport, Plummer, D.M. Zehner, G.W Fernando, Phys. Rev. B, 42 (1990) 1582-1597.
[27] M.J. Mehl, J.E. Osburn, D.A. Papaconstantopoulos, B.M. Klein,Phys. Rev. B 41, (1990) 10311-10323.
[28] T. Djaafri, A. Djaafri, F. Saadaoui, J. Supercond. Nov. Magn., 31 (2018) 2449–2458.
[29] Y. O. Ciftci, M. Evecen, Phase Transit. 91 (2018) 1206–1222.
[30] M. Born, K. Huang, Elasticity and stability, Dynamical Theory of Crystal Lattices, Clarendon, Oxford, 1954. pp142,

6th International Conference on Materials Science and Nanotechnology For Next Generation (MSNG2019)
October 16-18, 2019, Niğde, TURKEY (ORAL FULL TEXT)

A first-principles study of B2 TcSi alloyed with Mn,Re

İ. Kars Durukan[1*], and Y. Öztekin Çiftci[1]

Department of Physics, Faculty of Science, Gazi University, Ankara 06500, Turkey

The structural, elastic and electronic properties of TcSi alloyed with Mn,Re are investigated by using density functional theory (DFT). The study suggests that Mn and Re all tend to be substituted for an Tc site. $BxTc_{8-x}Si_8$ using (2x2x2) supercell in B2 structure are investigated by means of first-principles using CASTEP program. The results on the basic physical parameters, such as the bulk modulus, lattice constant, and elastic constant are presented. The obtained results are in agreement with the available and experimental and other theoretical values. The effect of the ratio of Mn and Re on TcSi is studied for the electronic band structure and density of states.

Keywords: TcSi, Ab initio, doping effect

Submission date:
Acceptance Date:

Corresponding authors: ilknurdurukan@gazi.edu.tr

1. Introduction

Intermetallic compounds are known to have attractive physical, chemical, mechanical electrical, and magnetic properties, which are generally superior to ordinary alloys [1]. Intermetallic compounds with structural properties B2 have been noted for several decades due to the high strength and high strength and high oxidation resistance required for engineering applications [2-5].

The mechanical and physical properties of B2 structure of intermetallic compounds, such as the transition-metal aluminides, have attracted much attention due to their low density, good corrosion, high melting temperature, high strength, and resistance for elevated temperature engineering applications [6,7] stiffness, strength, and oxidation resistance for high-temperature engineering applications [8–10].

In this study, The structural, elastic and electronic properties of TcSi compound alloyed with Mn, Re are investigated by using density functional theory (DFT).

2. Method of Calculation

All data presented in this study were performed using CASTEP program[11,12]. They are based on the density functional theory (DFT) using the projector-augmented-wave (PAW) method. The exchange correlation potential was considered within the generalized gradient approximation (GGA)[13,14]. Firstly, the optimization of lattice parameter and internal structure were determined. Then, band structure calculations were made using the calculations in the optimization. The valence-electron configurations for the Tc and Si were generated as $4f^1\ 4d^5\ 5s^2$, $3s^2\ 3p^2$, respectively. For optimization of the lattice parameters and atomic positions 14x14x14 Monkhorst and Pack [15] grid of k-points were used for integration in the irreducible Brillouin zone. The kinetic energy cut off is taken to be 700 eV for the plane-wave basis set.

3. Results and discussion:

In this study, $B_xTc_{8-x}Si_8$ (B= Mn, Re) was investigated in B2 (CsCl) phase. $Mn(Re)_1Tc_7Si_8$ crystal structure of the $BxTc_{8-x}Si_8$ in the structure is shown in Figure 1a. To determine the equilibrium geometry, we relaxed (ISIF=3 in VASP) the volume of unit cell and the

all atomic positions. With the relaxed equilibrium lattice constant, the Murnaghan equation of state[16] was fitted to the E (V) curves in order to determine the Bulk modulus (B).

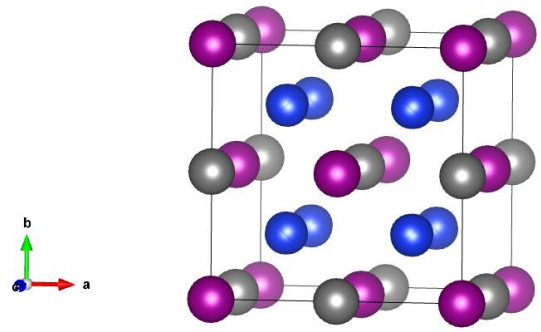


Fig.1: Crystal structure of Mn(Re)1Tc7Si8 compounds showing the three occupied sub-lattices. purple circles: Mn or Re atoms, Grey circles Tccatoms, Blue circles Si atoms..

It is seen from Table I, calculated lattice constant a_0, Bulk module B and derivative of bulk module B', and formation energy of B_xTc_8-xSi8 compound.

Table 1: Lattice constant, Bulk module and first derivative bulk module of B_xTc8-xSi8 (B= Mn,Re) compound.

Model	a_0(Å)	B(GPa)	B'
$Mn_1Tc_7Si_8$	5.907	242.822	4.653
$Mn_2Tc_6Si_8$	5.876	240.577	4.750
$Mn_3Tc_5Si_8$	5.826	238.690	4.689
$Mn_4Tc_4Si_8$	5.778	237.356	4.515
$Mn_5Tc_3Si_8$	5.736	233.106	4.443
$Mn_6Tc_2Si_8$	5.707	229.817	4.483
$Mn_7Tc_1Si_8$	5.645	227.165	4.595
Mn_8Si_8	5.593	226.079	4.669
$Re_1Tc_7Si_8$	5.949	250.355	4.608
$Re_2Tc_6Si_8$	5.953	254.102	4.586
$Re_3Tc_5Si_8$	5.958	257.590	4.546
$Re_4Tc_4Si_8$	5.964	261.175	4.512
$Re_5Tc_3Si_8$	5.969	264.742	4.511
$Re_6Tc_2Si_8$	5.972	268.388	4.486
$Re_7Tc_1Si_8$	5.978	272.203	4.489
Re_8Si_8	5.982	276.140	4.479
Tc_8Si_8	5.943	246.780	4.610

Elastic properties are very important properties for materials, which can be determined elasticity, mechanical stability, and stiffness of crystals that is essential to understand the chemical bonding and the cohesion of material [17]. In this study, the second-order elastic constants (Cij) are calculated using the "stress-strain" relations [18]. Calculated elastic constants are listed in Table II.

Table 2 Elastic constants Cij (GPa) of BxTc8-xSi8 (B= Mn,Re) compound.

Model	C_{11}	C_{12}	C_{44}
$Mn_1Tc_7Si_8$	398.1	169.3	87.0
Mn_2Tc6Si^8	383.8	168.9	88.4
Mn_3Tc5Si_8	375.1	170.3	88.7
$Mn_4Tc_4Si_8$	368.7	167.8	94.2
$Mn_5Tc_3Si_8$	354.5	164.3	91.3
$Mn_6Tc_2Si_8$	343.7	168.6	94.9
$Mn_7Tc_1Si_8$	345.5	170.6	101.6
Mn_8Si_8	348.4	173.1	113.4
$Re_1Tc_7Si_8$	414.5	172.1	88.9
$Re_2Tc_6Si_8$	418.5	175.9	90.5
$Re_3Tc_5Si_8$	422.7	179.9	91.4
$Re_4Tc_4Si_8$	426.2	184.1	92.6
$Re_5Tc_3Si_8$	431.1	186.7	94.0
$Re_6Tc_2Si_8$	435.9	189.6	95.9
$Re_7Tc_1Si_8$	441.4	192.5	97.9
Re_8Si_8	447.7	195.8	100.8
Tc_8Si_8	410.4	169.2	87.7

The traditional conditions for mechanical stability of cubic crystals are: C_{11}-C_{12}>0, C_{11}>0, C_{44}>0, C_{11}+2C12>0, C_{12}<B<C_{11}. Our calculated elastic constants satisfy these stability conditions for $B_xTc_{8-x}Si_8$ (B= Mn, Re). Therefore, B_xTc_8-xSi8 (B= Mn,Re) are mechanically stable to support the stability conditions.

In order to make sense of the electronic behavior of $B_xTc_{8-x}Si_8$ (B= Mn,Re), we have computed the electronic band structure. Electronic band structure of $Mn_2Tc_6Si_8$, $Mn_4Tc_4Si_8$ and $Mn_6Tc_2Si_8$ are shown in Figure 2. Fermi level is set 0 eV. Our calculation shows that these compouns are of metallic character due to there are no band gap near the Fermi level. E(Nf) values of $Mn_2Tc_6Si_8$ and $Mn_6Tc_2Si_8$ are -12.49 eV, -13,63 eV, respectively.

The total and partial density of states are also plotted in Figure 3. Clearly, the valence bands are located in three regions. The first region of valance band consists of Si - s states. The second region of the valence band is composed of Si– p and Tc-d states. The third region originates from the hybridization of Si p-states and Mn and Tc–d states. The fourth region of conduction band, above the Fermi energy level, the major contribution comes from Mn and Tc –d states. With the increase of the contribution of Mn, it is seen that the contribution of Mn in the total state density increases and the contribution of Tc decreases.

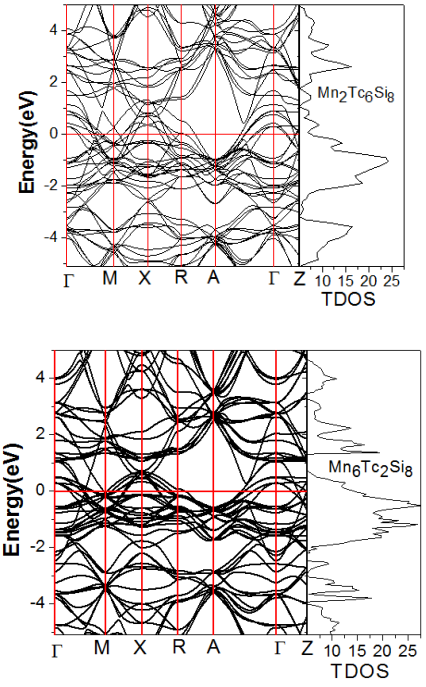


Fig.2: Electronic band structure for $Mn_2Tc_6Si_8$ and $Mn_6Tc_2Si_8$

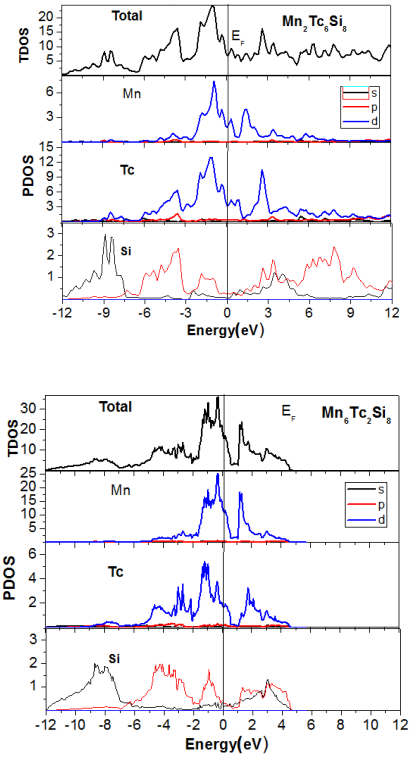


Fig.3: Calculated partial density of states for $Mn_2Tc_6Si_8$,$M_6Tc_2Si_8$

Conclusions

In this study, the first principles calculations have been performed to investigate the structural, electronic, elastic properties of $B_xTc_{8-x}Si_8$ (B= Mn,Re) compoud. According to elastic measurements, $B_xTc_{8-x}Si_8$ (B= Mn,Re) compoud. is mechanically stable. The computed band structures and density of states show that the studied $B_xTc_{8-x}Si_8$ (B= Mn,Re) is metallic in nature.

References:

[1]N.I. Medvsdeva, O.N. Mryasav,Y.N. Gornostryrev, Phys. Rev. B, 54 (1996) 13506.
[2] G. Schoeck, Acta Materialia, 49 (2001) 1179
[3] A.M. Russel, Advanced Eng. Mat. 5 (2003) 9.
[4] K.A. Gschneidner, A.M. Russel, A. Pechasky, Nature Materials, 2 (2003) 9.
[5] Z. Zhang, A.M. Russel, S.B. Biner, K.A. Gshneider, Intermetallic, 13(2005) 559.

[6] P. Lazar, R. Podloucky, Phys. Rev. B, 73 (2006) 104114.
[7] P. Gumbsch, R. Schroll, Intermetallics, 7 (1999) 447.
[8] N.S. Stoloff, C.T. Liu, S.C. Deevi, Intermetallics, 8 (2000) 1313.
[9] C.T. Liu, E.P. George, P.J. Maziasz, J.H. Schneibe, Mater. Sci. Eng. A, 258 (1998) 84.
[10] D.B. Miracle, R. Darolia, in: J.A. Westbrook, R.L. Fleischer (Eds.), (1994), Intermetallic Compounds. Practice, 2, Wiley, p. 53.
[11] M.D. Segall, P.J.D. Lindan, M.J. Probert, C.J. Pickard, P.J. Hasnip, S.J. Clark, M.C. Payne, J. Phys. Condens. Mater, 14 (2002) 2717.
[12] W. Zhu, H. Xiao, J. Comput. Chem., 29 (2008) 176.
[13] S.J. Clark, M.D. Segall, C.J. Pickard, P.J. Hasnip, M.I. Probert, K. Refson, M.C. Payne Z. Cristallogr. Mater., 220 (5/6) (2005) 567-570.
[14] J. P. Perdew and Y. Wang. Phys. Rev. B, 45 (1992) 13244.
[15] H. J. Monkhorst and J. D. Pack. Phys. Rev. B, 13(1976) 5188.
[16] F. D. Murnaghan, Proc. Natl. Acad. Sci. U. S. A., 30 (1944) 244–247.
[17]T. Djaafri, A. Djaafri, F. Saadaoui, Journal of Superconductivity and Novel Magnetism, 31 (2018) 2449–2458.
[18]G.V. Sin'ko, N.A. Smirnov, J. Phys. Condens. Matter, 14 (2002) 6989.

6th International Conference on Materials Science and Nanotechnology For Next Generation (MSNG2019)
October 16-18, 2019, Niğde, TURKEY (ORAL FULL TEXT)

Synthesis of The Ni-Al Intermetallic In The Al Matrix

Öyküm BAŞGÖZ[1], Ömer GÜLER[1], Ertan EVİN[2], Seval Hale GÜLER[1]

[1] Mersin University, Faculty of Engineering, Department of Metallurgical and Materials Engineering, Mersin, TURKEY
[2] Fırat University, Faculty of Engineering, Department of Metallurgical and Materials Engineering, Elazığ, TURKEY

The Ni–Al binary phase diagram contains Al_3Ni, Al_3Ni_2, Al_3Ni_5, NiAl, Ni_3Al five intermetallic compounds. Of these intermetallics, NiAl and Ni_3Al have the vast majority of scientific attention as they are considered candidate materials for high temperature structural because of high melting point (1638 °C for Ni_3Al peritectic, 1385 °C for NiAl alloy) and coating applications. Also in the Ni–Al binary system these two phases, relatively low densities, good strength and high temperature corrosion and oxidation resistance. For the fabrication, it seems that for particulate reinforcement of intermetallics, in-situ precipitation methods offer the best prospect for exploitation in the short term. In this study, 82.4 % Nickel powders and 17.6 % Aluminum powders were mixed homogeneously. Subsequently, mixed powder was added to Aluminium (Al) powders for 5 wt%, 10 wt% and 20 wt % ratios and were re-mixed. The samples which were prepared for 3 different ratios were compacted. The compacted samples were sintered at 1300 °C for 20 minutes. So, Ni-Al intermetallic reinforced Al-based composites were fabricated successfully. Ni-Al intermetalics were formed as in-situ during sintering of composite. The microstructures of obtained composites were examined via optical microscope. The mechanical behavior of the composite, including the hardness test. It was shown that increasing Ni-Al intermetallic amount improve the mechanical properties of composites.

Keywords: Intermetallic, Composite, Al matrix,, In-situ.

Corresponding author: oykumbasgoz@mersin.edu.tr

1. Introduction

Intermetallics are a unique group of materials composed of two (or more) types of metal (or metal and non-metal) atoms, which exist as solid compounds and differ in a structure from that of the constituent components. Since a great number of intermetallic phases have been recognized and examined, the most advanced works in the field of metallurgy and performance properties have been carried out for intermetallic phases from the Ni–Al, Fe–Al and Ti–Al binary systems. The main research efforts have been focused on NiAl, Ni_3Al, FeAl, Fe_3Al, TiAl, Ti_3Al and $TiAl_3$ based alloys [1]. Of these intermetallics, NiAl and Ni_3Al have by far received the vast majority of scientific attention as they are considered candidate materials for high temperature structural and coating applications. This is not surprising considering that these compounds have the highest melting points in the Ni–Al binary system, relatively low densities, good strength and high temperature corrosion and oxidation resistance [2]. The most attractive properties of the Ni_3 Al intermetallics include: a high tensile and compression strength at temperature of 650-1100 °C an increase of flow stress with increasing temperature—an anomalous positive temperature dependence of the yield strength (at 600–900 °C) is a characteristic feature of the Ni3Al phase and its alloys; a high corrosion resistance in oxygen and carbon enriched atmospheres up to 1100 °C, due to a formation of a continuous surface alumina layer [3-5]. In this work Al matrix has been reinforced with Ni_3Al intermetallic. The microstructures of obtained composites were examined via optical microscope. The hardness test was applied to samples. It was shown that increasing Ni-Al intermetallic amount improve the mechanical properties of composites.

2. Experimental details

In the experiments, 5%, 10% and 20% of Ni-Al powder mixture was added to Al matrix. For this purpose, 86.4% Ni (Merck) powder and 17.6% Al (Roth) powder were first mixed in a mechanical stirrer for 30 minutes. Subsequently, this powder mixture was added to the Al matrix separately in 5%, 10%, 20% by weight and the new powder mixture was mixed in the mechanical mixer for a further 15 minutes. The resulting powders were then made into pellets having a diameter of 12 mm and a height of 6 mm under a stretch of 500 MPa. The resulting pellets were heat-treated at 700 °C. Then the internal structure of the obtained samples were examined under optical microscope and the microhardness of the samples were taken and the mechanical properties of the composites were determined.

3. Results and discussion

The Ni-Al mixture was pelleted without addition to the Al matrix and heat-treated at 700 °C. The microstructure view of the obtained structure is given in Fig. 1a.

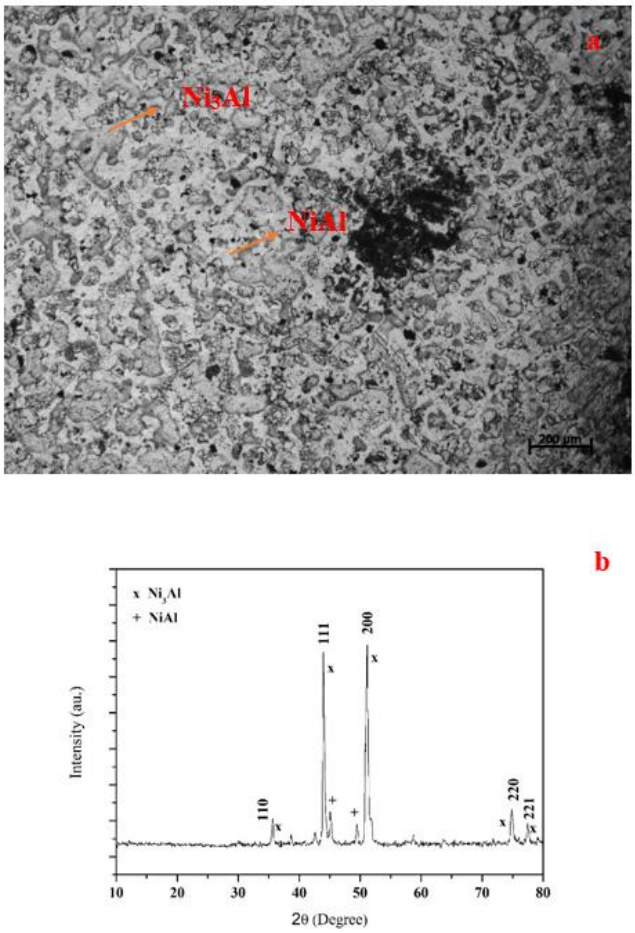
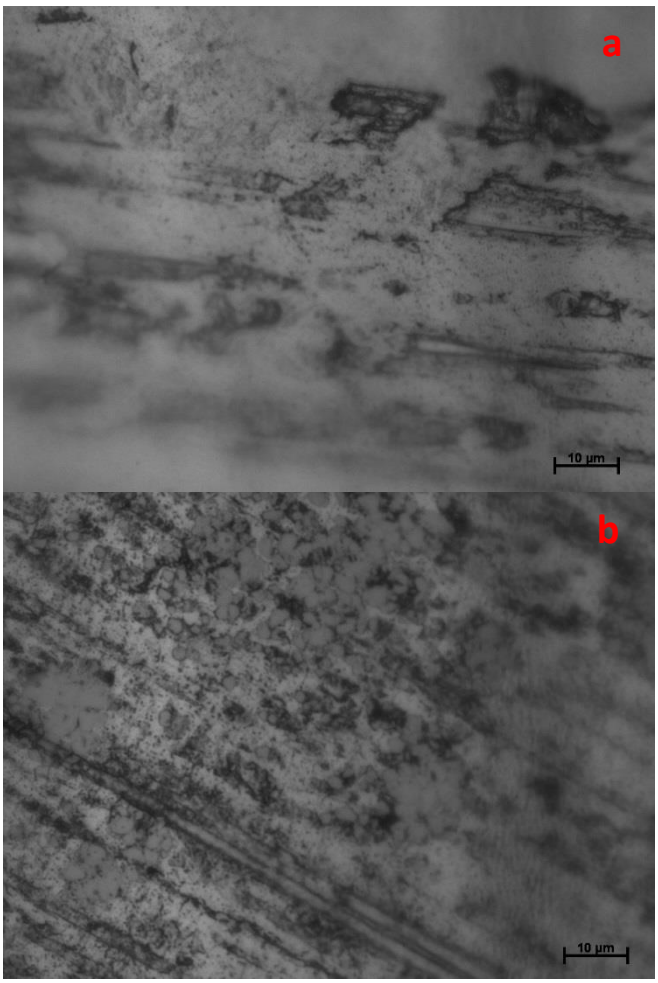


Figure 1. a) *Optical microstructure* ***b)*** *XRD spectra of Ni_3Al intermetallic synthesized from Ni-Al powder mixture.*

As can be seen from the XRD spectra, two different phases were found in the structure. The most dominant phase of the microstructure is Ni_3Al. The other phase is the NiAl intermetallic found in white clumps. . In addition, it can be said that NiAl intermetallic are formed. XRD analysis shows that Ni-Al intermetallic synthesis is synthesized when the Ni-Al powder mixture is heat treated at 700 °C.

The microstructure images of the composites produced in Figure 2 are given. The black part is a void. Images are appearing blurred due to surface curvature.



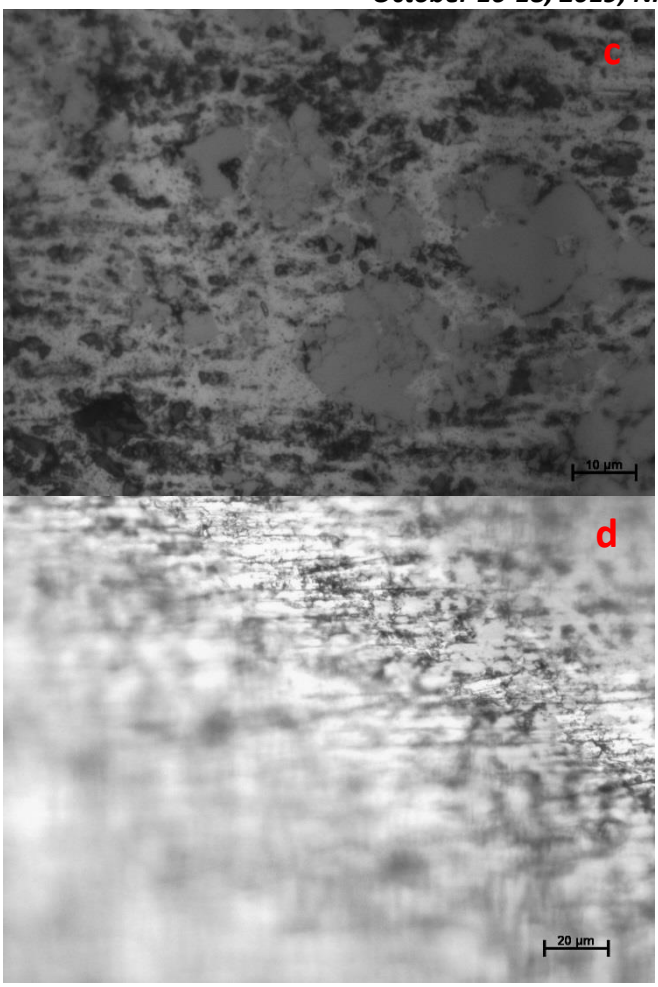


Figure 2. *Microstructures of* ***a)*** *Pure,* ***b)*** *5 wt. % composite,* ***c)*** *10 wt. % composite,* ***d)*** *20 wt.% composite.*

Five tests were performed for each sample surface. Measurements of Vickers hardness were performed to determine the microhardness values of the composites. Vickers hardness value was calculated by averaging the values obtained from each test (Fig. 3). The Vickers hardness tests were performed at a holding time 10s.

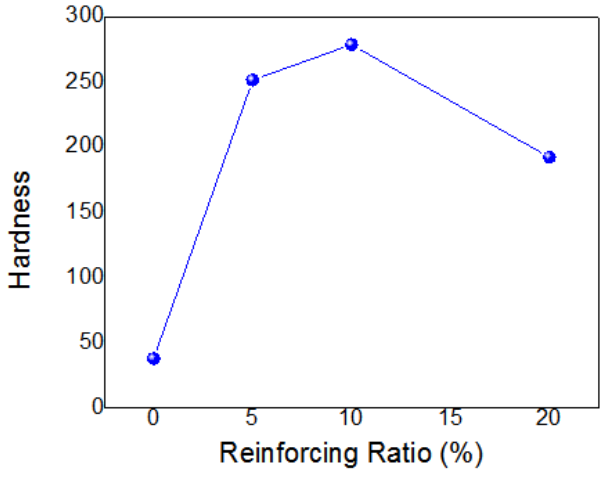


Figure 3. *Microhardness changing for different reinforcing ratio.*

The effect of the 5 % reinforcement rate on the hardness increase of the Al matrix was relatively limited. However, when the reinforcement ratio increased to 10%, the hardness increased to 251.4 HV. When the reinforcement ratio is increased to 20 % the hardness decrease 192 HV. The reason of this situation is test method. Because the area that is load on the phase which is cause of the low hardness values. 20 % reinforced Ni_3Al intermetallic composite has surface curvature and so the hardness value less than the other ratios.

4. Conclusion

Ni_3Al-Al in-situ composites were successfully synthesized. As a result of the study, it was analyzed that the synthesis of in-situ reactions to be successfully depends on sintering temperature and that NiAl phase is formed at this temperature besides Ni_3Al.

References:

[1] JOZWIK, P., POLKOWSKI, W., & BOJAR, Z. (2015). Applications of Ni3Al based intermetallic alloys—current stage and potential perceptivities. *Materials*, *8*(5), 2537-2568.

[2] MORSI, K. (2001). reaction synthesis processing of Ni–Al intermetallic materials. *Materials Science and Engineering: A*, *299*(1-2), 1-15.

[3] DEEVI, S. C., SIKKA, V. K., & LIU, C. T. (1997). Processing, properties, and applications of nickel and iron aluminides. *Progress in Materials Science*, *42*(1-4), 177-192.

[4] DEEVI, S. C., & SIKKA, V. K. (1996). Nickel and iron aluminides: an overview on properties, processing, and applications. *Intermetallics*, *4*(5), 357-375.

[5] JOZWIK, P., POLKOWSKI, W., & BOJAR, Z. (2015). Applications of Ni3Al based intermetallic alloys—current stage and potential perceptivities. *Materials*, *8*(5), 2537-2568.

6th International Conference on Materials Science and Nanotechnology For Next Generation (MSNG2019)
October 16-18, 2019, Niğde, TURKEY (ORAL FULL TEXT)

Investigation on the effect of Erbium Stabilized Bismuth (ESB) on operating temperature for Solid Oxide Fuel Cell (SOFC)

Mikail Yağız *, Selahattin Çelik *

* Niğde Ömer Halisdemir University, Faculty of Engineering, Mechanical engineering, Pr. Dr. T. Nejat Veziroğlu Clean Energy Application and Research Center, Niğde, TURKEY

Solid oxide fuel cells (SOFC) can operate high to temperatures, it is systems that work electrochemically and generate electricity. It is aimed to reduce the system cost by decreasing the SOFC operating temperature and to have a longer life. As a result of recent academic research, SOFC's are capable of operating moderate temperatures while producing the output of high temperature systems, moreover research on low temperatures (<600 °C). But for low temperature system, very costly and very good technological tools should be used. it is one of the most important problems that reduce low temperature performance. Although SOFC has a sufficiently high ionic conductivity, it does not operate at low temperatures. The use of erbium and bismuth oxide-based electrolytes shows high levels of oxygen ion transmission between electrolytes and the electrode, which removes an important barrier for the development of SOFC's. In addition to the high ionic conductivity of Erbium stabilized bismuth oxide (ESB), in the cathode layer achieved surface oxygen exchange rate, charge transfer, and oxygen decomposition. Furthermore Erbium stabilized bismuth oxide (ESB) synthesizing with traditional electrolyte materials GDC/YSZ/ScSZ of the coating with LSM in the cathode layer thus extends the innovative material field. Previous studies with ESB electrolytes made with these innovative materials, the highest a cell power produced was approximately 1.95 W/cm^2 at 650 ^{o}C. The high-performance increase is achieved by adding the appropriate amount of electrolytes to the cathode surface. in the light of all these studies; It is believed that higher power density levels can be achieved by depositing thin, dense and well-sintered ESB layers.

Keywords: Solid oxide fuel cells (SOFC), Erbium stabilized bismuth oxide (ESB), Lanthanum strontium manganite(LSM),low temperature (LT)

Corresponding author: yagizmikail.1071@gmail.com

1. Introduction

Solid oxide fuel cell is a simple working system consisting of anode, cathode and electrolyte layer are mechanisms that convert electricity and heat into high efficiency without combustion and mechanical movement. SOFCs are anode-supported, providing a wider choice of materials, higher material stability, better performance durability and lower production costs, and operate to around 800 ° C [1-2]. As a result of these studies, the commercial market in the energy conversion cycle of SOFCs was limited due to the high operating temperatures. Many studies have been conducted with conventional electrolyte materials GDC / YSZ / SDC / ScSZ. Although different types of electrolyte materials have been tested, average power densities reach a maximum temperature of 2 W/cm^2 at 800 °C[3]. Conventional yttria stabilized zirconia (YSZ) electrolyte is used to achieve long life, high stability and best performance at low operating temperatures. Yttrium oxide doped zirconium oxide (YSZ), zirconium based oxides, SOFC applications has become a popular due to its high ionic conductivity and stability and also which benefits from its high stability at a wide range of oxygen partial pressure. Other electrolyte materials, such as Gadolinium-doped Ceria (GDC) and Bismuth oxides

stabilized with lanthanide dopants have higher oxygen ion conductivity but worse stability at low oxygen partial atmosphere[4-5].

Erbium stabilized bismuth oxide (ESB) is synthesized for used in different materials both in the electrolyte and in the cathode layer. Bismuth oxide-based electrolytes have been recognized to be highly important for the application of solid oxide fuel cells because of the highest oxygen ion conductivity among all solid electrolytes. Erbium stabilized bismuth oxide electrolyte materials are mainly produced with mixture of standard compound (Bi_2O_3) and (Er_2O_3). in most applications, solid electrolytes will be used at an electrochemical potential of ESB which oxygen surface exchange coefficient have a better level with other electrolytes. Depending on the oxygen level, it increases the electrical conductivity in multi-layer ion transitions[6]. Studies have shown that double layer electrolyte, provide higher ion conductivity as depend on ratio ESB / GDC [7]. This is because the ESB layer will block electronic conduction through the GDC layer, and a sufficiently thick GDC layer will prevent decomposition of ESB [8-9]. in addition, ESB/GDC bilayer electrolytes, total specific resistance (ASR), can be reduced depending on thicknesses. Cathode layer in the same situation exhibits approximately 26% smaller cathode polarization of deposition of ESB on GDC [10]. it should be noted that as a result of the thin and dense accumulation of ESB structure, the increase in OCP results from this situation. [11-12]. Therefore, the production of thin and dense ESB/GDC layers is very important to increase OCP [13-14].

Compared with YSZ electrolyte material, GDC has better chemical compatibility with many perovskite cathode materials. In the commercial area, it is time-consuming and costly to prepare dense GDC thin layer on the surface of YSZ. Doped stabilized bismuth oxide (δ-Bi_2O_3) has been known as a promising electrolyte material with higher oxygen ions conductivity than both GDC and YSZ. The results of this study showed that intensive ESB is always used with YSZ and GDC electrolyte and cathode structure [15]. Joh et al. [16] replaced GDC with YSZ and used LSM -ESB as the cathode and obtained a peak power density at 700 °C higher than the GDC electrolyte state. Although the cathode structure of the LSM-ESB initially performed well, it was determined that these materials could work for a short time under LT-SOFC conditions. in the literature, innovative studies for SOFC in electrolyte and cathode layer are continuing. in this study, we investigated the resistance of LSM-ESB cells and the use of GDC and YSZ electrolytes in the LT-SOFC temperature range (450-650 ºC). The actual performance values of an ESB electrolyte layer and the I-V characterization values for the LSM-ESB cathode were examined.

2. Experimental details

Generally, commercial YSZ powder (TZ-8YS, Tosoh, Japan) is used in the studies and GDC powder is synthesized by appropriate reaction. For the LSM-ESB electrode ink, LSM powder and ESB powder synthesized by diffirent methods with the same or difference proportions can be mixed in as binder, plasticizer and solvent. With the mixture, both ESB and GDC electrolyte materials are sintered at different temperatures to produce cells [17].

3. Results and discussion

Figure 1 shows a comparison of Maximum Power Densities (MPDs) for SOFCs with various LSM-bismuth oxide cathodes at low to intermediate temperatures. For all temperatures, the LSM-ESB cathode connected achieves the highest performance for used with together to the ESB electrolyte. The effect of ESB electrolyte layer on LSM cathodes for low temperature SOFC was investigated. As a result of these comparisons, the effect of ESB electrolyte on LSM-ESB performance is valid and even greater at low temperature[19].

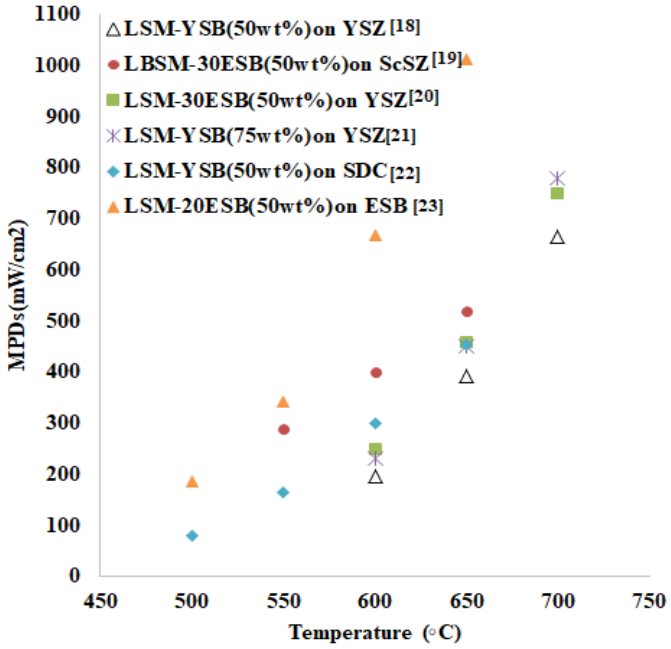


Figure 1. *Comparison of maximum power density of SOFCs using LSM-bismuth oxide based composite cathodes at IT ranges.*

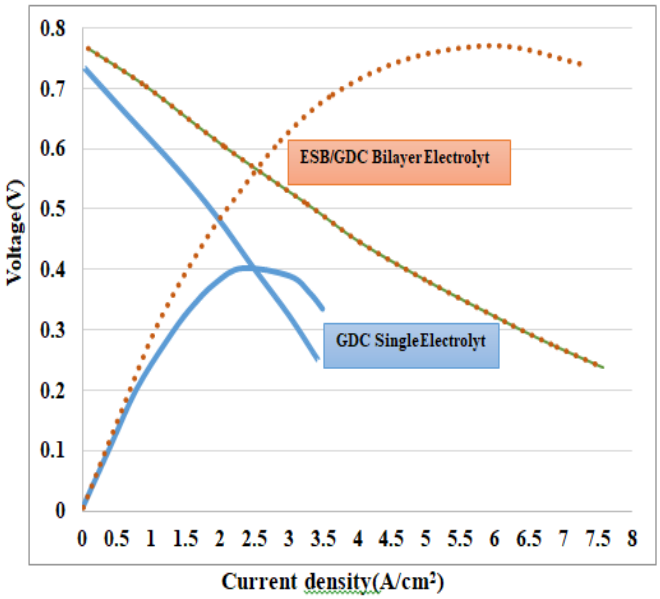


Figure 2. *I–V characteristics of the fuel cell samples with GDC single-layer and ESB/ GDC bilayer electrolyte at 650 °C[24].*

An increase in performance values was observed due to the fact the double layer of ESB electrolyte layer. Figure 2. shows for the bilayer cell, this increase in performance achieved on the single-layer GDC cell at 650 °C increased the maximum power density from 1.03 to 1.95Wcm^2 (93% increase)[24]. The most important factor leading to this dramatic improvement in power density, this is the ability of a bilayer electrolyte to increase open circuit potential (OCP). In this study, different cathode samples containing single and double layer electrolytes were examined, in SOFC applications, different studies will be tried by using two layer YSZ / GDC / ScSZ / ESB electrolytes, will lead to new research. It is also a very promising research topic at low operating temperatures.

4. Conclusion

The application of ESB is extremely important for both electrolyte and cathode layers. The presence of ESB in the LSM cathode is accelerate the cathode electrochemical reaction during the reduction of cathode polarization resistance. The use of LSM-ESB in the ESB / GDC / YSZ electrolyte in SOFC has the highest power levels of studies. The results of these studies show that ESB has become a popular research topic due to its electronic and ionic properties.

References:

[1] Brett DJL, Atkinson A, Brandon NP, Skinner SJ. Intermediate temperature solid oxide fuel cells. Chem Soc Rev 2008;37:1568-78.
[2] Wachsman ED, Marlowe CA, Lee KT. Role of solid oxide fuel cells in a balanced energy strategy. Energy Environ Sci 2012;5:5498-509.
[3] S. de Souza, S.J. Visco, L.C. De Jonghe, J. Electrochem. Soc. 144 (1997) L36.
[4] Fergus JW. Electrolytes for solid oxide fuel cells. J Power Sources 2006;162:30-40.
[5] Xiong Y, Yamaji K, Horita T, Sakai N, Yokokawa H. Hole and electron conductivities of 20 mol %-REO[sub 1.5] doped CeO [sub 2] (RE¼Yb, Y, Gd, Sm, Nd, La)lectrochem Soc 2004;151:A407.
[6] Park J-Y, Yoon H, Wachsman ED. Fabrication and characterization of high-conductivity bilayer electrolytes for intermediate-temperature solid oxide fuel cells. J Am Ceram Soc 2005;88:2402-8.
[7] J.Y. Park, E.D. Wachsman, J. Am. Ceram. Soc. 88(2005) 2402.

[8] K. Eguchi, T. Setoguchi, T. Inoue, H. Arai, Solid State Ionics 52 (1992) 165.
[9] E.D. Wachsman, G.R. Ball, N. Jiang, D.A. Stevenson, Solid State Ionics 52 - 213 (1992).
[10] J.S. Ahn, M.A. Camaratta, D. Pergolesi, K.T. Lee, H. Yoon, B.W. Lee, D.W. Jung, E. Traversa, E.D. Wachsman, J. Electrochem. Soc. (submitted for publication).
[11] E.D. Wachsman, P. Jayaweera, N. Jiang, D.M. Lowe, B.G. Pound, J. Electrochem. Soc. 144 (1997) 233.
[12] J.Y. Park, E.D. Wachsman, Ionics 12 (2006) 15.
[13] M.A. Camaratta, E.D. Wachsman, Solid State Ionics 178 (2007) 1411.
[14] M.A. Camaratta, E.D. Wachsman, J. Electrochem. Soc. 155 (2008) B135.
[15] Park J-Y, Yoon H, Wachsman ED. Fabrication and characterization of high-conductivity bilayer electrolytes for intermediate-temperature solid oxide fuel cells. J Am Ceram Soc 2005;88:2402-8.
[16] Joh DW, Park JH, Kim D, Wachsman ED, Lee KT. Functionally graded bismuth oxide/zirconia bilayer electrolytes for highperformance intermediate-temperature solid oxide fuel cells (IT-SOFCs). ACS Appl Mater Interfaces 2017;9:8443-9.
[17] Kang Taek Lee, Doh Won Jung, Hee Sung Yoon, Matthew A. Camaratta Nicolas A. Sexson, and Eric D. Wachsman ECS Transactions, 35 (1) 1861-1869 (2011)
[18] Z. Y. Jiang, L. Zhang, L. L. Cai and C. R. Xia, Electrochimica Acta, 54, 3059 (2009).
[19] J. L. Li, S. R. Wang, Z. R. Wang, J. Q. Qian, R. Z. Liu, T. L. Wen and Z. Y. Wen Journal of Solid State Electrochemistry, 14, 579 (2010).
[20] J. L. Li, S. R. Wang, Z. R. Wang, R. Z. Liu, T. L. Wen and Z. Y. Wen, *Journal of Power Sources*, 194, 625 (2009).
[21] Z. Jiang, Z. Lei, B. Ding, c. Xia, F. Zhao and F. Chen, *International Journal of Hydrogen Energy*, in press (2010
[22] Z. Y. Jiang, L. Zhang, K. Feng and C. R. Xia, *Journal of Power Sources*, 185, 40
[23] Kang Taek Lee, Doh Won Jung, Hee Sung Yoon, Matthew A. Camaratta Nicolas A. Sexson, and Eric D. Wachsman ECS Transactions, 35 (1) 1861-1869 (2011)
[24] Jin Soo Ahn a, Daniele Pergolesi b,c, Matthew A. Camaratta a, Heesung Yoon a, Byung Wook Lee a, Kang Taek Lee a, Doh Won Jung a, Enrico Traversa b,c, Eric D. Wachsman Electrochemistry Communications 11 (2009) 1504–1507.

6th International Conference on Materials Science and Nanotechnology For Next Generation (MSNG2019)
October 16-18, 2019, Niğde, TURKEY (ORAL FULL TEXT)

Surface Modification of Calcium Carbonate by Tumbling Ball Milling with Stearic Acid

Öner Yusuf TORAMAN*, Orkun ERSOY**, Harun KÖSE***

* Niğde Ömer Halisdemir University, Engineering Faculty, Department of Mining Engineering, Niğde, TURKEY
** Hacettepe University, Engineering Faculty, Department of Geological Engineering, Ankara, TURKEY
*** Niğtaş Company, Niğde, TURKEY

This paper investigates the surface modification of calcite ($CaCO_3$) obtained from the Niğde region of Turkey with stearic acid as modification agents, which are incorporated into the calcite with dry fine grinding in a laboratory scale tumbling ball mill. The effect of surface modification is evaluated by a floating test, which is characterized by the active ratio, colour properties and oil absorption. The results showed that modified calcite powder (BMC3) with a coating rate of 1.05%, a mean particle size of 10.18 μm, oil absorption ratio of 34%, Ry of 85.18% can be obtained with 30 min grinding+modification time, 30% ball filling ratio and 5% sample and ball mass ratio. The preliminary results obtained from the experiments indicate that dry surface modification with fatty acid may be an alternative method for the surface modification of calcite using a conventional ball mill.

Keywords: Calcium Carbonate, Ball Mill, Surface Modification, Stearic Acid
Corresponding author: otoraman@ohu.edu.tr

1. Introduction

Calcium carbonate ($CaCO_3$) containing calcite is most widely used filler in the plastics, rubber, paper, paint and ink industry [1]. In particular, its reaction with fatty and other organic acids, especially stearic acid, has been used for many years to improve their compatibility with, and dispersion in, polymers. The coated fillers are much more hydrophobic than the uncoated ones, which reduces water pick-up, and have also been shown to have an effect on polymer morphology and hence modifying the properties of polymers [2].

Conventional surface modification technologies, which consist of the heating mix modification and packing modification methods, have been applied widely in the treatment of fillers and pigments. However, conventional techniques have some drawbacks, such as weak stirring capabilities, low materials mixing degree, uneven dispersion between agent and materials, and, in particular, a lack of reaction foundation. Moreover, the modification effect is weak when using conventional techniques and the product quality is unstable. Thus, the improvement of mechanical performance of the product is not significant [3].

On the other hand, dry particle coating is a relatively new and alternative approach to wet coating methods and it has drawn attention of many researcher using different equipment such as high shear mixer, vibrating mill, planetary ball mill, and jet mill [4-7]. However, there is no study on surface modification in the tumbling ball mill. In this study, it was investigated the modification of calcite with stearic acid (SA), which is incorporated into the calcite with dry fine grinding in a tumbling ball mill. Moreover, before and after grinding+surface modification, calcite was characterized by the coating ratio and oil absorption method.

2. Experimental details

2.1. Samples and Reagents

Calcite powder used was supplied by the Niğtaş Company, Niğde, Turkey. A chemical analysis of the

sample is reported in *Table 1*. The sample was crushed to a nominal maximum size of -1.18 mm using a jaw crusher in a closed circuit with a 1.18 mm screen. The particle size distribution of the crushed sample was determined by dry screening, the results of which appear in *Fig. 1*. Chemical reagent (SA) which was used in the surface modification, were obtained from Sigma-Aldrich.

Table 1. Chemical composition of the sample (wt%).

$CaCO_3$	$MgCO_3$	Fe_2O_3	SiO_2	Al_2O_3	Total
99.5	0.2	0.01	0.01	0.02	99.74

Physical properties of chemical reagent used in the experimental studies is shown in *Table 2*.

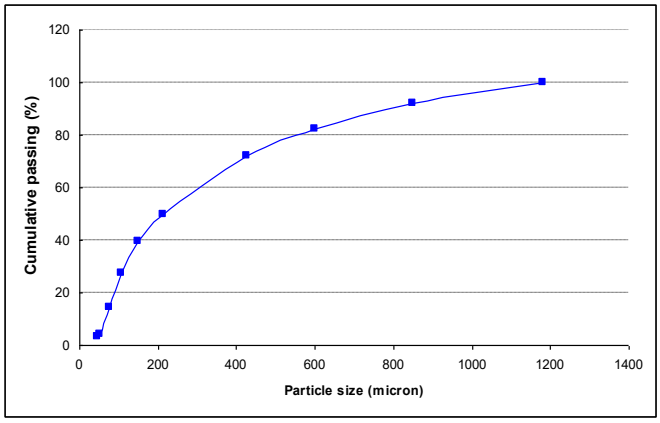


Fig 1. *Particle size distribution of feed sample.*

Table 2. Chemical reagent used in experimental studies.

Reagent	Density (g/cm^3)	Molecular formula	Molecular weight (g/mol)
Stearic acid	0.94	$C_{18}H_{36}O_2$	284.48

2.2. Test and Evaluation Method

Laboratory scale modification tests were conducted in a laboratory-scale ball mill made of stainless steel with the dimensions 200×200 mm. The grinding media were stainless steel balls with a density of 8000 kg/m^3 and with three different diameters (i.e., 1, 2, and 3 cm). The grinding experiment was performed as a batch process; after each test, all media and ground samples were removed from the mill and the media separated from the products by dry sieving.

The critical speed (N_c), ball filling ratio (J_b), and powder filling ratio (f_c) were calculated using Eqs. (1), (2) and (3), respectively:

$N_c = 42.3/[(D-d)]^{0.5}$ (rpm) (1)

(D = mill diameter and d = ball diameter, in meters)

J_b = [(mass of balls/ball density)/mill volume] x 1/0.6 (2)

f_c = [(mass of powder/powder density)/mill volume] x 1/0.6 (3)

The effect of the surface modification was evaluated by the floating test, which measures the ratio of the floated product to the overall weight of the sample, after they are mixed in water and stirred vigorously.

$AR(\%) = M_p/(M_p+M_t)*100$ (4)

where AR is the active ratio (%), M_p the mass of the floated product and M_t the mass of the non-floated product [8]. A greater active ratio implies better surface modification effects [3]. The samples were characterized with the Mastersizer Hydro 2000 laser diffraction particle size analyzer (Malvern, UK). Analyses of the colour properties of the samples with a Datacolor Elrepho spectrophotometer were performed.

An organization called Commission Internationale del'Eclairage (CIE) determined the standard values that are used worldwide to measure color. The values used by CIE are called L*, a*, and b*, and the color measurement method is called CIELAB. Symbol L* (Lightness) represents the difference between light (“pure white”) (where L*=100) and dark (“black”) (where L*= 0); a* (Redness-Greenness) represents the difference between green (−a*) and red (+a*); and b* (Yellowness-Blueness) represents the difference between yellow (+b*) and blue (−b*) [9]. The colour measurement method is called CIELAB. The CIELAB values are calculated from the red green and blue filters of the colorimeters and are particularly suited to describing near white samples according to the following equations [10]:

$L^*=116(Y/Y^n)^{1/3}-16$ (5)

$a^*=200[((X/X^n)^{1/3}-(Y/Y^n)^{1/3}]$ (6)

$b^*=200[((Z/Z^n)^{1/3}-(Y/Y^n)^{1/3}]$ (7)

where X, Y and Z are the tristimulus values for the samples arising from the colourimetric system and X^n, Y^n and Z^n are those of a surface colour choosen as the nominal white stimulus. Using this system and colour that correspons to a place on the Cylindrical CIELAB color space system was shown in *Fig. 2*.

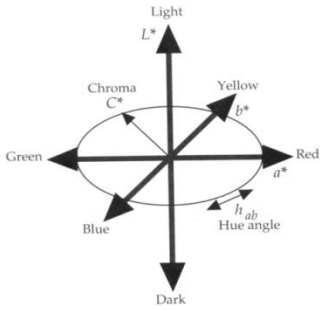


Fig 2. *Cylindrical CIELAB colour space [11].*

Summary of experimental conditions is also shown in *Table 3.*

Table 3. Summary of experimental conditions.

Item	Experimental condition
Ball filling ratio (J_b)	0.30
Powder filling ratio (f_c)	0.05
Operational speed (% of N_c)	90
Grinding time	BMC1: 10 min BMC2: 20 min BMC3: 30 min
Ball size distribution (10-20-30 mm)	30%-40%-30%
Modifying reagent ratio (% of powder mass)	1% Stearic acid
Material of grinding media	Stainless steel
Powder feed size	-1.18 mm

3. Results

3.1 Coating ratio of modified $CaCO_3$

It is desirable that coated calcite products used in the industry have an active rate value close to 100%. Active ratios of feed and coated products can be seen from *Table 4*. It can be seen from *Table 4*, the coating ratios of $CaCO_3$ was obtained 0.96-1.05% with 1% SA.

Table 4. Coating ratios of coated products.

Product	Coating ratio, ‰
BMC1	9.85
BMC2	9.6
BMC3	10.5

3.2 Particle size distribution of modified $CaCO_3$

Table 5 shows the summary of particle size distributions coated products.

Table 5. Particle size distributions of coated products.

Product	d_{50}, µm	d_{97}, µm	-2 µm, %	d_{100}, µm
BMC1	16,89	111,65	13,51	208,93
BMC2	11,45	61,36	15,36	120,22
BMC3	10,18	47,96	16,48	79,43

3.3 Oil absorption of modified $CaCO_3$

The decrease in the dop oil absorption rate is regarded as an indication of the coating quality. It can be seen from *Table 6*, the dop oil absoption of $CaCO_3$ was obtained 26-34% with 1% SA.

Table 6. Dop oil absorption ratios of coated products.

Product	DOP oil absorption, g/100g ≤
BMC1	26
BMC2	32
BMC3	34

3.4 Colour properties of modified $CaCO_3$

Colour parameters (Ry, L*, a*, b*) of feed sample and products coated are shown in *Table 7*. Whiteness is an important specification of micronized mineral filler products, and it is important for marketing purposes that whiteness be high (≥95%). Notably, the lightness *(L*)* values of the ground calcite products was obtained 93.9-94.6 with 1% SA.

Table 7. Colour parameters of coated products.

Product	Ry	L*	a*	b*
BMC1	85,59	94,14	0,24	1,76
BMC2	86,66	94,59	0,29	1,98
BMC3	85,18	93,96	0,24	1,5

4. Conclusions

In this study, surface modification with stearic acid as modification reagent incorporated with dry fine grinding in a tumbling ball mill was investigated. The results showed that modified calcite powder (BMC3) with an coating rate of 1.05%, a mean particle size of 10.18 µm, oil absorption ratio of 34%, Ry of 85.18% can be obtained with surface modification method under 1% modifier reagent dosage with 30 min grinding+modification time, 30% ball filling ratio and 5% sample and ball mass ratio. The preliminary results obtained from the experiments indicate that dry surface modification with fatty acid may be an alternative method for the surface modification of calcite using a conventional ball mill.

5. Acknowledgement

The authors would like to thank Niğde Ömer Halisdemir University Industrial Raw Materials & Building Materials Application & Research Center and the Nigtaş company (Niğde, Turkey) for their support in this work.

Nomenclature

d_{50} Average particle size, µm
d_{97} 90% cumulative weight passing size of the ground product, µm
d_{100} 100% cumulative weight passing size of the ground product, µm
SSA Specific surface area, m^2/g
SA Stearic acid
Ry Brightness of calcite
L* Lightness of calcite
a* Redness-greenness of calcite
b* Yellowness-blueness of calcite

References:

[1] SOLOMON, D.H., HAWTHORNE, D.G., 1983. Chemistry of Pigment and Fillers, Willey & Sons, NY, p.108.
[2] HANCOCK, M., ROTHON R.N. (EDS.), 2003. Particulate-filled Polymer Composites, Rapra Technology Limited, United Kingdom, p.57.
[3] DING, H., LU, S., DENG, Y., DU, C.X., 2007. Mechano-activated surface modification of calcium carbonate in wet stirred mill and its properties, *Trans. Nonferrous Met. Soc. China*, 17, p.1100-1104.
[4] JEONG, S.B., YANG, Y.C., CHAE, Y.B., KİM, B.G., 2009. Characteristics of the treated ground calcium carbonate powder with stearic acid using the dry process coating system, *Materials Transactions*, 50(2), p.409-414.
[5] LEFEBVRE, G., GALET, L., CHAMAYOU, A., 2011. Dry coating of talc with fumed silica: Influence of the silica concentration on the wettability and dispersibility of the composite particles, *Powder Technology*, p.372-377.
[6] SATO, A., SERRIS, E., GROSSERAU, P., THOMAS, G., CHAMAYOU, A., GALET, L., BARON, M., 2012. Effect of operating conditions on dry particle coating in a high shear mixer, *Powder Technology*, 229, p.97-103.
[7] HAIT, S.K., CHEN, Y., 2014. Optimization of milling parameters on the synthesis of stearic acid coated $CaCO_3$ nanoparticles, *J.Coat.Technol. Res.*, 11(2), p.273-282.
[8] SEKULIC, Z., MIHAJLOVIC, S., DAKOVIC, A., KRAGOVIC, M., STANIC, T., 2009. Modification of calcite with stearic acid using the solution method, *7th Industrial Minerals Symposium and Exhibition*, p.218-224, İzmir.
[9] SHARAFUDEEN, R., 2012. The manufacturing process parameters affecting color and brightness of TiO_2 pigment, International Journal of Industrial Chemistry (IJIC), 3(27), p.1-7.
[10] CHRISTIDIS, G.E., SAKELLARIOU, N., REPOUSKOU, E., MARKOPOULOS, TH., 2004. Influence of organic matter and iron oxides on the colour properties of a micritic limestone from Kefalonia, Bulletin of the Geological Society of Greece vol. XXXVI, p.72-79.
[11] OCHS, M. J., 2000. Development of a Linear Version of the CIECAM97s Color Appearance Model (https://www.cis.rit.edu/research/thesis/bs/2000/ochs/thesis.htm

6th International Conference on Materials Science and Nanotechnology For Next Generation (MSNG2019)
October 16-18, 2019, Niğde, TURKEY (ORAL FULL TEXT)

Investigation of Surface Modification by Dry Ball Milling Using Stearic Acid+Sodium Oleate Mixture

Öner Yusuf TORAMAN*, Orkun ERSOY**, Harun KÖSE***

* Niğde Ömer Halisdemir University, Engineering Faculty, Department of Mining Engineering, Niğde, TURKEY
** Hacettepe University, Engineering Faculty, Department of Geological Engineering, Ankara, TURKEY
*** Niğtaş Company, Niğde, TURKEY

In this study, surface modification with stearic acid+sodium oleate mixture as modification reagent incorporated with dry ultra-fine grinding in a tumbling ball mill was investigated. The results showed that modified calcite powder (YK-2) with an coating rate of 0.95%, a mean particle size of 12.92 μm, oil absorption ratio of 19%, Ry of 84.17% can be obtained with surface modification method under total 1% modifier reagent dosage with 1.8 m/s stirring velocity, 20 min grinding+modification time, 30% ball filling ratio and 5% sample and ball mass ratio. This results indicate that dry surface modification with fatty acid mixture may be an effective method for the surface modification of calcite using a conventional ball mill.

Keywords: Surface Modification, Calcite, Dry Ball Milling, Stearic Acid, Sodium Oleate
Corresponding author: otoraman@ohu.edu.tr

1. Introduction

The coated fillers are much more hydrophobic than the uncoated ones, which reduces water pick-up, and have also been shown to have an effect on polymer morphology and hence modifying the properties of polymers [1]. Conventional surface modification technologies, which consist of the heating mix modification and packing modification methods, have been applied widely in the treatment of fillers and pigments. However, conventional techniques have some drawbacks, such as weak stirring capabilities, low materials mixing degree, uneven dispersion between agent and materials, and, in particular, a lack of reaction foundation. Moreover, the modification effect is weak when using conventional techniques and the product quality is unstable. Thus, the improvement of mechanical performance of the product is not significant [2]. On the other hand, dry particle coating is a relatively new and alternative approach to wet coating methods and it has drawn attention of many researcher using different equipments such as high shear mixer, vibrating mill,

planetary ball mill, and jet mill [3-6]. However, there are no closure studies in the tumbling ball mill.

In this study, it was investigated the modification of calcite with stearic acid (SA)+sodium oleate (SO), which is incorporated into the calcite with dry fine grinding in a ball mill. Moreover, $CaCO_3$ before and after grinding+surface modification was characterized by the coating ratio and oil absorption method.

2. Experimental details

2.1. Samples and Reagents

Calcite powder used was supplied by the Niğtaş Company, Niğde, Turkey. A chemical analysis of the sample is reported in *Table 1*. The sample was crushed to the maximum sizes of −1.18 mm – 0.850 mm – 0.600 mm and – 0.425 mm using a jaw crusher in a closed circuit. The obtained products were denoted as YK-1, YK-2, YK-3 and YK-4, respectively. Chemical reagents which was used in the surface modification, were obtained from Sigma-Aldrich.

Table 1. Chemical composition of the sample (wt%).

$CaCO_3$	$MgCO_3$	Fe_2O_3	SiO_2	Al_2O_3	Total
99.5	0.2	0.01	0.01	0.02	99.74

Physical properties of chemical reagents used in the experimental studies are shown in *Table 2.*

Table 2. Chemical reagent used in experimental studies.

Reagent	Density (g/cm³)	Molecular formula	Molecular weight (g/mol)
Stearic acid	0.94	$C_{18}H_{36}O_2$	284.48
Sodium oleate	1.02	$C_{18}H_{33}NaO_2$	304.4

2.2. Test and Evaluation Method

Modification tests were conducted in a laboratory-scale ball mill made of stainless steel with the dimensions 200×200 mm. The grinding media were stainless steel balls with a density of 8000 kg/m^3 and with three different diameters (i.e., 10, 20, and 30 mm). The grinding experiment was performed as a batch process; after each test, all media and ground samples were removed from the mill and the media separated from the products by dry sieving.

The critical speed (N_c), ball filling ratio (J_b), and powder filling ratio (f_c) were calculated using Eqs. (1), (2) and (3), respectively:

$N_c = 42.3/[(D-d)]^{0.5}$ (rpm) (1)

(D = mill diameter and d = ball diameter, in meters)

J_b = [(mass of balls/ball density)/mill volume] x 1/0.6 (2)

f_c = [(mass of powder/powder density)/mill volume] x 1/0.6 (3)

The effect of the surface modification was evaluated by the floating test, which measures the ratio of the floated product to the overall weight of the sample, after they are mixed in water and stirred vigorously.

The samples were characterized with the Mastersizer Hydro 2000 laser diffraction particle size analyzer (Malvern, UK). Analyses of the colour properties of the samples with a Datacolor Elrepho spectrophotometer were performed.

An organization called Commission Internationale del'Eclairage (CIE) determined the standard values that are used worldwide to measure color. The values used by CIE are called L*, a*, and b*, and the color measurement method is called CIELAB. Symbol L* (Lightness) represents the difference between light ("pure white") (where L*=100) and dark ("black") (where L*= 0); a* (Redness-Greenness) represents the difference between green (−a*) and red (+a*); and b* (Yellowness-Blueness) represents the difference between yellow (+b*) and blue (−b*) [7]. The colour measurement method is called CIELAB. The CIELAB values are calculated from the red green and blue filters of the colorimeters and are particularly suited to describing near white samples according to the following equations [8]:

$L^*=116(Y/Y^n)^{1/3}-16$ (4)

$a^*=200[((X/X^n)^{1/3}-(Y/Y^n)^{1/3}]$ (5)

$b^*=200[((Z/Z^n)^{1/3}-(Y/Y^n)^{1/3}]$ (6)

where X, Y and Z are the tristimulus values for the samples arising from the colourimetric system and X^n, Y^n and Z^n are those of a surface colour choosen as the nominal white stimulus.

Summary of experimental conditions is also shown in *Table 3.*

Table 3. Summary of experimental conditions.

Item	Experimental condition
Ball filling ratio (J_b)	0.30
Powder filling ratio (f_c)	0.05
Operational speed (% of N_c)	90
Grinding time	20 min
Ball size distribution (10-20-30 mm)	30%-40%-30%
Modifying reagent ratio (% of powder mass)	0.5% Stearic acid+0.5% Sodium oleate
Material of grinding media	Stainless steel
Powder feed size	YK-1: -1180 µm YK-2: -850 µm YK-3: -600 µm YK-4: -425 µm

3. Results

3.1 Coating ratio of modified $CaCO_3$

It is desirable that coated calcite products used in the industry have an active rate value close to 100%. Active ratios of feed and coated products can be seen from *Table 4.* It can be seen from *Table 4*, the coating ratio of $CaCO_3$ was obtained 0.94-1.01% with 0.5% SO+0.5SA.

Table 4. Coating ratios coated products.

Product	Coating ratio, ‰
YK-1	9,4
YK-2	9,5
YK-3	9,9
YK-4	10,1

3.2 Particle size distribution of modified $CaCO_3$

Table 5 shows the summary of particle size distributions coated products.

Table 5. Particle size distributions of coated products.

Product	PSD					SSA m^2/g
	d_{10} µm	d_{50} µm	d_{97} µm	% of particles of diameter <2 µm	d_{100} µm	
YK-1	1,65	14,66	67,21	12,79	120,22	1,31
YK-2	1,19	12,92	73,59	16,74	138,03	1,61
YK-3	1,29	16,53	163,33	15,66	316,22	1,46
YK-4	1,43	19,94	201,65	14,22	416,86	1,34

3.3 Oil absorption of modified $CaCO_3$

The decrease in the dop oil absorption rate is regarded as an indication of the coating quality. Depending on the coating quality of the coated calcite products, the amount of dop oil absorption is reduced by 50% or more. It can be seen from *Table 6*, the dop oil absoption of $CaCO_3$ was obtained 18-22% with 0.5% SO+0.5SA.

Table 6. Dop oil absorption ratios of coated products.

Product	DOP oil absorption, g/100g ≤
YK-1	18
YK-2	19
YK-3	20
YK-4	22

3.4 Colour properties of modified $CaCO_3$

Colour parameters (Ry, L*, a*, b*) of feed sample and products coated are shown in *Table 7*. Whiteness is an important specification of micronized mineral filler products, and it is important for marketing purposes that whiteness be high (≥95%). Notably, the lightness *(L*)* values of the ground calcite products was obtained 93.2-94.0 with 0.5% SO+0.5SA.

Table 7. Colour parameters of feed and coated products.

Product	Ry	L*	a*	b*
YK-1	85,29	94,01	0,21	1,62
YK-2	84,17	93,52	0,16	1,44
YK-3	83,42	93,20	0,09	1,49
YK-4	84,01	93,46	0,11	1,64

4. Conclusions

In this study, surface modification with SA+SO mixture as modification reagent incorporated with dry fine grinding in a tumbling ball mill was investigated. The results showed that modified calcite powder (YK-2) with an coating rate of 0.95%, a mean particle size of 12.92 µm, oil absorption ratio of 19%, Ry of 84.17% can be obtained with surface modification method under total 1% modifier reagent dosage with 20 min grinding+modification time, 30% ball filling ratio and 5% sample and ball mass ratio. The preliminary results obtained from the experiments indicate that dry surface modification with fatty acid mixture may be an effective method for the surface modification of calcite using a conventional ball mill.

5. Acknowledgement

The authors would like to thank Niğde Ömer Halisdemir University Industrial Raw Materials & Building Materials Application & Research Center and the Niğtaş company (Niğde, Turkey) for their support in this work.

Nomenclature

d_{10} 10% cumulative weight passing size of the ground product, µm
d_{50} Average particle size, µm
d_{97} 90% cumulative weight passing size of the ground product, µm
d_{100} 100% cumulative weight passing size of the ground product, µm
SSA Specific surface area, m^2/g
SA Stearic acid
SO Sodium oleate
Ry Brightness of calcite
L* Lightness of calcite
a* Redness-greenness of calcite
b* Yellowness-blueness of calcite

References:

[1] HANCOCK, M., ROTHON R.N. (EDS.), 2003. Particulate-filled Polymer Composites, Rapra Technology Limited, United Kingdom, p. 57.
[2] DING, H., LU, S., DENG, Y., DU, C.X., 2007. Mechano-activated surface modification of calcium carbonate in wet stirred mill and its properties, *Trans. Nonferrous Met. Soc. China*, 17, p.1100-1104.
[3] JEONG, S.B., YANG, Y.C., CHAE, Y.B., KİM, B.G., 2009. Characteristics of the treated ground calcium carbonate powder with stearic acid using the dry process coating system, *Materials Transactions*, 50(2), 409-414.

[4] LEFEBVRE, G., GALET, L., CHAMAYOU, A., 2011. Dry coating of talc with fumed silica: Influence of the silica concentration on the wettability and dispersibility of the composite particles, *Powder Technology*, 372-377.

[5] SATO, A., SERRIS, E., GROSSERAU, P., THOMAS, G., CHAMAYOU, A., GALET, L., BARON, M., 2012. Effect of operating conditions on dry particle coating in a high shear mixer, *Powder Technology*, 229, 97-103.

[6] HAIT, S.K., CHEN, Y., 2014. Optimization of milling parameters on the synthesis of stearic acid coated $CaCO_3$ nanoparticles, *J.Coat.Technol. Res.*, 11(2), 273-282.

[7] SHARAFUDEEN, R., 2012. The manufacturing process parameters affecting color and brightness of TiO_2 pigment, International Journal of Industrial Chemistry (IJIC), 3(27), 1-7.

[8] CHRISTIDIS, G.E., SAKELLARIOU, N., REPOUSKOU, E., MARKOPOULOS, TH., 2004. Influence of organic matter and iron oxides on the colour properties of a micritic limestone from Kefalonia, Bulletin of the Geological Society of Greece, vol. 36, 72-79.

6th International Conference on Materials Science and Nanotechnology For Next Generation (MSNG2019)
October 16-18, 2019, Niğde, TURKEY (ORAL FULL TEXT)

The Effect of Ceramic Grinding Media on Stirred Milling and Experimental Testing of Media Wear

Öner Yusuf TORAMAN*, Ahmet TEYMEN*, Orkun ERSOY**, Harun KÖSE***

* Niğde Ömer Halisdemir University, Engineering Faculty, Department of Mining Engineering, Niğde, TURKEY
** Hacettepe University, Engineering Faculty, Department of Geological Engineering, Ankara, TURKEY
*** Niğtaş Company, Niğde, TURKEY

Grinding media selection has a major influence on mill parameters such as energy efficiency, internal wear and operating costs. Ceramic beads are usually classified according to their chemical composition and physical properties such as bulk density, hardness and fracture toughness. In this paper, three different ceramic beads supplied from different companies are compared in terms of grinding performance, self-wear resistance and strength of beads. As a result, it has been shown that there is a relationship between the chemical content of the grinding media and abrasion and compressive strength.

Keywords: Grinding Media, Stirred Milling, Media Wear, Impact Strength
Corresponding author: otoraman@ohu.edu.tr

1. Introduction

In the mining industry, operating costs are the most expensive and energy consuming processes and generally driven by energy consumption and wear. Wear of grinding media is by far the most important wear issue tumbling and stirred mills. The mining industry is faced with severe challenges due to media composition and characteristics, selection for their own application. Suppliers are presenting different products with specific properties and price. For grinding media selection, there is a compromise between grinding efficiency, wear resistance and cost [1].

The high intensity stirred mills further extend the energy benefits of this technology by using higher stirrer speeds and smaller grinding media [2]. Media selection has a major influence on mill parameters such as energy efficiency, internal wear and operating costs. An inert grinding environment is beneficial to avoid mineral surface degradation and obtain downstream processing and cost advantages [3]. Ceramic beads have a profound implication to these parameters and the availability of an economic ceramic media could give significant benefits to the users of mills [4]. They are usually classified according to their chemical composition and physical properties such as bulk density, hardness and fracture toughness. The bulk density has a large influence on the mill power draw. Hardness and fracture toughness give an indication of the bead's wear resistance [3].

Mill media selection, evaluation the media wear and the operation of stirred mills have been discussed in several authors [5-8].

In this paper, three different ceramic beads supplied from different companies are compared in terms of grinding performance, self-wear resistance and impact strength of beads.

2. Experimental details

2.1. Materials

Calcite ($CaCO_3$) powder used was supplied by the Niğtaş Co., Niğde, Turkey. A chemical analysis of the sample is reported in *Table 1.* Grinding aids (0.2% MEG, TEA and Glycerol complex) which were used in the grinding performance tests, were obtained from Sigma-Aldrich. *Table 2*, *Table 3* and *Table 4* also show the chemical and physical properties of different grinding beads called GM01, GM02 and GM03.

Table 1. Chemical composition of the sample (wt%).

$CaCO_3$	$MgCO_3$	Fe_2O_3	SiO_2	Al_2O_3	Total
99.5	0.2	0.01	0.01	0.02	99.74

Table 2. Chemical composition of grinding medias (wt%).

	GM01	GM02	GM03
Fe2O3	0.192	0.227	0.149
MgO	0.691	1.663	0.685
Al2O3	87.978	84.917	89.958
SiO2	4.796	7.658	7.232
SO3	0.406	0.557	0.029
K2O	0.060	0.075	0.115
Na2O	0.199	0.118	0.569
TiO2	0.080	0.064	0.128
Co3O4	0.502	0.502	0.083
ZnO	0.007	0.009	0.012
SrO	0.010	0.000	0.008
ZrO2	0.000	0.000	0.628
BaO	0.357	0.000	0.000
WO3	2.381	3.037	0.000
CaO	0.966	1.277	0.191

Table 3. Bulk and real densities of the samples.

	GM01	GM02	GM03
Bulk density, Kg/L	2,06	2,10	1,98
Real density, g/cm^3	3,60	3,60	3,60

Table 4. Physical properties of grinding medias.

	Composition	Density (g/cm^3)	Hardness
GM01	Al_2O_3 (~%88)+SiO_2 (%5)+Others (%7)	3.6	>1170 HV
GM02	Al_2O_3 (~%85)+SiO_2 (%8) Others (%7)	3.6	>1150 HV
GM03	Al_2O_3 (~%90)+SiO_2 (%8) Others (%2)	3.6	>1190 HV

2.2. Test Method

2.2.1. Self-wear in water

600 g grinding media and 200 g water were added into the vertical stirred mill to grind for some time (3-6-10 h). Grinding was conducted at a speed of 600 rpm.

2.2.2. Self-wear without water

600 g grinding media was added into the vertical stirred mill to grind for some time (8-16-24 h). Grinding was conducted at a speed of 600 rpm.

2.2.3. Milling performance with calcite powder

Vertical stirred media mill *Fig.1* was used in order to provide robust grinding and impacting forces. Also some detailed parameters of the mill used are listed in *Table 5*.



Fig 1. *Vertical stirred media mill used.*

Table 5. Parameters of vertical stirred mill.

Parameters	Vertical stirred mill
Motor power (kw)	0.5
Grinding chamber volume (l)	0.75
Operation speed (rpm)	600

Approximately 900 g grinding media and 45 g calcite powder were added into the vertical stirred mill to grind for 10 min. Summary of experimental conditions is shown in *Table 6.*

Table 6. Summary of experimental conditions.

Item	Experimental condition
Bead filling ratio	0.70
Sample filling ratio	0.05
Grinding time	10 min
Temperature	Room temperature
Material of grinding media	GM01, GM02, GM03
Grinding media size	3-4 mm
Powder sample	
Specific gravity	2.7 g/cm^3
Particle size (average)	23.48 µm
Specific Surface Area	0.941 m^2/g

2.2.4. Strength measurement

Uniaxial compression tests were performed on the studied ceramic beads. A digital point load tester with a loading capacity of 3000 kN was used to sensitively determine the strength of the ceramic beads. Ten samples of each ceramic bead type were broken to determine the strength of the ceramic beads. First, the specimens were centred between the loading plates and then the load was gradually increased manually until fracture occurred. *Fig. 2* shows the uniaxial compression test performed by adapting the point load tester, and some broken bead samples.

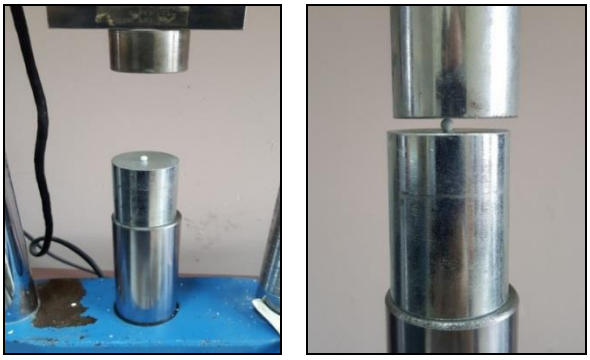


Fig 2. *Uniaxial compression test.*

2.2.5. Calculation on wear-rate

The media wear-rate can be calculated by equation "wear-rate=*a/b/t*", where *a* is the media loss (g), after milling, *b* is the initial media charge (kg), and *t* is the milling time (h). The unit of wear-rate is $g.kg^{-1}h^{-1}$ [9].

3. Results

3.1. Grinding tests

Table 7 shows the summary of particle size distributions of feed and milled products. It was found that grinding efficiency of all beads was very similar. As a result of grinding tests, both the average particle sizes (D_{50}) and specific surface areas (SSA) are approximately the same within the 3 balls.

Table 7. Particle size distributions of feed and milled products.

Media type	Particle size, µm			Specific Surface Area, m^2/g
	D_{50}	D_{97}	<2 µm % of particles of diameter	
Feed	23,48	89,43	8,38	0,94
GM01	2,90	13,83	39,81	2,44
GM02	2,94	16,04	40,39	2,47
GM03	3,09	19,58	40,21	2,36

3.2.Self-wear tests

Self-wear is a simple and easy way, that's why it is commonly used. *Fig. 3* shows the self-wear curves of different grinding media in water versus time. It can be seen from the *Fig. 3* that GM01 and GM03 beads have higher self-wear rate in water. The lower wear of GM02 may be due to the relatively higher WO_3, MgO and SiO_2 content in the chemical content.

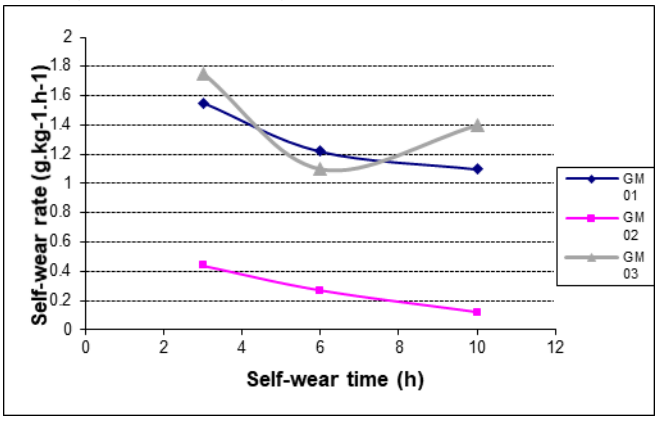


Fig 3. *Self-wear curves of beads in vertical stirred mill.*

Fig 4. also shows the cumulative wear curves of different grinding media without water versus self-wear time. It can be seen from the *Fig. 4* that GM02 has lower cumulative wear rate less than GM01 and GM03.

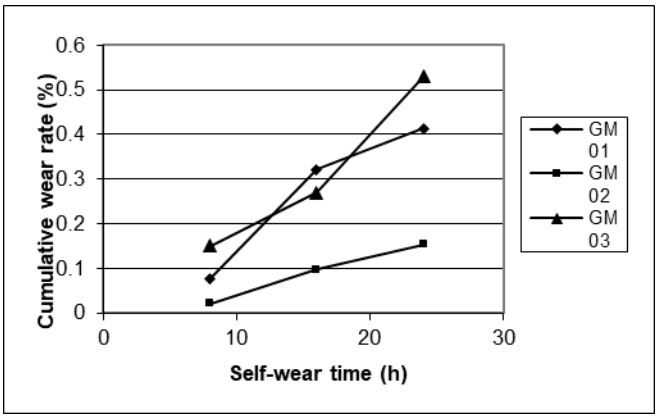


Fig 4. *Cumulative wear curves of beads in vertical stirred mill.*

Fig 5. shows typical SEM photos of media surfaces before and after 24 h self-wear test. As can be seen from the SEM images, the GM01 ceramic ball was fairly rough at the beginning, but after the abrasion test it became quite smooth surface, and the GM02 ceramic ball surface was not very rough, so the wear after test was also small. As a result, SEM images confirm the results in *Fig 3* and *Fig 4.*

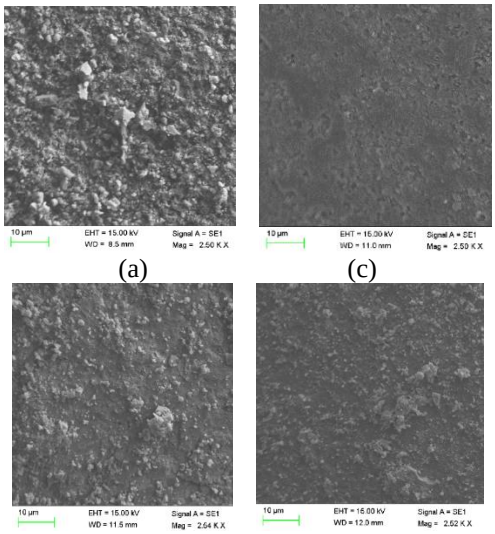


Fig 5. SEM photos of media surfaces before (a) GM01 (b) GM02 and after (c) GM01 (d) GM02 24 h self-wear test.

3.3.Strength test

After the strength test, *Table 8*, the strength of the GM01 and GM02 ceramic beads were 354,8 kg and 347 kg, respectively, while the value of GM03 was 240,5 kg. The slightly lower strength of the GM03 can be explained by the fact that WO_3 and Co_3O_4 contents are 0.000% and 0.083% respectively.

Table 8. Point load strength test results.

Grinding media type	Strength (kg)	% standard deviation
GM01	354,8±44,0	15,0
GM02	347,6±71,1	31,1
GM03	240,5±37,2	13,2

4. Conclusions

The following results were obtained in experimental studies:

1. According to the grinding tests, both the average particle sizes (D_{50}) and specific surface areas (SSA) are approximately the same for 3 balls.
2. GM01 and GM03 beads have higher self-wear rate in water. The lower wear of GM02 is due to the relatively higher WO_3, MgO and SiO_2 content in the chemical content.
3.GM02 has lower cumulative wear rate less than GM01 and GM03.
4. GM01 ceramic ball was fairly rough at the beginning, but after the abrasion test it became quite smooth surface, and the GM02 ceramic ball surface was not very rough, so the wear after test was also small. SEM images also confirm the test results.
5. After the compressive strength test, the strength of the GM01 and GM02 ceramic beads were 354,8 kg and 347 kg, respectively, while the value of GM03 was 240,5 kg. The slightly lower strength of the GM03 can be explained by the fact that WO_3 and Co_3O_4 contents are 0% and 0.083% respectively.

5. Acknowledgement

The authors would like to thank Niğde Ömer Halisdemir University Industrial Raw Materials & Building Materials Application & Research Center and the Niğtaş company (Niğde, Turkey) for their support in this work.

References:

[1] CLERMONT, B., PHILIPPE, C., 2012. Do's and Don'ts of measuring ceramic beads wear in the lab and in the industry.
[2] GAO, M., YOUNG, M., ALLUM, P., 2002. IsaMill Fine Grinding Technology and Its Industrial Applications At Mount Isa Mines. 34th Annual Meeting of the Canadian Mineral Processors, Ottawa, Canada.
[3] RULE, C.M., KNOPJES, L., CLERMONT, B., PHILIPPE, C., 2008. Fine grinding-Developments in ceramic media technology and result improved plant performance at Anglo Platinum, *The Southern African Institute of Mining and Metallurgy*, s.53-62.
[4] CURRY, D.C., CLERMONT, B., 2005. Improving the efficiency of fine grinding-developments in ceramic media technology, Randol Conference 2005.
[5] GRAVES, G.A., BOEHM, T., 2007. Mill media considerations for high energy mills, *Minerals Engineering*, 20, 342-347.
[6] FARBER, B., DURANT, B., BEDESI, N., 2010, Effect of Media Size and Mechanical Properties on Milling efficiency and Media Consumption, *Comminution 10*, Cape Town.
[7] KOTZE, H., 2012. Selecting ceramic media: Part 1-Theory, *Chem. Eng. Technol.*, 35(11), 2051-2057.
[8] KOTZE, H., BEDESI, N., 2015. Selecting ceramic media: Part 2-Evaluating the wear, *International Journal of Mineral Processing*, 136, 45-49.
[9] KING, J., LI, Q., WANG, A., HE, C., ZHOU, J., DENG, H., XU, R., 2015. Evaluation of grinding media wear-rate by a combined grinding method, *Minerals Engineering*, 73, 39–43.

6th International Conference on Materials Science and Nanotechnology For Next Generation (MSNG2019)
October 16-18, 2019, Niğde, TURKEY (ORAL FULL TEXT)

A Study of BeO Luminophosphores Synthesized with Different Calcination Conditions

V. Altunal*, A. Ozdemir, V. Guckan, and Z. Yegingil
Department of Physics, Faculty of Art and Sciences, Cukurova University, Adana 01330, Turkey

Beryllium Oxide (BeO) has been used extensively in the electronics and nuclear industry since 1950s, due to its many unique features, structurally, chemically and physically. So, it has also attracted the attention of many researchers working in different areas. However, BeO ceramics is used nowadays as Optically Stimulated Luminescence (OSL) dosimeters in radiation dosimetry applications since they are tissue equivalent materials. In short, the OSL technique is the emission of light as a result of optically stimulating a previously irradiated material. In this study, various luminescence characteristics of BeO ceramics, such as Thermoluminescence (TL) glow curves, OSL decay curves, and Radioluminescence (RL) emissions have been achieved controllably by polymeric sol–gel method. In this approach, beryllium sulfate tetra hydrate Be(SO4)x4(H_2O), citric acid and ethylene glycol were used as the source of Be^{2+}, the chelating agent and the solvent agent, respectively. The effect of calcination conditions on luminescence characteristics of BeO ceramics was discussed. High OSL and TL signals were obtained from BeO pellets calcinated at 1000 °C, for 4h. We concluded that the usage of appropriate calcination conditions in BeO sol-gel synthesis is a good starting operation to achieve a promising OSL dosimeter with high luminescent efficiency.

Keywords: Beryllium oxide (BeO), Sol-gel synthesis, Calcination Conditions, Radiation Dosimetry, Luminescence

**Corresponding author*:valtunal@cu.edu.tr

1. Introduction

BeO is a widely used material in the field of Optically Stimulated Luminescence (OSL) dosimetry with Al_2O_3:C material due to its superior physical and chemical properties as well as its superior luminescence and dosimetric properties [1, 2]. The material known as Thermalox 995 (Materion Corporation) is produced for the electronic industry. Thermoluminescence (TL) and OSL signals have been reported in many studies [3-7] and as a result of ongoing studies, a BeO based OSL dosimetry reader system has been produced [8-10]. The produced OSL reader system has become the second most widely used dosimetry system after the OSL reader system (from Epsilon Landauer) designed for Al_2O_3: C nanoDot dosimeters.

Thermalox 995 as BeO ceramic chips of 99.5% purity contains many impurities such as Si, Mg, Fe, Al, B, and Ca [6, 11, 12]. Such impurities in a material not produced as a luminescence dosimeter prevent access to precise information about the source and mechanism of TL and OSL emissions from the material. Therefore, the defects that will be created in the structure by producing for dosimetric purposes will provide us with more accurate information about the luminescence mechanism of the material. Certainly, different conditions that may occur during the synthesis process of a material may change the structural properties of the material as well as the luminescence properties. Perhaps in this way a more suitable material for dosimetric use can be synthesized.

BeO material was produced in different forms by using different synthesis methods and various structural, surface, physical and chemical properties were investigated in the literature [2, 12-20].

In this study, BeO ceramics as prepared pellets from the nano-powders were synthesized via sol-gel method. The calcination process of the material was carried out in two stages and the effects of calcination temperature and duration on luminescence signals were investigated in detail. We investigated whether the usage of appropriate calcination conditions in BeO sol-gel synthesis is a good starting operation to achieve a promising OSL dosimeter with high luminescent efficiency, or not.

2. Material and Method

All the chemicals with high purity were purchased from Sigma Aldrich. Deionized water prepared using New Human Power ultra-purification system (Human Corporation, Korea) and used throughout synthesis. The typical synthesis process begins with dissolving beryllium sulphate tetra hydrate ($Be(SO_4)x4H_2O$, %99.9) salts in ethylene glycol ($C_2H_6O_2$, 99.8% purity) solution diluted with predetermined proportion of deionized water. After the mixture became transparent at 80 °C for about half an hour, citric acid salts were added to the solution and the solution temperature was raised to about 250 °C. Translucent gel formation was observed after two hours of stirring and heating. The resulting gel was in sticky form and subjected to 1-hour heat treatment at 500 °C to remove it from the beaker. After the required heat treatment, the charred material was milled in agate mortar and subjected to secondary heat treatment to burn the organics formed during synthesis and to obtain pure BeO powders. This second heat treatment was our calcination process. In this study, while calcination temperatures were selected as 800, 900, 1000, 1100 and 1200 °C, the duration times at calcination temperatures determined according to TL, OSL and RL signals were 2, 4, 6, 8, 10 and 24 hours. After the calcination process, BeO pellets were prepared by using pure BeO powders obtained for ease of use in luminescence measurements. Here, applied pressure was 500 kgforce/cm^2 and duration time was 1 min. Finally, to correct trap structures and achieve a uniform crystal structure, prepared pellets were sintered at 1600 °C, for 4 h. The photo of the BeO ceramic pellet obtained after sintering was presented with commercially used Thermalox995 BeO chip and nanodot Al_2O_3:C dosimeter for comparison in Fig. 1.

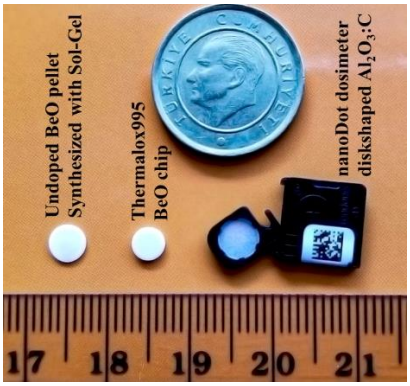


Fig. 1. BeO pellet (synthesized via sol-gel method), Thermalox995 BeO chip, and nanoDot Al_2O_3:C OSL dosimeter

After the synthesis and pellet preparation, the luminescence characteristics of the materials were first examined by using TL and OSL methods in ^{90}Sr-^{90}Y beta radiation source induced DA-20 model RisØ TL / OSL reader system which is equipped with bialkali model 9235 QA photomultiplier tube for detection and blue LEDs ($\lambda \sim$ 470 nm) for light stimulation. TL and OSL signals were detected using a Hoya U-340 nm filter in front of PMT. In OSL measurements, BeO pellets were irradiated with 0.5 Gy beta doses and preheated at 100 °C, 10 s. Then, OSL readout were performed using 200 s blue light stimulations in continuous wave OSL mode (CW-OSL mode). TL measurements were carried out by heating the initially 0.5 Gy irradiated pellets from the room temperature up to 650 °C with 3 °C/s heating rate without preheating procedure.

RL emissions of the BeO pellets were obtained from a homemade X-ray Luminescence system equipped with an 4-40 kV X-ray tube and USB-2000 model Ocean Optics fiber spectrometer which is produced for low sensitivity applications.

3. Results and Discussion:

3.1. RL emissions

Fig. 2. shows the RL emissions obtained from the BeO pellets calcinated at different calcination temperature of 800, 900, 1000, 1100 and 1200 °C for 4 h. As seen from the Fig. 2., the maximum RL emission intensity was obtained from the BeO pellets calcinated at 1000 °C. The appropriate calcination temperature for BeO pellets synthesized via sol-gel method was selected as 1000 °C. After the determination of the appropriate calcination temperature, BeO materials were synthesized

in similar way and calcinated at 1000 °C for different calcination durations of 2, 4, 6, 8, 10, and 24 hours. Fig. 3. shows the RL emissions obtained from the BeO pellets calcinated at 1000 °C for different durations. As seen from the Fig. 3., the maximum RL emission intensity was obtained from the BeO pellets calcinated at 1000 °C for 4 h. The appropriate calcination duration for BeO pellets synthesized via sol-gel method was selected as 4 h.

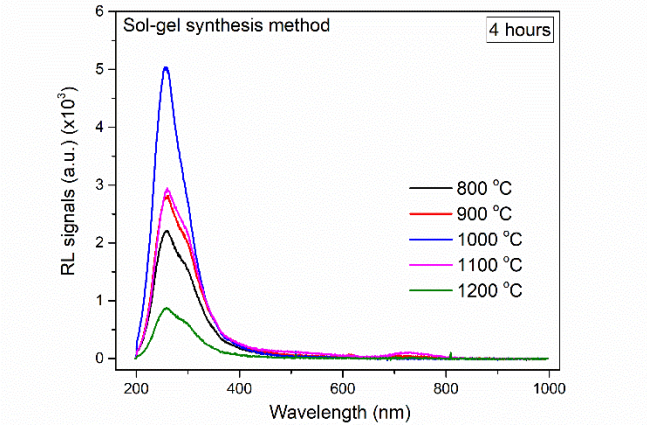


Fig. 2. RL emissions of BeO pellets calcinated at different temperatures for 4 h.

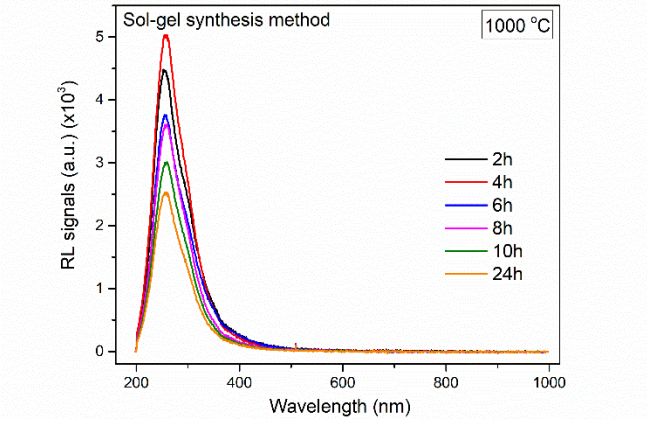


Fig. 3. RL emissions of BeO pellets calcinated at 1000 °C for different durations.

On the other hand, all the obtained RL emissions shows the same broad highly sensitive emission peak located between 200 and 500 nm. This dominant luminescence emission (3-4 eV and 4.9 eV) is originated from the radiative annihilation of the self-trapped excitons in BeO [2, 12]. Additionally, in Fig. 2., an unexpected peak was observed between 700 and 800 nm. This observed emission is associated with the oxygen defects in BeO may act as anion defects in the structure. It is known that such anion defects occurring during synthesis in the structure may show large emissions at high wavelengths in RL measurements.

3.2. TL Glow Curves

TL glow curves of BeO pellets calcinated at different calcination temperature of 800, 900, 1000, 1100 and 1200 °C for 4 h were obtained after 0.5 Gy irradiations and presented in Fig. 4. TL readouts were performed by heating each sample from room temperature up to 650 °C with a heating rate of 3 °C/s. As seen from the Fig. 4., the maximum TL signal intensity was obtained from the BeO pellets calcinated at 1000 °C. Similarly, Fig. 5. shows the TL glow curves obtained from the BeO pellets calcinated at 1000 °C for different durations of 2, 4, 6, 8, 10, and 24 hours. As seen from the Fig. 5., the maximum TL signal intensity was obtained from the BeO pellets calcinated at 1000 °C for 4 h. Considering all the TL glow curves of BeO samples, It can be said that different calcination conditions do not change the structure of traps formed in BeO, but that the traps can change the electron trapping densities.

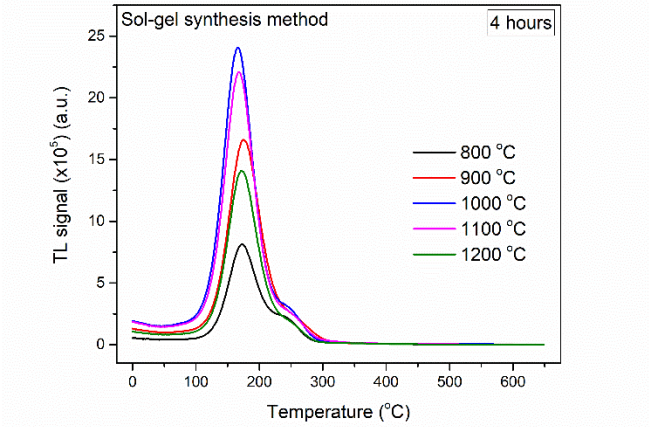


Fig. 4. TL glow curves of BeO pellets calcinated at different temperatures for 4 h.

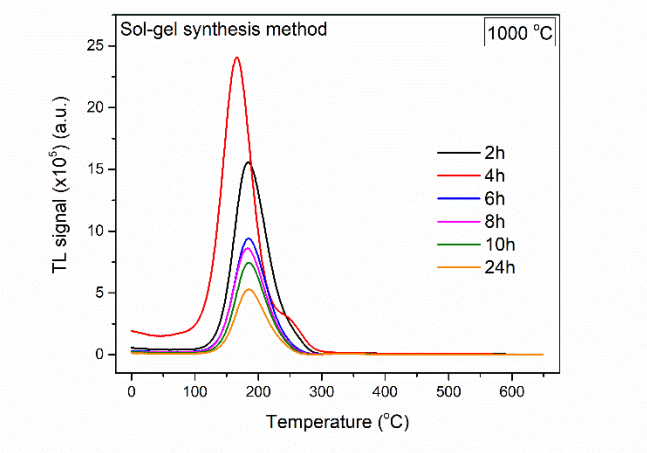


Fig. 5. TL glow curves of BeO pellets calcinated at 1000 °C for different durations.

3.3. OSL Decay Curves

Fig. 6. shows OSL decay curves of 0.5 Gy irradiated BeO pellets which was calcinated at different temperature of 800, 900, 1000, 1100 and 1200 °C for 4 h. The OSL decay curves were obtained by stimulating the blue lights for 200 s followed by a preheat treatment of 100 °C, 10s. As seen from the Fig. 6., the maximum OSL signal intensity was obtained from the BeO pellets calcinated at 1000 °C as for RL and TL signals. In order to see more clearly the total trapped charge population, inset Fig. 6. provides integrated OSL signals obtained by collecting data from 0 to 200 s against the calcination temperature. As results obtained from the maximum OSL signals, the total charge population gave the maximum value for the sample calcined at 1000 °C because the structure of the OSL decay curves did not change. In addition to calcination temperature study, OSL decay curves were obtained from the BeO pellets calcinated at 1000 °C for different durations of 2, 4, 6, 8, 10, and 24 h (see Fig. 7). As seen from the Fig. 7., the maximum OSL signal intensity was obtained from the BeO pellets calcinated at 1000 °C for 4 h. Considering the total trapped charge population from a different perspective, the integrated OSL signals were presented in inset Fig.7. against the calcination durations. Considering all the OSL decay curves of BeO samples, the total charge population gave the maximum value for the sample calcined at 1000 °C for 4 h because different calcination conditions do not change the structure of OSL traps in BeO.

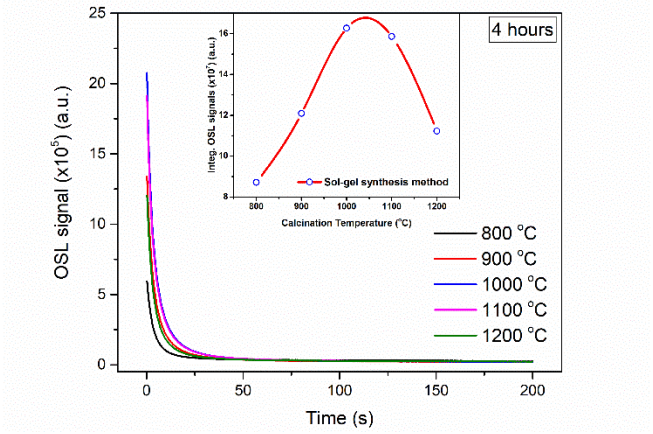


Fig. 6. OSL decay curves of BeO pellets calcinated at different temperatures for 4 h. Inset: Integrated OSL signals of BeO pellets calcinated at different temperatures for 4 h.

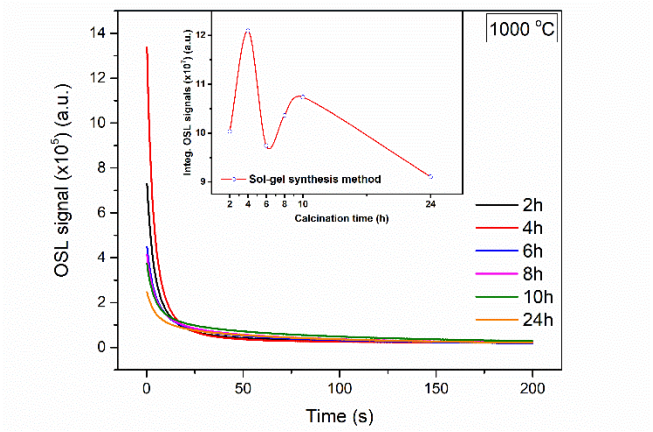


Fig. 7. OSL decay curves of BeO pellets calcinated at 1000 °C for different durations. Inset: Integrated OSL signals of BeO pellets calcinated at 1000 °C for different durations.

4. Conclusions

It was demonstrated that undoped BeO powders were synthesized via sol-gel technique and prepared as ceramic pellet. All the RL emissions are in well agreement with previously reported emissions. It was clearly shown that TL and OSL signals can be used in radiation measurement applications. In future studies, dosimetric properties of the material should be examined

using TL and OSL methods for different calcination conditions.

References:

[1] E.G. Yukihara, S.W. McKeever, Optically stimulated luminescence: fundamentals and applications, John Wiley & Sons2011.
[2] V. Altunal, V. Guckan, A. Ozdemir, A. Sotelo, Z. Yegingil, Effect of sintering temperature on dosimetric properties of BeO ceramic pellets synthesized using precipitation method, Nuclear Instruments and Methods in Physics Research Section B: Beam Interactions with Materials and Atoms 441 (2019) 46-55.
[3] H.O. Albrecht, C.E. Mandeville, Storage of Energy in Beryllium Oxide, Physical Review 101(4) (1956) 1250-1252.
[4] C.R. Rhyner, W.G. Miller, Radiation dosimetry by optically-stimulated luminescence of BeO, Health Phys 18 (1970) 681-684.
[5] E. Tochilin, N. Goldstein, W. Miller, Beryllium oxide as a thermoluminescent dosimeter, Health Phys 16(1) (1969) 1-7.
[6] S.W. McKeever, M. Moscovitch, P.D. Townsend, Thermoluminescence dosimetry materials: properties and uses, (1995).
[7] E. Bulur, H.Y. Goksu, OSL from BEO ceramics: New observations from an old material, Radiation Measurements 29(6) (1998) 639-650.
[8] M. Sommer, J. Henniger, Investigation of a BeO-based optically stimulated luminescence dosemeter, Radiat Prot Dosimetry 119(1-4) (2006) 394-7.
[9] M. Sommer, A. Jahn, J. Henniger, Beryllium oxide as optically stimulated luminescence dosimeter, Radiation Measurements 43(2-6) (2008) 353-356.
[10] A. Jahn, M. Sommer, W. Ullrich, M. Wickert, J. Henniger, The BeOmax system – Dosimetry using OSL of BeO for several applications, Radiation Measurements 56 (2013) 324-327.
[11] D.R. Vij, N. Singh, Thermoluminescence dosimetric properties of beryllium oxide, J Mater Sci 32(11) (1997) 2791-2796.
[12] V. Altunal, V. Guckan, A. Ozdemir, N. Can, Z. Yegingil, Luminescence characteristics of Al-and Ca-doped BeO obtained via a sol-gel method, J Phys Chem Solids (2019).
[13] V.S. Kortov, I.I. Milman, A.I. Slesarev, V.S. Kijko, New Beo Ceramics for Tl Esr Dosimetry, Radiat Prot Dosim 47(1-4) (1993) 267-270.
[14] V.S. Kortov, I.I. Milman, Luminescence properties of transparent BeO:Li ceramics, Radiat Prot Dosim 65(1-4) (1996) 355-358.
[15] V. Pustovarov, V.Y. Ivanov, M. Kirm, A. Korotaev, A. Kruzhalov, G. Zimmerer, E. Zinin, Time-resolved luminescent VUV spectroscopy of F-and F+-centres in single BeO crystals, Nuclear Instruments and Methods in Physics Research Section A: Accelerators, Spectrometers, Detectors and Associated Equipment 470(1) (2001) 353-357.
[16] I.N. Ogorodnikov, M.D. Petrenko, V.Y. Ivanov, Low-temperature luminescence and thermoluminescence from BeO:Zn single crystals, Optical Materials 62 (2016) 219-226.
[17] V. Altunal, Z. Yegingil, T. Tuken, T. Depci, A. Ozdemir, V. Guckan, N. Nur, K. Kurt, E. Bulur, Optically stimulated luminescence characteristics of BeO nanoparticles synthesized by sol-gel method, Radiation Measurements 118 (2018) 54-66.
[18] S.V. Nikiforov, I.G. Avdyushin, D.V. Ananchenko, A.N. Kiryakov, A.F. Nikiforov, Thermoluminescence of new Al2O3-BeO ceramics after exposure to high radiation doses, Appl Radiat Isotopes 141 (2018) 15-20.
[19] X. Wang, R. Wang, C. Peng, T. Li, B. Liu, Synthesis and sintering of beryllium oxide nanoparticles, Progress in Natural Science: Materials International 20 (2010) 81-86.
[20] M. Zahedifar, M. Mehrabi, M. Modarres, S. Harooni, Thermoluminescece properties of BeO: Mg nanoparticles produced by sol-gel method, Journal of Nanostructures 1(3) (2011) 199-203
.

6th International Conference on Materials Science and Nanotechnology For Next Generation (MSNG2019)
October 16-18, 2019, Niğde, TURKEY (ORAL FULL TEXT)

Structural and Optical Properties of ZnO Grown By Spin Coating Method Using Different Substrates

Mehmet Selim ASLAN[1], Mustafa AKYOL[2], Ahmet EKİCİBİL[1]

[1]Department of Physics, Art and Science Faculty, Çukurova University, Adana, Turkey
[2]Department of Materials Engineering, Faculty of Engineering, Adana Alparslan Türkeş Science and Technology University, Adana, Turkey

In this study, ZnO was grown with spin coating method which is simple to apply by using different substrates such as ITO and silicon. ZnO, a low cost transparent and conductive semiconductor, has a wide band gap energy of 3.37 eV and a high binding energy of 60 meV, which are very suitable for optoelectronic applications. The morphological, structural and optical characteristics of ZnO thin films were examined by SEM, XRD and UV-Vis spectroscopy. The surface and cross-section images of the obtained ZnO thin films prove that the thin films are uniformly distributed over the entire surface and that the thin films are approximately 800 nm thick. XRD results showed that the sharpness of the peaks is a sign of high crystallinity. Optical results show that the transmission of the thin films produced is quite high.

Keywords: Semiconductors, Thin Films, Spin Coating Method, Zinc Oxide (ZnO).

Corresponding author: mehmetselimaslan34@gmail.com

1. Introduction

In this study, Zinc Oxide (ZnO) thin films were grown on different substrates such as Si and glass by using spin coating method. The optical and structural properties of the thin films were examined by using XRD, SEM and UV-VIS mechanisms. ZnO is an important semiconductor material with a wide band gap of 3.37eV and a large exciton binding energy of about 60 meV. ZnO has a n type electrical conductivity from the Zn atoms in the interstitial sites and oxygen vacancies. Because of its remarkable physical properties. Zinc oxide has been used in many applications such as gas sensors [1,2], transparent conductor electrode in solar cells [3,4], light emitting diodes [5,6] and in spintronic where it is used as a functional DMS (Diluted Magnetic Semiconductor) [7].

We preferred the spin coating method as well as the methods commonly used in this study, such as vacuum evaporation [8], electrochemical deposition [9-11], reactive sputtering [12], thermal and chemical oxidation [13], Molecular beam epitaxy [14], sputtering [15].



Figure 1. *Spin Coating Device*

2. Experimental details

ZnO thin films were produced by using spin coating method which is simple to apply using different substrates such as Si and Glass. Firstly, the substrates were cut to the desired dimensions and after cleaning, coating process was realized. Spin coating process was performed by spinning the substrates at 500 rpm for 5 second and 3000

rpm for 55 second. Spin coated samples were dried on a hot plate at 200 °C for 10 minutes to evaporate solvent and stabilizer residues. After coating and drying, it was annealed for 1 hour at 450 ° C. Spin coating and drying processes were repeated three times to obtain sufficient film thickness.

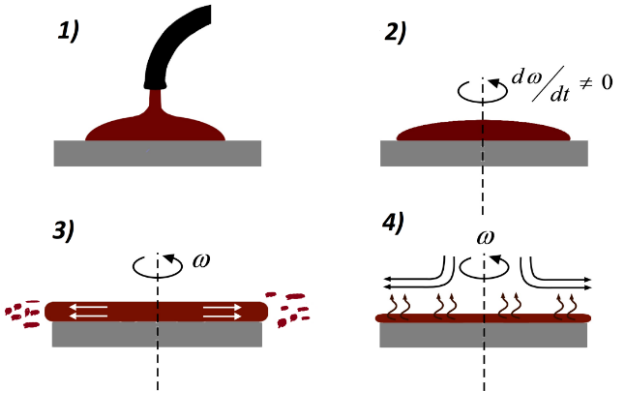


Figure 2. *Phases of spin coating method: 1) Phase of instillation of solution to surface, 2) Acceleration phase, 3) Phase of dissolution of solution to whole surface, 4) Evaporation phase.*

The spin coating method can be examined in four main parts as shown in Figure 2. In the first stage, the solution is dripped onto the ITO coated glass. In the second step, the material is rotated on the z-axis with the previously set rotation speed. In the third stage, the solution can be explained as the spreading of the solution to the surface after the dripping and rotating operations. In the last stage, the solvent evaporates homogeneously over the entire surface area. The process is repeated several times to obtain the desired thickness. In addition, the rotational speed is another important parameter in terms of coating thickness.

3. Results and discussion

The structure of the ZnO thin films were examined by X-ray diffraction (XRD) and then using Scherrer's formula the crystal size of this thin films was calculated.

$$D = \frac{0{,}9\lambda}{\beta cos\theta}$$

D is the average crystallite size (diameter), λ = 0.15406 nm, β is the full width at half-maximum (FWHM, rad), and θ is the Bragg angle (°). The average crystallite size of ZnO and Cu_2O were found as 28.61 and 32.25 nm, respectively.

Table 1. *Crystal sizes of ZnO Thin Films*

Samples Number	Angle 2θ (°)	D (nm)	FWHM (deg)
MSA-4	31.5519	28.35	0.2558
MSA-4	34.2049	26.21	0.3070
MSA-4	36.0422	24.91	0.2814
MSA-5	31.6983	28.22	0.2047
MSA-5	34.3491	26.10	0.2303
MSA-5	36.2026	24.81	0.3070

Using Scherrer's formula, we calculated the average crystal size of ZnO thin films to be approximately 28 nm.

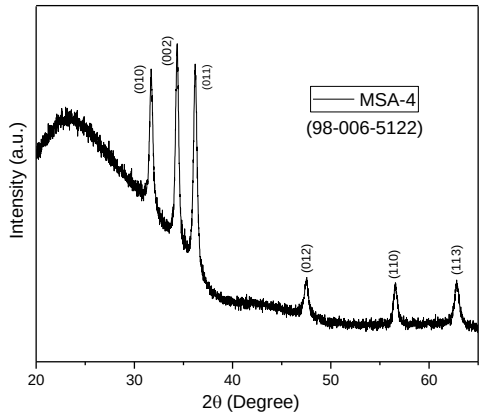


Figure 3. *XRD pattern of ZnO thin films coated on the glass substrate.*

Figure 3 shows the XRD pattern of the ZnO thin film coated on the glass substrate. All peaks belong to ZnO and match the JPDS card number (98-006-5122).

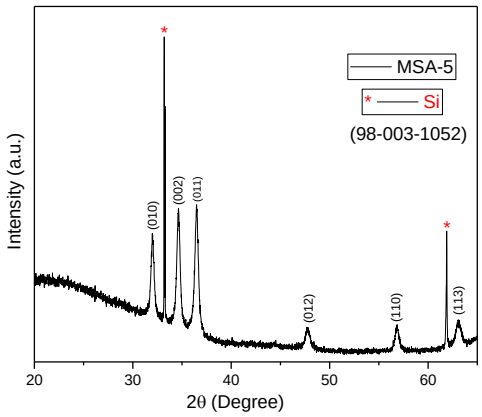


Figure 4. *XRD pattern of the ZnO coated on the Si substrate.*

The XRD pattern of ZnO coated on the Si substrate is given in figure 4. 2θ=33,11 and 2θ=62,38 peaks belong to Si and the other peaks belong to ZnO.

Morphology of the thin films are investigated by Scanning Electron Microscopy (SEM). According to the results obtained, it was observed that the coatings had a very homogeneous structure.

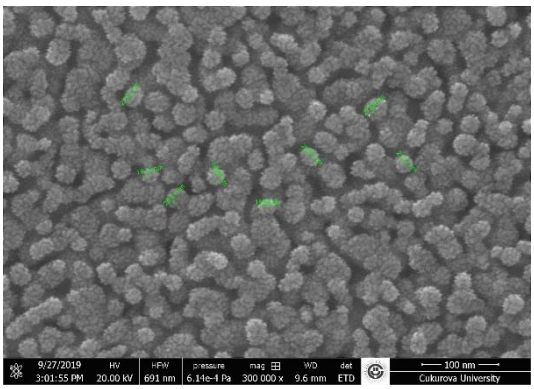


Figure 5. *Typical view SEM images of ZnO coated on the glass substrate.*

Figure 5 shows the SEM image of the ZnO thin films coated on the glass substrate. The grains diameter was approximately between 20 nm and 30 nm.

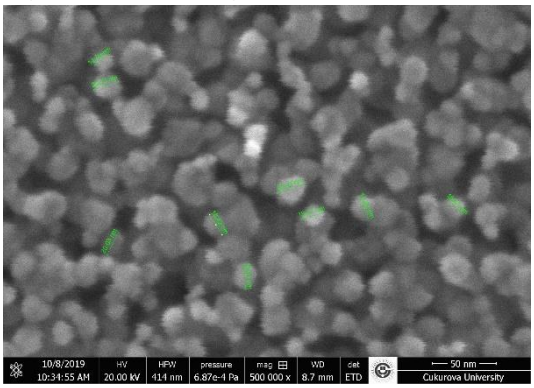


Figure 6. *Typical view SEM images of ZnO coated on the Si substrate.*

The SEM image of ZnO coated on the Si substrate is given in figure 6. The grains diameter was approximately between 15 nm and 25 nm.

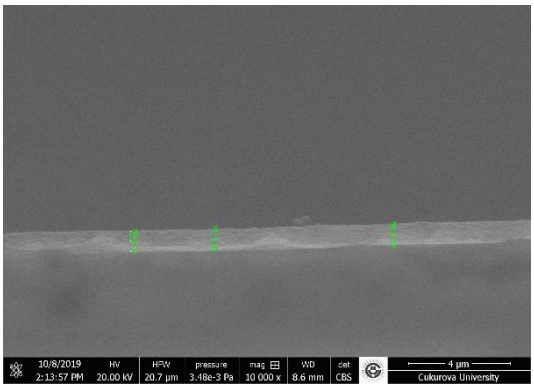


Figure 7. *Typical view cross-section SEM images of ZnO deposited on the Si substrate*

Figure 7 shows the cross-section view of the ZnO thin film coated onto the Si substrate. In the cross-section view, with a thickness of around 800 nm. This result clearly shows how homogeneous the film is distributed over the whole surface.

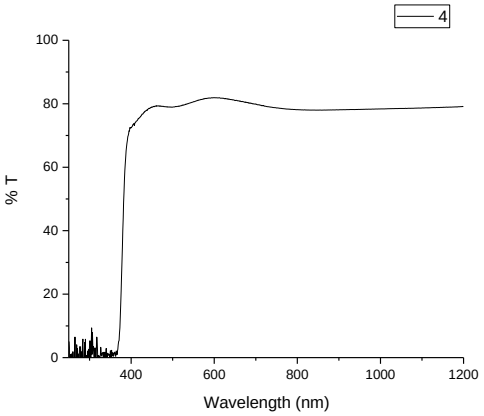


Figure 8. *UV-VIS transmittance spectra of ZnO thin films coated on the glass substrate.*

The optical properties of the coated samples were obtained by measuring the transmittance and absorbance at room temperature in the wavelength range of 380-1100 nm. It was observed that as thin film thickness increased, transmissions decreased. As you see in Figure 8. The transmission of ZnO films produced is about 80%.

4. Conclusion

In conclusion, the ZnO thin films were successfully grown on the Si and glass substrates by using spin coating method which is very simple to apply. Structure, morphological and optical properties of the thin films were investigated by using SEM, XRD and UV-VIS mechanisms. According to SEM results, the particle sizes of the coatings were between 20-30 for the glass substrate and between 15-25 for the Si substrate. The thickness of the ZnO thin films was determined about 800 nm by cross-section measurement. UV-VIS results show that the transmittance of ZnO thin films is about 80%.

5. Acknowledgement

I would like to thank the Çukurova University Central Research Laboratory (ÇÜMERLAB).

References:

[1] D.C. Look, D. Reynolds, C. Litton, R. Jones, D. Eason, G. Cantwell, Characterization of homoepitaxial p-type ZnO grown by molecular beam epitaxy, Appl. Phys. Lett., 81, 1830-1832, (2002).
[2] Q. Zhang, C. S. Dandeneau, X. Zhou and G. Cao, ZnO Nanostructures for Dye-Sensitized Solar Cells, Advanced Materials. 21, 4087–4108 (2009).
[3] Y.I. Alivov, E. Kalinina, A. Cherenkov, D.C. Look, B. Ataev, A. Omaev, M. Chukichev, D. Bagnall., Fabrication and characterization of n-ZnO/p-AlGaN heterojunction light-emitting diodes on 6H-SiC substrates, Appl. Phys. Lett., 83, 4719-4721, (2003).
[4] J. A. Anta, E. Guillén, R. Tena-Zaera, ZnO-based dye-sensitized solar cells, Journal of Physical Chemistry C. 116 11413 (2012).
[5] A. N. Afaah, Z. Khusaimi, M. R. Mahmood, A Review on Zinc Oxide Nanostructures: Doping and Gas Sensing, Advanced Materials Research 667, 329-332 (2013).
[6] R. Ahmad, N. Tripathy, Y. Hahn, High-performance cholesterol sensor based on the solution-gated field effect transistor fabricated with ZnO nanorods, Biosensors and Bioelectronics 45, 281 (2013).
[7] S. J. An, G. Yi, Near ultraviolet light emitting diode composed of n-GaN/ZnO coaxial nanorod heterostructures on a p-GaN layer, Applied Physics Letters, 91,123109 (2007).
[8] K. P. Muthe, J. C. Vyas, S.N.Narang et al., "Astudy of the CuO phase formation during thin film deposition by molecular beam epitaxy," Thin Solid Films, 324, 37–43, (1998).
[9] P. DeJongh, D. Vanmaekelbergh, J. Kelly, Cu_2O: electrodeposition and characterization, Chem. Mater. 11, 3512–3517 (1999).
[10] A. K. Mukhopadhyay, A. Chakraborty, A. Chatterjee, S. K. Lahiri, Galvanostatic deposition and electrical characterization of cuprousoxide thin films, Thin Solid Films, 209, 92–96 (1992).
[11] S. Jeong, A. Mittiga, E. Salza, A. Masci, S. Passerini, Electrodeposited ZnO/Cu_2O heterojunction solarcells, Electrochim.Acta, 53, 2226–2231 (2008).
[12] S. Ghosh, D. K. Avasthi, P. Shah et al., "Deposition of thin films of different oxides of copper by RF reactive sputtering and their characterization," Vacuum, 57,377–385 (2000).
[13] M. T. S. Nair, L. Guerrero, O. L. Arenas, and P. K. Nair, "Chemically deposited copper oxide thin films: structural, optical and electrical characteristics," Applied Surface Science, 150, 143–151 (1999).
[14] T. Oshima, M. Nohara, T. Hoshina, H. Takeda, T. Tsurumi, Characterization of Cu_2O thin film grown by molecular beam epitaxy, Key Eng. Mater., 582, 157–160 (2014).
[15] S. Ishizuka, T. Maruyama, K. Akimoto, Thin-film deposition of Cu_2O by reactive radio-frequency magnetron sputtering, Jpn. J. Appl. Phys., 786, 39 (2000).

6th International Conference on Materials Science and Nanotechnology For Next Generation (MSNG2019)
October 16-18, 2019, Niğde, TURKEY (ORAL FULL TEXT)

The Effect of Iron Nanoparticles on Methane Yield in Anaerobic Treatment

O. B. Gokcek*, H. Muratçobanoğlu*, R. A. Mert* and S. Demirel*

* Department of Environmental Engineering, Faculty of Engineering, Nigde Omer Halisdemir University, TURKEY

Along with the development of industry, a large amount of fossil fuels is consumed which caused climate change and deficiency of energy, thus human begins to quest for renewable energy sources that lessen greenhouse gases emission. Therefore, Bioenergy with low greenhouse gas emission and lower price which meets growing energy demand plays a important role in promoting renewable alternatives. As renewable bioenergy, methane can be generated under anaerobic conditions from various substrates. Anaerobic process; high concentrations of biodegradable substrates are removed and the use of methane in the produced biogas is a biochemical process with the advantages of energy recovery. The anaerobic disintegration process consists of four stages involving different microorganisms. These steps are hydrolysis, acidogenesis, acetogenesis and methanogenesis, respectively. In the first stage of hydrolysis, complex molecules such as protein, carbohydrate and fats are converted into amino acid, monosaccharide and fatty acids which are monomers. The monomers of organic compounds, the final product of the hydrolysis step, are introduced into the second step, acidogenesis, and are converted by the acidogenic bacteria into volatile fatty acids, ketones, alcohols, hydrogen and carbon dioxide products. Acetogenesis, which is the previous step before methane production, products produced during the acidogenesis stage and which cannot be used directly by the archaeological group, are converted by acetic acid, hydrogen and carbon dioxide, which are the main substrates of archaea. The biogas produced during the methanogenesis stage, which is the final stage of anaerobic disintegration, generally consists of 48-65% methane, 36-41% CO2, 17% nitrogen, and 1% hydrogen sulfide-like gases. Anaerobic disintegration technology widely used at industrial wastewaters with high organic pollution, complex wastewaters containing resistant chemical components, treatment sludges, wastewater at thermophilic temperatures, and in recent years has been widely used in the decomposition of urban and industrial organic solid wastes. Supplement of additives, such as mineral nutrients, metal oxide nanoparticles, bioaugmentation, and enzyme, stimulates methane production as well as improves process stability. Because many bacteria have developed pathways to obtain iron in the form of nutrients or electronic acceptor/donor, the iron is vital to the living organisms. Iron nanoparticles (Fe^0/Fe_2O_3/Fe_3O_4) have created an enhanced anaerobic environment with low H_2 content (or partial pressure) as well as low oxidation-reduction potential after being added to the anaerobic digestive system. As the electron donors for AD system, iron nanoparticles can not only accelerate sludge hydrolysis-acidogenesis but also change the fermentation type to increase the acetic acid concentration and ultimately promote methane yield. In this study, the effects of iron nanoparticles used in literature on methane yield in anaerobic treatment process were discussed.

Keywords: Iron nanoparticle, Anaerobic treatment, Methane, Renewable bioenergy

Corresponding author: begumgokcek@ohu.edu.tr

1. Introduction

In the world and in our country, energy demand is constantly increasing due to population growth and technological advances. Energy is an indispensable resource for meeting basic human needs. Today, renewable energy sources have been brought to the agenda in order to meet the increasing energy needs of societies in a reliable, uninterrupted and clean manner. It is possible to produce efficient, low cost and continuous production from renewable energy sources with developing technological innovations. In addition, renewable energy sources make significant contributions to national economies today. In this context, studies on renewable energy production with natural resources (solar, wind, hydro) and biofuels (biogas, biodiesel, bioethanol) have increased in recent years [1].

Biogas; It is the energy source formed by fermentation of organic substances in airless environments. Biogas, which contains 60-70% methane, 30-40% carbon dioxide and small amounts of hydrogen sulfide, hydrogen, carbon monoxide and nitrogen, is a colorless and flammable gas mixture [2].

Biogas, a biofuel; It is a clean, environmentally friendly and highly efficient energy source obtained by processing all kinds of organic waste [3]. Biogas production is possible by decomposing organic parts of domestic, animal, urban, industrial and agricultural wastes in anaerobic environment. Bioenergy has attracted the attention of many scientists and researchers who have tried to produce innovative solutions for the last decade. Nanotechnology is one of the emerging branches of science and it deals with materials having one of the dimensions less than 100 nm. Nanotechnology can be applied in bioenergy field for the purpose of feedstock modification and catalysis that is more efficient. Nanomaterials include nanoparticles (NPs), nanofibers, nanotubes; nanosheets and others have been employed for bioenergy production [4]. NPs have a high surface to volume ratio, which increases the chemical reaction sites. It is generally hypothesized that trace metals increase in biogas production during anaerobic digestion [5]. Trace metals worked as an electron donor in an anaerobic digestion process. They increase the total consumption of hydrogen methanogens and activity. NPs such as iron, cobalt and nickel have been reported that were successfully increasing the production of methanogens in digester sludge [6]. Iron itself is a non-toxic and low-cost electron donor that can be applied to numerous redox reactions [7].

The AD process is carried out by a serial of biochemical processes. In this process, bacteria and methanogens co-work together by means of electron transfer to obtain energy. The electron transfer can be done indirectly (Indirect interspecies electron transfer = IIET) or directly (Direct interspecies electron transfer = DIET). In recent years, studies have been carried out to increase the DIET between bacteria and methanogens by using conductive materials such as iron nanoparticles.

Abdelsalam et al. [8] found that the addition of Fe NPs (20 mg L−1) and Fe3O4 NPs (20 mg L−1) in AD of cattle slurry significantly increased the biogas yield by 1.5 and 1.7 times, respectively. Juntupally et al. [9] reported that addition of Fe2O3 NPs (12.5 mg L−1) enhanced methane production by 1.7–1.8 times. Wang et al. [10] found that the presence of 10 mg/g total suspended solids (TSS) nano zerovalent iron and 100mg/g TSS Fe2O3 NPs increased methane production in AD of waste activated sludge. A certain amount of iron nanoparticles can increase the biogas yield of the sludge AD system. However, the methanogenic effect of the system will decrease when the iron nanoparticles dosage exceeds the tolerance range of the methanogen [11]. In this study, the effects of iron nanoparticles used in literature on methane yield in anaerobic treatment process were discussed.

2. Effect of Biogas Yield

The iron homeostasis is critical mechanism for archaea microorganisms, as for all forms of life. In fact, Fe^{2+} and Fe^{3+} ions are essential for power generation and DNA replication, amongst other vital functions [12]. Nano iron particles can exhibit unique physical and chemical properties due to their small sizes and high specific area [13]. Because of this point, nano-sized iron particules have been widely investigated as a metallic additive in the field of anaerobic digestion [14]. According to implementation dosage, nano-sized iron based particles (1-100 nm) as additive could have negative or positive effect on anaerobic digestion processes [15].

Ali et al. [16] studied the effects of Fe_3O_4 on the AD of municipal solid waste under mesophilic conditions. Results showed that Fe_3O_4 caused the enhancement of methane production rate up to 117%. Also, Su et al. [17] and Liu et al. [17] concluded that the addition of iron-based nanoparticles could provide resistance against the formation of hydrogen sulfide (H_2S) and increased stability by pH buffering. According to Romero-Guiza et al. [22], enhanced methane yields were reported for all Fe additions (Fe^0/Fe_2O_3/Fe_3O_4). Their study showed that the

reduction of the Fe(III) oxides on the surface promoted microbial hydrolysis-acidification of complex matters, and therefore provided more organic matter for methanogenesis and more biogas production.

Casals et al. [12] controlled the dosage of Fe^{+2}/Fe^{+3} ions during an AD process. Results showed that the Fe_3O_4NPs (100 ppm of 7 nm) dispersed in the reactor and gradually dissolved in form of Fe^{+2}/Fe^{+3}acting as effective elements. Therefore, the concentration of Fe^{+2}/Fe^{+3} ions in optimal range during the AD process and boost the bacterial activity leading to 180% higher biogas production rate during the process. Note that results show not only an enhancement of biogas production, but also that this is richer in methane (8% more CH_4 respect controls in the final measure) [15].

Nanoscale zero-valent iron (NZVI) has been widely investigated as a metallic additive in the field of biogas production. Suanon et al. [18] showed that the application of 100 mg/L NZVI (160 nm) in batch reactors enhanced the methane production up to 25.2%. The effects of NZVI on the archaea during the anaerobic digestion of raw manure in a batch reactor were also investigated by [20-21] They reported that addition of 20 mg/L of NZVI to biodigester stimulates the methanogenic archaea and increases its activity and subsequently increasing biogas and methane production up to 45 and 59%, respectively. On the contrary, Yang et al. [19] showed that NZVI NPs(55 nm) with a concentration of 1 mM (56 mg/L) inhibited methanogenesis more than 20% during the anaerobic digestion process since iron, despite of being essential, at higher concentrations, is toxic.

3. Conclusion

For optimal biogas production, it is crucial to coordinate complex microbial processes in anaerobic reactors. Researches have shown that; controlling the DIET mechanism is an important strategy for anaerobic disintegration of organic wastes. NPs used for this purpose seem to be able to promote DIET-based electron transfer between bacteria and methanogens. In this study, effects of iron NPs on AD performance were reviewed. The influence of adding iron NPs on biological waste treatments was highlighted. The mechanisms including the DIET on AD were addressed. The research needs on the proper use of iron NPs to have enhanced AD without adverse impact to the involved microorganisms and the environment were discussed.

References:

[1] ZHANG, L., LOH, K-C., ZHANG, J. 2019. Enhanced Biogas Production from Anaerobic Digestion of Solid Organic Wastes: Current Status and Prospects. Bioresource Technology Reports, 5, 280-296.

[2] HAMED, M., EL-MASHAD, ZHANG, R., 2010. Biogas Production From Co-Digestion Of Dairy Manure And Food Waste. Bioresource Technology 101 (11), 4021-4028.

[3] LIN, R., CHENG, J., ZHANG, J., ZHOU, J., CEN, K., MURPHY JD., 2017. Boosting Biomethane Yield And Production Rate With Graphene: The Potential Of Direct Interspecies Electron Transfer In Anaerobic Digestion. Bioresource Technology, 239, 345-352.

[4] ANTONİO F, ANTUNES F, GAİKWAD S, Ingle Ap. Nanotechnology For Bioenergy And Biofuel Production. Green Chem. Sustain: Technol., Springer International Publishing; 2017. P. 3e18.

[5] GANZOURY MA, ALLAM NK. Impact Of Nanotechnology On Biogas Production: A Mini-Review. Renew Sustain Energy Rev 2015;50:1392e404.

[6] KRONGTHAMCHAT K, RİFFAT R, DARARAT S. Effect Of Trace Metals On Halophilic And Mixed Cultures İn Anaerobic Treatment. Int J Environ Sci Technol 2006;3:103e12.

[7] ZHANG, L., ZHANG, J., ZEHGN, G., DONG, H., CHEN, Y., HUANG, C., ZHU, Y., XU, R., CHENG, Y., HOU, K., CAO, W., FANG, W., 2018a. Multivariate Relationships Between Microbial Communities And Environmental Variables During Co-Composting Of Sewage Sludge And Agricultural Waste İn The Presence Of Pvp-Agnps. Bioresour. Technol. 261, 10–18.

[8] ABDELSALAM, E., SAMER, M., ATTİA, Y.A., ABDEL-HADİ, M.A., HASSAN, H.E., BADR, Y., 2016. Comparison Of Nanoparticles Effects On Biogas And Methane Production From Anaerobic Digestion Of Cattle Dung Slurry. Renew. Energy 2016 (87), 592 598.

[9] JUNTUPALLY, S., BEGUM, S., ALLU, S.K., NAKKASUNCHİ, S., MADUGULA, M., ANUPOJU, G.R., 2017. Relative Evaluation Of Micronutrients (Mn) And İts Respective Nanoparticles (Nps) As Additives For The Enhancedmethane Generation. Bioresour. Technol. 238, 290–295.

[10] WANG, T., ZHANG, D., DAİ, L., CHEN, Y., DAİ, X., 2016. Effects Ofmetal Nanoparticles On Methane Production From Waste-Activated Sludge And Microorganism Community Shift İn Anaerobic Granular Sludge. Sci. Rep. 6, 25857.

[11] YANG, Y., GUO, J., HU, Z., 2013. Impact Of Nano Zero Valent İron (NZVI) On Methanogenic Activity And Population Dynamics İn Anaerobic Digestion. Water Res. 47, 6790.

[12] CASALS, E., BARRENA, R., GARCIA, A., GONZALEZ, E., DELGADO, L., M. BUSQUETS-FIT, FONT, X., ARBIOL, J., GLATZEL, P., KVASHNINA, K., SANCHEZ, A., PUNTES, V., 2014. Programmed Iron Oxide Nanoparticles Disintegration In Anaerobic Digesters Boosts Biogas Production, Small, 10, 2801-2808.

[13] FERNÁNDEZ-GARCÍA, M., RODRIGUEZ, J.A., 2011. Metal oxide nanoparticles, Encycl. Inorg. Bioinorg. Chem.

[14] QIANG, H., LANG, D.-L., LI, Y.-Y., 2012. High-Solid Mesophilic Methane Fermentation Of Food Waste With An Emphasis On Iron, Cobalt, And Nickel Requirements, Bioresour. Technol., 103, 21-27.

[15] BANIAMERIAN HAMED., IISFAHANI P. G., TSAPEKOS P., ALVARADO-MORALES M., SHAHROKHI M., VOSSOUGHI M., ANGELIDAKIA I., 2019. Application Of Nano-Structured Materials In Anaerobic Digestion: Current Status And Perspectives, Chemosphere, 229, 188-199.

[16] ALI, A., MAHAR, R.B., SOOMRO, R.A., SHERAZI, S.T.H. 2017. Fe3O4 Nanoparticles Facilitated Anaerobic Digestion Of Organic Fraction Of Municipal Solid Waste For Enhancement Of Methane Production, Energy Sources, Part A Recover. Util. Environ. Eff., 39, 1815-1822.

[17] SU, L., SHI, X., GUO, G., ZHAO, A., ZHAO Y., 2013. Stabilization Of Sewage Sludge In The Presence Of Nanoscale Zero-Valent Iron (NZVI): Abatement Of Odor And Improvement Of Biogas Production, J. Mater. Cycles Waste Manag., 15, 461-468.

[18] SUANON, F., SUN, Q., LI, M., CAI, X., ZHANG, Y., YAN, Y., YU, C.-P., 2017. Application Of Nanoscale Zero Valent Iron And Iron Powder During Sludge Anaerobic Digestion: Impact On Methane Yield And Pharmaceutical And Personal Care Products Degradation, J. Hazard Mater., 321, 47-53.

[19] YANG, Y., ZHANG, C. & HU, Z., 2013. Impact Of Metallic And Metal Oxide Nanoparticles On Wastewater Treatment And Anaerobic Digestion. Environ. Sci. Proc. Impacts. 15, 39–48.

[20] ABDELSALAM, E., SAMER, M., ATTIA, Y.A., ABDEL-HADI, M.A., HASSAN, H.E., BADR Y., 2017. Effects Of Co And Ni Nanoparticles On Biogas And Methane Production From Anaerobic Digestion Of Slurry, Energy Convers. Manag., 141, 108-119.

[21] ABDELSALAM, E., SAMER, M., ATTIA, Y.A., ABDEL-HADI, M.A., HASSAN, H.E., BADR, Y., 2017. Influence Of Zero Valent Iron Nanoparticles And Magnetic Iron Oxide Nanoparticles On Biogas And Methane Production From Anaerobic Digestion Of Manure, Energy, 120, 842-853.

[22] M.S.ROMERO-GÜIZA J.VILA J.MATA-ALVAREZ J.M.CHIMENOS S.ASTALS., 2016 The Role Of Additives On Anaerobic Digestion: A Review., 38, 1486-1499

6th International Conference on Materials Science and Nanotechnology For Next Generation (MSNG2019)
October 16-18, 2019, Niğde, TURKEY (ORAL FULL TEXT)

The Wear Resistance Of Austenitic Stainless Steels Ceramic Coated By Thermal Spray Coating Method

U. Calıgülü[1], M. Türkmen[2], H. Durmuş[3] and Z. Aydeniz[4]

[1,4]Department of Metallurgy and Materials Eng, Faculty of Technology, Elazig, Turkey.
[2] Institute of Transportation Technology, Kocaeli, Turkey.
[3]Department of Metallurgy and Materials Eng, Faculty of Eng, Manisa, Turkey.

In this study, ceramic aluminum alloy Al2O3-13TiO2 oxide powder was coated on surface of substrate at different sizes (0-100 100 / 100-200 0 / 200-300) using plasma spray method on the surface of the commercially supplied AISI 304 and AISI 316L austenitic stainless steel. The powders used were the powders with chemical compositions Al2O3-13TiO2, TiO2 99%, and ZrO2 8Y2O3, respectively. In the coatings made with aluminum alloy, the coating thickness ranged between 180 and 300 µm. The difference in thickness of these coatings was realized to determine how corrosion and wear resistance varied depending on the thickness of the coating. After the coating process, the samples were subjected to metallographic processes (bakelite-sanding-polishing) and made suitable for mechanical and microstructure analysis. It was made based on pin-on disc method using CSM Tribometer for wear test of floor materials and coatings. It was determined that Al2O3 ceramic coatings made by using plasma spray coating method increased the wear resistance of AISI 304 and 316L stainless steel materials.

Keywords: AISI 304, AISI 316L, Al_2O_3, Thermal Spray Coating, Wear.

Corresponding author: zeliha.topcu06@hotmail.com

1. Introduction

Stainless steels are generally steels containing approximately 11% chromium in their composition. Due to this chromium content, a ductile, thin oxide layer which is attached to the surfaces with a great force is formed. Therefore, they are passivated against chemical environments. This oxide layer is a layer that is formed in environments containing oxygen and can regenerate itself in case of deterioration due to external factors. In addition to this chromium rate, the additions of nickel and molybdenum are also the factors increasing this corrosion resistance. In general, stainless steels are examined under 4 different groups according to their microstructures. These are named as ferritic, martensitic, duplex, and austenitic steels. The most commonly used types in austenitic stainless steels are AISI 200 and 300 series alloys. In addition, alloy additives and special alloy composition have a great influence on the weldability and microstructure of weld zone. AISI 300 series of these alloys generally contain 8-20% Ni and 16-25% Cr [1].

Due to their superior thermal, mechanical, chemical and electrical properties, ceramic materials are preferred in critical applications recently. The most common and easy-to-apply ceramic coating process is based on heating ceramic in powder form and spraying it on the substrate surface. Oxide ceramic coatings such as alumina (Al_2O_3), zirconia (ZrO_2) and chromia (Cr_2O_3) produced by thermal spray methods are widely used in many industrial applications requiring high wear resistance. Alumina is known as an expandable ceramic. It is a hard refractory material and a good corrosion resistant insulator. Moreover, it is an abundant raw material. Alumina is often used together with titania (TiO_2). As TiO_2 amount increases, the fracture toughness of the coating increases but its hardness along with wear resistance decreases. Therefore, a low amount of titania is preferred. Plasma sprayed alumina coatings are used in automotive industry to isolate metal substrates because of their high hardness and good electrical insulation properties. Electronic circuits are then manufactured on these coatings. Alumina coatings are also used in computer memory discs to

provide electrical insulation and form a wear-resistant surface [2].

Obtaining high heat with plasma makes it possible to use ceramic and metal based alloy powders having high melting point in coating applications. Ceramics are in an important coating material position because of advantages of its properties such as high wear and hardness properties, the prevalence and cheapness of its raw material, corrosion, oxidation, low thermal conductivity and high number of thermal cycles. Depending on the use of plasma energy, plasma spray coating technology allows the machinability (coating) of materials with high melting temperature as coating material [3-4].

According to DIN 50320 in 1979, wear is the undesired surface deformation caused by the separation of small particles from the surface by mechanical factors as a result of contact of materials used with other materials (solid, liquid, gas). Accordingly, in order to talk about wear, there must be friction, a change on material surface and a mechanical effect which is slow but continuous and occurs even though it is undesired [5]. Damages caused by wear causes high costs. The replacement of worn and thus unusable parts is an additional cost. Wear types include adhesive wear, abrasive wear, fatigue wear, and corrosion wear [6]. This classification is made by taking into account the factors such as the load applied to the worn surface, size and type of the abrasive particle, contact shape and contact geometry. The highest wear loss is usually seen in the abrasive wear type [7].

Special aluminum alloy (AA2024-T4) and Al bronze (Cu alloy) surface was coated with various oxide and carbide powders using atmospheric plasma spraying method. Microstructure, hardness, surface roughness, joint strength and thermal expansion properties of the coating layers obtained on the surface were examined [8]. Kaptan investigated the effect of primary and secondary plasma gases (Ar and H2) on microstructure and mechanical properties in WC-Co coating applied using plasma spray process [9]. Aslan produced biocompatible coatings formed with single-layer and double-layer powders using hydroxyapatite (HAP) and TiO2 powders with plasma spray coating method on the surfaces of AISI 316L stainless steel materials used as implant materials [10]. Kiper examined the wear behaviors of steel coatings in different quality formed with thermal spray method on aluminum under dry shear conditions [11].

In this study, commercially supplied AISI 304 and AISI 316 L austenitic stainless steels were coated with oxide mixture obtained by adding TiO_2 powders in Al_2O_3 and Al_2O_3 with different percentages and plasma spray method was used. It was aimed to improve the wear properties of the steel and minimize the wear losses with the coating to be made on the surface of AISI 304 and AISI 316L austenitic stainless steel.

2. Experimental method

AISI 304 and AISI 316L austenitic stainless steel materials commercially supplied in 500x1000 mm dimensions were cut into 20x20 mm dimensions with Ermaksan Brand laser cutting machine for wear tests. AISI 304 and AISI 316L austenitic stainless steels were coated with oxide mixture obtained with TiO_2 powders added into Al_2O_3 and Al_2O_3 at different percentages by using plasma spray method. It was coated with 50-µm thick Ni_20Cr powder as powder binder. Table 1 shows the chemical analyses of the materials and Table 2 shows powder properties of the sandblasted samples. Sulzer Metco Diamond Jet DJF (Figure 1) plasma spray system was used. Coating process was applied with Thermal Spray test device. Three coating thicknesses were applied for each material (Table 3)..

Material	Elements (% Weight)									
	C	N	Cr	Ni	Mn	Si	S	P	Mo	Fe
AISI 304	0.08	-	18-20	8-12	2	1	0.03	0.45	-	Remaining
AISI 316L	0.03	0.1	16-18	10-14	2	0.75	0.03	0.45	2-3	Remaining

Table 1. Chemical analysis of AISI 304 – AISI 316 materials

Oxide Powders	Powder Grain Size	Powder Morphology	Chemical Composition
Aluminum Oxide **Al_2O_3** Amdry 6220	-22+5µm	Angular	Al_2O_3 13TiO_2

Table 2. Properties of powder used in the experimental study

Material	0-100µm	100-200µm	200-300µm
AISI 304	N_1	N_2	N_3

AISI 316L	N_4	N_5	N_6

Table 3. The samples used in the experimental study



Figure 1. Thermal Spray Coating (Plasma) Unit

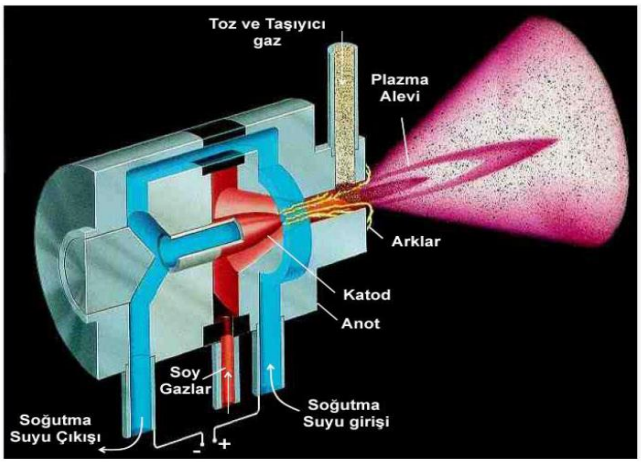


Figure 2. Thermal Spray Coating (Plasma) System [12].

For the wear test to AISI 304 and 316L austenitic stainless steels coated with ceramic powders, 5 N load was applied in the CSM Tribometer device. It was carried out at 15 cm/s wear rate, 500 m sliding distance, 20 °C temperature and 50% humidity level.

3. Experimental Results

3.1. Microstructure Examination

In the coatings made with aluminum alloy on surfaces, the coating thicknesses varying between 180- 300 µm were obtained. The difference in these coating thicknesses was thought to be associated with the fact that the plasma spray system was not automatic. Figure 3 shows micro images of N-Reference N_1, N_2, N_3, N_4, N_5 and N_6 samples provided with surface coating process made on the surface of AISI 304 and 316L austenitic stainless steel by using plasma spray method with ceramic Al_2O_3-13TiO_2.

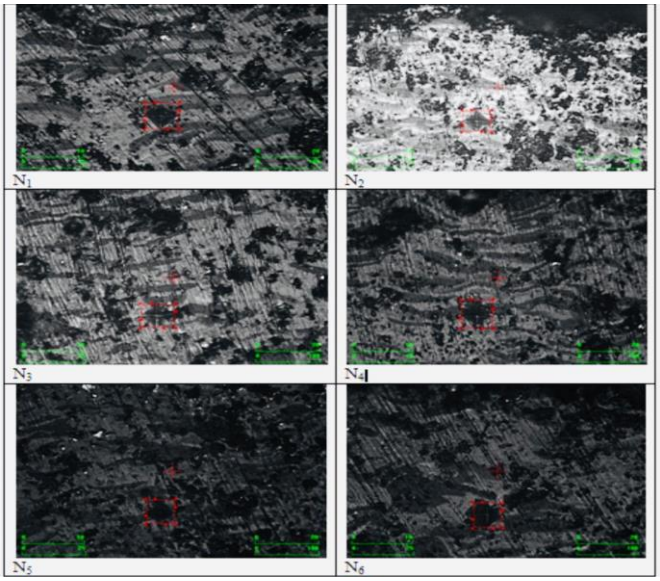


Figure 3. Microstructure images of N_1, N_2, N_3, N_4, N_5, N_6 samples

The photos show the optical microscope images of the coating made with plasma spray method. Oxide coatings made on AISI 304 and 316L austenitic stainless steels adhered homogeneously to the substrate. No factor that can cause any crack on the coatings and substrate material surface or a separation of the coating from the sample was observed. There were lamellar structures and porosities on the oxide coated surfaces. The observed lamellar structure was the regions deforming after molten Al_2O_3 alloy hit the substrate material and solidified.

3.2. Investigations of Microhardness Analysis

Figure 4 shows hardness values of the samples subjected to microhardness test.

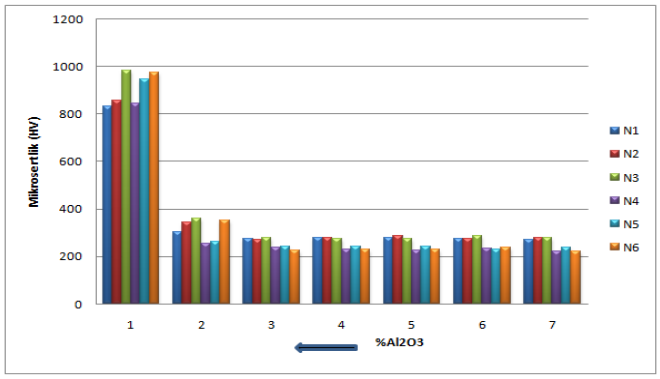


Figure 4. Microhardness values of the samples

In the measurement made from the coated material region, the hardness values were observed to be at maximum level. In this region, the hardness values of the samples N_3, N_5, N_6 were higher compared to the other samples. The arithmetic mean of the hardness values was around 900 HV.

In the measurement made on the coating area, namely the joint area, microhardness was observed to be higher compared to the hardness values taken from the main material of the sample. Again, in the hardness measurements in this area, a significant difference in microhardness of the samples N_3, and N_6 was also determined. The arithmetic mean of the hardness values was around 300 HV. The hardness in Al_2O_3 coated N_3, and N_6 samples was caused by the decrease in porosity amount and better resistance provided by oxides by forming new phases between themselves. In addition, the powder size of both Al_2O_3 coated N_3, and N_6 samples was 200-300 µm. Another reason for this increase was the powder size. The arithmetic mean of the hardness values of the substrate material was around 250 HV.

In the hardness measurement taken from the joint point of coating, the hardness values of AISI 316 L stainless steel were observed to be 50-80 HV lower than AISI 304 stainless steel.

3.3. Examination of EDS Analysis

As a result of EDS analysis taken from the surface of coated AISI 304 and 316 L stainless steel, it was determined that coatings formed on the surface. Figure 5 shows the EDS image and graph of the sample N_3.

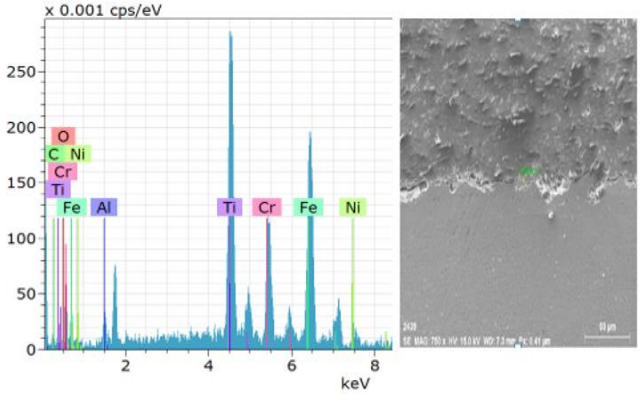


Figure 5. Point EDS analysis image and graph taken from the intermediate region of the sample N_3.

When the analysis images conducted at this point were examined, it was determined that the oxide structure had maximum peak in coating region and there were C and Al elements. When it comes to the substrate material from the coating, the element having the maximum peak was Ti. Besides, there were also Fe, Cr, and Ni elements. Figure 6 shows point EDS analysis image and plot taken from the joint point of the sample N_6.

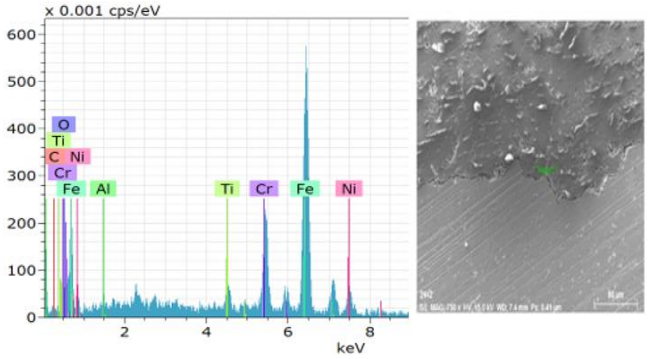


Figure 6. Point EDS analysis image and plot taken from the intermediate region of N_6 sample.

In the point EDS analysis taken from the substrate material of the sample N_6, the element making peak in the coating region was Ti. Apart from this value, the data of the sample N_3 were similar with the point EDS analysis taken from the base material.

3.4. Examination of XRD Analysis

Figure 7 shows the XRD plot showing phases and compounds of the sample N_3 among N-Reference samples. When XRD plot of the sample N_3 was

examined, there were phases such as Al_2O_3, Al_2Zr_3, Ti_3O_5, $NiAl_{32}O_{49}$, $Al_2Ti_7O_{15}$, AlNiZr, Cr_2O_3 and $NiCrO_4$ in coating layer. These compounds were seen to be oxide-containing compounds in general.

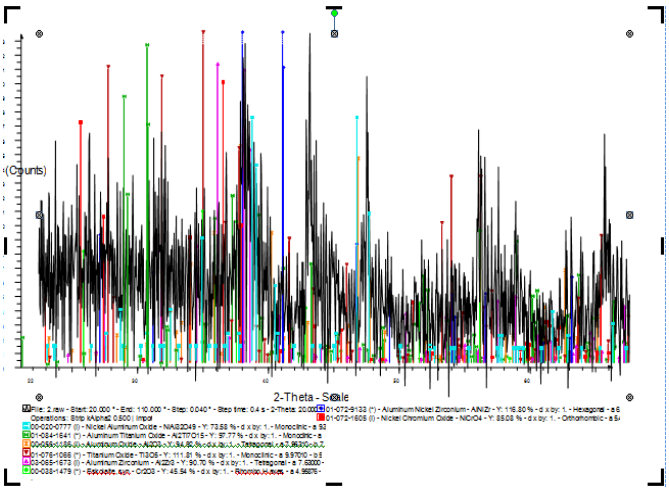
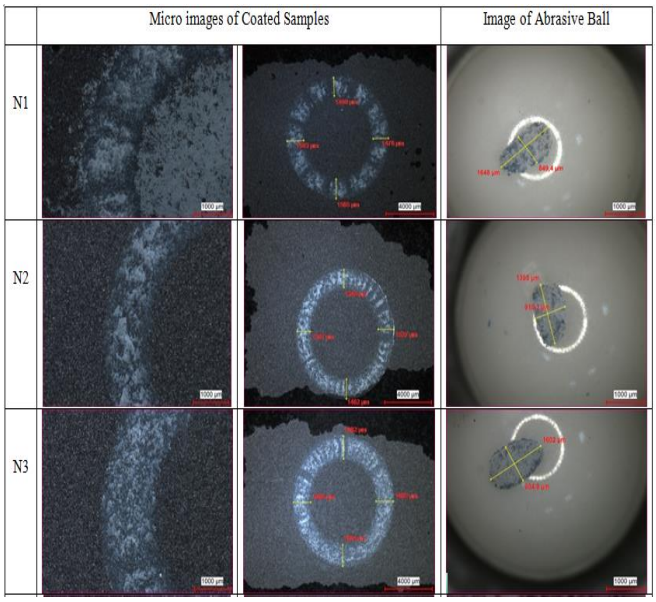


Figure 7. XRD plot showing phases and compounds of the sample N_3.

3.5. Wear Examination

Figure 8 shows optical images of the samples subjected to wear test.



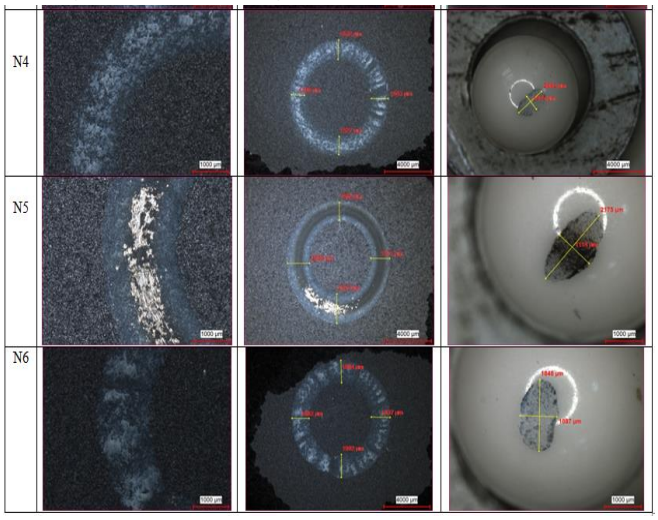


Figure 8. Optical images of the samples after wear test

When the wears forming on the surfaces of test samples subjected to wear test in wear test device and the ceramic balls used as abrasive were compared in terms of surface area, the wear measurements of AISI 304 steels varied between 1300-1600 µm and the trace measurements in the balls varied between 850-1650 µm. In AISI 316L steel, the wear measurements varied between 1300-2400 µm and the trace measurements in the balls varied between 1000-2650 µm. When these values were compared, AISI 304 steel was observed to show higher wear resistance compared to 316L steel.

Results and plots of N-Reference samples conducted on wear test device are shown below. Mass loss was measured in wear path periods in the samples N_1, N_2, N_3, N_4, N_5 and N_6 subjected to wear test under the same tribological conditions. Mass loss-number of turns of these samples are given in Table 4 and the corresponding plot is presented in Figure 9.

Table 4. Mass losses of the samples based on number of turns

Number of turns	1 x2000	2 x2000	3 x2000	4 x2000	5 x2000	6 x2000	7 x2000
N1	0.988	0.982	0.995	0.999	1.007	1.009	1.000
N2	0.496	0.739	0.976	0.991	0.991	1.027	1.009
N3	1.015	1.016	1.011	1.011	1.016	1.011	1.011
N4	1.087	1.091	1.085	1.082	1.084	1.079	1.076
N5	1.069	1.078	1.068	1.069	1.072	1.074	1.072
N6	1.086	1.087	1.085	1.083	1.080	1.086	1.082

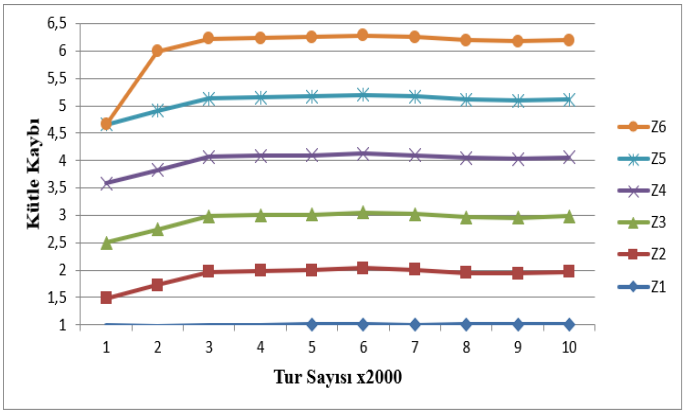


Figure 9. Mass losses of the samples based on the number of turns

In general, when the wear initiations depending on number of turns were examined in the plot, the sample N_1 was observed to have approximately constant mass loss in the first 4 (x2000) number of turns. It was observed that the sample N_1 moved up to 5th turn by increasing minimally after 4th turn and then exposed to a small but constant amount of mass losses. The mass losses of the samples N_2, N_3,N_4 and N_5 increased up to 3rd turn and there were ups and downs at minimal level in the following turns. It is observed that the mass loss in the sample N_6 increased rapidly in the 1st and 2nd turns, this mass loss increased more slowly in the turn range of 2-3 and there were ups and downs at minimal level in the next turns. Based on this behavior of the coated samples, it was thought that secondary and brittle phases formed depending on heat input and also a small amount of wear resistance decreased in the coating with the formation of these secondary phases.

4. General Conclusions

1. When the wear marks of the samples were examined, the widest wear mark was observed in the sample N_5 sample (2890 µm); whereas, the narrowest wear mark was observed in the sample N_2 sample (1348 µm).
2. Mass losses per turn were N2, N1, N3, N5, N6, and N4, respectively in ascending order. The results varied depending on the grain size.
3. It was determined that the coating process made with Al_2O_3 powders using Plasma Spray Coating method, one of the Thermal Spray Coating Methods, increased the wear resistance of AISI 304 and 316L austenitic stainless steels.

5. Acknowledgement

This study was supported by Firat University Scientific Research Projects (FUBAP) management unit (Project No: TEKF.18.11).

References:

[1] Ak, H.D., 2014, Geleneksel Toz Metalurjisi Yöntemiyle Üretilen AISI 304L ve AISI 316L Östenitik Paslanmaz Çeliklerin Özelliklerine Sinterleme Koşullarının Etkisi, Yüksek Lisans Tezi, İstanbul Teknik Üniversitesi, Fen Bilimleri Enstitüsü.

[2] Akın, U.,2003, Alüminyum Altlık Üzerine Isıl Püskürtme Yöntemiyle Kaplanan Seramik ve Seramik-Polimer Kaplamaların Aşınma Davranışlarının İncelenmesi, Yüksek Lisans Tezi, İstanbul Teknik Üniversitesi, Fen Bilimleri Enstitüsü.

[3] Lugscheider E.,Jokiel P., Plasmaspritzen-Verfahren, Anwendungen, Enteicklungen, Metal Heft 3, 230-235, 1993.

[4]Esschnauer H.,Lugscheider E., Fortschrittebeimthermisvhen Spritzen, Metal Heft 3, 218-224, 1985.

[5] Bourithis, L.,Papadimitriou, G.D., 2009.TheEffect Of Microstructureand Wear Conditions On TheWearResistance Of Steel Metal Matrix Composites Fabricated With PTA Alloying Technique.

[6] Timur, M., 2014. Otomotiv Fren Balatalarının Sürtünme Sonucu Oluşan Aşınma Direncinin ve Termal Etkileşiminin Otomatik Test Sistemi İle Tespit Edilmesi,Doktora Tezi, Trakya Üniversitesi Fen Bilimleri Enstitüsü, Edirne.

[7] Şimşek, M., 2014. Mikro Ark Oksidasyon İle Al2O3 Kaplanmış AA7075 Alaşımının Kuru ve Yağlı Şartlarda Sürtünme ve Aşınma Davranışının İncelenmesi, Doktora Tezi,Süleyman Demirel üniversitesi Fen Bilimleri Enstitüsü, Isparta.

[8] Özel S., Alüminyum Alaşımı ve Bronzu Yüzeyine Oksit ve Karbür Bileşiklerinin Plazma Sprey Yöntemiyle Kaplanmasının Araştırılması, Fırta Üniversitesi, Doktora Tezi, 1-5.

[9] Kaptan S., Plazma Sprey Gazlarının Tungsten Karbür Kaplama Özellikleri Üzerine Etkileri, Osmangazi Üniversitesi, Yüksek Lisans Tezi, 22-29.

[10] Aslan O., Plazma Sprey Yöntemiyle Tek ve Çift Katmanlı Kaplanan AISI 316 Çeliğinin Korozyon Davranışlarının İncelenmesi , Yüksek Lisans Tezi, Afyon

Kocatepe Üniversitesi Fen Bilimleri Enstitüsü, 2015.11-14.

[11] Kiper G., Alüminyum Üzerinde Isıl Püskürtme Yöntemiyle Oluşturulan Çelik Kaplamaların Aşınma Davranışlarının İncelenmesi, Yüksek Lisans Tezi, İstanbul Teknik Üniversitesi Fen Bilimleri Enstitüsü, 2003, 23-26.

[12] Smolka K., Thermisches Spritzen, DVS-Verlag, 2002,50-57

6th International Conference on Materials Science and Nanotechnology For Next Generation (MSNG2019)
October 16-18, 2019, Niğde, TURKEY (ORAL FULL TEXT)

The Effects of Natural Wollastonite on Mechanical and Durability Properties of Standard Mortars

Hatice Öznur ÖZ*, Hasan Erhan YÜCEL*, Muhammet GÜNEŞ*, Çağlar DUYMAZ*

* Nigde Omer Halisdemir University, Faculty of Engineering, Department of Civil Engineering, Nigde, TURKEY

Wollastonite an inert material includes mainly CaO and SiO_2. Wollastonite mineral has been used in concrete and mortar production due to its special acicular particle structure. In this study, natural wollastonite (NW) obtained from Balıkesir region of Turkey was used in the production of standard mortar (SM) in the ratios of 0%, 3%, 6%, 9% and 12% instead of cement. Compressive strength, flexural strength and ultrasonic pulse velocity (UPV) of SMs incorporating NW were measured at 28 and 90 days. In addition, to determine the effects on durability properties of SMs of NW, water sorptivity and rapid chloride permeability tests were performed at 28 and 90 days. The test results indicated that mechanical and durability performance of the SMs improved up to 3% replacement ratio of NW. NW does not have a dense acicular particle structure, therefore, increasing ratio of NW affected adversely the mechanical and durability properties of SMs.

Keywords: Natural Wollastonite, Standard Mortars, Mechanical and Durability Properties.

Corresponding author: mgunes@ohu.edu.tr

1. Introduction

Wollastonite (calcium-meta-silicate ($CaSiO_3$)) is an inert, white color and acicular micro fiber composed naturally of calcium oxide (CaO) and silica (SiO_2) in equal proportions (nearly 45%) [1, 2]. Wollastonite micro-fibers are characterized by loose acicular particles of non-uniform sizes with diameter typically [3]. The acicular particle structure of wollastonite microfibers are defined by their aspect ratio. Wollastonite is marketed as low aspect ratio (generally 5:1 or less) and high aspect ratio (generally 12:1 or more [4]. In addition, when the previous studies performed with production of wollastonite reported that the 20:1 aspect ratio for wollastonite is accepted as high [5]. Tensile strength of wollastonite varies from about 2700-4100 MPa and modulus of elasticity ranges between 300 and 530 GPa. Therefore, refined wollastonite microfibers are frequently used in plastics, ceramics, paints and are readily present commercially [3, 6-8]. In addition, previous studies indicated that wollastonite microfibers due to its acicular particle shape have been used as a reinforcing filler/material in cementitious composites (i.e., high strength concrete, concrete pavements, cement board) [2, 3, 9, 10]. High purity wollastonite is compatible with a hydrating cementitious system as it is chemically and temperature resistant. Due to wollastonite being an inert material, it has been think that it has no effect on the heat of hydration liberated during the hydration process [3, 11]. Moreover, wollastonite microfibers are founded as imbedded in cementitious materials achieved high stability without surface or bulk deterioration with time [12]. Kalla et al. [10] indicated that 15% wollastonite used instead of cement increased about 12% the compressive strength of concrete at 90 days. Moreover, Mathur et al. [13] reported that 10% wollastonite used instead of cement increased 28–35% the compressive strength of concrete at 28 and 56 days, respectively. According to the literature studies, wollastonite used instead of cement has been observed beneficial effects in terms of especially compressive strength on concrete/mortar. It is known that it is very important to use high volume of alternative cementitious materials to reduce the consumption volume of ordinary Portland cement due to its high carbon footprint [7]. Therefore, in this study, the effects on standard mortars (SMs) of wollastonite obtained from Balıkesir region of Turkey were investigated. Compressive strength, flexural

strength, ultrasonic pulse velocity, water sorptivity coefficient and rapid chloride permeability values of SMs were determined at 28 and 90 days.

2. Experimental details

In this study, CEM I 42.5 R ordinary Portland cement and natural wollastonite (NW) provided from Balıkesir Region was used in the design of mortar mixes. Physical and chemical properties of these materials are listed in Table 1. The particle size distributions, SEM images and XRD analysis of cement and NW are given in Figure 1, 2 and 3, respectively. Scarce acicular particle structure of NW proved to be wollastonite with XRD analysis can be seen from the SEM image. In addition, the standard sand called as the CEN reference sand was used in the SMs. CEN sand is round grain and contains silica in the ratio of about 98%.

Table 1. Physical and chemical properties of cement and NW.

Chemical Analysis (%)	Cement	NW
CaO	62.58	30.87
SiO_2	20.25	46.34
Al_2O_3	5.31	5.83
Fe_2O_3	4.04	6.05
MgO	2.82	2.97
SO_3	2.73	-
K_2O	0.92	0.09
Na_2O	0.22	-
Loss of Ignition	2.96	5.85
Specific Gravity	3.15	3.12
Blaine Fineness (m^2/kg)	326	-

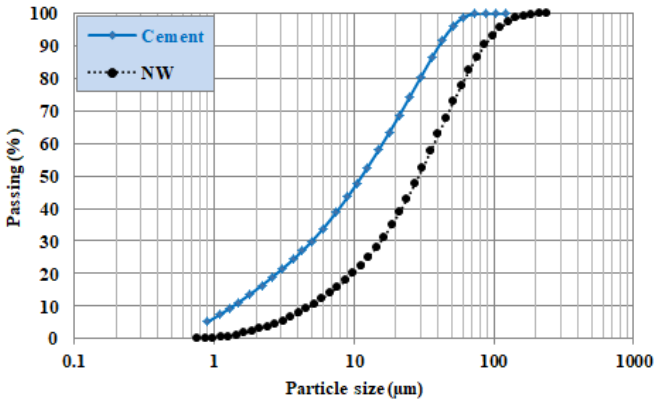
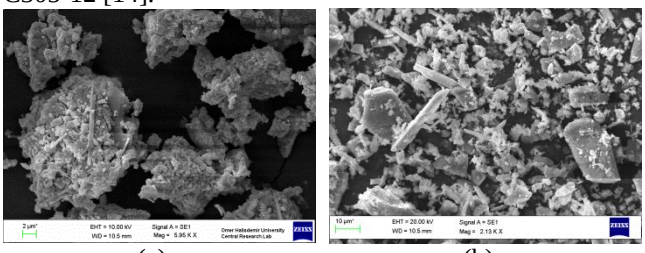


Figure 1. *The particle size distributions of cement and NW.*

All of SM mixes were listed in Table 2. NW was used at 3% increments instead of cement. Thus, SMs containing NW in the ratios of 0%, 3%, 6%, 9% and 12% were defined as SM0, SM3, SM6, SM9 and SM12, respectively. SMs were produced according to ASTM C305-12 [14].



(a) (b)

Figure 2. *SEM images of (a) cement and (b) NW samples*

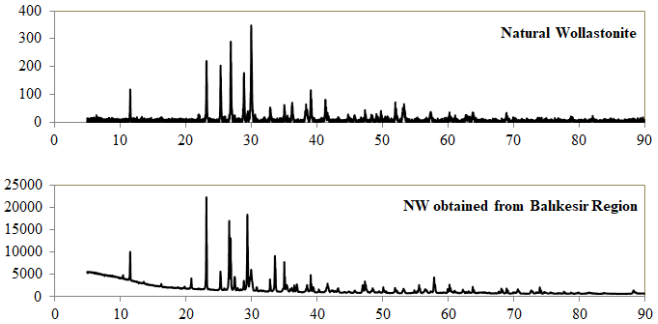


Figure 3. *XRD analyses of natural wollastonite and NW obtained from Balıkesir Region*

Table 2. Mix proportions of SM mixes (kg/m^3).

Mix	w/p*	Cement	NW	Water	CEN Sand	SDF*
SM0	0.48	500	0	242	1375	17.4
SM3	0.48	485	15	242	1375	16.9
SM6	0.48	470	30	242	1375	16.7
SM9	0.48	455	45	242	1375	16.6
SM12	0.48	440	60	242	1375	16.4

* w/p*: water/powder material (cement+NW), SDF*: slump flow diameter (cm)

Slump flow diameters of SMs were determined in accordance with ASTM C1437-15 [15]. The slump flow diameter of SMs is given in Table 2. Due to the acicular shape of NW reduced workability of SMs [7]. The compressive strength, flexural strength and UPV values of

the SM mixes were measured confirm to ASTM C349-14 [16], ASTM C348-14 [17] and ASTM C597-16 [18], respectively. The compressive test was applied to 6 pieces by using specimens broken in flexural test. The flexural and UPV tests were conducted on 3 prismatic specimens. The water sorptivity and rapid chloride permeability tests were applied on the three samples of 50 mm height and 100 mm diameter. In the water sorptivity test, firstly, the specimens were dried in oven at 100±5 °C through 24 h. Then, the sides of the specimens were coated with a waterproof material. The volume of water absorbed by the specimens was calculated and water sorptivity coefficients of SMs were determined. Rapid chloride permeability test was performed according to ASTM C1202 [19]. All test results were obtained by calculating the averages of results obtained from specimens. The tests were done at 28 and 90 days.

3. Results and discussion

Figure 4, 5 and 6 present compressive strength, flexural strength and UPV of SMs, respectively. The development of mechanical performance was influenced by NW content. SM incorporating 3% NW exhibited compressive strength, flexural strength and UPV higher than that of the control mixture at 28 and 90 days. This can be explained with the role of wollastonite in bridging the micro-cracks leading to a delay in micro-crack coalescence thanks to its acicular particle structure [3, 20]. However, this improvement in mechanical properties of SM reduced at higher NW content and thus, SM6, SM9 and SM12 exhibited lower mechanical performance than the control mixture at 28 and 90 days. This strength decrease can be attributed to higher contents of wollastonite indicating towards weak bond formation with increase in content of NW. [21, 22]. In addition, previous studies [20, 23] reported that mechanical properties of concrete/mortar improved up to 10% wollastonite content and after this value wollastonite decreased generally the mechanical performance of concrete/mortar. According to the data obtained in this study, the decrease of mechanical properties of SM mixes after 3% NW content can be explained by the fact that NW mineral does not have dense acicular structure as seen in Figure 2 [24].

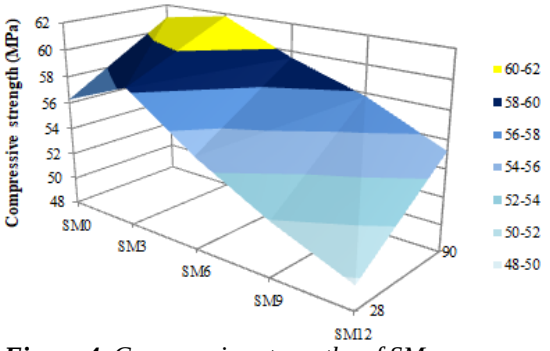


Figure 4. *Compressive strengths of SMs*

In Figure 7 and 8 the variation in water sorptivity coefficients and rapid chloride permeability of SMs are demonstrated. The durability performance of SM improved for the 3% content of the NW at 28 and 90 days. Similarly, Mathur et al. [13] reported that wollastonite reduced the water absorption percentage of concrete. Moreover, water sorptivity coefficients and rapid chloride permeability tested specimens of mixtures incorporating 6%, 9% and 12% NW was higher than that of SM0 mixture. This can be explained with the increased proportion of NW weakening the bond in the matrix and the inability to observe the acicular structure in most of the particles [22, 24].

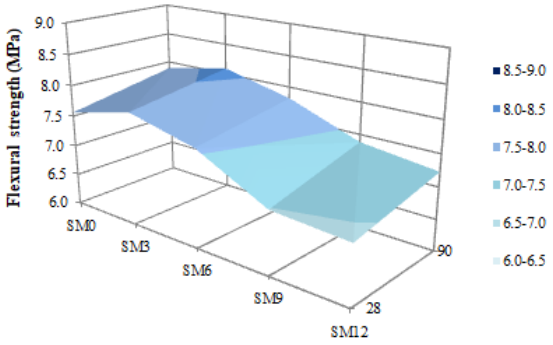


Figure 5. *Flexural strengths of SMs*

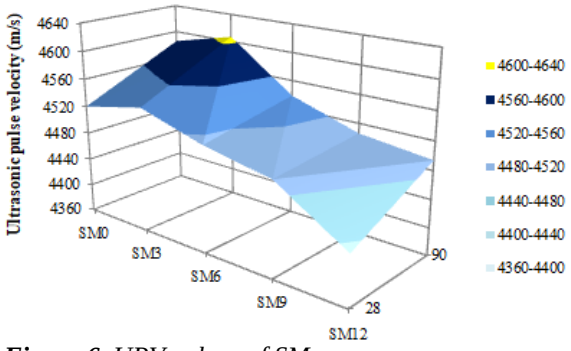


Figure 6. *UPV values of SMs*

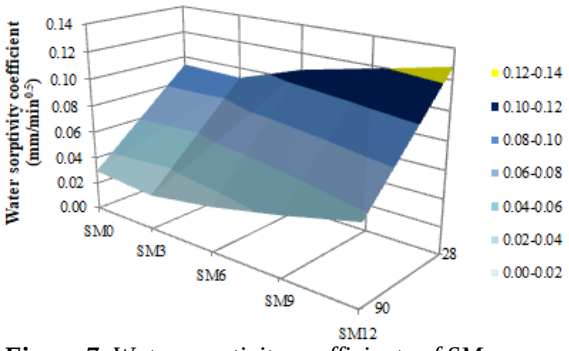


Figure 7. *Water sorptivity coefficients of SMs*

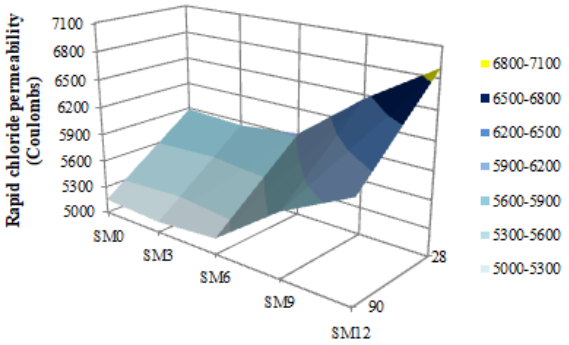


Figure 8. *Rapid chloride permeability values of SMs*

4. Conclusion

In this study, the effects of NW mineral obtained from Balikesir Region of Turkey on SMs were investigated in terms of mechanical and durability properties at 28 and 90 days. As a result of experimental studies, the following results were achieved.

- SM mixture incorporating 3% NW wollastonite exhibited higher mechanical and durability performance with respect to control mixture. This development can be attributed to acicular particle structure and thus, bridging feature of NW wollastonite. When NW wollastonite was used instead of cement in the ratios of 6%, 9% and 12%, this wollastonite was found that mechanical and durability properties were negatively affected. According to the previous studies, wollastonite use in the ratios of 10% is known to improve mechanical and durability properties of mortar or concrete. Therefore, the negative effect on the structure of the mortar in the increasing ratios usage (6%, 9% and 12%) of NW obtained from Balikesir Region can be attributed to the fact that the NW wollastonite does not have a dense acicular particle structure and thus weakens the bond with the matrix.

References:

[1] SHARMA, S.K., ‘‘Properties of SCC containing pozzolans, Wollastonite micro fiber, and recycled aggregates’’, Heliyon, 2019; 5: e02081

[2] SOLIMAN, A.M., NEHDI, M.L., ‘‘Effect of natural wollastonite microfibers on early-age behavior of UHPC’’ J. Mater. Civ. Eng., 2012; 24 (7): 816-824

[3] DEY, V., KACHALA, R., BONAKDAR, A., MOBASHER, B., ‘‘Mechanical properties of micro and sub-micron wollastonite fibers in cementitious composites’’, Constr. Build. Mater., 2015; 82: 351-359

[4] HANER, S., ÇUHADAROĞLU, D., ‘‘Vollastonit: Bir Gözden Geçirme’), Jeoloji Müh. Derg., 2013; 37(1): 63-82

[5] FATTAH, H., ‘‘Wollastonite, New aspects promise growth’’, Ind. Miner., 1994; 21-43

[6] BEAUDOIN, J.J., LOW, N.M.P., ‘‘Flexural strength and microstructure of cement binders reinforced with wollastonite micro-fibres’’, Cem. Concr. Res., 1993; 23: 905-916.

[7] KHAN, R.I., ASHRAF, W., ‘‘Effects of ground wollastonite on cement hydration kinetics and strength development’’, Constr. Build. Mater., 2019; 218: 150-161

[8] DEMIDENKO, N.I., PODZOROVA, L.I., ROZANOVA, V.S., SKOROKHODOV, V.A., SHEVCHENKO, V.Y., ‘‘Wollastonite as a new kind of natural material (a review)’’, Glas. Ceram., 2001; 58(47): 308-311.

[9] BEAUDOIN, J.J., LOW, N.M.P., “The flexural toughness and ductility of Portland cement-based binders reinforced with wollastonite fibers”, Cem. Concr. Res., 1994; 24(2): 250-258

[10] KALLA, P., MISRA, A., GUPTA, R.C., CSETENYI, L., GAHLOT, V., ARORA, A., ‘‘Mechanical and durability studies on concrete containing wollastonite-fly ash combination’’, Constr. Build. Mater., 2013; 40: 1142-1150

[11] BEAUDOIN, J.J., LOW, N.M.P., ‘‘Mechanical properties of high performance cement binders reinforced with wollastonite micro-fibres’’, Cem. Concr. Res. 1992; 22: 981-989

[12] BEAUDOIN, J.J., LOW, N.M.P., “Stability of portland cement-based binders reinforced with natural wollastonite microfibers”, Cem. Concr. Res., 1994; 24(5): 874–884

[13] MATHUR, R., MISRA, A.K., GOEL, P., ‘‘Influence of wollastonite on mechanical properties of concrete’’, J. Sci. Ind. Res., 2007; 66: 1029-1034

[14] ASTM C305–12, ‘‘Standard practice for mechanical mixing of hydraulic cement pastes and mortars of plastic consistency’’, Annual Book of ASTM Standards, 2017

[15] ASTM C1437–15, ‘‘Standard test method for flow of hydraulic cement mortar’’, Annual Book of ASTM Standards
[16] ASTM C349–14, ‘‘Standard test method for compressive strength of hydraulic-cement mortars (using portions of prisms broken in flexure)’’, Annual Book of ASTM Standards, 2017
[17] ASTM C348–14, ‘‘Standard test method for flexural strength of hydraulic-cement mortars’’, Annual Book of ASTM Standards, 2017
[18] ASTM C597–16, ‘‘Standard test method for pulse velocity through concrete’’, Annual Book of ASTM Standards, 2016
[19] ASTM C1202, ‘‘Standard test method for electrical indication of concrete's ability to resist chloride ion penetration’’, Annual Book of ASTM Standards, 2012.
[20] KUMAR, J.B., RAMUJEE, K., ‘‘Mechanical & durability characteristics of wollastonite based cement concrete’’, J. Civ. Eng., 2017; 7(1): 1-7
[21] JINDAL, A., RANSINCHUNG R.N., G.D., KUMAR, P., ‘‘Behavioral study of self-compacting concrete with wollastonite microfiber as part replacement of sand for pavement quality concrete (PQC)’’, Int. J. Trans. Sci. Tech.
[22] WAHAB, M.A., LATIF, I.A., KOHAIL, M., ALMASRY, A., ‘‘The use of wollastonite to enhace the mechanical properties of mortar mixes’’, Constr. Build. Mater. 2017; 152: 304-309
[23] KALLA, P., RANA, A., CHAD, Y.B., MISRA, A., CSETENYI, L., ‘‘Durability studies on concrete containing wollastonite’’, J. Clean. Pro. 2015; 87: 726-734
[24] ÖZ, H.Ö., YÜCEL, H.E., DUYMAZ, Ç., GÜNEŞ, M., ‘‘The effects of natural wollastonite on early age strengths of standard mortars’’, International Turkic World Congress on Science and Engineering, 686-695, 17-18 June 2019, Niğde – Turkey

6th International Conference on Materials Science and Nanotechnology For Next Generation (MSNG2019)
October 16-18, 2019, Niğde, TURKEY (ORAL FULL TEXT)

The Effect to Copper Matrix of CNT and Graphene Together Reinforcements

Karun KATMER*, Ömer GÜLER*, Seval Hale GÜLER*, Öyküm BAŞGÖZ*

* Mersin University, Faculty of Engineering, Department of Metallurgical and Materials Engineering, Mersin, TURKEY

In this study, Carbon nanotubes (CNTs) were synthesized by chemical vapour deposition. Graphene nanoplatelets (GNPs) were synthesized by liquid phase exfoliation method. CNTs and GNPs were mixing with with each other for equal ratio. Later, this hybrid reinforcement was added to copper matrix for 0.05 wt % ratio. The composite powder were compacted for 500 MPa and sintered at 1000 ºC. The obtained sample was compared with pure copper sample which was produced at same condition. The hardness of composite was higher than pure copper sample about 10 %. The resistivity of composite was less than pure copper sample. Consequently, CNT and Graphene together reinforcing improves the properties of copper.

Keywords: Nanohybrid composite, Carbon nanotube (CNT), Graphene nanoplate(GNP.)
Corresponding author: oykumbasgoz@mersin.edu.tr

1. Introduction

The use of nanocomposites has increased in associate with the widespread use of composite materials in industrial products. Nowadays, with the increasing industrialization, the search for the most appropriate efficiency in electrical applications has always been the research object. And in this context, composite materials exhibiting superior electrical properties in electrical applications have attracted the attention of scientists.

Since the discoveries of carbon nanotubes (CNTs) by Iijima and graphene nanoplatelets (GNP) by Novoselov et al., they have received a great attention as raw materials for the development of nanomaterials due to their excellent thermal, electrical and mechanical properties, low density and high specific surface area. Nowadays, enormous efforts have been devoted to the use of CNT and graphene in various applications, such as energy storage field effect transistors (FETs), electrodes and sensors [1-3]. Graphene and carbon nanotube hybrid structure is one of the promising graphene derivatives, which have great potential applications in areas such as energy storage, supercapacitor and building blocks composite. Experimental works have shown that nicely aligned hybrid structures between graphene and carbon nanotube are achievable. Their highly tailorable structures endow them with highly tunable mechanical properties. It is worth mentioning that other properties of the graphene and CNT hybrid structures are also of great interest, such as chemical properties and thermal transport properties [4].

However, the desire to address the limitations of individual graphene such as zero bandgap and challenges associated with functionalization, has triggered a new approach in which graphene is exploited as a scaffold platform to anchor other nanomaterials [5]. To this end the combination of one-dimensional (1D) carbon nanotubes (CNTs) and two-dimensional (2D) graphene materials to generate three-dimensional (3D) carbon nanotube–graphene hybrid has attracted great attention owing to their intriguing properties via the synergistic effects of these two materials on their electrical, optical, and electrochemical properties in comparison with their individual components [6].

So in this study CNT-GNP hybrid structure reinforced to Copper (Cu) matrix to improve the electrical properties thanks to the reasons above mentioned. In this connection copper matrix nanohybrid composites having 0.05 % volume fraction of nanotube and graphene concentrations were produced by using powder metallurgy method. CNT and Graphene were used as reinforcements materials. Carbon nanotubes were produced by Chemical Vapor Deposition, and Graphene was produced by Liquid Phase Exfoliation Process. Hexagonal graphite was preferred as the starting material for this purpose. Hexagonal graphite

was sonicated in a solvent. At the end of sonication process, stacked graphene layers were separated from each other. The produced powders were grained homogeneously with copper powders with high energy milling. After that the powders were compacted under high pressure and sintered in an atmosphere of inert gas at a temperature of 950 ° C. Abrasion, hardness, electrical conductivity and contact behavior of the produced Nano Hybrid composites were investigated. Internal structures of the samples were examined by Scanning Electron Microscopy (SEM). As a result of these analyzes, conclusions were made about how the amount of carbon nanotube and graphene change the mechanical and electrical properties of composite meterials.

2. Experimental details

In this work CNT and Graphene were used as reinforcements materials. Carbon nanotubes were produced by Chemical Vapor Deposition, and Graphene was produced by Liquid Phase Exfoliation Process.

2.1 Synthesized of the CNT

The silicon substrate placed at the middle of the furnace was cleaned 4 times with a vacuum of 10^{-3} Torr. After Argon (Ar) gas flowing at a flow rate of 1lt /min was heated to 650 ℃ beneath the atmosphere. Then C_2H_2 gas was and Ar gas flushed. Finally, the furnace was naturally cooled in Ar atmosphere.
The resulting powder was allowed to stand for 3 hours in a mixture of nitric acid (Sigma-Aldrich 438073) and hydrochloric acid (Sigma-Aldrich 258148) to remove the amorphous carbon structures present in the powder. The powders were then washed with distilled water and dried in an oven at 150 ° C for 10 hours. As a result, CNTs were successfully produced by CVD method.

2.2 Synthesized of the Graphene

Expanded hexagonal graphite which is expanded interlayer surface was used as a precursor material to synthesized graphene nano plates via liquid phase exfoliation method. N-Methyl-2- pyrrolidone (NMP) was used as the solvent for separating the layers bounding by Van der Waals bonds. Graphene Production Process was used in this study has been shown in Figure 1.

For this production 0.01 gram expanded graphite was mixed in 100 ml NMP with ultrasonic homogenizer (Sonix-Vibra Cell) at % 70 amplitude for 2.5 hours. The mixed solution was separated for 2 hours at 6000 RPM in a brand centrifuge. The precipitated graphene layers were washed 3 times with ethanol (Isolab) and to clean from NMP. In the magnetic stirrer, alcohol was evaporated and graphene nanotubes were obtained.

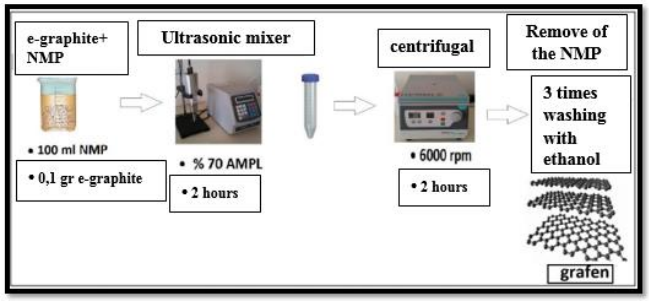


Figure 1. *Graphene Production Flow Chart.*

2.3 Mechanical Alloying Process

Mechanical alloying process was using to prepared the compositions by adding graphite and MWCNT particles at a rate of 0.05 % by volume to the copper powder which is used as the main matrix. Sample added to a 250 ml stainless steel grinding vessel were homogenized with high speed planatery grinder (Retsch) using a 12mm and 50mm diameter ball with rete on 15:1 powder ball ratio with 1.1 g zinco stearate (Aldrich) lubricant and homogeneously for a total of 12 hours. The obtained composite powder sample were compacted at 500 MPa pressure. For the sintering process, under 0.5 lt/min. Ar gas was flueshed through the horizontal tube furnace and sintered at 950 ° C for 1 hour. The obtained sintered samples were cold pressed again at 500 MPa to reach full density and sintered for a second time at 1000 °C.

3. Results and discussion:

Figure 2 showed that the SEM image of the sample for 100.000x magnification.

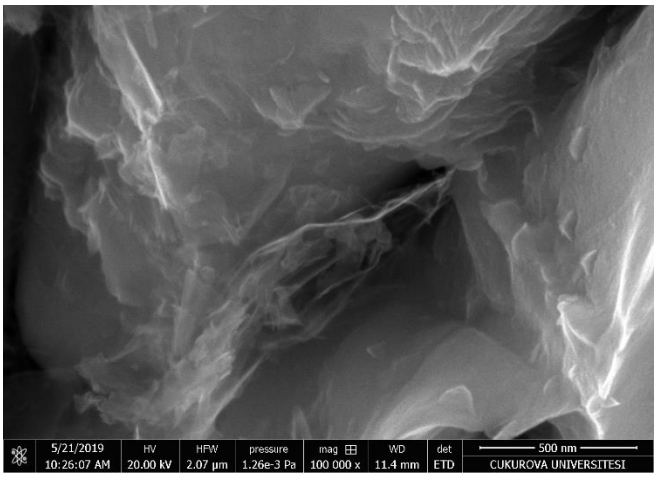


Figure 2. *SEM image of the sample.*

Since both the CNT and the graphene nanoplate have very small particle size, the SEM images of the composites were taken at 100,000x magnification. Some of the

reinforcements particles were placed on the matrix while others were embedded in the copper matrix by the effect of grinding or forging.

Measurements of Vickers hardness were performed to determine the microhardness values of the composites. Vickers hardness value was calculated by averaging the values obtained from each test (Figure 3). The Vickers hardness tests were performed at a holding time 10s. Composite samples with only CNT or graphene reinforced only have better hardness values than nano-hybrid composites. This is because graphene cannot form the desired strong interface bond due to agglomerate the CNT structure.

Zhang et al. In the results of the microhardness of graphene reinforced copper matrix composites of the [7] study, a significant increase in copper matrix hardness obtained by adding a small amount of GNS was attributed to the reinforcing effect of GNS. The hardness value of 0.05 % CNT-GNP nano hybrid composite is 58.44 HV.

Direct current was used with the help of the device installed in the furnace with conductivity tester (Agilent 34401A) and electrical conductivity measurements of the samples were carried out at room temperatures.

Four prob conductivity measurement method was used for electrical conductivity measurement. electrical conductivity values are given as% IACS. The% IACS (International Annealed Copper Standard) is the conductivity measurement standard made by accepting 100% self-conductivity of fully densely annealed pure copper, and 100 % IACS=58 MSiemens/m [8]. The resistances of the produced samples were first measured and the equation and the self-conductivity values given in equation (1) were found.

$$\rho = Rx\left(\frac{A}{L}\right) \quad (1)$$

In the equation, Resistance R (ohm), σ Self conductivity (MS/m), L thickness of the sample (m), A represents the cross-sectional area (m^2). The obtained conductivity values were converted to % IACS. The electrical conductivity of the synthesized composite was found to be 86.1% IACS for 0.05 % CNT-GNP. The electrical conductivity value for the pure Cu is 85.2 % IACS.

In this study, specific wear rates were calculated according to equation (2) by subjecting the wear sample produced at the specified distances (500m, 1000m, 1500m) and different loads (5N, 10N, 15N).

$$k = \left(\frac{\Delta V}{P.L}\right) \quad (2)$$

In here, the k; specific wear rate, ΔV; volume change, P; load to which it is exposed, L; indicates the distance taken.

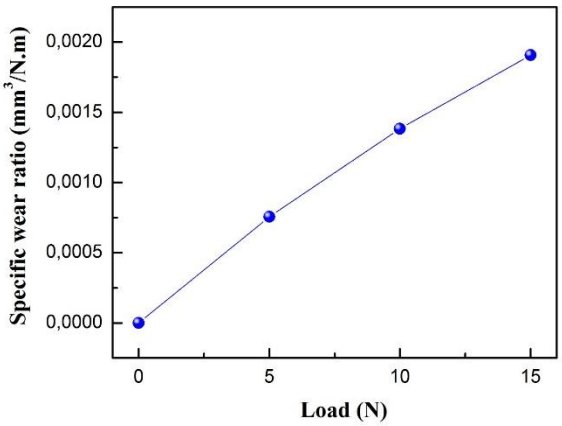


Figure 3. *Specific wear rates of the composite for different loads and different wear distances.*

Figure 4 shows the material loss during the opening and closing of the contacts. This result is in parallel with the wear results.

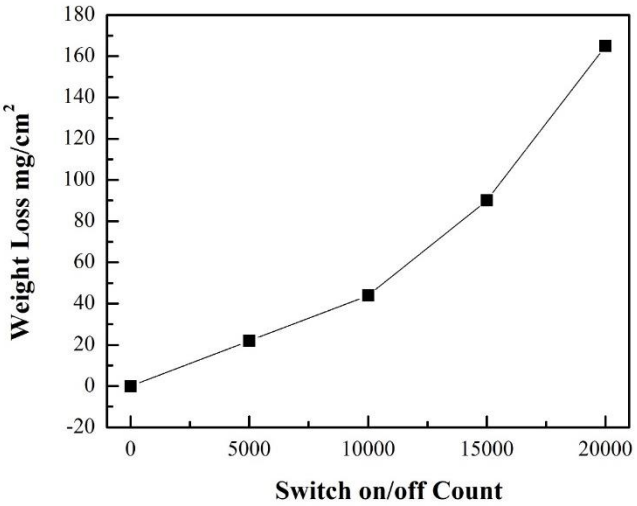


Figure 4. *Loss of material in composite material by number of contacts.*

It is seen that the loss of material in the nanohybrid composite material decreases as the number of opening/ closing increases.

The contacts were subjected to 5000, 10000 and 20000 switching operations under 5 A alternating current conditions. At the end of the process, the losses of substances in the contacts are explained before Figure 5 has been showed SEM image of nano hybrid composite after 2000 cycles.

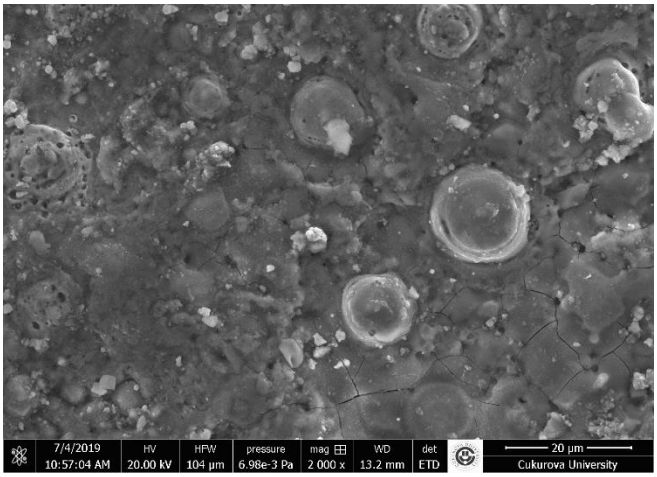


Figure 5. *SEM image of nano hybrid composite after 2000 cycles.*

At the end of 20000 cycles, SEM of the contact was investigated and the erosion behavior was evaluated. It has been observed that the melts and melts formed on the surfaces of the moving contacts are transformed into droplets and carried to the fixed contact. It is considered that material transport in the form of droplets from the moving contact to the fixed contact is effected by gravity.

4. Conclusions

In this study, nanohybrid composite was obtained by adding CNT and Graphene in various ratios to pure copper powder by powder metallurgy method. The effect of reinforcement elements on the wear behavior and electrical conductivity of the composite samples was investigated. In addition, micro hardness and contact properties of the obtained composites were examined and the effect of reinforcement ratios on mechanical and electrical properties was investigated. As a result of the study, it was seen that the hybrid structure improved the properties of copper. The electrical conductivity and hardness values were 86.1% IACS and 58.44 HV respectively.

Acknowledgements

The authors would like to acknowledge for the financial support of Mersin University Department of Scientific Research Projects (Project No. 2019-1-TP2-3468).

References:

[1] IIJIMA, S. (1991). Helical microtubules of graphitic carbon. *nature*, *354*(6348), 56.
[2] NOVOSELOV, K. S., GEIM, A. K., MOROZOV, S. V., JIANG, D., ZHANG, Y., DUBONOS, S. V., ... & FIRSOV, A. A. (2004). Electric field effect in atomically thin carbon films. *science*, *306*(5696), 666-669.
[3] CHE, J., CHEN, P., & CHAN-PARK, M. B. (2013). High-strength carbon nanotube buckypaper composites as applied to free-standing electrodes for supercapacitors. *Journal of Materials Chemistry A*, *1*(12), 4057-4066.
[4] XIA, K., ZHAN, H., & GU, Y. (2017). Graphene and carbon nanotube hybrid structure: a review. *Procedia IUTAM*, *21*, 94-101.
[5] IJEOMAH, G., SAMSURI, F., ZAWAWI, M. A. MD, OBITE, F. , Carbon Nanotube-Graphene hybrid: Recent Synthesis Methodologies and Applications, International Journal of Engineering Technology and Science, 7 (2017).
[6] DANG, V. T., NGUYEN, D. D., CAO, T. T., LE, P. H., & PHAN, N. M. (2016). Recent trends in preparation and application of carbon nanotube–graphene hybrid thin films. *Advances in Natural Sciences: Nanoscience and Nanotechnology*, *7*(3), 033002.
[7] LI, J. F., ZHANG, L., XIAO, J. K., & ZHOU, K. C. (2015). Sliding wear behavior of copper-based composites reinforced with graphene nanosheets and graphite. *Transactions of Nonferrous Metals Society of China*, *25*(10), 3354-3362.
[8] BRODIE, B. C. (1859). XIII. On the atomic weight of graphite. *Philosophical Transactions of the Royal Society of London*, (149), 249-259.

6th International Conference on Materials Science and Nanotechnology For Next Generation (MSNG2019)
October 16-18, 2019, Niğde, TURKEY (ORAL FULL TEXT)

Production of Copper Oxide Thin Films for Photovoltaic Applications by Sol - Gel Dip Method and Investigation of Their Optical Properties

U. Calıgülü[1], M. H. Boz[1]

[1]*Department of Metallurgy and Materials, Faculty of Technology, Elazig, Turkey*

CuO nanoparticles have attracted much attention in recent years due to their superior properties as they differ from the volume of nano-sized copper oxide with the decrease in crystal size. High interfacial area, overactive surface, and unusual optical, electrical, electronic and catalytic properties have made these particles attractive in photovoltaic applications. In this study, electro-optical properties of CuO thin films which were prepared by using sol-gel dip method and kept at 300ºC, 350ºC, 400ºC, 450ºC, 500ºC for 1 hour were examined depending on temperature change. Surface morphology of the prepared thin films was investigated by using Atomic Force Microscope (AFM Park System XE-100E). The crystalline structure of the films was investigated by using the scanning electron microscope (SEM) and X-ray diffraction method (XRD) and it was determined that CuO thin films showed structural changes due to temperature effect. Forbidden energy ranges of the samples were found to be between 3.6 eV and 3.93 eV. In addition, it was determined that thin films can be produced with less cost and work for photovoltaic applications.

Keywords: CuO, Sol-Gel Dip, Photovoltaic Applications, Optical Properties

Corresponding author: ugurcaligulu@gmail.com

1. Introduction

Copper oxide (CuO), whose band gap energy value is around 1.4 eV, is an important p-type semiconductor oxide material among many metal oxide materials. CuO is a semiconductor material which has monoclinic crystal structure, is non-toxic, inexpensive, easy to be synthesized and abundant in nature. Therefore, CuO thin films have been widely investigated for various applications in various areas of technology such as biosensors, gas sensors, solar cells, lithium ion batteries, and thin film transistors [1-5]. The copper oxide properties as well as the effect of temperature, thickness and doping on the properties of films have been investigated. It has been aimed to use the produced films in usage areas and photovoltaic applications in a cost-effective manner by changing reaction temperature [6-13]. In addition, CuO and ZnO have been combined and their photovoltaic properties [14] and their efficiency in solar cells has been investigated in the developed studies [15-16] and it has been found as a result of these studies that copper oxide is a good material for photovoltaic applications [17]. Many methods such as sol-gel [18], and dip coating [19] have been investigated and photovoltaic properties have been planned to be improved by synthesizing various nano structures with sol-gel method [21]. Moreover, it can be understood from these studies that it has become a promising candidate [28-30] for semiconductors, photocatalysts [22], piezoelectric devices [23], light emitting diodes [24], organic photovoltaic cells [25] and gas sensors [26-27] and the focus of the study [31-35]. In her study, Özge Hasançebi (2006) prepared copper oxide thin films using sol-gel method and investigated the optical, electrical, and structural properties of these films. She examined the effects of temperature, thickness and doping on such properties of films [10]. In their study, Meyer et al., (2012) tried to obtain maximum efficiency from the optical and electronic properties of semiconductors with copper oxide compound for photovoltaic applications [11]. In the study

conducted by Claudia Malerbi et al., on absorption coefficient of bulk and thin film Cu_2O, they investigated whether Cu_2O was appropriate for photovoltaic applications or not [17]. G. Martínez-Saucedo et al., examined the conversion of cupric oxide (CuO) to copper oxide (Cu2O) thin films with rapid thermal annealing (RTA) applications [19].

In this study, copper oxide (CuO or Cu_2O) thin films were produced using sol-gel dip coating method and the study was completed successfully. The effects of the temperature change on the morphological and optical properties of the prepared CuO thin films were investigated.

2. Experimental method

A copper acetate and ethanol solution stirred at different molars was prepared. ITO glasses were coated using sol-gel dip coating method. Copper Acetate Cu $(CH_3COO)_2$ and ethanol (C_2H_5OH) were used as the base material. While 2-methoxyethanol was used as the solvent, dimethylaminoethanol ($C_4H_{11}NO$) was used as the stabilizer. The amount of copper acetate was calculated for 10 ml solution. 0.90815 g copper acetate was added into 10 ml ethanol and mixed with a magnetic stirrer at 60^OC and 500 rpm for 1 hour. After measuring the pH value, NaOH amount was calculated for 10 ml methoxyethanol to bring the pH value between 8-10. 10 ml methoxyethanol and 0.3999 g NaOH were added and mixed in the magnetic stirrer at 70°C and 500 rpm for 10 minutes. In order for the pH value of copper acetate solution to be between 8-10, 3 drops of NaOH solution were added while stirring the solution in the magnetic stirrer.

ITO glasses were cleaned with acetone, methyl alcohol and deionized water, respectively for 10 minutes using an ultrasonic bath. The surfaces of the ITO glasses cleaned with nitrogen gas were dried. The cleaned ITO glasses were dipped into the prepared solution using sol-gel dip coating device. For dipping process, ITO glasses were kept in the solution for 24 hours. After the dipping process was completed, the sample was kept in the oven for 1 hour to complete the coating process. This process was repeated 5 times only by changing the temperature (300°C, 350°C, 400°C, 450°C, and 500°C) (Figure 1).

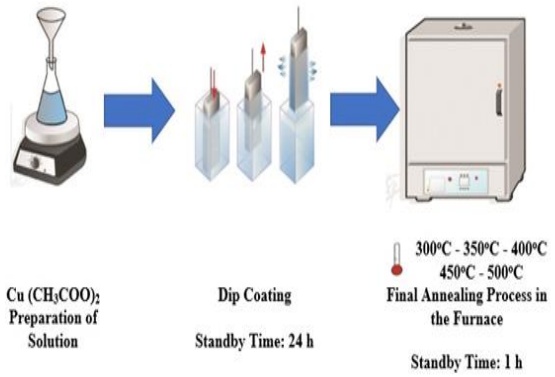


Figure 1. Thin film coating process with Sol-Gel Dip Method

The surface morphology of the prepared thin films was examined using Atomic Force Microscope (AFM Park System XE-100E). The crystal structure of the films was examined with Scanning Electron Microscope (SEM) and their characteristic properties were examined by using X-Ray Diffraction Method (XRD). All measurements were conducted at room temperature.

3. Results and Discussions

Sol-gel dip coating method is a low-cost method and suitable especially for photovoltaic application and the production of CuO thin films. The surface morphology and grain size analysis of thin films coated with CuO solution were characterized by Park System XE – 100E Atomic Force Microscope (AFM) in 2D (40 μm × 40 μm). Atomic force microscope is a device providing 3D images of the surfaces with a sharpened needle tip of materials found in atomic dimensions. It is based on imaging as a result of contact of the needle tip with the surface by using different tips in accordance with the purposes. It has 3 different methods as contact method, non-contact method and tapping method.

Figure 2 shows 2-dimensional (40 μm × 40 μm) AFM images of the thin films coated with CuO and ethanol mixture.

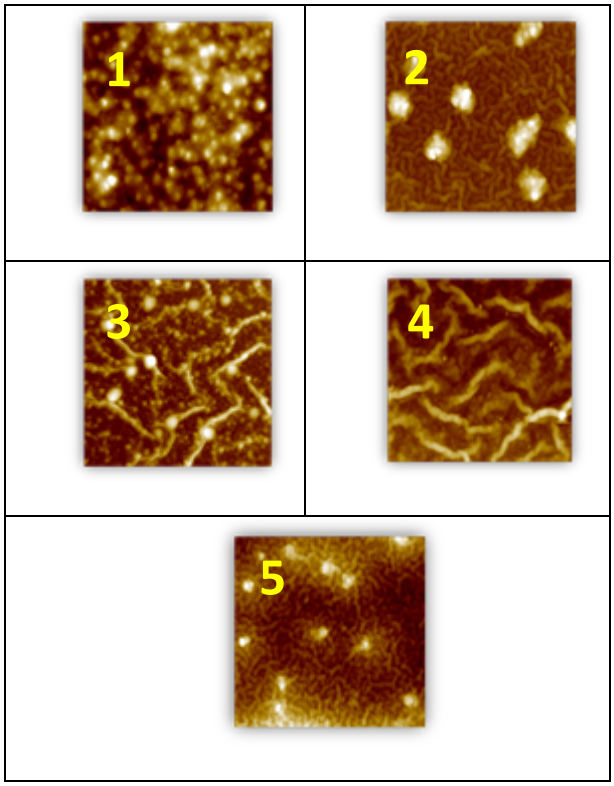


Figure 2. 2D (40µx40µ) AFM Surface Images of the Prepared Nano-Structured Thin Films
1 : 300ºC , 2 : 350ºC , 3 : 400ºC , 4 : 450ºC, 5 : 500ºC

When the AFM images were examined, it was seen that all films had a smooth and different surface and there was inconsistency in the surface images. This inconsistency in the surface morphology depended on the temperature, growing conditions and growing process of the thin films. The resulting structures were observed to have a micro-fiber morphology. Fiber thicknesses forming the sample varied depending on temperature changes (Figure 2).

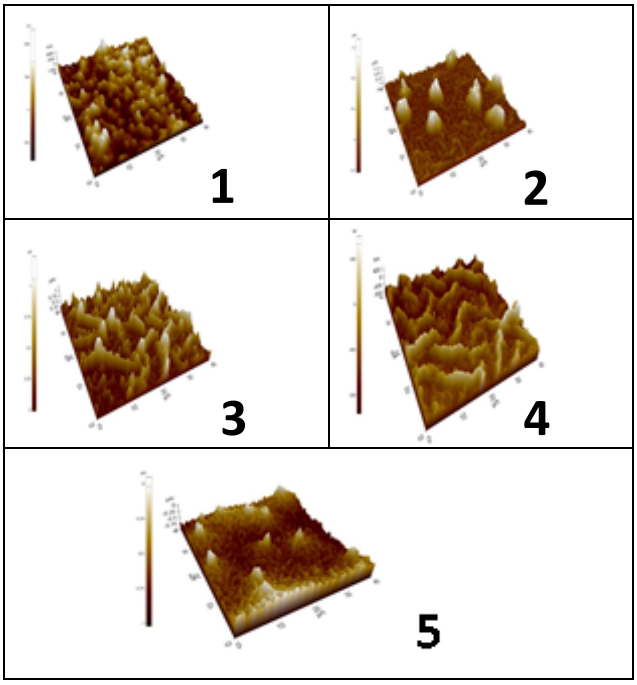


Figure 3. 3D (40µx40µ) AFM Surface Images of the Prepared Nano-Structured Thin Films

Figure 3 shows 3D AFM surface photographs of the samples 1, 2, 3 and 4. Surface roughness values of the films increased with increasing temperature values. The fact that defect densities increased in the structures of CuO films depending on temperature caused an increase in surface roughness due to the defects in the crystal structure and surface distribution. Another reason for the increase in surface roughness was that the increase in temperature values increased the number of nucleation centers and this caused an increase in the surface roughness [35].

3.1. Optical Properties of CuO Thin Films

Surface properties are important since it affects the electrical and optical properties throughout photovoltaic applications. The crystal structure of thin films coated with CuO solution was examined by SEM (Scanning Electron Microscope). Basically, scanning electron microscope is based on the principle of collecting and examining the signals resulting from the physical interaction of electron beam with the surface of examined sample.

The crystal structure of thin films coated with CuO solution was examined in 2 dimensions (2 µm × 2 µm) using Zeiss EVO MA10 Scanning Electron Microscope (SEM). Figure 4 shows 2D (2 µm × 2 µm) SEM images of the thin films coated with CuO and ethanol mixture and processed at 300ºC, 350ºC, 400ºC, 450ºC, and 500ºC.

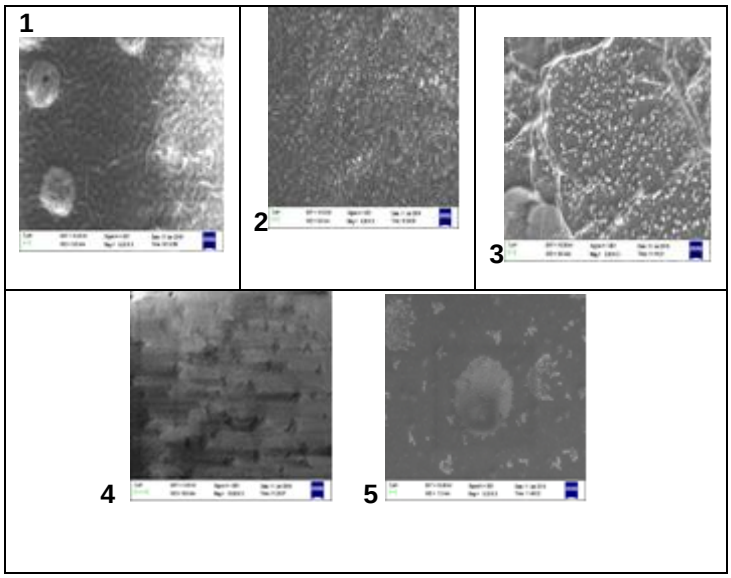


Figure 4. (2µx2µ) SEM Surface Images of the Prepared Nano-Structured Thin Film
1: 300ºC, 2: 350ºC, 3: 400ºC, 4: 450ºC, 5: 500ºC

Starting from 300 °C, the surface of the films showed a uniform particle morphology without a significant trend in particle size. Besides, the presence of larger pores is observed for films treated at higher temperatures. Based on these results, the formed pores are thought to be composed of Cu_2O reduced to more metallic copper (Figure 4).

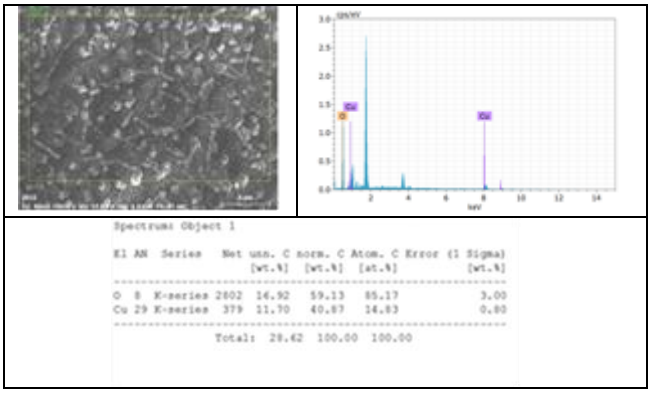
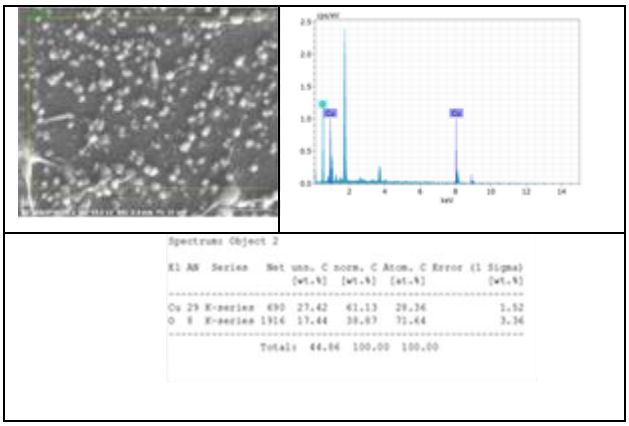


Figure 5. 300ºC EDX Analysis of the Prepared Nano-Structured Thin Films



Figurec 6. 400ºC EDX Analysis of the Prepared Nano-Structured Thin Films

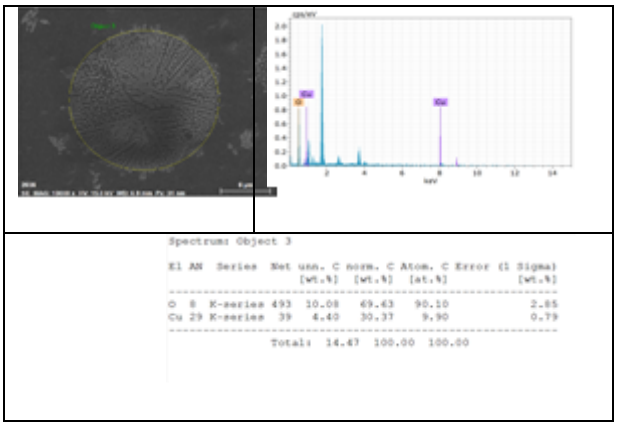


Figure 7. 500ºC EDX Analysis of the Prepared Nano-Structured Thin Films

The changes of thin films produced by Sol – Gel dip coating method depending on temperature were calculated by taking EDX analysis from 3 different temperatures. When the SEM images and XRD analysis of the surfaces were examined, it was determined that the structural properties changed with temperature changes and the resulting fiber structures showed variation in thickness depending on temperature (Figures 5-6-7). When XRD analysis taken from the surfaces of thin films produced with Sol – Gel dip coating method was examined, Cu, O and Si phases were determined in the produced thin films. It was thought that the Cu and O phases were the main phases of the solution prepared in producing thin film, Si phase was in the ITO glasses and it was the phase that would not affect thin film negatively

Absorption T(λ), reflection R(λ), and permeability A(λ) measurements of the produced films were taken with Shimadzu UV-VIS-NIR 3600 model spectrophotometer in the wavelength range of 200–1000 nm. All measurements were made at room temperature. Figures 8, 9, and 10 show these characterized curves, respectively.

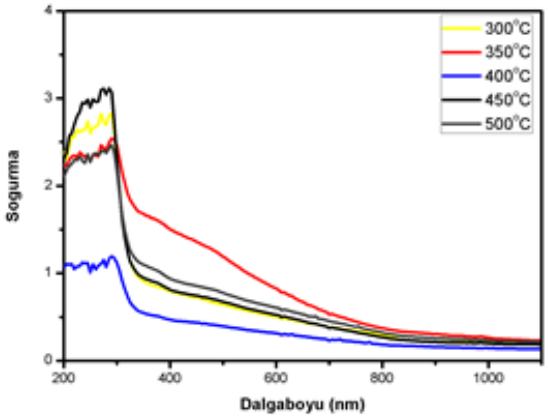


Figure 8. Absorption Graphs of the Samples

Figure 8 shows the absorption spectrum of CuO based thin films annealed at different temperatures recorded in the wavelength range of 200-1100 nm. Due to high transparency of the samples, the average absorption in the visible region was between 1% and 3%. Higher absorption was observed in 450°C sample compared to the other films in this range. This high absorption value was thought to be caused by the low film thickness compared to the other samples (Figure 8).

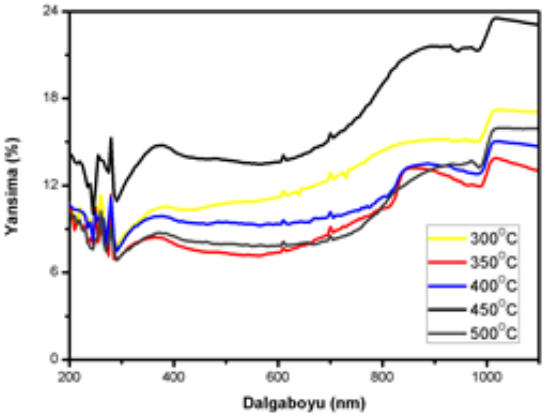


Figure 9. Reflection Graphs of the Samples

Figure 9 shows reflection curves of CuO nano-structured thin films. When Figure 9 was examined, it was clearly remarkable that the sample annealed at 450°C exhibited a higher reflection spectrum compared to the other four samples. It was seen that the reflection values varied in wavelength range of 200-1100 nm and there were nonlinear changes in the reflection rates (Figure 9).

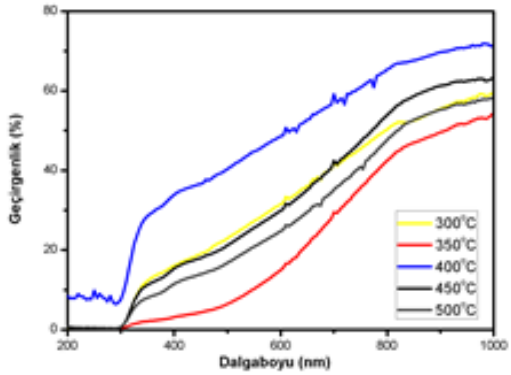


Figure 10. Permeability Graphs of Samples

Figure 10 shows permeability curves of the samples. When the permeability curves of the samples were examined, it was observed that the permeability values varied between 40% and 70% and the intensity of the light passing through the films decreased and optical density values increased due to a certain amount of increase in the thickness of the films after 300°C. This was thought to be caused by the decrease in the permeability values of the films (Figure 10).

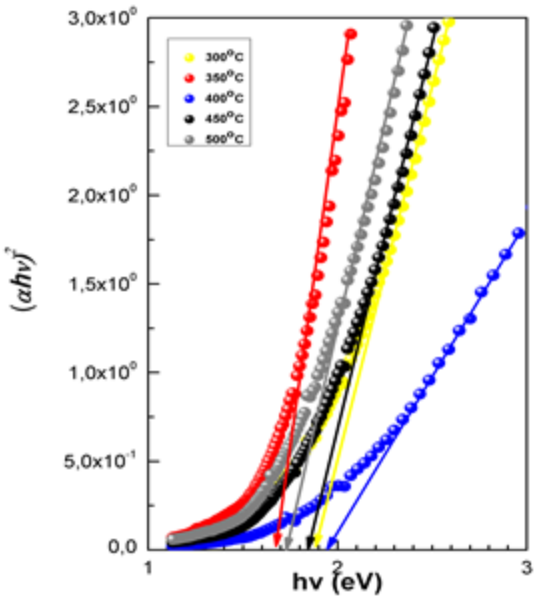


Figure 11. $(ahv)^2$ – hv (eV) Graph of the samples

Another parameter determined by using optical measurement results of semiconductor materials was the forbidden energy range. One of the methods for direct determination of the forbidden energy range of semiconductors is to use the optical method by benefiting from the basic absorption spectrum. The region which is known as the excitation of a photon with known energy from valence band to the transmission band and named as the region where the absorption shows a sharp increase is defined as the basic absorption region. Two types of transition events occur in the semiconductors at the basic absorption boundary. These are called as direct band transition and indirect band transition.

The optical method used to determine the forbidden energy ranges of semiconductors also provides information about optical transitions.

In this method, the forbidden energy range of the semiconductor material was determined from $(\alpha h\nu)^2 \sim h\nu$ variation graph plotted using the basic absorption spectrum. The energy value of the point at which the linear part of this change intersected $h\nu$ axis at $(\alpha h\nu)^2=0$ gave the forbidden energy range of the semiconductor [32]. In calculating the forbidden energy range: following formula was used;

$$\alpha h\nu = A(h\nu - E_g)^m$$

[33]. Where, α; absorption coefficient, $h\nu$; photon energy, E_g; Forbidden Energy Range, n=½ (for direct passes) and A; constant. If m value is 2, the material has indirect band gap; if it is ½, then it has direct band gap.

Temperature	***E_g (eV)***
300^{O}C	1.89
350^{O}C	1.67
400^{O}C	1.93
450^{O}C	1.83
500^{O}C	1.73

Table 1. Forbidden Energy Parameters of the Films

Figure 11 shows the graphs showing the forbidden energy range of the produced CuO thin films. With the help of the curves given in Figure 11, the forbidden energy ranges of the samples were determined and indicated in Table 1.

The optical band ranges of the well-known p-type semiconductor CuO were between 1.3 eV- 2.1 eV [34]. When the obtained results were examined, it was found that the forbidden energy parameters of CuO thin films were between ideal optical band ranges.

3.2. General Conclusions

- CuO based nano-structured thin films were successfully produced without addition and at different temperatures using sol-gel dip-coating method.
- It was determined as a result of these investigations, the nano structure of CuO based thin films varied depending on temperature.
- This study conducted on the production of semiconductor film which has an important place in technological applications is important especially in terms of producing CuO thin films as an alternative to other expensive production methods and allowing to change their properties further with addition possibility.
- When AFM images were examined, it was seen that all films had smooth and different surfaces and there was inconsistency in surface images. This inconsistency in surface morphology was thought to be dependent on the temperature, growing conditions and growing process of the thin films.
- When the optical properties of CuO thin films were examined, it was found that the surface of films exhibited a uniform particle morphology starting from 300 °C without a significant trend in particle size. It was also observed that larger pores formed for the films processed at higher temperatures (350, 400, 450 and 500 °C).
- When EDX analysis was examined, it was determined that the structural properties of CuO thin films changed with temperature changes and thickness changes occurred depending on the temperature in the formed fiber structures.
- When XRD analysis taken from the surfaces of thin films produced using sol-gel dip-coating method was examined, Cu, O and Si phases were determined in the produced thin films.
- When UV-VIS-NIR analysis was examined, it was found that the average absorption in the visible region was about between 1% and 3% due to the high transparency of the samples and 450^{o}C sample had a higher absorption than all other films in this range. It was clearly remarkable that the sample annealed at 450^{o}C had a higher reflection spectrum

compared to the other four samples. Reflection values varied in the wavelength range of 200-1100 nm and non-linear changes in reflection rates were observed.

- When the permeability curves of the samples were examined, it was determined that the permeability values varied between 40% and 70%, it was seen that the intensity of light passes through the films decreased depending on the increase of a certain amount in thickness and optical intensity values increased after 300ºC. This was thought to be caused by the decrease in the permeability values of the films.
- The optical band gaps of CuO which is a p-type semiconductor were between 1.3 eV- 2.1 eV. When the forbidden energy ranges of the samples were examined, it was found that the optical band gaps were between 1.67 eV- 1.93 eV and the forbidden energy parameters were in the ideal band range.

Acknowledgement

This study was supported by Firat University Scientific Research Projects (FUBAP) management unit (Project No: TEKF.18.16).

4. References

[1] Gençer, Ö., 2009 Bakır ve Bakır Oksit Nanopartiküllerinin Ultrasonik Sprey Piroliz (Usp) Yöntemi ile Üretimi Yüksek Lisans Tezi İstanbul Teknik Üniversitesi, Fen Bilimleri Enstitüsü, İstanbul

[2] Sönmezoğlu, S., Koç, M., Akın, S., 2012 İnce Film Üretim Teknikleri Erciyes Üniversitesi Fen Bilimleri Enstitüsü Dergisi, Kayseri

[3] Aydın, R., Şahin, B., Bayansal, F, 2016 SILAR yöntemi ile üretilen CuO filmlerin yapısal, morfolojik ve optik özelliklerine ikili katkılamanın (Zn, Li) etkisi, Sakarya Üniversitesi Fen Bilimleri Dergisi, 20.Cilt, 3.Sayı, s. 481-487

[4] Yakuphanoglu, F., Caglar, M., Caglar ve Y., Ilican, S. (2010), ‘‘Electrical characterization of nanocluster n-CdO/p-Si heterojunction diode, ’’ *Journal of Alloys and Compounds*, 506, 188-193

[5] Nasibulin, A. G., Shurygina, L. I. and Kauppinen, E. I., 2005. Synthesis of Nanoparticles Using Vapor-Phase Decompositionof Copper (II) Acetylacetonate, *Colloid Journal*, 67, 1–20.

[6] Hong, Z., Cao, Y. and Deng J., 2002. A convenient alcohothermal approach for low temperature synthesis of CuO nanoparticles, *Materials Letters*, 52, 34–38.

[7] Tetsuya Kida et al.,2007. Synthesis and Application of Stable Copper Oxide Nanoparticle Suspensions for Nanoparticulate Film Fabrication, *J. Am. Ceram. Soc.*, 90, 107–110.

[8] Şahin, B., Çomaklı, K., Çomaklı, Ö., Yılmaz, M., Nanoakışkanlar ile ısı transferinin iyileştirilmesi, *Mühendis & Makine, 47*, 29-34.

[9] N.R. Karthikeyan, N. R., John Philip, J. and Raj., 2008. Effect of clustering on the thermal conductivity of nanofluids, *Materials Chemistry and Physics*, 109, 50-55.

[10] Hasançebi, Ö., 2006 Electrical, Structural and Optical Properties of Copper Oxide Thin Films Prepared by Sol-Gel Method, Yüksek Lisans Tezi, Ankara University, Ankara,

[11] B.K. Meyer, A. Polity, D. Reppin, M. Becker, P. Hering, P.J. Klar, T. Sander, C. Reindl, J. Benz, M. Eickhoff, C. Heiliger, M. Heinemann, J. Bläsing, A. Krost, S. Shokovets, C. Reppin, C. Ronning, Binary copper oxide semiconductors: from materials towards devices, Phys. Status Solidi B 249 (2012) 1487–1509.

[12] Özüilerigiden, S., 2012 Yarı İletken Oksit Filmlerin Gaz Sensörleri Üzerine Uygulanması ve Optimizasyonu, Yüksek Lisans Tezi Dokuz Eylül Üniversitesi, Fen Bilimleri Enstitüsü, İzmir

[13] S. Rühle, A.Y. Anderson, H. Barad, B. Kupfer, Y. Bouhadana, E. Rosh-Hodesh, A. Zaban, All-oxide photovoltaics, J. Phys. Chem. Lett. 3 (2012) 3755–3764.

[14] T. Dimopoulos, A. Peić, P. Müllner, M. Neuschitzer, R. Resel, S. Abermann, M. Postl, E.J.W. List, S. Yakunin, W. Heiss, H. Brückl, Photovoltaic properties of thin film heterojunctions with cupric oxide absorber, J. Renew. Sustain. Energy Rev. 5 (2013) 011205

[15] W. Shockley, H.J. Queisser, Detailed balance limit of efficiency of pn junction solar cells, J. Appl. Phys. 32 (1961) 510–519.

[16] B.P. Rai, Cu2O solar cells: a review, Sol. Cells 25 (1988) 265–272.

[17] C. Malerba, F. Biccari, C.L. Azanza, M. D’Incau, P. Scardi, A. Mittiga, Absorption coefficient of bulk and thin film Cu2O, Sol. Energ. Mater. Sol. Cells 95 (2011) 2848–2854.

[18] Jeffrey B.C., George, W., 1990 Scherer Sol-gel Science: The Physics and Chemistry of Sol-gel Processing, s. 908, Gulf Professional Publishing.

[19] G. Martínez-Saucedoa, R. Castanedo-Péreza, G. Torres-Delgadoa, A. Mendoza-Galvána, O. Zelaya Ángel, 2017 Cuprous oxide thin films obtained by dip-coating method using rapid thermal annealing treatments.

[20] Ateş, H., Bahçeci E., 2015 Nano Malzemeler için Üretim Yöntemleri, Gazi Üniversitesi Fen Bilimleri Dergisi Part:C, Tasarım ve Teknoloji

[21] Dağ, M., 2015 Nanoyapıların Fotovoltaik Özelliklerinin İncelenmesi, İstanbul Üniversitesi Fen Bilimleri Enstitüsü, Yüksek Lisans Tezi, İstanbul
[22] Lv Y, Zhang Z, Yan J, Zhao W, Zhai C, Liu J. Growth mechanism and photoluminescence property of hydrothermal oriented ZnO nanostructures evolving from nanorods to nanoplates. J. Alloys Compd. 2017; 718: 161–169.
[23] Liu S, Wang L, Feng X, Wang Z, Xu Q, Bai S, Qin Y, Wang Z.L., Ultrasensitive 2D ZnO Piezotronic Transistor Array for High Resolution Tactile Imaging. Adv. Mater. 2017; 29.
[24] Kim D, Fu Y, Kim S, Lee W, Lee K.H, Chung H.K, Lee H.J, Yang H, Chae H. Polyethylenimine Ethoxylated-Mediated All-Solution-Processed High-Performance Flexible Inverted Quantum Dot-Light-Emitting Device, ACS Nano. 2017; 11: 1982–1990.
[25] Wang K, Liu C, Meng T, Yi C, Gong X. Inverted organic photovoltaic cells. Chem. Soc. Rev. 2016; 45: 2937–2975.
[26] Zhu L, Zeng W. A novel coral rock-like ZnO and its gas sensing. Mater. Lett. 2017; 209:244–246.
[27] Xu J, Xue Z, Qin N, Cheng Z, Xiang Q. The crystal facet-dependent gas sensing properties of ZnO nanosheets: Experimental and computational study, Sensors Actuators, B Chem. 2017; 242: 148–157.
[28] Lupan O, Postica V, Gröttrup J, Mishra A.K, De Leeuw N.H, Carreira J.F.C, Rodrigues J, Ben Sedrine N, Correia M.R, Monteiro T, Cretu V, Tiginyanu I, Smazna D, Mishra Y.K, Adelung R. Hybridization of zinc oxide tetrapods for selective gas sensing applications. ACS Appl. Mater. Interfaces. 2017; 9: 4084–4099.
[29] Penner R.M. A Nose for Hydrogen Gas: Fast, Sensitive H2Sensors Using Electrodeposited Nanomaterials. Acc. Chem. Res. 2017; 50:1902–1910.
[30] Xu D, Song K, Li Y, Jiao L, Zhong S, Ma J, Bao L, Zhang L, Song J, Sc2O3doped Bi2O3-ZnO thin films varistor prepared by sol-gel method. J. Alloys Compd. 2018; 746: 314–319.
[31] Yang H, Nie S, Preparation and characterization of Co-doped ZnO nanomaterials, Mater. Chem. Phys. 2009; 114: 279–282.
[32] Aydin C, Farklı Molar Oranlarında, Eşit Miktarlarda Mn-Ni Katkılandırılmış ZnO Esaslı Nano Yapılı İnce Filmlerin Yüzey Morfolojisi, Optik Sabitleri ve Dispersiyon Enerji Parametreleri, Fırat Üniversitesi Mühendislik Bilimleri Dergisi 2018; 29(2): 221–232.
[33] Aydin C, Aydin H, Yakuphanoglu F. Amorf Yarıiletken InTe İnce Filminin Üretilmesi ve Karakterizasyonu, Academic Platform Journal of Engineering and Science 2019, 7-2, 245-254.
[34] Dhanya S.M., Shailendra K., Choudhary R. J., Avinash D. W., Mahaveer K. J., Subrahmanyam A., Synthesis of Cu2O from CuO thin films: Optical and electrical, AIP Advances 2015, 5, 047143.
[35] Hasan, A.F.H., 2017 Bakır Oksit İnce Filmler Üzerine Bakır Oksit Nano-Parçacıkların Biriktirilmesi ve İncelenmesi, Süleyman Demirel Üniversitesi, Fen Bilimleri Enstitüsü, Fizik Anabilim Dalı, Isparta.

6th International Conference on Materials Science and Nanotechnology For Next Generation (MSNG2019)
October 16-18, 2019, Niğde, TURKEY (ORAL FULL TEXT)

The Effects of Induction Surface Hardening Process on Microstructure and Mechanical Properties of GGG40 Cast Iron

H. Dikbas[1], U. Caligulu[2], O. Yigit[3] and U. Gencsoy[4]

[1]*Department of Mechanical and Metal Technology, Vocational School of Technical Science, Elazig, Turkey*
[2,3,4]*Department of Metallurgy and Materials Eng, Faculty of Technology, Elazig, Turkey.*

In this study, the effects of surface hardening process with induction made on GGG40 spheroidal graphite cast irons (SGC) on the microstructure, hardness and tensile strength were investigated. For this purpose, surface hardening heat treatment with induction was applied to GGG40 SGC samples at 0.90 min feed rate at 900 ºC. In this study, we investigated the effect of the surface hardening heat treatment on the surface roughness of the SiC substrate. Microhardness measurements were also made on the surfaces by using the Vickers hardness scale (HV). Tensile tests were carried out at 1 mm / min of tensile speed under 50000 N of load in accordance with TS 287 EN 895 standard in order to determine the tensile strengths of heat treated and non-heat treated ductile cast iron GGG40 (SGC) samples. Fracture surface morphology of the samples was examined by using SEM-EDS and X-ray analyses. As a result of the examinations, it was found that the surface hardening heat treatment increased the tensile strength and surface hardness of the test samples.

Keywords: GGG40, Induction hardening, tensile strength, microstructure, microhardness.

Corresponding author: ugurcaligulu@gmail.com

1. Introduction

Spheroidal graphite cast iron (SGC) is defined as a group of materials having mechanical properties of steel and manufacturing properties of cast iron. SGCs have the strength of gray cast irons approximately two times and can be cast much more easily than steel. Moreover, the great cost advantage in its production has expanded its usage area gradually every passing day compared to both steel and other cast irons. Today, spheroidal graphite cast irons have been used successfully especially in the automotive industry. Depending on the development of spheroidal graphite cast iron technology, the ways to improve further the mechanical properties of SGC have been sought. However, it has been understood in the studies that it is impossible to gain another morphology to graphite other than sphere which has led researchers to conduct studies on improving mechanical properties through the modification of the matrix [1].

Induction surface hardening is an alternative type of heat treatment used in cases where hardness is not required on the whole part. Induction surface hardening is a process of heating the surface of work piece rapidly to austenitic conditions and rapid cooling for the conversion of a hard martensitic layer. Water or density-adjusted oil is used as the cooling medium. In this way, while some parts of the pieces are hardened, the other parts remain soft. Water hardening is not seen at the highest cooling rate in cooling the heated steel piece in the case where the temperature difference between the piece and water is the highest but it is seen when the difference is 350 and 400°C. This situation seen in water is valid at 400°C in other liquids such as oil. Water-hardening hardens three times better than oil hardening. Water hardening is the most effective and common system used in the industry because it is economical and easy. In oil hardening, the cooling power of oil is 1/3 of water. In addition to cooling in water and oil, air cooling is rarely done [2]. Induction surface hardening process is generally used in the automotive industry to harden the surface of materials such as

gearwheel, crankshaft, and shaft. In addition, this method is preferred because it makes the mechanical properties of low carbon steels and cast iron to the desired conditions [3].

In a study conducted by Ayday to improve the surface properties of SGCs, it was observed that the surfaces of samples hardened with induction were composed of martensite structure and residual austenite and this layer showed an even distribution on the surface [4]. In their study, Baydoğan et al. successfully applied boronizing and austempering process to GGG40 class ductile iron to combine the advantages of both procedures into a single treatment. This new process formed a 30-µm thick boride layer on the surface and was protected from acicular ferrite and austenite with the surface matrix structure [5]. In the studies conducted by Sert et al., on SGCs, they observed that the hardness of the samples increased with the decrease in austempering time [6]. In their study, Totik et al., evaluated the wear behavior of induction hardened AISI 4140 steel. It was determined that the wear coefficients in normalized samples were higher than the induction hardened samples [7]. In their study, Ghaderi et al. investigated the effect of chemical composition and austempering time on mechanical properties and tribological properties by subjecting cast irons having different chemical composition to austempering process under different austempering times such as 30, 60, 90, 120 minutes [8]. Hung et al., subjected spheroidal graphite cast iron containing 3.5% C, 2.8% Si to austempering process for 0.5, 1, 2, 3 hours at 420 °C austempering temperature [9]. Alabeedi et al., investigated the erosion resistance in spheroidal graphite cast iron with the process they made upon slightly laser-molten of the surface and they suggested that this was 110 times more durable than untreated state [10]. In their study, Haseeb et al. performed austempering process on spheroidal graphite cast iron at 360 °C for 2 minutes in lead bath after austenitizing at 860°C for 2 hours. In order to obtain the same hardness with the material obtained by the austempering process, spheroidal graphite cast iron in the same composition was cooled in salt water after austenitizing at 860°C for 2 hours. Finally, a tempering process of 350 ° C was performed to remove the stresses in the material [11]. Erdoğan et al., observed that austempering temperature had a significant effect on fatigue strength and the coarse ausferritic structure forming at high austempering temperatures led to decrease the fatigue strengths of the samples. In addition, as a result of their experimental studies, fatigue strength of all heat treated samples was determined to be better than the cast SGC [12]. Fredriksson et al., investigated the solidification of spheroidal graphite cast iron and small changes in the alloy (Mg, C, Ni, Si) exhibited a variable graphite distribution during solidification [13].

In this study, the effect of induction surface hardening heat treatment applied to GGG40 SGC samples at 900 °C with 0.90 min feed rate on hardness, microstructure and wear behavior was investigated.

2. Experimental Method

2.1. Materials and Preparation Techniques

SGC test samples with the diameter of 30 mm and the length of 120 mm which were cast commercially before the treatment were machined in CNC lathe and made appropriate for the test by bringing them to 10 mm diameter and 100 mm length (Figure 1). Tables 1, 2, and 3 show the chemical, physical and mechanical properties of GGG40 SGC sample, respectively.



Figure 1. Macro Image of GGG40 Test Sample

Chemical composition of GGG40 Spheroidal graphite cast iron (% weight)				
C 3.4	Si 2.3-3.1	Mn 0.1-0.3	S 0.2 max	P 0.1max
Chemical composition of GGG40 test sample (% weight)				
C 3.55	Si 2.45	Mn 0.159	S 0.014	P 0.028

Table 1. Standard Chemical Composition of GGG40 Ductile Graphite Cast Iron

Specific weight	Typical microstructure	Electrical conductivity	Thermal expansion coefficient
7.2 g/m^3	At least 80% ferrite	20-100 °C -36.5 watt / m ^{0}C	20-100 °C - 11.10 - 6 / m ^{0}C

Table 2. The Physical Properties of GGG40 Ductile Graphite Cast Iron

Yield strength	Tensile strength	Hardness	Elasticity module	Fatigue strength
250 N/mm^2	400 N/mm^2	160-190 HB	165 N/mm^2	220 N/mm

Table 3. The Mechanical Properties of GGG40 Ductile Graphite Cast Iron

2.2. Heat Treatments

Induction surface hardening heat treatment was applied to the GGG40 quality SGC samples in the cast condition. By passing SGC test samples in case condition through induction coils, rapid and homogeneous heat penetration from surface to center was achieved. By spraying water on the piece surfaces coming out of the induction, martensitic structure was formed from the surface of the piece to 1 mm depth. With this operation, a martensitic structure formed from the targeted surface to 1 mm depth (Water was used as the coolant.). The schematic view of the induction process is as shown in Figure 2. The test samples were processed with a 50kW induction machine at 900 ºC with 0.90 min. feed rate in a thermo induction company

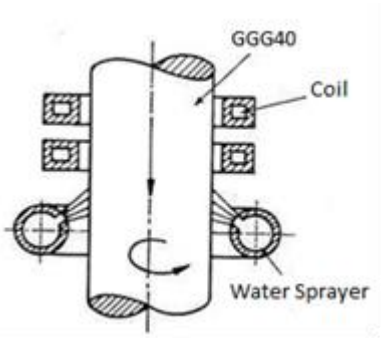


Figure 2. Schematic View of Induction Surface Hardening

2.3. Metallographic examination

Spheroidal graphite cast iron samples which were in cast state and were subjected to induction surface hardening process were cut in 10x10 mm dimensions to examine the microstructures and metallographic examinations were conducted. Conventional cleaning and polishing method was used and after sandpapering with 80, 120, 240, 500, 800 and 1000 mesh sandpaper, respectively, they were made ready for etching by polishing with a 3-µm diamond paste. Etching process was conducted by using 2% Nital for 2 seconds. In order to display the microstructures of the prepared samples, each sample was examined with Nikon MA2000 optic microscope and JEOL brand JSM-7001F scanning electron microscope.

2.4. Microhardness Tests

Six hardness values were obtained from the regions exposed to metallographic process at certain intervals to the samples which were subjected to induction surface hardness process along with SGC samples in cast state to investigate the microhardness of the test samples. The hardness tests were conducted in EMCOTEST DuraScan brand microhardness device by applying 50 gr load, with 1.3 mm intervals from the center axis of the samples and at 10 sec. feed rate.

2.5. Tensile Test

Tensile test was applied to the samples in order to see the effects of heat treatment on the tensile strength and to compare the tensile strengths of the test samples subjected to induction surface hardening heat treatment with SGC samples in cast state. The tensile test was conducted on the test samples under 50.000 N load and at 1 mm/min tensile rate in the SHIMADZU AG-X 50 KN brand tensile device in the laboratory of Fırat University Faculty of Technology Department of Metallurgy and Materials in accordance with the standards (Figure 3, Figure 4).



Figure 3. The Test Sample Subjected to the Tensile Process

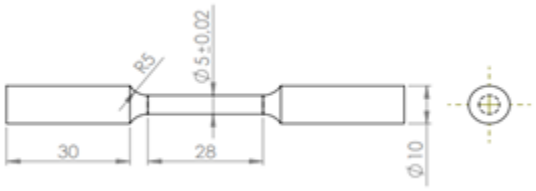


Figure 4. Sample Size According to TS138 EN Tensile Test Standard

3. Results and Discussions

3.1. Metallographic Study Results

Figure 5 shows Ferrite + Pearlite matrix microstructures of SGC

samples used in this test. As seen in the following figures, it was observed that Ferrite formed around Graphite in the internal structure of the material. Along with these ferrite rings, pearlite formation was observed in the other parts and typical "bull's eye" structure formed.

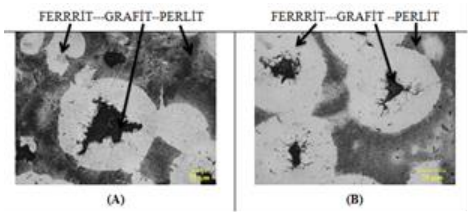


Figure 5. Microstructures (A) and (B) of the SGC (GGG40) samples in the cast state are shown in Pearlite SGC (Etching: 2% Nital X200)

SGC samples, whose microstructure was ferrite+pearlite, were subjected to induction surface hardening heat treatment at 900 ºC with 0.90 min. feed rate and the effects of induction surface hardening process on the hardness and microstructure of these samples were examined. The microstructure image of the induction sample is as indicated in Figure 6(A). As seen in the figure, the difference between the induction zone and the internal structure was clearly visible. In the left part of the figure, martensitic structure formed by the effect of heat in the part subjected to induction and caused an increased hardness in the outer shell part. No change was observed in the other region and the structure contained ferrite+pearlite. It was seen from this that a ductile structure on the inside part of this structure and a hard structure on its exterior part were obtained. Figure 6 shows microstructure images of the induction sample (B) [14].

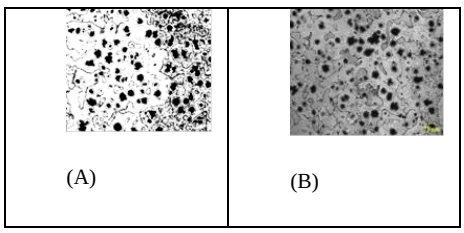


Figure 6. Induction Samples (Etching: 2% Nital X50)

3.2. Microhardness Test Results

Figure 7 shows the hardness results of SGC in cast state and SGC samples subjected to induction process in this test. It was determined according to the results given in the graph that total mean hardness value of SGC samples in cast state was 195.73 HV and the total mean hardness value of the induction samples was 282.57 HV. According to these obtained data, the hardness of the induction sample increased by 144.36% compared to SGC in cast state. Hardness values of the induction samples were obtained by taking the values from the regions close to the shell and from the inner regions. As seen from here, the mean hardness value of the material increased with the effect of hardening in the shell.

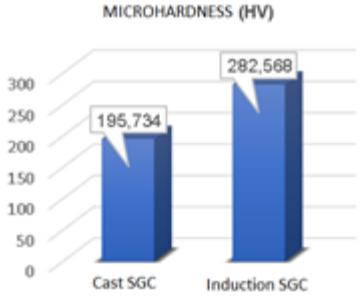


Figure 7. Average Hardness Values of SGC and OSGC Samples

3.3 Tensile Test Results

Tensile strength of GGG40 Spheroidal graphite cast iron in cast state was 400N/mm^2. Figure 8 shows the mean tensile strength of the heat treated other materials. As can be seen from the figure, the tensile strength increased with the effect of heat treatment (Figure 8). An increase of 29% was observed in the mean tensile strength of the samples subjected to induction surface hardening process.

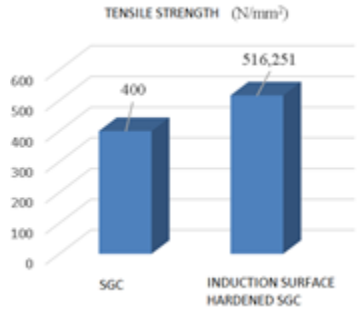


Figure 8. The Tensile Strength Mean Values of SGC and Induction Surface Hardened SGC Samples

3.4. EDS Analysis

Figure 9 shows EDS analysis graph taken 10 µm away from the fracture surface of the samples subjected to induction surface hardening process as a result of the tensile test. As understood from the EDS analysis results (Table 4), it was determined from the percentages of alloy elements that the material used in the tests was SGC. As a result of EDS analysis; 20.54% C, 0.18% Mg, 1.33% Si, and 77.94% Fe elements were determined in the microstructure.

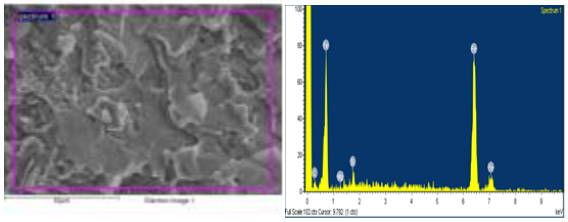


Figure 9. EDS Analysis Graphics from Fracture Surfaces

Chemical Composition (% mol.)					
	C	Mg	Si	Fe	Total
% Weight	20.5	0.18	1.33	77.94	100
% Atomic	54.1	0.24	1.50	44.15	100

Table 4. Chemical Composition of EDS Analyzes from Fracture Surfaces

4. Conclusions

1. As a result of EDS analysis taken from the fracture surfaces of GGG40 sample subjected to induction surface hardening process as a result of tensile test, it was determined that the material used was SGC and there were 20.54% C, 0.18% Mg, 1.33% Si, and 77.94% Fe elements in the microstructure.

2. Martensitic structure was formed by the effect of heat in the induction samples and caused an increase in the hardness of outer shell part.

3. The increase of the mean hardness value of the samples subjected to induction surface hardness process was due to the fact that the hardness measurement was performed from the regions close to the surface. The hardness of the induction sample increased by 144.36% compared to SGC in the cast state.

4. Tensile strength increased with the effect of heat treatment. An increase of 29% was observed in the tensile strength of the samples subjected to induction surface hardening process.

5. Acknowledgement

This study was supported by Firat University Scientific Research Projects (FÜBAP) management unit (Project No: TEKF.16.06).

References:

1. Akray İ., Küresel grafitli dökme demirlere uygulanan yüzey işlemlerinin aşınama direncine etkisinin incelenmesi, Yüksek Lisans Tezi, İstanbul Teknik Üniversitesi, Fen Bilimleri Enstitüsü, İstanbul, 2007.

2. Zakharov B., Heat Treatment of Metals, University Press of Pasific, 10-175, 2002.

3. Demirci A.H., Mühendislik Malzemeleri Önemli Endüstriyel Malzemeler ve Isıl İşlemleri, Uludağ Üniversitesi Mühendislik-Mimarlık Fakültesi, 77-78, 2004.

4. Ayday A., Elektrolitik Plazma Teknolojisi İle Küresel Grafitli Dökme Demir Malzemesinin Yüzey

Özelliklerinin Geliştirilmesi, Doktora Tezi, Sakarya Üniversitesi, Fen Bilimleri Enstitüsü, Sakarya, 2013.

5. Baydoğan M., Akray S.İ., Successive Boronizing and Austempering for GGG-40 Grade Ductile Iron, Journal of Iron and Steel Research, International, Volume 16, Issue 2, Pages 50-54, 2009.

6. Okay F., Sert H., Habalı K., Gül F., Östemperlenmiş Küresel Grafitli Dökme Demirin Aşınma Davranışı Üzerinde PVD Yöntemi İle TiN Kaplamanın Etkisi, Gazi Üniversitesi Müh. Mim. Fak. Der. 25(4), 787-794, 2010.

7. Totik, Y., Sadeler R., Alltun, H., The effects of induction hardening on wear properties of AISI 4140 steel in dry sliding conditions, Materials & Design, Volume 24, Issue 1, Pages 25-30, 2003.

8. Ghaderi, A.R., Nili Ahmadabadi, M., Ghasemi, H.M., Effect of Graphite Morphologies of Cu-Ni Austempered Ductile Iron, Materials Science and Technology, C:6, 245-256, 2003.

9. Hung, F.Y., Chen, L.H., Lui, T.S., A Study on Erosion of Upper Bainitic ADI and PDI, Materials and Desing, C: 260, 1003-1012, 2006.

10. Alabeedi K.F., Abboud J.H., Benyounis K.Y., Microstructure and Erosion Resistance Enhancement of Nodular Cast Iron by Laser Melting, Wear, vol. 266, 925-933, 2009.

11. Haseeb, A.S.M.A., Aminual, Islam, Md., Mohar Ali Bepari, Md., Tribolgical Behaviour of Quenched and Tempered, and Austempered Ductile Iron at the Same Hardness Level, C:244, 15-19, 2000.

12. Ovalı İ., Kılıçlı V. Erdoğan M., Arakritik Östenitleme Sıcaklıklarından Östemperlenmiş Küresel Grafitli Dökme Demirde Östemperleme Sıcaklığının Mikroyapı ve Yorulma Dayanımı Üzerine Etkisi, Uluslararası Demir & Çelik Sempozyumu, 114-121, 2012, Karabük, Türkiye.

13. Fredriksson H., Stjerndahl O., Tinoco S., On The Solidification of Nodular Cast Iron and Its Relation to The Expansion and Contraction, Meterials Science and Engineering A, vol. 413-414, 363-372, 2005.

14. Hayrynen K.L., Keough J.R, Kovacs B.V., Determination of mechanical properties in various ductile irons after subjecting them to long term elevated temperature, DIS Project No:28 Final Report, North Olmsted., Ohio, 1-56: 1999.

6th International Conference on Materials Science and Nanotechnology For Next Generation (MSNG2019)
October 16-18, 2019, Niğde, TURKEY (ORAL FULL TEXT)

Pt doping Effect on the Stability of Ru Nanoparticles as Ru@Pt core-shell structure: A Molecular Dynamics Investigation

S. SENTURK DALGIC
Department of Physics, Faculty of Science, Trakya University, Edirne 22030, Turkey

Recently, renewable energy devices such as Fuel Cells for converting chemical energy into electric power with no fossil fuels have great considerable attention. It is known that the Pt-Ru nanoparticles are known as the most active anodic electro catalysts for polymer electrolyte fuel cells and methanol fuel cells. In this work, the stability of the core-shell Ru@Pt structure, which was created by doping Pt atoms on the Ru nanoparticles, has investigated by molecular dynamics (MD) method. The different atomic structures of Ru nanoparticles are also used. The changes in both the atomic structure and coordination number of constituents have discussed by doping concentration and shell thickness. The results have compared with experiments and those obtained by other morphologies. It was noted that the core-shell structured of Ru@Pt nanoparticles are stable for the Pt shell at least one atom thick.

Keywords: Ru-Pt, Core-Shell, Molecular Dynamics

Submission date:
Acceptance Date:

Corresponding authors: serapd@trakya.edu.tr dserap@yahoo.com

1. Introduction

Ruthenium (Ru) has great attention as a catalyst because of its high catalytic activity. Ru nanocrystals (NCs) show an important role in many catalytic interactions [1-4]. In addition, Ru based catalysts are preferable because of environmental and industrial perspectives. It is known that naturally occurring bulk Ru forms a hexagonal close-packed (hcp) structure and maintains this structure at high temperatures and high pressures. The structure and size control of Ru nanocrystals (NCs) are well studied by experimentally [1-4]. Very recently, the Ru nanoparticles (NPs) with face-centered cubic (fcc) structures were discovered and reported [2]. The size-dependent structural stability of hcp and fcc Ru-NPs were also analyzed by experiments [1]. It has found that hcp Ru NPs larger than 3.5nm have shown lower catalytic activity than that of fcc Ru NPs of the same size. In contrast, hcp Ru NPs of 2nm has exhibited a more considerable catalytic activity than that of fcc Ru NPs of the same size [1]. On this line, Ru based alloy catalysts are designed by taking consideration of both size and shape effects on the catalytic activity of the Ru NPs. Platinum (Pt) is one of the noble metals which was demonstrated as the excellent anode material used with Ru nanostructures in fuel cell catalysts [5,6]. Among the Ru-Pt nanostructures, it has shown that Ru@Pt core-shell type nanostructures are improved their catalytic activities because of the strain effect from Ru core [7].

There are several reports about the deposition of Pt atoms on the Ru substrate as Ru@Pt core-shell nanostructures using experimental techniques [7-10]. Alayoglu and co-workers have shown that the bimetallic Ru-Pt NPs have different catalytic activity according to their architecture, such as alloy and core-shell NPs, etc. [9].

The Ru core greatly influenced the chemical action of the Ru@Pt core-shell system in the Ru@Pt spherical NP that affects significant changes in the structural properties of the Pt shell [9]. Xie and co-workers have reported the superior catalytic activity of Ru@Pt core-shell NPs with ordered core structure in contrast to amorphous one, which was studied earlier studies [10]. In very recent experiments, the catalytic activity of Ru@Pt NPs on the weakened CO adsorption has studied by constructing the ordered, and amorphous Ru core of NPs supported on carbon nanotubes (CNTs) [11].

To date, the molecular dynamics (MD) investigations on atomic ordering and stability of Ru@Pt NPs have been rare reported [9]. In this work, we first obtain

the stability of truncated octahedral Ru@Pt NPs with ordered fcc Ru core.

2. Materials and Method

The structural and thermal stability of unsupported Pt doped the Ru nanoparticles have investigated by the classical MD simulations, as implemented DLPOLY code [12] is used. Truncated octahedral (TO) shaped of Ru nanoparticle with 1289 atoms is used to construct as a core-shell Ru@Pt NPs. Here, two different Pt composition of TO Ru@Pt NPs was created as the MD sample of our calculations. In order to understand the structural and morphological stability of TO Ru@Pt NPs, two different model potential form is used.

Model Potential 1: The Sutton-Chen (SC) Potential:

The SC many-body potentials are used to describe the interatomic interactions in the Ru@Pt TO nanoparticles. Petkov and co-workers have developed SC parameters for Ru using the procedure given in the literature [13-15]. For Pt and Ru, parameters are taken from [14] and [15], respectively.

In the SC framework, the total energy for a system can be written as an equation (1) given by

$$U = \sum_i U = \sum_i \varepsilon \left[\frac{1}{2} \sum_{j \neq i} V(R_{ij}) - c\sqrt{\rho_i} \right] \quad \textbf{(1)}$$

where V (R_{ij}) is a repulsive pair interaction function between the i and j atomic cores defined by

$$V(R_{ij}) = \left(\frac{a}{R_{ij}} \right)^n . \quad (2)$$

The local electron density function of atom i defined by

$$\rho_i = \sum_{j \neq i} \left(\frac{a}{R_{ij}} \right)^n . \quad (3)$$

In above Eqs (1-3), the Rij is the distance between atoms i and j; ϵ sets the overall energy scale parameter, a and c are a length and dimensionless parameter scaling the attractive terms, respectively; n and m are integer parameters such that n>m.

Model Potential 2: Tight-Binding (TB) Potentials:

Based on the tight-binding (TB) model [16], the energy of a single atom can be divided into two parts: The attractive potential, E_B^i and the repulsive interaction term, E_R^i which is usually assumed to be pairwise, and described by a sum of -

Born-Mayer ion-ion repulsions :

$$E_B^i = -\left\{ \sum_j \xi_{\alpha\beta}^2 \exp\left[-2q_{\alpha\beta} \left(\frac{r_{ij}}{r_0^{\alpha\beta}} - 1 \right) \right] \right\}^{1/2} \quad (4)$$

Where r_{ij} represents the distance between atoms i and j; r_0 is the interatomic distance between the nearest neighbor atoms, ξ is an effective hopping integral parameter, and q describes its dependence on the relative interatomic distance. The α and β variables represent different lattice of unlike neighboring atoms.

$$E_R^i = \sum_j A_{\alpha\beta} \exp\left[-p_{\alpha\beta} \left(\frac{r_{ij}}{r_0^{\alpha\beta}} - 1 \right) \right] \quad (5)$$

where A is dependent on the experimental values of the lattice parameter. The parameter p is related to the compressibility of the bulk metal. For the hetero-interactions, an arithmetic mean was taken for the parameters related to the distance, $p_{\alpha\beta}$, $q_{\alpha\beta}$ and $r_0^{\alpha\beta}$, while a geometric mean was taken for parameters related to the strength, $A_{\alpha\beta}$ and $\xi_{\alpha\beta}$. Both attractive and repulsive energies, described well the cohesive energy of the system as given by .

$$E_C = \sum_i \left(E_R^i + E_B^i \right) \quad (6)$$

The TB potential parameters for Pt is taken from Ref. [16]. For Ru, the TB parameters are obtained by fitting some physical properties to the experimental values of bulk Ru [17]. core-shell TO Ru@Pt NPs were simulated by NVT canonical ensemble and Nose-Hoover thermostat. The time step was that 1fs in all simulations. The Verlet-leapfrog

algorithm was applied for the integral equation of motions. That nanoparticle was heated from 25K up to high temperatures with a temperature increment of 50K.

3. Results and discussion:

In this work, first, the thermal stability of the free-standing of Ru and Pt NPs have investigated by MD simulations. The morphological changes of the unsupported fcc Ru TO NPs of 1289 atoms under heating are given in Fig.1a by the snapshots from the front view using OVITO at three different temperatures, [18]. The corresponding g(r) distribution function at 850K is shown in Fig. 1b. The liquid structure is observed in Fig. 1b. Thus, it has noted that TO shaped Ru NPs have melted at 850K using SC potential. However, the corresponding melting temperature of TO Ru NPs is higher than that of the temperature obtained by SC potentials.

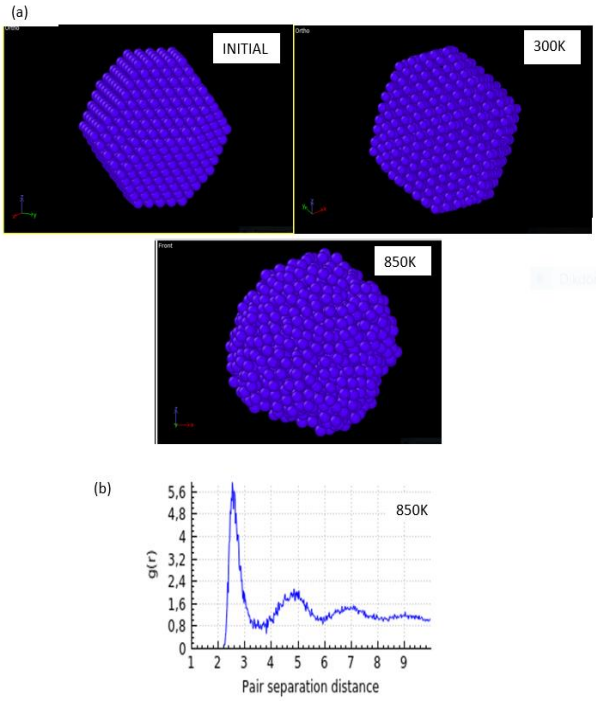


Fig.1: Ru NPs with TO morphology under heating (a)snapshots at three different temperatures (b) g(r) pair distribution function at 850K.

The truncated octahedral (TO) shaped of Ru nanoparticle is used to construct two different core-shell NPs, with compositions of $Ru_{0.78}@Pt_{0.22}$ and $Ru_{0.412}@Pt_{0.588}$ as given in Fig. 2.

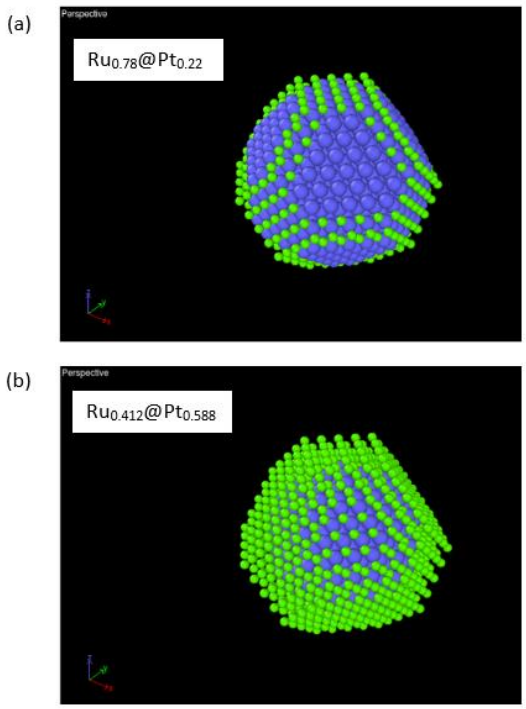


Fig.2: Snapshots of the initial geometries of Ru@Pt TO NPs.

As seen in Fig. 2, for the composition of $Ru_{0.78}@Pt_{0.22}$ core-shell TO nanoparticle, Pt atoms are placed at the corner, edge, and vertices of Ru TO nanoparticle. Thus Pt atoms do not cover the whole Ru atoms. However, for the composition of $Ru_{0.412}@Pt_{0.588}$, the Pt atoms cover all Ru atoms where at least one atomic layer.

The morphological deformations in the core-shell Ru@Pt NPs studied with SC potentials are given in Fig.3 by the snapshots of the front view using the OVITO.

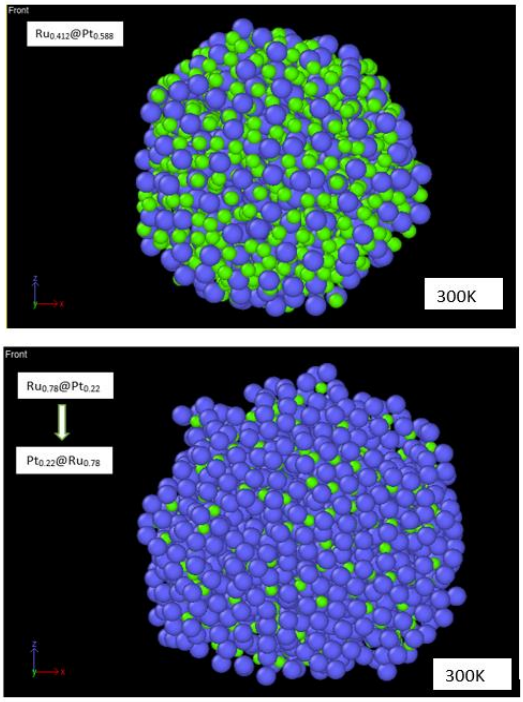


Fig.3: The snapshots from front view of the *TO-Ru@Pt nanoparticles studied with Model 1 SC potential*

The local atomic ordering of NPs is one of the important property which can be defined by different analysis methods such as bond angle analysis (BAA) or common neighbor analysis (CNA). The changes in the local atomic structure of the NPs are also defined using OVITO. The obtained local atomic structures of Ru@Pt NPs are shown in Fig. 4

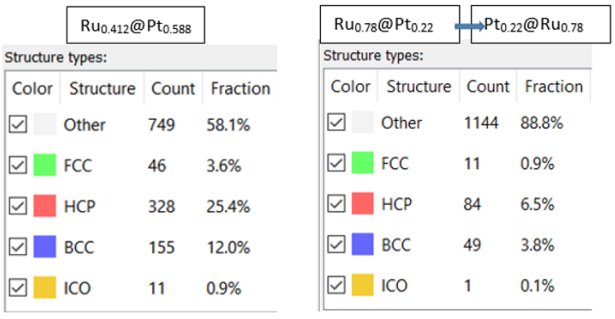


Fig.4: The local atomic structures of NPs defined by BAA method

It has noticed from Fig. 3 that the NPs studied with SC potentials show a different tendency in their structural changes from initial to 300K under the heating process. The thermally induced morphology of both core-shell Ru@Pt NPs is sphere at 300K. As seen in Fig. 3 that the $Ru_{0.412}@Pt_{0.588}$ nanoparticle with a thick layer of Pt represents as a core-shell structure of Pt@Ru while the $Ru_{0.78}@Pt_{0.22}$ nanoparticle has an alloy formation. For the stable core-shell nanoparticle, the layer thickness of the Pt shell must be at least one atom thick. However, it has obtained that both core-shell NPs studied with SC potential have melted at 300K.

The alternative potential of TB is also used. The thermally induced stability and morphology of the $Ru_{0.412}@Pt_{0.588}$ have calculated by TB potential. Fig. 5 shows the front view and cross-section of half nanoparticle of $Ru_{0.412}@Pt_{0.588}$.

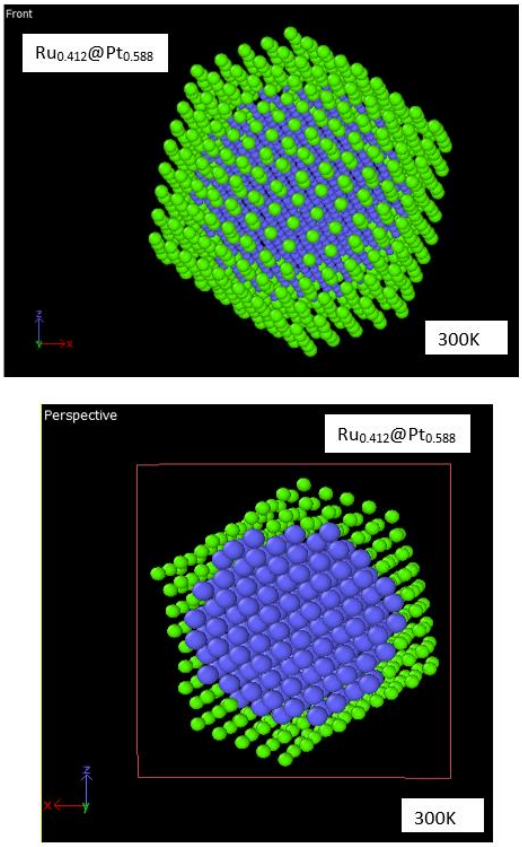


Fig.5: The snapshots from front view and cross sections of half nanoparticle of $Ru_{0.412}@Pt_{0.588}$.

The core-shell structure is maintained for the nanoparticles shown in Fig. 5. At the same time, the melting is just started in the shell of Pt atoms. The corresponding changes in the local atomic structure is given in Fig. 6. The common neighbor analysis (C N A) of $Ru_{0.412}@Pt_{0.588}$ has also summary in Fig. 6 for 300K.

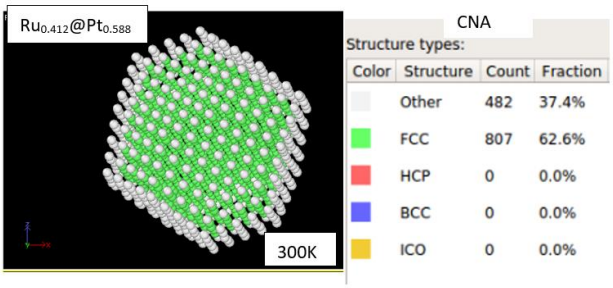


Fig.6: The local atomic structure of $Ru_{0.412}@Pt_{0.588}$ defined by CNA Method.

This local atomic structure analysis given in Fig. 6 shows that the FCC structure is still valid at 300K while it was disappeared in the C N A of the corresponding nanoparticle studied with SC potentials given in Fig. 2.

Conclusions

It was presented that highly stable FCC core-shell type truncated octahedral (TO) NPs as Ru@Pt is studied with TB potentials and MD simulation method. The thermally induced structural and morphological changes in the TO shaped Ru@Pt nanoparticles have determined by the classic simulation method using two different potentials for comparison. The fcc structure of Ru core is maintained at high temperatures when it was covered with the Pt shell at least one atomic thick. Results are in good agreement with experimental data.

The stability of Ru based core-shell NPs, such as Ru@Pt nanoparticles with different morphologies can be investigated by MD simulations using TB or EAM type potentials. This work will progress on this line and reported shortly.

References:

[1] C. Song, O. Sakata, L. S. R. Kumara, S. Kohara, A. Yang, K. Kusada, H. Kobayashi, H. Kitagawa, Sci. Rep. 6, (2016) 31400
[2] K. Kusada, H. Kobayashi, T. Yamamoto, S. Matsumura, N. Sumi, K. Sato, K. Nagaoka, Y. Kubota, H. Kitagawa, J. Am. Chem. Soc. 135 (2013) 5493−5496.
[3] G. Chen, J. Zhang, A. Gupta, F. Rosei, D. Ma, New. J. Chem, 38 (2014) 1827-1833.
[4] L. Xu, J. Yang, Physical Sciences Reviews, 3 (2018)
[5] G. S. Park, C. Pak, Y. S. Chung, J. R. Kim, W. S. Jeon, Y. H. Lee, K. Kim, H. Chang, D. Seung, J. Power Sources, 176 (2008) 484−489.
[6] N. Kakati, J. Maiti, S. H. Lee, S.H. Jee, B. Visvanathan, Y. S. Yoon, Chem. Rev. 114 (2014) 12397−12429.
[7] S. Alayoglu, A. U. Nilekar, M. Mavrikakis, B. Eichhorn, Nat. Mater., 7 (2008) 333−338.
[8] S. Alayoglu, P. Zavalij, B. Eichhorn, Q. Wang, A. I. Frenkel, P. Chupas, ACS Nano, 3 (2009) 3127−3137.
[9] P. Ochal, J L. G de la Fuente, M. Tsypkin, F. Seland, S. Sunde, N. Muthuswamy, M. Ronning, D. Chen, S. Garcia, S. Alayoğlu, B. Eichhorn, J. Electroanal. Chem., 655 (2011) 140−146.
[10] J. Xie, Q. Zhang, L. Gu, S. Xu, P. Wang, J. Liu, Y. Ding, Y. F. Yao, C. Nan, M. Zhao, Y. You, Z. Zou, Nano Energy, 21 (2016) 247-257.
[11] J. Zou, M. Wu, S. Ning, L. Huang, X. Kang, S. Chen, ACS Sustainable Chem. Eng., 7 (2019) 9007−9016.
[12] DL_POLY: a molecular dynamics simulation package was written by W. Smith, T.R. Forester, and I.T. Todorov obtained from the websitehttp://www.ccp5.ac.uk/DL_POLY
[13] A. P. Sutton, J. Chen, Philos. Mag. Lett., 61 (1990) 139
[14] Y. Kimura, Y. Qi, T. Cagin and W. Goddard III, MRS Symp. Ser., 554 (1999) 43.
[15] B. Prasai, Y. Ren, S. Shan, Y. Zhao, H. Cronk, J. Luo, C-J. Zhong, V. Petkov, Nanoscale, 7 (2015) 8122-8134.
[16] F. Cleri, V. Rosato Phys. Rev. B **48**, (1993) 22
[17] S. Senturk Dalgic, unpublished results
[18] OVITO: A. Stukowski, Modelling Simul. Mater. Sci. Eng. 18, (2010) 015012.

6th International Conference on Materials Science and Nanotechnology For Next Generation (MSNG2019)
October 16-18, 2019, Niğde, TURKEY (ORAL FULL TEXT)

Optimizations of Ball Milling Process in Reduced Graphene Oxide produced by Modified Hummers Method

B. Terzi [1,2]*, Ö. Ateş Sönmezoğlu [2], and S. Sönmezoğlu[1,3]

[1]Nanotechnology R&D Laboratory, Karamanoğlu Mehmetbey University, Karaman, Turkey
[2]Department of Bioengineering, Karamanoğlu Mehmetbey University, Karaman, Turkey
[3]Department of Metallurgical and Materials Engineering, Karamanoğlu Mehmetbey University, Karaman, Turkey

Graphene is a two-dimensional carbon nanolayer with a unique atomic thickness, and it is one of the most widely studied materials recently. Besides having excellent optical and electrical properties, its superior mechanical, chemical and thermal properties have made graphene popular for industrial and scientific research. Generally, chemical process is used to produce graphene, since other methods have some disadvantages, such as limited scalability and high costs. One of the most important steps in this chemical process is exfoliation process that helps to increase the distance between the graphene sheets to produce reduced graphene oxide. Although the sonication process, mostly used in graphene exfoliation, gives good quality graphene flakes as well as being simple and easy method, it requires a long process time which causing destruction of the structure of graphene, and also its scalability is limited. Therefore, recently, ball milling process has been developed for graphene exfoliation process to handle these limitations. As well scalable exfoliation processes for continuous graphene production. Herein, graphene oxides (GO) with different degrees of times have been prepared by ball milling process to produce high-quality graphene nanosheets. The prepared graphene oxides have been examined by X-ray diffraction (XRD), Raman spectroscopy and Fourier transform infrared (FTIR) spectra. As a consequence, the best optimized milling time has been established as 4h to prepare graphene oxide.

Keywords: Ball milling processing, Modified Hummers method, Reduced graphene oxide

Corresponding author: begumterzi19@gmail.com

1. Introduction

Carbon (C) is an element with the atomic number 6 and is a member of group IV A in the periodic table. It is the main ingredient for life on the planet, the fourth most abundant element in nature, and forms the basis of all organic chemistry [1]. Due to the variety of bonds made by the carbon atom, carbon-based materials can exist in many structures with different chemical and physical properties. Carbon allotropes: i) fullerene C60 (zero-dimensional abbreviated with 0D) ii) carbon nanotubes (one-dimensional abbreviated with 1D), iii) graphene (two-dimensional abbreviated with 2D) and iv) graphite (three-dimensional abbreviated with 3D). Among them, graphene was isolated in 2004 by Geim and Novoselov [2]. Graphene, one of the important allotropes of carbon atoms, is the building block of graphite. In the sp^3 hybrid, a single layer of carbon atoms in densely packed honeycomb crystal structure introduces its structure, which is connected to another graphene layer by van der Waals forces. Due to its single atomic thickness, it is the lightest, thinnest 2D material known. Graphite is formed by overlapping graphene layers, the distance between the two graphene layers is approximately 3.35 A° and the distance of C-C bonds in the structure is about 1.4 A°. Thanks to its strong carbon bond structures, it is the most robust material and is 100 times more durable than steel, as well as being easily bendable and flexible. Its flexibility gives it an advantage in terms of its coating properties on different materials. Graphene, which is the only nonmetal that can conduct electricity, has a higher

conductivity value than copper. It is a stable material and not chemically reactive, which is reflected in its electronic properties [1]. Specifically the superior properties of graphene make it an important component for biosensors as transducer.

There are number of processing methods for production of graphene as follows: chemical vapor deposition (CVD), mechanical exfoliation of graphite or graphite oxide or chemically reduction etc. [3-5]. Compared to other techniques, the most commonly used process to obtain graphene is the chemically reduction of graphene oxide. Graphene oxide has been synthesized by Brodie [6], Staundenmaier [7], Offeman and Hummers [8], where strong acid and oxidants have been used in chemical methods. In the Hummers method, sulfuric acid (H_2SO_4), potassium persulfate ($K_2S_2O_8$), phosphorus pentaoxide (P_2O_5) are added to the graphite. It is continuously stirred at a certain temperature then washed and filtered. In subsequent processes, H_2SO_4 and potassium permanganate ($KMnO_4$) are added in an ice bath to obtain a brown solution with water and hydrogen peroxide (H_2O_2). After washing with HCl, dialysis is performed and graphite oxide is obtained. One of the important steps to produce the reduced graphene oxide by chemical reduction is the exfoliation process which helps to increase the distance between the graphene sheets to produce reduced graphene. In this work, an optimization was performed to investigate ball milling times for exfoliation of graphene. Analysis of X-ray diffraction (XRD), Raman spectroscopy and Fourier transform infrared (FTIR) spectra were utilized to think about the physical properties.

2. Experimental details

In this work, reduced graphene oxide (rGO) was obtained and characterization studies of ball milling times were performed. Oxidation, exfoliation and reduction experiments for the manufacture of rGO were performed according to the modified hummers' method. According to modified hummers method; firstly, sodium nitrate and sulfiric acid are prepared in an ice bath then graphite powder and potassium permanganate are added to the solution. After that, solution is stirred in an oil bath at 50 °C for 2 h. Add some ddH_2O and hydrogen peroxide to the mixture, then stand overnight at room temperature and after added HCl. Centrifugation, washing and filtering performed. In order to get rid of acid residues, the process is completed by dialysis for a few days followed by drying. N-methyl-2-pyrrolidone (NMP) was used for ball milling solution and the samples that are physically shredded in the ball milling process appear dark black with the solvent (Fig. 1). In the reduction process, the solution containing GO and H_2O water is sonicated for 10 minutes. After sonication, the solution is transferred to the magnetic stirrer and stirred for 3 hours, followed by the addition of hydrazine hydrate as a reducing agent. The system is maintained in the oil bath at 95 °C for 24 h. After 24 h, the system is turned off and allowed to cool then subjected to washing and filtration with a glass funnel and allowed to dry. The characterizations of products were utilized using XRD, Raman spectroscopy and FTIR equipments.



Figure 1. *Ball milling process used in experiments*

3. Results and discussion

FT-IR analysis was performed to examine the functional groups in the GO structure obtained from the experiments. FT-IR analysis shows carboxylic acid groups, hydroxyl, epoxy and alkoxy groups in GO structure. Accordingly, stresses that graphene oxide is synthesized successfully; 1713 cm^{-1} for C = O stretching of carboxyl groups, 3116 cm^{-1} for OH stretching of carboxyl and hydroxyl groups, 1215 cm^{-1} for CO stretching, 1042 cm^{-1} for CO stretching of alkoxy groups [9,10]. The presence of functional groups such as epoxy, carboxyl and hydroxyl was found to be in the GO structure obtained by Hummers method as a result of the interaction of IR radiation with the FT-IR method. It is seen that functional groups in the structure are removed from the structure as a result of reduction (Fig 1).

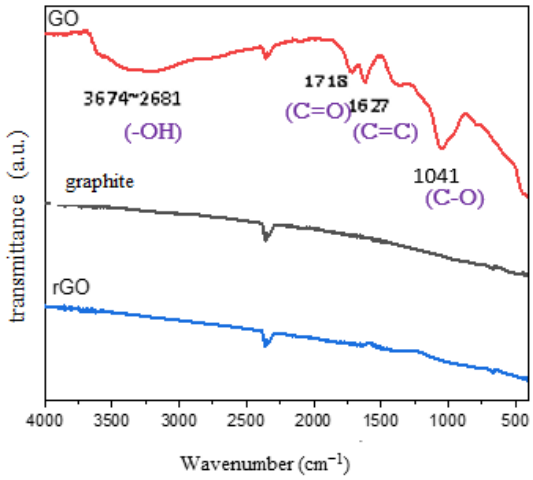


Figure 1. *SEM and EDX images of samples with 60 minutes FT-IR analysis of rGO, graphite and GO.*

When the ball milling times were compared, it was found that long ball milling times could lead to more breakage in the functional groups and cause random bonding, as shown in fig 2. Therefore, the short grinding time of the ball was found to be sufficient.

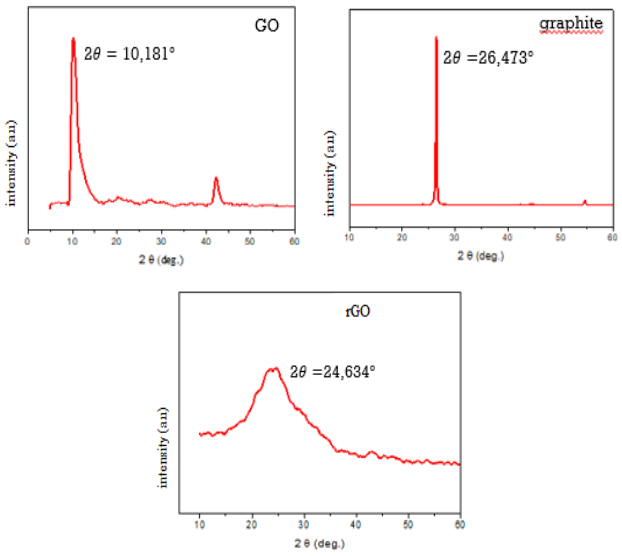


Figure 2. *FT-IR analysis of GO for ball milling times.*

The crystal properties of GO and rGO has been studied using X-ray diffraction (XRD). As shown in Fig 3, the XRD peak becomes wider and less dense than graphite due to defects in the rGO page and other oxygen functional groups

Figure 3. *X-ray difraction patterns of graphite, GO and rGO.*

When ball milling times are compared, it is seen that high times can initiate the reduction reaction (Fig 4). Therefore, the 4-h ball milling time was found to be more suitable for exfoliation before reduction.

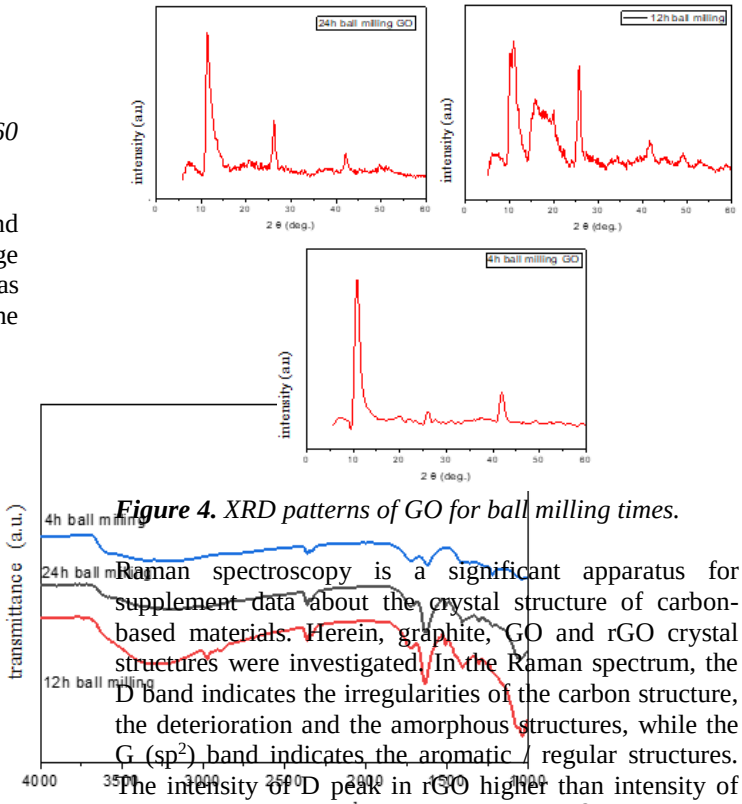


Figure 4. *XRD patterns of GO for ball milling times.*

Raman spectroscopy is a significant apparatus for supplement data about the crystal structure of carbon-based materials. Herein, graphite, GO and rGO crystal structures were investigated. In the Raman spectrum, the D band indicates the irregularities of the carbon structure, the deterioration and the amorphous structures, while the G (sp^2) band indicates the aromatic / regular structures. The intensity of D peak in rGO higher than intensity of peak D in GO. The fig 5 shows that new sp^2 structures are formed instead of functional groups which are removed as a result of reduction reaction and the amount of regular structure increases.

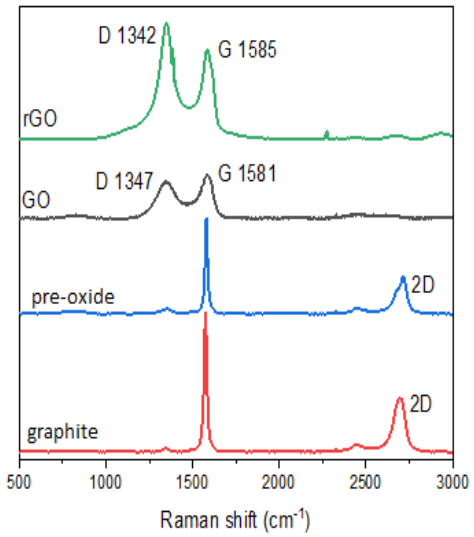


Figure 5. *XRD patterns of GO for ball milling times.*

Fig 6 shows Raman results after ball milling times. It was decided that, the ration of D and G peak intensities most suitable at 4 h for exfoliation. While there is not much difference in D/G ratios between 12 and 24, it is though that the long ball milling time increases the inter layer distance also it may breaks the functional groups. This is undesirable as this will affect the efficiency of the reduction.

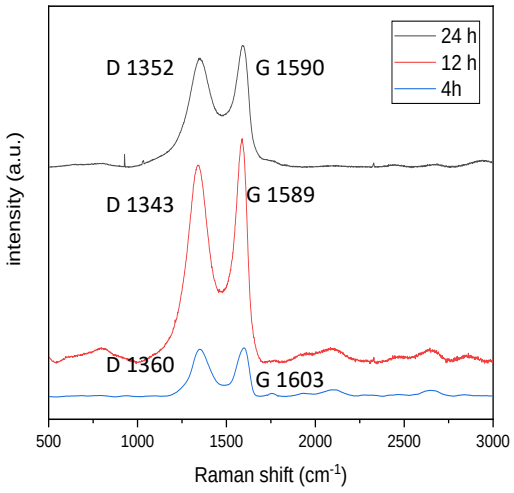


Figure 6. *Raman graphics after ball milling.*

The ratio of D and G bands (I_D/I_G) is a measure of irregularity in the structure and, it provides information about defects in the layer. Table 1 shows the D and G band ratios of GO and rGO samples.

Table 1*: I_D/I_G ratios of GO and rGO samples.*

	rGO	**GO-4h**	**GO-12h**	**GO-24h**
I_D/I_G	1.3	0.96	0.88	0.89

4. Conclusion

Modified Hummers method was used and ball milling optimization was studied for exfoliation process in this work. Ball milling times (4h, 12h, 24h) were compared for the production of reduced graphene oxide. It is suggested that high ball milling times can cause deformations in structure and optimum ball milling time is determined as 4h. As a result of this study, it is aimed to use rGO for future GMO biosensor applications.

References:

[1] NETO, AC., GUINEA, F., PERES, NM., NOVOSELOV, KS., GEİM, AK. (2009). "The electronic properties of graphene". *Rev. of mod. Phys.*, *81*(1), (2009), 109.

[2] NOVOSELOV, KS., GEIM, AK., MOROZOV, SV., JIANG, D., ZHANG, Y., DUBONOS, SV., FIRSOV, AA. "Electric field effect in atomically thin carbon films". *Science*, *306*(5696), (2004), 666-669.

[3] DREYER, DR., RUOFF, RS., BIELAWSKI, CW. "From conception to realization: an historial account of graphene and some perspectives for its future". *Angew. Chem. Int. Ed. 49*(49), (2010), 9336-9344.

[4] PUMERA, M. "Graphene-based nanomaterials and their electrochemistry." *Chem. Soc. Rev.* 39, (2010), 4146-4157.

[5] GÓMEZ-NAVARRO, C., MEYER, JC., SUNDARAM, RS., CHUVILIN, A., KURASCH, S., BURGHARD, M., KAISER, U. "Atomic structure of reduced graphene oxide". *Nano lett.*, *10*(4), (2010). 1144-1148.

[6] BRODIE, BC. "Sur le poids atomique du graphite". *Ann. Chem. Phys*, 1860, 59.466: e472.

[7] STAUDENMAIER, L. "Verfahren zur darstellung der graphitsäure." *Berich. der deuts. Chem. Gesells.* 32.2, (1899), 1394-1399.

[8] HUMMERS Jr, WILIAM S., RICHARD E. OFFEMAN. "Preparation of graphitic oxide." *J. of the A. Chem. S.* 80.6, (1958), 1339-1339.

[9] SONG, J., XINZHI W., CHANG-TANG C. "Preparation and characterization of graphene oxide." *J. of Nano.* 2014, (2014).

[10] TIYEK, İ., ERSOY, MS., ALMA, MH., DONMEZ, U., YILDIRIM, B., SALAN, T., YILDIZ, K. "Modifiye Hummers Yöntemiyle Grafen Oksit (GO) Sentezi ve Karakterizasyonu". *Gazi Üniv. Fen Bilim. Derg. Part C: Tas. ve Tekn.* *4*(2), (2016), 41-

6th International Conference on Materials Science and Nanotechnology For Next Generation (MSNG2019)
October 16-18, 2019, Niğde, TURKEY (ORAL FULL TEXT)

Synthesis of TiO_2@reduced graphene oxide (rGO) nanocomposites by hydrothermal method for Photocatalytic Applications

A.Culu[1,2]*, S. Sönmezoğlu[1,2]

[1]Nanotechnology R&D Laboratory, Karamanoğlu Mehmetbey University, Karaman, Turkey
[2]Department of Metallurgical and Materials Engineering, Karamanoğlu Mehmetbey University, Karaman, Turkey

Since it has superior properties such as thermodynamically stable, strong oxidative ability and non-toxicity, TiO_2 has been considered as one of the most promising photo-catalyst material compare to other alternative materials. However, the - usage of TiO_2 has disadvantages in some cases, such as the rapid transition of the electron-space pair and absorption of a narrow solar spectrum range. One of the most preferred methods to overcome these limitations is the formation of nanocomposites with reduced graphene oxide (rGO). Besides extending absorption spectrum, such a composite structure facilitates the charge transportation and separation in a photocatalytic system owing to considerable opto-electronic properties of graphene, including excellent mobility, specific surface area, and good optical transparency.

In this work, TiO_2 nanoparticles@reduced graphene oxide (rGO) nanocomposite photocatalysts were synthesized by growing TiO_2 nanoparticles onto the surface of rGO nanosheets through hydrothermal method. To get this nanocomposite, we primarily prepared graphene oxide (GO) using a modified Hummers technique, and then as-obtanied GO nanosheets were converted rGO during simultaneously production with TiO_2 nanoparticles by hydrothermal process. The prepared nanocomposites were characterized by scanning electron microscopy, X-ray diffraction, Raman spectroscopy, and UV/Vis spectroscopy. We evaluated the photocatalytic activities of these nanocomposites via photo-degradation of rhodamine B (RhB) under ultra-violet light irradiation. Surprisingly, photocatalytic activity of this nanocomposite has been weakened with integration of rGO inside TiO_2 nanoparticles due to the disappearance of surface functionalities with reduction.

Keywords: rGO, TiO_2, nanocomposites, photocatalytic activity

Corresponding author: ayseculu95@gmail.com

1. Introduction

Semiconductor photocatalysts (ZnO, TiO_2, MnO_2, Cu_2O, Fe_2O_3, SnO_2) have been used as photocatalysts for the separation of various environmental pollutants.[3] TiO_2 was found to be the most suitable photocatalytic process. TiO_2 does not cause corrosion, but also has a wide pH range and high photochemical stability.[4] However, in practical applications, some disadvantages of using TiO_2, such as the fast coupling of the electron-space pair and the use of a small amount of sunlight, are still a commercial problem[1]. Therefore, in recent years, it has become important to search for alternative materials that can be used as effectively as graphene-metal oxide as photocatalytic material. One of the most commonly used methods to address these problems is the formation of nanocomposites with reduced graphene oxide (rGO).[2]

In TiO_2 / rGO nanocomposite, electrons can be transported on rGO plates. Reduced graphene oxide layers provide effective separation of electron - hole pair.[7] Electrons trapped on the GO layers react with O_2 adsorbed to produce reactive oxygen that reacts with water to produce hydroxyl radicals.[6] Thus, hydroxyl radicals break down the dye rodamine-B (rhB). Reactive cavities on TiO_2 react with surface orifices which are reactive species for degradation of the rhB dye and

adsorbed water or hydroxyl group to produce surface hydroxyl radicals to which rhB molecules can be directly oxidized.[7]

2. Experimental details

For the synthesis of titanium nanoparticles, 100 ml of ethanol was first mixed with 0.4 ml of 0.1 M potassium chloride with a magnetic stirrer. To the mixture was added 2.2 ml of TTIP (titanium tetraisopropoxide).(Wang et al 2006) Stirring was continued for a further 10 minutes and the mixture turned white. The mixture was allowed to stand at room temperature for 24 h. After 24 hours, it was filtered and dried in a vacuum oven at 50 ° C. [8]
Graphene oxide was obtained by oxidation using the Hummers method. Graphite powders, sulfuric acid (H2SO4), phosphorus pentaoxide (P2O5), potassium persulfate (K2S2O8) were used as oxidizing acid. First, P_2O_5 and $K_2S_2O_8$ added to sulfuric acid were stirred in a magnetic stirrer until a homogeneous mixture was obtained, then graphite powder was added and stirred in reflux system at 80 ° C for 4-5 hours. After cooling to room temperature, the mixture was washed with de-ionized water and allowed to dry overnight at room conditions. Graphite powder was added to the mixture and stirring was continued. During this process, $KMnO_4$ was added slowly by controlling the temperature continuously. After the addition was complete, the mixture was stirred at 35 ° C for 2 hours. After 2 hours, it was diluted with de-ionized water. Subsequently, after some further de-ionization was added, H_2O_2 was added. When the mixture reached room temperature, it was washed with 10% HCl after filtration. To remove acid residues, it was washed several times with deionized water and filtered dried. As a result of the milling process, graphite oxide structure is obtained by separating the layers of graphite oxide layer. In other words, the purpose of this step is to flake the graphene oxide structure. Ball milling is used to reduce the amount of oxygen along with impurities in the graphite oxide structure. For this process, N-methyl-2-pyrrolidone was used as a solvent and the graphene oxide powder was carried out in a ball mill in the air medium by flaking together with the solvent for a certain period of time. The product obtained was dried in a vacuum oven to remove moisture by backwashing and filtering. For nanocomposite, TiO_2 and graphene oxide powders were also dissolved in ionized water and a homogeneous mixture was obtained. The homogeneous mixture obtained was transferred to the teflon vessel and remained in the hydrothermal system for 12 hours at 120 ° C. It was then dried by filtration and backwashing.

3. Results and discussion

The crystallographic structure of the as-obtained pure TiO_2 and TiO@rGO nanocomposite was evinced by XRD measurements. From XRD pattern in Fig1(a), TiO_2 was purely formed at anatase phase which these peaks are indexed to desired crystal planes. After incorporating rGO under the hydrothermal reaction, the carbon peak in TiO@rGO nanocomposite weakly appeared which is resulting that the TiO_2 nanoparticles is separately formed due to destruction of functional groups in graphene surface during the reduction process and thus titanium oxide cannot hold onto the surface well. This event is undesirable for photocatalytic measurements.
The photocatalytic activities of pure TiO_2 and TiO@rGO nanocomposite were analyzed by the degradation rhB dye under UV-light irradiation, and in Fig. 6, the results were shown. It is clear that the TiO@rGO nanocomposite exhibited a weaker photocatalytic activity than pure TiO_2.

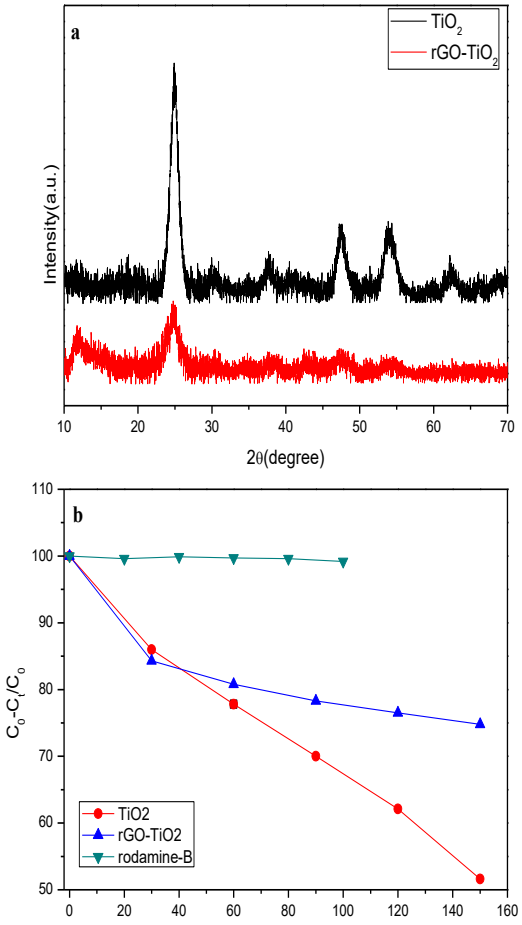


Figure 1 *(a): TiO_2 and rGO-TiO_2 XRD pattern, (b) TiO_2 and rGO-TiO_2 Photocatalytic Degradation*

4. Conclusion

From the experimental findings, it was understood that the rGO-TiO_2 composite structure had no photocatalyst effect. This is attributed to the fact that the nanocomposite structure does not form because the TiO_2 cannot hold onto the surface because nearly all of the functional groups in the rGO structure are broken while the composite structure is produced by hydrothermal.

References:

[1] UMAR, I.G., ABDUL HALİM, A., 'Heterogeneous photocatalytic degradation of organic contaminants over titanium dioxide: A review of fundamentals, progress and problems'.J. Photochem. Photobiol. C. 9, (2008) 1- 12.

[2] MAEDA, K., 'Photocatalytic water splitting using semiconductor particles: History and recent developments', Journal of Photochemistry and Photobiology C: Photochemistry Reviews.12,(2011) 237-268.

3] TSUYOSHİ, O., AKİRA, F., 'Photoelectrochemical properties of TiO_2 photocatalyst and its applications for environmental purification'. J. Photochem. Photobiol. C. 13, (2012) 247-262.

[4] HYUNWOONG, P., YİSEUL, P., WOOYUL, K., WONYONG, CH., 'Surface modification of TiO_2 photocatalyst for environmental applications'.J. Photochem. Photobiol. C. 15, (2013) 1-20.

[5] BO-TAO, Z., XİAOXİA, Z., HAİ-FANG, L., JİN-MİNG, L., 'Application of carbon-based nanomaterials in sample preparation: A review'.Anal. Chim. Acta. 784, (2013) 1-17.

1. [6] XİAOQİANG, A., JİMMYC, Y.,' Graphene-based
2. photocatalytic composites'. RSC Adv. , (2011) 1426-1434.

[7] ROYA, S., FATEMEH, H., 'A Novel & Effective Visible Light-driven TiO2/Magnetic Porous Graphene oxide Nanocomposite for Degrading Dye pollutant'. RSC Advances.6,(2016) 49459-49468.

[8] WANG, Y., XU, H., WANG, X., ZHANG, X., JİA, H., ZHANG, L., QİU, J., 'A General Approach to Porous Crystalline TiO_2 , $SrTiO_3$, $BaTiO_3$ Spheres'J.Phys.Chem.B. 110, (2006) 13835-13840.

6th *International Conference on Materials Science and Nanotechnology For Next Generation (MSNG2019)*
October 16-18, 2019, Niğde, TURKEY (ORAL FULL TEXT)

Magnetic Properties of NiGe/Au/C60 Thin Films at 5 K

Dogan KAYA[a,b,*], Mustafa AKYOL[c], Yitao WANG[b], Quanmin GUO[b], Faruk KARADAG[d], Ahmet EKICIBIL[d]

[a] Cukurova University, Vocational School of Adana, Department of Electronics and Automation, Adana, Turkey
[b] University of Birmingham, School of Physics and Astronomy, Nanoscale Physics Research Laboratory, Birmingham, United Kingdom
[c] Adana Alparslan Turkes Science and Technology University, Faculty of Engineering, Materials Engineering Department, Adana, Turkey
[d] Cukurova University, Faculty of Art and Sciences, Department of Physics, Adana, Turkey

Exploring intrinsic magnetism of magnetic semiconductor layers provides great potential applications in semiconductor spintronics applications. Therefore, we first investigated NiGe interlayer between ferromagnetic (FM) Ni and semiconductor (SC) Ge layers via a high-vacuum physical vapor deposition technique. Following we studied the effect of diamagnetic (DM) contribution of the C_{60} layer on NiGe/Au thin film. Magnetization vs. temperature (*M(T)*) between 5 K and 300 K and applied field (*M(H)*) up to 3 T obtained Physical Property Measurement System (PPMS) with a Vibrating Sample Magnetometer (VSM) head. *M(T)* results indicated that the DM signal arises from the C_{60} layer and Si substrate and below 50 K paramagnetic contribution becomes dominant in the sample. We observed large saturation (M_s) and remanent magnetization (M_r) and a negative hysteresis loop shift that is pinned magnetization (M_p) due to NiGe interlayer. The Ni layer in the sample results in the coercive field but there is no exchange interaction due to the absence of an antiferromagnetic (AFM) signal in the sample.

Keywords: Magnetization, Temperature dependence, hysteresis loop, NiGe/Au film, Fullerene

Corresponding author: dogankaya@cu.edu.tr

1. Introduction

Magnetic semiconductor interfaces become an important subject due to the natural spin-related properties for spintronics applications, such as insulating barrier for spin transistor and spin light-emitting diodes applications [1]. Such a combination of ferromagnetic (FM) and semiconductor (SC) interface properties provide no long-range ordered magnetization [2-4]. Fe, Co, and Ni are mostly used as a FM layer and Si, Ge, and Ga are uses as a SC layer. So controlling the magnetic properties of the FM layer, such as Curie temperature, magnetization, is possible by creating FM/SC interlayer. Moreover, FM/SC systems also provide potential applications in transistor technology due to intrinsic tunneling resistance [5]. In the literature, NiGe [6, 7], Fe_2YSi (Y = Cr, Mn, Fe, Co, Ni) [8], BaNiGe [9], FeGe [10], Fe on Si [11], MnGe [12], β-FeSe [13], Fe on GaAs [14] are studied and resistivity, thermal conductivity, Hall effect, and magnetic susceptibility with transport measurements are key subjects for the FM/SC systems. Although for device applications, Si is the most preferred material due to its semiconducting nature and easy to obtain, Ge provides similar properties addition with higher charge density and intrinsic mobility [3, 15]. FM nature of Ni exhibits realistic applications due to its high Curie temperature of T_C=630 *K* [16] in magnetic recording media [17], corrosion-resistant coating [18], solar thermal energy conversion [19]. Therefore, NiGe interlayer is an interesting system due to a small lattice mismatch and low resistivity. Differently, fullerene molecule (C_{60}) is a DM

order and provides magnetic and superconducting properties when it is doped with alkali metals. Therefore, C_{60} has a potential to control the magnetic properties of FM/SC systems.

In this paper, we studied the effect of the DM C_{60} layer on NiGe/Au thin film. The formation of NiGe layer between FM/SC Ni-Ge film contributes to the magnetic properties of the sample. Magnetization vs. temperature between 5 K and 300 K and applied external field up to 3 T measurements reveal remanent magnetization (M_r), saturation magnetization (M_s), coercive field (H_c), exchange bias (H_e), and pinned magnetization (M_p).

2. Experimental details

The sample was prepared in EDWARDS 306 evaporator under high-vacuum of 10^{-7} mbar using tantalum boats. We first evaporated Ni (0.4 mm pieces with high purity 99.99%) on a p-type Si wafer without annealing the sample and then Ge (0.5 mm with high purity 99.9985%) layer formed on it. Following, on the top of Ge, a thin Au layer was deposited to prevent the sample from oxidation or contamination. Finally, C_{60} molecules were deposited on the Au layer. To determine magnetic properties, a Quantum Design Physical Property Measurement System (PPMS) with a vibrating sample magnetometer (VSM) head was used for the magnetization as a function of a applied field, *M(H)* up to 3 T and temperature, *M(T)* at field cooled (FC) and zero-field cooled (ZFC). *M(H)* and *M(T)* measurements were performed via parallel applied field at 5 K and sweeping the temperature between 300-5 K, respectively.

3. Results and discussion

We first measured magnetic moment vs. temperature (Figure) between 5 K and 300 K for NiGe/Au/C_{60} films in FC (red) and ZFC (black) and an external magnetic field of 500 Oe is applied parallel to the film plane. There is no phase transition is observed below 300 K. The film exhibits first a decrease in magnetization with decreasing temperature and an upturn below 50 K. Such a rise is mostly observed at low temperature which can be attributed to the DM signal of the C_{60} layer on the top of the sample and Si substrate contribution [20]. Below 50 K PM contribution is become dominant in the sample. This signal is due to an anisotropic magnetization of the unidirectional aligned C_{60} layer. The applied field is strong enough to overwhelm the DM signal additional with a PM contribution.

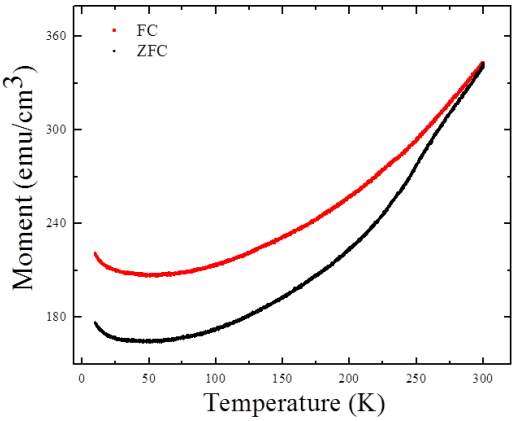


Figure 1. *Magnetic moment vs. temperature (between 5 K and 300 K) of NiGe/Au/C_{60} films measured in FC (red) and ZFC (black) for external magnetic field applied parallel to the film plane of 500 Oe.*

Magnetization vs. applied field (up to 3 T) measurements were performed at 5 K and 300 K. The hysteresis loop of the sample is presented in Figure2(a) with before (red circle) and after (blue circle) background subtraction. The increase above 0.4 T is due to DM signals in the sample. These DM signals arise from the C60 layer and Si substrate [21]. To evaluate FM Ni layer magnetic contribution, we need to subtract all DM background from the total magnetization. First, we found the slope by linear fitting above between 1.5 T to 3 T where the DM signal is linear. Following we subtract this DM signal from the total magnetization to obtain FM and PM signals. After background subtraction, the hysteresis loop (blue circle) is presented in Figure2(a). The saturation magnetization (Ms=|(Ms+−Ms−)/2|), remanent magnetization (Mr=|(Mr+−Mr−)/2|), coercive field (Hc=|(Hc+− Hc−)/2|), and exchange bias (He=|(Hc++Hc−)/2|) can be determineD by finding positive (Mr+, Ms+ and Hc+) and negative (Mr-, Ms- and Hc-) intercept of moment and field. Ms can be extracted from the intercepts of the moment axis which is found to be 618.8 emu/cm3. The loop in Figure2(b) exhibits an open-loop near the coercivity. Mr and Hc are calculated as 118.9 emu/cm3 and 458.4 Oe, respectively. These values can be controlled by the Ge layer which forms a thin NiGe interlayer. Here, we observed almost zero exchange bias for this system. This is because there is no antiferromagnetic (AFM) contribution from any layer.

The loop also exhibits a vertical shift which induces a small number of pinned moments, pinned magnetization (Mp=|(Ms++Ms−)/2|), that do not flow the applied field [22]. Mp is found to be 17 emu/cm3 that is probably because of NiGe interlayer.

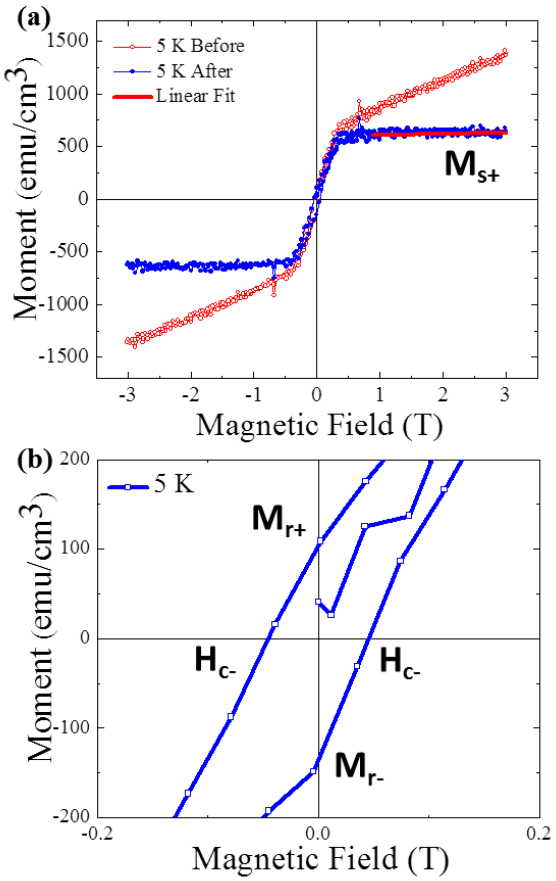


Figure 2. *M(H) plot for NiGe/Au/C_{60} sample at 5 K and the field is applied parallel to the substrate (a) The hysteresis loop of the sample before (red circle) and after (blue circle) DM background subtraction. The saturation magnetization (M_s) found by linear fitting (red line). (b) The remanent magnetization (M_r), coercive field (H_c), and exchange bias (H_e) are determined intercepts of x, y-axis as shown in the enlarged plot around the origin.*

4. Conclusion

In this study we investigated the C_{60} formation on NiGe/Au layer and determined magnetic properties at 5 K via magnetization of the sample as a function of applied field up to 3 T and temperature between 5 K and 300 K. We observed strong DM signal arises from the C_{60} layer and Si substrate on M(T) plot with an upturn below 50 K due to PM order. The hysteresis loop examined after subtraction of DM signal from the total magnetization, a large M_s, and M_r calculated along with M_p due to thin NiGe interlayer. While the sample exhibits H_c, no He observed at a low temperature of 5 K. This is because there is no AFM contribution in the sample.

5. Acknowledgement

The authors are thankful for the financial support of Cukurova University Scientific Research Funding Grand No: FBA-2018-10813.

References:

[1] S. Sugahara, S. Sugahara, Spin metal-oxide-semiconductor field-effect transistors (spin MOSFETs) for integrated spin electronics, in: IEE Proceedings - Circuits, Devices and Systems, 2005, pp. 355-365.
[2] C. Zhang, Y. Mao, R. Wang, H. Xiao, L. Xu, Z. Xia, C. Yang, Sign reversal of spontaneous exchange bias in Mn0.7Fe0.3NiGe alloy, J. Magn. Magn. Mater., 444 (2017) 12-15.
[3] M. Swain, S. Singh, D. Bhattacharya, A. Singh, R.B. Tokas, C.L. Prajapat, S. Basu, Micro-structural characterization of low resistive metallic Ni germanide growth on annealing of Ni-Ge multilayer, AIP Advances, 5 (2015) 077129.
[4] S. Singh, S. Basu, M. Gupta, M. Vedpathakz, R.H. Kodama, Investigation of interface magnetic moment of Fe⁄Ge multilayer: A neutron reflectivity study, J. Appl. Phys., 101 (2007) 033913.
[5] E.I. Rashba, Theory of electrical spin injection: Tunnel contacts as a solution of the conductivity mismatch problem, Phys. Rev. B, 62 (2000) R16267-R16270.
[6] C. Yan, J.M. Higgins, M.S. Faber, P.S. Lee, S. Jin, Spontaneous Growth and Phase Transformation of Highly Conductive Nickel Germanide Nanowires, ACS Nano, 5 (2011) 5006-5014.
[7] I.S. Edelman, D.A. Velikanov, A.V. Chernichenko, D.A. Marushchenko, E.V. Eremin, I.A. Turpanov, G.V. Bondarenko, Y.E. Greben'kova, G.S.

Patrin, Magnetic and magneto-optical properties of Ni–Ge layered films, Physica E, 42 (2010) 2301-2306.
[8] H. Luo, Z. Zhu, L. Ma, S. Xu, H. Liu, J. Qu, Y. Li, G. Wu, Electronic structure and magnetic properties of Fe2YSi (Y = Cr, Mn, Fe, Co, Ni) Heusler alloys: a theoretical and experimental study, J. Phys. D: Appl. Phys., 40 (2007) 7121-7127.
[9] S. Johnsen, A. Bentien, G.K.H. Madsen, M. Nygren, B.B. Iversen, Crystal structure and transport properties of nickel containing germanium clathrates, Phys. Rev. B, 76 (2007) 245126.
[10] R. Jaafar, D. Berling, D. Sébilleau, G. Garreau, Epitaxial Fe-Ge thin films on Ge(111): Morphology, structure, and magnetic properties versus stoichiometry, Physical Review B: Condensed matter and materials physics, 81 (2010) 155423.
[11] V.F. Motsnyi, J.D. Boeck, J. Das, W.V. Roy, G. Borghs, E. Goovaerts, V.I. Safarov, Electrical spin injection in a ferromagnet/tunnel barrier/semiconductor heterostructure, Appl. Phys. Lett., 81 (2002) 265-267.
[12] C. Zeng, S.C. Erwin, L.C. Feldman, A.P. Li, R. Jin, Y. Song, J.R. Thompson, H.H. Weitering, Epitaxial ferromagnetic Mn5Ge3 on Ge(111), Appl. Phys. Lett., 83 (2003) 5002-5004.
[13] D. Li, D. Pan, W. Liu, X. Li, M. Chen, S. Li, Y. Li, J. Tan, D. Sun, Z. Wang, Z. Han, Z. Zhang, Controllable Phase Transition for Layered β-FeSe Superconductor Synthesized by Solution Chemistry, Chem. Mater., 29 (2017) 842-848.
[14] D.M. Gillingham, M. Tselepi, A. Ionescu, S.J. Steinmuller, H.E. Beere, D.A. Ritchie, J.A.C. Bland, Smoothening of ultrathin Fe films grown on GaAs(100) observed by scanning tunneling microscopy and Brillouin light scattering, Phys. Rev. B, 76 (2007) 214412.
[15] C. Shen, T. Trypiniotis, K.Y. Lee, S.N. Holmes, R. Mansell, M. Husain, V. Shah, X.V. Li, H. Kurebayashi, I. Farrer, C.H.d. Groot, D.R. Leadley, G. Bell, E.H.C. Parker, T. Whall, D.A. Ritchie, C.H.W. Barnes, Spin transport in germanium at room temperature, Appl. Phys. Lett., 97 (2010) 162104.
[16] T.G. Kollie, Measurement of the thermal-expansion coefficient of nickel from 300 to 1000 K and determination of the power-law constants near the Curie temperature, Phys. Rev. B, 16 (1977) 4872-4881.
[17] C. Ross, Patterned Magnetic Recording Media, Annu. Rev. Mater. Res., 31 (2001) 203-235.
[18] Y.S. Huang, X.T. Zeng, X.F. Hu, F.M. Liu, Corrosion resistance properties of electroless nickel composite coatings, Electrochim. Acta, 49 (2004) 4313-4319.
[19] Y. Yin, Y. Pan, S. Rubanov, M.M. Bilek, D.R. McKenzie, Sputtered nanocrystalline nickel thin films for solar thermal energy applications, Nanosci. and Nanotec. Lett., 1 (2009) 32-36.
[20] J. Heremans, C.H. Olk, D.T. Morelli, Magnetic susceptibility of carbon structures, Phys. Rev. B, 49 (1994) 15122-15125.
[21] R.C. Haddon, Magnetism of the carbon allotropes, Nature, 378 (1995) 249-255.
[22] P.W. Huang, J.H. Huang, C.H. Yen, C.Y. Cheng, F. Xu, H.C. Ku, S.F. Lee, Coexistence of exchange bias and magnetization pinning in the MnOx/GaMnAs system, J. Phys.: Condens. Matter, 23 (2011) 415801.

6th International Conference on Materials Science and Nanotechnology For Next Generation (MSNG2019)
October 16-18, 2019, Niğde, TURKEY (ORAL FULL TEXT)

The Effects of Borax addition on Microstructure, Wettability and Mechanical Properties of High Temperature Nickel Based (630) Super Alloy Produced by Mechanical Alloying

Rasiha Nefise MUTLU*, and Ahmet Murat GİZİR

Mersin University, Faculty of Science and Letters, Department of Chemistry, Mersin, TURKEY

Nickel based super alloys can be classified as a high temperature alloy. These materials, which consist of a mixture of at least one metal and another element, find extensive use in military, aerospace, medical and electronics applications, as well as any other operations requiring durable, oxidation resistance, heat-resistant components. By mixing micrometric metal powders at certain ratios and pressing high pressure is aimed to produce a new material. The effect of $Na_2[B_4O_5(OH)_4]\bullet 8H_2O$ (B) binder on the formed alloys was also investigated. The obtained samples were subjected to the sintering process under the N_2(g) atmosphere. The samples were heated to 900◦C as a speed of 10 ◦C dk-1. It was kept at 900 ◦C for 45 minutes. It was then allowed to stand for 15 minutes in a 1000 ° C heated oven and then cooled by the speed of 10 ◦C dk-1. As hardness and density measurements of these samples; Brinell hardness and Archimedes water displacement method used respectively. Micro and crystal structures of these samples determined with scanning electron microscope (SEM) images and X-Ray diffraction (XRD) patterns. The contact angle method also used for determinate the wettability properties.

Keywords: Super Alloy, Mechanical Alloying, Borax, Contact Angel

*Corresponding author: esifen@gmail.com

1. Introduction

With the developing technology, the need for durable and easy to produce materials has increased. This increased the importance of new and advanced material manufacturing. New products and new market formations that have emerged as a result of developments in material technology affect all sectors. Especially in recent years, “advanced materials” have become increasingly important as materials with superior physical, chemical and mechanical properties, lighter, less space and high added value [1, 2]. When new materials are produced, the structure of the material can be controlled by controlling the material at the atomic level in the production stage and the desired mechanical and chemical properties such as toughness, brittleness, hardness and corrosion resistance can be obtained. They are advanced light alloy materials such as niobium, vanadium and titanium, micro alloy steels, duplex alloy stainless steels, ultra-strong steels, nickel, cobalt and titanium-based super alloys and aluminum-lithium alloys. On the other hand, the applications of aluminum and magnesium alloys in the automotive sector and the applications of aluminum-lithium alloys developed in low density in the aviation sector are examples of the introduction of advanced metallic materials into our daily lives [3]. Powdered metal injection methods such as sintering, hot pressing, metal powders are compacted and high-quality parts can be produced using advanced manufacturing technology called metal powder metallurgy [4].

Nickel based super alloys that is effective at temperatures of 500-1200 °C and above can be classified as a high temperature alloy [5-7]. These materials, which consist of a mixture of at least one metal and another element, find extensive use in military, aerospace, medical and electronics applications, as well as any other operations requiring durable, oxidation resistance, heat-resistant components. They show high strength and stability at extreme temperatures, as well exceptional environmental [8]. The production of such materials by

means of mechanical alloying will produce many different shaped product, durable, fast-to-produce and economical [4, 9, 10].

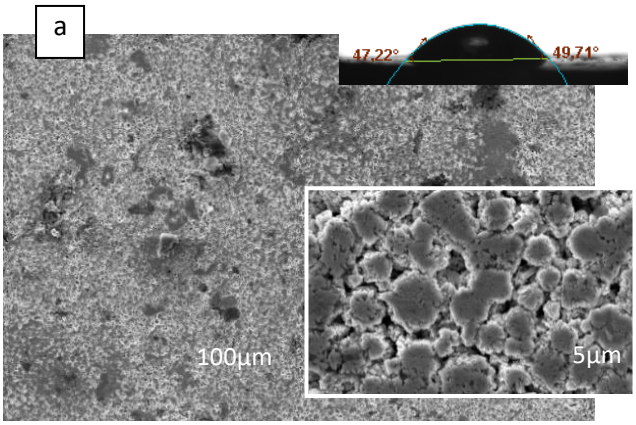
In this study, nickel-based inconel (630) alloy is formed with micrometric powders, sintered and borax is added to improve its properties.

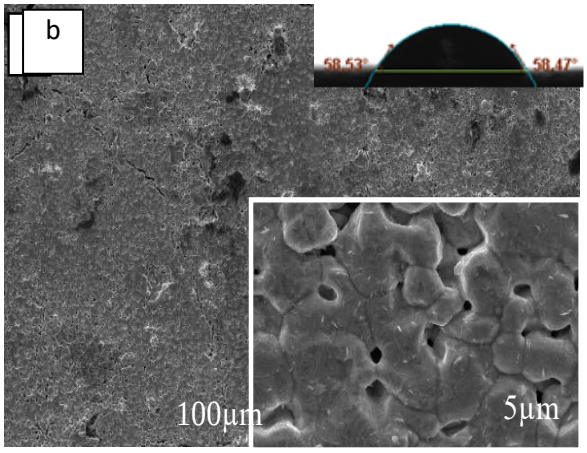
2. Experimental details

By mixing micrometric metal powders at certain ratios and pressing high pressure is aimed to produce a new material. The effect of $Na_2[B_4O_5(OH)_4]\bullet 8H_2O$ (B) binder on the formed alloys was also investigated. The obtained samples were subjected to the sintering process under the N_2(g) atmosphere. The samples were heated to 900◦C as a speed of 10 ◦C dk-1. It was kept at 900 ◦C for 45 minutes. It was then allowed to stand for 15 minutes in a 1000 ° C heated oven and then cooled by the speed of 10 ◦C dk-1. Samples were subjected to density test based on Archimedes water removal principle and Brinel hardness test. Before the density test, dry weights were taken with the help of precision scales. Then, the samples were put into pure water and the temperature of the water was boiled in a magnetic heater up to 100 ° C and when the temperature of the water reached this temperature, it was kept at this temperature for 4 hours. The reason for this is to ensure that the pure water is distributed homogeneously between the grains and pores of the sample. The samples in the purified water boiled at this temperature for 4 h were then cooled to room temperature. The cooled samples were suspended in pure water precision scales with a sensitivity of 0.0001 g and then dried and weighed again. Brinell hardness test was applied in order to examine the strength properties of samples which were pressed and heat treated. Traces were left on the specimens with a load of 31.25 N with a steel ball tip with a radius of 2.5 mm and the radii of these traces were taken out by means of optical microscope.
SEM images were recorded with Nova NovaSEM with high vacuum and 20.00 kV EHT. XRD none-sintered and sintered samples were obtained from PANalytical – Empyrean XRD instrument with 45kV tube voltage, 40 mA tube current and 0.013 ° / min scanning rate and Cu - Kα radiation.

3. Results and discussion

The SEM images and contact angels of pressed, pressed-sintered and sintered with borax addition Inconel samples are given in Fig.1. When looking at the SEM images of only the pressed sample given in Fig. 1.a, the inter-particle voids can be clearly observed. The contact angle is less than 90 degrees as expected. This means that the water drop on the surface flows into the pores. When the pressed sample is subjected to sintering, see Fig.1.b. As seen in the inter-particle gaps began to close, but there are still gaps. The contact angel of the sintered samples are increased also. SEM images of the sintered sample after the addition of borax to the composition are given in Fig. 1.c. The addition of borax closes the gaps between the grains and makes the structures seen as rounded on the surface sharper. This means that new crystal structures begin to form. In addition, the contact angle increased further.





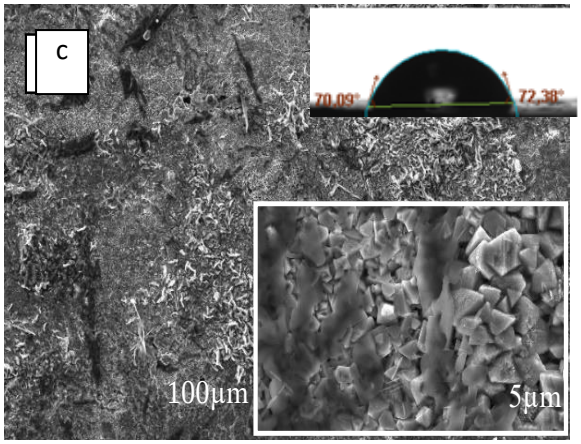


Figure 1. *SEM images and contact angels of INC-non sintered, INC-Sintered and INC-B samples*

XRD pattern of the samples are given in Fig.2. When the XRD measurement of the non-sintered sample is examined, the XRD patterns of each element are composed of superimposed severe peaks and small different peaks. When the sample is sintered, the intensity of the peaks decreases and a more amorphous structure is formed. The addition of borax added to the composition produces sharper and less common peaks. This means the formation of a more pronounced crystal structure. In addition, iron boride, nickel boride structures are formed.

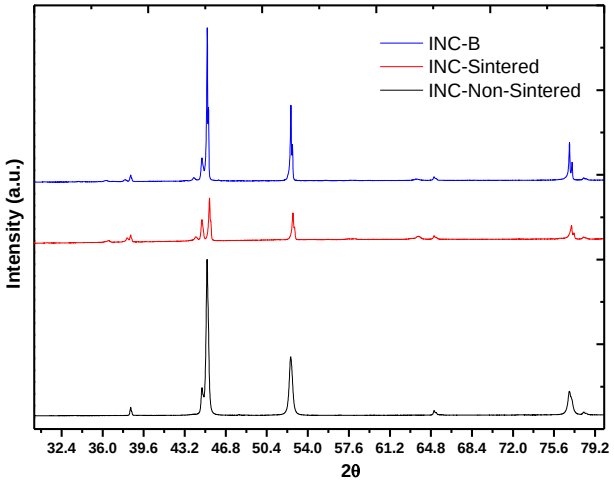


Figure 2. *XRD patterns of INC-non sintered, INC-Sintered and INC-B samples*

The Hardness and theoric density of samples are given in Fig.3. The mean radius of the traces left on the samples with a load of 31.25 N in the hardness test was obtained with the help of optical microscope. Finally, Brinell hardness value (HB, N / mm2) of the samples whose average radius was calculated was calculated by the following formula.

$$\text{Brinell hardness value (HB, N/mm}^2\text{)} = \frac{2P}{\pi D\left(D - \sqrt{D^2 - d^2}\right)} \quad (1)$$

P, D and d given in equation (1) are named as the loaded load (kg), the largest and smallest track radii, respectively.

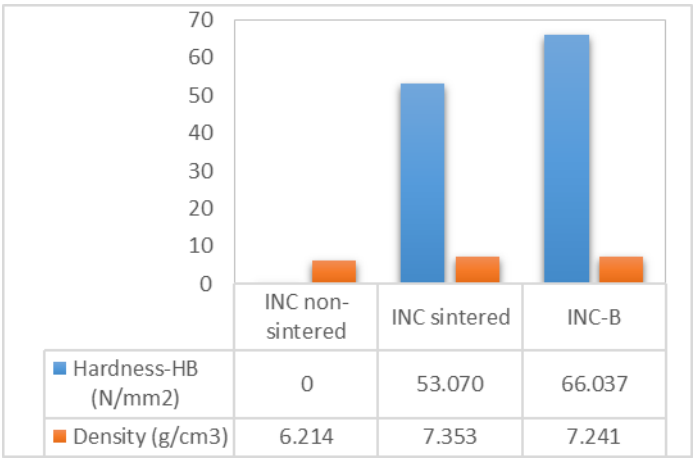
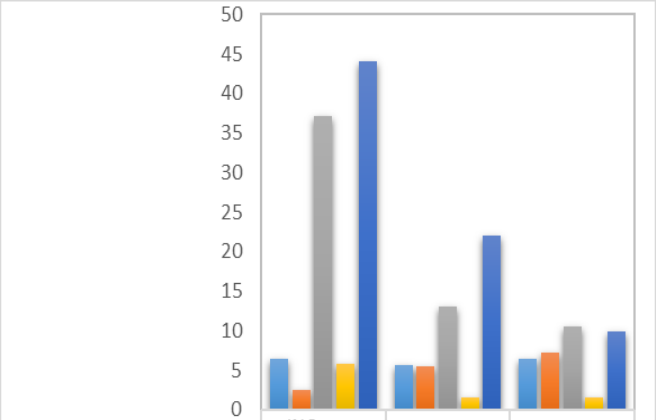


Figure 3. *The Hardness and theoric density of INC-non sintered, INC-Sintered and INC-B samples*

The hardness value of the non-sintered sample could not be calculated because the sample was dispersed during the test. When the hardness values in Fig.3 are examined, it is seen that the hardness value of the sintered sample is lower than that of the borax added sintered sample. The addition of borax is increased the hardness. However, considering the theoretical densities, the addition of borax does not cause a significant change, while the sintering process increases the density due to the shrinkage in volume.

The bulk density (g / cm2), apparent solid density (g / cm2), apparent and total porosity values (%) and water absorption (%) values obtained by the archimedes density test are given in Fig.4[11, 12]



	INC non-sintered	INC sintered	INC-B
Bulk density (g/mm3)	6.469	5.730	6.524
Visible solid density (g/mm3)	2.574	5.559	7.292
apparent porosity (%)	37.165	13.074	10.539
Water absorption %	5.745	1.537	1.615
total porosity %	44.111	22.073	9.909

Figure 4. *The bulk density (g / cm2), apparent solid density (g / cm^2), apparent and total porosity values (%) and water absorption (%) values of INC-non sintered, INC-Sintered and INC-B samples*

Calculations were made by giving the density and % porosity equations below with the help of the weight values taken after the recorded dry, suspended in water and after being removed from the water.

$$\text{Bulk Density (g/cm}^3\text{)} = \frac{W_K}{W_D - W_A} \times \rho_{sivi} \quad (2)$$

$$\text{Visible Solid Density (g/cm}^3\text{)} = \frac{W_K}{W_K - W_A} \times \rho_{sivi} \quad (3)$$

$$\text{Visible Porosity (\%)} = \frac{W_D - W_K}{W_D - W_A} \times 100 \quad (4)$$

$$\text{Water Absorption (\%)} = \frac{W_D - W_K}{W_K} \times 100 \quad (5)$$

$$\text{Total Porosity (\%)} = 1 - \frac{\rho_{bulk}}{ptheoric} \times 100 \quad (6)$$

WK, WA, WD in the above equations are referred to as dry weight, weight suspended in water, and weight weighed after being removed from water. Figure 4 shows that bulk density and density are increased with sintering and addition of borax, while apparent porosity, water absorption and total porosity are decreased. These results are consistent with other measurements.

4. Conclusion

It was demonstrate, although pores of powder alloys are covered by sintering, there are still pores on the surface. Borax addition reduced these pores and increased contact angle, density, hardness and crystal properties and decreased porosity. This, increased the quality of the alloy produced.

5. Acknowledgement

The authors are thankful to the Mersin University research fund (2019-1-AP4-3460) and TUBITAK for their financial support.

References:

[1] C.-J. Tong, M.-R. Chen, J.-W. Yeh, S.-J. Lin, S.-K. Chen, T.-T. Shun, S.-Y. Chang, Metallurgical and Materials Transactions A, 36 (2005) 1263-1271.
[2] L.A. Dobrzański, Journal of Materials Processing Technology, 175 (2006) 133-148.
[3] E. Ghassemieh, Materials in automotive application, state of the art and prospects, New trends and developments in automotive industry, InTechOpen, 2011.
[4] B. BAKSAN, R. GÜRLER, Osmangazi Üniversitesi, Metalurji Enstitüsü, Eskişehir, (2003).
[5] G.A. Rao, K.S. Prasad, M. Kumar, M. Srinivas, D. Sarma, Materials science and technology, 19 (2003) 313-321.
[6] I. Choudhury, M. El-Baradie, Journal of Materials Processing Technology, 77 (1998) 278-284.
[7] M. Nalbant, A. Altın, H. Gökkaya, Materials & design, 28 (2007) 1334-1338.
[8] A. Thakur, S. Gangopadhyay, International Journal of Machine Tools and Manufacture, 100 (2016) 25-54.
[9] J.S. Benjamin, Metallurgical transactions, 1 (1970) 2943-2951.
[10] A.N. Acar, A.K. Ekşi, A. Ekicibil, Journal of Molecular Structure, 1198 (2019) 126876.
[11] A.N. Acar, R.N. Mutlu, A.K. Ekşi, A. Ekicibil, B. Yazıcı, Anti-Corrosion Methods and Materials, 65 (2018) 558-571.
[12] A.N. Acar, A.K. Ekşi, A. Ekicibil, Politeknik Dergisi, 21 (2018) 341-350.

[2] K. Mahmood, H.W. Kang, S.B. Park, H. J. Sung, Appl. Mater. Interfaces, 5 (2013) 3075−3084.
[3] J. Sun, Q. Dai, F. Liu, H. Huang, Z. Li, X. Zhang, Y. Wang, Sci. China. Phys. Mech. Astron., 54 (2011) 102–105.
[4] D. Hwang, O. Min-Suh, J. Lim S. Park, J. Phys. Appl. Phys., 40 (2007) 387–412.
[5] K.K. Banger, Y. Yamashita, K. Mori, R.L. Peterson, T. Leedham, J. Rickard, H.Sirringhaus, Nat. Mater., 10 (2011) 45.
[6] J. Xia, A. Wang, X. Liu, Z. Su, Appl. Surf. Sci., 257 (2011) 9724–9732.
[7] S. Ilican, Y. Caglar, M. Caglar, J. Optoelectron. Adv. Mater., 10 (2008) 2578–2583.
[8] W.Y. Zhang, D.K. He, Z.Z. Liu, L.J. Sun, Z.X. Fu, J. Optoelectron. Adv. Mater. Rapid Commun., 4 (11) (2010) 1651–1654.
[9] L.H. Van, M.H. Hong, J. Ding, J. Alloys Comp., 449 (1) (2008) 207–209.
[10] M.H. Aslan, A.Y. Oral, E. Mensur, A. Gul, E. Basaran, Solar Energy Mater. Solar Cells, 82 (2004) 543–552.
[11] O.A. Novodvorsky, L.S. Gorbatenko, V.Y. Panchenko, O.D. Khramova, Y.A. Cherebilo, C. Wenzel, J.W. Bartha, V.T. Bublik, K.D. Shcherbachev, Semiconductors, 43 (2009) 419–424.
[12] O.A. Novodvorsky, L.S. Gorbatenko, V.Y. Panchenko, O.D. Khramova, Y.A. Cherebilo, C. Wenzel, J.W. Bartha, V.T. Bublik, K.D. Shcherbachev, Semiconductors, 43 (2009) 419–424.

6th International Conference on Materials Science and Nanotechnology For Next Generation (MSNG2019)
October 16-18, 2019, Niğde, TURKEY (ORAL FULL TEXT)

Conformational and Infrared Spectrum Analysis of Glycine

Nihal KUŞ*, Saliha ILICAN

* Eskisehir Technical University, Faculty of Science, Department of Physics, Eskisehir, TURKEY

In this study, molecular structure and conformational analysis of glycine (Gly) were studied by DFT/B3LYP-6-311++G(d,p) method. The structure has seven conformers belong to calculations of N-C-C=O, H-O-C=O and C-C-N-H torsional motions, and three of them are main conformers. Vibrational frequencies of Gly determined for all conformers. Highest occupied molecular orbital (HOMO) - lowest unoccupied molecular orbital (LUMO) energy gaps for the main three conformers were determined.

Keywords: Glycine, DFT, Conformer, Vibrational frequency.

Corresponding author: nkus@eskisehir.edu.tr

1. Introduction

Glycine (*Gly*) is the simplest amino acid which forms the building block of protein. It's not an essential amino acid, and the body takes it from chemicals. *Gly* is used for treating schizophrenia, stroke, sleep problems, metabolic syndrome, and metabolic disorders. Most importantly, it is also used in cancer prevention and memory development. *Gly* has a wide application area and both theoretical and experimental studies are reported (Coussan and Tarczay, 2016; Bazsó, et al., 2012; Kieninger et al., 1998). Stepanian and coworkers (1998) studied matrix isolation *Gly* in argon gases. They observed three main conformers in the matrix. Also they calculated of infrared (IR) frequencies and intensities with DFT/Becke3LYP method with aug-cc-pVDZ basis set and Møller-Plesset second-order perturbation theory (MP2) method. Reva et al. (1995) studied IR spectra of *Gly* isolated in neon (Ne), argon (Ar) and krypton (Kr) matrices. They identified three different conformers of *Gly* in the matrix gases. The near-infrared (NIR) spectrum of *Gly* in Ar and Kr matrices was studied by Bazsó et al. in 2012. *Gly* and *Gly*·water complex were inverstigated in low-temperature matrices by Coussan and Tarczay (2016). They irradiated of matrix isolated *Gly* and *Gly*·water complex with IR-laser (MID and NIR) and observed spectral changes.

In the present study, the conformers of *Gly* were studied. It was found seven minimal form. Highest electronic energy difference (ΔE) between Gly_1 and Gly_7 was *ca.* 29.7 kJ mol^{-1}. The vibration energies calculated using density functional theory (DFT) for all conformations were plotted. HOMO and LUMO energy gaps were calculated for the main three conformers.

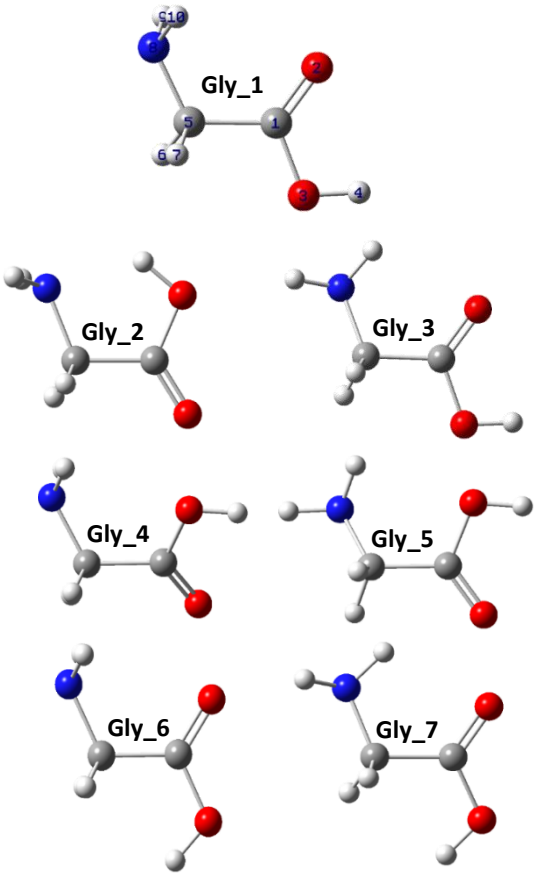


***Figure 1**. The structure of the conformers for Gly, calculated by B3LYP/6-311++G(d,p) level.*

2. Theoretical calculations

The optimized geometries and energies of the possible conformers of *Gly* calculations were performed using the DFT implementation in the Gaussian 09 (Frisch et al., 2009) program package. The calculations were achieved using the 6-311++G(d,p) basis set. The three-parameter hybrid density functional which is called B3LYP, includes Becke's gradient exchange correction (Becke, 1993) and the Lee, Yang and Parr (Lee et al., 1998).

3. Results and discussion

If the fragments NH_2, CH_2, CO, and OH are assumed to be rigid, *Gly* has three rotational degrees of freedom related to their connecting bonds C−N, C−C, and C−O, respectively. *Gly* has seven conformers with minimum energies, while three of them (Gly_1, Gly_2 and Gly_4) are the main conformers. All conformers are given in Fig. 1. Reva and coworkers (1995) was found three main conformers in the Ne, Ar, and Kr matrices.

Table 1. *Calculated electronic energies obtained from Becke3LeeYangParr/6-311++G(d,p) calculations.*

Conformer	E hartree	E+ZPV hartree	Gibbs hartree	Entalpy hartree	ΔE kJ mol^{-1}	ΔE(ZPV) kJ mol^{-1}	ΔG kJ mol^{-1}	ΔEntalpy kJ mol^{-1}
Gly_1	-284.530	-284.450	-284.479	-284.444	0	0	0	0
Gly_2	-284.529	-284.449	-284.478	-284.443	1.78	3.16	3.71	2.46
Gly_3	-284.527	-284.448	-284.477	-284.441	6.06	5.78	6.53	5.64
Gly_4	-284.527	-284.448	-284.478	-284.441	6.37	6.47	3.80	6.56
Gly_5	-284.525	-284.446	-284.475	-284.439	11.16	11.31	11.69	11.08
Gly_6	-284.521	-284.442	-284.471	-284.435	23.48	22.50	22.46	22.74
Gly_7	-284.518	-284.439	-284.468	-284.433	29.69	28.34	28.76	28.48

It can be noticed that the electronic, zero point vibrational and gibbs energy difference between the conformers 1 and 2 are 1.78, 3,16 and 3.71 kJ mol^{-1} (Table 1).

Stepanian and co workers were found zero-point vibrational energies difference about 2.32 kJ mol^{-1} when they calculated with DFT/cc-pVDZ level. They also calculated with different level of theory and found almost same energies as we found in our present study (Stepanian et al., 1998). Coussan and Tarczay (2016) were found eight different conformers with different energies. One of them same with our study. It was Gly_6 but different orientation of N-H2. We also found in the calculation but it was not as a minimum in the scan about C1-C5-N-H9 dihedral angle Therefore it was not a different conformer just H2 in N-H2 was different state.

In the calculated IR spectra, C=O stretching bonds were observed as the most intense vibrating bonds for all conformers of *Gly*. C=O stretching vibrations for all conformers were 1815, 1843, 1818, 1808, 1820, 1850, 1850 cm^{-1}, respectively. Gly_1 and Gly_5 have more intense bonds than the other conformers (318 and 352 km mol^{-1}, respectively). It is interesting to note that the OH stretching peak of the 3488 cm^{-1} and OH bending peak of the 1410 cm^{-1} are very intense bands in the Gly_2. This is because the N atom is close to the H4 and bending and stretching vibrations affected by the H-bonding therefore it could be indicated N…..H-O H bond in the conformer Gly_2 was much stronger than the other conformers. Distance between N and H4 was calculated as 1.935 Å.

The calculated IR spectra for the three main conformers using DFT/B3LYP/6-311++G(d,p) level were agreed with the previous reports who were studied about IR spectra of conformers for *Gly* (Reva et al., 1995; Stepanian et al., 1998; Bazsó et al., 2012; Coussan and Tarczay, 2016).

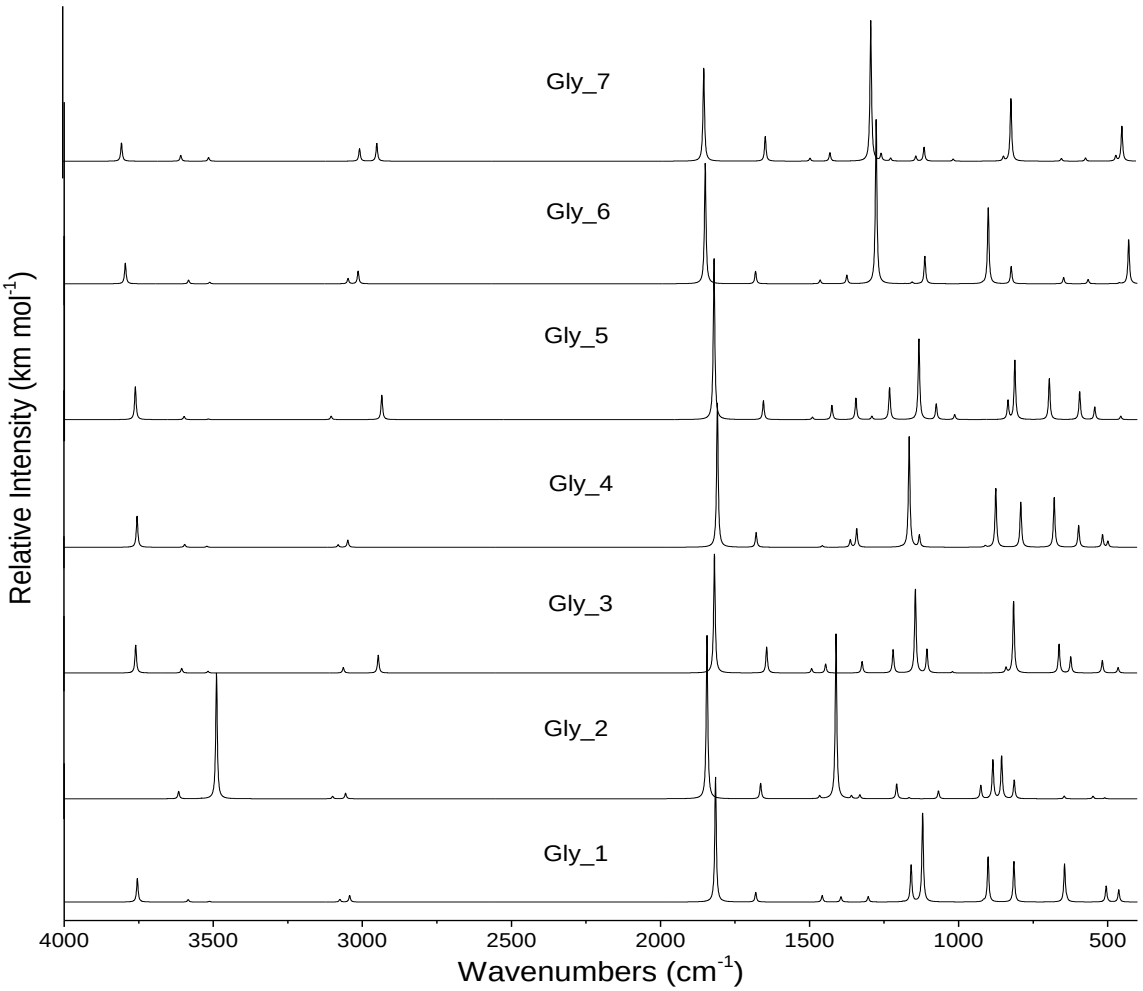


Figure 2. *IR spectra of the conformers for Gly, calculated by DFT/B3LYP/6-311++G(d,p) level.*

Table 2. *Mulliken charge values[a] for all conformers of Gly, obtained from B3LYP/6-311++G(d,p) calculations[b].*

Atom	Gly_1	Gly_2	Gly_3	Gly_4	Gly_5	Gly_6	Gly_7
C1	0.064251	0.121546	0.126251	0.023161	0.099420	0.027982	0.076986
O2	-0.285992	-0.288073	-0.313379	-0.284221	-0.293362	-0.266968	-0.288063
O3	-0.168655	-0.191845	-0.170693	-0.191476	-0.212568	-0.157828	-0.152161
H4	0.283067	0.296259	0.284964	0.288547	0.289851	0.242735	0.238143
C5	-0.355896	-0.330366	-0.359367	0.309950	0.320883	-0.287626	-0.292338
H6	0.197517	0.193922	0.194615	0.200627	0.190348	0.181385	0.162102
H7	0.197513	0.200534	0.171700	0.200491	0.167208	0.181490	0.175068
N8	-0.414183	-0.507856	-0.392727	-0.425588	-0.391942	-0.414463	-0.383050
H9	0.241188	0.249114	0.234342	0.249176	0.233317	0.246637	0.241220
H10	0.241188	0.121546	0.224292	0.249232	0.238611	0.246656	0.222094

[a] In units of electron; e = $1.60217646 \times 10^{-19}$ C.
[b] See Fig. 1 for atom numbering.

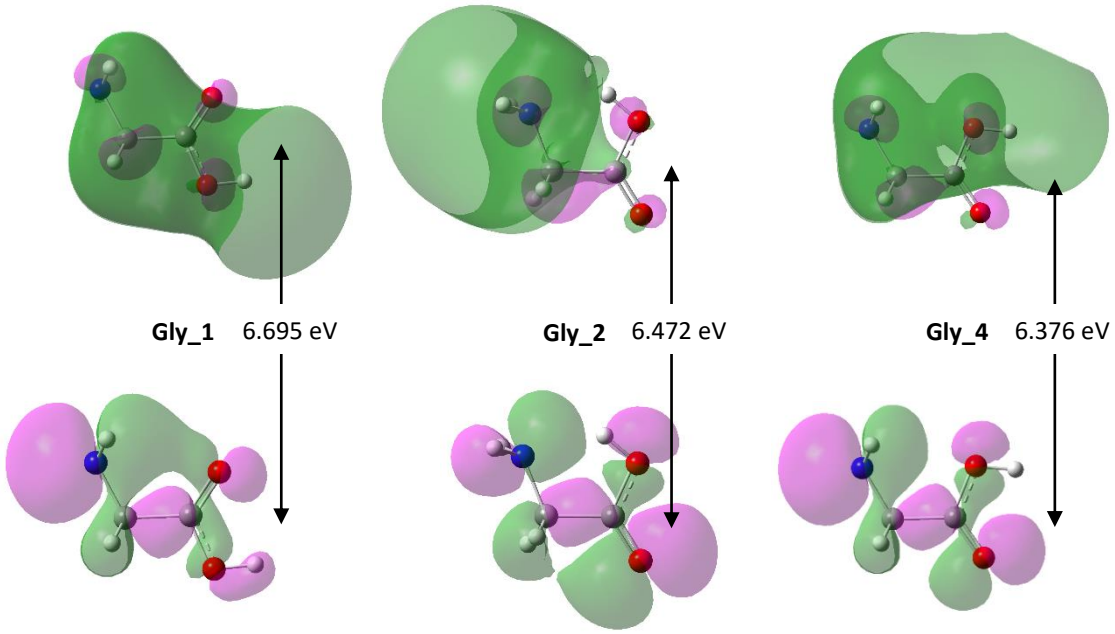


Figure 4. *HOMO-LUMO energy gap diagram for the main three conformers, calculated by B3LYP/6-311++G(d,p) level.*

According to molecular orbital theory; As the molecules are formed, the atoms form the orbitals of the molecule by mixing the atomic orbitals that allow them to form molecules close to each other at the required bond distance. HOMO and LUMO energies are the basic orbitals involved in chemical reactions. The gap between HOMO and LUMO energy values is defined as the chemical stability of the molecule. The closer the energy levels of the interacting molecular orbitals are, the easier the interaction. In this work, the energy differences between HOMO and LUMO for the main three conformers are calculated by B3LYP/6-311++G(d,p) level, and plotted in Fig. 4.

4. Conclusion

In this study conformational structure of *Gly* was studied using DFT method. Calculated with DFT/B3LYP/6-311++G(d,p) level IR spectral characteristics for the seven conformers of the *Gly* were determined. The theoretical simulation results of the IR frequencies and intensities for the conformers of *Gly* were plotted. HOMO-LUMO energy gaps were calculated for three main conformers. The gap of Gly_4 is about 6.38 kJ mol^{-1} and so, it is more interact for the other main conformers.

5. Acknowledgement

This work was supported by Eskisehir Technical University Commission of Scientific Research Project under Grant No: 19ADP143.

References:

Bazsó, G., Magyarfalvi, G. Tarczay, G. (2012). Near-infrared laser induced conformational change and UV laser photolysis of glycine in low-temperature matrices: Observation of a short-lived conformer. J. Mol. Struct., 1025, 33-42.

Becke, A.D. (1988). Density-functional exchange-energy approximation with correct asymptotic behavior. Phys. ReV. A, 38, 3098–3100.

Coussan, S., Tarczay, G. (2016). Infrared laser induced conformational and structural changes ofglycine and glycine·water complex in low-temperature matrices. Chem. Phys. Lett., 644, 189-194.

Frisch, M.J., Trucks, G.W., Schlegel, H.B., Scuseria, G.E., Robb, M.A., Cheeseman, J.R., Scalmani, G., Barone, V., Mennucci, B., Petersson, G.A., Nakatsuji, H., Caricato, M., Li, X., Hratchian, H.P., Izmaylov, A.F., Bloino, J., Zheng, G., Sonnenberg, J.L., Hada, M., Ehara, M., Toyota, K., Fukuda, R., Hasegawa, J., Ishida, M., Nakajima, T., Honda, Y., Kitao, O., Nakai, H., Vreven, T., Montgomery, J.A., Peralta, Jr. J.E., Ogliaro, F., Bearpark, M., Heyd, J.J., Brothers, E., Kudin, K.N., Staroverov, V.N., Kobayashi, R., Normand, J., Raghavachari, K., Rendell, A., Burant, J.C., Iyengar, S.S., Tomasi, J., Cossi, M., Rega, N., Millam, J.M., Klene, M., Knox, J.E., Cross, J.B., Bakken, V., Adamo, C., Jaramillo, J., Gompert, R., Stratmann, R.E., Yazyev, O., Austin, A.J., Cammi, R., Pomelli, C., Ochterski, J.W., Martin, R.L., Morokuma, K., Zakrzewski, V.G., Voth, G.A., Salvador, P., Dannenberg, J.J., Dapprich, S., Daniels, A.D., Farkas, O., Foresman, J.B., Ortiz, J.V., Cioslowski, J., Fox, D.J. (2009). Gaussian 09, Revision A.0.2, Gaussian, Inc., (Wallingford CT).

Kieninger, M., Suhai, S. Ventura, O. N. (1998). Glycine conformations: gradient-corrected DFT-studies. J. Mol. Struct. Theochem., 433, 193-201.

Lee, C., Yang, W., Parr, R.G. (1988). Development of the Colle-Salvetti correlation-energy formula into a functional of the electron density. Phys. ReV. B, 37, 785–789.

Reva, I. D., Plokhotnichenko, A.M., Stepanian, S.G., Ivanov, A.Y., Radchenko, E.D., Sheina, G.G., Blagoi, Y.P. (1995). The rotamerization of conformers of glycine isolated in inert gas matrices. An infrared spectroscopic study. Chem. Phys. Lett., 232, 141-148.

Selvarengan, P., Kolandaivel, P. (2004). Potential energy surface study on glycine, alanine and their zwitterionic forms. J. Mol. Struct. Theochem., 671, 77-86.

Stepanian, S. G., Reva, I. D., Radchenko, E. D., Rosado, M. T. S., Duarte, M. L. T. S., Fausto,| R., Adamowicz, L. (1998). Matrix-Isolation Infrared and Theoretical Studies of the Glycine Conformers. J. Phys. Chem. A, 102, 1041-1054.

6th International Conference on Materials Science and Nanotechnology For Next Generation (MSNG2019)
October 16-18, 2019, Niğde, TURKEY (ORAL FULL TEXT)

Investigation of Structural and Morphological Properties of Ultrafine Ni/B_2O_3 Core/Shell Magnetic Nanoparticles (MNPs)

Idris Adanur[1], Mustafa Akyol[2] and Ahmet Ekicibil[1]

[1]Department of Physics, Art and Science Faculty, Çukurova University, 01330 Adana, Turkey
[2]Department of Materials Engineering, Faculty of Engineering, Adana Alparslan Türkeş Science and Technology University, 01250 Adana, Turkey

In this study, we investigated the structural and morphological properties of ultrafine Ni and Ni/B_2O_3 core/shell MNPs that they were synthesized by polyol process using Polyvinylpyrrolidone (PVP) and Oleic Acid (OAc) as surfactants. The X-Ray Diffraction (XRD) analysis was performed to examine the structural properties of MNPs. The crystallite size of MNPs was calculated as ~3.59, ~3.88 nm from the XRD pattern for Ni and Ni/B_2O_3, respectively, which can be called as ultrafine MNPs. To investigate morphological and elemental properties, Scanning Electron Microscopy (SEM) and Energy Dispersive Spectroscopy (EDS) analysis were performed. It is observed that Ni and Ni/B_2O_3 core/shell MNPs are homogeneously distributed through the sample. The particle size of Ni and Ni/B_2O_3 core shell MNPs are determined as ~4.21 and ~2.94 nm from the SEM images, respectively, which is consistent with the XRD data.

Keywords: Ni, B_2O_3, Polyvinylpyrrolidone (PVP), Polyol Process

Corresponding author: adanuridris@gmail.com

1. Introduction

The core/shell magnetic nanoparticles (MNPs) are one of the attractive type of nanoparticle due to their interesting physical, chemical and biological properties for the nanotechnology applications like high-density magnetic recording media, catalysts, medical diagnostic and cancer treatments [1-3]. However, one of the main problem of nanoscale particles is low stability. Therefore, core/shell type NPs provide good advantages in terms of physical, chemical and biological properties. Core/shell nanoparticles are composed of ferromagnetic (FM) or superparamagnetic (SPM) core in the center and antiferromagnetic (AFM) or ferrimagnetic (FiM) shell in the outer layer. AFM or FiM shell, which is oxidized layer, have many important roles on the core surface like magnetic core stabilization, surface functionalization, cooperative magnetic switching and leads to effective exhance coupling and exchange bias (EB). Due to this all advantages enhaces magnetization stability of core. In the literature, it is reported that the insulator matrices like SiO_2, Al_2O_3, C, BN and B_2O_3 are very important for industrial applications when they are coated on mangetic nanoparticles [4-10]. Nickel (Ni) is one of the 3*d* ferromagnetic materials and have an important place in nanotechnology applications. In this study, Ni and Ni/B_2O_3 core/shell MNPs were synthesized by the polyol reduction process. Structural and morphological were investigated in detail.

2. Experimental details

The Ni and Ni/B_2O_3 core/shell MNPs were synthesized by the polyol reduction process. In this process, 0.8755 g Ni(acac)2, 30 ml ethylene glycol (EG) 0.1112 g Polyvinylpyrrolidone (PVP) and 2.5 ml oleic acid (OAc) were added in a three-necked flask. The solution was heated to 100°C under argon atmosphere by stirring at 800 rpm. Then, 30 ml sodium borohydride (NaBH4)-dimethylformamide (DMF) solution was injected in solution and heated to 140°C for 1 h. The solution immediately turned black, indicating Ni nanoparticles were formed. After 1 h, the solution was cooled to room temperature. Then, the Ni nanoparticles centrifuged and washed with hexane and ethanol. Finally, a sum of Ni powder was added in a three-necked flask. The 50 ml boric acid-EG solution was injected in a three-necked

flask drop by drop. After 2 h, 30 ml DMF-$NaBH_4$ solution was added in solution at room temperature for 1 h. Then, the solution again centrifuged, washed and dried 1 day in a drying-oven.

The structural and morphological properties of the samples was carried out by X-Ray Diffraction (XRD) technique with wavelength of 1.54 Å Cu-K radiation and Scanning Electron Microcope (SEM). The element contents in the samples were determined by Energy-Dispersive x-ray Spectrum (EDS).

3. Results and discussion

The X-ray diffraction (XRD) analysis was performed in the range of $35° \leq 2\theta° \leq 80°$ for Ni and Ni/B_2O_3 core/shell MNPs, which is shown in Figure 1. The characteristic (111), (200) and (220) Ni peaks were obtained for two samples. But no observed any B_2O_3 peak. It is due to the B_2O_3 is amorphous phase on the Ni nanoparticle. It is noted that when the B_2O_3 is coated on Ni, the intensity of Ni peaks decreases. It indicates that B_2O_3 is successfully coated and form of Ni/B_2O_3 core/shell structure. The peaks shift to the low angle when B_2O_3 is coated. This is related to changes in the lattice parameter due to the B_2O_3 coating. The crystallite size of samples were calculated by using Debye-Scherrer formula [11]

$$D_c = \frac{\kappa\lambda}{\beta cos\theta}$$

where λ is the X-ray wavelength (1.5406 Å), κ is the crystallite shape factor (0.94), β is the peak full width at half maximum (in radians) at observed peak angle θ. The crystallite size of Ni and Ni/B_2O_3 core/shell MNPs were determined ~3.59 and 3.88 nm, respectively, which can be called as ultrafine MNPs. The other crystallographic parameters are shown in Table 1.

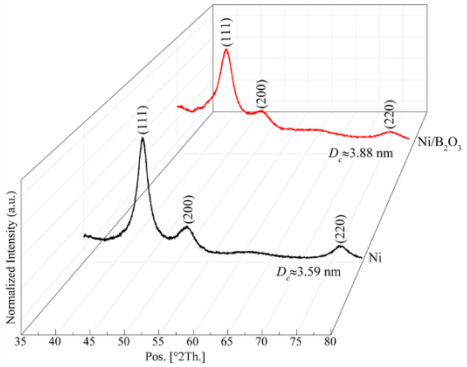


Figure 1. The powder X-ray diffraction patterns of Ni and Ni/B_2O_3 MNPs.

Tablo 1. Structural parameter of Ni and Ni/B_2O_3 core/shell MNPs.

Sample	Crystal Structure and Space Group	a (Å)	V (Å³)	D_c (nm)
Ni	Cubic Fm-3m	3.530	44.010	3.59
Ni/B_2O_3	Cubic Fm-3m	3.528	43.922	3.88

The Scanning electron microscopy (SEM) analysis was performed to examine morphological properties of samples at high magnification. SEM images of samples are shown in figure 2a-d. It is observed that the shape of the nanoparticles is nearly spherical for two samples. However, it is clear that the Ni MNPs tend to aggregate partly (Figs. 2a,b). But when the amorphous B_2O_3 was coated, highly homogeneous distribution was observed (Figs. 2c,d). This may be due to the insulator nature of the B_2O_3 [12]. The particle size distribution of samples were calculated randomly selected 100 particles, which is shown in Figure 2e,f. The particle size of Ni and Ni/B2O3 core/shell MNPs were determined as ~4.21 and 2.94 nm, respectively. This calculated values are consisted with XRD result (see Fig.1). Energy dispersive spectroscopy (EDS) analysis was also performed to determine atomic and weight percent for samples. The obtained results are shown in Table 2. In the EDS analysis, no other impurity elements were observed in the structure of samples.

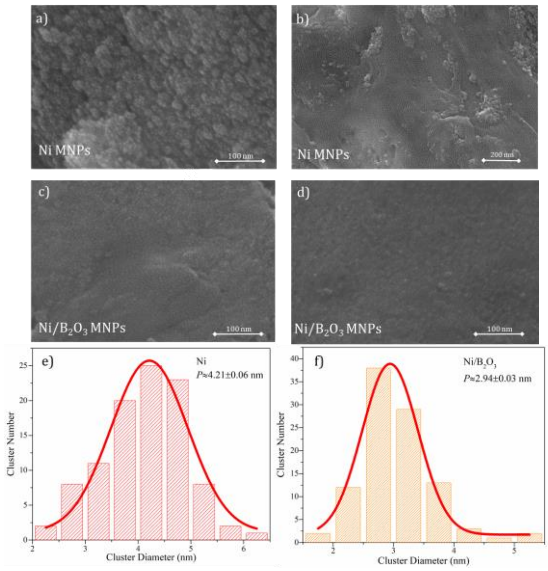


Figure 2. SEM images of a-b) Ni MNPs, c-d) Ni/B_2O_3 MNPs. e-f) Cluster size distribution of samples.

Table 2. EDS analysis of Ni and Ni/B_2O_3 core/shell MNPs.

Sample	Ni (%)	B (%)	O (%)
Ni	93.22	-	6.78
Ni/B_2O_3	78.79	9.01	12.20

4. Conclusion

In conclusion, Ni and Ni/B_2O_3 core/shell MNPs were successfully synthesized via polyol reduction process. The X-ray diffraction analysis was performed for Ni and Ni/B_2O_3 core/shell MNPs. The crystallite size of Ni and Ni/B_2O_3 were calculated as ~ 3.59 and ~3.88 nm, respectively. Scanning Electron Microscopy (SEM) and Energy Dispersive Spectroscopy (EDS) analysis were performed. It is observed that Ni and Ni/B_2O_3 core/shell MNPs are homogeneously distributed through the sample. The particle size of Ni and Ni/B_2O_3 core shell MNPs is determined as ~4 and ~3 nm from the SEM images, respectively.

5. Acknowledgement

This work was supported by Çukurova University (Adana/Turkey) under the Project No. of FDK-2019-11498.

References:

[1] M.C. Roco, Nanoparticles and nanotechnology research, Journal of Nanoparticle Research 1(1) (1999) 1-6.

[2] X.-C. Sun, X.-L. Dong, Magnetic properties and microstructure of carbon encapsulated Ni nanoparticles and pure Ni nanoparticles coated with NiO layer, Materials research bulletin 37(5) (2002) 991-1004.

[3] D.L. Leslie-Pelecky, R.D. Rieke, Magnetic properties of nanostructured materials, Chemistry of materials 8(8) (1996) 1770-1783.

[4] F.C. Fonseca, G.F. Goya, R. Jardim, R. Muccillo, N. Carreno, E. Longo, E. Leite, Superparamagnetism and magnetic properties of Ni nanoparticles embedded in SiO 2, Physical review B 66(10) (2002) 104406.

[5] W. Liu, W. Zhong, H. Jiang, N. Tang, X. Wu, W. Du, Synthesis and magnetic properties of FeNi 3/Al 2 O 3 core-shell nanocomposites, The European Physical Journal B-Condensed Matter and Complex Systems 46(4) (2005) 471-474.

[6] J. Jiao, S. Seraphin, X. Wang, J.C. Withers, Preparation and properties of ferromagnetic carbon-coated Fe, Co, and Ni nanoparticles, Journal of Applied Physics 80(1) (1996) 103-108.

[7] H. Tokoro, S. Fujii, T. Oku, Microstructures and magnetic properties of boron nitride-and carbon-coated iron nanoparticles synthesized by a solid phase reaction, Journal of Materials Chemistry 14(2) (2004) 253-257.

[8] C. Luo, S.H. Liou, L. Gao, Y. Liu, D.J. Sellmyer, Nanostructured FePt: B 2 O 3 thin films with perpendicular magnetic anisotropy, Applied Physics Letters 77(14) (2000) 2225-2227.

[9] Z. Zhang, J. Yu, J. Zheng, I. Skorvanek, J. Kovac, X. Dong, Z. Li, S. Jin, H. Yang, Z. Guo, Structure and magnetic properties of boron-oxide-coated Fe (B) nanocapsules prepared by arc discharge in diborane, Physical Review B 64(2) (2001) 024404.

[10] X. Zhang, X. Dong, H. Huang, B. Lv, J. Lei, S. Ma, W. Liu, Z. Zhang, Synthesis, structure and magnetic properties of B2O3/H3BO3-coated Fe nanocapsules, Materials Science and Engineering: B 143(1-3) (2007) 76-80.

[11] İ. Adanur, M. Akyol, A. Ekicibil, Effect of reducing agent and surfactant on the morphology, structural and magnetic properties of Ni magnetic nanoparticles, Philosophical Magazine Letters 98(8) (2018) 319-329.

[12] V. Singh, V. Srinivas, Evolution of Ni: B 2 O 3 core-shell structure and magnetic properties on devitrification of amorphous NiB particles in air, Journal of Applied Physics 106(5) (2009) 053910.

6th International Conference on Materials Science and Nanotechnology For Next Generation (MSNG2019)
October 16-18, 2019, Niğde, TURKEY (ORAL FULL TEXT)

Molecular Dynamics Simulations of Hydrogenated Silicon Nanoparticles

S. SENTURK DALGIC
Department of Physics, Faculty of Science, Trakya University, Edirne 22030, Turkey

In this work, the stability and structure of cubic shaped hydrogenated Si nanoparticles in different sizes have investigated under heating by molecular dynamics simulation (MD) method. The temperature dependence of cohesive energy and pair correlation function have also calculated. The changes in structure have discussed with the coordination number analysis. The results have compared with experiments and those obtained by other morphologies. It was observed that the stability of nanoparticles depends on size and shape. The hydrogen termination plays a positive role in stabilizing the structure and morphology of cubic Si nanoparticles. The average coordination number of hydrogenated silicon nanoparticles depends on the size. It was observed the liquid-like state of outer shells /the solid core of the nanoparticles during heating.

Keywords: Ru-Pt, Core-Shell, Molecular Dynamics

Submission date:
Acceptance Date:

Corresponding authors: serapd@trakya.edu.tr dserap@yahoo.com

1. Introduction

In recent years, silicon (Si) nanostructures have attracted considerable interest both in applied and fundamental science [1-4]. Due to quantum confinement, Si nanomaterials have different properties from bulk for a wide variety of applications in photocatalysis, optoelectronics, the drug-delivery, photovoltaics, and LiBs. The study on the physical properties and structure of Si nanostructures is a significant research area of silicon nanotechnology and poorly understood.

On the other hand, there are several reports on the amorphous and crystalline silicon nanostructures such as nanoparticles, nanowires and nanofilms have studied with first-principle calculations using density functional theory (DFT) or classical molecular dynamics (MD) simulation method [1-3,5-7].

On this line, the growth and dynamics of Si nano-clusters, Si quantum dots (SiQDs), and Si nanoparticles is another interesting subject for optoelectronics and other technologic applications. It was demonstrated that the functionalization of Si Nano surfaces by taking consideration of hydrogen-terminated was improved their optoelectronic properties.

Using the DFT calculations, Amanda and co-workers have shown that the hydrogen-terminated SiQDs have different optoelectronic properties according to their architecture and size [2,3]. The near-cubic morphologies exhibit superior spectral resolution. It was found that the shape-dependent band gaps of hydrogen terminated SiQDs affect in their luminescent properties.

To date, the molecular dynamics (MD) investigations on the stability of hydrogen terminated Si nanostructures have been reported by some researchers [8-11]. Different potential applications in MD simulations were presented to determine the interactions between the hydrogen and Si atoms. Most of the potential applications were based on the original Tersoff potential of Si [12]. Hansen and Vogl studied hydrogen absorption on hydrogenated Si surfaces [8]. Qi and co-workers have reported the stability of core-shell structured Si-H nanomaterials using Tersoff type potentials [9]. Mota and co-workers proposed Tersoff type potential for hydrogenated a-Si [10]. Recently, Amanda and Wilson

have studied optoelectronic properties of hydrogen terminated Si nanoparticles [11]. In this work, different potentials are applied to study the stability of hydrogenated Si nanoparticles by MD simulations using DLPOLY code [13].

2. Materials and Method

The structural and thermal stability of hydrogenated silicon nanoparticles was investigated by the classical MD simulations, as implemented DLPOLY code [13]. Cubic shaped silicon nanoparticles are considered to construct as hydrogen-terminated silicon NPs. Here, different sizes of hydrogenated silicon NPs were created as the MD sample of our calculations. In order to understand the effect of Si-H interactions on the stability of hydrogenated Silicon NPs, three different potential functions are used in MD simulations.

Tersoff Potential:

The Tersoff potential is used to describe Si-Si, Si-H and H-H for Si-H interactions [1,11,12,15] and adopted in the DLPOLY [13].

The three-body Tersoff potential (TP) was based on the bond-order concept with the strength of a bond between two atoms depends on the local atomic environment [12]. The interatomic potential energy between i and j atoms is given by

$$V_{ij} = f_c(r_{ij})[Aa_{ij}\exp(-\lambda_1 r_{ij}) - Bb_{ij}\exp(-\lambda_2 r_{ij})] \quad (1)$$

$$f_c(r_{ij}) = \begin{cases} 1, r < R-D \\ \frac{1}{2} - \frac{1}{2}\sin\left[\frac{\pi}{2}\frac{(r-R)}{D}\right], R-D < r < R+D \\ 0, \mathrm{r} > \mathrm{R}+\mathrm{D} \end{cases} \quad (2)$$

where a_{ij} and b_{ij} terms are the bond order parameters for the repulsive and attractive part of the potential energy, V_{ij} respectively. These parameters describe how the bond-order formation energy affected by the presence of other neighboring atoms such as the positions of k atoms. The potential parameters and details of the potential can be found in elsewhere [8-15].

Morse Potential

The MD simulations were carried out for Si-H and H-H interactions using Morse potential while the Si-Si interactions using TP force field was used.

Morse potential form is given by

$$V(r_{ij}) = E_0\left[\left(1-\exp(-k(r_{ij}-r_0)\right)^2 - 1\right] \quad (3)$$

Where the related parameters of E_0, k and r_o are taken from Galashev [1].

Lennard- Jones Potential

Moreover, Lennard-Jones (LJ) (12,6) potentials were considered to determine the interatomic interactions between the Si - H and H-H. The LJ potential form is given by

$$V(r_{ij}) = 4\varepsilon\left[\left(\frac{\sigma}{r_{ij}}\right)^{12} - \left(\frac{\sigma}{r_{ij}}\right)^{6}\right] \quad (4)$$

For Si-H and H-H interactions, LJ potential parameters are deduced from the values given in literature [15]

All MD simulations were performed in Isochoric-Isothermal (NVT) ensemble under heating. The equations of atomic motions with a time step as 1fs have integrated by the leapfrog Verlet Velocity algorithm. Brendsden thermostat controlled the temperature of the system with 0.1 value in all simulations. The optimization procedure was applied to obtain the equilibrium structures at 1K. Then the optimized NPs were heated up to 2800K with an increment of 50K.

3. Results and discussion:

In this work, first, the thermal stability of the free-standing cubic silicon NPs have presented by MD simulations. First, the MD results with Tersoff potential

of Si are illustrated for cubic Si_{239} NPs.The morphological and structural changes of the truncated cubic silicon NPs of 239 atoms under heating are given in Fig.1 by the snapshots from the front view and selected radial distribution functions using OVITO. It has noted in Fig.1 that truncated cubic shaped Si_{239} NPs have morphological changes from cubic form to sphere at corresponding temperatures of 1K to 1000K, respectively. The melting temperature of that Si_{239} nanoparticle was determined as 1200K, which is lower than that of the Tersoff potential simulated result for bulk Si melting (Tmbulk=3300K). It is evident in Figs 1 that both the hight of the primary and second peak of rdfs of Si decrease with temperature increases.

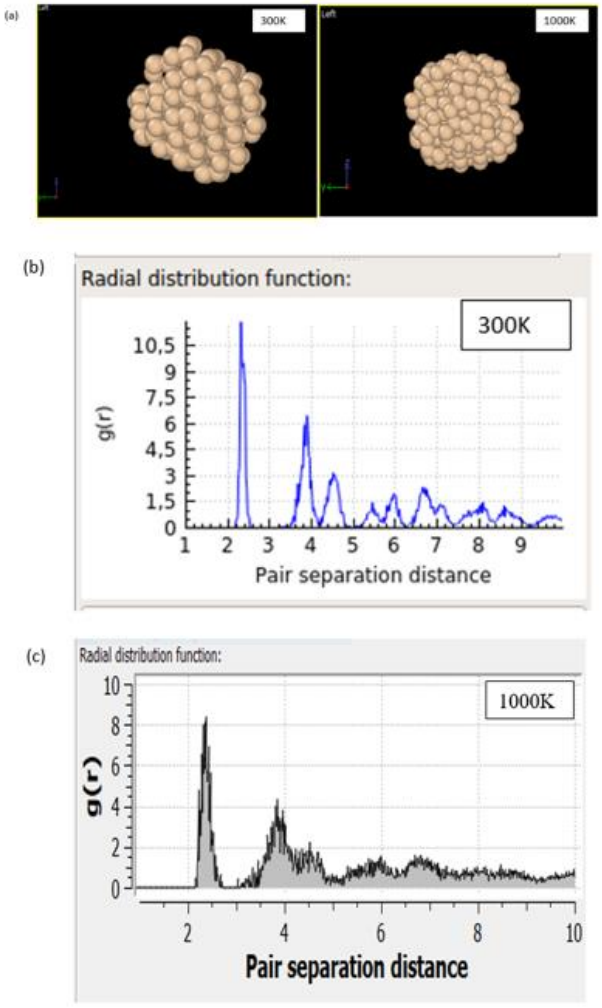


Fig.1: The Snapshots of the Si_{239} cubic NPs (a) at selected temperatures and corresponding rdfs at (b) 300K and (c)1000K

As indicated in Fig. 1 that it is possible to observe the size-dependent melting for Si nanocubes with the Tersoff potential as opposed to the SW potential.

In order to construct the hydrogenated Si nanoparticles, the truncated cube given in Fig.1 was used. The 172 hydrogen atoms were terminated on Si_{239} nanocube. The stability of hydrogen-terminated nanocube of Si0.58H0.42 compositions is shown in Fig. 2 using different potential applications for Si-H and H-H interactions while Tersoff potential was used for Si-Si interactions. The snapshots of $Si_{0.58}H_{0.42}$ and corresponding rdfs are taken from OVITO given in Fig2.

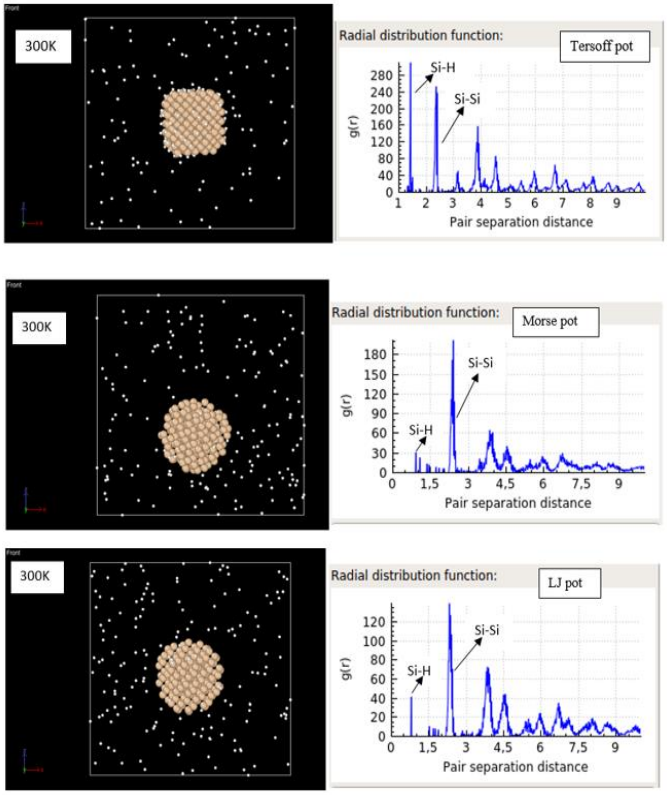


Fig.2: The Snapshots of the hydrogenated $Si_{239\ cubic}$ NPs and corresponding rdfs at 300K using different potential applications for Si-H interactions.

It is clear in Fig2 that the Si-H interactions for Tersoff potential is stronger than other potential applications. For this reason, that the more hydrogen atoms terminated on Si cube are still observed at 300K in contrast to others. The comparison of morphologies in

Fig2 that the hydrogenated Si_{239} cube has maintained its cubic shape when others are almost spherical morphology.

As indicated in previous studies that hydrogen stabilize the Si_{239} cube of both morphology and structure when Tersoff potential is used for all interaction in $Si_{0.58}H_{0.42}$ It can be observed the same behaviour for that nanoparticles at higher temperatures as given in Fig. 3. The snapshots and corresponding rdf values of hydrogenated cubic Si_{239} are illustrated in Fig3 for comparison with non-hydrogenated one as given in Fig. 1. As indicated in Fig1 that these snapshots in Fig.3 also provide the liquid skin evidence of Si_{239} cube by increasing temperature while hydrogen atoms are bonding. Thus surface melting is clear in both all Si cubes, namely hydrogenated and non-hydrogenated ones where the inner region stays ordered until the melting temperature.

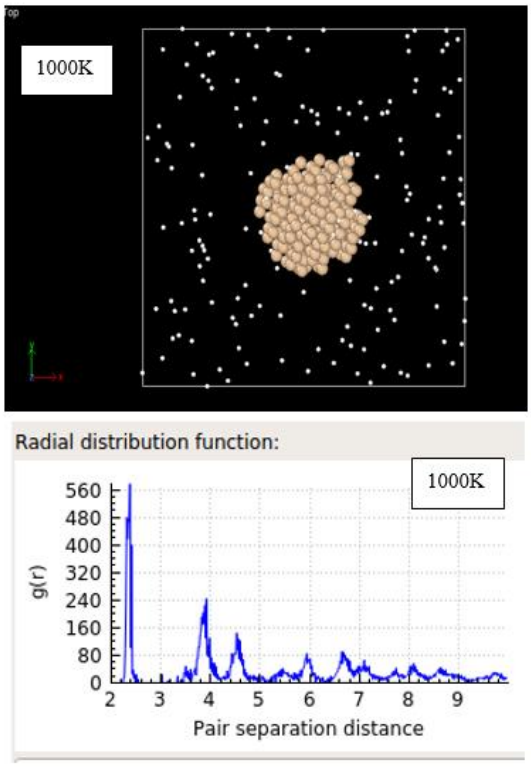


Fig.3: The Snapshots of the hydrogenated $Si_{239\ cubic}$ *NPs and corresponding rdfs at 1000K using Tersoff potential for Si-H interactions*

It has noted that the hydrogen atoms also stabilize the Si cubes at higher temperatures by comparison of the rdfs peaks in Fig.3 with those obtained in Fig. 1c.

The coordination number analysis (CNA) method is also used to calculate average coordination number of non-hydrogenated and hydrogenated cubic Si_{239} NPs and given in Fig.4 for hydrogenated Si_{239} .

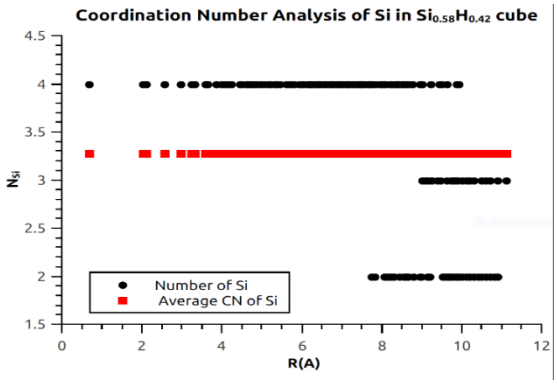


Fig.4: The Coordination numbers of Si atoms in hydrogenated cubic Si_{239} *NPs*

It has noticed from Fig. 4 that the average coordination number value is 3.2803 for hydrogen terminated Si_{239} NPs by compared with the value of 3.2468 for non-hydrogenated one. Those values are computed from the MD results with Tersoff potentials and are in good agreement with previous first principle calculations [2].

Conclusions

In summary, the molecular dynamics (MD) method has been used to simulate the hydrogenated cubic Si nanoparticles. The thermal stabilities of hydrogenated silicon nanoparticles during heating process have studied with different potentials using MD simulations. The cohesive energy of the hydrogenated Si nanoparticles has larger values compare with free standing nanoparticles, which suggest hydrogen can stabilize the surface of Si nanoparticles. The simulated results based on Tersoff based potential functions are in good agreement with previous studies and experiments. It can suggest that Tersoff potential is sufficiently well for the simulation of hydrogenated silicon materials. This work will progress on this line and reported shortly.

References:

[1] A. Y. Galashev, Mol. Phys, 107 (2009) 2555-2565.
[2] H. F. Wilson, L. McKenzie-Sell, A. S. Barnard, J. Mater. Chem. C, 2 (2014) 9451-9451.
[3] A. S. Barnard, H. F. Wilson, J. Phys. Chem. C, 119 (2015) 7969-7977.
[4] J.F. Algorri, D. C. Zografopoulos, A. Ferraro, B. García-Cámara, R. Vergaz, R. Beccherelli, J. M. Sánchez-Pena, Nanomaterials, 9 (2019) 30.
[5] S. Senturk Dalgic (unpublished results)
[6] L.W. Chen, Y. Shibuta, M. Kambara, T. Yoshida, J. Phys. D: Appl. Phys., 46 (2013) 425302-425308.
[7] H. Li, R. Xu, Z. Bi, X. Shen, J. Electronic Materials, 46 (2017) 3826-3830.
[8] U. Hansen, P. Vogl, Phys. Rev. B,57 (1998) 13295-13304.
[9]W. H. Qi, S.T. Lee,Chem. Phys. Lett.483(2009) 247-249.
[10] F. de Brito Mota, J. F. Justo, A. Fazzio, J. Appl. Phys. 86 (1999) 1843-1847.
[11] H. F. Wilson, A. S. Barnard, J. Phys. Chem. C, 118 (2014) 2580-2586.
[12] J. Tersoff, Phys. Rev. Lett, 56 (1986) 632.
[13] DL_POLY: a molecular dynamics simulation package was written by W. Smith, T.R. Forester, and I.T. Todorov obtained from the websitehttp://www.ccp5.ac.uk/DL_POLY
[14] OVITO: A. Stukowski, Modelling Simul. Mater. Sci. Eng. 18, (2010) 015012.
[15] M. Neek-Amal, R. Asgari, and M. R. Rahimi Tabar, Nanotechnology,20 (2009) 135602-135610.

6th International Conference on Materials Science and Nanotechnology For Next Generation (MSNG2019)
October 16-18, 2019, Niğde, TURKEY (ORAL FULL TEXT)

Cu_2ZnSnS_4 (CZTS) Based Thin Films Solar Cells

M.A. Olgar[1,2]*

[1]Department of Physics, Niğde Ömer Halisdemir University, Nigde, Merkez, Turkey
[2]Nanotechnology Application and Research Center, Niğde Ömer Halisdemir University, Nigde, Turkey

CZTS (e) thin films prepared using two-stage process that sputter deposition of metallic Cu, Zn and Sn layers, thermal evaporation Se cap layer to form Cu/Sn/Zn/Cu and Cu/Sn/Zn/Cu/Se metallic stacks followed annealing process in sulfur vapor atmosphere for CZTS and without sulfur for CZTSe thin film fabrications at different reaction temperatures for various reaction times. It was seen that Cu composition has notable effect on the structural properties of CZTSe thin films. The CZTS thin films prepared employing various reaction time displayed remarkable changes in their Raman spectra of films. Overall, it was observed that composition of the metallic precursor and sulfurization procedure (temperature and time) has noticeable impacts on the properties of CZTS thin films.

Keywords: Cu_2ZnSnS_4 (CZTS), Thin film, Sputtering

**Corresponding authors*: mehmetaliolgar@ohu.edu.tr

1. Introduction

Thin film solar cell technology has attracted great attention due to high power conversion efficiency and promising developments in the PV industry. CdTe and Cu (In, Ga)Se_2 (CIGS) based solar cells are materials commonly used in thin film solar cell technology since their conversion efficiency have already surpassed 20% value [1, 2]. However, toxicity of Cd and scarcity of In and Ga have been shown as a big issue for further development such kind of solar cells. In this context, Cu_2SnZnS_4 (CZTS) thin film is an alternative material in place of CdTe and CIGS materials because it contains earth-abundant and environmental-friendly raw materials. In addition, CZTS has p-type conductivity, optical band gap of 1.4-1.5 eV and high absorption coefficient ($\geq 10^4$ cm^{-1}) that makes this compound proper for solar cell applications [3]. The current record conversion efficiency for CZTS-based solar cell is still 12.6% [4] by using selenium (Se) and sulfur (S) together in the compound but Shockley-Queisser theoretical limit for CZTS-based solar cell is above 30%. There are several reasons that influence performance of the solar cell such as composition of the films [5, 6], sulfurization temperatures and dwell time of reactions [7, 8], stacking order of the precursor layers etc [9, 10]. Therefore, growth parameters of CZTS thin films such as deposition technique or sulfurization procedure play important role in the quality of CZTS structure. CZTS thin films are usually fabricated using DC and RF magnetron sputtering [11], thermal evaporation [12], e-beam evaporation [13], pulsed laser deposition (PLD) [14] spray pyrolysis [7]. In this study, effect of deposition parameters such as composition, sulfurization temperature, time etc. on the properties of CZTS (e) thin films was summarized.

2. Experimental details

Precursor layers Cu, Zn and Sn were deposited on Mo-coated glass using DC magnetron sputtering. The base pressure and operating pressure of the vacuum chamber was about 10^{-6} and 10^{-3} torr respectively. Metallic stacking order was arranged as Mo/Cu/Sn/Zn/Cu. In addition, for fabrication of CZTSe thin films, Se cap layer was deposited on top of the metallic stack (Mo/Cu/Sn/Zn/Cu/Se).

The precursor films were then annealed in graphite box with placing high purity (99.98%) elemental sulfur near the precursor as to convert metallic films to CZTS structure. The tubular furnace was heated to reaction temperature (550 °C) and then samples were pushed to the heating zone as to simulate rapid thermal processing. Before the sulfurization process, the furnace was evacuated roughly with aid of pump and filled with mix gas (95%Ar+5%H_2) as to get rid of air before initiation of the sulfurization process. In order to investigate effect of the Cu-composition and reaction temperatures, Cu-poor (Cu/Zn+Sn<1) and Cu-rich (Cu/Zn+Sn>1) compositions and 525, 550, 575 and 600 °C temperatures were selected for fabrication of CZTSe thin films.

To investigate impact of sulfurization time, Mo/Cu/Sn/Zn/Cu stacking order was deposited in the same manner and then sulfurization process was carried out at 500 °C for different reaction times (4, 8, 12 min).

Chemical composition of the films was determined using Oxford Instruments Inca X-act energy dispersive X-ray spectroscopy (EDX) system. In order to confirm formation of kesterite CZTS phase and other phases Renishaw inVia Spectrometer was employed for Raman spectroscopy using an excitation wavelength of 633 nm. Surface morphology of samples was characterized using JEOL JSM 6610 scanning electron microscope (SEM).

3. Results and discussion:

3.1. Impact of Cu-composition and reaction temperature

The atomic percentage and atomic ratio of precursor (Cu/Sn/Zn/Cu) and CZTS thin films were listed in Table 1. The Cu-poor samples were marked as a "A" type samples and and Cu-rich samples were denoted as "B" type and the followed numbers present their annealing temperatures. For example, A550 sample represents the sample that it has Cu-poor composition and annealed at 550 °C.

Table 1. Atomic ratio of Cu-poor CZTSe thin films.

Atomic Ratio	A525	A550	A575	A600
Cu/(Zn+Sn)	0.75	0.84	0.74	0.94
Zn/Sn	1.03	1.21	1.38	2.43
Se/Metal	0.94	0.95	0.92	0.80

Table 2. Atomic ratio of Cu-rich CZTS thin films.

Atomic Ratio	B525	B550	B575	B600
Cu/(Zn+Sn)	1.19	1.11	1.12	1.29
Zn/Sn	1.16	1.10	1.34	1.37
Se/Metal	0.86	0.87	0.85	0.79

As can be seen in the Table 1, all CZTS thin films exhibited Cu-poor (Cu/(Zn+Sn) <1) and Zn-rich composition Zn-rich (Zn/Sn>1), as targeted. On the other hand, CZTS thin films listed in Table 2 showed Cu-rich (Cu/(Zn+Sn) >1) Zn-rich and Zn-rich (Zn/Sn>1) composition, as targeted too. As can be traced from these tables, annealing above the 575 °C temperature gave rise to Sn-loss hence Cu/Zn+Sn ratio got higher values for all films. The surface morphological structures of Cu-poor and Cu-rich samples demonstrated in Figure 1.

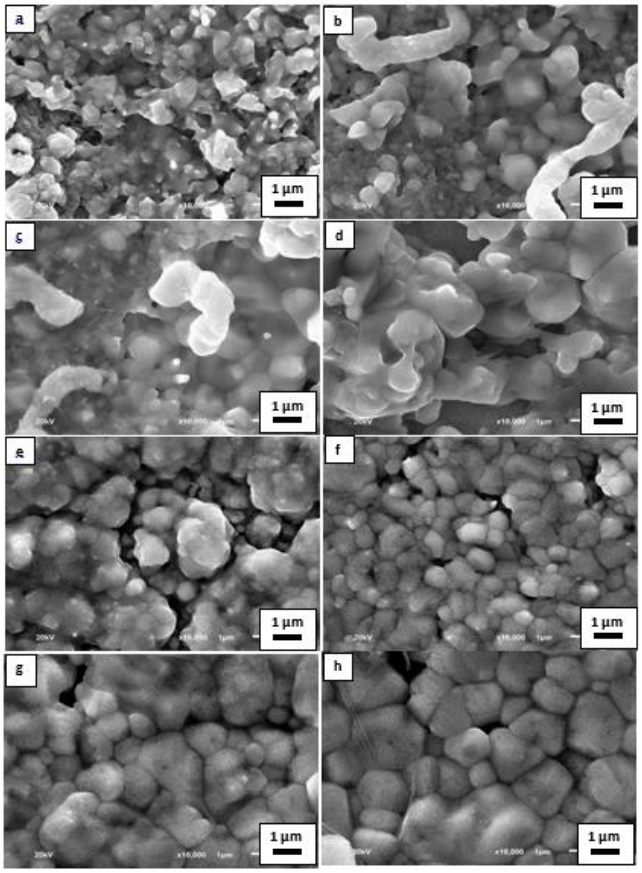


Fig. 1: SEM top views of ; a) A525, b) A550, c) A575, d) A600, e) B525, f) B550, g) B575, and h) B600 samples.

Although some of the samples show somewhat non-uniform and inhomogeneous surface structures, they display a rather dense structure irrespective of the composition and the reaction temperature. For the "A" type films, higher reaction temperatures improved fusion between the surface structures and yielded films that are more compact. Increasing the reaction temperature yielded similar results for the "B" type films also. As the annealing temperature increased, cracks within the layers disappeared, and the surface structures became larger and more compact [6].

3.2. Impact of reaction time

CZTS thin films were grown employed different reaction times (4, 8, 12 min) were denoted according to their sulfurization time. For example, CZTS-4 represents the

sample sulfurized at 500 °C for 4 min. The chemical composition of samples was listed in Table 3. As can be seen in the table, irrespective of the sulfurization time all samples showed Cu-poor and Zn-rich composition. As the reaction time increased some amount of Zn and Sn decreased for CZTS-8 and CZTS-12 films due to the high vapor pressure of these elements and/or their binary compounds.

Table 3. Chemical composition of metallic and CZTS samples.

Specimen	Atomic Ratio		
	Cu/(Zn+Sn)	Zn/Sn	S/Metal
Cu/Sn/Zn/Cu	0.83	1.22	-
CZTS-4	0.86	1.03	1.25
CZTS-8	0.87	1.12	1.24
CZTS-12	0.90	1.05	1.20

Raman spectra of CZTS samples obtained various reaction time was presented in Figure 2. As shown in the the figure, irrespective of the reaction time all films has a dominant peak in their Raman spectra at around 336-337 cm^{-1} that is attributed to CZTS phase. The other peaks associated with CZTS phase are marked in the figure. Peaks of $Cu_{2-x}S$ and Cu_2SnS_3 (CTS) were also observed for formation of CTS phase can be explained with the fact that longer sulfurization time may cause decomposition reactions in CZTS-8 and CZTS-12 thin films [15].

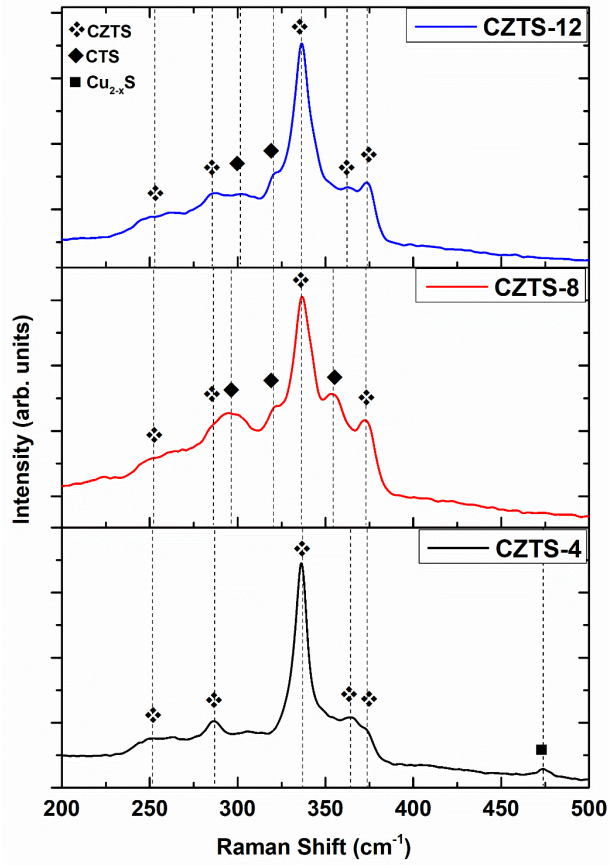


Fig. 2: Raman spectra of CZTS thin films sulfurized for different reaction time.

Conclusions

In this study, CZTSe and CZTS thin films were grown by two stage process includes sputter deposition of metallic Cu, Zn, Sn precursor layers and thermal evaporation of Se cap layer followed by annealing process with/without sulfur atmosphere at different reaction temperatures for various reaction times. It was observed that Cu composition has a substantial effect on the structural properties of CZTSe thin films. The CZTS thin films obtained using different reaction time displayed remarkable changes in their Raman spectra of the films. Overall, it was observed that composition of the metallic precursor and sulfurization procedure (temperature and time) has notable impacts on the properties of CZTS thin films.

References:

[1] M. Nakamura, K. Yamaguchi, Y. Kimoto, Y. Yasaki, T. Kato, H. Sugimoto, IEEE Journal of Photovoltaics (2019).
[2]M.A. Green, E.D. Dunlop, D.H. Levi, J. Hohl-Ebinger, M. Yoshita, A.W. Ho-Baillie, Progress in Photovoltaics: Research and Applications 27(NREL/JA-5K00-74116) (2019).
[3] W. Shockley, H.J. Queisser, J Appl Phys 32(3) (1961) 510-519.
[4] W. Wang, M.T. Winkler, O. Gunawan, T. Gokmen, T.K. Todorov, Y. Zhu, D.B. Mitzi, Adv Energy Mater 4(7) (2014) 1301465.
[1] M. Nakamura, K. Yamaguchi, Y. Kimoto, Y. Yasaki, T. Kato, H. Sugimoto, IEEE Journal of Photovoltaics (2019).
[2] M.A. Green, E.D. Dunlop, D.H. Levi, J. Hohl-Ebinger, M. Yoshita, A.W. Ho-Baillie, Progress in Photovoltaics: Research and Applications 27(NREL/JA-5K00-74116) (2019).
[3] W. Shockley, H.J. Queisser, J Appl Phys 32(3) (1961) 510-519.

[4] W. Wang, M.T. Winkler, O. Gunawan, T. Gokmen, T.K. Todorov, Y. Zhu, D.B. Mitzi, Adv Energy Mater 4(7) (2014) 1301465.
[5] K. Tanaka, Y. Fukui, N. Moritake, H. Uchiki, Solar Energy Materials and Solar Cells 95(3) (2011) 838-842.
[6] M.A. Olgar, Y. Atasoy, B.M. Basol, M. Tomakin, G. Aygun, L. Ozyuzer, E. Bacaksiz, J Alloy Compd 682 (2016) 610-617.
[7] H.T. Kim, D. Kim, C. Park, Molecular Crystals and Liquid Crystals 564(1) (2012) 155-161.
[8] M.A. Olgar, Superlattice Microst 126 (2019) 32-41.
[9] M.A. Olgar, J. Klaer, R. Mainz, S. Levcenco, J. Just, E. Bacaksiz, T. Unold, Thin Solid Films 615 (2016) 402-408.
[10] H. Yoo, J. Kim, Thin Solid Films 518(22) (2010) 6567-6572.
[11] S. Marchionna, P. Garattini, A. Le Donne, M. Acciarri, S. Tombolato, S. Binetti, Thin Solid Films 542 (2013) 114-118.
[12] A. Redinger, M. Mousel, R. Djemour, L. Gütay, N. Valle, S. Siebentritt, Progress in Photovoltaics: Research and Applications 22(1) (2014) 51-57.
[13] E.M. Mkawi, Y. Al-Hadeethi, E. Shalaan, E. Bekyarova, J Mater Sci-Mater El 29(23) (2018) 20476-20484.
[14] A.V. Moholkar, S.S. Shinde, A.R. Babar, K.U. Sim, Y.B. Kwon, K.Y. Rajpure, P.S. Patil, C.H. Bhosale, J.H. Kim, Solar Energy 85(7) (2011) 1354-1363.
[15] M.A. Olğar, A. Seyhan, Cumhuriyet Science Journal 40(3) 554-562.

6th International Conference on Materials Science and Nanotechnology For Next Generation (MSNG2019)
October 16-18, 2019, Niğde, TURKEY (ORAL FULL TEXT)

Graphene Doping By Ammonia And Pyridine

A. Altuntepe[1], R. Zan[1,2*]

[1]Niğde Ömer Halisdemir University, Nanotechnology Application and Research Center, 51200, Niğde,
[2] Niğde Ömer Halisdemir University, Department of Physics, 51200, Niğde, Turkey

Graphene is one of the most popular materials in recent years. There are a few methods for graphene synthesis; however, in order to obtain large scale and high homogenous graphene, the chemical vapor deposition method (CVD) is commonly employed. Graphene has remarkable properties, such as high optical transparency, conductivity, flexibility and durability. In addition to these outstanding properties of graphene, it has some drawbacks like high sheet resistance and missing energy band gap. These problems can be solved via doping or multilayer graphene synthesis. The synthesis of the doped graphene can increase the application areas of the graphene. In this study, ammonia (NH_3) and pyridine (C_5H_5N) were used as dopant for the synthesis of doped graphene. In addition, the pyridine was used both as carbon source and dopant. NH_3 flow rate was optimized for single layer and homogenous graphene synthesis. The study revealed NH_3 doping of the graphene layer was much more successful in terms of single layer graphene synthesis in comparison to the pyridine doping. However, few layers were synthesized using only C_5H_5N. Then, the pristine graphene, NH_3 and C_5H_5N doped graphene films were characterized to determine electrical and optical properties.

Keywords: CVD, Graphene, Ammonia, Pyridine

Corresponding author: recep.zan@ohu.edu.tr

1. Introduction

Graphene has superior properties such as high light transmittance, high conductivity and flexibility. These properties make graphene appliable in many areas of technology. There are a few methods for graphene synthesis and each has its own advantages over the others in terms of applications. Graphene was first isolated by mechanical exfoliation methods by Novoselov et. al. in 2004. Chemical vapor deposition (CVD) method is one of the most popular methods for graphene synthesis that provides large scale homogenous graphene synthesis [1, 2].

Although graphene has attractive properties, it has some handicaps such as missing band gap and high sheet resistance. These properties restrain graphene applications in particular in electronics. However, different methods could be used to overcome these issues. Chemical doping is commonly used to lower the sheet resistance of graphene film. In order to dope

graphene films, ammonia, pyridine, nitrogen and urea were used as dopants in the literature [3, 4].

Fast and non-disruptive tools to characterize graphene films are known to be Raman Spectrometer. Graphene has three main peaks called D, G and 2D in the Raman spectra. D peak generally represents defect or vacancy in the structure, G peak shows crystallinity of graphene film and 2D peak is related to the graphene film thickness. $I_{2D/G}$ is used to determine graphene film thickness and quality. If the intensity ratio between 2D and G peaks is $I_{2D/G} > 2$, it means single layer graphene is obtained [5].

In the present study, NH_3 and C_5H_5N were used as dopants during graphene synthesis. The effect of

NH_3 and C_5H_5N was investigated to lower sheet resistance of single layer graphene. NH_3 flow rate was investigated in order to synthesize doped graphene. Pyridine was used as both carbon source and dopant for the graphene synthesis.

2. Experimental

At the beginning, most of the growth such parameters like temperature, pressure, growth time and annealing time of graphene films were optimized to synthesize single layer graphene. In the current research, graphene was grown on 25 µm thick polycrystalline copper by CVD method. The CVD system consists of three-zone furnace and six mass flow controllers. Standard pre-cleaning (acetone, deionize water, isopropyl alcohol) was applied to copper substrates to remove possible organic contaminations. High purity (%99,9995) Methane (CH_4) as a carbon source and high purity (%99,9999) Hydrogen (H_2) gases were used for the pristine (un-doped) single layer graphene synthesis. The experimental chart that shows the growth process and related parameters was given in Figure 1. NH_3 flow rate effect on graphene doping was investigated. Different NH_3 flows from 5 sccm to 15 sccm were applied for in-situ graphene doping. Then C_5H_5N, which is in liquid form, was used both as carbon source and as dopant for the second approach of the research. Raman spectroscopy was used for the characterization of the pristine and doped graphene films.

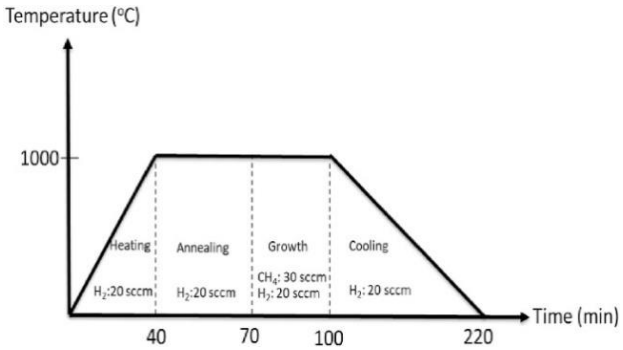


Figure 1 Experimental CVD process of graphene synthesis.

3. Results

The Raman spectroscopy of pristine single layer graphene is given in figure 2. Doped single layer graphene was synthesized using NH_3. The increase of NH_3 flow rate during the synthesis reduced the graphene film quality and the film thickness was increased. Single layer doped graphene with high homogenity was synthesized using 5 sccm NH_3. Figure 3 shows Raman spectroscopy results of the NH_3 doped graphene. The graphene film quality was decreased after 5 sccm NH_3. When the NH_3 flow increased over 15 sccm under given conditions multilayer graphene was synthesized and graphene quality decreased seriously.

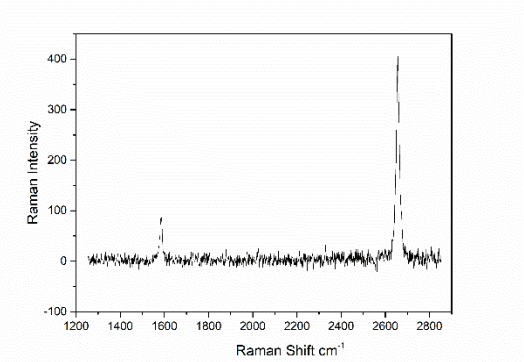


Figure 2 Raman spectroscopy of pristine graphene

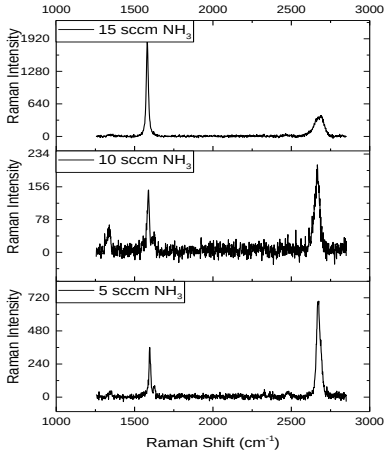


Figure 3 Raman spectroscopy of NH_3 doped graphene

Then, C_5H_5N was used as both carbon source and dopant during the synthesis. Only multilayer graphene was synthesized by C_5H_5N although many growth parameters were amended during the graphene synthesis. Raman spectrum of the graphene film was given in Figure 4 and this spectrum represents a few layer graphene films.

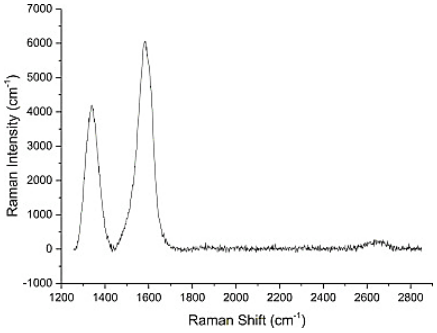


Figure 4 Raman spectroscopy of C_5H_5N *doped graphene*

4. Conclusion

NH_3 doped and C_5H_5N doped graphene films were synthesized successfully using CVD. Single layer and large-scale graphene films were fabricated via NH_3; however, only a few layered graphene was synthesized via C_5H_5N.

Acknowledgement

The authors gratefully acknowledge the funding from The Scientific and Technological Research Council of Turkey (TÜBITAK-117M401).

References

[1] A.K. Geim, K.S. Novoselov, The rise of graphene, Nanoscience and Technology: A Collection of Reviews from Nature Journals, World Scientific2010, pp. 11-19.
[2] M.J. Allen, V.C. Tung, R.B. Kaner, Honeycomb carbon: a review of graphene, Chemical reviews, 110 (2009) 132-145.
[3] L. Panchakarla, K. Subrahmanyam, S. Saha, A. Govindaraj, H. Krishnamurthy, U. Waghmare, C. Rao, Synthesis, structure, and properties of boron-and nitrogen-doped graphene, Advanced Materials, 21 (2009) 4726-4730.
[4] S. Das, M. Kim, J.-w. Lee, W. Choi, Synthesis, properties, and applications of 2-D materials: a comprehensive review, Critical Reviews in Solid State and Materials Sciences, 39 (2014) 231-252.
[5] Y. Hao, Y. Wang, L. Wang, Z. Ni, Z. Wang, R. Wang, C.K. Koo, Z. Shen, J.T. Thong, Probing layer number and stacking order of few-layer graphene by Raman spectroscopy, small, 6 (2010) 195-200.

6th International Conference on Materials Science and Nanotechnology For Next Generation (MSNG2019)
October 16-18, 2019, Niğde, TURKEY (ORAL FULL TEXT)

Growth of Cu_2ZnSnS_4 (CZTS) Thin Films Employing Various Sulfurization Pressures

M.A. Olgar[1]*, A.O. Sarp[2], A. Seyhan[1] and R.Zan[1]

[1]Department of Physics, Niğde Ömer Halisdemir University, Nigde, Merkez, Turkey
[2]Department of Electrical Electronic Engineering, Niğde Ömer Halisdemir University, Merkez, Turkey

CZTS thin films prepared using two-stage process that sputter deposition of metallic layers Cu, Sn and ZnS to form CuSn/ZnS/Cu metallic stack followed annealing process in sulfur vapor atmosphere using different annealing pressures at 550 °C for 3 min. EDX measurements of the films revealed that Zn-deficiency was observed in all CZTS thin films due to high vapor pressure of Zn. The XRD pattern of CZTS films showed diffraction peaks of kesterite CZTS phase regardless of the annealing pressure. In addition, minor peaks related to ternary CTS phase was observed in all films. Raman spectra of the films confirmed formation of kesterite CZTS phase and presented some other extra phases such as SnS_2 and $Cu_{2-x}S$ for some films. Overall, it was observed that all samples suffer from Zn-deficiency, however after more optimization process CZTS-40 may the most promising properties for solar cell applications.

Keywords: Cu_2ZnSnS_4 (CZTS), Thin film solar cell, Sputtering, Annealing pressure

**Corresponding authors*:mehmetaliolgar@ohu.edu.tr

1. Introduction

Thin film solar cell is the second-generation technology in the PV industry. Several different compounds have been used so far in this technology, such as amorphous silicon, CdTe and Cu (In, Ga)Se_2 (CIGS). Amongst these compounds, both CdTe and CIGS based solar cells have already reached 22.1% and 23.35% conversion efficiency [1, 2]. However, toxicity of Cd and scarcity of In and Ga may limit further development of such kind of thin film solar cells. Therefore, Cu_2SnZnS_4 (CZTS) thin film has been shown as an alternative material to CdTe and CIGS materials because it has earth-abundant and environmental-friendly materials (Cu, Zn, Sn, S), p-type conductivity and superior optical properties that are direct band gap of 1.4-1.5 eV and high absorption coefficient ($\geq 10^4$ cm^{-1}) [3]. Although Shockley-Queisser theoretical limit for CZTS-based solar cell is above 30%, the current record efficiency is still 12.6% [4]. The underlying reason for the gap between the theoretical limit and reported efficiency may be attributed to several parameters such as composition of the films [5, 6], sulfurization temperatures and dwell time of reactions [7, 8], stacking order of the precursor layers etc [9, 10]. Therefore, growth parameters of CZTS thin film are extremely important in terms of the quality of the films. The CZTS thin films are usually prepared either using vacuum based methods such as DC and RF magnetron sputtering [11], thermal evaporation [12], e-beam evaporation [13], pulsed laser deposition (PLD) [14] or non-vacuum required methods such as spray pyrolysis [7], dip-coating etc. [15]. Sputtering method is widely used for fabrication of CZTS thin films because it is feasible for large-scale fabrication, easy to control deposition parameters such as thickness, pressure etc. and enablement for homogenous thin film fabrications.

In this study, effect of the sulfurization pressure on the properties of CZTS thin films were studied. A new stacking order (Cu/Sn/ZnS/Cu) was proposed at the first time by own research group and utilized in this study. The compositional, structural, optical, and electrical properties of prepared samples were discussed in detail.

2. Experimental details

Metallic Cu, Sn and ZnS layers were deposited using DC and RF magnetron sputtering in a determined tacking order. DC power source was used for Cu, RF power source was used for Sn, and ZnS sputter targets. High purity Cu (5N), Sn (4N) and ZnS (4N) targets were used for film deposition. Sputtering chamber was evacuated to 10^{-6} torr in

advance deposition process. Sputter deposition of the films were performed under 10^{-3} torr operating pressure. Major part of Cu and Sn was co-sputtered on glass substrate with a substrate temperature of 200 °C as to obtain CuSn alloy. In this way, it was aimed to prevent Sn-loss from CZTS compound. The ZnS and Cu layers were deposited sequentially on top of CuSn alloy to form Glass/CuSn/ZnS/Cu metallic precursor film.

The precursor films were then annealed in graphite box with placing high purity (99.98%) elemental sulfur near the precursor as to convert metallic films to CZTS structure. The tubular furnace was heated to reaction temperature (550 °C) and then samples were pushed to the heating zone as to simulate rapid thermal processing. Before the sulfurization process, the furnace was evacuated roughly with aid of pump then different amount of mix gas (95%Ar+5%H_2) was sent and the precursor films were sulfurized. The sulfurized samples were denoted according to employing gas. For example, CZTS-20 represents the sample sulfurized under 20 sccm of 95%Ar+5%H_2 gas mixture (see Table 1).

Table 1. Growth parameters of CZTS thin films.

Sample ID	Stacking Order	Temperature & Time	Ar+H_2 (sccm)
CZTS-0	Glass/CuSn/ZnS/Cu	550 °C, 3 min	0
CZTS-20			20
CZTS-40			40
CZTS-60			60
CZTS-80			80
CZTS-100			100

Chemical composition of the films was determined using Oxford Instruments Inca X-act energy dispersive X-ray spectroscopy (EDX) system. The crystal structure of the films was investigated using RigakuSmartLab diffractometer with a CuKα radiation source (λ= 1.5405 Å). In order to confirm formation of kesterite CZTS phase and other phases Renishaw inVia Spectrometer was employed for Raman spectroscopy using an excitation wavelength of 633 nm.

3. Results and discussion:

The atomic percentage and atomic ratio of precursor (CuSn/ZnS/Cu) and CZTS thin films were listed in Table 2. As can be seen in the table, precursor film showed Cu-poor (Cu/(Zn+Sn) <1) and Zn-rich (Zn/Sn>1) composition and small value of S/Metal atomic ratio due to ZnS prior the sulfurization process. After reaction of the samples under 0, 20, 40, 60, 80 and 100 sccm of 95%Ar+5%H_2 mix gas, the atomic ratio of the samples showed remarkable variation in their atomic ratio. As shown in the table, with increasing the annealing pressure Zn-loss was observed in all composition of the samples (see Table 2). This situation may be explained by high vapor pressure of Zn [16].

The XRD patterns of CZTS thin films grown under different annealing pressures were displayed in Figure 1. As can be revealed in the figure, irrespective of the annealing pressures, all of the films displayed diffraction peaks at the estimated locations of CZTS (112) (2θ= 28.44°), (220/204) (2θ= 47.31°), and (312/116) (2θ= 56.17°) (JCPDS 26-0575) planes [17]. In addition to kesterite CZTS phase, two extra small peaks were observed in vicinity of 2θ= 14.75°, 34.50° that are attributed to formation of $CuSn_{3.75}S_8$ (JCPDS 01-066-2266).

Table 2. Atomic ratio of precursor and CZTS thin films prepared under different annealing pressures.

Sample	Atomic ratio		
	Cu/(Zn+Sn)	Zn/Sn	S/Metal
CuSn/ZnS/Cu	0.98	1.19	0.24
CZTS-0	1.10	0.84	0.94
CZTS-20	1.13	0.75	0.95
CZTS-40	1.19	0.67	0.94
CZTS-60	1.18	0.52	0.98
CZTS-80	1.30	0.54	0.98
CZTS-100	1.15	0.77	0.96

Overall, except minor peaks related to ternary phase all samples displayed almost pure CZTS crystal structure.

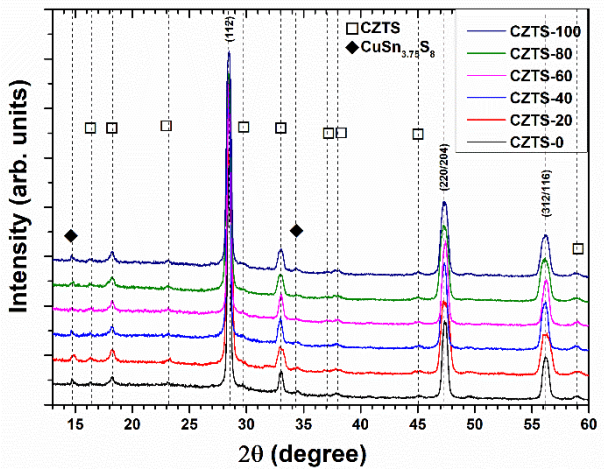


Fig.1: XRD pattern of CZTS thin films.

Some phases have similar diffraction patters with each other. Since CZTS (JCPDS 26-0575), ZnS (JCPDS 05-0566) and Cu_2SnS_3 (CTS) (JCPDS 027-0198) phases have similar XRD patterns, Raman spectroscopy of the samples was taken as a complementary technique as to distinguish these phases and confirm existence of kesterite phase. Figure 2 presents Raman spectra of CZTS thin films prepared employing various annealing pressures.

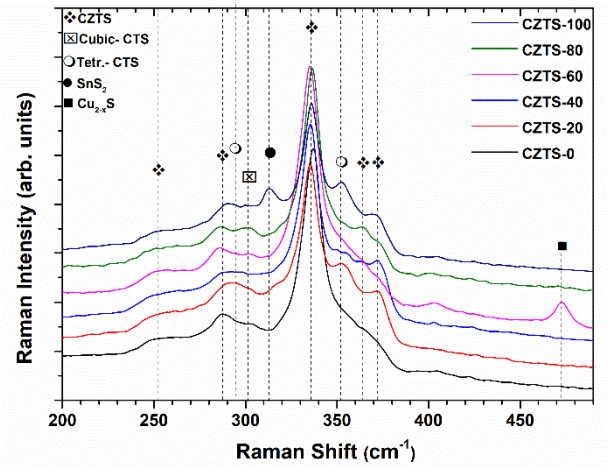


Fig.2: Raman spectra of CZTS thin films prepared in this study.

As can be seen in the figure, irrespective of the sulfurization pressure, all of the Raman spectra are dominated by a strong peak located around at 338 cm^{-1} that is attributed to kesterite CZTS phase [18]. Other characteristic peaks of CZTS phase were also marked in the figure. In addition to kesterite CZTS phase, some extra phases were also detected such as CTS, SnS_2 and $Cu_{2-x}S$ phases. Only CZTS-40 showed almost formation of pure kesterite CZTS phase.

Conclusions

In this study, CZTS thin films were grown successfully by a two-stage method includes sputter deposition metallic films followed by sulfurization process under different annealing pressures. EDX measurements showed that all CZTS thin films suffer from Zn-deficiency due to the high vapor pressure of Zn. XRD measurements revealed that regardless of the annealing pressure, all samples showed diffraction peaks of kesterite CZTS structure. Also, ternary CTS phase was observed in all films. Raman spectra of the samples confirmed formation of CZTS phase and extra some secondary phases such as CTS, SnS_2 and Cu_{2-x} S. Overall, although all CZTS samples displayed Zn-deficiency, CZTS-40 thin film may present more promising results after optimization of the sulfurization process.

Acknowledgements

This research was supported by The Scientific and Technological Research Council of Turkey (TUBITAK) with the project number of 118F530.

References:

[1] M. Nakamura, K. Yamaguchi, Y. Kimoto, Y. Yasaki, T. Kato, H. Sugimoto, IEEE Journal of Photovoltaics (2019).
[2] M.A. Green, E.D. Dunlop, D.H. Levi, J. Hohl-Ebinger, M. Yoshita, A.W. Ho-Baillie, Progress in Photovoltaics: Research and Applications 27(NREL/JA-5K00-74116) (2019).
[3] W. Shockley, H.J. Queisser, J Appl Phys 32(3) (1961) 510-519.
[4] W. Wang, M.T. Winkler, O. Gunawan, T. Gokmen, T.K. Todorov, Y. Zhu, D.B. Mitzi, Adv Energy Mater 4(7) (2014) 1301465.
[5] K. Tanaka, Y. Fukui, N. Moritake, H. Uchiki, Solar Energy Materials and Solar Cells 95(3) (2011) 838-842.
[6] M.A. Olgar, Y. Atasoy, B.M. Basol, M. Tomakin, G. Aygun, L. Ozyuzer, E. Bacaksiz, J Alloy Compd 682 (2016) 610-617.
[7] H.T. Kim, D. Kim, C. Park, Molecular Crystals and Liquid Crystals 564(1) (2012) 155-161.
[8] M.A. Olgar, Superlattice Microst 126 (2019) 32-41.
[9] M.A. Olgar, J. Klaer, R. Mainz, S. Levcenco, J. Just, E. Bacaksiz, T. Unold, Thin Solid Films 615 (2016) 402-408.
[10] H. Yoo, J. Kim, Thin Solid Films 518(22) (2010) 6567-6572.
[11] S. Marchionna, P. Garattini, A. Le Donne, M. Acciarri, S. Tombolato, S. Binetti, Thin Solid Films 542 (2013) 114-118.
[12] A. Redinger, M. Mousel, R. Djemour, L. Gütay, N. Valle, S. Siebentritt, Progress in Photovoltaics: Research and Applications 22(1) (2014) 51-57.
[13] E.M. Mkawi, Y. Al-Hadeethi, E. Shalaan, E. Bekyarova, J Mater Sci-Mater El 29(23) (2018) 20476-20484.
[14] A.V. Moholkar, S.S. Shinde, A.R. Babar, K.U. Sim, Y.B. Kwon, K.Y. Rajpure, P.S. Patil, C.H. Bhosale, J.H. Kim, Solar Energy 85(7) (2011) 1354-1363.
[15] T. Bayazıt, M.A. Olgar, T. Küçükömeroğlu, E. Bacaksız, M. Tomakin, Journal of Materials Science: Materials in Electronics (2019) 1-7.
[16] M.A. Olgar, E. Bacaksiz, M. Tomakin, T. Kucukomeroglu, B.M. Basol, Materials Science in Semiconductor Processing 90 (2019) 101-106.

[17] M.A. Olgar, M. Tomakin, T. Kucukomeroglu, E. Bacaksiz, Materials Research Express 6(5) (2019).

[18] P.A. Fernandes, P.M.P. Salome, A.F. da Cunha, J Alloy Compd 509(28) (2011) 7600-7606.

6th International Conference on Materials Science and Nanotechnology For Next Generation (MSNG2019)
October 16-18, 2019, Niğde, TURKEY (ORAL FULL TEXT)

Graphene as a Transparent Conductive Layer

R. Zan[1,2*]

[1] Niğde Ömer Halisdemir University, Nanotechnology Application and Research Center, 51200, Niğde, Turkey
[2] Niğde Ömer Halisdemir University, Department of Physics, 51200, Niğde, Turkey

With its remarkable properties such as a high optical transparency, conductivity, flexibility and durability, graphene has become one of the most attractive materials in recent years. Graphene layers can be obtained via various techniques; however, growing graphene through chemical vapor deposition (CVD) technique provides large-scale single layer graphene with high homogeneity. Besides many good properties, graphene has some drawbacks like high sheet resistance and missing energy band gap. The sheet resistance of the graphene is higher than its rival that is indium tin oxide (ITO). In order to employ graphene as transparent conductive electrode in many optoelectronic applications, the sheet resistance somehow should be lowered to be competitive with the ITO. In order to overcome this issue, doping the graphene layer can be employed. Thus, in situ doping was performed using ammonia in this study. The nitrogen doped graphene was synthesized using different growth recipes and was characterized using Raman spectroscopy and contactless sheet resistance and transmission measurement system.

Keywords: Graphene, ITO, PVD, CVD, n-doped graphene

Corresponding author: recep.zan@ohu.edu.tr

1. Introduction

Graphene has been one of the most attractive materials so far in literature. It has high transparency, high durability, high conductivity and these aspects make it versatile for large scale applications. Besides good properties, it has some drawbacks such as missing band gap and high sheet resistance [1]. Graphene can be used as a transparent conductive oxide (TCO) layer; however, high sheet resistance and missing band gap restrict graphene usage in electronic applications. Indium tin oxide (ITO) is traditionally used as TCO for optoelectronic applications. However, due highly to its brittleness and high cost, new TCO materials are investigated [2, 3]. Besides the drawbacks of ITO, it has low sheet resistance in comparison to the single layer graphene. Thus, the sheet resistance of graphene should be lower to be able to be used as TCO. There are a few methods for the decrease of graphene sheet resistance. These are multi-layer graphene synthesis and doping that could decrease the sheet resistance but meanwhile, some of the good properties such as transmission would be lost [4].

There are a few methods for graphene synthesis such as mechanical exfoliation, chemical exfoliation and chemical vapor deposition (CVD). One of the most widely used method is CVD because CVD provides large scale single layer graphene growth with high homogeneity [5].

To this end, in this research, a systematical study has been conducted regarding graphene and ITO fabrication to investigate sheet resistance of the films and their comparison. Graphene doping has been conducted in order to lower the sheet resistance of the graphene film. So, the doped graphene films were grown using ammonia (NH_3) with different recipes on copper substrates in the CVD furnace to find out the effect of the doping and growth process on the sheet resistance.

Additionally, ITO thin films with different thicknesses were obtained on glass substrates via physical vapor deposition (PVD) system. Then, the synthesized doped graphene and ITO films were characterized to find out the sheet resistance and optical transmittance.

2. Experimental details

In the present study, graphene was grown on 25 µm polycrystalline copper by CVD method. CVD system consists of 3-zone furnace along with 6 mass flow controller (Fig.1.). Pristine and doped graphene synthesis were conducted using this system. Standard pre-cleaning (acetone, deionize water, isopropyl alcohol) was used to abolish any possible contamination from copper surface that could hinder the growth of the graphene films. High purity (%99,9995) Methane (CH_4) was used as carbon source and high purity (%99,9999) Hydrogen (H_2) was used for decomposition at elevated temperature (1000°C).

Doped graphene films were grown by ammonia (NH_3) with different flow rates in addition to methane and hydrogen gases on the polycrystalline copper substrates.



Figure 1. CVD system used to synthesize of graphene

The PVD system was used for coating of ITO on glass substrate. 20, 40, 60, 80, 100 nm thick ITO films were coated at room temperature onto pre-cleaned glass substrates. The base pressure of the system was about $1x10^{-7}$ mbar. The sheet resistance and optical transmission measurements were conducted using contactless sheet resistance and transmission measurement system.



Figure 2. PVD system for coating ITO onto glass

3. Results

The sheet resistance of the ITO films was measured and the results were compared for different film thicknesses. The sheet resistance was observed to decrease with the increase of ITO film thickness. On the other hand, optical transmission decreased with increasing ITO film thickness. 80 nm ITO was determined as optimum film thickness to be employed as TCO.
Then NH_3 doped graphene was synthesized. Different NH_3 flow rate was used for doped graphene synthesis. Raman spectra of the doped graphene films was given in Figure 3. The graphene quality was decreased with the increase of NH_3 flow. 5 sccm NH_3 flow was determined as optimum flow rate for the synthesis of single layer doped graphene. Later, the doped graphene was transferred onto 80 nm ITO coated substrate.

The sheet resistance of the single layer doped graphene films have been found to be around ~350 Ω/sq with approximately 93% optical transmission. Still, ITO sheet resistance values were between 30 and 300 Ω/sq for different ITO thickness. While the sheet resistance increased with the decreasing thickness of the ITO film, the optical transmission improved.

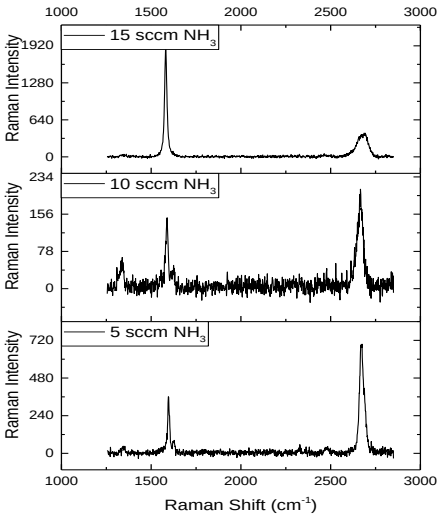


Figure 3 Raman spectroscopy of NH_3 doped graphene

4. Conclusion

ITO films with different thicknesses were successfully fabricated using PVD system and the sheet resistance of the films was measured. Simultaneously, large-scale single layer NH_3 doped graphene was synthesized and characterized. Based on the comparison between doped graphene and ITO, it can be concluded that graphene can be used as TCO. In addition, ITO and graphene can be used together on top of each other as hybrid electrode for opto-electronic applications.

5. References

[1] A.K. Geim, K.S. Novoselov, The rise of graphene, Nanoscience and Technology: A Collection of Reviews from Nature Journals, World Scientific2010, pp. 11-19.
[2] P. Liu, J. Yan, Z. Guang, Y. Huang, X. Li, W. Huang, Recent advancements of polyaniline-based nanocomposites for supercapacitors, Journal of Power Sources 424 (2019) 108-130.
[3] H. Liu, Y. Liu, D. Zhu, Chemical doping of graphene, Journal of materials chemistry 21(10) (2011) 3335-3345.
[4] L. Panchakarla, K. Subrahmanyam, S. Saha, A. Govindaraj, H. Krishnamurthy, U. Waghmare, C. Rao, Synthesis, structure, and properties of boron-and nitrogen-doped graphene, Advanced Materials 21(46) (2009) 4726-4730.
[5] H. Wang, T. Maiyalagan, X. Wang, Review on recent progress in nitrogen-doped graphene: synthesis, characterization, and its potential applications, Acs Catalysis 2(5) (2012) 781-794.

6th International Conference on Materials Science and Nanotechnology For Next Generation (MSNG2019)
October 16-18, 2019, Niğde, TURKEY (ORAL FULL TEXT)

Fabrication of SnS Thin Films For Solar Cell Applications

M.A. Olgar[1,2*], A.Çiriş[2], M. Tomakin[3] and R. Zan[1,2]

[1]Department of Physics, Niğde Ömer Halisdemir University, Nigde, Merkez, Turkey
[2]Nanotechnology Application and Research Center, Niğde Ömer Halisdemir University, Nigde, Turkey
[3]Department of Physics, Recep Tayyip Erdogan University, Rize, Merkez, Turkey

SnS thin films were prepared by annealing treatment of deposited films via RF magnetron sputtering technique in sputtering chamber using various annealing temperatures (225, 300, 375 °C). Chemical composition of SnS thin films displayed remarkable variations after annealing treatment especially at above 300 °C temperature that sulfur loss was observed. XRD pattern of samples showed formations of orthorhombic structure of SnS phase. However, lattice constant values of samples annealed below 375 °C showed more proper results with subject to theoretical value.

Keywords: Tin sulfide (SnS), Thin film, Sputtering, Solar cell

**Corresponding authors*:mehmetaliolgar@ohu.edu.tr

1. Introduction

Limited supply of In, Ga and toxicity of Cd have been demonstrated as a big problem for further development of Cu (In, Ga)Se_2 (CIGS) and CdTe based solar cells though they have conversion efficiency above 20% [1]. Cu_2SnZnS_4 (CZTS) thin film has emerged as a new and alternative material in place of CIGS due to the fact that it has similar crystal structure with CIGS and has suitable optical and electrical properties such as direct band gap of 1.4-1.5 eV, high absorption coefficient ($\geq 10^4$ cm^{-1}) and p-type conductivity [2]. However, the maximum conversion efficiency of CZTS based solar cell has been achieved by 12.6% so far [3, 4]. Low conversion efficiency may be attributed to several reasons. One of the most important reason mentioned amongst these reasons is formation of different secondary phases because CZTS compound consists of at least four different material (Cu, Zn, Sn, S). Therefore, another alternative and promising material, tin sulfide (SnS), has been extensively studied recently. SnS thin film is binary compound includes less kind of material and has suitable optical and electrical properties for solar cell applications such as band gap of around 1.3 eV, high absorption coefficient ($\geq 10^4$ cm^{-1}) [5, 6] and p-type conductivity [7].

Fabrication of SnS thin films have been reported via several different techniques such as sputtering [8], thermal evaporation [9], spray pyrolysis [10] etc. The theoretical conversion limit for SnS-based solar cell is higher than 30% [11], however the current record efficiency is comparatively too low (4.36%) [12]. The underlying reason for the gap between these values can be attributed to several reasons such as composition of the films, improper annealing parameters etc. Therefore, growth parameters of SnS thin films should be optimized as to improve conversion efficiency of SnS based solar cell. Several different optimization studies performed in the literature. For example, effect of substrate temperature, annealing temperature and time, composition of the films etc.

In this study, effect of in-situ annealing temperature (room temperature (RT), 225, 300, 375 °C) performed in the sputtering chamber after deposition of SnS films under vacuum atmosphere on the properties of SnS thin films was investigated.

2. Experimental details

SnS thin films were prepared by RF magnetron sputtering using high purity SnS target (4N). Before deposition process, the glass substrates were cleaned sequentially in methanol, aceton and distilled water using ultrasonic cleaner. Then, glass substrates were dried under flow of nitrogen gas. The base pressure and operating pressure of sputtering chamber were 10^{-6} and 10^{-3} torr respectively. After deposition of the SnS thin films, heater placed behind the samples on and samples annealed for 5 min and then left to natural cooling. The samples were denoted according their annealing temperature. For example, SnS-AD represents the sample obtained at room temperature and SnS-225 represents the sample annealed at 225 °C (see Table 1).

Table 1. Growth parameters of SnS thin films.

Sample	Annealing Temperature & Time
SnS-AD	-
SnS-225	225 °C, 5 min
SnS-300	300 °C, 5 min
SnS-375	375 °C, 5 min

Chemical composition of the films was determined using Oxford Instruments Inca X-act energy dispersive X-ray spectroscopy (EDX) system. The crystal structure of the films was investigated using Rigaku-SmartLab diffractometer with a CuKα radiation source (λ= 1.5405 Å).

3. Results and discussion:

The Sn/S atomic ratio and its variation with respect to temperature was shown in Figure 1. As can be seen in the figure, Sn/S atomic ratio values showed variation from 1.04 to 1.22 with increasing the annealing temperature from room temperature to 375 °C. It was seen that as the annealing temperature increased especially above 300 °C, remarkable S loss was observed in the sample (see Figure 1). Therefore, fabrication of SnS thin films under vacuum conditions might be optimized between 300 and 375 °C temperatures for obtaining desired composition.

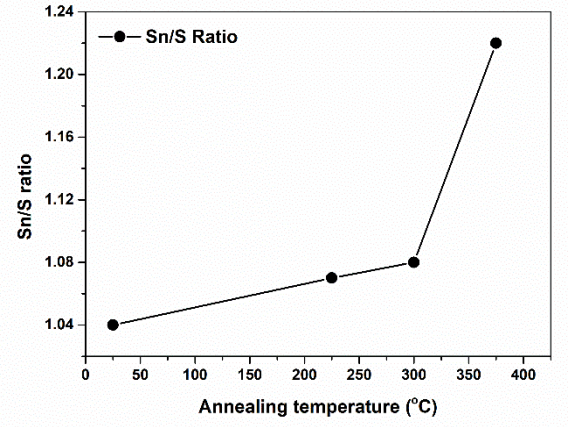


Fig. 1: Variation of atomic composition subject to annealing temperatures.

XRD pattern of SnS thin films obtained using different annealing temperatures were displayed in Figure 2. As can be seen in the figure, regardless of annealing temperature all annealed samples displayed preferential orientation along the (111) plane of orthorhombic phase of

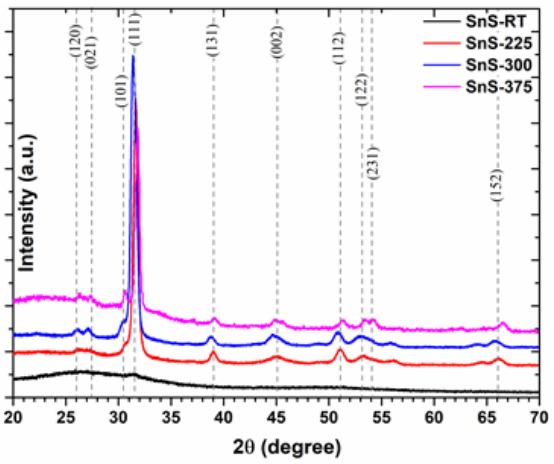


Fig. 2: XRD pattern of SnS thin films prepared in this study.

SnS (JCPDS 39-0354). Other diffraction of this phase marked in the figure. Only SnS-AD sample revealed amorphous structure due to not applying any annealing treatment hence crystallization was not occurred.

Lattice constants of these samples were calculated and compared with theoretical values as to determine the optimum annealing temperature. The calculated and theoretical values for lattice constants were listed in Table 2.

Table 2. Lattice constant values of SnS thin films.

Sample	a(A°)	b(A°)	c(A°)
RT	-	-	-
225°C	4.247	11.297	4.024
300 °C	4.287	11.278	4.051
375 °C	4.190	11.412	4.022
Theoretical	4.329	11.192	3.984

As shown in Table 2, lattice constant values of prepared SnS thin films are very close to theoretical values regardless of the annealing temperatures. However, the annealed samples below the 375 °C had closer values. This situation might be explained by variation in composition of films.

Conclusions

In this study, SnS thin films were fabricated successfully via RF magnetron sputtering that thin films were deposited on glass substrates and in-situ annealing treatment was exposed at different temperatures. EDX measurements showed that annealing temperature above 300 °C gave rise to notable S-loss in the samples. XRD measurements showed that orthorhombic SnS phase was formed regardless of the annealing temperature. However, increasing the annealing temperature above 300 °C may cause more deviation in lattice constant values with respect to theoretical values.

References:

[1] [1] M.A. Green, E.D. Dunlop, D.H. Levi, J. Hohl-Ebinger, M. Yoshita, A.W. Ho-Baillie, Progress in Photovoltaics: Research and Applications 27(NREL/JA-5K00-74116) (2019).
[2] M.A. Olgar, Superlattice Microst 126 (2019) 32-41.
[3] W. Wang, M.T. Winkler, O. Gunawan, T. Gokmen, T.K. Todorov, Y. Zhu, D.B. Mitzi, Adv Energy Mater 4(7) (2014) 1301465.
[4] H.R. Jung, S.W. Shin, K.V. Gurav, M.G. Gang, J.Y. Lee, J.H. Moon, J.H. Kim, Electronic Materials Letters 12(1) (2016) 139-146.
[5] Y. Kawano, J. Chantana, T. Minemoto, Current Applied Physics 15(8) (2015) 897-901.
[6] V. Steinmann, R. Jaramillo, K. Hartman, R. Chakraborty, R.E. Brandt, J.R. Poindexter, Y.S. Lee, L. Sun, A. Polizzotti, H.H. Park, Advanced Materials 26(44) (2014) 7488-7492.
[7] J. Vidal, S. Lany, M. d'Avezac, A. Zunger, A. Zakutayev, J. Francis, J. Tate, Appl Phys Lett 100(3) (2012) 032104.
[8] K. Hartman, J. Johnson, M.I. Bertoni, D. Recht, M.J. Aziz, M.A. Scarpulla, T. Buonassisi, Thin Solid Films 519(21) (2011) 7421-7424.
[9] S. Cheng, G. Conibeer, Thin Solid Films 520(2) (2011) 837-841.
[10] K.R. Reddy, P.P. Reddy, R. Miles, P. Datta, Optical materials 17(1-2) (2001) 295-298.
[11] W. Shockley, H.J. Queisser, J Appl Phys 32(3) (1961) 510-519.
[12] P. Sinsermsuksakul, L. Sun, S.W. Lee, H.H. Park, S.B. Kim, C. Yang, R.G. Gordon, Adv Energy Mater 4(15) (2014) 1400496.S.J. Pearton, D.P. Norton, K. Ip, Y.W. Heo, T. Steiner, J. Vac. Sci. Technol. B, 22 (2004) 932–9

6th International Conference on Materials Science and Nanotechnology For Next Generation (MSNG2019)
October 16-18, 2019, Niğde, TURKEY (ORAL FULL TEXT)

Microencapsulation of phase change material for electronic cooling applications

Yeliz KONUKLU[a,b*]

[a]Nigde Ömer Halisdemir University, Department of Chemistry, 51240, Nigde, Turkey

[b]Nigde Ömer Halisdemir University, Nanotechnology Application and Research Center, 51240, Nigde,Turkey

In order to use electronic devices more efficiently and safely, they need to be cooled down. Many heating and cooling applications benefit from using thermal energy storage in phase change materials (PCM). The basic purpose of this study is to develop microencapsulation of phase change materials with poly(melamine-urea-formaldehyde) (PMUF) shell which can be used in electronics cooling applications with appropriate melting temperature. Lauric acid and PMUF were used as capsule core and shell material respectively. Microcapsules were prepared with in situ polymerization method. The thermal properties of composites were analyzed using Differential scanning calorimetry (DSC) analysis. PMUF microcapsules were prepared successfully and can be used as energy storage material in thermal energy storage applications. Thanks to the use of prepared microcapsules in electronic devices, the cooling load of the device can be reduced and a safer and more efficient use can be achieved.

Keywords: Phase Change Material, Microencapsulation, Thermal Energy Storage, Lauric acid, electronical cooling.

Corresponding author: ykonuklu@ohu.edu.tr

1. Introduction

According to U.S. Air Force service, more than 55% of the disorders that occur in electronic devices are caused by the rise in temperature during use. In addition, users feel uncomfortable when the used electronic devices reach a temperature above 45 °C. For this specific reason, studies on the cooling of electronic devices have become important in recent years.

Thermal Energy Storage advantages of phase change materials (PCM) are considered in increasing of productivity of heating and cooling applications [1-3]. In order to prevent leakage problem in thermal energy storage applications, the PCMs microencapsulated in different shell materials [4-10].

In our previous studies polyMUF was used as shell material during microencapsulation of decanoic acid [11] and pentadecane [12].

In this study; the lauric acid microcapsules with polyMUF was developed for electronic cooling applications.

Microcapsules were analysed for their form stability and thermal properties using DSC.

2. Experimental details

Lauric acid with purity above 98.0% was used as PCM without any further purification. The properties of lauric acid was presented in Table 1. Melamine, urea and formaldehyde were used as monomers of capsule shell material.

Table 1. Properties of lauric acid

Molecular Formula	$C_{12}H_{24}O_2$
Molar mass	200.32 g/mol
Appearance(color)	white
Melting Point	43-44 °C

Lauric acid microcapsules (Table 2) were fabricated with the one step-in situ polymerization process technique (Konuklu et al; 2014). Lauric acid microcapsules were aanlysed for their thermal properties using DSC.

In order to determination of leakage of composites; the water bath at 95 °C was used in a for 45 min [11].

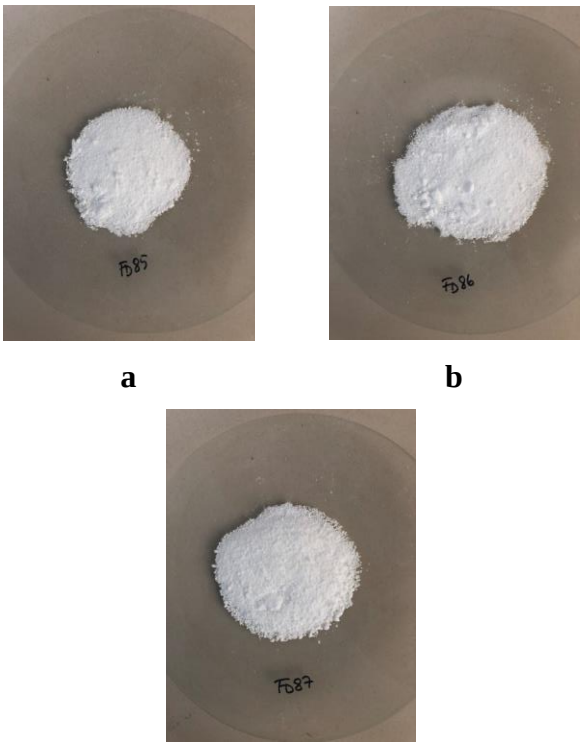
Table 2. Information about preparation of microcapsules

Sample	LA	Melamine	Formaldehyde

FD85	20g	2,30g	2,30g
FD86	24g	2,30g	2,30g
FD87	28g	2,30g	2,30g

3. Results and discussion

In this study LA/polyMUF microcapsules were developed. Fig. 1. presents the digital photos of the microcapsules at room conditions. As can be seen clearly; the prepared microcapsules are in the white powder form.



a **b**

c

Fig.1. Photos of microcapsules at a) FD85 b)FD86 c)FD87

Thermal resistance test results of microcapsules were evaluated due to their leakage free powder forms and usable form stable conditions. Fig. 2-4 shows photographs of microcapsules heated at 95ºC after 60 min. As can be seen in this photo after thermal resistance test the microcapsules show good heat resistance without PCM leakage.



a **b** **c**

Fig.2. Thermal resistance test a) FD85 b)FD86 c)FD87

The thermal properties of lauric acid and microcapsules were determined by DSC. The heating and cooling thermograms of LA microcapsules are presented in Figs. 3-5 and all DSC results are summarized in Table 2.

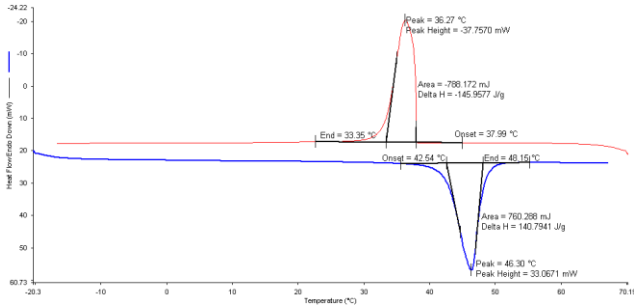


Fig. 3. *DSC analysis of FD85*

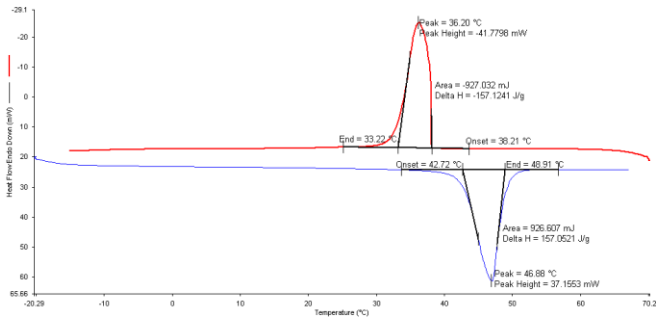


Fig. 4. *DSC analysis of FD86*

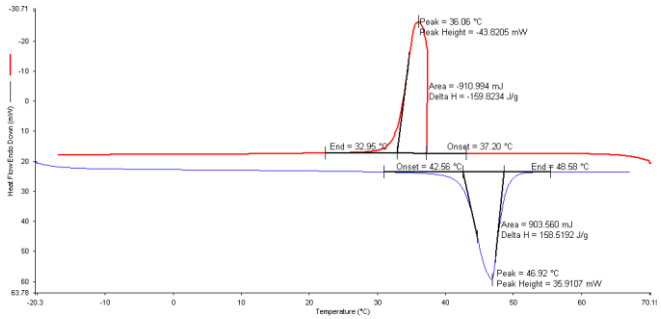


Fig. 5. *DSC analysis of FD87*

Table 3. DSC analyses of LA and LA microcapsules

	Tom (◦C)	Tpm (◦C)	Tem (◦C)	Hm (j/g)	Toc (◦C)	Tpc (◦C)	Tec (◦C)	Hc (j/g)
LA[13]	43.66	48.54	52.60	196.61	40.98	37.02	33.11	-205.19
FD85	42,54	46,30	48,15	140,79	37,99	36,27	33,35	-145,94
FD86	42,72	46,88	48,91	157,05	38,21	36,20	33,22	-157,12
FD87	42,56	46,92	48,58	158,51	37,20	36,06	32,95	-159,82

The melting and freezing temperatures of lauric acid were 43.66 ºC and 40.98 ºC, respectively. LA microcapsules FD85, FD86 and FD87 have melting/freezing temperatures of 42.54 ºC,37.99; 42.72ºC, 38.21 and 42.56 ºC, 37.20 ºC, respectively. Furthermore, the latent heats of melting and freezing are determined 196.61/-205.19 J/g for LA, 140.79/-145.94 J/g for FD85, 157.05/-157.12 J/g for FD86 and 158.51/-159.82 J/g for FD87 respectively. Higher ratios of LA caused higher latent heat storage capacity.

4. Conclusion

In this research, lauric acid microcapsules for were synthesized and characterized. Higher ratios of PCM caused higher latent heat storage capacity. Microcapsules obtained in this study is suitable for thermal energy storage applications especially for electronic cooling applications.

The overheating of the mobile phones not only shortens their lifetime but disturbs the users during use. In further studies; thanks to the use of developed micro-nano capsules in electronics, the cooling load of the device can be reduced and a safer and more efficient use can be achieved.

5. Acknowledgement

We would like to thank the Research Projects Unit of Nigde Ömer Halisdemir University (The Project Code: FEB2016/21-BAGEP) for their financial support for this study.

References:

[1] Konuklu, Y., Ostry, M., Paksoy, H. O., & Charvat, P. (2015). Review on using microencapsulated phase change materials (PCM) in building applications. Energy and Buildings, 106, 134-155.

[2] Farid, M. M., Khudhair, A. M., Razack, S. A. K., & Al-Hallaj, S. (2004). A review on phase change energy storage: materials and applications. Energy conversion and management, 45(9-10), 1597-1615.

[3] Sharma, A., Tyagi, V. V., Chen, C. R., & Buddhi, D. (2009). Review on thermal energy storage with phase change materials and applications. Renewable and Sustainable energy reviews, 13(2), 318-345.

[4] Ma, Y., Xie, Q., Wang, X., & Lu, J. (2019). Synthesis and characterization of microencapsulated phase change materials with comb-like acrylic co-polymer shell as thermal energy storage materials. Solar Energy, 179, 410-423.

[5] Fu, W., Zou, T., Liang, X., Wang, S., Gao, X., Zhang, Z., & Fang, Y. (2019). Characterization and thermal performance of microencapsulated sodium thiosulfate pentahydrate as phase change material for thermal energy storage. Solar Energy Materials and Solar Cells, 193, 149-156.

[6] Wang, Y., Liu, Z., Niu, X., & Ling, X. (2019). Preparation, Characterization, and Thermal Properties of Microencapsulated Phase Change Material for Low-Temperature Thermal Energy Storage. Energy & fuels, 33(2), 1631-1636.

[7] Weinstock, L., Sanguramath, R. A., & Silverstein, M. S. (2019). Encapsulating an organic phase change material within emulsion-templated poly (urethane urea) s. Polymer Chemistry, 10(12), 1498-1507.

[8] Su, W., Li, Y., Zhou, T., Darkwa, J., Kokogiannakis, G., & Li, Z. (2019). Microencapsulation of paraffin with poly (urea methacrylate) shell for solar water heater. Energies, 12(18), 3406.

[9] Han, S., Lyu, S., Chen, Z., Wang, S., & Fu, F. (2019). Fabrication of melamine–urea–formaldehyde/paraffin microcapsules modified with cellulose nanocrystals via in situ polymerization. Journal of materials science, 54(9), 7383-7396.

[10] Zhang, K., Zhou, Q., & Ye, H. M. (2019). Optimizing the Preparation of Semi-Crystalline Paraffin/Poly (Urea-Formaldehyde) Microcapsules for Thermal Energy Storage. Applied Sciences, 9(3), 599.

[11] Konuklu, Y., Paksoy, H. O., Unal, M., & Konuklu, S. (2014). Microencapsulation of a fatty acid with Poly (melamine–urea–formaldehyde). Energy conversion and management, 80, 382-390.

[12] Konuklu, Y., & Erzin, F. (2019). Preparation of pentadecane/poly (melamine-urea-formaldehyde) microcapsules for thermal energy storage applications. International Journal of Energy Research.

[13] Konuklu, Y., & Ersoy, O. (2017). Fabrication and characterization of form-stable phase change material/xonotlite microcomposites. Solar Energy Materials and Solar Cells, 168, 130-135.

6th International Conference on Materials Science and Nanotechnology For Next Generation (MSNG2019)
October 16-18, 2019, Niğde, TURKEY (ORAL FULL TEXT)

Investigation of Mechanical and Electrical Properties of Titanium Based Implant Materials

Yahya TAŞGIN *

* Department of Mechanical Engineering, Munzur University, 62000 Tunceli, Turkey

Titanium and titanium alloys are widely used as implant materials. These alloys can very well bond with the bone without a fibrous intermediate surface layer. Different types of dental and medical prostheses have been developed and continue to be developed by utilizing the various characteristics of titanium and titanium based alloys. This study covers general characterization of titanium and titanium alloys, application types, surface and interface properties of implants and various implant manufacturing techniques. Based on titanium as the base metal in implant applications, a comparison was made in order to see the positive and negative aspects of the alloying with different metals. Titanium has a very important place among implant materials used to date. A lot of research has been done on the biological compatibility of titanium with bone and its reliability has been proved. The major disadvantage of titanium is the reflection of its gray color under the mucosa. Therefore, non-metallic implants or hybrid implants have been developed in order to eliminate the aesthetic concern especially in the loss of anterior teeth. In this context, the recent researches on titanium and its alloys have been examined and recommendations have been made on future researches

Keywords: Titanium, Mechanic, Implant, Alloy

Corresponding author: yahyatasgin@munzur.edu.tr

1. Introduction

Tissues or organs may become incapacitated due to damages in living organisms. In order to make the damaged areas re-functional, real-like tissue or organ are produced instead of the bone damaged during surgery. These artificial bodies that are manufactured to fulfill the function of damaged tissue or organ are called implants. Implants are used in defective areas to treat bone structure disorders in patients due to congenital diseases, cancer, trauma, accident and so on [1]. In the selection of the implant material, it is necessary to consider the mechanical and biological properties of the bone as well as the physical conditions where the implant will be applied [2].

In the materials to be used as biomedical implant material; some properties such as lack of or little toxic elements, mechanical properties suitable for human tissue (such as bone), biocompatibility, corrosion and abrasion resistance are important. Stainless steel, Co-Cr alloys, pure Ta, pure Nb, Ti and Ti alloys are used as the most suitable metallic biomaterials with these properties. Among these materials, Ti and its alloys are preferred over other materials in terms of their biocompatibility, corrosion resistance and mechanical properties [3]. Titanium metal has an allotropic structure. Above 882 °C, it is on the β-phase (volume-centered cubic), below this temperature it is on the α–phase (hexagonal) structure. Apart from these equilibrium phases, non-equilibrium phases (α_I , α_{II}, ω) may occur depending on alloy ratios and cooling rate variables. α_I (hexagonal martensite), α_{II} (orthorhombic martensite) phases are formed by rapid cooling from β phase. The ω (hexagonal structure) phase is formed by slow quenching from the β phase or by aging at an average temperature [4]. Among these phases, the phase with the lowest elastic modulus is the semi-stable β phase and the phase with the highest elastic modulus is the ω phase [5]. Based on the amount of alloying elements, β-Ti is formed (as a result of quenching or air cooling). In stable alloys, there is no phase conversion by thermomechanical processes, whereas in semi-stable β, α precipitation or other transformations may occur [6]. Pure Ti is commonly used in dental implants, but it is insufficient when high strength is required, such as hard tissue replacement. To overcome this limitation, pure Ti has been replaced by α + β type Ti-6Al-4V [7]. The small amount of aluminum and vanadium added to the titanium increases the resistance of the alloy considerably more than the CpTi. While aluminum acts as α-stabilizer, vanadium plays a role in β-stabilization. By

adding these elements to titanium at the temperature at which the α-β transformation occurs, the transformation is suppressed and in this way both α- and β-forms are formed at room temperature. Therefore, titanium aluminum-vanadium (Ti-6Al4V) alloys have a two-phase structure of α and β grains. These alloys are still the most widely used biomaterials among different titanium alloys because they are easily obtainable, suitable for working conditions and have strong mechanical properties at low temperatures [8,9].

In addition to its mechanical properties, titanium is known to have excellent corrosion properties due to its very stable passive film layer which forms rapidly on the metal surface [10].

Titanium, as an extremely biocompatible metal, does not cause allergic reactions and is a relatively radiolucent element [11]. On the other hand, the elastic modulus of titanium is closer to the elastic modulus of the bone than other implant materials, so the force distribution on the bone implant surface is more regular.8 Although titanium implants are thermodynamically stable, small amounts of ion release appears. It is known that titanium released as a result of corrosion is well below the values of titanium taken with food [12]. Mechanically, titanium bends more easily than titanium alloys. Today, Ti-6Al-4V alloy is generally used in implant applications. The normal root-form treated titanium implants are approximately 1.5 times stronger than the compact bone and the treated Ti-6Al-4V alloy is 6 times stronger than the compact bone. Therefore, it allows designs of thinner cross-section [13].

2. Results and discussion:

When we investigate the reasons for using Titanium as a biomedical implant material, followings are the highlighted features:

- It does not cause allergic reactions as a biocompatible material
- It has good corrosion resistance (The passive film layer formed on the surface of titanium prevents corrosion)
- It has outstanding mechanical properties
- It is dvantageous depending on usage by experiencing different structures at different temperatures
- The fact that the elastic modulus of the titanium is close to the elastic modulus of the bone has highlighted the use of Ti.

In Table 1, sample numbers, trade name and composition of the material according to titanium ratios are given.

Table 1. *Sample numbers, trade name and compo- sition of the material according to titanium ratios.*

Sample	Name on production line (Sorted by titanium ratio)	Alloy of Material
1	Grade 1	Ti
2	Grade 9	Ti,Al,V
3	Grade 19	Ti,Zr,Cr,Mo
4	Grade 12	Ti, Ni
5	Grade 6	Ti,Sn
6	Grade 21	Ti,Nb
7	Grade 30	Ti,Co
8	Grade 7	Ti,Pb

In this research, our studies to add superior properties to the implant materials as a result of the alloying of titanium are presented in graphs.

When we examine Ti alloys in Brinel hardness which form many implant materials by making compound with different metals, in the graph given in Figure 1; it is seen that titanium and niobium (Nb) alloy is the hardest alloy with 365 HB in terms of hardness values, it is followed by Ti-Zr-Cr-Mo alloy with 350 HB. Ti-Pb alloy has the lowest value (155HB). Depending on the area to be used, the shape of the implant and the forces to be exposed in that area rather than the high or low hardness value are important for the titanium alloy to be used.

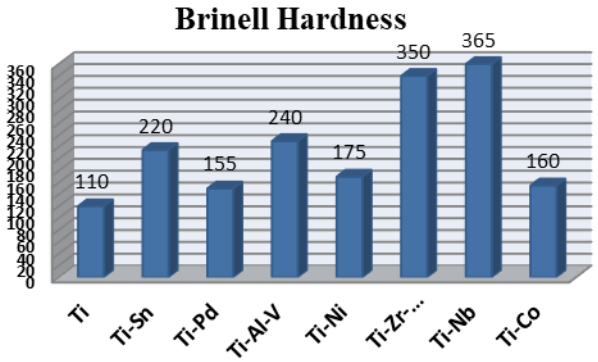


Figure 1. *Graphs of Brinell Hardness of the Samples*

When we examine the Elastic modulus of implant alloys in Figure 2, it is seen that Ti-Nb alloy is different from other alloys and the other alloys are between 100-130 Gpa. The properties and elasticity of the bone in the region where the implant is used is very important. Because one of the reasons for preference of titanium alloy is that the bone has a value close to its elasticity.

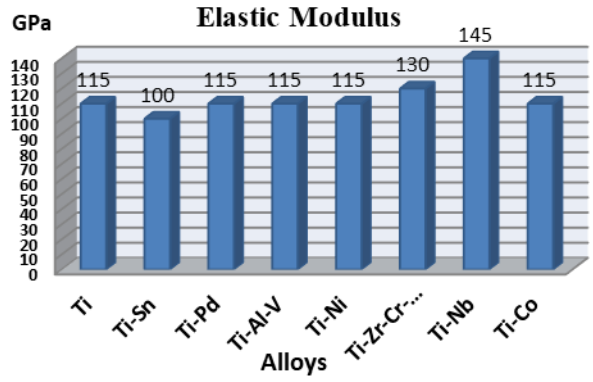


Figure 2. *Elastic Module Graphs of the Samples*

Titanium alloys are hard-structured so they are not expected an elongation at break. The elongation at break is determined to decrease after titanium alloying with (Ti-Pb, Ti-Co, Ti-Ni). (Figure 3) This has resulted that by increasing the hardness of all the metals alloying with titanium, alloy becomes harder than titanium and it shows no elongation at break.

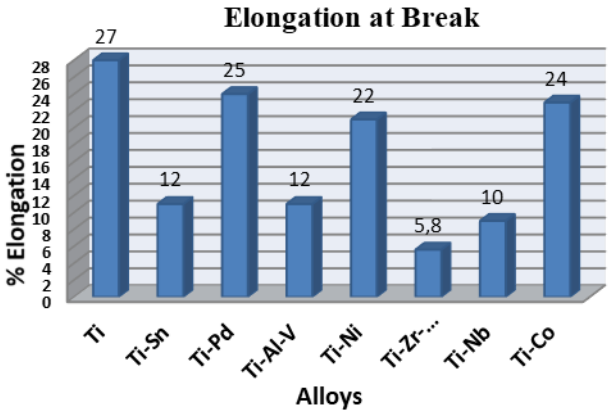


Figure 3. *Graphs of Elongation at Break of the Samples*

It is seen that Nb and Zr-Cr-Mo added to titanium increase the density in the alloy (540 MPa). The reason for the increase in density is due to the fine grain structure (Figure 4).

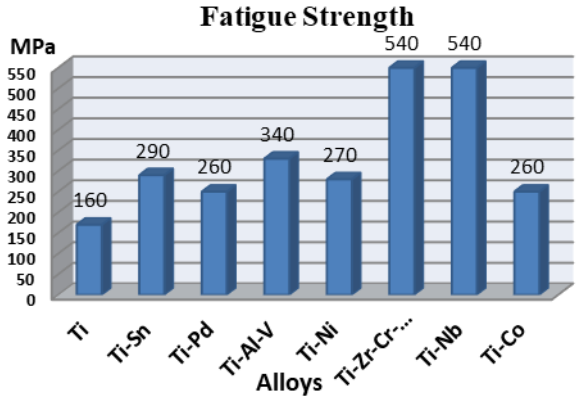


Figure 4. *Density Graphs of the Samples*

As a result of the alloying of titanium, an increase in the area of the material has been observed in general (Figure 5). This shows us that the reduction of the 38% area in the production of titanium can be seen as a result of alloying.

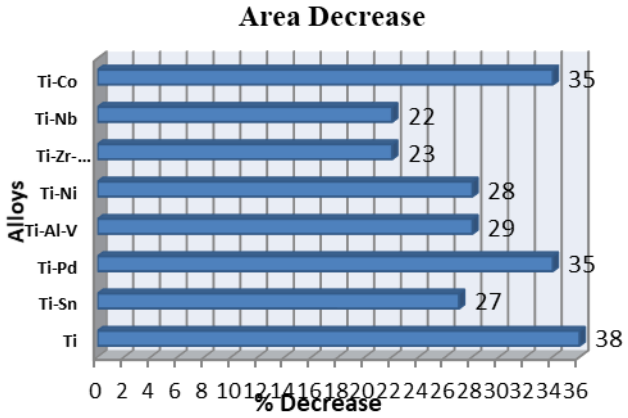


Figure 5. *Area Decrease Graphs of the Samples*

As a result of the torsion test applied to the titanium alloys, it is seen that with the moment and the material with equal diameter, the shear modulus has the highest value in Ti-Nb alloy with 52 Gpa (Figure 6).

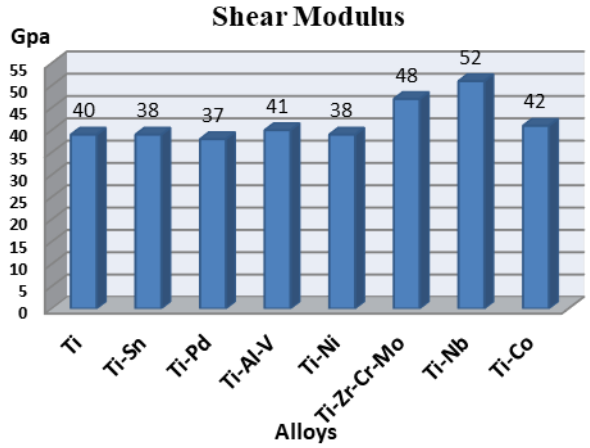


Figure 6. *Shear Modulus Graphs of the Samples*

As a result of the tensile tests applied to the titanium alloys, when we examine the graph shown in Figure 7, it is seen that the elastic and plastic deformation of the Ti-Nb and Ti-Zr-Cr-Mo alloys have the highest strength with 890-880 Mpa tensile strength and pure titanium has the lowest one with 240 Mpa tensile strength. This shows that alloying of titanium with some metals positively affects the tensile values.

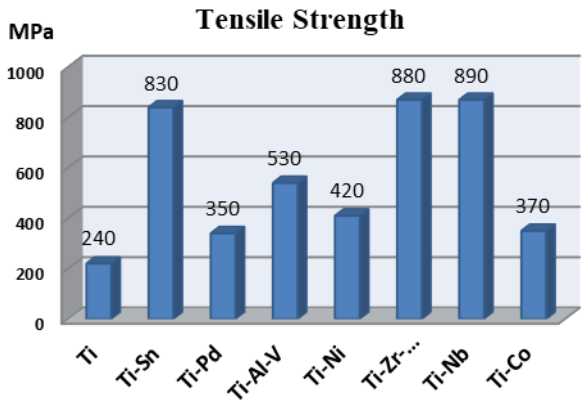


Figure 7. *Tensile Strength Graphs of the Samples*

Since the melting degree of niobium is 2477 ^{0}C, the Ti-Nb alloy has a melting degree of around 1750 ^{0}C, but in Figure 8 it is seen that the other alloys have similar melting degrees.

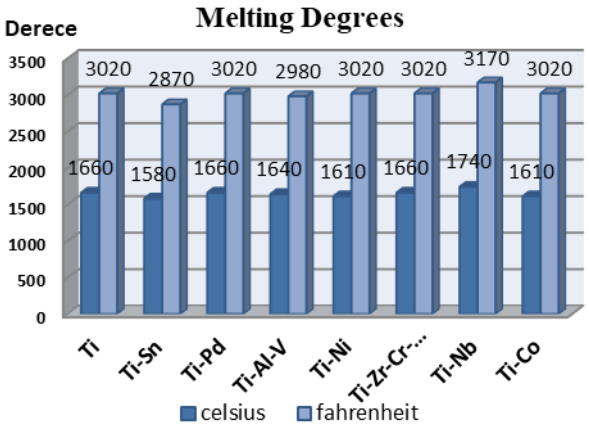


Figure 8. *Melting Degrees Graphs of the Samples*

The specific heat capacity of the steel is 450-480 J / kg ° K, the specific heat capacity of copper is 385 J / kg ° K and the specific heat capacity of aluminum is 900 J / kg ° K. These show that Titanium alloys are between 490-550 J / kg ° K in terms of heat transfer. The graph in Figure 9 shows that unalloyed titanium's is 530 J / kg ° K.

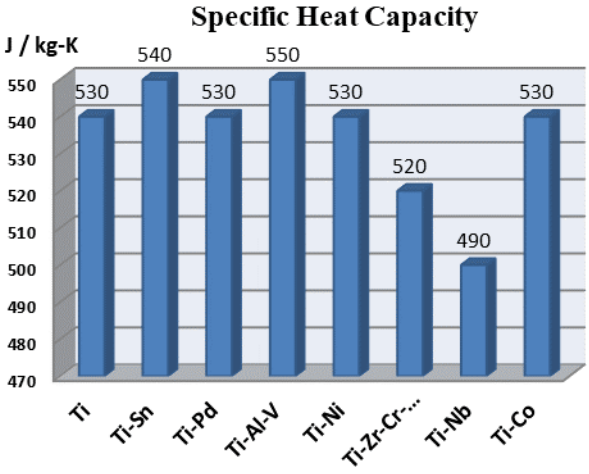


Figure 9. *Specific Heat Graphs of the Samples*

The electrical conductivity of titanium alloys is between 3.5 - 4.4 IACS. When Sn and Al whose melting degrees are low are added the value decrease can be seen in Figure 10.

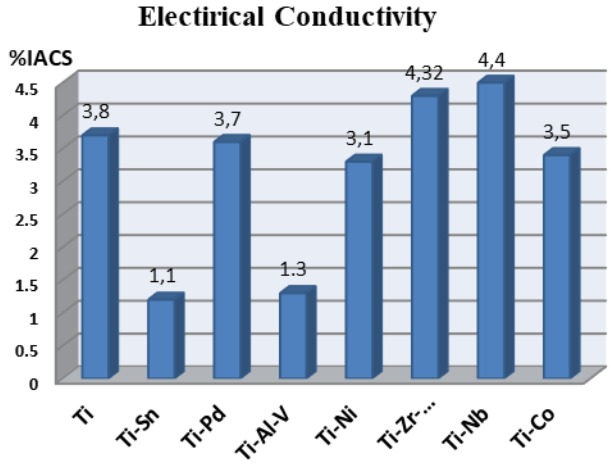


Figure 10. *Electirical Conductivity Graphs of the Samples*

Conclusions

In this study we investigate what kind of positive changes appear when we alloy Titanium, which is the first metal that comes to mind when we say implant material, with different metals, we obtain following results:

• Many Titanium alloys add favorably different properties.

• Ti-Nb and Ti-Zr-Cr-Mo alloys are found to be mechanically good alloys. However, it should be calculated that the size of the implant and details during processing may complicate the production.

• The location and shape of the implant impose restrictions on the use of alloys.

• Although mechanically compatible alloys are formed, they should be bioavailable and allergically investigated.

• The Ti-6Al-4V alloy used as a dental implant is hard and has good mechanical propertiesalthough it has Al.

As a result, in this study, since we have formed many alloys, many mechanical advantages have been determined. In the selection of the implant, it has been determined that not only the mechanical properties of a material, but also the biocompatibility, place of use and shape should be taken into consideration.

References:

[1] ENDERLE J.D., BLANCHARD M.S., BRONZİNO D.J., Biomaterials, Introduction to Biomedical Engineering, Academic Press, ABD, 220-222, 2012.

[2] NASAB M.B., HASSAN, M.R. Metallic Biomaterials of Knee and Hip - a review, Trends in Biomaterials and Artificial Organs, 24 (1), 69-82, 2010.

[3] TAVARES AMG, RAMOS WS, BLAS JCG, LOPES ESN, CARAM R, BATİSTA WW, SOUZA WW. "Influence of Si addition on the microstructure and mechanical properties of Ti-35Nb alloy for applications in orthopaedic implants". Journal of the Mechanical Behavior of Biomedical Materials, 51, 74-87, 2015.

[4] KİM HY, MİYAZAKİ S. "Martensitic transformation and superelastic properties of Ti-Nb base alloys". Materials Transactions, 56, 625-634, 2015.

[5] YOU L, SONG X. "A study of young's modulus T,-Nb-Zr alloys using d electrons alloy theory''. Scripta Materialia, 67, 57-60, 2012.

[6] DUBİNSKİY S. Ti-Nb-(Zr,Ta) Superelastic Alloys For Medical Implants: Thermomechanical Processing, Structure, Phase Transformations and Functional Properties. PhD Thesis, Ecole De Techologıe Superieure Unıversıte Du Quebec, Montreal, 2013.

[7] Lİ Y, YANG C, ZHAO H, QU S, Lİ X, Lİ Y. "New developments of Ti-based alloys for biomedical applications''. Materials, 7, 1709-1800, 2014.

[8] AKÇA K. Mandibuler Kennedy I ve II vakalarında uygulanan implant destekli sabit protezlerde kemigin farklı bukko-lingual açılanmasından kaynaklanan streslerin üç boyutlu sonlu elemanlar stres analiz yöntemi ile arastırılması. Hacettepe Üniversitesi, Ankara, 1988.

[9] ROACH M. Base metal alloys used for dental restorations and implants. Dent Clin North Am 2007; 51: 603-27.

[10] NİİNOMİ M. Mechanical biocompatibilities of titanium alloys for biomedical applications. J Mech Behav Biomed Mater 2008; 1: 30-42.

[11] KEDİCİ SP, AKSUT AA, KİLİCARSLAN MA, BAYRAMOGLU G, GOKDEMİR K. Corrosion behaviour of dental metals and alloys in different media. J Oral Rehabil 1998; 25: 800-8.

[12] BRUNE D, EVJE D, MELSOM S. Corrosion of gold alloys and titanium in artificial saliva. Scand J Dent , European journal of oral sciences, 90, 1982, 168-171.

[13] TUNALİ B. Multi-disipliner bir yaklaşımla oral implantolojiye giriş. İstanbul Üniversitesi Diş Hekimliği Fakültesi Yayınları 1996:

6th International Conference on Materials Science and Nanotechnology For Next Generation (MSNG2019)
October 16-18, 2019, Niğde, TURKEY (ORAL FULL TEXT)

Investigation of Electrical and Structural Properties of ZrO_2 Thin Films

B. Coşkun[1]*, M. Kurban[2]

[1]Department of Physics, Faculty of Arts and Sciences, Kırklareli University, Kırklareli, TURKEY
[2]Department of Electronics and Automation, Ahi Evran University, Kırşehir, TURKEY

ZrO_2 thin films was deposited on Si substrate by RF magnetron sputtering. The micro structural analyses of thin films were done by Scanning Electron Microscope and it was observed that the films were grown successfully in the form of big grains formed by the accumulation of small particles. The frequency dependent electrical properties of ZrO2 thin films has been investigated using capacitance–voltage (C–V) and conductance–voltage (G/ω–V) characteristics in the frequency range 120 kHz–400 kHz in the room temperature. Obtained results show that C–V and G/ω–V characteristics strongly depend on the frequency.

Keywords: ZrO_2, Dielectric Properties
*Corresponding E-mail: burhan.coskun@klu.edu.tr

1. Introduction

ZrO_2 has been very important for researchers in recent years with its interesting physical properties. It is a heat resistant material with excellent insulation and ceramic properties. It is extremely resistant to corrosion, erosion and abrasion. Having high dielectric constant (18-25), high melting point (2680 ± 15 ºC), high chemical stability and wide band range (4,7eV-7,8eV), ZrO_2 has become one of the most studied materials for the last twenty years. It has brought. It is a good material especially for metal oxide semiconductors (MOS). It has many desired properties such as high thermal stability, high refractive index and low thermal conductivity. ZrO_2 is an allotropic ceramic material. Pure ZrO_2 has a polymorph structure which can be found in monoclinic (m), tetragonal (t) and cubic (c) forms at different temperatures [1-4].

2. Experimental details

In this study, one side polished (100) oriented n-type semiconductor Silicon (Si) substrate material with dimensions of 20x20 mm^2 on which ZrO_2-1 and ZrO_2-2 thin films were investigated was used. In order to prevent scratching, contamination and damage, no chemical cleaning was applied to the infrastructure. After the Si (100)

Substructures were placed in the film growth chamber, the cover of the growth chamber was closed and the system was

vacuumed. When the base pressure fell below 1.10-7 Torr, the butterfly valve was closed and Argon gas was introduced into the film growth medium. The power value from the RF power supply unit was set to 125 W and pre-sputtering from the Zirconium target surface for 5 minutes. After this pre-sputtering and heating process, ZrO_2-1 and ZrO_2-2 thin films were applied at a constant substrate temperature of 200 oC using a Reactive RF Magnetron Sputtering technique, at a power value of 125 W and a magnification rate of 0.4Å / s. Si (100) was raised on infrastructures.

3. Results and discussion

The SEM image showing the surface morphology of the ZrO_2-1 and ZrO_2-2 sample is shown in Figure 1 a, b. As shown in Figure 1a, b the surface structure of the ZrO_2 sample consists of pellets and cavities of different sizes. The average size of the pellets was determined to vary in the range of ~ 120-280 nm. Similar agglomeration and voids were found in different regions of all sample.

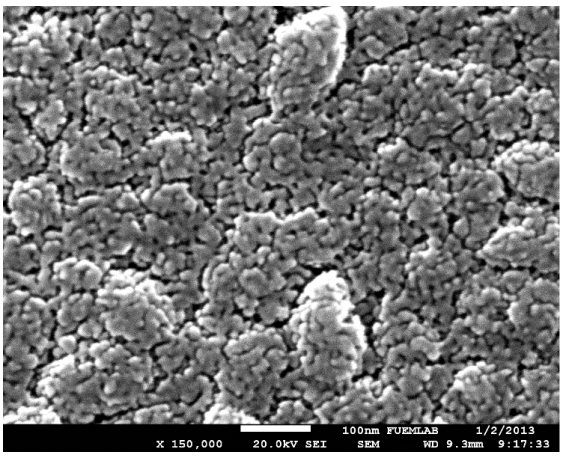


Figure 1a: SEM images of the ZrO_2 -1 sample

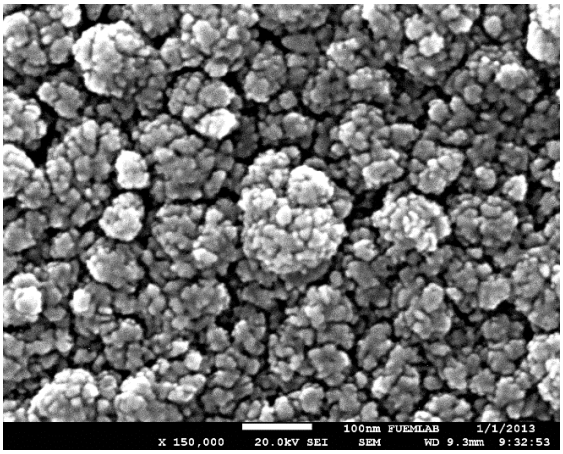


Figure 1b: SEM images of the ZrO_2 -2 sample

The Capacitance – voltage and Conductance-Voltage graphs were drawn with obtained G/ω-V data of photodiodes. The graphs were given in Fig. 2a, b, 3a, b. The C-V plots give a peak in the negative voltage region. As can be seen in these figures, the measured capacitance and conductance in depletion region decreases with increasing frequency in the frequency range 120 kHz– 400 kHz. Negative capacitance in heterocycle structures is often explained by interface states. The fact that the loads in the interface states follow the ac (alternating current) signal at low frequencies creates an additional capacity. However, at higher frequencies, interface loads cannot follow the ac signal, so they cannot provide additional capacity. Thus the capacity shifts to negative. In the conductivity voltage graphs, it was observed that the conductivity changes depending on the voltage and frequency. It has been determined that the conductivity increases depending on the frequency [5-7].

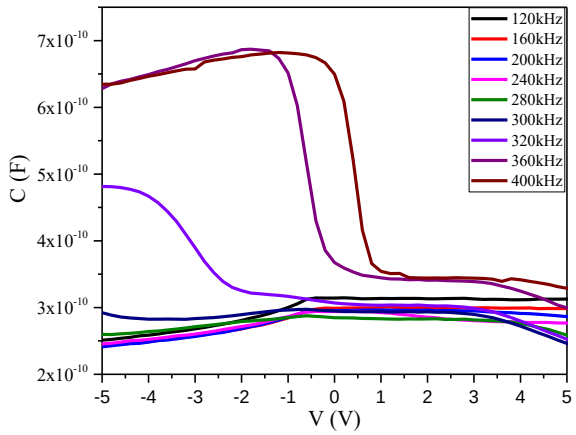


Figure 2a. Capacitance – voltage (C–V) characteristics of ZrO_2-1 film.

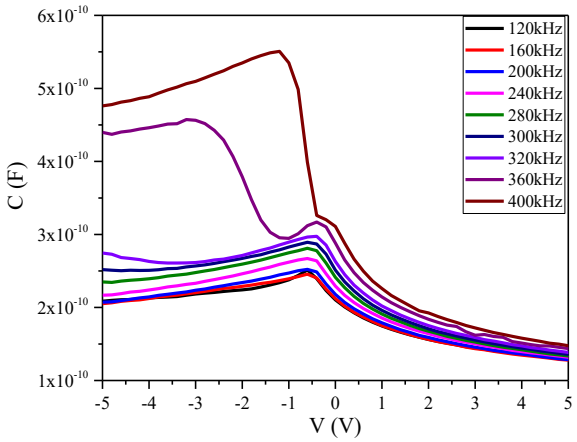


Figure 2b. Capacitance – voltage (C–V) characteristics of ZrO_2-2 films.

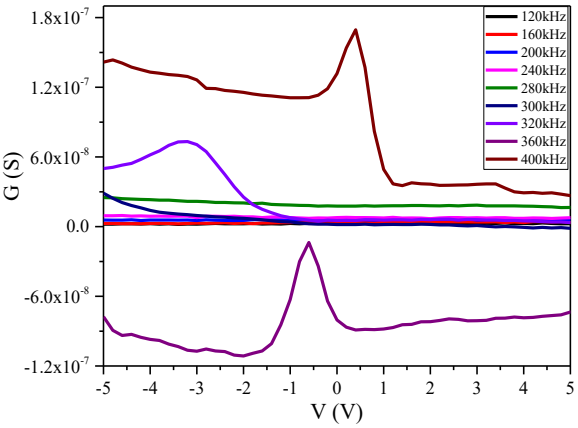


Figure 3a: The Conductance-Voltage (G-V) graph of ZrO_2-1 film

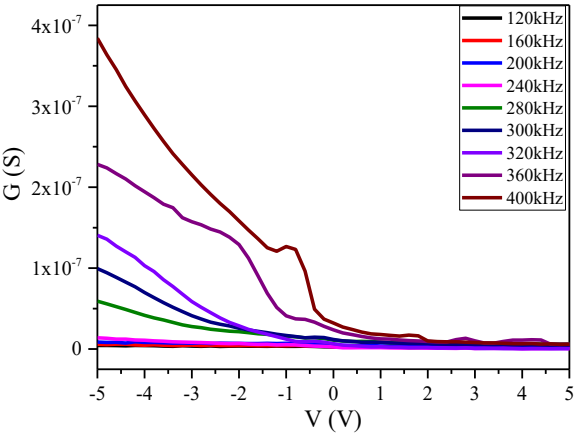


Figure 3b: The Conductance-Voltage (G-V) graph of ZrO_2-2 film

4. Conclusion

In this work, the photodiode properties of the ZrO_2 based devices have been investigated. The structural and electrical properties were determined by using SEM, Capacitance – Voltage, Conductance – Voltage measurements. Capacitance – Voltage and Conductance – Voltage characteristics of the photodiodes were assessed in various AC signal frequencies ranging from 120 kHz to 400 kHz. It is evaluated that the C–V and G/ω–V characteristics confirm that the series resistance and interface state densities are important parameters that strongly influence the electrical properties of the ZrO_2 thin films.

5. Acknowledgement

This work was supported by Firat University Scientific Research Office with project number 1110.

References:

[1] L. Weifeng, L. Xuanyong, H. Anping, K.C. Paul J Phys D: Appl Phys, 40 (2007), pp. 2293-2299
[2] A. T. Ravichandran, K. C. S. Pushpa, K. Ravichandran, K. Karthika, B. M. Nagabhushana, S. Mantha, K. Swaminathan, Superlattices and Microstructures 75, 533–542 (2014).
[3] H. H. Zhang, C. Y. Ma, Q. Y. Zhang, Vacuum 83, 1311–1316 (2009)
[4] J. Wang, S. Yang, X. Liu, S. Ren, F. Guan, M. Chen, Applied Surface Science 221, 272–280 (2004).
[5] Chattopadhyay P., Ray Chaudhuri B., 1992, Origin of the Anomalous Peak in the Forward Capacitance-Voltage plot of a Schottky Barrier diode, Solid State Electronics, 35(6), 875-878.
[6] Şafak Asar, Y., Asar T., Altındal Ş., Özçelik S., 2015, Journal of Alloys and Compounds, 628, 442-449.
[7] S. Karataş, F. Yakuphanoglu, F. M. Amanullah, Journal of Physics and Chemistry of Solids, 73-1, 2012, 46-51

6th International Conference on Materials Science and Nanotechnology For Next Generation (MSNG2019)
October 16-18, 2019, Niğde, TURKEY (ORAL FULL TEXT)

The investigation and comparison of the main electrical properties of Cr/*p*-type Si and Cr/*n*-type Si metal semiconductor structures

Şükrü KARATAŞ

Kahramanmaraş Sütçü İmam University, Faculty of Sciences and Arts, Department of Physics, 46100-Kahramanmaraş, Turkey

In our study, we investigated the main electrical properties of Cr/p-type Si and Cr/n-type Si metal-semiconductor (MS) Schottky structures, with series resistance silicon structures, using current-voltage (*I-V*) and capacitance-voltage (*C-V*) characteristics at the room temperature. The main electrical parameters such as ideality factor (*n*), barrier height (Φ_{bo}) and series resistance (R_S) of Cr/p-type Si and Cr/n-type Si metal-semiconductor (MS) Schottky structures were determined using the forward bias current–voltage (*I–V*) measurements. The values of ideality factor (*n*) and barrier height (Φ_{bo}) for the Cr/p-type Si and Cr/n-type Si metal-semiconductor obtained as 1.577; 1.335 and 0.692; 0.699 eV, respectively. Furthermore, the main electrical parameters such as ideality factor (*n*), barrier height (Φ_{bo}) and series resistance were evaluated using different methods developed by Cheung and Norde. Experimental results showed that the series resistance values obtained from Norde method were higher than those obtained from Cheung functions.

Keywords: Keywords: Electric properties, Si, Series resistance

Submission date:28 September 2019
Acceptance Date:30 Semtember 2019

Corresponding authors: skaratas@ksu.edu.tr

1. Introduction

Semiconductors are crystalline or amorphous substances with a full valence band and an empty conduction band. These two bands are separated by the band gap energy (E_g). The development of semiconductor electronics is reviewed briefly, beginning with the development of silicon devices (band gap E_g = 1.12 eV) after World War II. Thus, metal-semiconductor (MS) interfaces are an essential part of virtually all semiconductor electronic and optoelectronic devices [12,]. The physical properties of MS interfaces are widely studied, both for their basic physical properties and for their technological applications to electronic devices [1-3].

Metal semiconductor structures type dependent investigations have been done by various researchers. For example, Akkılıç et al., determined correlation between barrier heights and ideality factors of Cd/n-Si and Cd/p-Si Schottky barrier diodes [4]. Siad et al studied series resistance and diode parameter differences between Al/n-Si and Al/p-Si structures [5]. Karataş [6] has been investigated electrical properties of the Zn/p-Si and Sn/p-Si structures using *I-V* and *C-V* measurements at room temperature. Yıldız et al. investigated electrical characteristics of Au/SnO_2/n-Si and Al/SnO_2/p-Si Schottky contacts at different temperatures [7]. Arslan et al. published electrical characteristics of Pt/p-InGaN and Pt/n-InGaN Schottky barriers in various temperatures [8]. Korkut [9] investigated series resistances of the Pt/p-InP and Pt/n-InP Schottky diodes in the different temperatures.

In this study, our aim is to investigate experimentally investigate the relationship between the electrical properties obtained from the forward bias I-V characteristics of the Cr/p-type Si and Cr/n-type Si metal-semiconductor (MS) Schottky structures at absolute temperature (300 K).

2. Experimental details

In this study, cleaned and polished p-Si and n-Si wafers were used. The p and n-type silicon polished on one side (250-micrometer thickness, <100> oriented, 1-10 Ω-cm) was used as substrate. Firstly, the silicon substrate was cleaned by RCA process. After, the rectifier contacts were formed by evaporation of Cr dots with diameter of about 1.0 mm. All evaporation processes were carried out in a turbo molecular fitted vacuum coating unit at about 10^{-6} mbar. The current-voltage (I-V) measurements of the Cr/p-type Si and Cr/n-type Si metal-semiconductors were performed at room temperature using a Keithley 2400 source meter.

3. Results and discussion

The electrical characteristics of both Cr/p-type Si and Cr/n-type Si metal-semiconductors were monitored as a function of forward and reverse bias conditions at room temperature (300 K) and illustrated in Fig.1. As can be shown in the Fig. 1, for the both structures, the current curves increases exponentially with applied forward bias voltage.

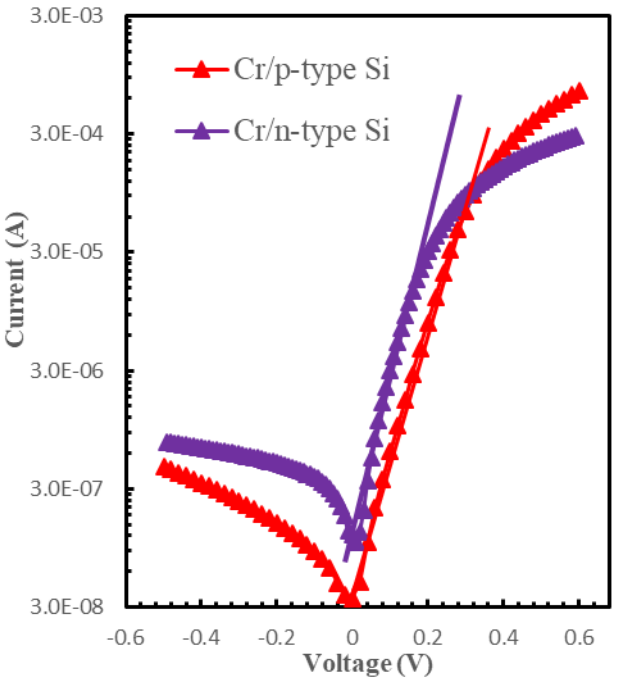


Fig. 1. The current–voltage plots of Cr/p-Si and Cr/n-Si structure at room temperature

From the thermionic emission (TE) theory, the experimental current-voltage characteristics are analyzed by following equation [1-3, 6, 10, and 11];

$$I = I_o \exp\left(\frac{qV}{nkT}\right)\left[1-\exp\left(-\frac{qV}{kT}\right)\right] \quad (1)$$

where q is the electron charge, V is applied voltage, n is the ideality factor, k is the Boltzman constant 1.38x10-23 $J\,K^{-1}$, T is the absolute temperature and I_o is the saturation current derived from the straight line intercept of lnI at V=0 and is given by;

$$I_o = AA^*T^2\exp\left(-\frac{q\Phi_{bo}}{kT}\right) \quad (2)$$

where A is the effective diode area, A* is the effective Richardson constant of 32 and 112 $Acm^{-2}K^{-2}$ for p-and n-type Si, respectively. The ideality factor (n) of the Cr/p-type Si and Cr/n-type Si structures are determined from the slope of the linear region of the forward bias ln(I)-V characteristics through the relation;

$$n = \frac{q}{kT}\left(\frac{dV}{d\ln I}\right) \quad (3)$$

In the same way, the barrier height (Φ_{bo}) is determined from the saturation current (I_o) and is given by the relation;

$$\Phi_{bo} = \frac{kT}{q}\ln\left(\frac{AA^*T^2}{I_o}\right) \quad (4)$$

Therefore, using Eq. (3) and Eq. (4) the values of the ideality factor (n), and barrier height (Φ_{bo}) of the Cr/p-type Si and Cr/n-type Si metal-semiconductors at room temperatures were calculated from the slopes of the linear region of the forward bias ln(I)-V plots in Fig. 1. The values 1.577; 1.335 and 0.692; 0.699 eV for the ideality factor (n) and barrier height (Φ_{bo}) of the Cr/p-type Si and Cr/n-type Si metal-semiconductors, respectively. As can be seen, the experimental ideality factors vary from diode to diode. This is that the reason for that might be the density of the interface state exists between metal and semiconductor junction. However, the values of barrier heights obtained from Fig. for Cr/p-type Si and Cr/n-type Si metal-semiconductors are in close agreement with each other. In the same time, the values of ideality factor, barrier height and the series resistance were evaluated using a method developed by Cheung and Cheung [12] who utilized the downward curvature of the forward bias current-voltage characteristics. According to Cheung function is analyzed by following equation;

$$\frac{dV}{d(lnI)} = n\frac{kT}{q} + R_s I \quad (5)$$

$$H(I) = V - n\left(\frac{kT}{q}\right)\ln\left(\frac{I}{AA^{*}T^{2}}\right) = IR_S + n\Phi_{bo} \quad (6)$$

Experimental *dV/d(ln I)* vs I and *H(I)* vs *I* plots of the of Cr/p-type Si and Cr/n-type Si metal-semiconductors at room temperature are presented in Fig. 2 and Fig.3, respectively. The slope and intercept of dV/dln(I)-I plots according to Eq. 5 would yield R_S and nkT/q, respectively. The values of idealitry factor (n) and series resistance (Rs) were found as 1.79 and 280 Ω for Cr/p-type Si metal-semiconductors and 1.04 and 1567 Ω for Cr/n-type Si metal-semiconductors, respectively. The experimental results clearly seen that there are relatively large difference between the values of n obtained from the forward bias ln *I–V* and the *dV/d (lnI)–I* plots. Also, the values of ideality factor (n) and series resistance (Rs) obtained from dV/d (lnI)–I plots for Cr/p-type Si and Cr/n-type Si metal-semiconductors were different from each other. This states can be attributed to the effect of the R_S and nature of bias voltage [13]. The value of n obtained from the slope of ln I–V plot corresponds to intermediate bias voltages, while that obtained from dV/dln(I)–I plots corresponds to high bias voltages. The slope and intercept of *H(I)-I* plots according to Eq. 6 would yield Rs and $n\Phi_{bo}$, respectively. The values of barrier height (Φ_{bo}) and series resistance (R_S) were found as 0.354 eV and 288 Ω for Cr/p-type Si metal-semiconductors and 0.346 eV and 1375 Ω for Cr/n-type Si metal-semiconductors, respectively. This is that series resistance values obtained from Cheung functions are in good agreement with each other.

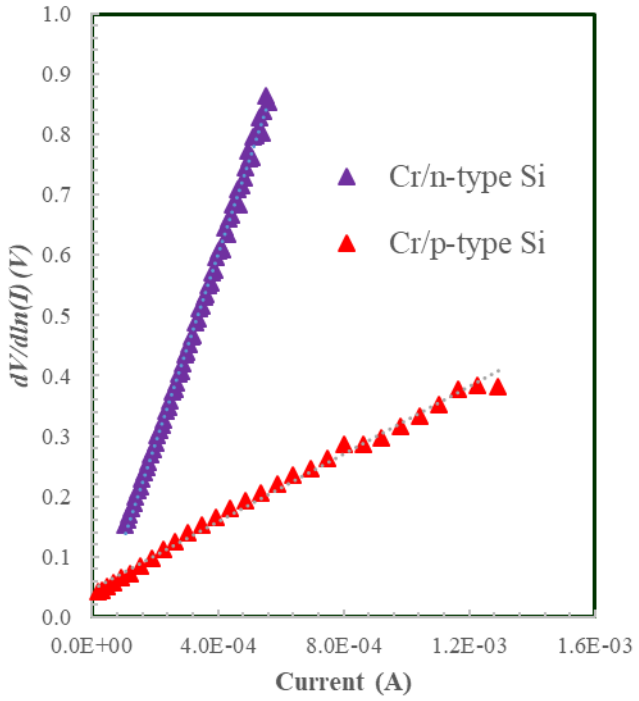


Fig. 2. The dV/dln(I)-I plots of Cr/p-Si and Cr/n-Si structure at room temperature

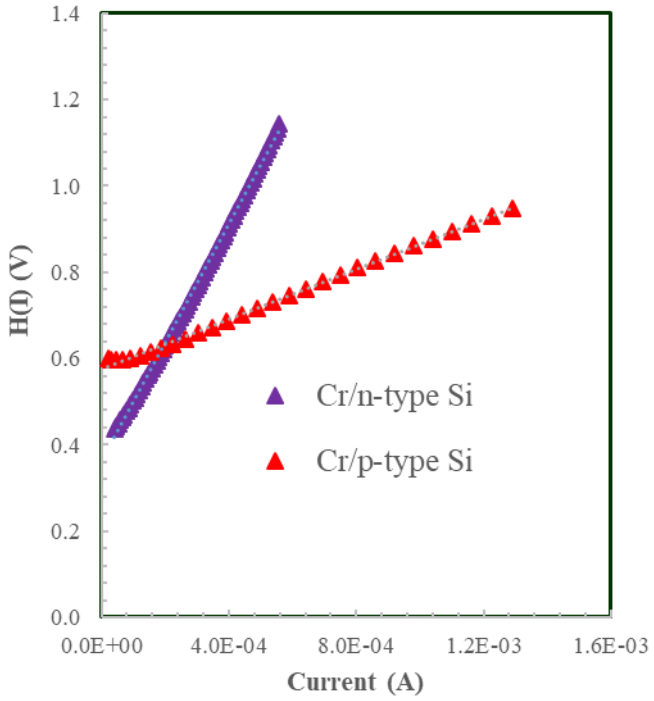


Fig. 3. The H(I)-I plots of Cr/p-Si and Cr/n-Si structure at room temperature

Norde [14] proposed an alternative method as different from Cheung's functions to determine values of the barrier height and series resistance of Cr/p-type Si and Cr/n-type Si metal semiconductors. According to this modified Norde method, barrier height (Φ_{bo}) and series resistance (R_S), both can be calculated using the following relation;

$$F(V) = \frac{V}{\gamma} - \frac{kT}{q}\ln\left(\frac{I(V)}{AA^{*}T^{2}}\right) \qquad (7)$$

where γ is an constant higher than the ideality factor. *F(V)-V* curves of the Cr/p-type Si and Cr/n-type Si metal-semiconductors at room temperature is shown in Fig. 4. According to this method the values of barrier height (Φ_{bo}) and series resistance (R_S) can be obtained from following equations, respectively;

$$\Phi_b = F(V_0) + \frac{V_o}{\gamma} - \frac{kT}{q} \qquad (8)$$

$$R_S = \frac{\gamma - n}{I_0} \quad \frac{kT}{q} \qquad (9)$$

where $F(V_0)$ is the minimum point of *F(V)* vs *V* plot, V_0 and *I* are the corresponding bias voltage and current values, respectively.

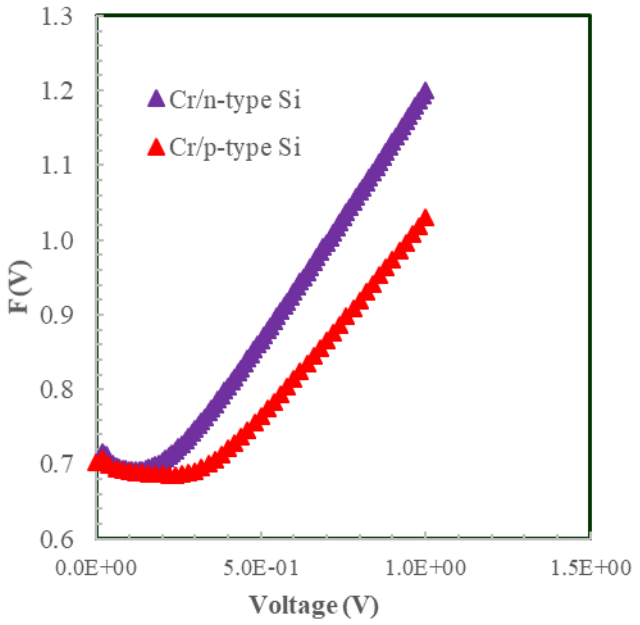


Fig. 4. The F(V)-V plots of Cr/p-Si and Cr/n-Si structure at room temperature

For fig.4, the values of barrier height (Φ_{bo}) and series resistance (R_S) were obtained using Eqs. (8) and (9). The values of Φ_{bo} and R_S were found as 0.493 eV and 385 Ω for Cr/p-type Si metal-semiconductors and 0.257 eV and 2106 Ω for Cr/n-type Si metal-semiconductors, respectively. The experimental showed that the Φ_{bo} and R_S values obtained from Cheung's method is lower than the one obtained from Norde method. These differences in the barrier height values obtained from various methods for the device may be attributed to the extraction from different regions of the forward-bias current–voltage plot [1-3, 6, 11, 15, and 16].

4. Conclusions

In this work, we investigated the main electrical properties such as ideality factor (n), barrier height (Φ_{bo}) and series resistance (R_S) of Cr/p-type Si and Cr/n-type Si metal-semiconductors using the current–voltage (I-V) characteristics at room temperature. The barrier height and series resistance values obtained from Cheung's method is lower than the one obtained from Norde method. These differences in the barrier height values obtained from different methods for the device may be attributed to the extraction from different regions of the forward-bias current–voltage plot. Furthermore, as above mentioned, this situation may because of that while Cheung's functions are only applied for the nonlinear region of forward bias *I–V* curve; Norde's functions are applied for the whole forward bias region of *I–V* curve of the diode.

5. Acknowledgement

This work was supported by Kahramanmaras Sütçü Imam University Scientific Research Project (Project number: 2019/2-40 M). We would like to thank Kahramanmaraş Sütcü Imam University for financial support of the research program.

References:

[1] R. T. Tung, Mater. Sci. Eng., R 35, 1 (2001).
[2] W. Mönch, Semiconductor Surf. And Interfaces, 2nd ed. (Springer, Berlin 1995).
[3] M. Sze, Physics of Semiconductor Devices, 2nd ed. (Wiley, New York, 1981).
[4] K. Akkiliç, A. T¨ürüt, G. Çankaya and T. Kiliçoğlu, Solid State Commun. 125(10), 551-556 (2003).
[5] M. Siad, A. Keffous, S. Mamma, Y. Belkacem and H. Menari, Appl. Surf. Sci. 236(1-4), 366-376 (2004).
[6] Ş. Karataş, Solid State Communications 135 500 (2005)
[7] D. E. Yıldız, S¸. Altındal, Z. Tekeli and M. Ozer, Mat. Sci. Semicon. Proc. 13(1), 34-40 (2010).
[8] E. Arslan, H. Çakmak and E. Ozbay, Microelectron. Eng. 100, 51-56 (2012).
[9] B. A. Gozeh, A. Karabulut, A. Yildiz, F. Yakuphanoğlu, J. All. Comp. 732 16 (2018).

[10] Y.P. Song, R.L. Van Meirhaeghe, W.H. Lafle´re, F. Cardon, Solid-State Elect. 29 633 (1986)
[11] B.A. H. Ameen, A. Yildiz, W. A. Farooq, F. Yakuphanoğlu, Silicon 11 563 (2019)
[12] S.K. Cheung, N.W. Cheung, Appl. Phys. Lett. 49 85 (1986)
[13] T. Kılıçoğlu, Thin Solid Films 516 967 (2008).
[14] H. Norde, J. Appl. Phys. 50 5052 (1979).
[15] Ş. Karataş, Microelectron. Eng. 87 1935 (2010)
[16] J.P. Sullivan, R.T. Tung, M.R. Pinto, W.R. Graham, J. Appl. Phys. 70 7403 (1991)

6th International Conference on Materials Science and Nanotechnology For Next Generation (MSNG2019)
October 16-18, 2019, Niğde, TURKEY (ORAL FULL TEXT)

Synthesis of Calcium Magnesium Acetate (CMA) Deicer from Dolomite

Sait KURŞUNOĞLU*, Ekin KÖKEN*, Soner TOP*

* Abdullah Gül University, Faculty of Engineering, Materials Science and Nanotechnology Engineering Department, Kayseri, TURKEY

Calcium magnesium acetate (CMA) is an environmentally friendly alternative to sodium and/or calcium chloride for the use of de-icing salt on highways. Owing to the several advantages such as low corrosion for asphalt and concrete structures and multi-purpose availability, it is highly preferred for the use of road-salt. In this study, dolomitic rocks were investigated to synthesize the CMA in laboratory conditions. For this purpose, the initial size of rocks was manually reduced and the dolomitic materials with a particle size range of less than 0.5 mm were prepared for experimental studies. The prepared materials were utilized in leaching tests where dilute acetic acid (CH_3COOH) solutions at a specific concentration of 40% were used for the dissolution of dolomite minerals. During leaching tests, the effects of leaching time (T, min), temperature (t, °C) as well as the ratio of solid to liquid (S/L) on the variations in dolomite dissolution were investigated. As a result of these investigations, it was determined that the average of dolomite dissolution rate were found to be 74.60% under the conditions of T = 180 min, t = 80 °C and S/L = 10%. The chemical constituents of the CMA as a final product was determined by crystallizing and evaporating of leach solutions at 80 – 90 °C with a heating control procedure. X-Ray diffraction (XRD) and Fourier-transform infrared spectroscopy (FTIR) analyses were used for the characterization of CMA products and the results showed that the CMA mainly comprises three main phases with different quantities: calcium magnesium acetate (59.7% – 66.1%), calcium acetate (25.7% – 31.5%) and magnesium acetate (8.2% – 9.3%).

Keywords: Road-Salt, Calcium Magnesium Acetate, Synthesis, Dolomitic Rocks.
Corresponding author: soner.top@agu.edu.tr

1. Introduction

Road salt is a conventional choice when dealing with deicing management of highways. However, it has been experienced from practical applications that the adverse effects of rock salt on road and concrete structures may outweigh its short-term benefits. In general, road salt refers sodium chloride (NaCl) in most cases and no matter how widely it is used, it could not be benefited effectively if the temperature is lower than -7 °C since NaCl has an endothermic nature [1]. In parallel with the ineffectiveness of NaCl in colder regions, the extent of chloride ions in salty solution penetrating into concrete structures results in a remarkable deterioration in such infrastructures of highways and bridges [2].

Therefore, researchers have attempted to focus on investigations with relation to more effective natural and/or artificial deicing salts. The deicers are generally divided into three main categories, which are sorted as chloride-based, acetate-based and inorganic-based ones [3, 4]. Common chloride-based deicers are NaCl, calcium chloride ($CaCl_2$) and magnesium chloride ($MgCl_2$) whereas, acetate-based deicers are Calcium-Magnesium Acetate (CMA) and Potassium Acetate (KAc). Inorganic-based deicers are mainly of sodium monohydrate and/or dehydrate phosphates [5]. Apart from these kinds of deicers, a complementary agent in deicing management could be mentioned as carbohydrate-based ones. Liquid carbohydrate-based agents mainly composed of cane or beet sugar do not aid in melting ice, however, they allows for diminishing the freezing point of ice [6]. Alternatives to road-salt are listed in Table 1 with their possible environmental impacts. Accordingly, calcium chloride ($CaCl_2$) with an effective temperature of -32 °C could be a leading hygroscopic alternative, capturing moisture from the contact environment and accelerating the melting procedure.

Table 1. Environmental impacts of several de-icers [modified after 2, 13].

Environm. Impact	**Rock salt (NaCl)**	**Calcium magnesium acetate (CMA)**	**Calcium Chloride ($CaCl_2$)**	**Magnesium Chloride ($MgCl_2$)**
Soil	Excessive Na^+ ions may corrupt the soil structure.	Potential substitutions of Ca^{++} and Mg^{++} ions may be observed in soils.	Chloride-based constituents may lead to heavy metal contamination in the long-term.	Similar to the one of CMA.
Ground water	Chloride loading or accumulation in groundwater may result in anoxia.	Acetate degradation can decrease the oxygen availability.	Heavy metal contamination could be stimulated if it mixes into groundwater.	Similar to the ones of NaCl and $CaCl_2$.
Vegetation	The use of NaCl around vegetated areas may influence up to 120 m downwind from commonly used roadways, which may result in a decrease of biodiversity.	Little or no remarkable effects are expected.	It could be worthwhile to plant growth.	Similar to the one of $CaCl_2$.
Highway infrastructure	Initiating and accelerating the rate of corrosion in concrete structures, it acts adversely.	It is less corrosive then chloride-based de-icers.	It could be a potential corrosive agent when stayed longer on wet surfaces.	Owing to the Mg-related reactions, infrastructures may deteriorate.
Effective temp. (°C)	-7	-27	-32	-18

Even if the alternatives to Rock salt listed in Table 1 can be consistent with the issues with respect to snow management, chloride-based de-icers have significant disadvantages such as corrosion and deterioration in concrete structures, potentially endangering the life [7 – 12].

Calcium Magnesium Acetate (CMA), a non-chloride deicing agent, was firstly introduced by DOT Company in the USA in the 1980s after an extensive research program initiated by the Federal Highway Administration (FHWA) [14]. The CMA has highly efficient at lower temperatures because of its eutectic temperature of −27 °C that is nearly 20 °C lower than that of rock salt [15]. The advantages of CMA can be summarized as follows:

•Utilization as a deicer in special engineering structures such as bridges, airports etc.
•Less corrosive to highway-related metals and concretes,
•Less endangering the soil, groundwater and biodiversity.

The only disadvantage of the CMA is expensiveness. The CMA approximately costs 10 – 20 times more than that of rock salt. The CMA is a physical mixture of magnesium acetate ($MgAc_2{\cdot}4H_2O$) and, calcium acetate ($CaAc_2{\cdot}H_2O$) both in their stable hydrated forms. Hence, it is possible to be synthesized considering rocks with different Ca/Mg bearing constituents. It was documented that acetic acid with different concentrations could be used to produce the CMA in laboratory conditions [16]. In terms of raw materials such as limestone, dolomite or dolomitic lime, the CMA production could be described by the following equation;

$CaMg(CO_3)_2 + 4HAc = CaAc_2 + MgAc_2 + 2CO_2 + 2H_2O$ (1)

In this study, dolomitic rocks were leached in dilute acetic acid solutions to produce the CMA. During experimental studies, the effects of leaching time (T, min), leaching temperature (t, °C) and solid-to-liquid ratio (S/L) on dolomite dissolution were investigated. As a result of leaching tests, the CMA as a product was characterized through X-Ray diffraction (XRD) and Fourier-transform infrared spectroscopy (FTIR) analyses.

2. Materials and methods

Representative dolomitic rocks to produce CMA were obtained from Nasdur Mining Company located in Hatay province in Turkey. The dolomitic rocks were crushed by a laboratory jaw crusher and then milled to a size of -0.5 mm with a ball mill. CMA synthesis was performed using -0.5 mm sized dolomite sample. The chemical constituents of dolomitic rocks were determined using a Minipal 4 Panalytical XRF (X-Ray Fluorescence) apparatus and the results are given in Table 2.

Table 2. Chemical analysis results of the dolomitic rocks used in this study.

Contents	CaO	MgO	Fe_2O_3	LOI
%	30.43	21.86	0.51	46.38

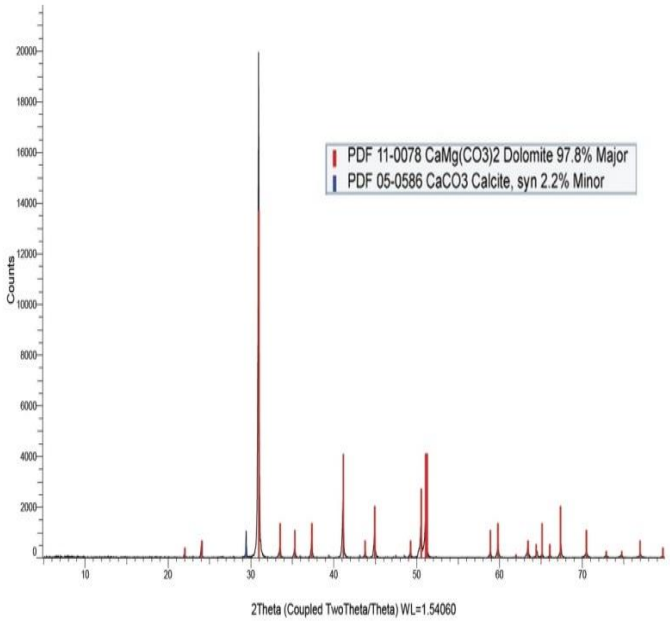


Figure 1. *XRD pattern of the dolomitic rocks*

For leaching tests, acetic acid solution with a specific concentration of 40% was prepared by diluting analytical grade glacial acetic acid (100% purity, Merck) in distilled water. The tests were executed in a 500-mL glass beaker. The leach slurry was mixed by a digital magnetic stirrer (MTOPS) at 400 rpm equipped with a temperature controller hot plate (MTOPS - MSDSM).

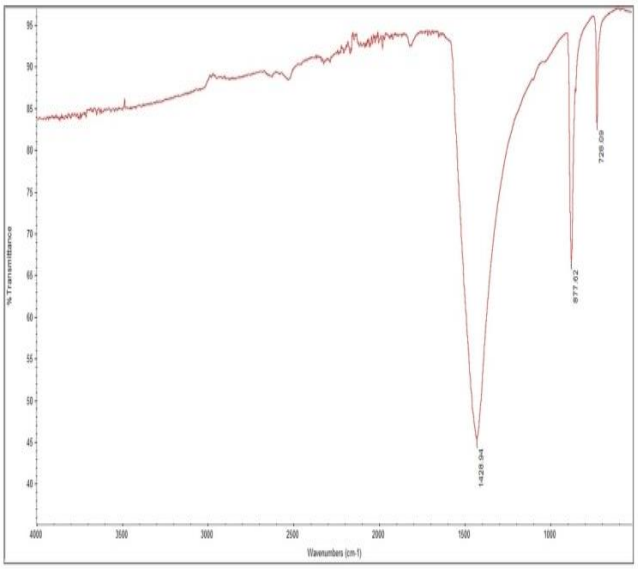


Figure 2. *FTIR pattern of the dolomitic rocks*

For each experiment, the required volume of distilled water was transferred into the reactor and following this procedure, it was heated to the desired temperature before adding ore sample to commence the leaching process. Once the leaching process has been completed, solid-liquid separation was conducted. The CMAs were synthesized from the obtained solutions with a heat-controlled procedure around 80 – 90 °C.

All the tests were duplicated and conducted at 1 atm pressure.

In order to characterize the CMA as product, the Bruker Discover D8 XRD device was used for XRD analyses. In addition, Nicolet 6700 FTIR with ATR (Attenuated Total Reflection) apparatus was used for FTIR analyses. The representative XRD and FTIR patterns of dolomitic rocks are given in Figure 1 and Figure 2, respectively.

3. Results and discussion

3.1. The effects of leaching temperature

For the evaluation of varying temperature effect on dolomite dissolution, 20 g of prepared sample was used in the experiments under the conditions of mixing speed of 400 rpm, acetic acid concentration of 40% (in total of 100 mL leach solution), and 1 h of leach duration. Under these conditions kept stable, leaching tests were performed at different temperatures (i.e. 25 °C, 40 °C, 60 °C and 80 °C).

The effect of temperature on the dissolution of dolomite was found to be significantly high. Particularly, in the experiment carried out at 80 °C, the dissolution rate of dolomite were more than two times than that of room temperature (25 °C) (Figure 3).

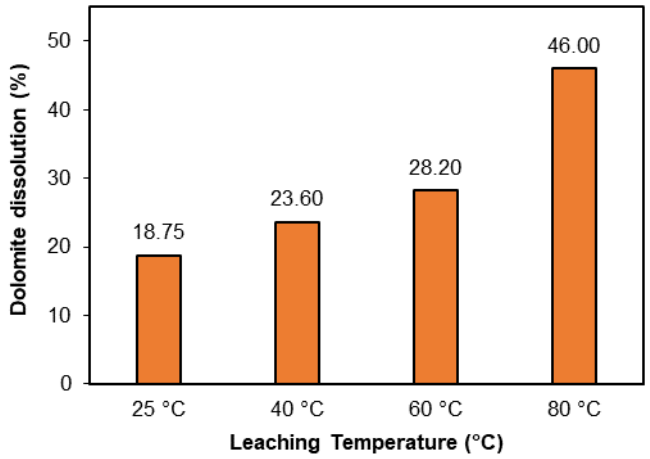


Figure 3. *Dissolution rates of dolomite with respect to varying temperatures.*

3.2. The effects of leaching time

In this evaluation, sample weight (20 g) mixing speed (400 rpm) and acetic acid concentration (40%) were the same as previously described, however, leaching temperature of 80 °C was adopted and under these conditions additional tests were conducted. Leaching tests were conducted up to 3 h and at each hour dolomite, dissolution rates were recorded. As seen in Figure 4, dolomite dissolution gradually increased with increasing leach duration. In the subsequent times, dolomite dissolution continued relatively slow. In other words, after a leach duration of 3h, the dolomite dissolution rate proportionally increased at a rate of 12% when compared the one obtained after 1h leach duration.

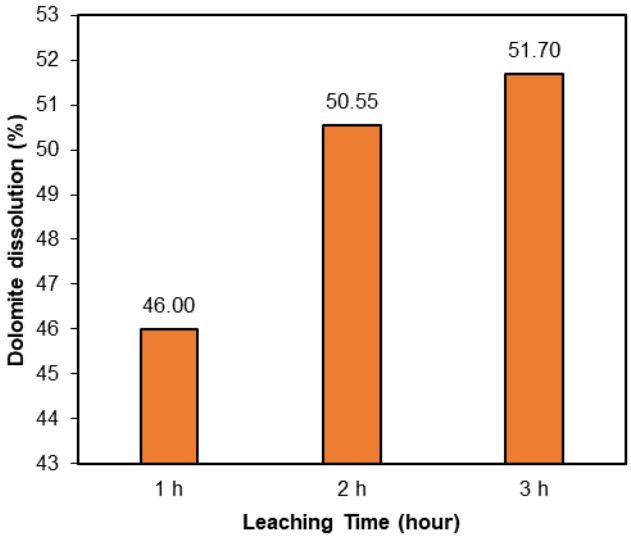


Figure 4. *Dissolution values at different leaching times*

3.3. The effects of solid weight

The dissolution tests were performed at three different S/L ratios (i.e. S/L ranging from 10% to 20%) when the concentration of the acetic acid was 40%, at a temperature of 80 °C, stirring speed of 400 rpm, and leaching duration of 180 min. The decrease in the S/L ratio resulted in an increase in the dissolution values. The maximum dolomite dissolution yielded in the experiments when S/L ratio of 10% was in charge (Figure 5).

3.4. Crystallization tests

After the solid-liquid separation, the leach solutions were gradually heated up to 80 – 90 °C in a 500 mL beaker. The CMAs were obtained at the bottom of the beaker by crystallization and evaporation. After an effective crystallization has been achieved, the CMAs were obtained from the beaker and prepared for the characterization tests. As a result of XRD and FTIR patterns of CMAs, more than 60% of the materials obtained were found as calcium magnesium acetate and the remainder are calcium acetate and magnesium acetate (Figure 6 and Figure 7). Furthermore, it was determined that FTIR analysis results are in a good agreement with the study of [16].

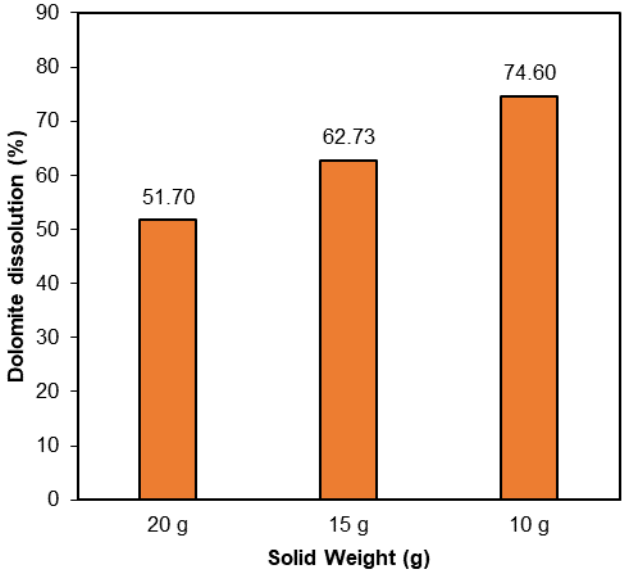


Figure 5. *Dissolution values at different solid ratios (in 100 mL solution)*

4. Conclusions

This research demonstrated that CMAs could be synthesized from the dolomite mineral after the leaching process with acetic acid. The experimental results showed that the dolomite dissolution was the highest when the concentration of the acetic acid was 40%, at a temperature of 80 °C, a solid/liquid ratio of 100 g/L, stirring speed of 400 rpm, a size fraction of – 0.5 mm, and leaching duration of 180 min. Under these conditions, 74.60% of dolomite was dissolved. The CMAs were synthesized from the leach solutions and characterized by XRD and FTIR analyses.

Significant CO_2 emissions were observed during during leaching operations. This released CO_2 can be stored attempted to extablish a closed-loop system in order to attain dry ice as byproduct. In future studies, it should be planned to investigate CMA production after calcination of dolomite. In this regard, positive/negative effects of calcination process on CMA production might be revealed.

5. Acknowledgement

Authors thank to mining engineers "Rüstem KARLIBAHAR and Eshabil YİĞİT" from Nasdur Mining Company for providing the materials.

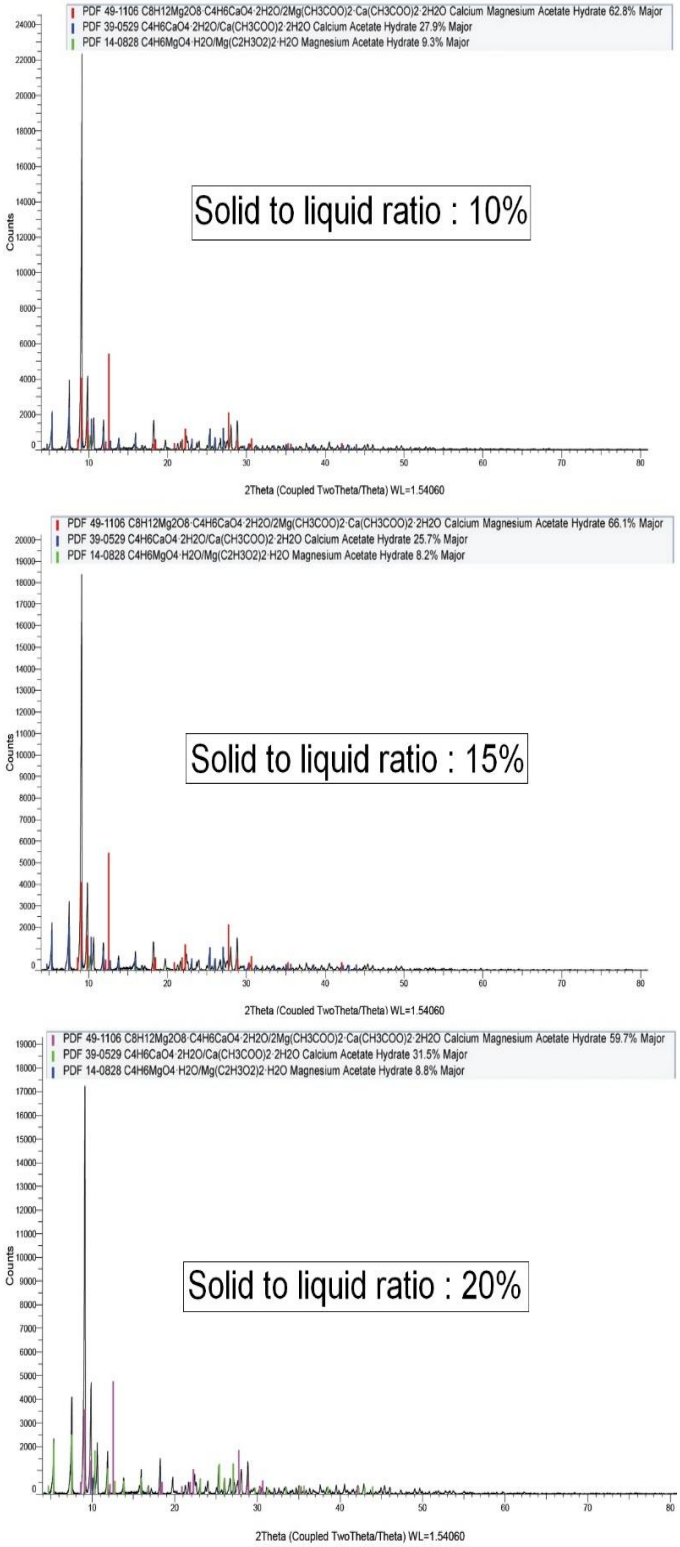


Figure 6. *The results of XRD analyses for the synthesized samples*

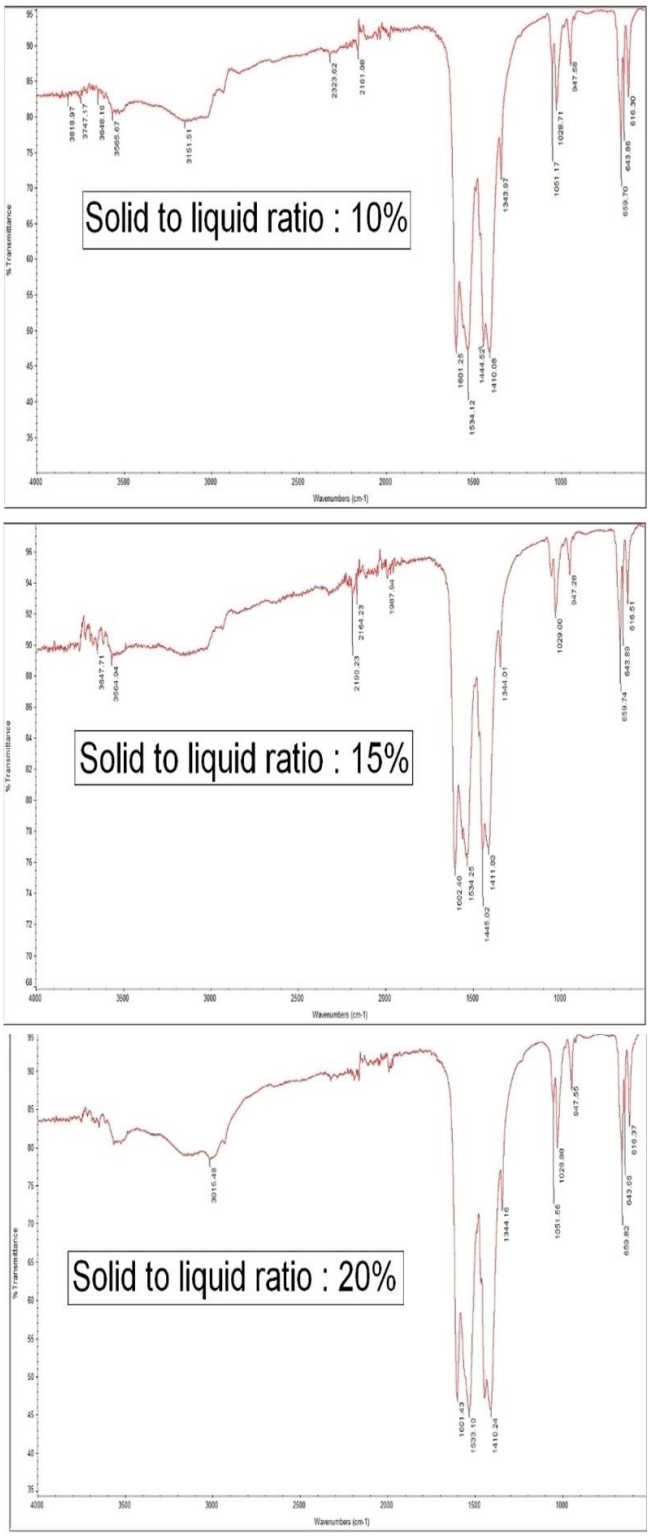


Figure 7. *The results of FTIR analyses for the synthesized samples*

References:

[1] AUTELITANO, F., RINALDI, M., GIULIANI, F., "Winter highway maintenance strategies: Are all the sodium chloride salts the same?". Construction and Building Materials. Vol. 226, pp. 945 – 952, 2019.

[2] National Academies of Sciences, Engineering, and Medicine (1991) Highway Deicing: Comparing Salt and Calcium Magnesium Acetate: Comparing Salt and Calcium Magnesium Acetate -- Special Report 235. Washington, DC: The National Academies Press. https://doi.org/10.17226/11405

[3] DAI, H.L., ZHANG, K.L., XU, X.L. YU, H.Y., "Evaluation on the effects of deicing chemicals on soil and water environment". Procedia Environ. Sci. Vol. 13: pp. 2122 – 2130, 2012.

[4] ZHANG, X., "The current situation of snow melting agent and its impact on the environment and countermeasures". Environ. Sanit. Eng. Vol. 25 (5), pp. 64-65, 2017.

[5] DUNN, S.A., SCHENK, R.U., "Alternative highway deicing chemicals", Transportation Research Board, Special Publication. Vol. 185, pp. 261 – 269, 1979.

[6] FORTIN, C., TJADEN, L., MULHERN, N. (2014). Chloride Free Snow and Ice Control Material. Transportation Research Synthesis, TRS 1411. Minnesota Department of Transportation, St. Paul, MN.

[7] FU, L., OMER, R., JIANG, C., "Field test of organic deicers as prewetting and anti-icingagents for winter road maintenance". Transp. Res. Rec.: J. Transp. Res. Board. Vol. 2272, pp. 130–135, 2012.

[8] FARNAM, Y., WIESE, A., BENTZ, D., DAVIS, J., WEISS, J., "Damage development in cementitious materials exposed to magnesium chloride deicing salt", Construction and Building Materials. Vol. 93, pp. 384-392, 2015.

[9] ALTHOEY, F, WISNER, B., KONTSOS, A., FARNAM, Y., "Cementitious materials exposed to high concentration of sodium chloride solution: Formation of a deleterious chemical phase change". Construction and Building Materials. Vol. 167, pp. 543-552, 2018.

[10] WANG, D., ZHU, Q., SU, Y., LI, J., WANG, A., XING, Z., "Preparation of MgAlFe-LDHs as a deicer corrosion inhibitor to reduce corrosion of chloride ions in deicing salts". Ecotoxicology and Environmental Safety, Vol. 174, pp. 164-174' 2019.

[11] MA, H., YU, H., TIAN, J., TAN, Y., DA, B., "The physical and mechanical properties of chloride-based deicers at 0~−30 °C". Construction and Building Materials. Vol. 211, pp. 721-729, 2019.

[12] SHI, X., DU, S., FU, L., "Environmental risks of snow and ice control materials, in Sustainable Winter Road Operations", Chapter 10, 2018, https://doi.org/10.1002/9781119185161.ch10

[13] KELTING, D.L., LAXSON, C.L. "Review of effects and costs of road de-icing with recommandations for winter roc management in the Adirondack Park", Adirondack

Watershed Institute Report (No: AWI2010-01), 84 pp., 2010.
[14] LEE, B.Y., CHOI, Y.S., KIM, Y.G., KIM, I.L., YANG, E., "A comparison study of performance and environmental impacts of chloride-based deicers and eco-label certified deicers in South Korea". Cold Regions Science and Technology. Vol. 143, pp. 43-51, 2017.
[15] LEINEWEBER, D.B., Production of Calcium Magnesium Acetate (CMA) from Dilute Aqueous Solutions of Acetic Acid, MSc Thesis, University of Wisconsin-Madison, 2002.
[16] OH, S.J., CHOI, G.G, KIM, J.K., "Preparation of Calcium Magnesium Acetate Deicer Using Raw Acetic Acid-Rich Bio-oil Obtained from Continuous Two-Stage Pyrolysis of Corncob". ACS Sustainable Chemistry & Engineering. Vol. 3, pp. 4362-4369, 2018. DOI: 10.1021/acssuschemeng.8b00013.

6th International Conference on Materials Science and Nanotechnology For Next Generation (MSNG2019)
October 16-18, 2019, Niğde, TURKEY (ORAL FULL TEXT)

Effect of High Temperature on the Strength of Geopolymer Concrete Produced from Industrial Tailings

Soner TOP[a], İrfan TİMÜR[b], Ekin KÖKEN[a], Sait KURŞUNOĞLU[a], Hüseyin VAPUR[c]

[a] Abdullah Gül University, Faculty of Engineering, Materials Science and Nanotechnology Engineering Department, Kayseri, TURKEY
[b] Bingöl University, Department of Biochemistry, Institute of Natural and Applied Science, Bingöl, TURKEY
[c] Çukurova University, Engineering Faculty, Mining Engineering Department, Adana, TURKEY

If the concrete is affected by high temperature, significant decreases in strength are observed. The temperature of the concrete at 250-300 °C is considered as a limit. It is stated that the damage occurring below this temperature is insignificant. As the temperature progresses into the concrete during the fire, the regions where the temperature rises above these limits are damaged and the carrier part of the structure decreases gradually.

In this study, we researched the strength properties of the geopolymer concretes produced from the mortar, which is a mixture of slag, fly ash and sodium silicate (Na_2SiO_3) solution. Uniaxial compressive strengths (UCS), point load strengths (PLS), and the stress-strain curves were revealed and the optimal condition for geopolymer concrete production were determined. After the optimum conditions were selected, the concrete specimens were exposured to high temperatures (400, 500 and 600 °C). Effect of the high temperatures on strength of the produced specimens were examined.

Keywords: Geopolymer, Concrete, High, Temperature.

Corresponding author: soner.top@agu.edu.tr

1. Introduction

Although the amount of energy obtained from renewable energy sources such as sun, wind, wave, stream, biomass and geothermal is increasing day by day, the use of fossil fuels, which are the main source of energy production, will continue for the next 100 years in line with the increasing energy demand. In addition, advances in flue gas treatment methods with advancing technology make the use of fossil fuels more environmentally sensitive. In particular, applications to bring fly ash to the industry are limited to the use of these materials only in cement-ready concrete plants in Turkey.

In parallel with the development of industrial applications, the utilization of residual materials accumulated more and more is of increasing importance. In the last 20 years, studies on the evaluation of such residual materials have continued on a limited scale in Turkey. Increasing environmental concerns have led to efforts to take measures on a global scale. In Turkey, the legislation on the control and evaluation of waste has been accelerated especially after 2000 with the regulations such as "Regulation on Waste Management", and "Regulation on the Landfill of Waste".

Fly ashes are the particles of powder size obtained from the flue gases with the help of cyclone and electrofilters as a result of burning of pulverized coals in thermal power plants and loss of carbon and volatile contents in these coals. The ash obtained in the lower part of the furnaces in the thermal power plant is called as bottom ash and its dimensions are higher compared to the fly ash [1-3]. Particle sizes of fly ashes vary between 0.5-150 µm. Crude ash can be formed by cooling the coal burned in water in the cyclone type furnaces [4].

Geopolymers are promising materials that can replace Portland cement concretes [5-6]. The major disadvantage of Portland cement is that the amount of CO_2 produced by humans is around 5-7% due to the production of portland cement [7-8]. CO_2 emissions during Portland cement production are not only caused by the calcination process during clinker production, but also by fossil fuels used to provide calcination heat. Both processes are equally responsible for CO_2 emissions [9-10]. Compared with traditional Portland cement, geopolymers have superior properties such as fire proofing, low price, environmental sensitivity, sound absorption [11-12].

The geopolymers described for the first time by Davidovits, who also have patents for most soil mineral based materials,

include AlO_4 and SiO_4 quadrangles that form 3-dimensional poly (sialate), poly (sialate-siloxo) and poly (sialate-disiloxo) polymeric chains [13-14]. The molecular sequences of geopolymer structures are shown in Figure 1. Si-O-Si and Si-O-Al chains are formed by establishing polymeric amorphous or semi-crystalline structures [15]. Geopolymerization reactions occurs between solid aluminasilicate oxides (minerals and inorganic by-products) and alkali metal silicate solutions (NaOH, KOH, etc.), at moderate temperatures (20-150 °C) and high basic conditions. Unlike zeolite crystals, geopolymer chemistry has a more amorphous particle structure. Figure 2 summarizes the procedure for obtaining geopolymer materials.

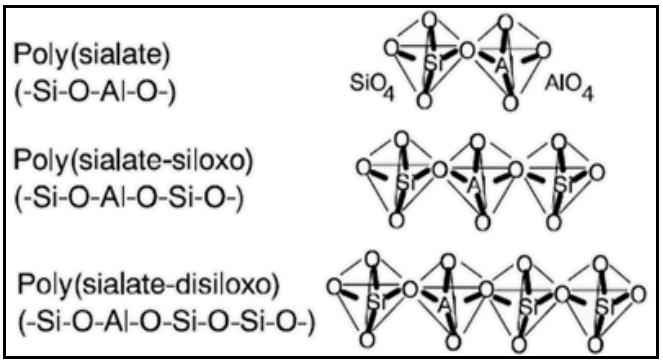


Figure 1. *Molecular sequences of polysialates (Connie et al., 2018)*

Polysialates and hydrosodalites are in the three-dimensional hexagonal molecule sequence. As a result of polycondensation, they give water by dehydratation and dehydration and reach a grain structure similar to zeolite rocks. Unlike zeolite crystals, three-dimensional hexagonal amorphous molecular bond structure of alumino silicate soil materials are geopolymers [16]. The simple formulation of geopolymers is given below.

$$X_q[-(SiO_2)_a\text{-}AlO_2]_q.nH_2O \quad (1)$$

Here; X is the metal cation (Ca^{2+}, K^+ or Na^+), a is 1, 2 or 3, and q is the degree of polycondensation.

Fly ashes, metakaolines, glass residues, red sludge, ashes of agricultural industry by-products (coconut, sugarcane, rice paddy, etc.), ferrochrome slag, concrete demolition residues are some materials containing aluminacilicate used to produce geopolymer concrete [17-24].

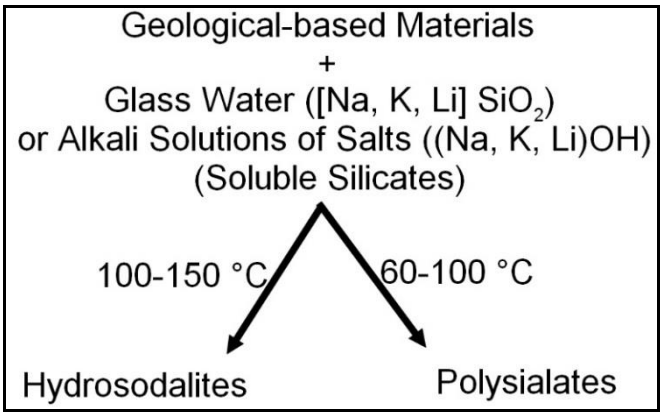


Figure 2. *Flow chart for producing geopolymer material*

The University of Queensland's Global Change Institute building was built entirely with geopolymer concretes from fly ash and blast furnace slag. Brisbane West Wellcamp Airport in South Queensland was established using 70000 tons of geopolymer concrete and was put into service in 2014 [25]. There are dozens of companies that produce geopolymer concrete worldwide [26-29].

In this study, we researched the strength properties of the geopolymer concretes produced from the mortar, which is a mixture of slag, fly ash and sodium silicate (Na_2SiO_3) solution. Uniaxial compressive strengths (UCS), point load strengths (PLS), and the stress-strain curves were revealed and the optimal condition for geopolymer concrete production were determined. After the optimum conditions were selected, the concrete specimens were exposured to high temperatures (400, 500 and 600 °C). Effect of the high temperatures on strength of the produced specimens were examined.

2. Materials and methods

Fly ashes were taken from Sugözü Thermal Power Plant in Yumurtalık District of Adana. All the fly ashes of Sugözü are less than 80 µm in size. Ferrochrome slags from Antalya and Elazığ ferrochrome plant and arc furnace slag from İskenderun were used for aggregate production. The slags were crashed by a laboratory type jaw crusher. In accordance with TS 802 standard, aggregates were prepared in accordance with the maximum grain size determined to be 12 mm [30]. A minimum of 95% sodium meta silicate (anhydrous) was obtained from TEKKİM chemical Inc. to provide geopolymerization. Sodium meta silicate contains 49.5% Na_2O and 46% SiO_2. XRF analyses were applied to the slags (Table 1). The density of the fly ash was determined as 2.33 g/cm^3 by a pycnometer. When the XRF analysis of the arc furnace slag obtained from the iron and steel plant is examined, it is seen that the slag contains a high percentage of iron. The iron content is followed by high calcium content.

Table 1. XRF analyses of the samples.

Content	SiO_2	Al_2O_3	CaO	Fe_2O_3	MnO	K_2O	TiO_2	SrO	BaO	ZrO_2	SO_3	Na_2O	CuO	MgO	Cr_2O_3	LOI#
Sugözü Fly Ashes	55.20	24.10	5.50	8.11	LA*	1.62	1.44	0.27	0.26	0.19	2.34	LA*	LA*	LA*	LA*	2.34
Elazığ Ferrochrome Slags	38.00	22.50	1.56	1.22	0.30	0.23	0.37	LA*	LA*	LA*	0.64	LA*	0.02	29.00	6.03	0.34
Antalya Ferrochrome Slags	41.70	14.20	25.45	1.22	0.10	LA*	0.25	LA*	LA*	LA*	0.31	LA*	0.02	12.30	3.56	1.41
Arc Furnace Slags	11.59	7.63	31.90	37.38	3.95	LA*	0.30	LA*	LA*	LA*	0.39	LA*	LA*	LA*	1.34	0.01

*Under detection limit, #Loss on ignition

In the slags obtained from Elazığ ferrochrome plant, which produces high carbon ferrochrome, major oxides are silicium, magnesium and aluminum oxides. Calcium content is very low and loss on ignition value is lower than Antalya ferrochrome slag.

Resistance of slag aggregates against thermal and degradation was determined by using saturated magnesium sulfate solution according to TS-EN 1367-2 Turkish Standard [31]. Samples weighing approximate 500 g between 10-14 mm in size were used from each aggregate group. The samples which were kept in saturated magnesium sulfate solution for 17 hours were filtered and dried in the oven for 24 hours and then immersed in the solution for 17 hours. In this way, the process was repeated 5 times and then sieved through a 10 mm sieve and the ratio of the portion passing through the sieve to the total sample mass and thermal and degradation resistance were calculated.

According to TS-EN 1097-2 Turkish Standard, Loss Angeles Abrasion Test was applied to the slags [32]. Slag aggregates between 8-12 mm were used in this test. 10 balls weighing 4263 g were placed in the Loss Angeles tester and the device was rotated 500 revolutions. The sample was then extracted and sieved through a 1.6 mm sieve. Wear loss values were found by proportional to the total mass used. Each experiment was repeated 2 times to obtain the mean values. In Table 2, when the los angeles wear values of the slag are examined, it is seen that the most resistant to slag is the arc furnace slag.

Table 2. Wear, thermal resistance and density values of slags.

Aggregate types	Antalya Ferrochrome Slags	Elazığ Ferrochrome Slags	Arc Furnace Slags
Los Angeles Abrasion (%)	16.46	15.28	15.08
Density (g/cm³)	3.12	3.25	3.99
Sulfate Soundness (%)	9.51	12.48	12.57

The slag with the highest density is again the arc furnace slag. According to the results of the magnesium sulphate test, the most resistant slag against thermal and climatic degradation were determined as Antalya ferrochrome slag.

The alkali solution containing 5M Na_2SiO_3 was used for geopolymerization. Tap water was used in the preparation of the solutions. The solutions were prepared 30 minutes before the mortar mixture was formed. The mortar mixture was poured into 5 x 5 x 5 cm molds immediately after preparation. The mixture was stirred for 5 minutes before pouring into the molds. A thin layer of grease was used for easy removal of concrete blocks from the molds. The molds were struck for 3 minutes to remove any air trapped in the mortars. After pouring the mortars into the molds, the molds were placed in the oven at predetermined temperature and left in the oven for 1 day. The curing process was then continued at room temperature. The ratio of aggregates to fly ash was mixed to be 0.66.

In order to measure uniaxial compressive strength, ELE brand concrete press was used. In accordance with ASTM C109 / C109M standard, cubic samples were placed in the loading section and loading process started by computer [33]. The loading speed was selected as 200 kgf/sec. When the cubic sample was broken, the compressive strength test was terminated. UCS values were determined by Equation 2.

$$\sigma = F / A \quad (2)$$

Where; F is pressure (kgf) and A is area (cm^2).

UCS values were converted to MPa. Point load strength of concrete blocks were measured with ELE brand point load resistance device. Protherm (PLF model) ash furnace was used for high temperature resistance tests.

3. Results and discussions

3.1. Effect of slag aggregate type on strength of geopolymer concrete

During the experiments, it was determined that the relative humidity rate ranged from 55 to 70%. The aggregates were mixed with Sugözü thermal power plant fly ashes, where the ratio of aggregates to fly ash was 0.66, which was best achieved in previous experiments. Then 5 M Na_2SiO_3 solution was added to the mixture to form the mortar and the mortar was poured into molds.

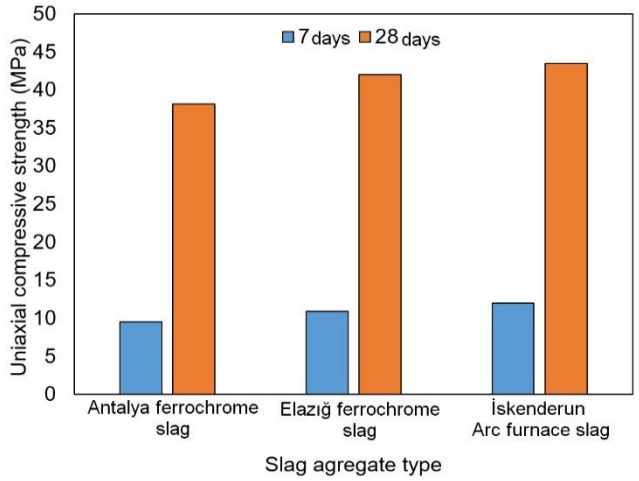


Figure 3. *Compressive strengths according to types of aggregate*

The uniaxial compressive strengths were measured on days 7 and 28 without applying temperature. As it can be seen from Figure 3, the best compressive strength values were obtained in experiments using arc furnace slags as aggregates. These results are consistent with the Los Angeles abrasion test results of the aggregates.

Additional experiments were carried out using arc furnace slag where the highest strength was obtained. In these experiments, arc furnace slag amounts were increased gradually and changes in strength were investigated. After the mortar mixtures were poured into the molds, the molds were cured in the oven at 70 °C for 1 day. The concrete samples were then stored at room temperature. It has been determined that the addition of aggregates up to 20% does not cause a decrease in strength but after the additions it starts to decrease. Especially with the addition of more than 50% of aggregate, strength was reduced by half (Figure 4). It was determined that unit volume weights increased with heavier aggregate ratio and heavier concretes were obtained. Point load strengths of the specimens were also measured. As can be seen in Figure 5, after the addition of 20% arc furnace slag, the strength of concrete samples decreases. These values were found to confirm the compressive strength values. In addition to these findings, the deformations of the concrete samples against strength were calculated.

As it can be seen from Figure 6, although the strength decreases as the aggregate amount increases, the deformation rates are close to each other.

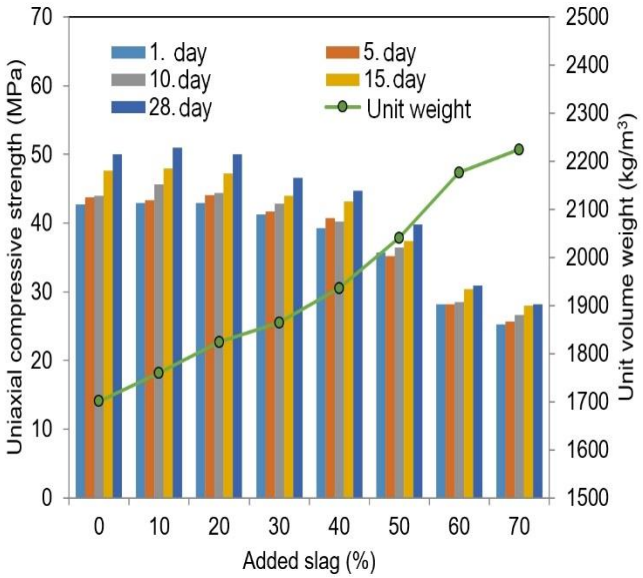


Figure 4. *Compressive strengths according to slag aggregate ratios of arc furnace*

Hard arc furnace slag has a significant effect on the formation of this result. The pre-breakage behavior of the concretes formed with stretchable aggregates such as calcined perlite or pumice is not seen in the concretes prepared by using harder arc furnace slag aggregates.

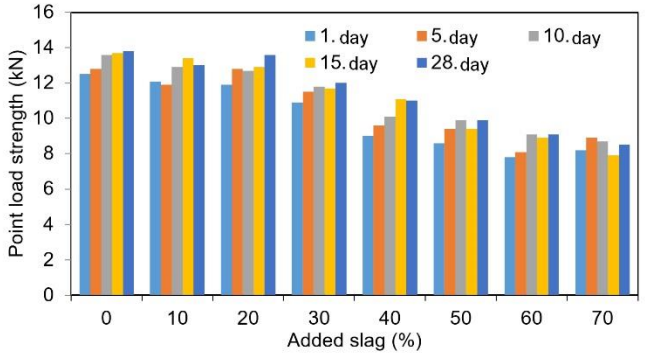


Figure 5. *Point load strengths according to slag aggregate ratios of arc furnace*

3.2. The effect of high temperatures on concrete strength

In order to observe the changes in strength of geopolymer concretes at high temperature, geopolymer concrete samples were exposed to 400, 500 and 600 °C temperature in ash furnace for 1 hour. Although no structural changes were observed in the samples, shallow capillary cracks were detected on their surfaces. The samples were then subjected to uniaxial compressive strength tests (Table 3). There was a decrease in the strength of the samples held at high temperature. While the strength losses at 400 degrees are around 10%, the strength losses at 500 and 600 degrees vary between 20-40%.

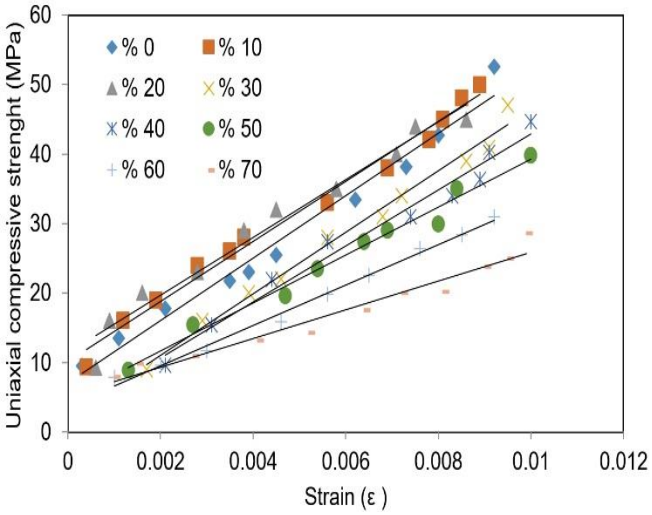


Figure 6. *Stress-strain curves according to added aggregate proportions*

As it can be seen in Figure 7, it is determined that the decreases in the strengths decrease as the amount of slag aggregates increases, even though the strength decreases with the increase in temperature.

Table 3. Changes in concrete strength at high temperatures (MPa).

Temp.	Aggregate amount (%)							
	0	10	20	30	40	50	60	70
-	50.03	51.02	50.03	46.59	44.73	39.82	30.9	28.15
400 ˚C	45.12	46.12	44.16	43.12	41.16	37.15	28.16	26.15
500 ˚C	34.15	36.15	37.46	34.46	34.46	30.46	24.46	23.16
600 ˚C	27.46	27.78	28.16	26.96	26.16	24.48	20.99	19.99

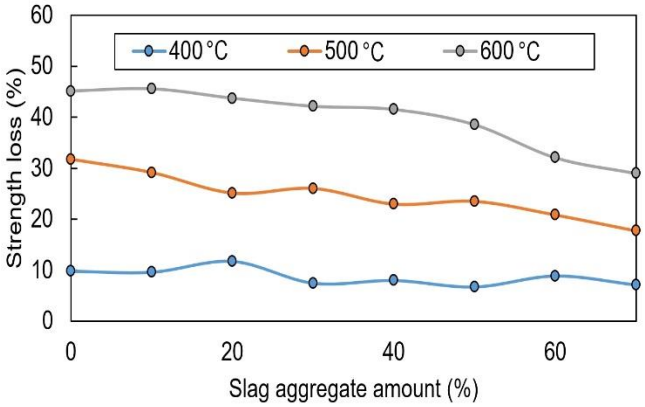


Figure 7. *Strength losses after heat treatments*

4. Conclusions

Exposure to fire is one of the most destructive process that concrete can face. The decrease in the strength of concrete under high temperature depends on the exposure time and the exposure temperature [34]. After the 500 °C threshold is passed, the compressive strength of concrete generally drops by 50% to 60%, and the concrete is considered fully damaged [35].

In this study, we researched the strength properties of the geopolymer concretes produced from the mortar, which is a mixture of slag, fly ash and sodium silicate (Na_2SiO_3) solution. Firstly, 3 different slag aggregates were used in geopolymer concrete and the concrete samples were formed. Slag aggregates used in the highest strength concrete were determined as arc furnace slags. It was determined that the addition of aggregates up to 20% does not cause a decrease in strength but after the additions it starts to decrease. In order to observe the changes in strength of geopolymer concretes at high temperature, geopolymer concrete samples were exposed to 400, 500 and 600 °C temperature in ash furnace for 1 hour. While the strength losses at 400 degrees are around 10%, the strength losses at 500 and 600 degrees vary between 20-40%. it was determined that the decreases in the strengths decrease as the amount of slag aggregates increases.

References:

[1] CELIK, A., YILMAZ, K., CANPOLAT, O., AL-MASHHADANI, M.M., AYGÖRMEZ,, Y., UYSAL, M., "High-temperature behavior and mechanical characteristics of boron waste additive metakaolin based geopolymer composites reinforced with synthetic fibers". Construction and Building Materials. Vol. 187, pp. 1190-1203, 2018.
[2] MOOSAVI, A., ASADI, S., SHORAKI, H.J., "Microstructure and mechanical properties of tabular alumina composites with geopolymer binder at elevated temperatures". Ceramics International. Vol. 45, Issue 7, Part A, pp. 9092-9098, 2019.
[3] GÖRHAN., G., KAHRAMAN, E., BAŞPINAR, M.S., DEMIR, İ., "Uçucu Kül Bölüm I: Oluşumu, Sınıflandırılması ve Kullanım Alanları". Yapı Teknolojileri Elektronik Dergisi. Vol. 2, pp. 85-94, 2008.
[4] TÜRKER, P., ERDOĞAN, B., KATNAŞ, F., YEĞINOBALI, A., "Türkiye'deki Uçucu Küllerin Sınıflandırılması Ve Özellikleri", Türkiye Çimento Müstahsilleri Birliği, Ankara, 112 s. (2009).
[5] ABDEL-GHANI, N.T., ELSAYED, H.A., ABDELMOIED, S., "Geopolymer synthesis by the alkali-activation of blastfurnace steel slag and its fire-resistance". HBRC Journal. Vol. 14 (2), pp. 159-164, 2018.
[6] ZHANG, P., ZHENG, Y., WANG, K., ZHANG, J., "A review on properties of fresh and hardened geopolymer mortar". Composites Part B: Engineering. Vol. 152, pp. 79-95, 2018.
[7] SHEN, W., CAO, L., LI, Q., ZHANG, W., WANG, G., LI, C., "Quantifying CO2 emissions from China's cement industry". Renewable and Sustainable Energy Reviews. Vol. 50, pp. 1004-1012, 2015.
[8] ROLFE, A., HUANG, Y., HAAF, M., PITA, A., REZVANI, S., DAVE, A., HEWITT, N.J., "Technical and environmental study of calcium carbonate looping versus oxy-fuel options for low CO2 emission cement plants". International Journal of Greenhouse Gas Control. Vol. 75, pp. 85-97, 2018.
[9] MCNULTY, E., "Geopolymers: An Environmental Alternative to Carbon Dioxide Producing Ordinary Portland Cement", Department of Chemistry, The Catholic University of America, Senior Comprehensive Paper, 22 s., (2009).
[10] MADDALENA, R., ROBERTS, J.J., HAMILTON, A., "Can Portland cement be replaced by low-carbon alternative materials? A study on the thermal properties and carbon emissions of innovative cements". Journal of Cleaner Production. Vol. 186, pp. 933-942, 2018.
[11] PAN, Z., TAO, Z., CAO, Y.F., WUHRER, R., MURPHY, T., "Compressive strength and microstructure of alkali-activated fly ash/slag binders at high temperature". Cement and Concrete Composites. Vol. 86, pp. 9-18, 2018.
[12] ASKARIAN, M., TAO, Z., ADAM, G., SAMALI, B., "Mechanical properties of ambient cured one-part hybrid OPC-geopolymer concrete". Construction and Building Materials. Vol. 186, pp. 330-337, 2018.
[13] DAVIDOVITS, J., "Geopolymers Inorganic Polymeric New Materials". Journal of Thermal Analysis. Vol. 37, pp. 1633-1656, 1991.
[14] SISOL, M., DRABOVA, M., MOSEJ, J., "Alkali activation of fresh and deposited black coal fly ash with high loss on ignition", Gospodarka Surowcami Mineralnymi. Vol. 30 (2), pp. 103-115, 2014.
[15] YUN-MING, L., CHENG-YONG, H., BAKRI, M.M.A., HUSSIN, K., "Structure and properties of clay-based geopolymer cements: A review". Progress in Materials Science. Vol. 83, pp. 595-629, 2016.
[16] KEYTE, L.M., LUKEY, G.C., VAN DEVENTER, J.S.J., "The effect of coal ash composition on properties of waste based geopolymers". International Symposium Of Research Students On Material Science And Engineering. pp. 1-13, 2004.
[17] NIKOLIC, V., KOMLJENOVIC, M., DZUNUZOVIC, M.N., MILADINOVIC, Z., "The influence of Pb addition on the properties of fly ash-based geopolymers". Journal of Hazardous Materials. Vol. 350, pp. 98-107, 2018.
[18] HAJIMOHAMMADI, A., NGO, T., KASHANI, A., "Glass waste versus sand as aggregates: The characteristics of the evolving geopolymer binders". Journal of Cleaner Production. Vol. 193, pp. 593-603, 2018.
[19] ASCENSAO, G., SEABRA, M.P., AGUIAR, J.B., LABRINCHA, J.A., "Red mud-based geopolymers with tailored alkali diffusion properties and pH buffering ability". Journal of Cleaner Production. Vol. 148, pp. 23-30, 2017.
[20] HASSAN, H.S., ABDEL-GAWWAD, H.A., VASQUEZ GARCIA, S.R., ISRADE-ALCANTARA, I., "Fabrication and characterization of thermally-insulating coconut ash-based geopolymer foam". Waste Management. Vol. 80, pp. 235-240, 2018.
[21] ARULRAJAH, A., KUA, T.A., SUKSIRIPATTANAPONG, C., HORPIBULSUK, S., SHEN, J.S., "Compressive strength and microstructural properties of spent coffee grounds-bagasse ash based geopolymers with slag supplements". Journal of Cleaner Production. Vol. 162. pp. 1491-1501, 2017.
[22] PATEL, Y.J., SHAH, N., "Enhancement of the properties of Ground Granulated Blast Furnace Slag based Self Compacting Geopolymer Concrete by incorporating Rice Husk Ash". Construction and Building Materials. Vol. 171, pp. 654-662, 2018.
[23] KARAKOÇ, M.B., TÜRKMEN, İ., MARAŞ, M.M., KANTARCI, F., DEMIRBOĞA, R., "Sulfate resistance of ferrochrome slag based geopolymer concrete". Ceramics International. Vol. 42 (1), pp. 1254-1260, 2016.
[24] VASQUEZ, A., CARDENAS, V., ROBAYO, R.A., GUTIERREZ, R.M., "Geopolymer based on concrete demolition waste". Advanced Powder Technology. Vol. 27 (4), pp. 1173-1179, 2016.

[25] RANGAN, B.V., "Geopolymer concrete for environmental protection". The Indian Concrete Journal. Vol. 88 (4), pp. 41-48, 2014.
[26] RENCA, (2019). Sustainable construction materials. http://renca.org/ (Accessed time: 22 May 2019).
[27] WAGNERS, (2019). Earth friendly concrete. https://www.wagner.com.au/main/what-we-do/earth-friendly-concrete/efc-home (Accessed time: 22 May 2019).
[28] KIRAN, (2019). Kıran geopolymer. http://www.geocement.in/geo_home.php (Accessed time: 23 May 2019).
[29] LUCIDEON, (2019). MIDAR Technology. https://www.lucideon.com/materials-technologies/midar-technology?source=AMPnewsletter_July18 (Accessed time: 23 May 2019).
[30] TS 802, 2016. Beton karışım tasarımı hesap esasları. 43 s.
[31] TS EN 1367-2, 2010. Agregaların termal ve bozunma özellikleri için deneyler bölüm 2: Magnezyum sülfat deneyi. 17 s.
[32] TS EN 1097-2, 2010. Agregaların mekanik ve fiziksel özellikleri için deneyler bölüm 2 : Parçalanma direncinin tayini için metotlar. 36 s.
[33] ASTM C109 / C109M-16a, Standard Test Method for Compressive Strength of Hydraulic Cement Mortars (Using 2-in. or [50-mm] Cube Specimens), ASTM International, West Conshohocken, PA, 2016, www.astm.org.
[34] KIZILKANAT, A.B., YÜZER, N., KABAY, N., "Thermo-physical properties of concrete exposed to high temperature". Construction and Building Materials. Vol. 45, pp. 157-161, 2013.
[35] HAGER, I., "Behaviour of cement concrete at high temperature". Bulletin Of The Polish Academy of Sciences, Technical Sciences. Vol. 61, No. 1, pp. 1-10, 2013.

6th International Conference on Materials Science and Nanotechnology For Next Generation (MSNG2019)
October 16-18, 2019, Niğde, TURKEY (ORAL FULL TEXT)

Addressing the Stability Issue of Perovskite Solar Cells using Low-Cost CuSCN Hole Transporting Material

S. AKIN

Department of Metallurgical and Materials Engineering, Karamanoglu Mehmetbey University, Karaman, TURKEY

Organic-inorganic perovskite solar cells (PSCs) are assembled from a complex ensemble of layers of disparate materials, each has a crucial function within the device structure. Specifically, hole-transporting materials (HTMs) have indispensable role in device architecture to achieve an outstanding efficiency and long-term stability. However, highly efficient HTMs are commonly consist of expensive and additive incorporated organic molecules such as spiro-OMeTAD and PTAA. Such materials limit the cost-effectiveness and device stability due to their complicated multi-step synthesis procedure and hygroscopic nature. Compared to the state-of-the-art spiro-OMeTAD, low-cost CuSCN showed a promising progress in the recent years owing to its high hole mobility and efficient hole extraction ability. Herein, CuSCN HTM has been systematically examined in the presence of different perovskite systems, i.e., single cation-, and mixed cation-based absorbers. CuSCN HTM showed a comparable efficiencies and exceptional stability in all perovskite compositions indicating the universality of such HTM. Consequently, a breakthrough efficiency approaching 21% with J_{SC} of 23.87 mA.cm^{-2}, V_{OC} of 1.12 V and FF of 0.78 has been achieved in triple cation perovskite-based PSCs. More importantly, devices employing CuSCN HTM exhibited a remarkable operational stability at maximum power point (MPP) tracking retaining ~85% of initial efficiency over 1000 h. These results highlight the great potential of the CuSCN HTM for achieving cost-effective and stable perovskite devices within different perovskite systems.

Keywords: Perovskite Solar Cells (PSCs), Hole-Transporting Materials (HTMs), Stability, CuSCN

Corresponding author: seckinakin@kmu.edu.tr

1. Introduction

With over 25% power conversion efficiency (PCE) [1], organic-inorganic perovskite solar cells (PSCs) have witnessed tremendous attention in the recent years [2-4]. As a key component in high efficiency device architecture, hole-transporting materials (HTMs) play a crucial role in terms of transferring photo-generated holes [2, 5]. In the regular (n-i-p) device configuration, either 2,2′,7,7′-tetrakis(N,N-di-p-methoxyphenyl-amine)9,9′-spirobifluorene (spiro-OMeTAD) or polymer-based poly(triarylamine) (PTAA) has been mostly employed as HTM [6, 7]. Despite the well-aligned energy levels, high hole mobility, and rapid hole extraction/collection of current HTMs, such materials limit the cost-effectiveness and device stability owing to their complicated multi-step synthesis procedure and hygroscopic nature [3, 4, 8, 9].

The poor stability of these HTMs is substantially associated by the highly hydrophilic bis(trifluoromethylsulfonyl)imide (Li-TFSI) dopant which tend to penetrate towards the inner layers and accelerate the degradation of perovskite and/or change the Fermi level of TiO_2 electron-transporting material (ETM) [4, 9]. Although organic and small molecule based different approaches have been reported so far [10-12]; inorganic HTMs attracted the greatest attention both in terms of low-cost and long-term stability. However, most of the inorganic HTM-based devices offering long-term stability have not yet reached the efficiency values of organic HTM-based devices.

Among various inorganic-based materials, copper thiocyanate (CuSCN) has been actively pursued by researchers as an extremely cheap, abundant p-type semiconductor that exhibits notably high hole mobility (10^{-2}–10^{-1} cm^2 V^{-1} s^{-1}) and a well-aligned work function (−5.3 eV) [13, 14]. In addition to individual convincing properties of CuSCN, the compatibility of current HTM within the device need to be considered for the large-scale deployment of PSCs. Especially, the band off-set between corresponding perovskite layer and HTM plays a major role in the determination of voltage loss. The high-quality perovskite surface with good crystallinity is another important factor that effects the photovoltaic performance [15]. Although CuSCN HTM-based PSCs in different perovskite structures performed a great progress over the past few years, there is no

any regular study showing the universality of such HTM within different perovskite systems.

In this study, the applicability of CuSCN HTM with various perovskite systems i.e., single cation-, double cation-, and triple cation-based perovskite absorbers, have been investigated systematically. The obtained results showed a similar trend in terms of long-term operational stability in all perovskite compositions as compared to spiro-OMeTAD. CuSCN HTM exhibited a remarkable improvement in operational stability of different perovskite structures. In addition, triple cation-based PSCs indicated an efficiency of 20.77% which is one the highest efficiencies among the CuSCN HTM based perovskite devices.

2. Experimental details

A 20-to 30-nm thick blocking layer of TiO_2 (c-TiO_2) was deposited on ultrasonically cleaned FTO substrates by spray pyrolysis at 450 °C from a precursor solution of titanium diisopropoxide bis(acetylacetonate) diluted in ethanol (1:9, volume ratio). Then, ~200-nm thick mesoporous TiO_2 (mp-TiO_2) film was deposited on the c-TiO_2 layer by spin coating of TiO_2 paste diluted in ethanol (1:6, weight ratio) at 5000 rpm for 10 s and sintered at 450 °C for 30 min.

Three different perovskite structures of MA-based $MAPbI_3$, MA/FA-based $MA_{0.15}FA_{0.85}Pb(I_{0.85}Br_{0.15})_3$, and MA/FA/Cs-based $Cs_{0.05}(MA_{0.15}FA_{0.85})_{0.95}Pb(I_{0.85}Br_{0.15})_3$ have been used in this work as a single, double, and triple cation-based perovskite structure, respectively. These structures have been determined on the basis of our experience and literature survey. For $MAPbI_3$ perovskite films, a precursor solution (1.3 M) of equal molar ratio of PbI_2 and MAI has been mixed in dimethylformamide/dimethylsulphoxide (9:1, volume ratio). For $MA_{0.15}FA_{0.85}Pb(I_{0.85}Br_{0.15})_3$ perovskite films, a precursor solution containing FAI (1.0 M), PbI_2 (1.1 M), MABr (0.2 M), and $PbBr_2$ (0.2 M) in dimethylformamide/dimethylsulphoxide (4:1, volume ratio). For $Cs_{0.05}(MA_{0.15}FA_{0.85})_{0.95}Pb(I_{0.85}Br_{0.15})_3$ perovskite films, CsI was pre-dissolved as a 1.5 M stock solution in DMSO was added to the double cation perovskite solution as Cs source.

The spin-coating procedure was performed on the mp-TiO_2 films in a two-step program at 1000 and 6000 rpm for 10 and 30 s, respectively. During the second step, 200 µL of chlorobenzene was poured on the spinning substrate 10 s prior to the end of the spinning. The substrates were then heated at 100 °C for 1 hour. After cooling down to room temperature, the CuSCN and spiro-OMeTAD films were coated by the following methods. Subsequently, a spiro-OMeTAD solution, prepared by dissolving 70 mM spiro-OMeTAD in 1 mL of chlorobenzene and doped with 200 mM tert-butylpyridine and 30 mM of lithium bis(triuoromethanesulfonyl)imide (Li-TFSI) from a stock solution in acetonitrile, was deposited on the top of perovskite film by spin coating at 4000 rpm for 20 s. Alternatively, to obtain CuSCN film, CuSCN powder was dissolved in diethyl sulfide (30 mg mL^{-1} in concentration). The solution was deposited on top of perovskite film by spin-coating at 6000 rpm for 30 s. Finally, 70-80 nm of gold counter electrode was deposited by thermal evaporation under high vacuum.

Current density-voltage (J-V) characteristics were recorded under ambient conditions (humidity of ca. 30%) upon illumination by applying an external potential bias to the cell while recording the generated photocurrent with a digital source meter (Keithley 2400), without device pre-conditioning. A 450 W xenon lamp (Oriel) was used as the light source. All measurements were conducted using a non-reflective metal mask with an aperture area of 0.16 cm^2 to define the active area of the device and avoid light scattering through the sides. Long-term photo-stability measurements were performed with a Biologic MPG2 potentiostat. The devices with a metal aperture mask were mounted on the sample holder flushed with nitrogen. The devices were measured with maximum power point tracking (MPPT) under constant one-sun illumination.

3. Results and discussion

In this study, three different perovskite absorbers have been employed to obtain PSCs in the stucture of FTO/c-TiO_2/mp-TiO_2/perovskite/spiro-OMeTAD or (CuSCN)/Au. Schematic illustration of the typical device architecture is given in Figure 1a. Digital images of perovskite devices employing spiro-OMeTAD and CuSCN HTMs are shown in Figure 1b and Figure 1c, respectively. For single cation perovskite devices, $MAPbI_3$ absorber layer has been used in the presence of either spiro-OMeTAD or CuSCN. The J-V curve of best-performing devices is shown in Figure 2a. The photovoltaic parameters extracted from the corresponding curve of the spiro-OMeTAD-based device yielded a short-circuit current (J_{SC}) = 22.29 $mA.cm^{-2}$, an open-circuit voltage (V_{OC}) = 1080 mV, and a fill factor (FF) = 75.2%, resulting in a PCE of 18.10%. Under the same conditions, the device with CuSCN as HTM yielded a J_{SC} = 22.16 $mA.cm^{-2}$, V_{OC} = 1082 mV, and FF = 75.1%, resulting in a PCE of 18.01%.

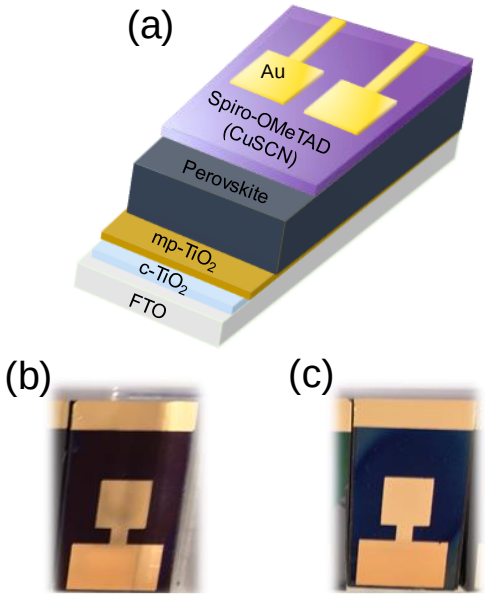


Figure 1. *(a) Schematic illustration of the typical device architecture. Digital images of perovskite devices employing (b) spiro-OMeTAD (c)CuSCN HTMs.*

J-V metrics for 10 independent devices based on spiro-OMeTAD and CuSCN HTMs showed a similar tendency with champion devices in a wide distribution (Figure 2b). 10 independent devices based on spiro-OMeTAD and CuSCN HTMs showed a similar tendency with champion devices in a wide distribution. Such a wide distribution in efficiency range can be attributed to the unstable nature and high defect-states of $MAPBI_3$ perovskite [16, 17]. Furthermore, to study the long-term stability of these devices, the operational stability of unencapsulated devices was monitored under continuous illumination at maximum power point tracking (MPPT) over 1000 h (Figure 2c). Apparently, the PSC containing CuSCN HTM revealed a relatively better stability than that of device containing spiro-OMeTAD HTM. After 1000 h, CuSCN HTM-based PSC retained only >28% of its initial efficiency, while the efficiency of spiro-OMeTAD HTM-based PSC dropped to <10% in only 200 h.

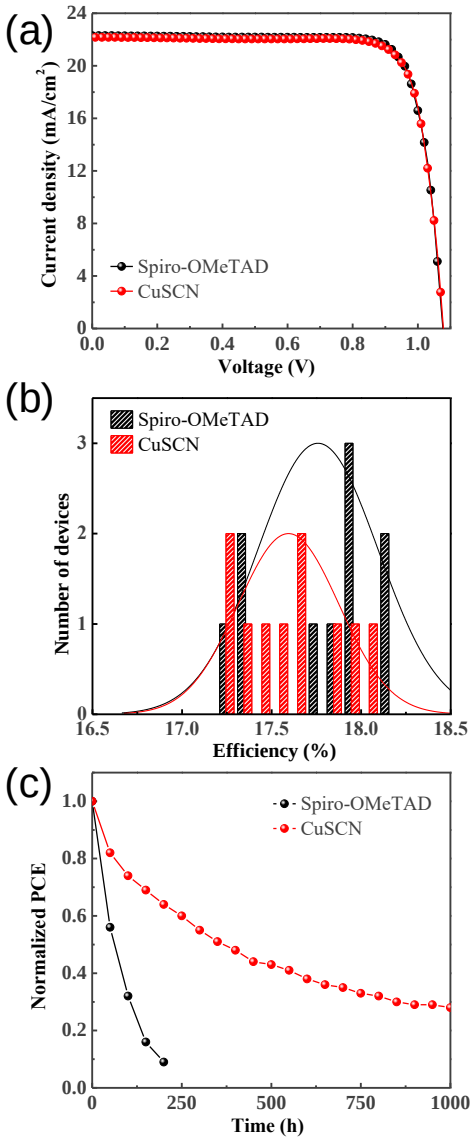


Figure 2. *(a) J-V curves of the best-performing single cation-based devices. (b) PCE histogram of 10 devices based on spiro-OMeTAD or CuSCN HTM. (c) Operational stability curves of un-encapsulated devices with spiro-OMeTAD or CuSCN HTM.*

Similar to single cation devices, $MA_{0.15}FA_{0.85}Pb(I_{0.85}Br_{0.15})_3$ absorber layer has been used for double cation perovskite devices in the presence of either spiro-OMeTAD or CuSCN HTMs. The J-V curve of best-performing devices is shown in Figure 3a. As compared to single cation-based devices, higher device performance was achieved for both HTMs. The champion PSCs yielded an outstanding efficiency of 20.04% and 19.94% for spiro-OMeTAD and CuSCN HTM-based perovskite devices, respectively. As shown in Figure 3b, it is clear that CuSCN HTM-based PSCs displayed not only remarkable performance, but also an outstanding reproducibility. Although an admirable efficiency with a

narrow distribution has been obtained for both systems, the resulting stability curves are still far from the commercialization goal. After 1000 h, CuSCN-based PSC retained ~60% of its initial efficiency, whereas spiro-OMeTAD-based device showed ~75% degradation from its initial performance (Figure 3c).

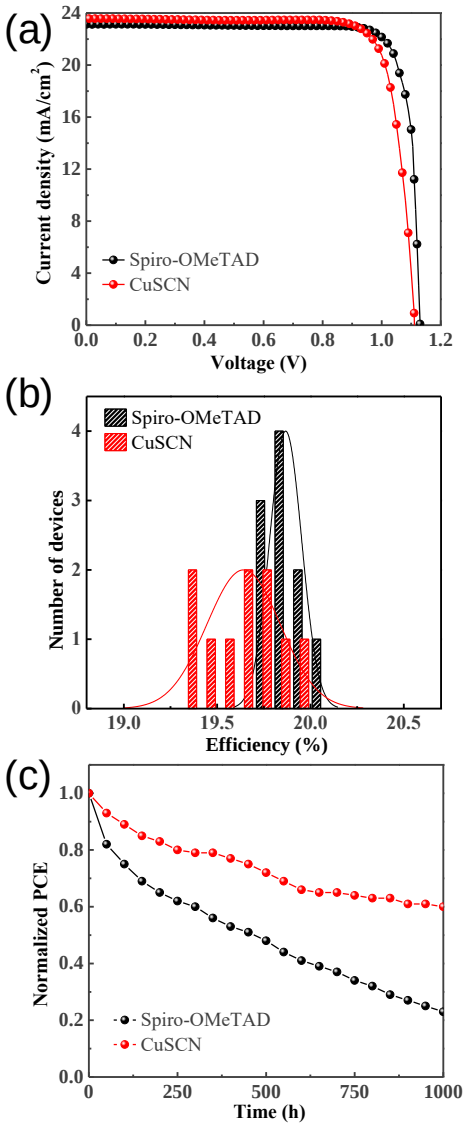


Figure 3. *(a) J-V curves of the best-performing double cation-based devices. (b) PCE histogram of 10 devices based on spiro-OMeTAD or CuSCN HTM. (c) Operational stability curves of un-encapsulated devices with spiro-OMeTAD or CuSCN HTM.*

With the addition of Cs^+ cation, improvements in all device parameters have been achieved. The J-V characteristics of the best PSCs based on spiro-OMeTAD and CuSCN as HTMs measured under 100 $mW.cm^{-2}$ illumination are shown in Figure 4a. Devices employing CuSCN as HTM showed a slightly lower efficiency of 20.77%, with J_{SC} = 23.87 $mA.cm^{-2}$, V_{OC} = 1120 mV, and FF = 77.8% as compared to spiro-OMeTAD-based devices (21.06%). The reproducibility of the PSCs employing spiro-OMeTAD and CuSCN as HTMs were also examined based on 10 identical devices as displayed in Figure 4b. The average efficiencies of spiro-OMeTAD and CuSCN-based devices are 20.88 ± 0.13% and 20.68 ± 0.11%, respectively.

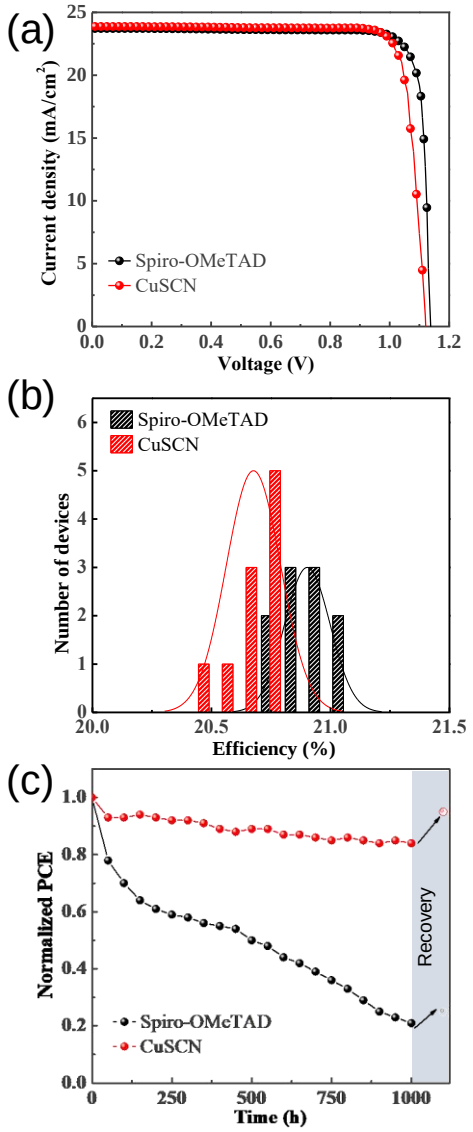


Figure 4. *(a) J-V curves of the best-performing triple cation-based devices. (b) PCE histogram of 10 devices based on spiro-OMeTAD or CuSCN HTM. (c) Operational stability curves of un-encapsulated devices with spiro-OMeTAD or CuSCN HTM.*

Although CuSCN possesses higher hole mobility (~10^{-3} $cm^2.V^{-1}.s^{-1}$) indicating higher J_{SC} value [18, 19], the photovoltaic performance of devices based on such HTM

was found to be rather poor because of the lower V_{OC} value. This can be ascribed to higher monomolecular recombination occurring within the CuSCN HTM-based devices [20]. Besides considerable efficiencies, the stability of PSC devices based on different HTMs was further examined under continuous illumination at MPPT over 1000 h. As presented in Figure 4c, device with CuSCN HTM exhibited relatively good stability, retaining ~85% of the initial efficiency. In contrast, the devices using doped spiro-OMeTAD showed a much faster degradation rate, retaining only 21% of the initial efficiency during the aging period. The rapid degradation of spiro-OMeTAD HTM-based perovskite devices can be attributed to the high concentration of p-dopant and other additives which accelerates the perovskite decomposition due to their hygroscopic and/or volatile character [2, 4, 8, 9]. Such a superb efficiency can be explained on the basis of perovskite composition whereas significant long-term stability can be attributed to the inorganic nature of CuSCN HTM [20, 21]. It is also noteworthy that CuSCN HTM-based perovskite devices showed a significant recovery in around 100 h and reached to 95% of its initial efficiency.

4. Conclusions

In this study, CuSCN semiconductor has been successfuly employed as HTM in three different perovskite systems. The photovoltaic performance of CuSCN HTM was analyzed as a function of perovskite structure. In conclusion, triple cation perovskite employing CuSCN HTM indicated a fascinating stability with admirable efficiency approaching 21%. This has been one of the highest efficiency for CuSCN HTM-based PSCs to date. This study obviously illustrates that CuSCN HTM employing triple cation perovskites are a novel architecture strategy on the road to industrialization of PSCs. This study provides an efficient and cost-effective way to stabilize the different perovskite structures and improve their operational stability, paving the way for the industrialization of the PSCs.

References:

[1] https://www.nrel.gov/pv/cell-efficiency.html, 2019.
[2] AKIN, S., ALTINTAS, Y., MUTLUGUN, E., SONMEZOGLU, S., "Cesium-Lead based Inorganic Perovskite Quantum-Dots as Interfacial Layer for Highly Stable Perovskite Solar Cells with exceeding 21% Efficiency". Nano Energy, 2019, 60, 557-566.
[3] LIU, Y.H., AKIN, S., PAN, L.F., UCHIDA, R., ARORA, N., MILIC, J.V., HINDERHOFER, A., SCHREIBER, F., UHL, A.R., ZAKEERUDDIN, S.M., HAGFELDT, A., DAR, M.I., GRATZEL, M., "Ultrahydrophobic 3D/2D Fluoroarene Bilayer-based Water-Resistant Perovskite Solar Cells with Efficiencies exceeding 22%". Sci Adv, 2019, 5, eaaw2543.
[4] SEO, J.Y., KIM, H.S., AKIN, S., STOJANOVIC, M., SIMON, E., FLEISCHER, M., HAGFELDT, A., ZAKEERUDDIN, S.M., GRATZEL, M., "Novel P-Dopant toward Highly Efficient and Stable Perovskite Solar Cells". Energ Environ Sci, 2018, 11, 2985-2992.
[5] VIDAL, S., IZQUIERDO, M., FILIPPONE, S., FERNANDEZ, I., AKIN, S., SEO, J.Y., ZAKEERUDDIN, S.M., GRATZEL, M., MARTIN, N., "Site-Selective Synthesis of -[70]PCBM-like Fullerenes: Efficient Application in Perovskite Solar Cells". Chem-Eur J, 2019, 25, 3224-3228.
[6] KIM, J., PARK, N., YUN, J.S., HUANG, S., GREEN, M.A., HO-BAILLIE, A.W.Y., "An Effective Method of Predicting Perovskite Solar Cell Lifetime Case Study on Planar CH3NH3PbI3 and HC(NH2)(2)PbI3 Perovskite Solar Cells and Hole Transfer Materials of spiro-OMeTAD and PTAA". Sol Energ Mat Sol C, 2017, 162, 41-46.
[7] KIM, Y., JUNG, E.H., KIM, G., KIM, D., KIM, B.J., SEO, J., "Sequentially Fluorinated PTAA Polymers for Enhancing VOC of High-Performance Perovskite Solar Cells". Adv Energy Mater, 2018, 8, 1801668.
[8] AKIN, S., LIU, Y.H., DAR, M.I., ZAKEERUDDIN, S.M., GRATZEL, M., TURAN, S., SONMEZOGLU, S., "Hydrothermally Processed CuCrO2 Nanoparticles as an Inorganic Hole Transporting Material for Low-Cost Perovskite Solar Cells with Superior Stability". J Mater Chem A, 2018, 6, 20327-20337.
[9] KIM, H.S., SEO, J.Y., AKIN, S., SIMON, E., FLEISCHER, M., ZAKEERUDDIN, S.M., GRATZEL, M., HAGFELDT, A., "Power Output Stabilizing Feature in Perovskite Solar Cells at Operating Condition: Selective Contact-Dependent Charge Recombination Dynamics". Nano Energy, 2019, 61, 126-131.
[10] DUAN, L.S., CHEN, Y., ZONG, X.P., LIU, R., SUN, Z., LIANG, M., WU, Q.P., XUE, S., "Facile Synthesis of Triphenylamine-based Hole-Transporting Materials for Planar Perovskite Solar Cells". J Power Sources, 2019, 435.
[11] OK, S.A., JO, B., SOMASUNDARAM, S., WOO, H.J., LEE, D.W., LI, Z., KIM, B.G., KIM, J.H., SONG, Y.J., AHN, T.K., PARK, S., PARK, H.J., "Management of Transition Dipoles in Organic Hole-Transporting Materials under Solar Irradiation for Perovskite Solar Cells". Nat Commun, 2018, 9.
[12] JEON, N.J., NA, H., JUNG, E.H., YANG, T.Y., LEE, Y.G., KIM, G., SHIN, H.W., SEOK, S.I., LEE, J., SEO, J., "A Fluorene-Terminated Hole-Transporting Material for Highly Efficient and Stable Perovskite Solar Cells". Nat Energy, 2018, 3, 682-689.
[13] MADHAVAN, V.E., ZIMMERMANN, I., ROLDAN-CARMONA, C., GRANCINI, G., BUFFIERE, M., BELAIDI, A., NAZEERUDDIN, M.K., "Copper Thiocyanate Inorganic Hole-Transporting Material for High-Efficiency Perovskite Solar Cells". Acs Energy Lett, 2016, 1, 1112-1117.

[14] PATTANASATTAYAVONG, P., YAACOBI-GROSS, N., ZHAO, K., NDJAWA, G.O.N., LI, J.H., YAN, F., O'REGAN, B.C., AMASSIAN, A., ANTHOPOULOS, T.D., "Hole-Transporting Transistors and Circuits Based on the Transparent Inorganic Semiconductor Copper(I) Thiocyanate (CuSCN) Processed from Solution at Room Temperature". Adv Mater, 2013, 25, 1504-1509.
[15] WANG, J.F., ZHU, L., ZHAO, B.G., ZHAO, Y.L., SONG, J., GU, X.Q., QIANG, Y.H., "Surface Engineering of Perovskite Films for Efficient Solar Cells". Sci Rep-Uk, 2017, 7, 14478.
[16] CHEN, B., RUDD, P.N., YANG, S., YUAN, Y.B., HUANG, J.S., "Imperfections and Their Passivation in Halide Perovskite Solar Cells". Chem Soc Rev, 2019, 48, 3842-3867.
[17] CHEN, Y.H., LI, N.X., WANG, L.G., LI, L., XU, Z.Q., JIAO, H.Y., LIU, P.F., ZHU, C., ZAI, H.C., SUN, M.Z., ZOU, W., ZHANG, S., XING, G.C., LIU, X.F., WANG, J.P., LI, D.D., HUANG, B.L., CHEN, Q., ZHOU, H.P., "Impacts of Alkaline on the Defects Property and Crystallization Kinetics in Perovskite Solar Cells". Nat Commun, 2019, 10.
[18] JUNG, M., KIM, Y.C., JEON, N.J., YANG, W.S., SEO, J., NOH, J.H., SEOK, S.I., "Thermal Stability of CuSCN Hole Conductor-based Perovskite Solar Cells". Chemsuschem, 2016, 9, 2592-2596.
[19] JIN, I.S., LEE, J.H., NOH, Y.W., PARK, S.H., JUNG, J.W., "Molecular Doping of CuSCN for Hole Transporting Layers in Inverted-Type Planar Perovskite Solar Cells". Inorg Chem Front, 2019, 6, 2158-2166.
[20] ARORA, N., DAR, M.I., HINDERHOFER, A., PELLET, N., SCHREIBER, F., ZAKEERUDDIN, S.M., GRATZEL, M., "Perovskite Solar Cells with CuSCN Hole Extraction Layers Yield Stabilized Efficiencies Greater than 20%". Science, 2017, 358, 768-771.
[21] ZHAO, K., MUNIR, R., YAN, B., YANG, Y., KIM, T., AMASSIAN, A., "Solution-Processed Inorganic Copper(I) Thiocyanate (CuSCN) Hole Transporting Layers for Efficient p-i-n Perovskite Solar Cells". J Mater Chem A, 2015, 3, 20554-20559.

6th International Conference on Materials Science and Nanotechnology For Next Generation (MSNG2019)
October 16-18, 2019, Niğde, TURKEY (ORAL FULL TEXT)

Surface Modification of Pumice in a Stirred Ball Mill

Serkan CAYIRLI[1], Hasan Serkan GOKCEN[2], Ece. Burcin DAGCI Yilmaz[1]

[1]Department of Mining Engineering, Faculty of Engineering, Nigde University, Nigde 51240, Turkey
[2]Department of Mining Engineering, Faculty of Engineering and Architecture, Eskisehir Osmangazi University, Eskisehir 26040, Turkey

This paper is aimed to investigate the grinding+surface modification of pumice from the Nevsehir region of Turkey with stearic acid (SA) as a modification agent in a laboratory stirred mill (using single unit). Experimental results were evaluated based on the stress intensity analysis, particle size and floating test which measures the active ratio (AR). In the grinding+surface modification tests, the active ratio of approximately 95% was achieved at 375 kJ/kg energy level. At this energy level and active ratio, d_{50} value was obtained 3.80μm. The results indicate that the hydrophilic surface of pumice becomes hydrophobic after the modification with SA.

Keywords: Pumice, Surface modification, Stirred ball mill

Corresponding authors: scayirli@ohu.edu.tr

1. Introduction

Turkey has a diverse mineral industry that produces more than 50 mineral commodities from about 4,500 known mineral deposits, including metals and industrial minerals. Pumice is one of them and is particularly used in the industries such as construction, agriculture, chemical, textile, dentistry and cosmetic to gain a variety of features to products. Especially, micronized pumice is preferred in the cosmetic and dentistry.

In order to use industrial mineral as filler, some specific physical and physicochemical properties are required. The most important one is that it should be milled to micronized sizes (first stage) (Fig. 1). In industrial scale, micronized material is usually produced by using mills such as tumbling mill, pendulum roller mill, ring roller mill, stirred mill, vibrating ball mills. The mentioned mills are operated in closed circuit by using a pneumatic separator to produce fine/ultra-fine products.

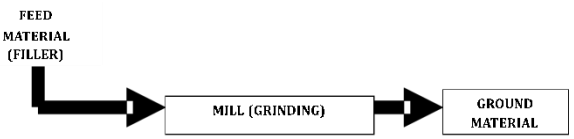


Fig. 1. Schematic diagram of milling process in industrial scale

Second stage is coating process (surface modification) after milling process. Conventional surface modification technologies, which consist of the heating mix modification and packing modification methods, have been applied widely in the treatment of fillers and pigments [1] (Fig. 2).

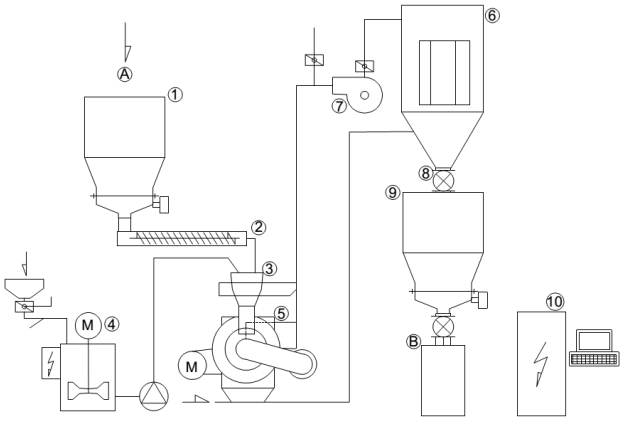


Fig. 2. Schematic diagram of the dry coating system (A: Micronized calcite, 1: Silo, 2: Feeding screw, 3: Spraying tank, 4:

Melting stearic acid, 5: Pin mill, 6: Filter, 7: Air fan, 8: Rotary valve, 9: Packaging) [2, 3]

However, conventional techniques have some drawbacks, such as weak stirring capabilities, low materials mixing degree, uneven dispersion between agent and materials, and, in particular, a lack of reaction foundation. Moreover, the modification effect is weak when using conventional techniques and the product quality is unstable [4]. Mechano-activated surface modification is a modification method that could provide better results than the conventional methods by utilizing mechano-chemical effects during ultrafine grinding. Mechano-chemical effects are physical, and mechanical changes occur in the near surface region where the solids come into contact with each other under mechanical forces [4-6].

Moreover, this method combines the surface modification and the ultra-fine grinding technique that is widely used to produce high quality mineral powder, together in one equipment [1, 7]. One of the mecano-chemical activated machines is stirred ball mills which are used in mineral processing applications. Due to a very high number of stress events per unit time and unit volume and due to appropriate stress intensity the specific energy consumption of stirred media mills for producing very fine particles is less than the one of tumbling and vibrating ball mills. The importance of stirred ball mills increases steadily because of an increasing demand for fine and very fine particles and because of the advantages of stirred ball mills compared to other mills [8].

In this study, both grinding and coating (grinding+surface modification) were carried out for pumice that is an alternative coated product using a laboratory-scale stirred ball mill (single unit).

2. Experimental details

The pumice sample used in the experiments was obtained from Miner Company (~ 100 kg) in Nevsehir. The density of pumice was found to be 2.30 g / cm^3 using helium pycnometer. Feed size analyzes of the samples are shown in Fig. 3.

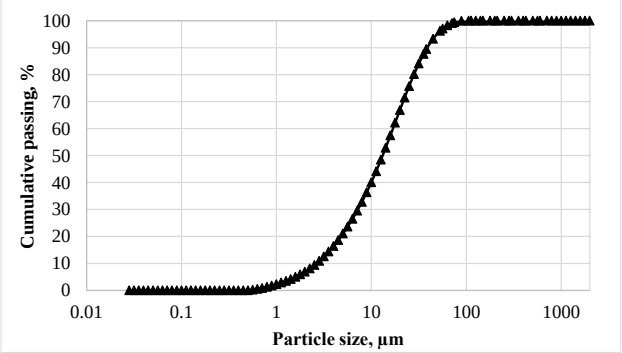


Fig. 3. The size distribution of the feed material.

Chemical analysis of the sample using XRF (X-Ray Fluorescence Spectroscopy-Panalytical Zetium), mineralogical analysis using XRD and image analysis using SEM were performed in the Central Research Laboratory of Niğde University. The result of the XRF analyze is shown in Table 1, the result of the XRD analyze is shown in Figure 4 and the result of the SEM analyze is shown in Figure 5.

Table 1. Chemical composition of the sample

Pumice	%
SiO_2	74.88
Al_2O_3	13.828
K_2O	4.796
Fe_2O	1.445
CaO	1.003
Na_2O	0.801
TiO_2	0.091
MnO	0.062
BaO	0.046
MgO	0.044
P_2O_5	0.004
LOI	3.1

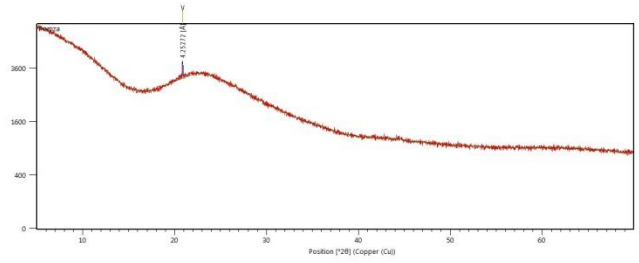


Fig. 4. XRD patterns of feed sample.

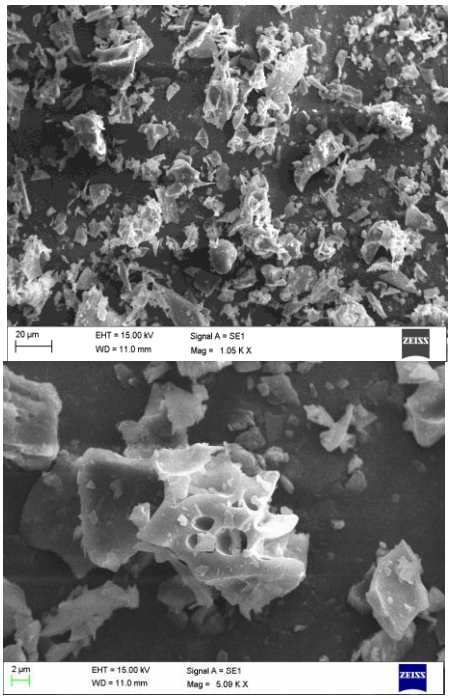


Fig. 5. Scanning electron microscope (SEM) photographs of the sample

Laboratory grinding+coating tests were conducted in a laboratory batch type stirred ball mill (Figure 6). It comprises a 1200 ml cylindrical steel grinding tank. For cooling purposes, the grinding chamber is also equipped with a water jacket. The stirrer axis is fitted with five slotted stainless steel shaft and arms. The shaft is stirred with a motor which has a power of 3 kW and run at RPMs from 50 to 3000 and can be used for dry grinding.



Fig. 6. Stirred ball mill

Grinding+coating tests were carried out in a dry stirred ball mill with varying tip speeds, media diameters. Surfa modification and the grinding performances were also evaluated using the stress energy model at different energy levels. The stress intensity "SI_{GM}" has been varied by changing the stirrer tip speed vtip (between 1 m/s and 10 m/s) as well as the grinding media size "d_{GM}" (between 3 and 4 mm). The stress intensity "SI" is proportional to the kinetic energy of a grinding media [9].

$$SI \infty SI_{GM} = v_{tip}^2 \times d_{GM}^3 \times \rho_{GM} \quad (1)$$

In this study, grinding+coating tests were conducted in a single unit (stirred mill), and process steps are illustrated in Fig. 7. Grinding+coating tests were performed under the conditions given in Table 2. The commercial stearic acid (SA) ($CH_3(CH_2)_{16}COOH$) was used as the surface modification agent in all tests.

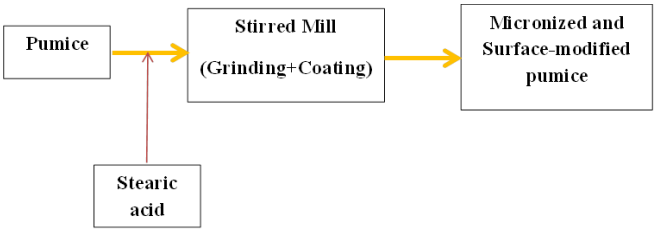


Fig. 7. The grinding+coating process steps.

Table 2. Grinding+coating test conditions

Mill volume (ml)	1200
Stirrer design	5-pin
Media type	Alumina, (3.6 g/cm^3)
Media filling (%)	60
Material load (%)	80
Stearic acid dosage (%)	1,2
Media size (mm)	3, 4
Tip speed (m/s)	1, 2, 4, 8, 10

The all grinding+coating tests were performed as a batch process in which samples were taken from the pot at the determined specific energy. After each test, all of the media and ground+coated samples were removed from the mill and the media were separated from the products by sieving.

A Wet Laser Diffraction Particle Sizer Malvern 2000 Ver. 2.00 with Hydro 2000 MU attachment (Malvern Co., Ltd., UK) was used for the particle size analysis of the feed and the ground+coated products. The effect of the surface modification was evaluated with a floating test, which measures the ratio of the floated product to the overall weight of the sample, after they are mixed in water and stirred vigorously.

$$AR\%=(Mp/(Mp+Mt))*100 \quad (2)$$

where AR is the active ratio (%), Mp the mass of the floated product and Mt the mass of the non-floated product [10]. A greater active ratio implies better surface modification effects [1, 7, 10].

3. Results and discussion

3.1. Effect of Stress Intensity on Pumice Active Ratio

In this section, the modification performances of pumice at three energy consumption were tested under same conditions. The change of the AR values as a function of the stress intensity (i.e. different tip speeds and media size) are shown in Fig. 8.

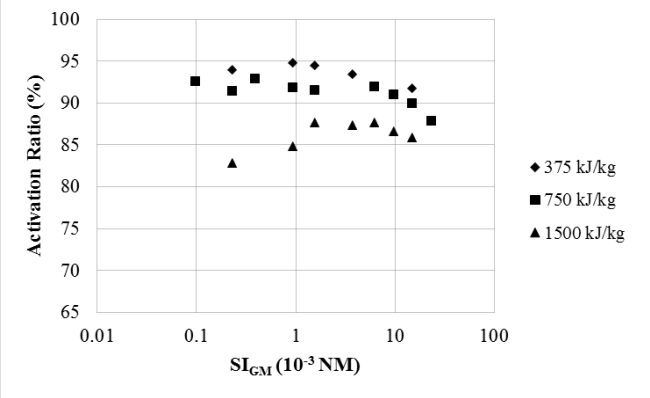


Fig. 8. The effect of stress intensity on AR at different energy input.

AR values increase with an increasing stress intensity down to a certain point and then slowly decrease for all energy levels. When the energy level decreases, there was a significant increase in the active ratios. It was found that the best results were obtained at 375 kJ/kg energy level. In the pumice grinding + coating tests, the active ratio of approximately 95% were achieved at 375 kJ/kg energy level, is illustrated in Fig. 9.

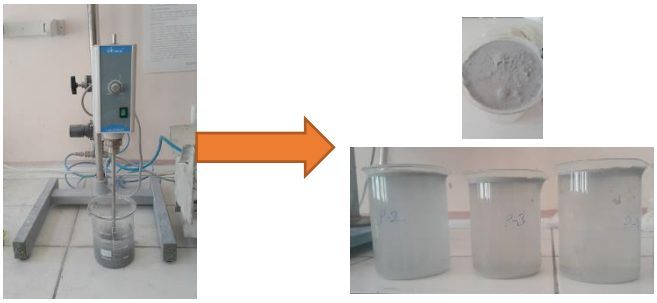


Fig. 9. Hydrophilicity (left) and hydrophobicity (right) of treated and untreated calcium carbonate.

3.2. Effect of Stress Intensity on Particle Size of Pumice

Within this section, the grinding performances of three different energy levels are shown in Fig. 10. d_{50} values decrease with an increasing stress energy down to a certain point and then slowly increases for all energy levels. At low stress intensities ($<1\cdot10^{-3}$ Nm) the d_{50} values is coarser than higher stress intensities, as the stress intensity is not sufficient to fracture the particles for all stirrer designs. Similar findings were observed in cement grinding by Racz [11]. He pointed out that, for dry stirred media milling if the stress intensity of grinding media is lower than the value for the particle breakage, the attrition of the surface rounding of the particles is carried out. Racz and Csöke [12], Cayirli and

Gokcen [13] and Cayirli et al. [14] also found out similar results in their dry grinding studies. Regarding all energy levels tested, optimum stress intensities changed to be in the range of $3*10^{-3}$ - $7*10^{-3}$ Nm. Finer sizes were obtained with 1500 kJ/kg energy consumption. In addition, above optimum stress intensities, the d_{50} values slowly increase and the grinding performance worsened.

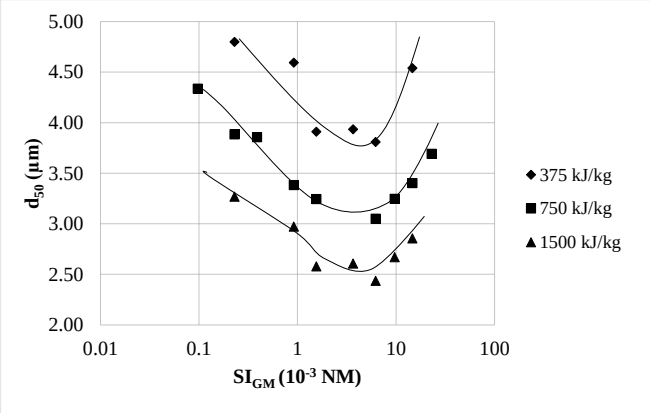


Fig. 10. The effect of stress intensity on product size at different energy input.

Comparing Fig. 8 to Fig. 10, it is understood that the AR is not more efficient as pumice is reduced to finer particle sizes. In the experiments conducted at 375-750 kJ/kg energy levels, it was observed that the coating was efficient compared to the high energy level (1500 kJ/kg). The possible explanation for the decrease in the AR for pumice, the amount of acid was not fed sufficiently as the particle size decreased. In addition, the relationship between surface area and AR should be examined.

4. Conclusions

In this experimental study, pumice powder was subjected to a surface treatment with stearic acid, using the dry coating system and stirred ball mill. The grinding+coating tests conducted showed that:

-For all energy levels, optimum stress intensities change to be in the range of $3*10^{-3}$ - $7*10^{-3}$ Nm.
-At low stress intensities ($<1\cdot10^{-3}$ Nm) the d_{50} values did not decrease, as the stress intensity is not sufficient to fracture the particles. In addition, above optimum stress intensities, the d_{50} values slowly increase and the grinding performance worsens.
-In the pumice grinding + coating tests, the active ratio of approximately 95% were achieved at 375 kJ/kg energy level. At this energy level and active ratio, d_{50} value was obtained 3.80µm.
- Pumice surfaces were changed hydrophilic to hydrophobic.

5. Acknowledgments

This work was supported by Nigde Omer Halisdemir University Scientific Research Projects Directorate (Project No. 2019/02/BAGEP). The authors would like to thank Mining Company (Nevsehir, Turkey) for providing the sample.

References

[1] DING, H., LU, S., DENG, Y., DU, C.X., 2007, Mechano-activated Surface Modification of Calcium Carbonate in Wet Stirred Mill and its Properties, Trans. Nonferrous Met. Soc. China 17, 1100–1104.
[2] JEONG, S., YANG, Y., CHAE Y., KIM, B., 2009, Characteristics of the Treated Ground Calcium Carbonate Powderwith Stearic Acid Using the Dry Process Coating System, Materials Transactions, 50(2), 409-414.
[3] www.hosakawa-alpine.com
[4] YOĞURTCUOĞLU, E., UÇURUM, M., 2011, Surface Modification of Calcite by Wet-Stirred Ball Milling and its Properties, Powder Technology, 214, 47–53.
[5] FRANK, S., STEFAN, M., JORG, S., WOLFGANG, P., 2005, The Influence of Suspension Properties on the Grinding Behavior of Aluminum Particles in the Submicron Site in Stirred Media Mills, Powder Technol. 156 103– 110.
[6] MOHAMED, I., WAKEEL, A., 2005, Effect of Mechanical Treatment on the Mineralogical Constitutes of Abu-Tar Tour Phosphate ore Egypt, Int. J. Miner. Process. 75, 1012– 1015.
[7] WU, W., LU S.C., 2003, Mechano-Chemical Surface Modification of Calcium Carbonate Particles by Polymer Grafting, Powder Technol. 137, 41–48.
[8] KWADE, A., SCHWEDES, J., 1997, Wet Comminution in Stirred Media Mill, Kona, 15, 91-101.
[9] KWADE, A. 1999, Determination of the Most İmportant Grinding Mechanism in Stirred Media Mills by Calculating Stress İntensity and Stress Number, Powder Technol., 105, 382–388.
[10] SHENG, Y.,ZHOU, J., TAO, N., YU, K., TIAN, Y., WANG, Z., 2004, Influence of Octadecyldi Hydrogen Phosphate on the Formation of Active Super-Fine Calcium Carbonate, Journal of Colloid and Interface Science, 272, 326-329.
[11] RÁCZ, Á., 2014, Reduction of Surface Roughness and Rounding of Limestone Particles in Stirred Media Mill, Chem. Eng. Technol., 37, 1–9.
[12] RÁCZ, Á., CSŐKE, B. 2016, Application of the Product Related Stress Model for Product Dispersity Control

in Dry Stirred Media Milling, Int. J. Mineral Process., 157, 28–35.
[13] CAYIRLI, S., GOKCEN, H.S. 2017, The Effect of Stirred Mill Orientation on Calcite Grinding. In: Conference Proceeding: 14th European Symposium on Comminution and Classification. Izmir, Turkey.
[14] ÇAYIRLI, S., GÖKÇEN, H. S., YÜCE. N., 2019, The Effect of Stirrer Design in Different Stirred Mill Orientations. IMCET (26th International Mining Congress and Exhibition), Antalya, 1017-1024.

6th International Conference on Materials Science and Nanotechnology For Next Generation (MSNG2019)
October 16-18, 2019, Niğde, TURKEY (ORAL FULL TEXT)

Electromagnetic shielding properties of Sn doped ZnO powder

F.Yakuphanoglu[1], A. Dere[2*], Osman Dayan[3], Canan Aksu Canbay[1]

[1] Firat University, Department of Physics, Elazig, 23200 TURKEY
[2]Firat University, Nanoscience and Nanotechnology Laboratory, Elazig, 23200 TURKEY
[3]Department of Chemistry, Faculty of Arts and Science, Çanakkale Onsekiz Mart University, Çanakkale, Turkey

The electromagnetic interference (EMI) properties of Sn doped ZnO materials prepared by hydrothermal method have been investigated. In previous study, the reflection and dielectric properties of Sn doped ZnO metal oxide materials have been investigated . In present study, we have investigated electrical conductivity of Sn doped ZnO materials to analyze electromagnetic shielding conduction mechanism. The obtained results indicate that electrical conductivity of ZnO based materials make a significant effect on electromagnetic shielding properties.

Keywords: Electromagnetic shielding, Sn, ZnO, dielectric

Corresponding author: a.dere@firat.edu.tr

1. Introduction

Radar absorbing materials have been great attention due to defense and military applications. In recent years, transparent metal oxide materials. The electromagnetic pollution is military and civil applications. The defense and radar applications need to new materials for transparent and flexible. Most of metal oxides are transparent and one of them is zinc oxide, ZnO. This material can be used for electromagnetic shielding effects due to its interesting electric and magnetic properties.

In previous study, we have investigated the electromagnetic shielding properties of Sn doped ZnO materials prepared by sol gel method [1].
In present study, Sn doped ZnO materials were prepared by hydrothermal to analyze electromagnetic conductivity of their.

2. Experimental details

The used precursors are zinc acetate, tin chloride and distilled water. Firstly, the nominal values of zinc acetate and tin chloride were dissolved in distilled water for 10 min. Then, the solution was ultrasonically stirred using a FYRONIX ultrasonic sonicatior. Then, the solution was poured into a Teflon holder. Then, the Teflon was put into FYRONIX nanomaterial production system. The reaction temperature and time were automatically programmed. The reaction was continued at 180 ^{o}C for 12 h. The obtained powders were dried at 50 ^{o}C for 1h. Then pellets of Sn doped ZnO powders were prepared using a FYRONIX 20 ton benchtop press. The electromagnetic shielding properties off samples were measured using a network analyzer.

3. Results and discussion

The electromagnetic shielding properties of Sn doped ZnO samples were measured as a function high frequency. Fig. 1 shows the electrical conductivity of Sn doped ZnO samples as function frequency ranging of 20 MHz to 20 GHz. As seen in Ffig.1, the electrical conductivity of samples are changed with increasing Sn doping and it increases with frequency. The decrease in electrical conductivity of ZnO is due to Sn doping. The Sn doping changes the electrical conductivity of ZnO. This change is due to the high resistance of Sn doping. The electrical conductivity plots of ZnO samples shows two regions. The first region is the low frequency and second region is the high frequency region. At lower frequencies, the change in conductivity is almost the same. Whereas, at higher frequencies, the electrical conductivity is changed with frequency. The samples

exhibited an alternating conductivity (AC). AC conductivity is related to electromagnetic shielding. The electromagnetic shielding is comprising from electric and magnetic components. The proportion of electromagnetic waves is different in metal, dielectric. The electromagnetic shielding is related to electrical conductivity, resistance and magnetic field.

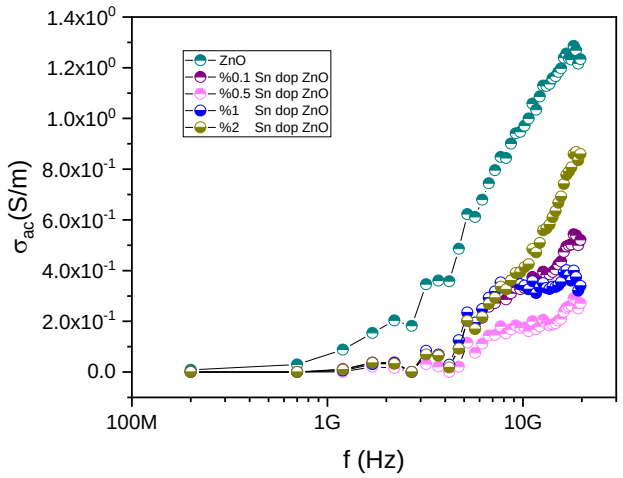


Fig.1 Electrical conductivity of Sn doped ZnO samples

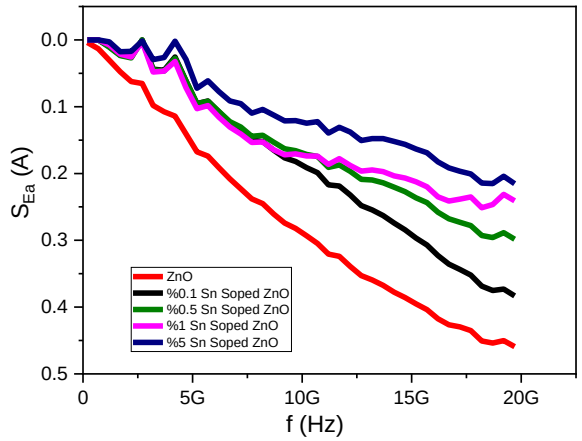


Fig.2. Plot of S_{EA} vs. frequency off Sn doped ZnO samples

Total EMI shielding effectiveness can given by the formula

$$S_{ET} = S_{EA} + S_{ER} + S_{EM} \quad (1)$$

Where S_{EA} is absorption of electromagnetic shielding, S_{ER} is the reflection of electromagnetic shielding and S_{EM} is the multiple reflections. Also, another important parameter is skin depth (δ) to analyze electromagnetic shielding effect. The skin depth is depth of penetration of electromagnetic wave in material.

The absorption losses are defined with conductivity (σ) real permeability (μ'), skin depth (δ) and thickness (t) of the shield material. The SEA value of Sn doped ZnO materials were determined using by the following,

$$S_{EA} = -20\frac{t}{\delta} log e = -8.68\frac{t}{\delta} = -8.68t(\frac{\sigma\omega\mu}{2})^{1/2} \quad (2)$$

The absorbing behavior of Sn doped ZnO samples is shown in Fig.2. As seen in Fig.2, S_{EA} values of Sn doped ZnO is decreased with decreasing S_{EA} values. The lowest SEA value was found to be for 5%Sn doping. The change in S_{EA} is almost linear with increasing frequency. Sn doping was used in ZnO to improve electrical conductivity to increase. The lowest S_{EA} was found to be %5. The change in S_{EA} is not linear behavior.

The electromagnetic shielding conductivity mechanism of Snb Doped ZnO samples is dependent of Sn doping. The mechanism of electrical conductivity is almost linear at higher frequencies. At higher frequencies, the Sn doped ZnO samples exhibited an insulator behavior. It is seen that Sn doping is a significant material for Zinc oxide material. The transparent electromagnetic shielding materials can be used environmental conditions. For electromagnetic applications. These materials also are flexible and are used in production of electromagnetic shielding materials.

Conclusions

Sn doped ZnO materilas has been synthesized by hydrothermal for electromagnetic shielding materials. The electrical conductivity and absorption properties of the samples have been investigated. It is found that the electrical conductivity and absorption losses of zin oxide can be controlled by Sn doping. The obtained results suggest that ZnO based materials can be used in electromagnetic shielding applications.

References:

[1] A. Dere, B. Coşkun, Electromagnetic Interference properties of Sn doped ZnO semiconductors, OEMT2018, İğne Ada, Kırklareli, 20-22 September, 2018.
[2] Aksoy, S., Ruzgar, S. (2019). Effect Of Nitrogen On Optical Properties Of Zno Film Deposited By Sol Gel Method. Journal of Materials and Electronic Devices, 1(1), 35-39

6th International Conference on Materials Science and Nanotechnology For Next Generation (MSNG2019)
October 16-18, 2019, Niğde, TURKEY (ORAL FULL TEXT)

Electromagnetic interference shielding properties of Pentacene thin film prepared by thermal evaporation

F.Yakuphanoglu[1]*, A. Dere[2], Osman Dayan[3], Burhan Coşkun[4], Canan Aksu Canbay[1]

[1] Firat University, Department of Physics, Elazig, 23200 TURKEY
[2]Firat University, Nanoscience and Nanotechnology Laboratory, Elazig, 23200 TURKEY
[3]Department of Chemistry, Faculty of Arts and Science, Çanakkale Onsekiz Mart University, Çanakkale, Turkey
[4]Department of Physics, Faculty of Arts and Sciences, Kırklareli University, Kırklareli, TURKEY

Pentacene is a promising material for organic electronic applications. . Also pentacene is known to have a ordered molecular structure. In the last decade pentacene has generally been studied as a transistor, but the effect of electromagnetic shielding has not been studied. In this study, electromagnetic interference shielding properties of pentacene will be investigated. Fort this the EMI properties of pentacene in the frequency range from 1 GHz to 20 GHz were studied. The obtained results revealed that pentacene organic semiconductor materials can be used as very effective, lightweight microwave shielding materials for spacecraft, aircraft, microelectronic and structural applications.

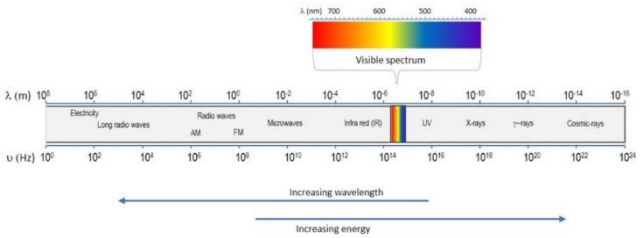
Keywords: Pentacene, electromagnetic interference shielding, dielectric.

Corresponding author: a.dere@firat.edu.tr

1. Introduction

Electromagnetic wave is the transfer of energy in waves by the effect of electric and magnetic fields perpendicular to each other.. Electromagnetic waves; radio waves, microwaves, visible light, ultraviolet rays, infrared rays, x-rays and gamma ligths, frequencies and energy. It is classified as in Figure 1 [1,2]. Natural electromagnetic fields and except natural electric fields electromagnetic and electrical sprawling from man-made sources areas have become a part of our daily lives. Nowadays we often use; Bluetooth devices, mobile phones, high voltage lines, radio stations, TV antennas, low and high frequency electrical appliances are all sources of electromagnetic waves. In Figure 2 shown that . electromagnetic wave types and energies.
EM shielding is the process of reducing EM field in a place made with conductive or magnetic materials. Also known as RF shielding for blocking EM radio frequency.

Pentacene is a generally used p-type organic semiconductor. pentacene is a semiconductor material with high diffusion length and high carrier mobility [3-6]. Therefore pentacene is mainly used in the production of transistors and diodes .But in this study of the pentacene thin film were investigated by electromagnetic shielding measurements.



Fiqure.1. is electromagnetic spectrum

Type	Wavelength (m)	Frequency (Hz)	Energy (eV)
Electricity	$5\ 10^{5}$	50 - 60	
Long wave, television	10^{5} - 10^{2}	< $3\ 10^{9}$	
Short wave, radio	10^{2} - 10^{-1}	10^{8} - $3\ 10^{9}$	< 10^{-5}
Microwaves	10^{-1} - 10^{-3}	$3\ 10^{9}$ - $3\ 10^{12}$	10^{-5} - 10^{-2}
Infrared light	10^{-3} - $7\ 10^{-7}$	$3\ 10^{12}$ - $3\ 10^{14}$	10^{-2} - 2
Visible light	$7\ 10^{-7}$ - $4\ 10^{-7}$	$4.3\ 10^{14}$ - $7.5\ 10^{14}$	2 - 3
Ultraviolet light	$4\ 10^{-7}$ - 10^{-9}	$7.5\ 10^{14}$ - $3\ 10^{17}$	3 - 10^{3}
X-rays	10^{-9} - 10^{-11}	$3\ 10^{17}$ - $3\ 10^{19}$	10^{3} - 10^{5}
Gamma rays	10^{-11} - 10^{-13}	$3\ 10^{19}$ - 10^{21}	> 10^{5}
Cosmic rays	10^{-13} - 10^{-20}	10^{21} - 10^{25}	

Fiqure.2. Electromagnetic wave types and energies.

2. Experimental details

The pentacene p-type organic semiconductor material was purchased from Sigma Aldrich. The molecular formula of this material is $C_{22}H_{14}$ and its molecular weight is 278.35 g / mol. The pentacene organic layer of about 200 nm was thermally evaporated on microscope glass layer. The electromagnetic shielding properties of the pentacene thin film were measured with the FYTRONIX Network Analyzer.

3. Results and discussion

Relative permittivity, and dielectric loss of pentacene thin film as a function of applied frequency in the range of 1-20 GHz and at room temperature is shown in Fig. 3. As seen in Fig. 3, it is depicted that the relative permittivity at high frequencies is gradually increase while the sudden changes is shown at low frequencies. this indicates that the relative dielectric constant is more stable and higher at high frequencies.

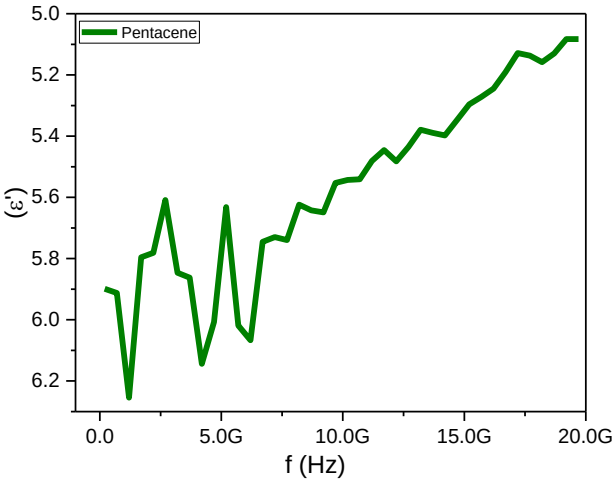


Fig. 3. Plot of the relative permittivity vs. frequency

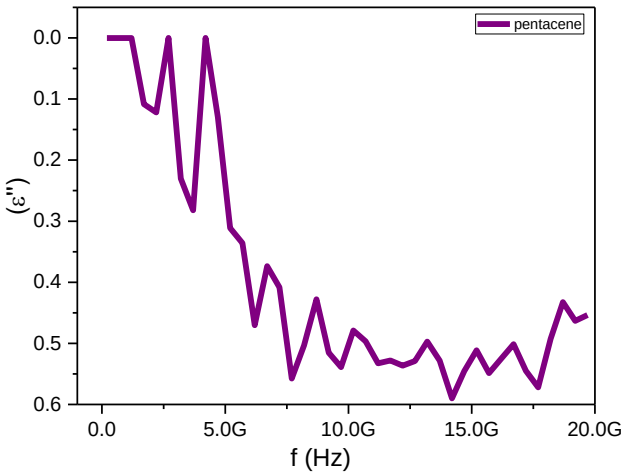


Fig. 4. Plots of the dielectric loss as a function of frequency.

The dielectric loss curve shown in figure 4 is the opposite of this situation. that is, dielectric loss increases at low frequencies and decreases at high frequencies.

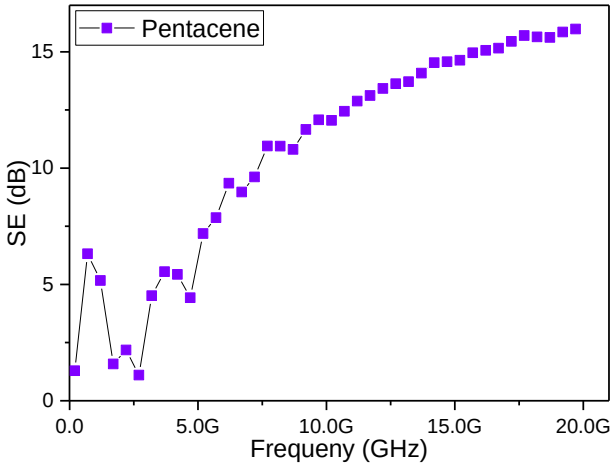
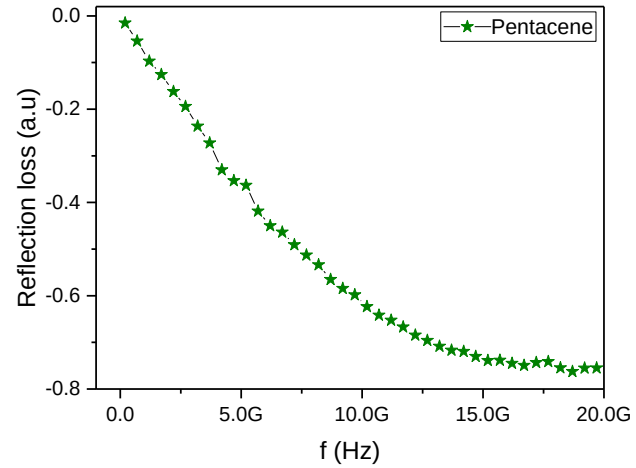


Fig.5. EMI SE of the pentacene thin film at frequency

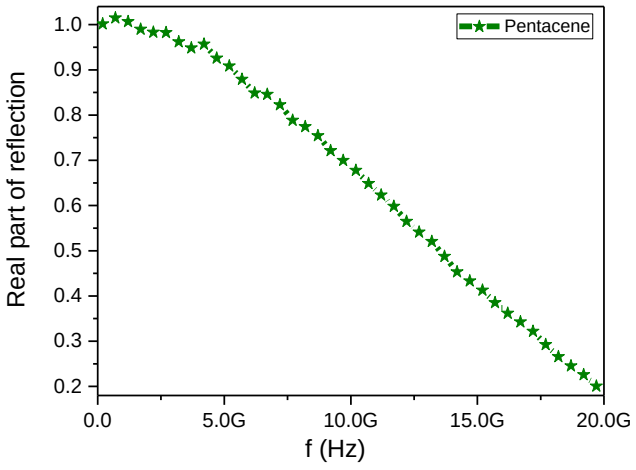
Fig. 5 shows the EMI shielding effectiveness (SE) of pentacene thin film. It is clearly seen that the EMI SE of pentacene thin film displays a increase dependence on frequency, the minimum standard shielding requirements for practical applications (above 20 dB)
SE value given in the figure is calculated by the following equation. The depth at which the electric field drops to 1/e of the incident value is called the skin depth (δ), which is given by the following formula:

$$\delta = (\pi \mu_r \mu_0 f \sigma)^{-1/2} \qquad (1)$$

where mr is the relative magnetic permeability and μ = 4πx10-7 H/m.
To investigate the effect of skin depth and the contribution of
absorption and reflection to total SE as a function of pentacene thin film are investigated
.



(a)



(b)

Fig.6. a) Frequency dependence of reflection loss, b) Frequency dependence of real part of reflection.

The real and parts of reflection and reflection loss are shown in Fig. 6. The imaginary part of the reflection namely reflection loss is decreased with the increasing frequency. Real and imaginary part of reflection analysis shows that dielectric polarization causes change in dielectric constant of pentacene thin film.

Conclusions

The electromagnetic shielding properties of pentacene thin film prepared by thermal evaporation method were investigated. It is seen that the SE of pentacene thin film is changed with the frequency. The obtained electromagnetic shield parameters suggest that pentacene can be used as shielding material for electromagnetic applications.

References:

[1] Zhimin Fan, Duola Wang, Yin Yuan, Youshan Wang, Zhongjun Cheng, Yuyan Liu∗, Zhimin Xie,∗ A lightweight and conductive MXene/graphene hybrid foam for superior electromagnetic interference shielding, Chemical Engineering Journal 381 (2020) 122696.
[2] Sonay Doğan, Ozan Kayacan, Aytaç Gören, Development of Polymer Composite Structures with Electromagnetic Shielding Characteristics, Journal of Textiles and Engineer, 30 March 2018.
[3] Chemical sensors using organic thin-film transistors (OTFTs), M. Demelas S.Lai, P.Cosseddu, A.Loi, M.Barbaro, A.Bonfiglio, Materials, Manufacturing and Applications
2015, Pages 375-396.
[4] Fullerene Thin Films as Photovoltaic Material, Nanostructured Materials for Solar Energy Conversion
2006, Pages 361-443.
[5] Fahrettin Yakuphanoglu,∗,W. Aslam Farooq, The effect of SiO2 dielectric layer on ultraviolet detecting properties of pentacene thin film transistor, Synthetic Metals 161 (2011) 132–135.
[6] Ahmed A. Al-Ghamdi, , Attieh A. Al-Ghamdi, , Yusuf Al-Turki, , F. Yakuphanoglu *,Farid El-Tantawy, Electromagnetic shielding properties of graphene/acrylonitrile
butadiene rubber nanocomposites for portable and flexible electronic devices, Composites Part B 88 (2016) 212-219.

POSTER PRESENTATIONS

6th International Conference on Materials Science and Nanotechnology For Next Generation (MSNG2019)
October 16-18, 2019, Niğde, TURKEY (POSTER FULL TEXT)

The Influence of Green Collector on Floatability of Coal

Hasan HACIFAZLIOĞLU[1], Dilek ŞENOL ARSLAN [2]*

[1]*Istanbul University-Cerrahpasa, Mining Engineering Department, Avcilar, Istanbul, Turkey.*
[2]**Abdullah Gul University, Engineering Faculty, Materials Science and Nanotechnology Engineering Department, Kayseri, Turkey.*

In this study, the potential of sunflower oil as green collector was examined as an alternative to the kerosene, which is an oil product as a collector. Coal flotation experiments and contact angle measurements were carried out with kerosene and sunflower oil. Plant eucalyptus oil was used as frother in all the flotation experiments. After that, the results obtained from flotation experiments were compared in terms of ash, combustible recovery and efficiency index while contact angle values compared to each other. The results show that sunflower oil is a vegetable oil that can be used as an alternative to the kerosene.

Keywords: Bituminous coal; sunflower oil; kerosene; flotation; contact angle.

Corresponding author: dilek.senol@agu.edu.tr

1. Introduction

Collectors which are organic compounds which make the mineral surface hydrophobic, are generally classified as anionic, cationic and non-ionic [1]. The collectors on the mineral surface reduce the stability of the hydrate layer, thus the mineral to form an interface with the air bubble. Compounds which are used as water-insoluble emulsions and which consist of hydrocarbon oils that make the surface hydrophobic by covering the mineral surface non-ionizing collectors. The most important of these are petroleum products such as kerosene, diesel and natural vegetable oils.

Petroleum products (usually kerosene) have been widely used in flotation process of fine coals (<0.5 mm) as collectors and consistently provided robust performance due to their unique capability to selectively adsorb on the surface of coal and render them hydrophobic. The dosage of collector has significant effect on flotation performance [2]. Since the petroleum product is non-polar oil, its disposal in an environmentally acceptable manner is challenging task. These products are also nonrenewable and highly flammable. Hence, a replacement for these products was initiated. Vegetable oils with negligible sulfur, nitrogen and heavy metal content are renewable, available and a non-polluting raw material. Because of these important characteristics, they are suitable candidates for purposes other than food. In this sense, vegetable oils are becoming more widely investigated for alternative uses such as biodiesel production and raw material for the chemical and other industries [3]. It was hypothesized that vegetable oils consisting of long-chain fatty acids which could act as both frother and collector, and having ester groups linked with the ability to behave as a frother, would improve the flotation recovery of the coal particles [4].

Mainly sunflower oil, soybean, cotton, olive, sesame, corn and many other vegetable oil types can be produced in Turkey. Turkey produces nearly 1 million tons of vegetable oil annually and 50% of this oil is sunflower oil [5] In this study, coal flotation with sunflower oil was performed and the results were compared with kerosene which is known as the best collector in the literature.

2. Experimental details

2.1. Materials

Coal sample used in the flotation experiments was collected from a thickener underflow stream of a coal washing plant treating the Zonguldak bituminous coal in Turkey. The results of the chemical analysis of the test sample are given in Table 1. In addition, the distribution of ash and combustibles according to the size fractions is given in Table 2. It indicates that about 50% of the coal has a particle size less than -38 µm and contains about 33.75% ash and 0.70% total sulfur. Thus, the sample may be characterized as a relatively high ash and low sulfur coal.

Table 1. Proximate analysis of the sample coal (on dry basis)

Analysis	Values
Ash content (%)	33.75
Volatile matter (%)	29.20
Fixed carbon (%)	37.50
Total sulfur (%)	0.70
Upper calorific value (kcal/kg)	5220

Table 2. The distribution of weight, ash and combustible recovery in the size fractions.

Size Fractions (µm)	Weight (%)	Ash (%)	Combustible Recovery (%)
500x300	3.51	8.20	4.86
300x212	10.12	7.10	14.20
212x150	14.40	13.30	18.84
150x125	4.62	9.60	6.30
125x63	9.58	22.30	11.24
63x38	4.98	44.60	4.13
-38	52.84	49.30	40.44
Total	100.00	33.75	-

For contact angle measurements, the coal sample was received in the form of lump-sized from the entrance of washery plant in Zonguldak (Turkey). Coal sample was cleaved 15×13×4 mm and coarse polishing with silicon carbide abrasive paper makes the coal flat surface.
Kerosene (from Tupras Company in Izmir from Turkey) and sunflower oil (from Kristal company in Izmir from Turkey) as collector and eucalyptus oil as frother (from Ciftcizade company in Antalya from Turkey) were used as received

2.2. Methods

2.2.1. Contact angle measurements

The surface wettability can be determined by measuring the some parameters such as the electrical potential and contact angle [6]. Contact angle is one of the common techniques to measure the wettability of material. Wetting refers to the study of how a liquid deposited on a solid (or liquid) substrate spreads out or the ability of liquids to form boundary surfaces with solid states. The wetting, as mentioned before is determined by measuring the contact angle which the liquid forms in contact with the solids or liquids.
In this study, the contact angle of kerosene and sunflower oil were carried out with Sessile Drop method by using Attension theta contact angle goniometer on a flat coal surface (Fig.1). The advancing contact angle measurements were carried out 10-20 seconds after the increase in the size of the drop. These values were determined through using the approach provided by Fowkes [7]. All the measurements were carried out at the room temperature (20-22°C).

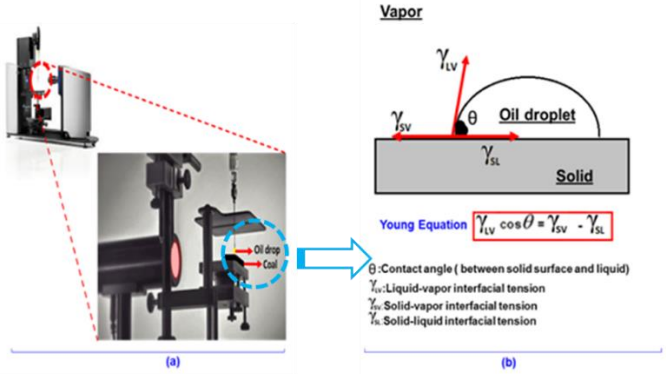


Figure 1. *(a) Shematic of contact angle goniometer. (b) schematic of wetting statics in the Young equation for solid-liquid-vapor system.*

The contact angle is defined as the angle formed by the intersection between of the solid-liquid interface and the liquid-vapor interface which is described by Young equation [8]. As illustrated in Fig.1(c) contact angle of oil droplet on a coal surface in an aqueous medium is defined

as the equilibrium of the oil droplet under the action of three interfacial tensions; liquid-vapor, solid-vapor and solid-liquid. This relation is known Young's equation is shown in Eq.(1)

$$\gamma_{LV}\cos\theta = \gamma_{SV} - \gamma_{SL} \quad (1)$$

where γ_{LV}, γ_{SV}, and γ_{SL} represent the liquid-vapor, solid-vapor, and solid-liquid interfacial tensions, respectively, and θ is the three phase contact angle. If θ is higher than 90°, the solid is hydrophobic or oil-wet, if θ is lower than 90°, the solid surface is hydrophilic or water wet.

2.2.2. Batch Flotation and Release Tests with Sunflower and Kerosene Collectors

Flotation tests were performed in a Denver machine with a cell capacity of 1.5 liters**.** The impeller speed was fixed at 1100 rpm. A pulp density of 10% was used in all experiments. For each flotation tests, the sample was mixed with tap water in the cell for 10 min to ensure the wetting of its surface. Sunflower oil (*2000 g/t*) was used as collector, and eucalyptus oil (*100 g/t*) was used as frother**.** Viscosity, density and oil-water interfacial tension of the sunflower oil were 72 mPa/s, 0.90 g/cm^3 and 22.00 mN/m, respectively. The measurement of these physical properties of the oil was carried out at 20 ºC. Similar conditions were used for determination of flotation performance of the kerosene collector. In the experiments 2000 g/t kerosene and 100 g/t eucalyptus oil as frother was used. The mechanism of particle-oil adsorption in coal flotation with kerosene and sunflower oil were schematized in Fig.2. The flotation process was achieved by mixing chemicals known as collectors (kerosene, sunflower oil) and frother (eucalyptus oil) with in the coal slurry. The collectors adsorb onto the coal surfaces, making these coal particles hydrophobic. Air was passed through the slurry in a tank known as a flotation cell. The new hydrophobic coal particles (coated with the collectors) attach to the bubbles, rising with them to the surface of the flotation cell, where they form a froth. The froth flows over the top edge of the flotation cell and moved the concentrate launder Fig 2 (a, b). Fig.2 (b) However, the selectivity of the collection mechanism was not perfect for sunflower oil flotation process. Some gangue minerals were also carried into the froth, largely by bad selectivity of sunflower oil and entrainment with the water rising with the bubbles. This was particularly the case for particles less than 10 µm in size. Some of the gangue particles follow the water between the bubbles as it drains back to the underlying slurry.

Kinetic flotation tests (for 30, 60 and 240 sec. froth skimming) were conducted to determine collecting potential of sunflower oil and kerosene, separately. The obtained concentrates were filtered, water with acetone washed, dryed in oven, weighted to calculate the yield, and analyzed for ash content. Before starting the kinetic flotation tests, "release test" procedure developed by [9] was applied in order to determine final washability limit of the coal sample. Release test was performed in order to determine the best washability result at varying stirring speeds in a Denver cell and at high reagent dosages *(*10 kg/t sunflower oil, 0.4 kg/t eucalyptus oil*).*

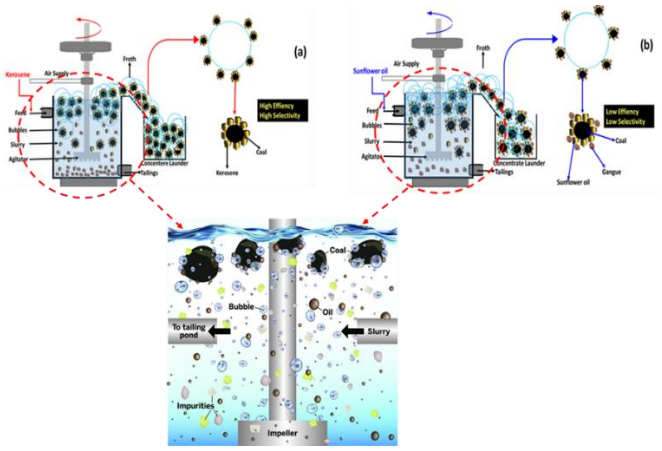


Figure 2. *The mechanism of particle-oil adsorption in coal flotation with kerosene (a) and sunflower oil (b). Detailed view of flotation cell [10] (c).*

The performance of any separation system can be evaluated based on the quality and quantity of the products produced. Many researchers evaluated the flotation performance using yield, recovery, assay, efficiency index, selectivity index, flotation kinetic parameters etc. In this study, the curve of combustible recovery versus concentrate ash was used to compare flotation performance [11].

3. Results and discussion

Release curves for sunflower oil and kerosene collectors are shown in Figure 3. According to Fig. 3 the collecting feature of the kerosene is better than the sunflower oil. Clean coal with a 8.73% ash with kerosene collector were

obtained with a combustible recovery value of 62.54%, while sunflower oil with 10.35% ash clean coal with a combustion recovery value of 55.48%. For a salable clean coal ash value (eg. 10% ash), the combustible recovery value (~ 70%) of the kerosene collector is higher than the combustible recovery value (~ 53%) of the sunflower oil. On the other hand, the results of kinetic flotation studies for sunflower oil and kerosene are presented in Figure 4.

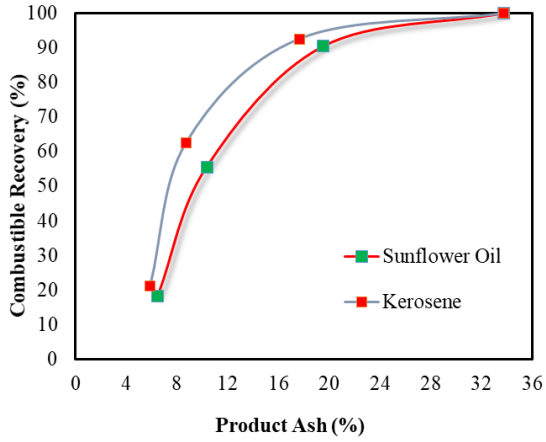


Figure 3. *Release test results with sunflower oil and kerosene.*

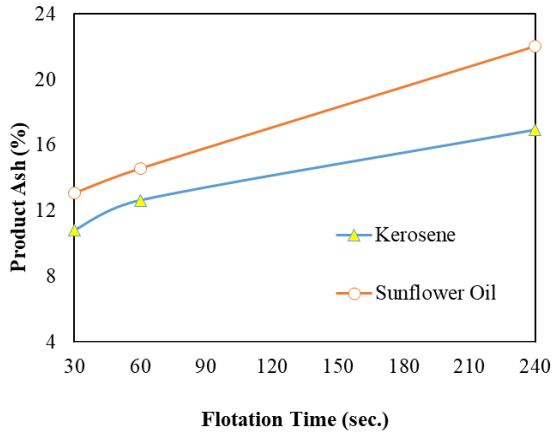


Figure 4. *Release test results with sunflower oil and kerosene.*

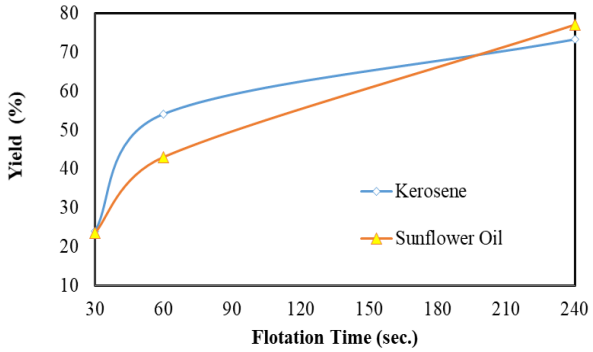


Figure 5. *Release test results with sunflower oil and kerosene.*

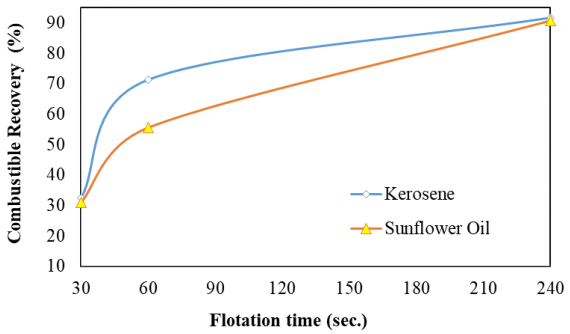


Figure 6. *(a) Product ash, (b) yield, and (c) combustible recovery values as a function of flotation time with kerosene and sunflower oil as collector.*

From Fig.6 results, it can be seen that, the combustible recovery values of both oil types are approximately the same during low (30 sec.) and high (240 sec.) flotation time. For example, the combustible recovery value of sunflower oil is 30.96%, while the kerosene is 32.35% at 30 seconds of flotation. The combustible recovery of sunflower oil is 90.72%, while the kerosene is 91.85% at 240 seconds of flotation. When the results are examined in terms of selectivity, it was seen that the kerosene was more selective. For example, the product ash obtained at the flotation time of 240 seconds was 16.95% with kerosene and 21.93% with sunflower oil. The clean coal ash obtained with sunflower oil is 4.98% higher than that of the kerosene.

4. Conclusion

The ash content of bituminous coal used in the metallurgical industry should be maximum 10%.

Otherwise, the desired coke quality cannot be obtained. As a result of this study, it was observed that sunflower oil could reduce the fine bituminous coal ash value from 33.75% to 6.50%. Although sunflower oil can produce clean coal with very low ash content, it has given poor results in terms of combustible recovery than that of kerosene. Its probable cause is that the surface coating ability of the sunflower oil is lower than kerosene. For obtain a clean coal with 10% ash, the combustible recovery value of sunflower oil is ~53%, while kerosene is ~70%. Kerosene has also given better results in terms of selectivity. The product ash obtained at the longest flotation time (240 sec.) is 16.95% with kerosene while 22.05% with sunflower oil. According to all results, the overall performance of sunflower oil is about 20-30% lower than kerosene. However, it should not be forgotten that sunflower oil is a renewable green collector while kerosene is non-renewable resource.

References:

[1] S.M. Bulatovic, Handbook of flotation reagents: chemistry, theory and practice: volume 1: flotation of sulfide ores, Elsevier2007.
[2] S. Dey, S. Pani, Effective processing of low-volatile medium coking coal fines of Indian origin using different process variables of flotation, International Journal of Coal Preparation and Utilization 32(6) (2012) 253-264.
[3] A.F. Valdés, A.B. Garcia, On the utilization of waste vegetable oils (WVO) as agglomerants to recover coal from coal fines cleaning wastes (CFCW), Fuel 85(5) (2006) 607-614.
[4] R.R. Klimpel, R.D. Hansen, Frothers, In Reagents in Mineral Technology, (Eds.), P. Somasundaran and B.M. Moudgil, Marcel Dekker (1987) 387–409 pp. New York.
[5] Anonym, http://www.bysd.org.tr/. 2017).
[6] G. Zhou, C. Xu, W. Cheng, Q. Zhang, W. Nie, Effects of oxygen element and oxygen-containing functional groups on surface wettability of coal dust with various metamorphic degrees based on XPS experiment, Journal of analytical methods in chemistry 2015 (2015).
[7] F.M.Fowkes, Attractive forces at interfaces Industrial and Engineering Chemistry 56 (1964) 40-52.
[8] T. Young, An essay on the cohesion of fluids, Philosophical Transactions of the Royal Society of London 95 (1805) 65-87.
[9] C. Dell, An improved release analysis procedure for determining coal washability, Journal of the Institute of Fuel 37 (1964) 149-150.
[10] T. Oi, M. Nomura, M. Musashi, T. Ossaka, M. Okamoto, H. Kakihana, Boron isotopic compositions of some boron minerals, Geochimica et Cosmochimica Acta 53(12) (1989) 3189-3195.
[11] M. Vanangamudi, K. Pillai, T. Rao, Effect of some operating variables on the efficiency index of a coal flotation operation, International Journal of Mineral Processing 8(1) (1981) 1-7.

6th International Conference on Materials Science and Nanotechnology For Next Generation (MSNG2019)
October 16-18, 2019, Niğde, TURKEY (POSTERL FULL TEXT)

The Investigation of Temperature Dependent Current – Transfer Mechanisms of Au/PVA/n-GaAs

E. Evcin Baydilli[1*], H. Uslu Tecimer[1], Ş. Altindal[2], H. Tecimer[1]

1Department of Electric-Electronic Engineering, Faculty of Engineering, Karabük University, Karabük 78050, Turkey
[2]Department of Physics, Faculty of Science, Gazi University, Ankara 06500, Turkey

Determination of current-transport mechanisms of (CTMs) of Schottky diode (SD) is quite important in order to improve the device performance. In this study, I_o (reverse saturation current), ideality factor (n) and zero-bias barrier height (Φ_{Bo}) of Au/PVA/n-GaAs are evaluated from forward bias semi-logarithmic I-V measurements at 200 K, 240 K, 320 K and 360 K. It is acquired that the forward bias I-V curve of the sample have three distinct linear regions which are called Region 1 (between 0.039 V and 0.338V), Region 2 (between 0.379 V and 0.595 V) and Region 3 (between 0.639 V and 0.918 V). Obtained results showed that while temperature increases, n value decreases and Φ_{Bo} value increases. Also, series resistance (R_s) values of sample were calculated by Ohm's Law for 200K, 240 K, 320 K and 360 K. Consequently, it is clarified that CTMs of Au/PVA/ n-GaAs MPS type SD are strongly depending on temperature and voltage.

Keywords: Current-transport mechanisms, Schottky diode, MPS, PVA.

Corresponding authors:esraevcin@gmail.com

1. Introduction

Metal-organic/polymer-semiconductor (MPS) type Schottky diodes (SDs) has become major component of the microelectronic circuit elements in today's technology. GaAs semiconductor has become competitive with Si in the technology world, due to increased need for semiconductor devices that working in the microwave frequency in the electronic industry. Furthermore, GaAs is preferred by the researchers because of its high electron mobility, semi-insulator property and direct band gap [1-3]. In consequence of all attributes of GaAs, in this study n-type GaAs has been used as the semiconductor material.

Recently, instead of low dielectric SiO2, high dielectric materials have been used as the interface material between the metal and semiconductor [4]. The presence of this layer prevents the diffusion to the MS interface, deactivates the surface states and increases the rectifying rate by decreasing the leakage currents [4]. Polyvinyl alcohol (PVA) used in this study has become attractive as an interface material due to its physical and chemical properties (high water solubility, high film forming capacity, etc.) [4-5]. In fact, the electrical conductivity of PVA and similar polymers is low. However, the electrical conductivity of PVA which can be modified by doping concentration, can be increased by doping materials such as Zn, Co, Ni [4-7]. In this study, the effect of interface material PVA, which has low production cost and easy processing, was examined on possible current-transmission mechanisms (CTMs) at several temperatures (200K, 240 K, 320 K and 360 K).

As is known, in order to improve the performance of semiconductor devices, it is important to describe the possible CTMs. Especially at low temperatures, the CTMs of the device becomes complex and one or more mechanisms can be dominant at the same time. As is known, at high temperatures, the Thermionic Emission theory (TE) applies because the carriers have sufficient energy to pass the potential barrier. However, due to carriers that do not have sufficient energy at low temperatures, one or more of the CTMs such as TFE, FE, To anomaly may be dominant at the same time [8-9].

Therefore, I-V measurements at different temperatures are important to determine the basic diode parameters of the device, such as ideality factor (n), zero-bias potential barrier height (ϕBo) and series resistance (Rs).

In literature, MPS type SDs prepared that was doped such as ZnO, Co, CdS, etc. to PVA used as interface material are of great interest [4,7,10]. In order to make comparisons with these studies and to investigate the temperature-dependent CTMs, the I-V measurements of Au/pure PVA/n-GaAs were taken at 200 K, 240 K, 320 K and 360 K.

2. Experimental details

The Au/PVA/n-GaAs sample has been prepared by using n-type Si doped GaAs wafer that is 300µm thickness and 1-10 Ω.cm resistivity as substrate. n-GaAs wafer has been divided into 1cm x 1cm pieces. Then wafer has been ultrasonically cleaned by acetone, isopropyl alcohol and deionized water for 5 minutes, respectively. After cleaning process, for back ohmic contact formation, unpolished side of wafer has been coated by Au metal with 99.999% purity and 150nm thickness by thermal evaporation method. For low ohmic contact resistance, wafer has been annealed at 500oC for 3 minutes in N2 atmosphere [11].

After process of back ohmic contact, wafer has been cleaned by HF+10H2O solution to uproot the native oxide layer. On the other hand, high purity PVA solution has been prepared and heated to 80oC for 3 hours. Then, for the arrangement of the PVA interface layer, PVA solution has been transferred to the polished side of n-GaAs wafer as nanofiber by electrospinning method. Lastly, Au metal has been coated on the PVA layer surface with the mask that has been had 150 nm dots about 1.00 mm diameter by thermal evaporating method to creation of Schottky contact.

For examination the temperature dependent I-V characteristics of Au/PVA/n-GaAs, current-voltage measurements have been taken by Keithley 2400 source meter for the temperatures 200 K, 240 K, 320 K and 360 K. Temperature control has been performed by Janis vpf-475 cryostat and the temperature change has been followed by Lake Shore 321.

3. Results and discussion:

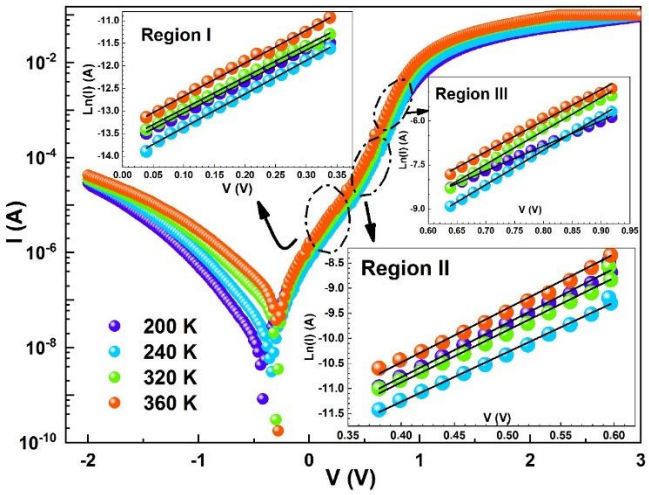


Fig.1. Semi-logarithmic forward and reverse bias I-V characteristics of Au/PVA/n-GaAs MPS type SBD at 200 K, 240 K, 320 K and 360 K.

Fig. 1 shows the forward and reverse bias lnI-V characteristics of Au/PVA/n-GaAs for the temperature of 200 K, 240 K, 320 K and 360 K. As can be seen in Figure 2, there are three linear distinct regions for both temperatures. These regions are Region 1 (between 0.039 V and 0.338V), Region 2 (between 0.379 V and 0.595 V) and Region 3 (between 0.639 V and 0.918 V). The slopes of linear regions remain almost constant as independent temperature. At the high voltage values, because of Rs effect, lnI-V curves are not linear for both temperatures. This type of I-V behavior of forward bias can be explained by TE mechanism [12,13]:

$$I = \underbrace{AA^{*}T^{2}\exp\left(-\frac{q}{kT}\phi_{Bo}\right)}_{I_o}\left[\exp\left(\frac{q\left(V-IR_s\right)}{nkT}\right)-1\right] = I_o\left[\exp\left(\frac{q(V-IR_s}{nkT}\right)-1\right] \quad (1)$$

Where A* is the effective Richardson constant and equals 8.16 A/cm2K2 for n-GaAs, A is the diode area and for our sample, it equals 7.85x10-3cm2. Other quantities are well-known physical quantities.

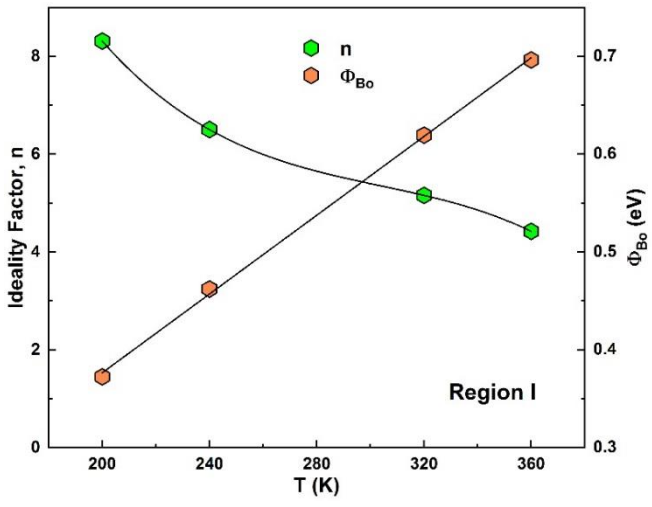
Table 1 shows the Io, n and ΦBo values for both three regions. Io and n values are specified from intercept and slope of the linear regions, respectively. ΦBo values are computed by using below [12,13]:

$$\phi_{Bo} = \frac{kT}{q} \ln\left[\frac{AA^{*}T^{2}}{I_0}\right] \qquad (2)$$

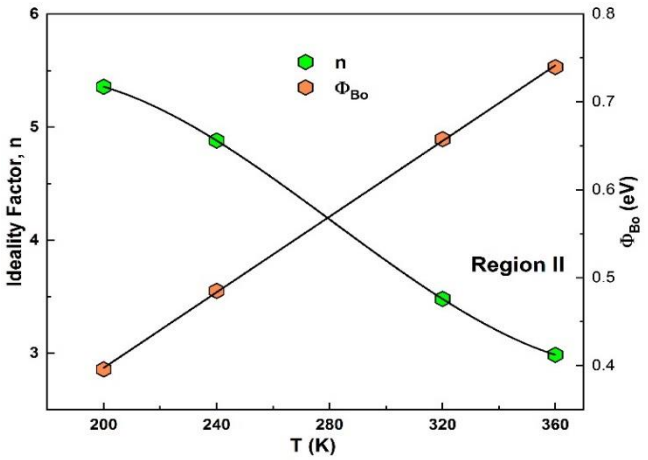
Table 1. Experimental n, I_0 and Φ_{B0} values of Au/PVA/n-GaAs for Region I, Region II and Region III for 200 K, 240 K, 320 K and 360 K.

	Region I			Region II			Region III		
T (K)	n	I_0 (A)	Φ_{B0} (eV)	n	I_0 (A)	Φ_{B0} (eV)	n	I_0 (A)	Φ_{B0} (eV)
200	8.31	1.07 E-06	0.37	5.36	2.76 E-07	0.40	6.80	1.15 E-06	0.37
240	6.50	7.44 E-07	0.46	4.88	2.45 E-07	0.48	4.06	6.88 E-08	0.51
320	5.16	1.17 E-06	0.62	3.48	2.94 E-07	0.66	3.17	1.91 E-07	0.67
360	4..42	1.51 E-06	0.70	2.98	3.75 E-07	0.74	3.04	5.15 E-07	0.73

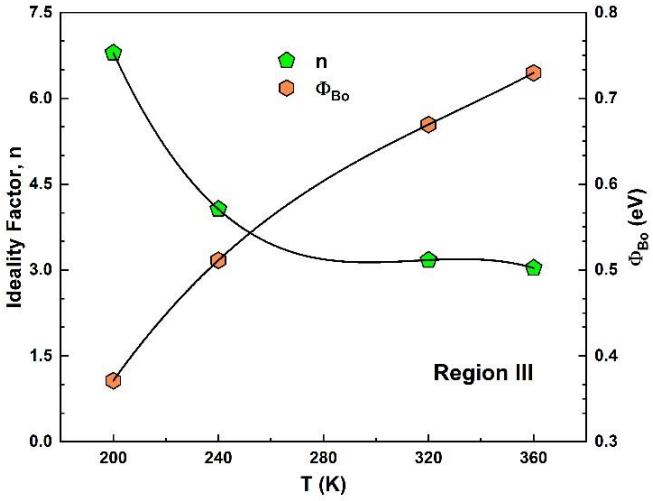
As can be seen in Table 1, when temperature increases, n values decrease but ΦBo values increase for both regions. It is clear that, this condition contrasts with negative temperature coefficient of barrier height [4,8-10]. At low temperatures, current flows through to patches of lower barrier heights and n becomes greater [4-11].



(a)



(b)



(c)

Fig. 2. Temperature dependent n and ΦB0 values of Au/ PVA/n-GaAs (a) for Region I, (b) for Region II and (c) for Region III.

Temperature dependent n and ΦBo changes are shown in Fig. 2 (a) for Region I, (b) for Region II and (c) for Region III. The deviation from classic TE theory can be seen Fig. 2, too. Nearly exponential decrease is observed in n values, as temperature increases. Expected n values for an ideal diode must be unit or intimate the unit [2,14-16]. Also, as temperature increases, ΦBo values must be decreased like Eg (Forbidden band gap) of semiconductor [14-16]. These low values of ΦBo causes the minor barriers at the metal-semiconductor interfaces [14-16]. So, charge carriers can pass from metal to the

semiconductor and CTMs are directed by these charges that flow through these patches. Thus, n values or current increases. All of these unexpected results are based on quantum mechanical tunneling mechanisms that FE (Field Emission) and TFE (Thermionic Field Emission) [8,10,17].

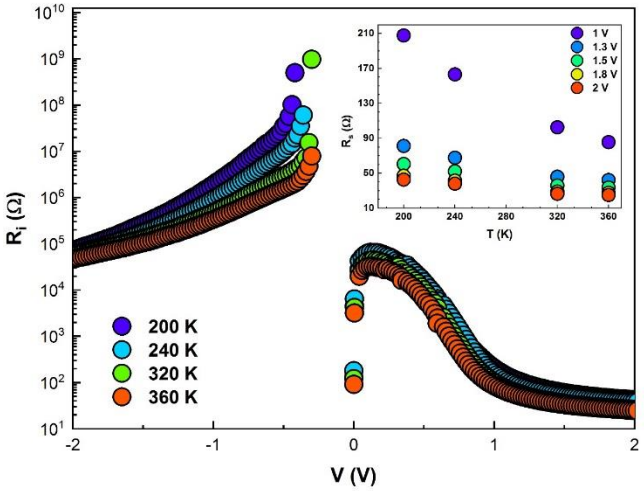


Fig. 3. R_i vs V as a function of temperature and Rs vs T plots of Au/PVA/n-GaAs.

Fig. 3 shows the temperature dependent Ri-V plots. Rs and Rsh parameters of Au/PVA/n-GaAs are determined from I-V characteristic of sample by using Ohm's Law:

$$R_i = \frac{dV_i}{dI_i} \qquad (3)$$

As seen in Fig. 3, Ri values are strongly depending on both temperature and applied voltage. As it is known, resistance value decreases with increasing temperature [18-19]. At sufficiently forward bias, the resistance of the diode becomes steady that value is the Rs. Likewise, if enough reverse bias is applied, the resistance of the diode is fixed again and that point is called Rsh (shunt resistance). Due to low leakage current, maximum Rsh value is at the lowest temperature region, 200 K. This result increases the rectifying rate of the SD at low temperature. The maximum Rs value is also at low temperature. Additionally, in the supplement plot in Fig.3 shows that when applied forward bias increase, Rs value decreases. This behavior can be attributed the recombination or generation mechanisms [19-21].

Conclusions

In conclusion, Au/PVA/n-GaAs MPS type SD was prepared by electrospinning and thermal evaporating methods. The semi-logarithmic current – voltage measurements were taken at 200K, 240 K, 320 K and 360 K to obtain a detailed information about possible CTMs. According to experimental results, it can be said that there is a deviation from thermionic emission theory because of barrier inhomogeneities at M/S interface. Especially at low temperatures, quantum mechanical tunneling mechanisms (FE and TFE) can be ascended. Also, Ri values of sample were determined that Ri values depend on both temperature and applied bias voltage.

References:

[1] F.A. Padovani, G.G. Sumner, Journal of Applied Physics 36 (1965) 3744–3747.
[2] S¸. Karatas¸, S¸. Altındal, Materials Science and Engineering: B 122 (2005) 133–139.
[3] A.T. Sharma, Shahnawaz, S. Kumar, Y.S. Katharria, D. Kanjilal, Nuclear Instruments and Methods in Physics Research Section B 263 (2007) 424.
[4] H. Tecimer, A. Türüt, H. Uslu, S¸. Altındal, ˙I. Uslu, Sens. Actuators A 199194–201 (2013)
[5] S. Alialy, H. Tecimer, H. Uslu, S. Altındal¸ J. Nanomed Nanotecnology 4,3 (2013), 167.
[6] O. Çiçek, H. Uslu Tecimer, S.O. Tan, H. Tecimer, Ş. Altindal, İ. Uslu, Composites Part B 98 (2016):260-268.
[7] S. O. Tan, Transactıons On Electron Devıces, 12 (2017), 5121-5127.
[8] E. Arslan, S¸. Altındal, S. Özcelik, E. Özbay, Journal of Applied Physics 105 (2009) 023705 (7 pages).
[9] V. Rajagopal Reddy, V. Janardhanam, C.H. Leem, C.J. Choi, Superlattices Microstruct. 67 (2014), 242–255.
[10] İ. Taşçıoğlu, S. O. Tan, F. Yakuphanoğlu, Ş. Altindal, Journal of Electronic Material, 10(2018), 6059-6066.
[11] A. Kaya, Ö. Sevgili, Ş. Altindal, M. K. Öztürk, Indian Journal of Pure aand Applied Physics, 1 (2015), 56-65.
[12] E.H. Rhoderick, R.H. Williams, Metal-Semiconductor Contacts (Clarendon, Oxford, 1988)
[13] S.M. Sze, Physics of Semiconductor Devices, 2nd edn. (Wiley, New York, 1981)
[14] R. Tung, Appl. Phys. Lett. 58, 2821–2823 (1991)
[15] J.H. Werner and H.H. Güttler, J. Appl. Phys. 69, 1522 (1991).

[16] R.F. Schmitsdorf, T.U. Kampen, W. Monch, Surf. Sci. 324, 249–256 (1995).
[17] E. Arslan, S. Altındal, S. Ural, Ömer A. Kayal, M. Öztürk and E. Özbay, Journal of Vacuum Science and Technology B: Nanotechnology and Microelectronics, 11(2018), 061209 (10pages).
[18] D. Donocal, M. Barus, M. Zdimal, Solid-State Electron, 34 (1991), 1365.
[19] H. Uslu, Ş. Altindal, İ. Polat, H. Bayrak, E. Bacaksız, Journal of Alloys and Compounds, 509 (2011), 5555-5561.
[20] V. Janardham, H.K. Lee, K.H. Shim, H.B. Hong, S.H. Lee, K.S. Ahn, C.J. Choi, J. Alloys Compd. 504 (2010) 146.
[21] S. Kh, M.M. Karimov, S.A. Ahmed, M.I. Moiz, Federov, Sol. Energy. Mater. Sol. C87 (2005) 61.

6th International Conference on Materials Science and Nanotechnology For Next Generation (MSNG2019)
October 16-18, 2019, Niğde, TURKEY (POSTERL FULL TEXT)

Investigation of Gamma Irradiation Effects on The Current-Voltage Characteristics of Au/n-Si/Ag Schottky Diodes (SDs)

Ahmet Kaymaz[1*], Şemsettin Altındal[2], Habibe Uslu Tecimer[1]

[1]Electrical and Electronic Engineering Department, Engineering Faculty, Karabuk University, TURKEY
[2]Physics Department, Science Faculty, Gazi University, TURKEY

The effects of ^{60}Co (γ-ray) irradiation on the electrical properties of Au/n-Si/Ag Schottky diodes (SDs) have been investigated by using current-voltage (I-V) measurements at room temperature. Au/n-Si/Ag SDs were exposed to dose 60 kGy irradiation to see the effects of ^{60}Co (γ-ray) on the fundamental electrical parameters of SDs such as zero bias barrier height (Φ_{B0}), ideality factor (n), series resistance (R_s) and shunt resistance (R_{sh}). These parameters have been calculated before and after irradiation by using the reverse and forward bias I-V measurements at room temperature. It is obtained that the barrier height and series resistance values increase while the ideality factor and shunt resistance values decrease after exposure the SDs to γ-ray source. On the other hand, the rectifying ratio values of SDs for before and after irradiation have been obtained as 276 and 36 respectively, at (± 3 V). In this case, experimental results confirm that γ-ray irradiation have significant effect on the electrical properties of SDs.

Keywords: Schottky diodes, I-V characteristics, radiation effects, gamma-ray effects.

Corresponding author: ahmetkaymaz@karabuk.edu.tr

1. Introduction

It is known that change in current-voltage (I-V) characteristics of semiconductor-based structures such as Schottky diodes (SDs), MOS capacitors, solar cells or other MS/MIS/MPS and MOS type structures is lower than the C-V characteristics when exposure them to the low-dose gamma-ray irradiation [1]. On the other hand, if it is used high-dose ^{60}Co-γ-ray source for investigating response of these structures, it could be seen apparently change in I-V characteristics [2]. SDs and other semiconductor-based structures form the basis of many electronic systems such as satellite, nuclear industry and medical applications. However, it is well known that space environment contains magnetic and electric fields, solar radiation, charged particles, galactic radiation, etc. [3,4] and it is also possible to encounter some similar effects in other applications. Due to these structures are fairly sensitive to electromagnetic radiation such as γ-rays [5], the radiation effect of these materials has to be understood very well. Therefore, the measurements of I-V characteristics of Au/n-Si/Ag Schottky diode has been performed before and after 60 kGy irradiation and the possible effects of the radiation is discussed in this study. In addition, the analysis of the measurements is carried out and thus, the basic diode parameters are determined by utilizing the linear region of the forward bias I-V characteristics. It has been found that effects of γ-irradiation can be listed as follows: a) it is seen significant degradation in the currents especially in reverse bias currents, b) it is occurred decrease in the ideality factor and shunt resistance, c) the zero bias barrier height and series resistance values increase and d) it is occurred significant decrease in the diode rectifying ratio value which represent the diode quality.

2. Experimental details

In order to produce SDs with a Metal-Semiconductor (MS) structure, Ag/n-Si SDs have been fabricated on P-doped (n-Si) wafer with (100) float zone, ~300 μm thickness and 0.4 Ω.cm resistivity. The first stage for fabrication of these structures is that n-Si wafer was dipped in $5H_2SO_4 + H_2O_2 + H_2O$ solution for about a minute to remove damaged surface layer and organic impurities. Thereafter, it was quickly dried with high-purity N_2 gas as soon as etching by H_2O+HCl solution and rinsing in de-ionized water with 18 MΩ resistivity. The other stage is that high purity Au (99.999%) was evaporated on the whole back side of the n-Si wafer in high vacuum thermal evaporation system at about 10^{-6} Torr and then it was thermally annealed at 500 ℃ for 3 min bin the nitrogen ambient for getting a low ohmic resistivity. In the final stage, rectifier contacts with $7.85x10^{-3}$ cm^2 area was grown on the front surface of the n-Si wafer using high purity Ag (99.999%). It is known that the formation of a natural oxide layer is inevitable, although MS structure production is intended. In this case, it could be said that the structures are actually Metal-Oxide-Semiconductor (MOS) not MS. It could be found more information in reference [6] for fabrication stage of Au/n-Si/Ag SDs. On the other hand, measurements of I-V characteristics are performed by using Keithley 2400 current-voltage source which can measure with 0.15% accuracy.

3. Results and discussion

The I-V characteristics of Au/n-Si/Ag Schottky diodes are measured in the wide range voltage (± 3 V) before and after γ-irradiation and they are given in Fig. 1. Plots of the currents are given as logarithmic in order to evaluate the reverse and forward bias currents together. The linear regions of the logarithmic currents are also given in this figure. It is clearly seen here that currents are deteriorated after γ-irradiation especially reverse bias current is affected a lot after radiation such as many of the previous studies [7-10]. Due to the values of reverse bias currents are quite small compared to the forward bias currents, effects of the radiation on these currents would be expected more because of the enhancement of trapped charge densities and restructure and reordering of them under electric field. Another reason for the increase of the reverse bias currents is attributed to the occurrence of new charge carriers and a great number of defects in close proximity provided path for charge carriers [7]. However, for obtaining more information about radiation effect, it should be detailed analyzed the other parameters such as zero bias barrier height (Φ_{B0}) and ideality factor (n). These parameters can be obtained using linear regions of the forward bias ln(I)-V characteristics.

It is well known that currents of SDs under a bias voltage can be given by Eq. (1). Here corresponds to the reverse saturation current and its formula can be written by Eq. (2) and other symbols are well known in the literature.

$$I = I_0 \exp\left(\frac{qV}{nkT} - 1\right) \quad (1)$$

$$I_0 = AA^*T^2 \exp\left(-\frac{q\phi_B}{kT}\right) \quad (2)$$

Using Eq. (1) and Eq. (2), it can be extracted formula of ideality factor and Schottky barrier height and they are given by Eq. (3) and Eq. (4) respectively for $V \geqslant 3Kt/q$.

$$n = \frac{q}{kT}\left(\frac{dV}{d(\ln I)}\right) \quad (3)$$

$$\Phi_{B0} = \frac{kT}{q}\ln\left(\frac{AA^*T^2}{I_0}\right) \quad (4)$$

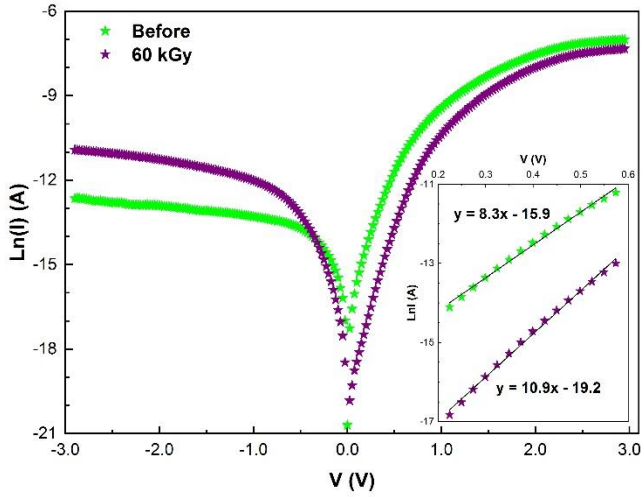


Figure 1*.The reverse and forward bias ln(I)-V characteristics of the Au/n-Si/Ag structure*

From slope of the linear region of the ln(I)-V characteristic, it can be obtained I_0, n and Φ_{B0}. On the other hand, it can be found series resistance (R_s) and shunt resistance (R_{sh}) values using ohm's laws. Additionally, resistance (R_i) values have been obtained for all bias voltage and plots of them are given in Fig. 2 while other parameters are demonstrated in Table 1.

Table 1. Basic diode parameters for Au/n-Si/Ag SD

	I_0 (A)	n	Φ_{B0}	R_s (Ω)	R_{sh} (Ω)	RR at ±3V
BEFORE	1.24×10^{-7}	4.66	0.741	3.26×10^{3}	9.00×10^{5}	276.05
60 KGY	4.59×10^{-9}	3.55	0.826	4.49×10^{3}	1.63×10^{5}	36.28

According to Table (1), I_0, n and R_{sh} values are decrease while Φ_{B0} and R_s values are increased after irradiation. After γ-irradiation, reduction of the carrier concentration in the depletion region of SDs through the emergence of recombination centers or traps caused by radiation damage, results by increase in the barrier height [11]. On the other hand, the increase/decrease of the ideality factor can be attributed in homogeneities of SD's interfaces and because of the other possible carrier mechanisms are effective or ineffective after irradiation such as diffusion theory, quantum mechanical tunneling and gaussian distribution when the ideality factor is bigger than unity. It is seen that saturation reverse current decrease significantly after irradiation. This situation can be explained because of the deep levels may act as recombination centers and frequently assume the role of the carrier recombination in inverse characteristics [11]. Additionally, due to the series resistance is increased and shunt resistance is decreased, the diode rectifying ratio value which represent the diode quality is decreased. Reduction of the diode rectifying ratio value after irradiation could be found in a lot of studies such as references [8,9,11].

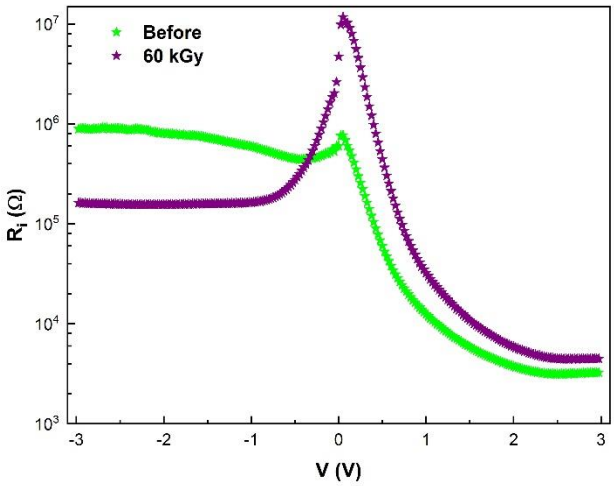


***Figure 2**. The forward and reverse bias Ri characteristics of the Au/n-Si/Ag structure*

4. Conclusion

In this study, the effects of ^{60}Co-γ-irradiation on the SDs are observed using reverse and forward bias I-V measurements at room temperature. Experimental results show effects of radiation apparently in that a) It is occurred significant degradation in the currents especially in the reverse bias currents, b) decrease in the ideality factor and shunt resistance, c) increase in the zero bias barrier height and series resistance values and d) significant decrease in the diode rectifying ratio value which represent the diode quality. This study shows that γ-ray induced defects play important role on the electrical properties of the structures, which have possible use in satellite, biomedical or industrial applications.

References:

[1] S. Kaya, E. Yilmaz, A. Kahraman, and H. Karacali, "Frequency dependent gamma-ray irradiation response of Sm_2O_3 MOS capacitors," Nucl. Instruments Methods Phys. Res. Sect. B Beam Interact. with Mater. Atoms, vol. 358, pp. 188–193, 2015.

[2] M. V. Kumar et al., "Influence of High Dose Gamma Irradiation on Electrical Characteristics of Si Photo Detectors," ECS J. Solid State Sci. Technol., vol. 6, no. 10, pp. 132–135, 2017.

[3] D. Binder, E. C. Smith, and A. B. Holman, "Satellite Anomalies From Galactic Cosmic Rays," IEEE Trans. Nucl. Sci., vol. 22, no. 6, pp. 2675–2680, 1975.

[4] P. Laha, I. Banerjee, P. K. Barhai, A. K. Das, V. N. Bhoraskar, and S. K. Mahapatra, "Effects of 6 MeV electron irradiation on the electrical properties and device parameters of $Al/Al_2O_3/TiO_2$/n-Si MOS capacitors," Nucl. Instruments Methods Phys. Res. Sect. B Beam Interact. with Mater. Atoms, vol. 283, pp. 9–14, 2012.

[5] K. Ali, S. A. Khan, and M. Z. MatJafri, "^{60}Co γ-irradiation effects on electrical characteristics of monocrystalline silicon solar cell," Int. J. Electrochem. Sci., vol. 8, no. 6, pp. 7831–7841, 2013.

[6] Ç. Bilkan and Ş. Altındal, "Investigation of the C-V characteristics that provides linearity in a large reverse bias region and the effects of series resistance, surface states and interlayer in Au/n-Si/Ag diodes," J. Alloys Compd., vol. 708, pp. 464–469, 2017.

[7] S. S. Barala, J. Singh, S. Ranwa, and M. Kumar, "Radiation Induced Response of $Ba_{0.5}Sr_{0.5}TiO_3$ Based Tunable Capacitors under Gamma Irradiation," IEEE Trans. Nucl. Sci., vol. 62, no. 4, pp. 1873–1878, 2015.

[8] A. Teffahi et al., "Effect of ^{60}Co γ-ray irradiation on electrical properties of $Ti/Au/GaAs_{1-x}N_x$ Schottky diodes," Curr. Appl. Phys., vol. 16, no. 8, pp. 850–858, 2016.

[9] G. A. Umana-Membreno, J. M. Dell, G. Parish, B. D. Nener, L. Faraone, and U. K. Mishra, "^{60}Co Gamma Irradiation Effects on n-GaN Schottky Diodes," IEEE Trans. Electron Devices, vol. 50, no. 12, pp. 2326–2335, 2003.

[10] A. Tataroğlu and Ş. Altindal, "Analysis of interface states and series resistance at MIS structure irradiated under ^{60}Co γ-rays," Nucl. Instruments Methods Phys. Res. Sect. A Accel. Spectrometers, Detect. Assoc. Equip., vol. 580, no. 3, pp. 1588–1593, 2007.

[11] Ö. Güllü, M. Çankaya, M. Biber, and A. Türüt, "Gamma irradiation-induced changes at the electrical characteristics of organic-based Schottky structures," J. Phys. D. Appl. Phys., vol. 41, no. 13, 2008.

6th International Conference on Materials Science and Nanotechnology For Next Generation (MSNG2019)
October 16-18, 2019, Niğde, TURKEY (POSTERL FULL TEXT)

The Influence of Green Collector on Floatability of Coal

Hasan HACIFAZLIOĞLU[1], Dilek ŞENOL ARSLAN [2]*

[1]*Istanbul University-Cerrahpasa, Mining Engineering Department, Avcilar, Istanbul, Turkey.*
[2]**Abdullah Gul University, Engineering Faculty, Materials Science and Nanotechnology Engineering Department, Kayseri, Turkey.*

In this study, the potential of sunflower oil as green collector was examined as an alternative to the kerosene, which is an oil product as a collector. Coal flotation experiments and contact angle measurements were carried out with kerosene and sunflower oil. Plant eucalyptus oil was used as frother in all the flotation experiments. After that, the results obtained from flotation experiments were compared in terms of ash, combustible recovery and efficiency index while contact angle values compared to each other. The results show that sunflower oil is a vegetable oil that can be used as an alternative to the kerosene.

Keywords: Bituminous coal; sunflower oil; kerosene; flotation; contact angle.

Corresponding author: dilek.senol@agu.edu.t

1. Introduction

Collectors which are organic compounds which make the mineral surface hydrophobic, are generally classified as anionic, cationic and non-ionic [1]. The collectors on the mineral surface reduce the stability of the hydrate layer, thus the mineral to form an interface with the air bubble. Compounds which are used as water-insoluble emulsions and which consist of hydrocarbon oils that make the surface hydrophobic by covering the mineral surface non-ionizing collectors. The most important of these are petroleum products such as kerosene, diesel and natural vegetable oils.

Petroleum products (usually kerosene) have been widely used in flotation process of fine coals (<0.5 mm) as collectors and consistently provided robust performance due to their unique capability to selectively adsorb on the surface of coal and render them hydrophobic. The dosage of collector has significant effect on flotation performance [2]. Since the petroleum product is non-polar oil, its disposal in an environmentally acceptable manner is challenging task. These products are also nonrenewable and highly flammable. Hence, a replacement for these products was initiated. Vegetable oils with negligible sulfur, nitrogen and heavy metal content are renewable, available and a non-polluting raw material. Because of these important characteristics, they are suitable candidates for purposes other than food. In this sense, vegetable oils are becoming more widely investigated for alternative uses such as biodiesel production and raw material for the chemical and other industries [3]. It was hypothesized that vegetable oils consisting of long-chain fatty acids which could act as both frother and collector, and having ester groups linked with the ability to behave as a frother, would improve the flotation recovery of the coal particles [4].

Mainly sunflower oil, soybean, cotton, olive, sesame, corn and many other vegetable oil types can be produced in Turkey. Turkey produces nearly 1 million tons of vegetable oil annually and 50% of this oil is sunflower oil [5] In this study, coal flotation with sunflower oil was performed and the results were compared with kerosene which is known as the best collector in the literature.

2. Experimental details

2.1. Materials

Coal sample used in the flotation experiments was collected from a thickener underflow stream of a coal washing plant treating the Zonguldak bituminous coal in Turkey. The results of the chemical analysis of the test sample are given in Table 1. In addition, the distribution of ash and combustibles according to the size fractions is given in Table 2. It indicates that about 50% of the coal

has a particle size less than -38 µm and contains about 33.75% ash and 0.70% total sulfur. Thus, the sample may be characterized as a relatively high ash and low sulfur coal.

Table 1. Proximate analysis of the sample coal (on dry basis)

Analysis	Values
Ash content (%)	33.75
Volatile matter (%)	29.20
Fixed carbon (%)	37.50
Total sulfur (%)	0.70
Upper calorific value (kcal/kg)	5220

Table 2. The distribution of weight, ash and combustible recovery in the size fractions.

Size Fractions (µm)	Weight (%)	Ash (%)	Combustible Recovery (%)
500x300	3.51	8.20	4.86
300x212	10.12	7.10	14.20
212x150	14.40	13.30	18.84
150x125	4.62	9.60	6.30
125x63	9.58	22.30	11.24
63x38	4.98	44.60	4.13
-38	52.84	49.30	40.44
Total	100.00	33.75	-

For contact angle measurements, the coal sample was received in the form of lump-sized from the entrance of washery plant in Zonguldak (Turkey). Coal sample was cleaved 15×13×4 mm and coarse polishing with silicon carbide abrasive paper makes the coal flat surface.
Kerosene (from Tupras Company in Izmir from Turkey) and sunflower oil (from Kristal company in Izmir from Turkey) as collector and eucalyptus oil as frother (from Ciftcizade company in Antalya from Turkey) were used as received

2.2. Methods
2.2.1. Contact angle measurements

The surface wettability can be determined by measuring the some parameters such as the electrical potential and contact angle [6]. Contact angle is one of the common techniques to measure the wettability of material. Wetting refers to the study of how a liquid deposited on a solid (or liquid) substrate spreads out or the ability of liquids to form boundary surfaces with solid states. The wetting, as mentioned before is determined by measuring the contact angle which the liquid forms in contact with the solids or liquids.
In this study, the contact angle of kerosene and sunflower oil were carried out with Sessile Drop method by using Attension theta contact angle goniometer on a flat coal surface (Fig.1). The advancing contact angle measurements were carried out 10-20 seconds after the increase in the size of the drop. These values were determined through using the approach provided by Fowkes [7]. All the measurements were carried out at the room temperature (20-22°C).

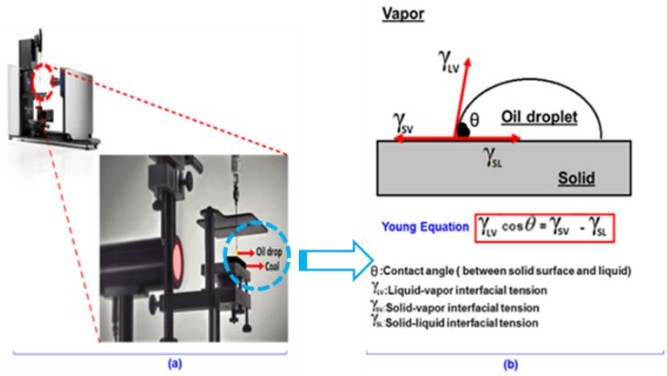


Figure 1. *(a) Shematic of contact angle goniometer. (b) schematic of wetting statics in the Young equation for solid-liquid-vapor system.*

The contact angle is defined as the angle formed by the intersection between of the solid-liquid interface and the liquid-vapor interface which is described by Young equation [8]. As illustrated in Fig.1(c) contact angle of oil droplet on a coal surface in an aqueous medium is defined as the equilibrium of the oil droplet under the action of three interfacial tensions; liquid-vapor, solid-vapor and solid-liquid. This relation is known Young's equation is shown in Eq.(1)

$$\gamma_{LV}\cos\theta = \gamma_{SV} - \gamma_{SL} \quad (1)$$

where γ_{LV}, γ_{SV}, and γ_{SL} represent the liquid-vapor, solid-vapor, and solid-liquid interfacial tensions, respectively, and θ is the three phase contact angle. If θ is higher than 90°, the solid is hydrophobic or oil-wet, if θ is lower than 90°, the solid surface is hydrophilic or water wet.

2.2.2. Batch Flotation and Release Tests with Sunflower and Kerosene Collectors

Flotation tests were performed in a Denver machine with a cell capacity of 1.5 liters**.** The impeller speed was fixed at 1100 rpm. A pulp density of 10% was used in all

experiments. For each flotation tests, the sample was mixed with tap water in the cell for 10 min to ensure the wetting of its surface. Sunflower oil (*2000 g/t*) was used as collector, and eucalyptus oil (*100 g/t*) was used as frother**.** Viscosity, density and oil-water interfacial tension of the sunflower oil were 72 mPa/s, 0.90 g/cm^3 and 22.00 mN/m, respectively. The measurement of these physical properties of the oil was carried out at 20 ºC. Similar conditions were used for determination of flotation performance of the kerosene collector. In the experiments 2000 g/t kerosene and 100 g/t eucalyptus oil as frother was used. The mechanism of particle-oil adsorption in coal flotation with kerosene and sunflower oil were schematized in Fig.2. The flotation process was achieved by mixing chemicals known as collectors (kerosene, sunflower oil) and frother (eucalyptus oil) with in the coal slurry. The collectors adsorb onto the coal surfaces, making these coal particles hydrophobic. Air was passed through the slurry in a tank known as a flotation cell. The new hydrophobic coal particles (coated with the collectors) attach to the bubbles, rising with them to the surface of the flotation cell, where they form a froth. The froth flows over the top edge of the flotation cell and moved the concentrate launder Fig 2 (a, b). Fig.2 (b) However, the selectivity of the collection mechanism was not perfect for sunflower oil flotation process. Some gangue minerals were also carried into the froth, largely by bad selectivity of sunflower oil and entrainment with the water rising with the bubbles. This was particularly the case for particles less than 10 µm in size. Some of the gangue particles follow the water between the bubbles as it drains back to the underlying slurry.

Kinetic flotation tests (for 30, 60 and 240 sec. froth skimming) were conducted to determine collecting potential of sunflower oil and kerosene, separately. The obtained concentrates were filtered, water with acetone washed, dryed in oven, weighted to calculate the yield, and analyzed for ash content. Before starting the kinetic flotation tests, "release test" procedure developed by [9] was applied in order to determine final washability limit of the coal sample. Release test was performed in order to determine the best washability result at varying stirring speeds in a Denver cell and at high reagent dosages *(*10 kg/t sunflower oil, 0.4 kg/t eucalyptus oil*).*

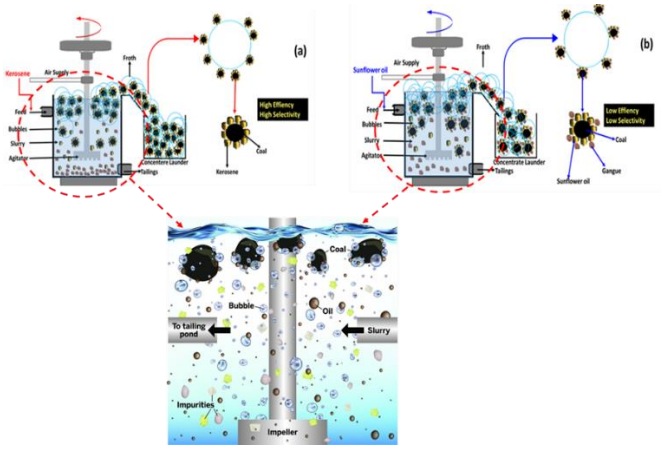


Figure 2. *The mechanism of particle-oil adsorption in coal flotation with kerosene (a) and sunflower oil (b). Detailed view of flotation cell [10] (c).*

The performance of any separation system can be evaluated based on the quality and quantity of the products produced. Many researchers evaluated the flotation performance using yield, recovery, assay, efficiency index, selectivity index, flotation kinetic parameters etc. In this study, the curve of combustible recovery versus concentrate ash was used to compare flotation performance [11].

3. Results and discussion

Release curves for sunflower oil and kerosene collectors are shown in Figure 3. According to Fig. 3 the collecting feature of the kerosene is better than the sunflower oil. Clean coal with a 8.73% ash with kerosene collector were obtained with a combustible recovery value of 62.54%, while sunflower oil with 10.35% ash clean coal with a combustion recovery value of 55.48%. For a salable clean coal ash value (eg. 10% ash), the combustible recovery value (~ 70%) of the kerosene collector is higher than the combustible recovery value (~ 53%) of the sunflower oil. On the other hand, the results of kinetic flotation studies for sunflower oil and kerosene are presented in Figure 4.

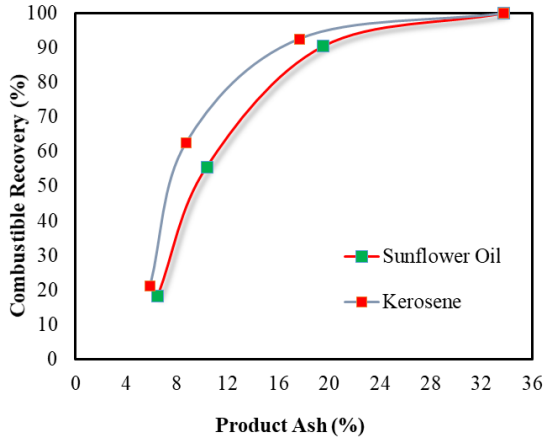


Figure 3. *Release test results with sunflower oil and kerosene.*

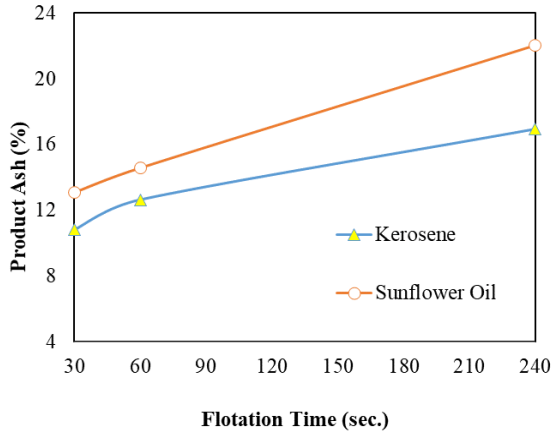


Figure 4*. Release test results with sunflower oil and kerosene.*

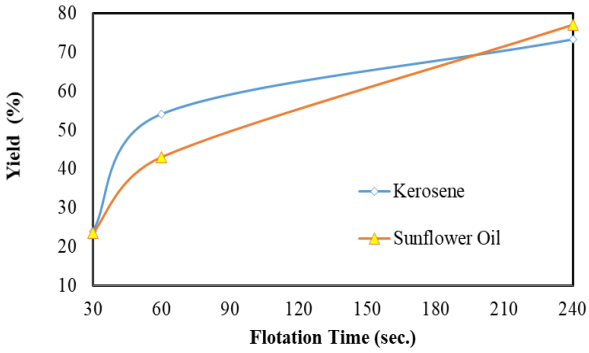


Figure 5. *Release test results with sunflower oil and kerosene.*

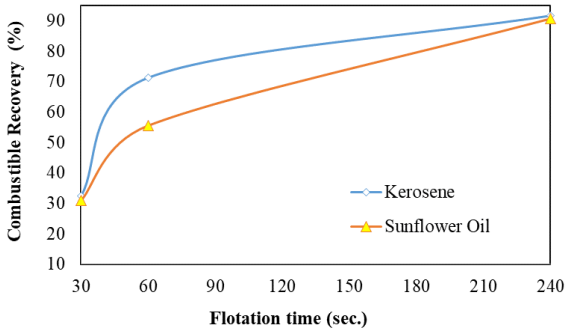


Figure 6. *(a) Product ash, (b) yield, and (c) combustible recovery values as a function of flotation time with kerosene and sunflower oil as collector.*

From Fig.6 results, it can be seen that, the combustible recovery values of both oil types are approximately the same during low (30 sec.) and high (240 sec.) flotation time. For example, the combustible recovery value of sunflower oil is 30.96%, while the kerosene is 32.35% at 30 seconds of flotation. The combustible recovery of sunflower oil is 90.72%, while the kerosene is 91.85% at 240 seconds of flotation. When the results are examined in terms of selectivity, it was seen that the kerosene was more selective. For example, the product ash obtained at the flotation time of 240 seconds was 16.95% with kerosene and 21.93% with sunflower oil. The clean coal ash obtained with sunflower oil is 4.98% higher than that of the kerosene.

4. Conclusion

The ash content of bituminous coal used in the metallurgical industry should be maximum 10%. Otherwise, the desired coke quality cannot be obtained. As a result of this study, it was observed that sunflower oil could reduce the fine bituminous coal ash value from 33.75% to 6.50%. Although sunflower oil can produce clean coal with very low ash content, it has given poor results in terms of combustible recovery than that of kerosene. Its probable cause is that the surface coating ability of the sunflower oil is lower than kerosene. For obtain a clean coal with 10% ash, the combustible recovery value of sunflower oil is ~53%, while kerosene is ~70%. Kerosene has also given better results in terms of selectivity. The product ash obtained at the longest flotation time (240 sec.) is 16.95% with kerosene while 22.05% with sunflower oil. According to all results, the overall performance of sunflower oil is about 20-30% lower than kerosene. However, it should not be forgotten that sunflower oil is a renewable green collector while kerosene is non-renewable resource.

References:

[1] S.M. Bulatovic, Handbook of flotation reagents: chemistry, theory and practice: volume 1: flotation of sulfide ores, Elsevier2007.
[2] S. Dey, S. Pani, Effective processing of low-volatile medium coking coal fines of Indian origin using different process variables of flotation, International Journal of Coal Preparation and Utilization 32(6) (2012) 253-264.
[3] A.F. Valdés, A.B. Garcia, On the utilization of waste vegetable oils (WVO) as agglomerants to recover coal from coal fines cleaning wastes (CFCW), Fuel 85(5) (2006) 607-614.
[4] R.R. Klimpel, R.D. Hansen, Frothers, In Reagents in Mineral Technology, (Eds.), P. Somasundaran and B.M. Moudgil, Marcel Dekker (1987) 387–409 pp. New York.
[5] Anonym, http://www.bysd.org.tr/. 2017).
[6] G. Zhou, C. Xu, W. Cheng, Q. Zhang, W. Nie, Effects of oxygen element and oxygen-containing functional groups on surface wettability of coal dust with various metamorphic degrees based on XPS experiment, Journal of analytical methods in chemistry 2015 (2015).
[7] F.M.Fowkes, Attractive forces at interfaces Industrial and Engineering Chemistry 56 (1964) 40-52.
[8] T. Young, An essay on the cohesion of fluids, Philosophical Transactions of the Royal Society of London 95 (1805) 65-87.
[9] C. Dell, An improved release analysis procedure for determining coal washability, Journal of the Institute of Fuel 37 (1964) 149-150.
[10] T. Oi, M. Nomura, M. Musashi, T. Ossaka, M. Okamoto, H. Kakihana, Boron isotopic compositions of some boron minerals, Geochimica et Cosmochimica Acta 53(12) (1989) 3189-3195.
[11] M. Vanangamudi, K. Pillai, T. Rao, Effect of some operating variables on the efficiency index of a coal flotation operation, International Journal of Mineral Processing 8(1) (1981) 1-7.